

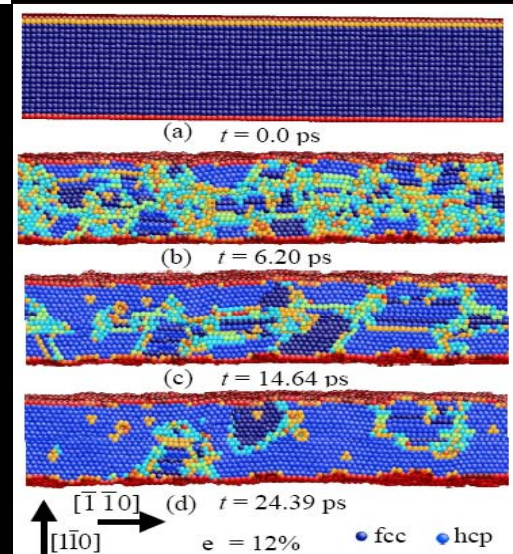
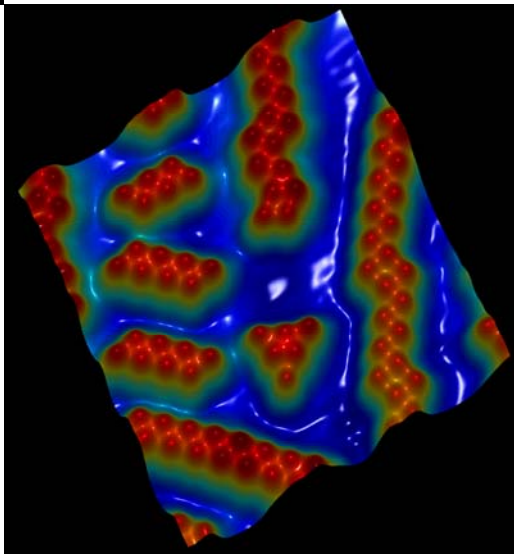
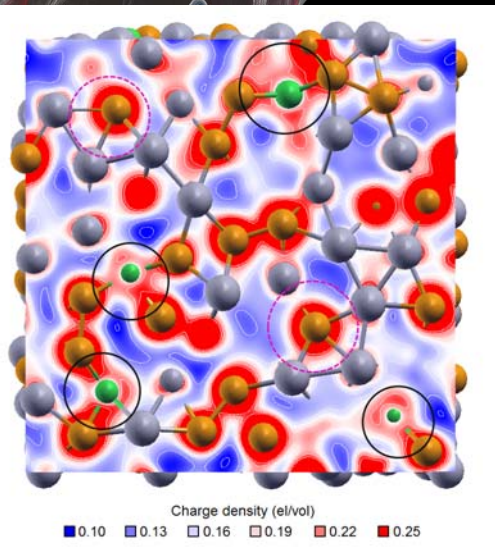
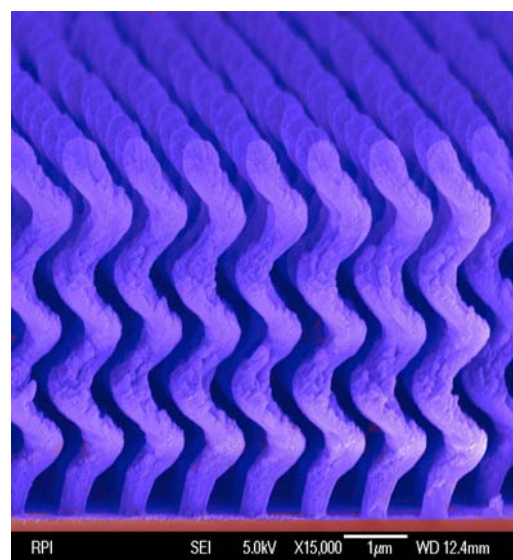
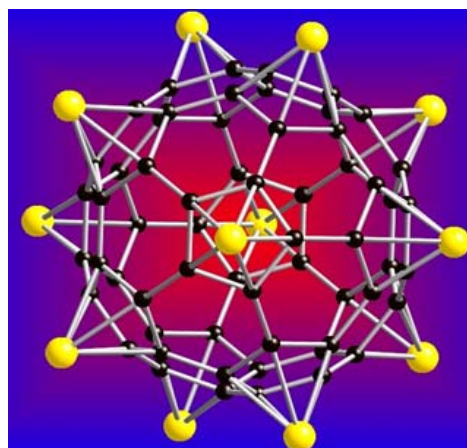
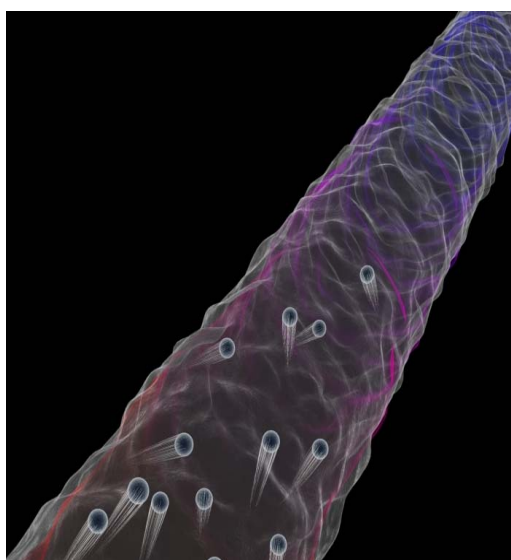
DOE - BES Contractors Meeting

# Physical Behavior of Materials

Airlie Conference Center, Warrenton, VA

March 16 - 19, 2008

*PROGRAM and ABSTRACTS*



**U.S. Department of Energy**  
**Office of Basic Energy Sciences**  
*Division of Materials Sciences and Engineering*



# Cover

**Top Left** - A very low thermal conductivity observed in silicon nanowires makes it possible to achieve a breakthrough ZT of 0.6 at room temperature in rough Si nanowires of ~50 nm diameter. (A. Majumdar, P. Yang, LBNL)

**Top Middle** - The lithium coated fullerene (Li<sub>12</sub>C<sub>60</sub>), with Li atoms capping the pentagonal faces of the fullerene is identified as a promising material for hydrogen storage. This material is not only stable, but can store up to 120 hydrogen atoms in molecular form. (P. Jena, VCU)

**Top Right** - A side view image of a completed 3D spiral photonic crystal structure with 3 unit cells, respectively. In similarly grown vertically-aligned carbon nanotube arrays, a total reflectance of 0.045% and a corresponding absorptance of 99.955% (a new world record) has been achieved. This may enable a much improved selective thermal emission and efficiency of thermophotovoltaic energy conversion. (S-Y. Lin, RPI)

**Bottom Left** - Effect of Al (green) on electronic structure of the Zr<sub>47</sub>Cu<sub>46</sub>Al<sub>7</sub> metallic glass. (E. Ma, JHU)

**Bottom Middle** - A 120 Angstrom x 120 Angstrom STM image of “photoswitching” azobenzene molecules that convert between two different mechanical configurations (cis and trans isomers) when irradiated with light on the surface of Au(111). (M. F. Crommie, LBNL)

**Bottom Right** - MD simulations of the cross sectional view of a strained (12%) Cu thin film showing the evolution of the film structure as it undergoes structural transition from an initial fcc lattice (dark blue) in (a) to the hcp phase (light blue) (b-d). Hcp phase nucleates at the film’s surface in (b). Maroon atoms are surface atoms and other colored atoms are inside dislocation cores. (D. Maroudas, Univ. MA)

**This document was produced under contract number DE-AC05-06OR23100 between the U.S. Department of Energy and Oak Ridge Associated Universities.**

## Foreword

This volume summarizes the scientific content of the 2008 Research Program Meeting; “Physical Behavior of Materials,” sponsored by the Division of Materials Sciences and Engineering (DMS&E) of the Office of Department of Energy, Basic Energy Sciences (BES). The primary purpose of these BES Program Meetings is to provide an environment for the exchange of new information and ideas among grantees and contractors, and to foster synergistic activities among researchers. For the grantees, it facilitates an overview of the program useful to define a future scope for the program and identify promising new research directions. These meetings are designed to stimulate cross cutting and inspiring of new ideas, as it brings together leading experts in diverse fields of interest.

This inaugural meeting was held March 16-19, 2008, at the Airlie Conference Center, in Warrenton, Virginia. The meeting was chaired by Gerbrand Ceder (MIT) and Harry A. Atwater, Jr. (Caltech), and attended by over 80 scientists, with 26 oral and 46 poster presentations in two different poster sessions. We were very pleased to have Prof. Mildred S. Dresselhaus of MIT as our keynote speaker. She inspired us with her talk entitled; *“For our energy future: materials issues, breakthroughs and challenges”*. The Physical Behavior of Materials program covers a very broad range of research activities, as suggested by its name. We organized this year’s presentations into seven different sessions using their subject similarities. These sessions were: (1) Nano-Enabled Behavior, (2) Novel Electronic Materials, (3) Interfaces / Surfaces, (4) Hydrogen / Fuel Cells, (5) Magnetism / Spintronics, (6) Thermoelectrics / Structural Properties, and (7) Photovoltaics / Photon related.

We gratefully acknowledge the contributions of all the participants for their investment of time and for their willingness to share their ideas with the meeting participants. We also want to gratefully acknowledge the excellent support of Sophia Kitts and Deborah Grubb from the Oak Ridge Institute of Science and Education, and Christie Ashton of our Division, and the staff of the Airlie Conference Center.

Refik Kortan  
Program Manager,  
Division of Materials Sciences and Engineering  
Office of Basic Energy Sciences  
Department of Energy

March 2008



*Basic Energy Sciences*

*Division of Materials Sciences and Engineering*

## "PHYSICAL BEHAVIOR OF MATERIALS"

### Contractors Meeting

March 16-19 2008, Airlie Center, VA

Meeting Chairs :

**Gerbrand Ceder** (MIT) and **Harry A. Atwater, Jr.** (Caltech)

#### Sunday, March 16, 2008

3:00 – 6:00 pm	Registration
5:00 – 6:00 pm	Reception (No Host)
6:00 – 7:00 pm	***** Dinner *****
7:30 – 8:00 pm	<i>Welcome</i> <i>Division and Program Updates</i> Harriet Kung Director, Division of Materials Science and Engineering Refik Kortan Program Manager, Physical Behavior of Materials

8:00 – 8:45 pm Mildred S. Dresselhaus, *MIT* (Invited Talk)  
“For Our Energy Future: Materials Issues, Breakthroughs and Challenges”

## Monday, March 17, 2008

7:00 – 8:00 am Breakfast

### **Session I**

#### **Nano-Enabled Behavior**

Chair: Zhifeng Ren, Boston College

8:15 – 8:45 am Peidong Yang, *LBNL*

8:45 – 9:15 am Zhong Lin Wang, Georgia Tech

9:15 – 9:45 am Michael Crommie, *LBNL*

9:45 – 10:00 am \*\*\*\*\* Break \*\*\*\*\*

### **Session II**

#### **Novel Electronic Materials**

Chair: Arto V. Nurmikko, Brown University

10:00 – 10:30 am Eugene E. Haller, *LBNL*

10:30 – 11:00 am Angelo Mascarenhas, *NREL*

11:00 – 11:30 am Antoine Kahn, Princeton

11:30 – 12:00 am Gerbrand Ceder, *MIT*

12:00 – 1:30 pm \*\*\*\*\* Lunch \*\*\*\*\*

1:30 – 3:00 pm **Time for Interactions & Discussions**

3:00 – 5:30 pm **Poster Session I**

5:30 – 6:30 pm \*\*\*\*\* Dinner \*\*\*\*\*

**Session III** **Interfaces / Surfaces**  
Chair: Feng Liu

6:30 – 7:00 pm Darryl Smith, LANL

7:00 – 7:30 pm Amanda Petford-Long, ANL

7:30 – 8:00 pm Dimitrios Maroudas, Univ Mass

8:00 – 8:30 pm Gary L. Kellogg, SNL

8:30 – 10:00 pm **Continuation of Poster Session I**

**Tuesday, March 18, 2008**

7:00 – 8:00 am Breakfast

**Session IV** **Hydrogen / Fuel Cells**  
Chair: Anil Virkar

8:15 – 8:45 am Puru Jena, Virginia Commonwealth Univ.

8:45 – 9:15 am Lutgard C. DeJonghe, LBNL

9:15 – 9:45 am Ragaiy Zidan, WESTINGHOUSE SAVANNAH RIVER CO

9:45 – 10:00 am \*\*\*\*\* Break \*\*\*\*\*

**Session V**                      **Magnetism / Spintronics**  
Chair: Kannan M. Krishnan, Washington Univ

10:00 – 10:30 am    Karl A. Gschneidner, Ames

10:30 – 11:00 am    Yuri Suzuki, LBNL

11:00 – 11:30 am    Frank Tsui, North North Carolina Univ.

11:30 – 12:00 am    Jing Shi, UC Riverside

12:00 – 1:30 pm    \*\*\*\*\* Lunch \*\*\*\*\*

1:30 – 3:00 pm        **Time for Interactions & Discussions**

3:00 – 5:30 pm        **Poster Session II**

5:30 – 6:30 pm        \*\*\*\*\* Dinner \*\*\*\*\*

**Session VI**                      **Thermoelectric / Structural Properties**  
Chair: Takeshi Egami, ORNL

6:30 – 7:00 pm        Gang Chen, MIT

7:00 – 7:30 pm        Armen Khachaturyan, Rutgers

7:30 – 8:00 pm        Naushad Ali/Shane Stadler, So Illinois Univ

8:00 -- 8:30 pm      Evan Ma, Johns Hopkins Univ

8:30 – 10:00 pm      ***Continuation of Poster Session II***

**Wednesday, March 19, 2008**

7:00 – 8:00 am      Breakfast

***Session VII***

**Photovoltaics / Photon Related**

Chair: David Waldeck, Univ of Pittsburgh

8:15 – 9:00 am      Paul Alivisatos, LBNL (Invited Talk)

9:00 -- 9:30 am      Harry Atwater, Caltech

9:30 – 10:00 am      Shawn-Yu Lin, RPI

10:00 – 10:30 am      Shengbai Zhang, NREL, RPI

10:30-- 11:15 am      Closing Remarks

11:15 am      \*\*\*\*\* Lunch and Adjourn \*\*\*\*\*  
(Optional Box Lunches Available)

## Table of Contents

Nanomechanics at Hard-Soft Interfaces .....	1
<b>Arun Majumdar, Peidong Yang, Renkun Chen, and Allon Hochbaum,</b>	
Characterization of Functional Nanomachines .....	2
<b>Michael Crommie, C. Bustamante, M. L. Cohen, J.M.J. Frechet, S. G. Louie, D. Trauner, A. Zettl</b>	
Structure-Optical-Thermal Relationships of Carbon Nanotubes .....	6
<b>Stephen B. Cronin and Li Shi</b>	
Imaging Carrier Generation, Transport, and Collection in Nanostructured Materials .....	10
<b>Lincoln J. Lauhon</b>	
Manipulation of Carbon Nanotubes and Field Emission of Semiconducting Nanowires .....	14
<b>Zhifeng Ren</b>	
Structure-Optical-Thermal Relationships of Carbon Nanotubes .....	20
<b>Li Shi and S. B. Cronin</b>	
Nanogenerators for Self-Powered Nanotechnology .....	24
<b>Zhong Lin Wang</b>	
Lattice Dynamical Properties of Ferroelectric Thin Films at the Nanoscale .	27
<b>Xiaoxing Xi</b>	
Nanowire for Photonics and Energy Conversion .....	31
<b>Peidong Wang</b>	
Atomic Processes and Defects in Wide-Bandgap Semiconductors .....	33
<b>Andrew M. Armstrong, Robert M. Fleming, Sam M. Myers, Alan F. Wright</b>	
Doped Semiconductor Nanomaterials for Solid State Lighting Applications .....	37
<b>Frank Bridges, Sue Carter, and Jin Z. Zhang</b>	
First Principles Prediction of Structure and Thermodynamics of Complex Oxides.....	41
<b>Gerbrand Ceder</b>	
Theoretical and Experimental Studies of Ion Beam Synthesized Nanocrystals .....	44
<b>Daryl Chrzan, Joel W. Ager III, and Eugene E. Haller</b>	
The Electronic Materials Program at LBNL.....	48
<b>E. E. Haller, J. W. Ager III, D. C. Chrzan, O. D. Dubón, Z. Liliental-Weber, W. Walukiewicz</b>	
Interfaces of Polymer Electronic Devices.....	52

Defect Chemistry Study of Nitrogen Doped ZnO Thin Films.....	56
<b>Lei L. Kerr, Andre Sommer, David C. Look, Zhaoqiang Fang, Xiaonan Li, and Timothy J. Coutts</b>	
Luminescence, Structure, and Growth of Wide-Bandgap InGaN Semiconductors .....	60
<b>S. R. Lee, D. D. Koleske, M. H. Crawford, G. Thaler, D. M. Follstaedt, and N. A. Missert</b>	
Superconducting Materials .....	64
<b>Qiang Li, A. Moodenbaugh, and W. Si</b>	
Novel Ordered Semiconductor Alloys .....	68
<b>A. Mascarenhas, W. E. McMahan, and S.-H. Wei</b>	
Magnetic and Optical Properties of Ferromagnetic ZnO Nanoparticles .....	72
<b>Matthew D. McCluskey, Leah Bergman, and You Qiang</b>	
Hybrid Inorganic Nitride/Organic Semiconductor Heterostructures.....	76
<b>Arto V. Nurmikko and Jung Han</b>	
Addressing Fundamental Questions for Graphene Films Synthesized On Silicon-Carbide.....	80
<b>Taisuke Ohta, Eli Rotenberg, Karsten Horn, Thomas Seyller, and Andreas K. Schmid</b>	
Hetero-Junctions of Boron Nitride and Carbon Nanotubes: Synthesis and Characterization .....	84
<b>Yoke K. Yap</b>	
Proximity Effects in Conducting Oxide Heterostructures.....	89
<b>J. A. Eastman, D. D. Fong, P. H. Fuoss, P. Zapol, A. Bhattacharya and G. B. Stephenson</b>	
Adhesion and Wetting.....	93
<b>J. E. Houston</b>	
Atomic Scale Surface Phenomena .....	97
<b>Gary L. Kellogg</b>	
Towards Quantitative Understanding of Strain Induced Nano-Scale Self-Assembly from Atomic-Scale Surface Energetics and Kinetics .....	101
<b>Feng Liu</b>	
Surface Engineering by Simultaneous Action of Multiple External Fields ....	105
<b>Dimitrios Maroudas and M. Rauf Gungor</b>	
Interfaces in Electronics and Structural Materials .....	109
<b>Y. Mishin</b>	
Interfacial Materials Program .....	113
<b>A. K. Petford-Long, O. Auciello, S. Hong and S. Nakhamanson</b>	

Electronic Processes in Solid State Organic Electronic Materials.....	117
<b>Darryl L. Smith</b>	
Atomic Scale Surface Phenomena: Localized Corrosion.....	121
<b>K. R. Zavadil, N. A. Missert, P. J. Feibelman, P. G. Kotula and N. Vasiljevic</b>	
The State of Water in Proton Conducting Membranes.....	125
<b>Harry R. Allcock, Digby D. MacDonald, Alan J. Benesi and David Lee</b>	
High Performance Nano-Crystalline Oxide Fuel Cell Materials: Defects, Structures, Interfaces, Transport, and Electrochemistry .....	129
<b>S. A. Barnett, D. Ellis, L. D. Marks, T. O. Mason, K. Poeppelmeier and P. W. Voorhees</b>	
NMR Characterization of Complex Metal Hydrides.....	133
<b>Robert C. Bowman, Jr., Son-Jong Hwang and Chul Kim</b>	
An Ab-Initio Study of the Low-Temperature Phases of Lithium Imide.....	137
<b>Gerbrand Ceder</b>	
NMR of Hydrogen Motion in Ionic Hydrides .....	138
<b>Mark S. Conradi</b>	
Nanocomposite Proton Conductors .....	142
<b>Lutgard C. DeJonghe, Jeffrey A. Reimer and Philip N. Ross</b>	
A Surface Stress Paradigm for Studying Catalyst and Storage Materials Relevant to the Hydrogen Economy .....	146
<b>Cody Friesen</b>	
Issues and Challenges in Hydrogen Storage.....	150
<b>P. Jena</b>	
Complex Hydrides – A New Frontier for Future Energy Applications Toward Reversibility through Mechanochemistry and Nanostructuring .....	155
<b>V. K. Pecharsky, M. Pruski, L. S. Chumbley, V. S.-Y. Lin and P. Jena</b>	
Thermodynamic and Kinetic Studies on High Temperature Proton Conductors Using Thin Films and Porous Bodies.....	159
<b>Anil V. Virkar, Hyung-Tae Lim, Ravikanth Abbaraju and James Wright</b>	
Elucidation of Hydrogen Interaction Mechanisms with Metal-Doped Carbon Nanostructures.....	163
<b>Ragaiy Zidan, Polly Berseth and Ashley Stowe</b>	
Extraordinary Responsive Magnetic Rare Earth Materials: Bonding, Crystallography and Magnetism in Complex Intermetallic Compounds .....	167
<b>K. A. Gschneidner, Jr. V. K. Pecharsky, L. S. Chumbley, T. A. Lograsso, G. J. Miller, A. I. Goldman, B. N. Harmon and R. J. McQueeney</b>	
Exchange Anisotropy, Engineered Coercivity and Spin Transport In Atomically Engineered L1 <sub>0</sub> Heterostructures.....	171
<b>Kannan M. Krishnan</b>	

Field-Structured Composites .....	175
<b>J. E. Martin, D. Read, G. Venturini and R. Anderson</b>	
Spin-Dependent Effects in Ferromagnetic Semiconductor and Manganite Thin Films.....	179
<b>Jing Shi</b>	
Magnetization Dynamics and Cooperative Phenomena in Spin and Charge Frustrated Correlated Electron Materials.....	182
<b>Hariharan Srikanth, M. H. Phan, Natalie Frey, James Gass, Manuel Angst, Brian Sales, David Mandrus, C. N. Chinnasamy and Vincent Harris</b>	
Spin Polarized Functionality through Complex Oxide Heteroepitaxy .....	186
<b>Yuri Suzuki</b>	
Coupled Phenomena in Magnetoelectric Multiferroics .....	190
<b>Xiaoli Tan, R. William McCallum and Vladimir Antropov</b>	
Structure and Magnetism in Novel Group IV Element-Based Magnetic Materials.....	194
<b>Frank Tsui</b>	
Understanding the Spin-Lattice Coupling in Multiferroic Oxides .....	198
<b>Trevor A. Tyson</b>	
Understanding Compound Phase Transitions in New Heusler Alloy Magnetocaloric Materials .....	203
<b>Naushad Ali and Shane Stadler</b>	
Surface Wave Mediated Near-Field Heat Transfer .....	207
<b>Gang Chen</b>	
Atomistic and Mesoscopic Study of Metallic Glasses .....	211
<b>Takeshi Egami, Paso George and Jamie R. Morris</b>	
Bridging Atomistic and Continuum Scales in Phase-Field .....	215
Modeling of Solid-Liquid Interface Dynamics and Coalescence	
<b>Alain Karma</b>	
Phase Field Approach for Strain-Induced Magnetoelectric Effect in .....	219
Multiferroic Composites	
<b>Y. Ni and A. G. Khachatryan</b>	
Enhanced Thermoelectric Performance of Rough Silicon Nanowires.....	222
<b>Allon I. Hochbaum, Renkun Chen, Arun Majumdar and Peidong Yang</b>	
Electric Field Effects in Liquid Crystals with Dielectric Dispersion .....	226
<b>Oleg D. Laventovich and Sergij V. Shiyankovskii</b>	
Amorphous Structures and Polymorphs of Metallic Glasses .....	230
<b>E. Ma</b>	
Mesoscale Interfacial Dynamics in Magnetoelectric Nanocomposites .....	234

Complex Amorphous Transition-Metal Dielectrics .....	238
<b>R. Bruce van Dover</b>	
Designing Nanoparticle/Nanowire Composites and Nanotree Arrays as Electrodes for Efficient Dye-Sensitized Solar Cells .....	203
<b>Yiyang Wu</b>	
Magnetolectric Epitaxial Thin Layer Two Phase Composites .....	242
<b>Dwight Viehland and Jiefang Li</b>	
Suspensions of Monodisperse Nanoparticles as Model Systems for Probing Heat Transfer Mechanisms in Nanofluids .....	245
<b>Bao Yang, Michael R. Zachariah</b>	
Overview of the Helios Solar Energy Research Center .....	249
<b>Paul Alivisatos</b>	
Plasmonic Photovoltaics .....	251
<b>Harry A. Atwater and Thomas J. Watson</b>	
Engineering Optical Conductivity in Short Period Oxide Superlattices.....	254
<b>Xiaofang Zhai, C. Mohapatra, A. Shah, A. Bhattacharya, J. G. Wen, J. M. Zuo and J. N. Eckstein</b>	
Investigation of Metallic Photonic Crystals for the Modification of Thermal Emission .....	257
<b>Shawn-Yu Lin</b>	
Nanophosphors: Fundamental Science of Insulators in the Nanoscale Regime.....	259
<b>Ross E. Muenchausen</b>	
Theory on Defects and Doping Bottlenecks in Semiconductors, Wide-Gap Materials, and their Nanostructures .....	267
<b>Shengbai Zhang</b>	

## **Session I: Nano-Enabled Behavior**

## **Nanomechanics at Hard-Soft Interfaces**

Arun Majumdar, Peidong Yang, Renkun Chen, Allon Hochbaum  
Lawrence Berkeley National Laboratories

The overall program goal is to advance the fundamental understanding of complex phenomena at the interface of soft and hard nanomaterials. The research focuses on two areas:

(i) understanding of transport of liquids, ions, and molecules in nanofluidic channels;  
(ii) understanding the origin of mechanical forces generated by molecular reactions at interfaces, and creating ways to transduce them into measurable signals. The first area explores the science and engineering of molecular and ionic transport in confined or low dimensional liquids. Progress in this area will lay the foundations of integrated nanofluidic circuits for manipulating single molecules, as well as new approaches for energy-efficient separations of liquid mixtures. The second area will focus on the origin of mechanical forces generated from ligand-receptor reactions at interfaces, and ways to manipulate these forces to produce measurable signals. While mechanical forces from ligand-receptor binding are widely exploited in signal transduction at cell membranes, they have rarely been utilized in non-biological settings. This project will explore the science of molecular mechanics at interfaces and develop electronic and optical transduction mechanisms for observing reactions. The eventual goal is to somehow mimic the olfactory or the immune system in detecting and distinguishing molecules with very high sensitivity and selectivity.

## **Program Title:** Characterization of Functional Nanomachines

**Principal Investigator:** M. F. Crommie

**Mailing address:** University of California at Berkeley, Physics Department, 366 LeConte Hall #7300, Berkeley, CA 94720-7300

**e-mail:** crommie@berkeley.edu

**Co-investigators:** C. Bustamante, M. L. Cohen, J. M. J. Frechet, S. G. Louie, D. Trauner, A. Zettl

**Program Scope/Definition:** The goal of this project is to develop and characterize mechanical devices at the nanoscale. We are following two paths toward this goal. First, we are harnessing naturally occurring biomotors to take advantage of the molecular mechanisms provided by Nature. Second, we are purposefully designing new synthetic molecular machines in a molecule-by-molecule fashion. This project is aimed at clarifying the mechanisms by which nanomachines convert chemical to mechanical energy, and at examining their utility for new applications. Our program should yield two new categories of functional nano-assemblies in the area of synthetically fabricated nanomachines. The first involves chemically engineered molecules, purposefully designed with specific mechanical functions in mind. The second involves exploitation of the unique properties of carbon nanotubes to create novel, nanomechanical devices. We intend to integrate these nanomachine elements to help form the basis of a new molecular-mechanical nanotechnology with applications in areas of importance to DOE such as chemical and photosensing, computation, power generation, and active surface control.

This project has seven co-investigators whose expertise span physics, chemistry, and biology. We believe that an interdisciplinary approach is best for addressing the problems that face researchers in the area of molecular machines and motors, where multiple fields often intersect. The experimental tools utilized by our collaboration range from synthetic chemistry, surface science, and scanned probe techniques (Frechet, Trauner, and Crommie), to photolithography, wet biology, and laser tweezers (Zettl and Bustamante). Frechet and Crommie work closely to develop new, synthetic nanomachines at the single molecule level, while Zettl and Bustamante collaboratively share lithographic techniques for mesoscopic to nanoscopic surface patterning and nanomachine integration. Trauner's complimentary activities range from chemical synthesis to protein engineering and *in vivo* biological measurement. Cohen and Louie provide theoretical support through the use of *ab initio* density functional techniques and molecular dynamics calculations.

**Recent Progress:** We have made recent progress in a wide range of experimental activities that span synthesis and actuation of new nanomachine molecular elements, exploration of chemical-to-mechanical energy conversion in biomotors, and fabrication of nanotube-based nanomachines that operate on new nanomechanical principles (such as electromigration). Our theoretical activities strongly support our experimental research, and have helped to explain nanomechanical energy conversion and dissipation in different molecular systems (such as in functionalized azobenzene and multiwall carbon nanotubes).

In this presentation I will emphasize our activities in just one of these areas: chemical synthesis and optical actuation of new molecular machine elements. I will describe our progress at developing new molecules capable of converting the energy of light into mechanical work at

the single molecule level. The use of light to actuate molecular machines is an exciting new area because it has the potential benefits of not requiring nanoscale electrical contact, of having extremely high bandwidth, and of benefitting from a wide range of optically active molecular candidates. Most previous work in this area has focused on exploring ensembles of molecules in solution. Our work is aimed at understanding and controlling the photomechanical properties of nanomachine elements on surfaces and at the single molecule level. We believe that this poorly studied regime forms a critical area for future nanomachine applications.

One of our recent successes in this area has been the first observation of reversible photomechanical switching in a single molecule tethered to a crystal surface.<sup>1</sup>

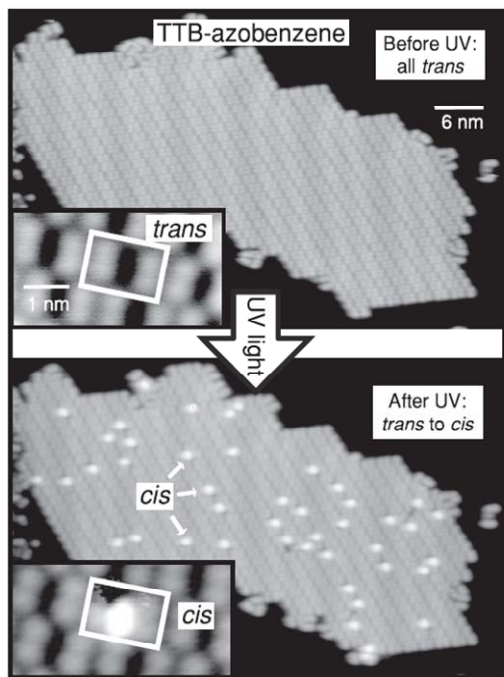


Fig. 2: Photoisomerization of individual TTB-azobenzene molecules on Au(111) from *trans* to *cis*. Same island of TTB-azobenzene molecules is shown before (upper image) and after (lower image) a 3 hr exposure to 90 mW/cm<sup>2</sup> UV irradiation at 375 nm. After UV exposure 45 TTB-azobenzene molecules have switched from the *trans* to the *cis* state. Inset zoom-in images show UV-induced switching (before and after) from *trans* to *cis* for a single molecule (identified by white box).

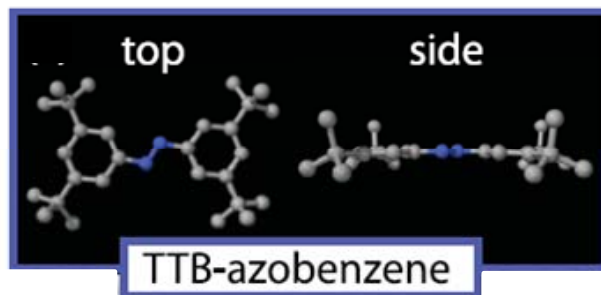
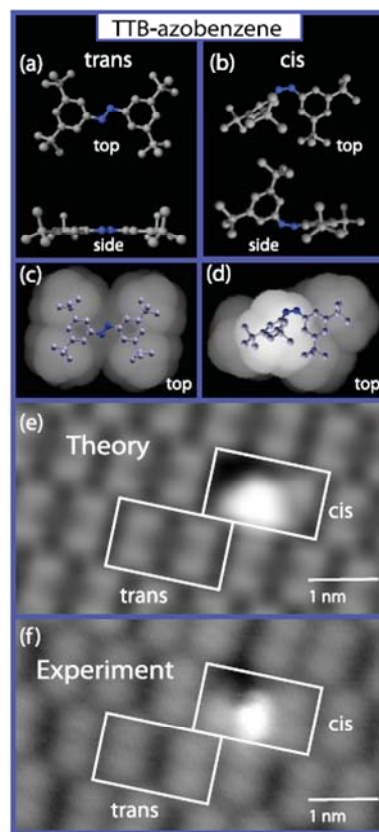


Fig. 1: Sketch of azobenzene molecule functionalized with four tert-butyl legs designed to decouple it from a surface and enable photomechanical switching. This molecule is referred to as tetra-tert-butyl azobenzene (TTB-azobenzene).

We have chemically engineered azobenzene derivatives (Fig. 1) that mechanically switch via the absorption of a single photon while adsorbed to a metal surface, and we have observed reversible switching at the single-molecule level (Fig. 2) using scanning tunneling microscopy (STM). This photo-actuated single-molecule mechanical switching has been confirmed through comparison of our molecular images to density functional theory calculations of switched molecule electronic structure (Fig. 3). These results signify a new level of molecular-mechanical control, and open new scientific possibilities for understanding photonically coupled mechanical processes at the single molecule level, as well as new possibilities for single-molecule photomechanical applications.

We have explored the phenomenology of this photoswitching by measuring the wavelength-dependence,<sup>2</sup> the local environment dependence, and the chirality dependence of single photoswitching molecules of tetra-tert-butyl-azobenzene (TTB-AB) on a Au(111) surface. Using STM single-molecule imaging, we have determined the precise number of photoswitched TTB-AB molecules at a gold surface as a function of optical exposure and optical wavelength (Fig. 4). This has allowed us to determine the critical forward and reverse switching cross-sections for this molecule when it is placed at a surface and illuminated with either UV or optical wavelengths.<sup>2</sup> Molecules found in the dominant

Fig. 3: Simulated *trans* and *cis* TTB-azobenzene structures compared to experiment. (a) Calculated *trans* geometry. (b) Calculated *cis* geometry. (c) Calculated *trans* electronic local density of states (LDOS) isosurface. (d) Calculated *cis* LDOS isosurface [same parameters as in (c)]. (e) Simulated STM image of TTB-azobenzene using tiled single-molecule LDOS isosurfaces from (c) and (d). (f) Experimental STM image of TTB-azobenzene molecules.



close-packed surface configuration on Au(111) were found to saturate using 375nm light at a 50% fraction of *cis* to *trans* isomers. This leads to equal forward and reverse molecular photoswitching cross sections of  $2.3 \times 10^{-23} \text{ cm}^{-2}$ . Although this overall rate is much lower than seen for molecules in solution, the asymmetry (or lack of it) observed in forward and reverse switching rates at this wavelength for the surface molecule system is comparable to that observed in solution phase molecules. Visible (444nm) radiation, on the other hand, leads to a forward / reverse asymmetry of only 25%. This is significantly different from the more than 1000% switching asymmetry seen for this same molecule (at this wavelength) in solution. The photoswitching asymmetry of surface bound TTB-AB molecules is thus greatly reduced compared to solution phase molecules, a fact that poses a hindrance for some switching applications. This is likely due to changes in optical absorption and relaxation properties for surface-bound molecules compared to molecules in solution phase. This result presents us with the new challenge of how to increase asymmetry in photomechanical switching rates for surface bound molecules.

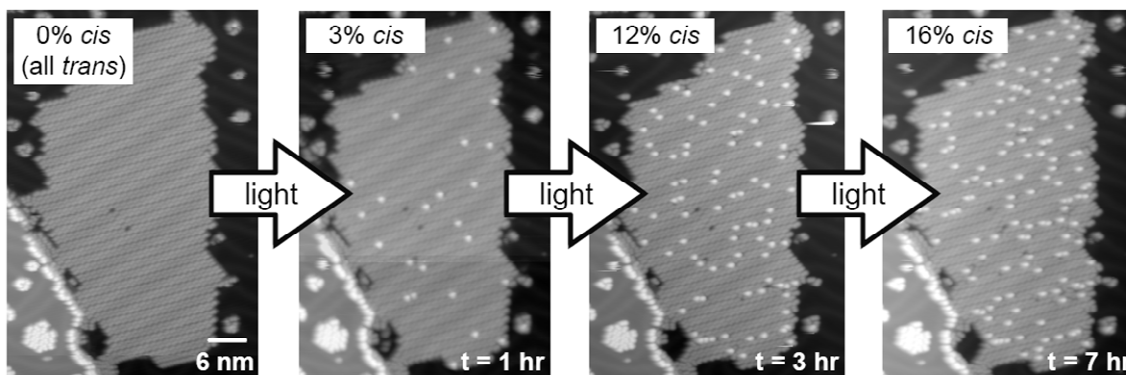


Fig. 4: Sequential images of a single island of TTB-azobenzene on Au(111) after successive exposures to 375 nm UV light. First image is the pre-exposure configuration of uniformly *trans* isomers. The three following images were acquired after 1 hr, 3 hr, and 7 hr total exposures to UV light, and show increasing number of photoswitched *cis* isomers of TTB-azobenzene.

We have additionally explored the effect of local surface environment on the photoswitching properties of optomechanically active molecules. We find that the photoswitching rate of TTB-AB depends strongly on how it is locally configured on Au(111).

TTB-AB exhibits three different structural phases, each of which exhibits a completely different photoswitching probability. One of these phases surprisingly exhibits "self-patterned" spatial stripes of enhanced photoswitching probability that are spaced 10nm apart. These results highlight the importance of molecule-molecule and molecule-surface interactions in determining molecular photoswitching properties at a surface.

We have gained new insight into the specific mechanism by which TTB-AB molecules photoswitch at a gold surface by examining the chirality of initial state (*trans* isomer) and final state (*cis* isomer) molecular products. We observe that TTB-AB assembles into "self-selected" chiral islands of *trans* isomers on Au(111) (right-handed versus left-handed). By examining the chirality of single molecules of optically switched *cis* isomers, we are able to determine chirality-dependent photoswitching selection rules for TTB-AB at a surface. These selection rules rule out certain switching mechanisms, and provide evidence for a new surface switching modality.

**Future Plans:** Our future plans in this particular area of our overall Nanomachine Project will emphasize three thrust topics: (a) Assembly of photomechanical molecules into functional nanomachines, (b) Exploration of new photomechanical molecular elements, and (c) Exploration of new substrate systems to enhance photomechanical switching properties. Now that we have carefully characterized a range of single-molecule photoswitching properties at a surface, we are eager to assemble photoswitching molecules into functional arrays. An example of such a functional assembly would be a nanometer-scale molecular "nanocrawler" capable of light-induced locomotion across a surface. This goal dovetails with topic (b), since assembly of such a nanomachine will require the design and synthesis of new photoswitching molecules capable of bonding in pre-determined arrangements at a surface. Topic (c) is an important area of future work, as we hope to improve surface nanomachine performance by engineering the substrates utilized in this work. We find that surface-molecule interactions play a large role in photomechanical switching rates, and so we hope to control these effects through the use of new semiconducting and tunable substrates. One particularly exciting substrate is graphene, which provides a tunable surface electron density through the use of backgating. We have begun exploring backgated graphene devices as continuously tunable nanomachine substrates, and we intend to push forward in this area.

### References:

[1] "Reversible Photomechanical Switching of Individual Engineered Molecules at a Metallic Surface", Matthew J. Comstock, Niv Levy, Armen Kirakosian, Jongweon Cho, Frank Lauterwasser, Jessica H. Harvey, David A. Strubbe, Jean M. J. Frechet, Dirk Trauner, Steven G. Louie, and Michael F. Crommie, *Phys. Rev. Lett.* **99**, 038301 (2007).

[2] "Measuring Reversible Photomechanical Switching Rates for a Molecule at a Surface", Matthew J. Comstock, Niv Levy, Jongweon Cho, Luis Berbil-Bautista, Daniel A. Poulsen, Jean M.J. Frechet, and Michael F. Crommie, accepted for publication in *Applied Physics Letters*.

Program Title: Structure-Optical-Thermal Relationships of Carbon Nanotubes  
 Principal Investigator: Stephen Cronin  
 Institution: University of Southern California  
 Address: 3737 Watt Way, Los Angeles, CA 90089  
 Email: scronin@usc.edu  
 DOE Grant Number: DE-FG02-07ER46376  
 Collaboration: Prof. Li Shi, University of Texas, Austin

### Program Scope or Definition

This research aims to better understand the relationships between the crystal structure of different single wall carbon nanotubes (SWCNTs) and their optical and thermal properties as well as the electron transport and heat dissipation mechanisms. We have designed the following three experiments to explore several poorly understood phenomena in nanotubes. These experiments are being executed via the collaboration between the Cronin group and the Shi group.

1. Establish the structure-optical property relationships of carbon nanotubes using Raman and fluorescence spectroscopy on well-defined nanotubes, characterized by transmission electron microscopy (TEM).
2. Determine the structure-thermal property relationships of carbon nanotubes of different diameters and chiral angles, by performing thermal, optical, and TEM measurements on the same nanotube.
3. Quantify the temperature rise/distribution and contact thermal resistance in current-carrying carbon nanotubes, using Scanning Thermal Microscopy (SThM) and Spatial Mapping of Raman Spectroscopy (SMRS).

### Recent Progress

1.) *Optical Measurement of Thermal Transport:* During the first half year of this project, we have performed optical measurements of thermal transport using different laser powers to heat suspended single walled carbon nanotubes  $\sim 5\mu\text{m}$  in length<sup>1</sup>. The temperature change along the length of a nanotube is determined from the temperature-induced downshift in the  $G$  band Raman frequency, as shown in Figure 1. The spatial temperature profile ( $\Delta T(x)$ ) reveals the ratio of the contact thermal resistance ( $R_{c,left}$ ) and ( $R_{c,right}$ ) to the intrinsic thermal resistance of the nanotube ( $R_{NT}$ ). Moreover, the obtained temperature profiles allow differentiation between diffusive and ballistic phonon transport. If the phonon transport were ballistic, the temperature rise would result in a constant  $\Delta T(x)$  regardless of the contact resistances. This was not observed in any of the samples we measured.

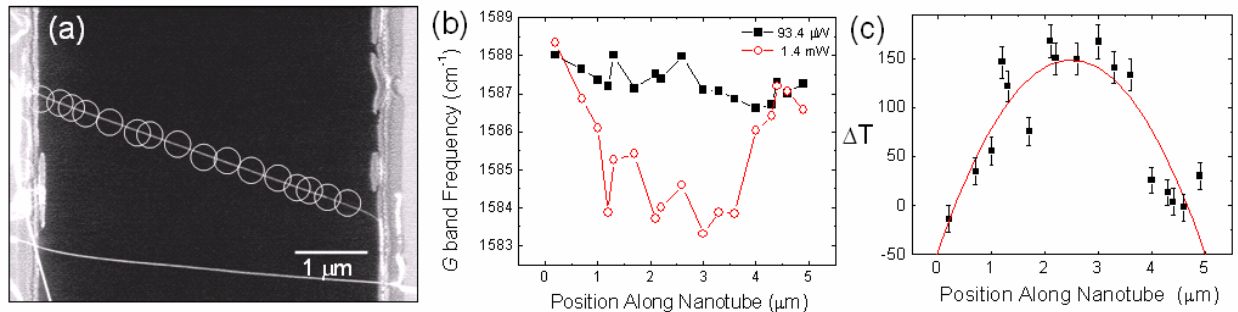


**Figure 1.** (a) SEM image of carbon nanotubes suspended over a 4.7  $\mu\text{m}$  trench. (b)  $G$  band Raman frequency measured along the length of the nanotube in (a) at different laser powers. (c) Laser heating profile of the suspended nanotube shown in (a). Error bars reflect the uncertainties in the  $G$  band shift and its temperature coefficient.

By assuming diffusive heat transport, the measured temperature profile can be modeled using the Fourier heat equation. Solving for  $\Delta T(x)$  we have:

$$\Delta T(x) = \frac{\dot{Q} \left[ -\frac{x^2}{(\kappa A)^2} + x \left( \frac{L}{(\kappa A)^2} + \frac{R_{c,right} - R_{c,left}}{\kappa A} \right) + R_{c,right} R_{c,left} + \frac{L}{\kappa A} R_{c,left} \right]}{\frac{L}{\kappa A} + R_{c,left} + R_{c,right}},$$

where  $\dot{Q}$  is the rate at which heat is generated in the nanotube by the incident laser,  $L$  and  $A$  are the length and geometric cross section of the suspended nanotube,  $x$  is the distance of the laser spot from the left edge of the trench,  $\kappa$  is the thermal conductivity of the nanotube and  $R_{c,left}$  and  $R_{c,right}$  are the contact thermal resistances at the two ends of the nanotube. This complicating looking but otherwise simple algebraic expression is a quadratic equation that can be represented as  $ax^2 + bx + c = 0$ . Although  $\dot{Q}$  is unknown, we can solve for the ratio of the thermal contact resistance to the thermal resistance of the nanotube itself as:

$$\frac{R_{c,left}}{R_{NT}} = \frac{-\alpha + \sqrt{\alpha^2 + 4\beta}}{2L} \quad \text{and} \quad \frac{R_{c,right}}{R_{NT}} = -1 + \frac{\alpha + \sqrt{\alpha^2 + 4\beta}}{2L},$$

where  $\alpha=b/a$  and  $\beta=c/a$ .

This measurement scheme was implemented on a total of 4 suspended nanotubes. Their data is summarized in the table below. Diffusive transport is observed in all nanotubes measured and the ratio of thermal contact resistance to intrinsic nanotube thermal resistance is found to range by almost four orders of magnitude, from 0.02 to 17.

Sample	$a$ (K/ $\mu\text{m}^2$ )	$b$ (K/ $\mu\text{m}$ )	$c$ (K)	Length ( $\mu\text{m}$ )	$P_{\text{laser}}$ (mW/ $\mu\text{m}^2$ )	$R_{c,left}/R_{NT}$	$R_{c,right}/R_{NT}$
1	31	155	<15	5.0	13	0.02	0.02
2	48	118	27	2.6	16	0.08	0.08
3	<0.2	16	26	5.0	25	0.32	17
4	3.6	-7.9	144	4.7	3.1	1.59	0.13

**Table 1.** Summary of the temperature rise profile measurements of four suspended nanotubes.

2.) *Optical Measurement of Electronic Heat Dissipation:* During this funding period, we also investigated electron transport and heat dissipation mechanisms, optically. By measuring the Raman spectra of individual suspended carbon nanotubes under high voltage biases, we directly observe optical phonon emission. Interestingly, the LO and TO modes of the optical  $G$  band phonons behave differently with respect to voltage bias, indicating preferential electron-phonon coupling and non-equilibrium phonon populations.

Figure 2 shows an SEM image of the device measured, together with the voltage dependence of the  $G$  band optical phonons. The  $G_+$  band (TO) is observed to downshift by more than  $26\text{cm}^{-1}$ , indicating significant heating, while the  $G$  (LO) band on average doesn't change by more than  $1\text{cm}^{-1}$ . These results imply that the TO and LO phonons are in a state of extreme

thermal non-equilibrium. From the  $26\text{cm}^{-1}$  downshift, we estimate the temperature of the TO band to be approximately  $1000^\circ\text{C}$ , while the LO band doesn't change by more than  $40^\circ\text{C}$  under the applied bias voltage. The orthogonality of the LO and TO phonon bands enables them to remain in a state of extreme non-equilibrium. The selective nature of the preferential heating can be explained by the Kohn anomaly, which affects in the TO and LO bands differently. Preferential heating of the  $G_+$  phonon was observed in 4 out of 15 devices measured in this study.

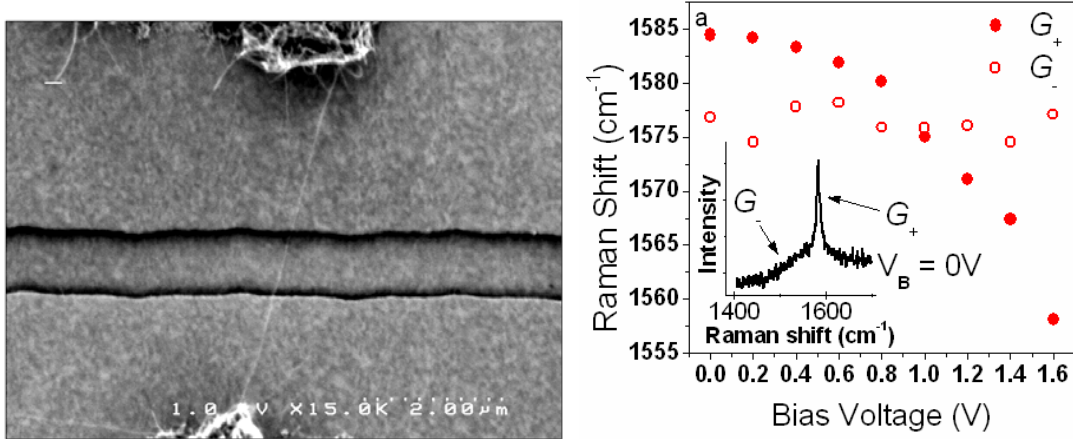


**Figure 2.** Left: SEM image of a suspended carbon nanotube grown on top of Pt electrodes. Right:  $G$  band Raman spectral data versus bias voltage.

Figure 3 shows the electrically measured resistance, plotted as a function of the optically measured phonon population. The data are fit using the Landauer model, in which the nanotube resistance is expressed as

$$R(V, T) = R_c + \frac{h}{4q^2} \frac{L + \lambda_{\text{eff}}(V, T)}{\lambda_{\text{eff}}(V, T)},$$

where  $R_c$  is the contact resistance,  $L$  is the nanotube length, and  $\lambda_{\text{eff}} = (\lambda_{\text{ac}}^{-1} + \lambda_{\text{op,ems}}^{-1} + \lambda_{\text{op,abs}}^{-1})^{-1}$  is the bias and temperature dependent electron mean free path. It is clear from the figure that modeling with only phonon emission is not sufficient to explain the data, and that instead, scattering by phonon absorption must also be included in the model. From the fit to this model, we can determine the key scattering parameters.

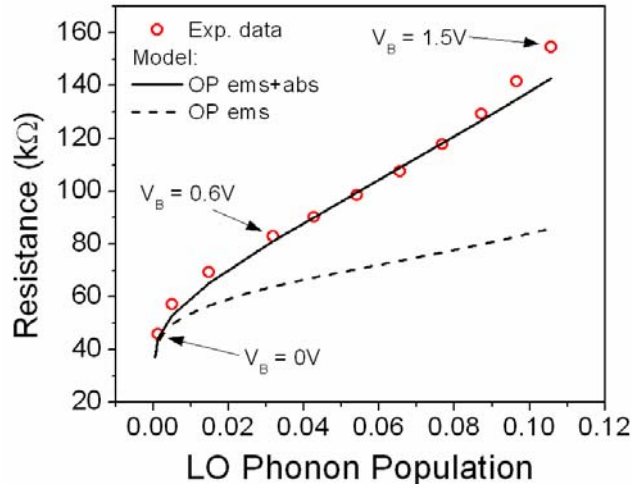


**Figure 3.** Electrical resistance plotted as function of phonon population. The two models shown are for OP scattering through emission plus non-equilibrium OP absorption and through OP emission alone.

There is a voltage threshold above which electrons simply don't have enough energy to emit an optical phonon. This threshold is given by  $V_{bias}=E_{ph}L/e$ , where the phonon energy  $E_{ph}\approx 0.2\text{eV}$ . Below this threshold, electronic conduction is ballistic. Above this threshold, the electron must travel a certain distance in the electric field in order to accumulate enough kinetic energy to emit a phonon of energy  $E_{ph}$ . This threshold length is given by  $E_{ph}L/eV_{bias}$ . Once the electron's energy exceeds  $E_{ph}$ , it travels an additional distance  $\lambda_{op}^{\min}$  (on average) before emitting a phonon, since the emission process is not instantaneous. Putting this together, the scattering length for optical phonon emission is given by:

$$\lambda_{op,ems}=\frac{E_{ph}L}{eV}+\lambda_{op}^{\min}.$$

For optical phonon absorption, the scattering length is given by

$$\lambda_{op,abs}=\lambda_{op}^{\min}\cdot\frac{1+N_{op}(300K)}{N_{op}(T_{op})},$$

where  $N_{op}(T)$  is the optical phonon population. In this model, there is only one fitting parameter,  $\lambda_{op}^{\min}$ . By fitting this model to our data, as shown in Fig. 3, we find values for  $\lambda_{op}^{\min}$  ranging from 18nm to 35nm from a total of 4 metallic nanotubes measured. One semiconducting nanotube measured showed a value of 9nm.

Combining Raman, thermal, and electrical measurements on the same individual suspended nanotube allows us to better understand several poorly understood phenomena, including the key scattering parameters in electron transport and the relative magnitude of the thermal contact resistance.

### Future Plans

For the remaining four months of the first year and the second year of this project, we have planned the following experiments:

1. Perform thermal, TEM and Raman measurements on the same nanotube so that the contact resistance obtained using the Raman measurement can be eliminated from the measured thermal conductance using the micro-device.
2. Establish the structure-optical property relationships of carbon nanotubes using Raman and fluorescence spectroscopy on well-defined nanotubes, characterized by TEM.
3. Quantify the temperature rise/distribution and contact thermal resistance in current-carrying carbon nanotubes using Scanning Thermal Microscopy combined with Spatial Mapping of Raman Spectroscopy

### References to publications of DOE sponsored research that have appeared in 2005-2007 or that have been accepted for publication.

1. I-K. Hsu, R. Kumar, A. Bushmaker, S. B. Cronin, M. T. Pettes, L. Shi, T. Brintlinger, M. S. Fuhrer, J. Cumings, "Optical Measurement of Thermal Transport in Suspended Carbon Nanotubes," *Appl. Phys. Lett.*, accepted (2008).
2. Adam W. Bushmaker, Vikram V. Deshpande, Marc W. Bockrath, and Stephen B. Cronin, "Direct Observation of Mode Selective Electron-Phonon Coupling in Suspended Carbon Nanotubes", *Nano Lett.*, 7, 3618 (2007).

**Program Title:** Imaging carrier generation, transport, and collection in nanostructured materials

**Principle Investigator:** Lincoln J. Lauhon, Morris E. Fine Junior Professor  
Department of Materials Science and Engineering, Northwestern University  
2220 Campus Drive, Evanston, IL 60208 e-mail: lauhon@northwestern.edu

### **Program Scope**

The objective of our program is to develop a fundamental, quantitative understanding of charge transport between and within components of nanostructured materials to support the design and optimization of new materials for energy conversion. Our experimental approach is based on combining electrical transport measurements with near-field scanning optical microscopy (NSOM) and electrostatic force microscopy (EFM) to spatially map carrier collection efficiency in semiconductor nanowire heterostructures and hybrid nanowire-organic devices. Appropriate combinations of spatially-resolved, time-resolved, and spectrally-resolved sources and detectors are used to isolate and quantify various steps in the energy conversion process, including carrier generation, exciton diffusion, majority/minority carrier transport, and collection by metal contacts. This experimental base enables research in three thrust areas: quantitative transport measurements, new concepts for nanowire photodetectors and photovoltaics, and carrier generation and collection in hybrid materials.

### **Prior Work**

The current program, which began in the summer of 2007, was founded on exploratory research supported by university seed funding. Our prior work established that scanning photocurrent microscopy (SPCM) could be used to determine the diffusion lengths of minority carriers in semiconductor nanowires with a resolution limited by the optical source.<sup>1,2</sup> More recently, the related technique of electron beam induced current (EBIC) was used to study the diameter dependence of the diffusion length in n-type silicon nanowires at even higher resolutions.<sup>3</sup> We found that the effective diffusion length was approximately equal to the nanowire diameter due to the dominance of surface recombination. This work highlighted the need to develop appropriate strategies for surface passivation if nanowires are used to collect minority carriers. EBIC is not the ideal tool for surfaced passivation studies, however, as the electron beam may damage both inorganic and organic passivation layers. SPCM measurements with an NSOM can enable high-resolution measurements without risk of sample damage.

The activities of the current program include: (1) the application of NSOM-based SPCM and EFM to nanowires and nanowire-thin film hybrids; (2) the development of time-resolved and energy-resolved SPCM; and (3) the development of models of the photocurrent response to enable extraction of key materials parameters related to carrier generation and collection.

### **Recent Progress**

The focus of our efforts in the first year has been the application of SPCM to doped silicon nanowires to establish the origins of the local photocurrent response. We expect the response to be determined by, and potentially provide insight into, the absorption cross-section, the nature of the contacts, doping level, carrier mobility and lifetime, the local potential, and traps and other defect states.

Figure 1 shows the SPCM response of an n-type silicon nanowire with one Ohmic and one Schottky contact. The photocurrent response is limited to the region near the Schottky contact under zero or reverse-bias (Fig. 1c) because the potential drop is primarily at the contact. Flat band conditions can be achieved by forward biasing the contact (Fig. 1b,c), which equalizes the response with the nanowire channel. Unexpectedly, a larger forward bias produces a localized response at the Schottky contact rather than a response throughout the channel. Contrary to what one would expect from a simple 1-D device model, the nanowire Schottky contact is not behaving as an efficient majority carrier injector under forward bias. We have found that the SPCM signal is highly sensitive to local fields, and that contrast is often seen at contacts that would be classified as Ohmic based on I-V characterization. The spatial extent of the

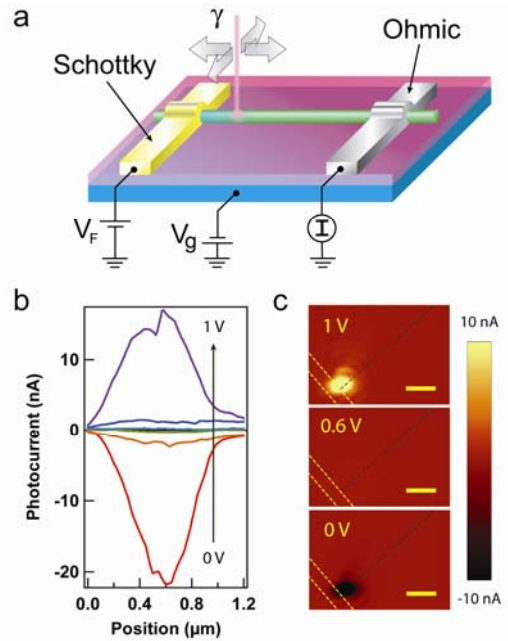


**Figure 1** a) Schematic of EBIC and SPCM measurements of n-Si nanowire Schottky diodes. b) Line profiles of the SPCM images in c) showing the photocurrent peak near the Schottky contact at various applied biases. c) SPCM images taken at 0 V, 0.6 V, and 1 V forward bias.

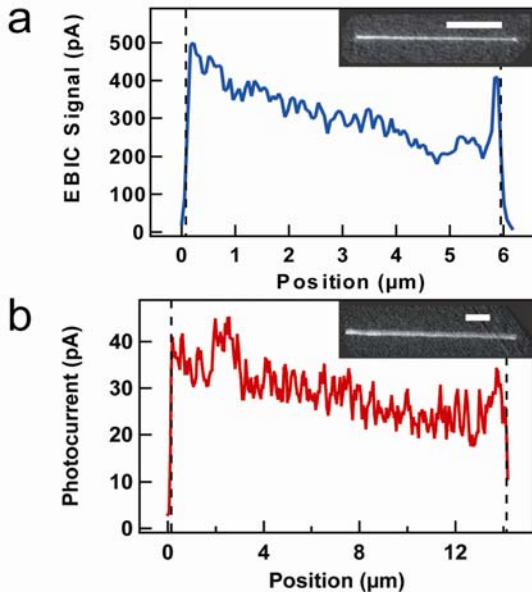


**Figure 2** Comparison of SPCM and EBIC signals for n-type silicon nanowires. a) Line profile of the EBIC signal along the nanowire device channel. b) Line profile of the SPCM signal along the nanowire device channel. Dashed lines indicate the position of the electrodes. The insets show the full images. Scale bars are 2  $\mu\text{m}$ .

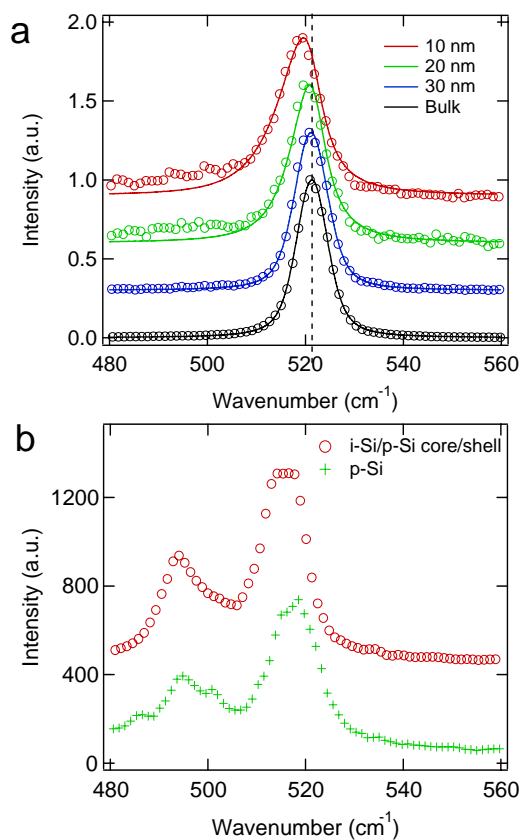
potential drop associated with the contacts is not well-resolved using the confocal microscope objective, so we are also using NSOM as a higher resolution illumination source.

Figure 2 shows a comparison of EBIC and NSOM-SPCM studies on Ohmically contacted n-type silicon nanowires. Four-terminal measurements of the respective devices indicate negligible contact resistance. Qualitatively, the response is much more uniform than for the Schottky-contacted device of Fig. 1; there is signal throughout the device channel and the response near the contacts is not especially large. This suggests that the potential drop occurs nearly uniformly throughout the channel, providing an electric field that generates the small excess minority carrier

current detected in the measurement. The magnitude of the response, and the slope, scale smoothly with bias (not shown), but the response remains uniform, suggesting that the diffusion/drift length of the carriers remains less than or equal to the probe size. Intriguingly, the photocurrent is slightly greater near one end of the nanowire. In both devices, this corresponds to the end nearest the catalyst tip. The larger signal corresponds to a slightly larger nanowire resistance, which could arise from either a tapered shape, and hence narrower diameter, or a variation in doping level and hence carrier concentration.

We have reason to believe that there are slight variations in the doping level along the nanowire due to unintended surface doping during vapor-liquid-solid (VLS) growth. In brief, VLS growth relies on a metal catalyst particle to selectively decompose reactants and produce one-dimensional nanowire growth. If vapor-solid (VS) surface reactions are not completely suppressed, the preferential adsorption of one species in the gas phase could lead to a non-uniform radial composition profile. We have explored this hypothesis in two parallel efforts involving single nanowire Raman spectroscopy and Local Electrode Atom Probe (LEAP) tomography.

In silicon heavily doped with boron, a Fano-like resonance appears in the Raman spectrum that enables an approximate determination of the active dopant concentration. Figure 3 shows Raman spectra of silicon nanowires of varying sizes and doping levels. To establish an approach to dopant level determination, the effects of finite size and surface disorder in intrinsic silicon nanowires were first explored (Fig. 3a). Below  $\sim 30$  nm, it becomes necessary to include the effects of confinement when fitting the Raman spectra of nanowires. With the effects of confinement in hand, one can address the additional line-shape changes induced by doping. The spectra of boron-doped nanowires (Fig. 3b) reveal an additional feature, however- a second peak at reduced wavenumber-shift. We have determined that this extra peak arises from a disordered surface layer of more heavily doped silicon by comparison to a spectrum of a nanowire that has an intentional intrinsic core/doped shell structure. Efforts to fit these more complex spectra and extract the dopant concentrations in the two components are ongoing.



**Figure 3** Raman spectra from single silicon nanowires. a) Single nanowire spectra versus diameter showing confinement-induced broadening. b) Spectra from boron-doped silicon nanowires showing new peak due to coating of disordered heavily doped coating. The upper spectrum is from an intentionally grown core-shell structure.

In separate efforts supported by the NSF, we have found evidence of a non-uniform doping distribution in boron-doped silicon and phosphorous-doped germanium nanowires using LEAP tomography. LEAP tomography combines field ion microscopy with time-of-flight mass spectroscopy to produce a 3-D reconstruction of sample composition with single atom sensitivity and sub-nanometer resolution.<sup>4</sup> Even in the absence of obvious overgrowth of a heavily doped surface layer, the surfaces of Si and Ge nanowires appear slightly enriched in dopant atoms, consistent with the interpretation of our SPCM measurements on phosphorous doped silicon nanowires.

### **Future Plans**

Our future plans are to develop a more complete understanding of the SPCM response in optimized silicon nanowires prior to extending measurements to thin films. This will involve three primary tasks: (1) correlation of the conductivity and SPCM profile with doping levels in nanowires using single nanowire Raman spectroscopy and LEAP tomography; (2) passivation of nanowires to increase the minority carrier diffusion length, which can be measured by SPCM; and (3) building a model of the photocurrent response that incorporates all physical processes found to be relevant in the preliminary studies. With this foundation, we will extend our approach to include time and energy-resolved measurements of nanowires and hybrid organic-inorganic materials.

### **References from Prior Work**

1. Gu, Y., Kwak, E. S., Lensch, J. L., Allen, J. E., Odom, T. W. & Lauhon, L. J. Near-field scanning photocurrent microscopy of a nanowire photodetector. *Applied Physics Letters* **87** (2005).
2. Gu, Y., Romankiewicz, J. P., David, J. K., Lensch, J. L. & Lauhon, L. J. Quantitative measurement of the electron and hole mobility-lifetime products in semiconductor nanowires. *Nano Letters* **6**, 948-952 (2006).
3. Allen, J. E., Hemesath, E. R., Perea, D. E., Lensch, J. L., Li, Z. Y., Yin, F., Gass, M. H., Wang, P., Bleloch, A. L., Palmer, R. E. & Lauhon, L. J. High-resolution detection of Au catalyst atoms in silicon nanowires. *Nature Nanotechnology, AOP.* (2008).
4. Perea, D. E., Allen, J. E., May, S. J., Wessels, B. W., Seidman, D. N. & Lauhon, L. J. Three-dimensional nanoscale composition mapping of semiconductor nanowires. *Nano Letters* **6**, 181-185 (2006).

## Manipulation of Carbon Nanotubes and Field Emission of Semiconducting Nanowires

Principal Investigator: Zhifeng Ren

Department of Physics, Boston College, Chestnut Hill, Massachusetts 02460

*In this program, we have carried out studies in two fields: 1) the behavior of carbon nanotubes under a bias voltage inside a transmission electron microscope equipped with a scanning electron microscope, 2) field emission property of carbon nanotubes and semiconducting nanowires. We discovered superplasticity in carbon nanotubes, and excellent field emission properties on carbon nanotubes and semiconducting nanowires including Si nanowires and ZnO nanobelts.*

### Electrical breakdown of MWCNTs inside a TEM

CNTs are potentially the smallest building blocks for future generation electronic devices. Rational design of any device requires a fundamental understanding of the electronic properties, of which SWCNTs have been well understood. Consequently, electronic devices such as field-effect transistors, nanotube-nanotube junctions, and integrated logic circuits based on SWCNTs have been realized. In contrast, understanding transport properties of MWCNTs has proceeded more slowly because of their extremely complex structure. A MWCNT consists of many nested SWCNTs in which each has a different electronic structure. All the transport studies carried out so far use a “side contact” in which nanotubes are spread on a pre-patterned Au electrode, with only the outermost wall contacted to the electrodes, and the inner carbon walls not in direct contact with the electrodes. As such, parallel conduction paths along the inner walls are limited in their contribution to the overall conductance. Indeed, experiments have shown that current flows only in the outermost wall in side-contacted MWCNTs. Collins *et al.* attempted to characterize the conductivity of *side-contacted* MWCNTs by using an electric breakdown technique. Their results are promising but are complicated by the tunneling barrier due to the side contact geometry. In this project, we realized an *end contact* geometry, in which every wall of the MWCNTs is contacted by the electrodes. This is a more generic contact configuration for the study of transport in multilayer systems. Consequently, we were able to reveal the transport properties of each wall within a MWCNT.

Our experimental setup is shown in Figs. 1(a) and 1(b). A MWCNT is end-contacted and free standing in high vacuum ( $10^{-8}$  Torr), inside a HRTEM equipped with an STM probe. In such an arrangement, atomic-scale imaging and *I-V* measurements (Fig. 1c) were carried out concurrently. Figure 1(b) shows a MWCNT grown on a carbon fiber by CVD. A contact was made on the left between an STM probe and the nanotube tip by the deposition of amorphous carbon using electron beam radiation.

When applying a bias of about 2 V, the catalyst particle on the nanotube tip is molten and moves rapidly toward the STM probe. The encapsulated nanotube tip is broken after the catalyst particle passes through, leaving each wall being contacted by the amorphous carbon or the STM probe. On the other end (right) of the nanotube, each wall is contacted to the carbon fiber because of the tip growth mechanism.

The electronic properties of each wall are probed using the electric breakdown method. When passing a current of  $240 \mu\text{A}$ , breakdown occurs at the midpoint of the nanotube, resulting in the formation of a clean six-wall nanotube segment, which was eliminated wall-by-wall by electric breakdown. The loss of one wall under a constant bias of 3 V results in an instant current drop, as shown in Fig. 1(c). The current drops are approximately 13, 17, 25, and  $31 \mu\text{A}$  for the 6<sup>th</sup>, 5<sup>th</sup>, 4<sup>th</sup>, and 3<sup>rd</sup> wall breakdown (the innermost wall is labeled as the first wall), respectively. The sequential wall-by-wall breakdown was recorded by HRTEM in our experiments. Figure 2 shows clearly that one wall is removed after each current drop, and each wall is removed sequentially from the outermost wall (6<sup>th</sup>) to the innermost wall (2<sup>nd</sup>). HRTEM indicates that the breakdown eventually results in the formation of either a DWCNT or a SWCNT. Remarkably, HRTEM detects that each breakdown is initiated in the *middle* of the nanotube, *not* at the contact, indicating the electron transport

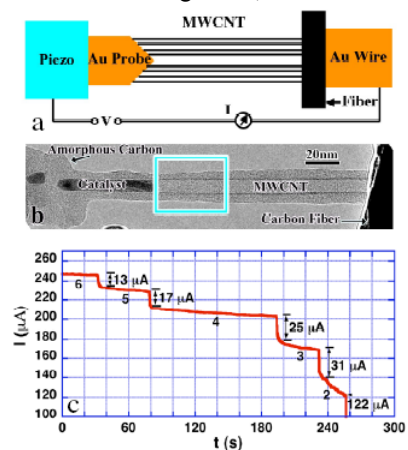


**Fig. 1.** (a) and (b) show that a MWCNT grown on a carbon fiber was side contacted by a STM probe, which is further attached to a piezomanipulator. (c) The current-time (*I-t*) curve of the breakdown of the MWCNT, the numbers below the plateau indicate the total wall number.

is not ballistic.

Intuitively, the wall-by-wall breakdown may occur sequentially from the outermost to innermost walls. Surprisingly, our HRTEM reveals that this (Fig. 2) is only one of the three possible burning patterns. The breakdown can proceed alternatively between the outer and the inner walls. Figure 3 shows the breakdown of a five-wall nanotube. Initially, a hole is formed on the surface of the outermost wall [Fig. 3(a)]. After 5 min, the entire wall is broken with the residue shown in Fig. 3(b). This triggers a current drop of  $8 \mu\text{A}$  [Fig. 3(e)]. Surprisingly, the next breakdown occurs from the innermost wall [Fig. 3(c)]. Remarkably, we found a large current drop of  $24 \mu\text{A}$  once the inner wall is broken, proving unambiguously that the inner wall is carrying a significant amount of current. The third breakdown also occurs from the inside [Fig. 3(d)], causing another  $24 \mu\text{A}$  current drop. It should be noted that all the breakdowns are initiated in the middle of the clean MWCNT segment, indicating the electron transport is not ballistic.

Figure 4 presents the third observed behavior in which the breakdown takes place sequentially from the innermost wall (1st) to the outermost wall (4th), completely reversing the burning sequences observed in the nanotube shown in Fig. 2, until a SWCNT is formed. The current drops are  $6$ ,  $12$ , and  $14 \mu\text{A}$  for the 1<sup>st</sup>, 2<sup>nd</sup>, and 3<sup>rd</sup> wall breakdown [Fig. 4(f)], respectively. It is interesting to note the interplay between the wall-diameter dependence of the current drop and the breakdown sequence. Figure 4(f) shows that the amount of current drop increases with increasing wall diameter, consistent with the results of Bourlon *et al.*, but opposite of what is shown in Fig. 2, where the breakdown starts from the outermost wall.

We studied the breakdown mechanism. The observation (Figs. 2–4) that the breakdown is initiated in the middle of the nanotube (not at the contacts) indicates that it is caused by resistive heating. This is also supported by the defect generation and migration along the nanotubes. Typical defects observed are kinks (Fig. 2), holes, and sliding between different walls. These are apparently heat-stimulated imperfections. From the lattice spacing of  $4 \text{ \AA}$ , we estimate that the temperature in the middle of the nanotubes is between  $2000$  and  $3000 \text{ }^\circ\text{C}$  at the breakdown voltage of  $3 \text{ V}$ . From the Fourier law, the middle section of the nanotube is the hottest spot; therefore it is not difficult to understand that the breakdown occurs in the middle of the nanotube.

These observations naturally imply that the transport in the MWCNTs is not ballistic and that significant scattering occurs as carriers traverse the length of the nanotubes. To this end, an estimate of the carrier mean free path ( $\lambda_{\text{MF}}$ ) is useful. From the Einstein relation, the conductance is given by  $G = (\pi dm/L)e^2 D \nu$ , where  $d$  is the averaged tube diameter,  $m$  is the number of walls,  $L$  is the length of the nanotube between the end contacts,  $D = V_F \lambda_{\text{MF}}/2$  is the diffusion constant, and  $\nu = 2\Delta E/\pi(\hbar V_F)^2$  is the density of states, where  $V_F$  is the Fermi velocity and  $\Delta E$  is the energy measured from the Fermi level which we replace with the thermal energy  $k_B T$  at room temperature. The mean free path is thus given by  $1/\lambda_{\text{MF}} = \pi d m \rho G_0 (k_B T/\hbar V_F)$ , with  $\rho = R/L$  the resistance per unit length and  $G_0 = 2e^2/h = 1/(13 \text{ k}\Omega)$ . Using the experimental values  $m = 6$ ,  $R = 20 \text{ k}\Omega$ ,  $d = 12 \text{ nm}$ , and the length of the nanotube  $L = 200 \text{ nm}$ , we obtain an averaged  $\lambda_{\text{MF}} = 13 \text{ nm}$ , which agrees excellently with that reported by Javey *et al.* Since the averaged mean free path is much shorter than the length of the nanotube, the transport is diffusive and electron heating is unavoidable at large bias and power input. Although we observed defect generation and migration in the nanotube walls under high bias conditions, and the breakdown might be initiated from the defect site, the defects

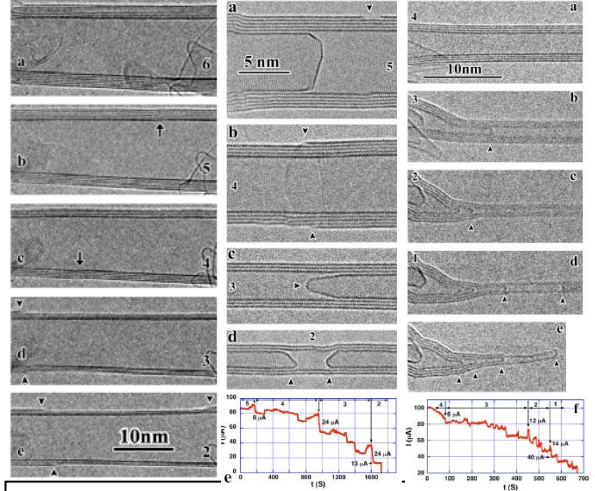


**Fig. 2** (left). Sequential HRTEM images showing that the six-wall nanotube is removed wall-by-wall from the outermost (a) to the innermost (e). The numbers indicate the total number of walls. The arrows mark kinks. The arrow heads denote the residue of the 4<sup>th</sup> and the 3<sup>rd</sup> walls after breakdown.

**Fig. 3** (middle). A MWCNT breaks in a sequence alternatively between the outermost and innermost wall. The numbers mark the number of walls in the broken segments. The arrowheads denote the breaking locations. The vertical arrows in (e) mark the current drop when a wall is removed. The outermost wall opens a hole (a) and breaks completely (b). The innermost wall is broken (c), and the second innermost wall is broken (d). (e) The I-t curve.

**Fig. 4** (right). The four walls of the MWCNT in (a) are sequentially removed from the innermost to outermost wall [(b)-(d)]. (e) The residue of the four broken walls. (f) The I-t curve. The numbers mark the total number of walls in the broken segments. The arrowheads denote the breaking locations. The vertical arrows in (f) mark the current drop when one wall is removed.

were found to emerge and then disappear from anywhere in the nanotube randomly; therefore, this cannot account for our results that the breakdown always starts from the middle of the nanotube. We conclude that the middle part of the nanotube is the hottest spot, and the transport in our nanotube is diffusive rather than ballistic.

### Superplasticity of CNTs observed inside a TEM

A SWCNT with an initial length of 24 nm [Fig. 5(a)] was formed *in situ* by the electrical breakdown of a MWCNT described above. The STM probe was used to pull the SWCNT to increase the strain [Fig. 5(b)–5(d)], at a constant bias of 2.3 volts. At tensile failure, the SWCNT was 91 nm long, showing a tensile elongation of 280%; its diameter was reduced 15-fold, from 12 to 0.8 nm. As the SWCNT segment was clamped between the layers of the MWCNT, the possibility of wall-sliding during elongation is ruled out. The diameter of the elongated nanotubes should not have changed significantly if wall-sliding had occurred.

A 280% tensile strain and 15-fold reduction in diameter are unprecedented in a SWCNT. Ropes of single-walled and multiwalled CNTs break at strains of less than about 6% and 12%, respectively, which is significantly less than those seen in our research. We propose that the super-elongation we observed is due to a fully plastic deformation mechanism that occurs at high temperatures.

During deformation at a bias of 2.3 V, the temperature in the middle of the SWCNT is estimated to be more than 2,000 °C. At such high temperatures, defects and diffusion are fully activated, leading to plastic flow in the nanotube. Indeed, during the tensile-loading experiments, kinks frequently emerge, propagate, and then disappear along the nanotube walls. The kink motion in CNTs proves conclusively that nanotubes are extremely ductile at high temperatures.

In addition to kink motion, we show below that vacancy/atom diffusion and dislocation climb also play significant roles in the elongation. In addition to the above described super plastic deformation of SWCNTs, using the same technique, we also observed exceptional ductile behavior in DWCNTs and TWCNTs at temperatures above 2000 °C, with tensile-elongation of 190% and 130%, respectively. Concurrent atomic-scale microstructure observations reveal that the super-elongation is attributed to a high temperature creep deformation mechanism mediated by atom/vacancy diffusion, dislocation climb, and kink motion at high temperatures.

We have found that super-elongation is never observed when nanotubes are pulled at room temperatures. Figure 8 shows the tensile-elongation of a DWCNT at room temperature. The total elongation is 7%, and the diameter reduction is 2%, which is much less than that in the nanotubes pulled at high temperatures.

We pulled about fifty nanotubes, including S/D/MWCNTs, either at room temperature or at high temperature (with a bias voltage of about 2.2 V). The elongation is usually larger than 50% for the nanotubes pulled at high temperatures. The limiting factor to the elongation is that the nanotubes generally experience electrical breakdown very easily and/or undergo wall sliding before substantial elongation. The elongation is generally less than 10% when the nanotubes are pulled at room temperature, which is about five or more times lower than that for the nanotubes pulled at high temperatures. Therefore, it is evident that high temperature plays a key role in the super-elongation of the nanotubes.

### Field emission of CNTs

Based on the growth of long length (up to 2.2 mm) of aligned CNTs on single crystal magnesium oxide (MgO) by CVD as shown in Fig. 6, we have also achieved on growth of long length of CNTs on Si substrates. However, as-grown samples were found not to be great field emitters due to the screening effect. To improve the

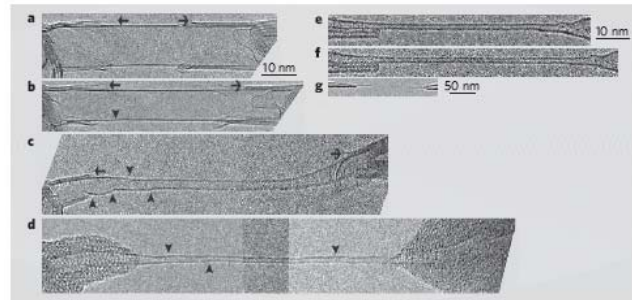


**Fig. 5.** *In Situ* tensile elongation of an individual SWCNT viewed in an HRTEM. (a)-(d), tensile elongation of a SWCNT under a constant bias of 2.3 V. Arrowheads mark kinks, arrows indicate features at the ends of the nanotube that are almost unchanged during elongation. (e)-(g), tensile elongation of a SWCNT at room temperature without bias. Initial length is 75 nm (e); length after elongation (f) and at the breaking point (g) is 84 nm, (g) low magnification image of the SWCNT breaking in the middle.

field emission current density, post-growth thermal annealing was conducted at 850 °C for 1 h in vacuum plus at 465 °C for 2 h in air.

The CNTs of 10 – 20 nm in diameter and 25 – 200  $\mu\text{m}$  in length were synthesized on silicon wafer (as-doped n-type, resistance 0.001  $\Omega\text{cm}$ , [100] orientation, Recticon Enterprises, Inc.) by CVD. Briefly, at first an 11 nm thick film (3 nm Fe / 4 nm Al / 4 nm Fe) was deposited as a catalyst on the silicon wafer by RF magnetron sputtering. CNT growth was carried out in a tube furnace by a thermal CVD technique. The catalyst layer was first heat-treated at 740 – 780 °C in 200 Torr of flowing  $\text{H}_2$  (100 sccm, 99.999% purity) for 10 min to form the required catalyst particles and to enhance the catalyst activity, followed by flowing  $\text{C}_2\text{H}_4$  (100 sccm 99.6% purity) while keeping the flowing  $\text{H}_2$ , the pressure was adjusted to one atmosphere by controlling the exhaust valve for CNTs growth for 5 – 60 mins depending on the length requirement. After growth, the sample was cut into two parts; one, designated as as-grown, was used for field emission measurement directly, and another was annealed in vacuum as described above.

Figures 7(a) and 7(b) show the SEM top view of the morphologies of the as-grown and annealed CNTs films. From the SEM images, we determined that annealing appeared to roughen the surface of the CNTs [Fig. 7(b)]. The density of the CNTs seems decreased after annealing. Moreover, from the tilted view [Figs. 7(c) and 7(d)], it looks like that some intertwined CNTs on the surface in the as-grown sample [Fig. 7(c)] has been separated by annealing [Fig. 7(d)].

The field emission measurements were carried out in a diode configuration. The anode was a molybdenum disk with a diameter of 3 mm, and the gap between the sample surface and the anode was about 270  $\mu\text{m}$ . The vacuum level was kept at about  $1 \times 10^{-6}$  Torr during the measurements. Before the emission current measurement, an electrical conditioning was conducted to get stable field emission. The measured emission current density as a function of the macroscopic electric field is shown in Fig. 8. A turn-on electric field of 2.6  $\text{V}/\mu\text{m}$  was obtained at an emission current density of 0.01  $\text{mA}/\text{cm}^2$  for the as-grown samples (represented by the open triangles), and 2.5  $\text{V}/\mu\text{m}$  for the annealed samples (represented by the solid circles). An emission current density of 1  $\text{mA}/\text{cm}^2$  was obtained at 4.6  $\text{V}/\mu\text{m}$  for the as-grown samples, which is higher than that of the annealed ones (3.8  $\text{V}/\mu\text{m}$ ) [Fig. 8(a)]. The Fowler-Nordheim plots for the measured samples are shown in Fig. 8(b). It is clearly shown that the measured data have a linear relationship, which confirmed the field emission nature. From the intercepts and slopes of the Fowler-Nordheim plots assuming a work function of 5 eV, we estimated that the total real emitting areas are  $1.4 \times 10^{-12}$   $\text{cm}^2$  and  $1.2 \times 10^{-10}$   $\text{cm}^2$  for the as-grown and annealed samples, respectively. The larger emitting area for the annealed sample is the result of oxidation that removes some amorphous carbon and exposes CNTs.

It is found that the highest obtained emission current density (79  $\text{mA}/\text{cm}^2$ ) for the annealed samples is much higher than that (19  $\text{mA}/\text{cm}^2$ ) of the as-grown samples (Fig. 9). Annealing is demonstrated to be an effective way to improve the emission current density. Such high current

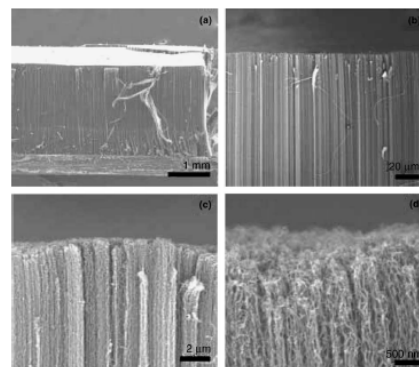


**Fig. 6.** SEM images of CNTs grown on single crystal MgO substrates coated with Fe film. (a) Low magnification showing the length of CNTs and the thickness of MgO substrate (500  $\mu\text{m}$ ); (b) medium magnification showing the good alignment; (c) and (d) high magnification showing the wavy nature of the alignment.

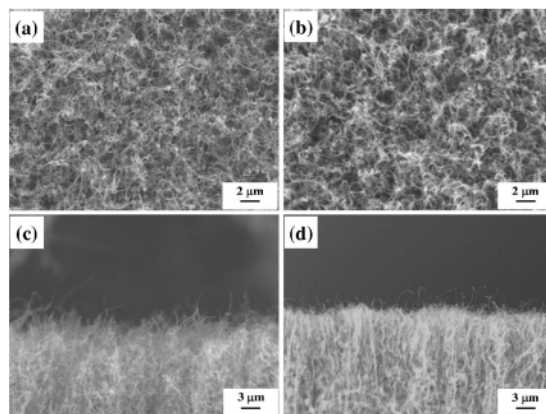


**Fig. 7.** SEM micrographs of carbon nanotubes. (a) Top view of the as-grown sample, (b) top view of the annealed sample, (c) side view of the as-grown sample, and (d) side view of the annealed sample.

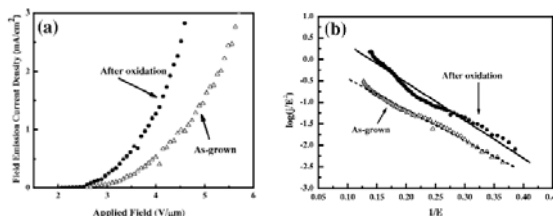


**Fig. 8.** Field emission property. (a) Emission current density dependence of electrical field and (b) Fowler-Nordheim plots.

density is a big step towards the understanding and the application of using carbon nanotubes as high current sources in microwave devices. It is very interesting to point out that the vacuum of  $1 \times 10^{-6}$  at the beginning of measurement quickly deteriorated when the current density went up, which prevented us from obtaining even higher current. If a pulse power source was used, it would be possible to obtain an even higher current density.

For any practical application, stability of emission current density is essential. We have carried out the stability test at a starting current density of about  $31.6 \text{ mA/cm}^2$  at about  $1 \times 10^{-6}$  Torr. After 12 h of continuous dc emission, the current density dropped from  $31.6$  to  $28.4 \text{ mA/cm}^2$ , about 10 % degradation (shown in Fig. 10), which is very good considering the large current density.

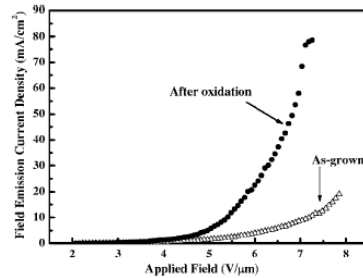


**Fig. 9.** Field emission current density (up to  $80 \text{ mA/cm}^2$ ) dependence of electric field.

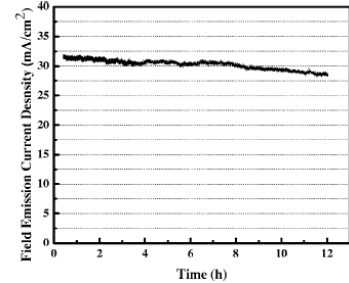


**Fig. 10.** Field emission current density stability as a function of time.

### Field emission of ZnO nanobelts

We have designed a new approach, molten salt-assisted thermal evaporation, and we demonstrated that this approach can produce aligned ultralong ZnO nanobelts over a large area. The key point of this new approach is the evaporation of metal Zn powder in a liquid environment of molten sodium chloride (NaCl) salt.

In a typical synthesis, 1 g of metal Zn powder was mixed with 8 g of NaCl and 4 mL of NP-9 (surfactant) in an agate mortar, then ground for 30 min by hand. The ground mixture was loaded into an alumina crucible covered with a gold (Au) sheet leaving about a 10% opening for vapor release. The whole assembly was placed in a box furnace and heated up to  $800 \text{ }^\circ\text{C}$  and held at that temperature for 2 h, then cooled to room temperature in air. Transparent, aligned ultralong ZnO nanobelts were obtained on the Au cover facing the vapor.

A side-view camera photograph of the as-grown ZnO nanobelts on the Au substrate is shown in Fig. 11(a), indicating that the nanobelts can grow to several millimeters in length. Figure 11(b) shows the SEM image of the as-grown ZnO nanobelts. Figure 11(c) shows a TEM image of an individual belt and its selected area electron diffraction (SAED) as the inset. The rectangular SAED spot pattern can be indexed based on a hexagonal wurtzite cell with lattice parameters  $a = 3.25$  and  $c = 5.21 \text{ } \text{Å}$ . Fig. 11(d) shows an HRTEM image of the belt shown in Fig. 11(c). The clear lattice fringes demonstrate that the nanobelt is highly crystallized. The spacing of  $0.52 \text{ nm}$  corresponds to the (0001) planes of ZnO. Detailed study of the SAED pattern indicates that the nanobelt grows along  $[0\bar{1}14]$ , with its top/bottom surface  $\pm(2\bar{1}10)$  and the side surfaces  $\pm(0\bar{2}2\bar{1})$ .

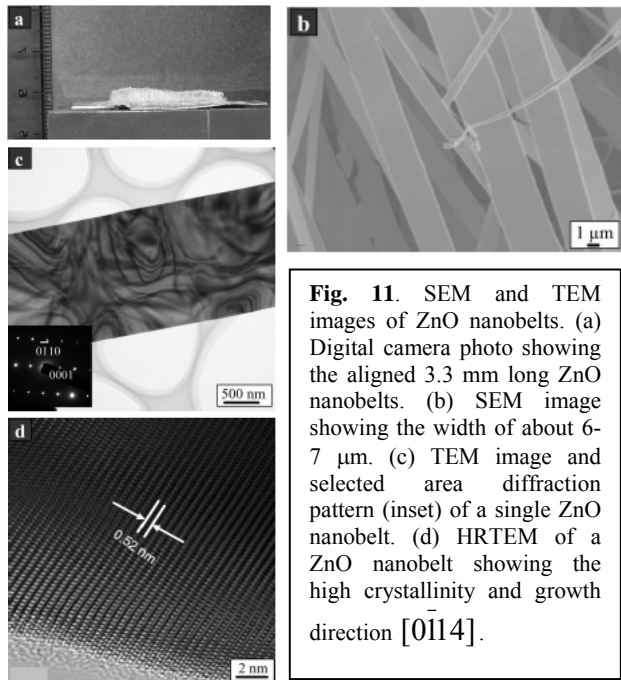


**Fig. 11.** SEM and TEM images of ZnO nanobelts. (a) Digital camera photo showing the aligned  $3.3 \text{ mm}$  long ZnO nanobelts. (b) SEM image showing the width of about  $6\text{--}7 \text{ } \mu\text{m}$ . (c) TEM image and selected area diffraction pattern (inset) of a single ZnO nanobelt. (d) HRTEM of a ZnO nanobelt showing the high crystallinity and growth direction  $[0\bar{1}14]$ .

A typical field emission  $I - V$  curve of the ZnO nanobelts is shown in Fig. 12(a). For the as-grown ZnO nanobelts, a turn-on electric field is  $1.3 \text{ V}/\mu\text{m}$ . An emission current density of  $1 \text{ mA/cm}^2$  (the minimum to produce the luminance of  $300 \text{ cd/m}^2$  for video graphics array field emission display with a typical high-voltage phosphor screen efficacy of  $9 \text{ lm/W}$ ) was achieved at  $2.9 \text{ V}/\mu\text{m}$ . Figure 12(b) shows the Fowler-Nordheim plot for the nanobelts, which fits well with the linear relationship given by  $\text{Log}(J/F^2) = \text{log}(A\gamma^2/\phi) - B\phi^{3/2}/\gamma F$ , where  $A = 1.54 \times$

$10^{-6} \text{ A eV V}^{-2}$ ,  $B = 6.83 \times 10^3 \text{ eV}^{-3/2} \text{ V } \mu\text{m}^{-1}$ ,  $\gamma$  is the field enhancement factor, and  $\phi$  is the work function of the emitting materials.

It is generally accepted that the intrinsic field enhancement of an individual nanowire is approximately proportional to the aspect ratio  $\ell/r$ , where  $\ell$  and  $r$  are the length and radius of the nanowire, respectively. In our present work, the average length of the ZnO nanobelts is 3.3  $\mu\text{m}$ , and the thickness of the belts is in the scale of nanometers. Therefore, the as-grown ZnO nanobelts have a very high field enhancement factor in the range of  $10^4 - 10^5$ , which was confirmed by calculating the field enhancement factor  $\gamma$  of  $1.4 \times 10^4$  from the slope of the straight line in Fig. 12(b), assuming  $\phi = 5.3 \text{ eV}$  for ZnO. Thus, we believe that the enhanced field emission of the aligned ultralong ZnO nanobelts is the result of their high field enhancement factor.

Acknowledgment: The work is supported by DOE DE-FG02-00ER45805.

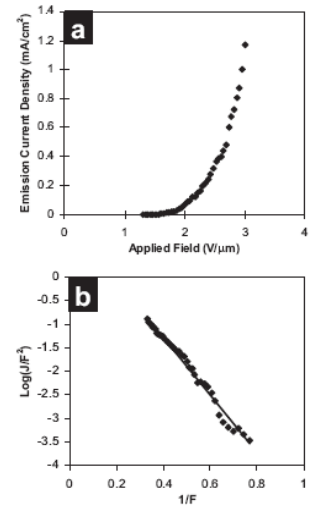


**Fig. 12.** Field emission from ZnO nanobelts. a)  $J$ - $F$  curve of the nanobelts. b) Fowler-Nordheim plot corresponding.

Program Title: Structure-Optical-Thermal Relationships of Carbon Nanotubes  
Principal Investigator: Li Shi  
Institution: University of Texas at Austin  
Address: 1 University Station, Austin, TX 78712  
Email: lishi@mail.utexas.edu  
DOE Grant Number: DE-FG02-07ER46377  
Collaboration: Prof. S. B. Cronin, University of Southern California

### **Program Scope or Definition**

This research aims to better understand the relationships between the crystal structure of different single wall carbon nanotubes (SWCNTs) and their optical and thermal properties as well as the electron transport and heat dissipation mechanisms. We have designed the following three experiments to explore several poorly understood phenomena in nanotubes. These experiments are being executed via the collaboration between the Cronin group and the Shi group.

1. Establish the structure-optical property relationships of carbon nanotubes using Raman and fluorescence spectroscopy on well-defined nanotubes, characterized by transmission electron microscopy (TEM).
2. Determine the structure-thermal property relationships of carbon nanotubes of different diameters and chiral angles, by performing thermal, optical, and TEM measurements on the same nanotube.
3. Quantify the temperature rise/distribution and contact thermal resistance in current-carrying carbon nanotubes, using Scanning Thermal Microscopy (SThM) and Spatial Mapping of Raman Spectroscopy (SMRS).

### **Recent Progress**

Carbon nanotubes are being explored for a broad range of applications including computing, thermal management, and energy conversion because of their superior electrical, mechanical, and thermal properties. Existing reported thermal conductivity measurement values of carbon nanotubes vary by over an order of magnitude. The variation is often attributed to different qualities of the nanotube samples. However, the crystal structures of the CNT samples in these thermal measurements were usually not well characterized.

During the first half year of this project, we have fabricated a modified design of a suspended micro-heater device to conduct thermal, TEM, and optical characterizations of individual nanotubes grown between the two suspended membranes of the device. Figure 1 shows the scanning electron micrograph (SEM) of the device. It consists of two adjacent  $20\ \mu\text{m} \times 20\ \mu\text{m}$  low-stress silicon nitride ( $\text{SiN}_x$ ) membranes each suspended with six  $420\text{-}\mu\text{m}$ -long and  $2\text{-}\mu\text{m}$ -wide  $\text{SiN}_x$  beams. One platinum resistance thermometer (PRT) serpentine is patterned on each membrane. A hole etched through the wafer under the suspended device allows for TEM measurement of the nanotube. To fit the device into the TEM holder, the thickness of the wafer is thinned down to about  $200\ \mu\text{m}$ . To grow a SWCNT between the two membranes of the micro-device, a sharp probe is used to deliver catalytic nanoparticles containing Fe, Mo and  $\text{Al}_2\text{O}_3$  onto the two membranes of the device. The device is then loaded into an  $800\text{-}900\ \text{°C}$  tube furnace with flowing methane. This chemical vapor deposition (CVD) method produces individual

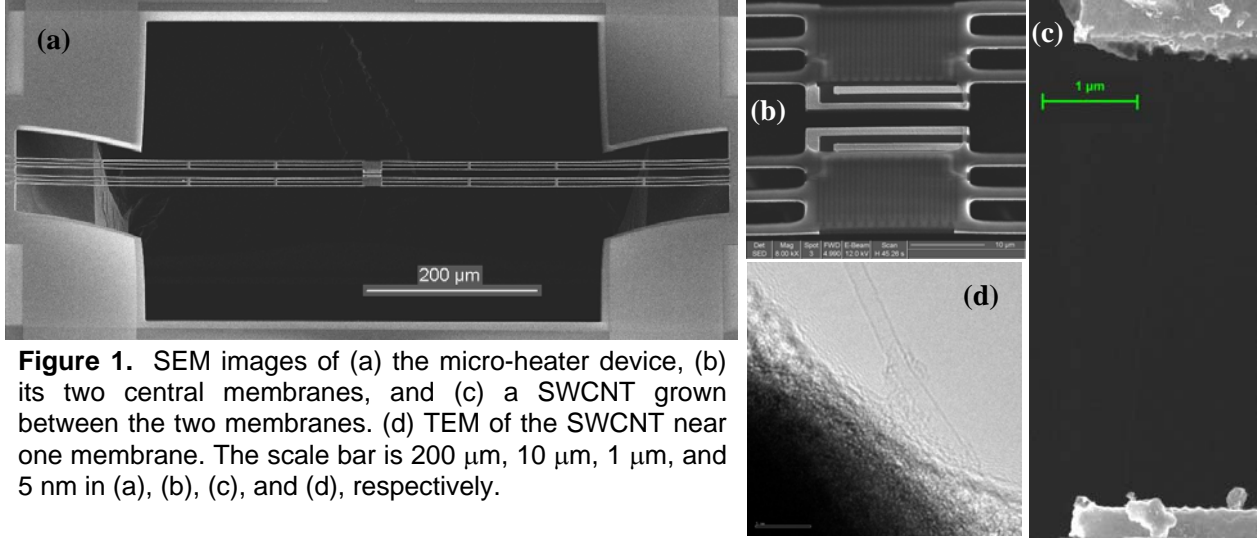


**Figure 1.** SEM images of (a) the micro-heater device, (b) its two central membranes, and (c) a SWCNT grown between the two membranes. (d) TEM of the SWCNT near one membrane. The scale bar is 200  $\mu\text{m}$ , 10  $\mu\text{m}$ , 1  $\mu\text{m}$ , and 5 nm in (a), (b), (c), and (d), respectively.

suspended SWCNTs bridging the two membranes, as shown in Fig. 1(c). TEM is used to characterize the diameter of the nanotubes. Figure 1(d) shows the TEM image of one nanotube with its diameter determined to be 1.6 nm.

The thermal conductance of the nanotube is measured with the sample placed in an evacuated cryostat of a temperature range between 4 and 800 K. The thermal conductance is obtained according to the following procedure. When a direct current ( $I$ ) is supplied to one PRT to raise the temperature of one membrane, part of the Joule heat generated is conducted through the nanotube to the other (sensing) membrane. The two PRTs are used to measure the temperature rises on the heating and sensing membranes at different  $I$  values, *i.e.*  $\Delta T_h(I) \equiv T_h(I) - T_h(I = 0)$  and  $\Delta T_s(I) \equiv T_s(I) - T_s(I = 0)$ , respectively. The thermal conductance ( $G_b$ ) of the six beams supporting each membrane and the thermal conductance ( $G_s$ ) of the nanotube sample are obtained as  $G_b = (Q_h + Q_L) / (\Delta T_h + \Delta T_s)$  and  $G_s = G_b \Delta T_s / (\Delta T_h - \Delta T_s)$ , where  $Q_h$  is the Joule heat dissipation in the PRT on the heating membrane and  $Q_L$  is the Joule heat dissipation in one of the two identical Pt leads supplying the current to the heating PRT.

Table 1 Diameter ( $d_t$ ), length ( $L_t$ ), and growth temperature ( $T_g$ ) of different nanotube samples. N/A = not available

	Sample 1	Sample 2	Sample 3	Sample 4	Sample 5	Yu et al.	Pop et al.
$d_t$ (nm)	N/A	N/A	1.63±0.01	1.13±0.26	1.84±0.20	N/A	1.7
$L_t$ ( $\mu\text{m}$ )	3.57±0.04	4.60±0.01	4.72±0.04	2.90±0.32	4.64±0.17	2.76	2.6
$T_g$ ( $^{\circ}\text{C}$ )	865	810	810	810	825	900	800-825

Figure 2 shows the obtained thermal conductance of five SWCNT samples measured in this work. The dimensions and the growth temperatures of these samples are shown in Table 1. The sample shown in Fig. 1(c-d) is Sample 3 in the Table. The measurement results show that the thermal conductance increases with temperature until about 500 K, beyond which the thermal conductance starts to decrease as a result of Umklapp phonon scattering. Compared with the calculated ballistic thermal conductance of a (18, 0) nanotube of 1.41 nm diameter, the measured thermal conductance results are approximately proportional to the ballistic thermal conductance

at temperatures below 500 K. Figure 3 shows the macroscopic thermal conductivity calculated from the measured thermal conductance, diameter, and length of three nanotube samples without accounting for the contact thermal resistance. The thermal conductivity is greater than 1000 W/m K above room temperature, reaches a peak of about 3000 W/m K at about 500 K, and exceeds that for diamond above 500 K.

The thermal conductivity peak is rather broad, and occurs at a much higher temperature than the corresponding temperatures of about 100 K for bulk graphite and diamond. This feature manifests that the influence of the Umklapp process is significant in the nanotube only at a much higher temperature than that for graphite and diamond. All these above observations suggest that phonon scattering at the two end boundaries or with defects in the finite-length nanotube dominate over the Umklapp process at temperatures below 500 K.

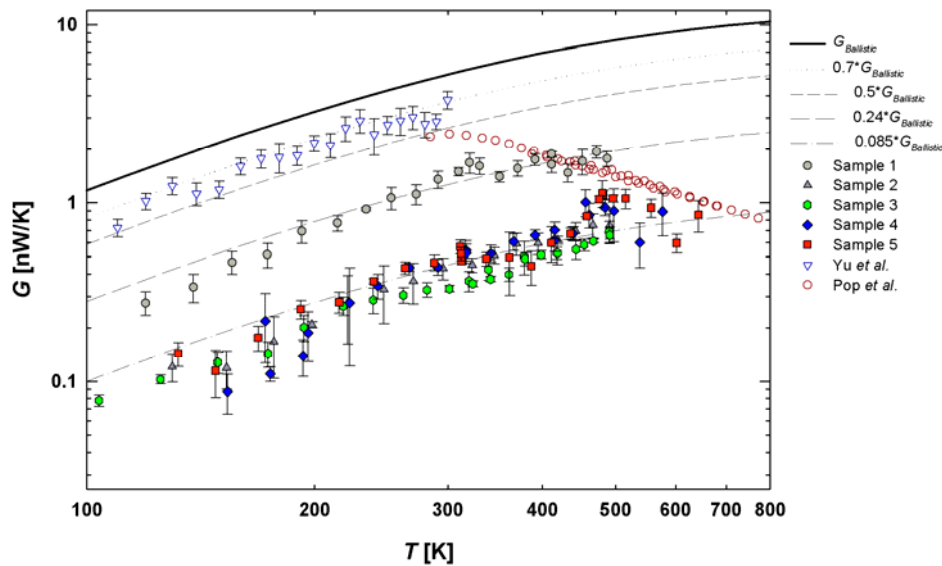


Fig. 2. Thermal conductance ( $G$ ) as a function of temperature for five SWCNT samples measured in this work and a sample measured in our previous work [Yu et al., Nano Lett. 5, 1842 (2005)]. Also plotted are different fractions of the ballistic thermal conductance ( $G_{Ballistic}$ ) of a 1.41 nm diameter, (18, 0) SWCNT calculated by Mingo and Broido, Phys. Rev. Lett. 95, 096105 (2005), and the thermal conductance extracted based on an electron transport model from the current-voltage characteristic of a SWCNT under high-bias self heating [Pop et al., Nano Lett 6, 96 (2006)].

The measured thermal conductance results exhibit a large variation up to a factor of 9 between samples grown at different temperatures, showing generally increasing thermal conductance with the growth temperature although the nanotube length and diameter vary among the samples. Moreover, the temperature dependence of the thermal conductance of our samples contrast with Pop et al.'s recently reported thermal conductance results extracted based on an electron transport model from the current-voltage characteristic of a SWCNT under high-bias self heating.

To better understand the variation and discrepancy, the contact thermal resistance to another nanotube sample grown on the suspended device has been characterized at the Cronin group using a Raman spectroscopy based technique [1] developed during the award period. The ratio of the contact thermal resistance to the intrinsic thermal resistance of the nanotube is determined to be 0.11 and 0.045, respective, for the left and right contact to the nanotube. The results are in

agreement with the calculation based on a fin heat transfer model between the nanotube and the supporting substrate. Combined Raman, thermal, and TEM measurement on the same nanotube will allow us to better understand whether the discrepancy between the different results is due to the differences in the contact thermal resistance and defect concentration or errors in the measurement method or the model.

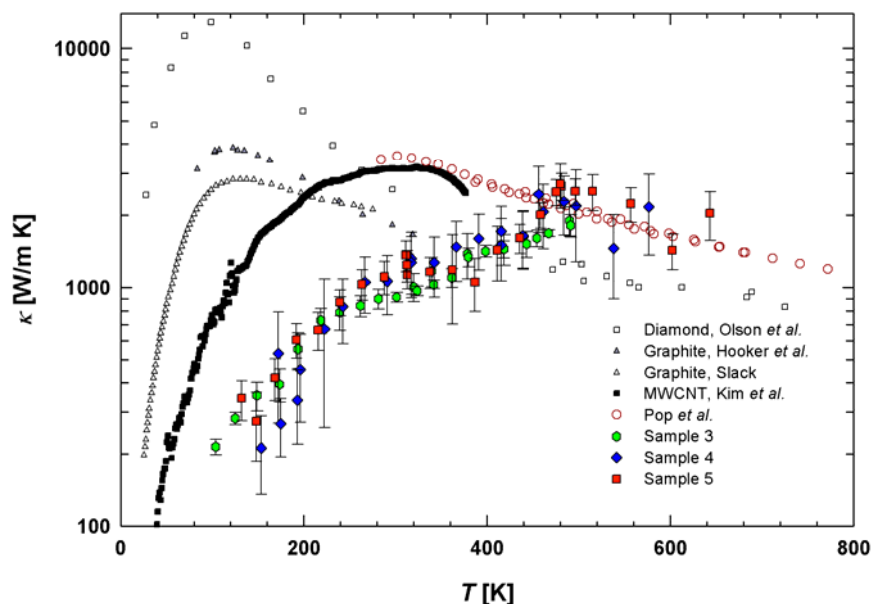


Fig. 3. Thermal conductivity ( $k$ ) as a function of temperature ( $T$ ) of three SWCNTs of this work, one CNT by Pop *et al.* [Nano Lett 6, 96 (2006)], one MWCNT by Kim *et al.* [Phys. Rev. Lett. 87, 215502 (2001)], graphite [Slack Phys. Rev., 127, 694 (1962); Hooker *et al.*, Proc. Royal Society London, Series A, Mathematical and Physical Sciences, 284, 1396 (1965)], and diamond [Olson *et al.*, 47, 14850 (1993)]

### Future Plans

For the remaining four months of the first year and the second year of this project, we have planned the following experiments:

1. Perform thermal, TEM and Raman measurements on the same nanotube so that the contact resistance obtained using the Raman measurement can be eliminated from the measured thermal conductance using the micro-device.
2. Establish the structure-optical property relationships of carbon nanotubes using Raman and fluorescence spectroscopy on well-defined nanotubes, characterized by TEM.
3. Quantify the temperature rise/distribution and contact thermal resistance in current-carrying carbon nanotubes using Scanning Thermal Microscopy combined with Spatial Mapping of Raman Spectroscopy

### References to publications of DOE sponsored research that have appeared in 2005-2007 or that have been accepted for publication.

1. I-K. Hsu, R. Kumar, A. Bushmaker, S. B. Cronin, M. T. Pettes, L. Shi, T. Brintlinger, M. S. Fuhrer, J. Cumings, "Optical Measurement of Thermal Transport in Suspended Carbon Nanotubes," Appl. Phys. Lett., accepted (2008)

# Nanogenerators for Self-Powered Nanotechnology

Zhong Lin Wang

School of Materials Science and Engineering, Georgia Institute of Technology, Atlanta GA 30332-0245  
USA

E-mail: zhong.wang@mse.gatech.edu

Developing novel technologies for wireless nanodevices and nanosystems are of critical importance for in-situ, real-time and implantable biosensing, defense technology, and even wearable personal electronics. A nanodevice requires a power source, which may be provided directly or indirectly by charging of a battery. It is highly desired for wireless devices to be self-powered without using battery. Therefore, it is essential to explore innovative nanotechnologies for converting mechanical energy, vibration energy, and hydraulic energy into electric energy that will be used to power nanodevices without using battery.

## 1. The principle of nanogenerators

We have demonstrated an innovative approach for converting nanoenabled technology for converting mechanical energy into electricity with the use of piezoelectric ZnO nanowires that can be grown effectively on any substrates (metals, ceramics, polymers, textile fibers) and any shape of substrates. Using piezoelectric ZnO nanowire (NW) arrays, we discovered an innovative phenomenon on converting nano-scale mechanical energy into electric energy [1, 2]. The measurements were performed by atomic force microscope (AFM) using a Si tip coated with Pt. In the AFM contact mode, a constant normal force of 5 nN was maintained between the tip and sample surface. The tip scanned over the top of the ZnO NWs, which were thus bent and then released (Fig. 1). The operation mechanism of the electric generator relies on the unique coupling of piezoelectric and semiconducting dual properties of ZnO.

## 2. DC nanogenerator driven by ultrasonic wave

In order to increase the output power, the essential task is to enable a large number of nanowires generating electricity continuously and simultaneously without using an AFM. We must make an innovative design to drastically improve the performance of the nanogenerator in following aspects. First, we must eliminate the use of AFM for making the mechanical deformation of the NWs so that the power generation can be achieved by an adaptable, mobile and cost-effective approach over a larger scale. Secondly, all of the NWs are required to generate electricity simultaneously and continuously, and all the electricity can be effectively collected and output. Finally, the energy to be converted into electricity has to be provided in a form of wave/vibration from the environment, so the nanogenerator can operate “independently” and wirelessly. We have developed an innovative approach that uses ultrasonic waves to drive a nanogenerator built from an array of vertically aligned ZnO NWs [3, 4].

The experimental set up is schematically shown in Fig. 2, in which an array of aligned ZnO NWs is covered by a zigzag Si electrode coated with Pt. The Pt coating is not only for enhancing the

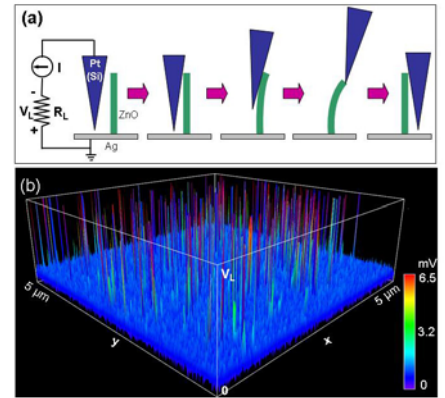


**Figure 1.** (a) Experimental set up and procedures for generating electricity by deforming a piezoelectric NW using a conductive AFM tip. (b) Output voltage image map of ZnO NW arrays.

conductivity of the electrode but also for creating a Schottky contact at the interface with ZnO. The NWs were grown on either GaN substrates, which served as a common electrode for directly connecting with an external circuit. The asymmetric piezoelectric-potential across the width of a ZnO NW and the Schottky contact between the metal electrode and the NW are the two key processes for creating, separating, preserving/accumulating, and outputting the charges. A top electrode is designed to achieve the coupling process and to replace the role played by the AFM tip, and its zigzag trenches are to act as an array of aligned AFM tips. The DC nanogenerator is driven by ultrasonic wave. Once the wave is on, a current output of 30 nA has been received from a nanogenerator of 2 mm<sup>2</sup> in size. The design is novel and cost-effective and has the potential to meet the requirements outlined above. The approach is the basic platform for optimizing and improving the performance of the nanogenerator for its applications in nanotechnology.

### 3. Fiber nanogenerators

Using piezoelectric ZnO nanowires (NWs) grown radially around textile fibers, a low-cost approach has been demonstrated for converting low-frequency (< 10 Hz) vibration/friction energy into electricity (Fig. 3). The design is based on two inter-twisted fibers that form a pair of “teeth-to-teeth brushes”, with one fiber covered with Au coated NWs and the other just by bare NWs. A relative brushing of the NWs rooted at the two fibers produces electricity owing to a coupled piezoelectric-semiconductor process. The optimum instantaneous output power density of a fabric is anticipated to reach up to ~5 W/m<sup>2</sup>. The research establishes the fundamental methodology of scavenging light-wind energy and body movement (heart beating, foot steps) energy using fabric based nanomaterials, making it possible for making flexible and foldable “power shirt/curtain/tent”.

The textile-fiber based nanogenerator has demonstrated the following innovative advances in comparison to the DC nanogenerators reported previously. First, using ZnO NWs grown on fibers, it is possible to fabricate flexible, foldable and wearable power source in any shape (such as “power shirt”). Secondly, the nanogenerator operates at low-frequency in the range of conventional mechanical vibration, foot steps and heart beating, greatly expanding the application range of nanogenerators. Finally, since the ZnO NW arrays were grown using chemical synthesis at 80 °C on a substrate with any curvature and materials nature, the fields to which the nanogenerators can be applied to have been greatly expanded

### Summary

The principle and technology demonstrated here have the potential of converting mechanical movement energy (such as body movement, muscle stretching, blood pressure), vibration energy (such as acoustic/ultrasonic wave), and hydraulic energy (such as flow of body fluid, blood flow, contraction of blood vessel) into electric energy that may be sufficient for self-powering nanodevices and nanosystems.

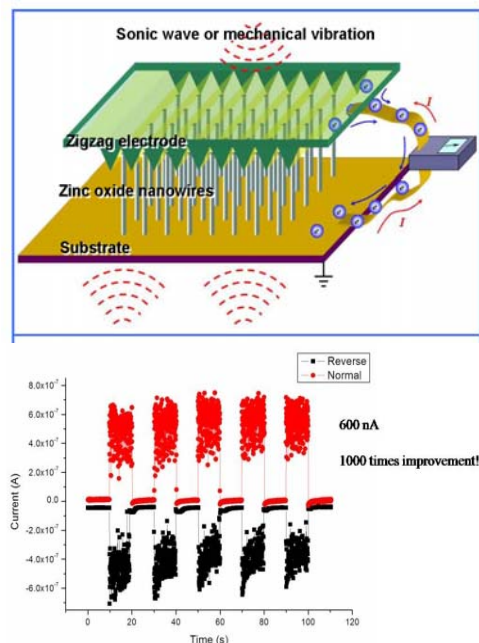
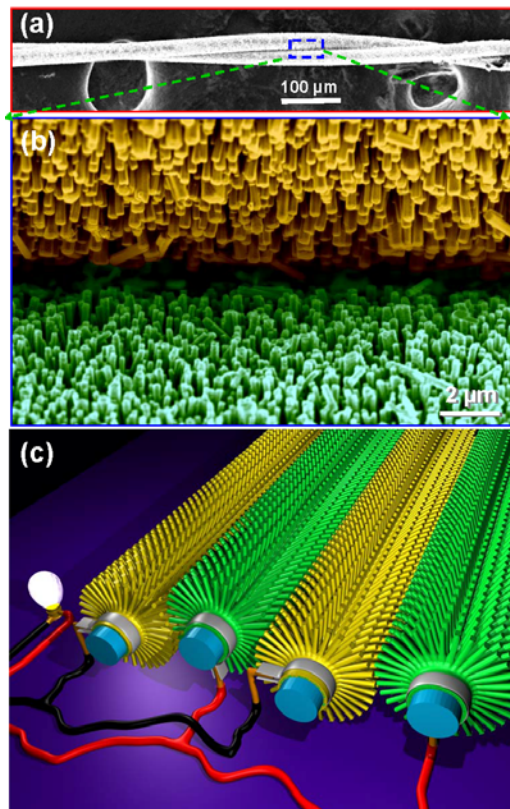


**Figure 2.** Schematic diagram showing the direct current nanogenerator built using aligned ZnO nanowire arrays with a zigzag top electrode. The nanogenerator is driven by an external ultrasonic wave or mechanical vibration and the output current is continuous. The lower plot is the output from a nanogenerator when the ultrasonic wave was on and off. The output current reached 600 nA for a 3 mm<sup>2</sup> size nanogenerator.

The prototype technology established by the DC nanogenerator set a platform for developing self-powering nanosystems with important applications in implantable in-vivo biosensing, wireless and remote sensing, nanorobotics, MEMS, sonic wave detection and more.

**Figure 3.:** (a) Scanning electron microscopy (SEM) image of two entangled microfibers that were covered radially with piezoelectric ZnO nanowires, with one of them coated with gold. The relative scrubbing of the two “brushes” generates electricity. (b) A magnified SEM image at the area where the two “brushes” meet teeth-to-teeth, with the top one coated with gold and the bottom one is as-synthesized ZnO nanowires. (c) A schematic illustration of the microfiber-nanowire hybrid nanogenerator, which is the basis of using fabrics for generating electricity.



### Acknowledgements.

This research was supported by BES-DOE, NSF, NASA, DARPA and NIH.

### References:

- [1] Z.L. Wang and J.H. Song “Piezoelectric Nanogenerators Based on Zinc Oxide Nanowire Arrays”, *Science*, 312, 242 (2006).
- [2] P.X. Gao, J.H. Song, J. Liu and Z.L. Wang “Nanowire Nanogenerators on Plastic Substrates as Flexible Power Source”, *Adv. Mater.*, 19, 67 (2007).
- [3] X.D. Wang, J.H. Song J. Liu, and Z.L. Wang “Direct current nanogenerator driven by ultrasonic wave”, *Science*, 316, 102 (2007).
- [4] Xudong Wang, Jin Liu, Jinhui Song, Zhong Lin Wang “Integrated Nanogenerators in Bio-Fluid”, *Nano Letters*, 7, 2475 (2007).
- [5] Yong Qin, Xudong Wang and Zhong Lin Wang ”Microfiber-Nanowire Hybrid Structure for Energy Scavenging”, *Nature*, 451 (2008) 809.

**Program Title: Lattice Dynamical Properties of Ferroelectric Thin Films at the Nanoscale**

**Principle Investigator: Xiaoxing Xi**

**Address: Penn State University, 104 Davey Lab, University Park, PA 16802**

**Email: xxx4@psu.edu**

## **Program Scope**

The objective of the program is to obtain a fundamental understanding of the lattice dynamical properties of epitaxial ferroelectric thin films at the nanoscale using Raman scattering. To study ferroelectric films at the nanoscale, ultraviolet (UV) excitation is used for the Raman experiments. Ferroelectrics have bandgaps in the UV range (e.g. about 3.4 eV for SrTiO<sub>3</sub>). When the Raman spectra are excited above the bandgap energy, the ferroelectric film absorbs the UV light, thus reducing or eliminating the substrate contribution to the spectra. UV excitation near the bandgap also leads to strong resonance enhancement of the Raman signal.

It is difficult to measure the ferroelectric phase transition temperature  $T_c$  in nanoscale ferroelectric systems and UV Raman spectroscopy is an effective technique for this important measurement. From the symmetry selection rules, phonons in cubic and paraelectric crystals are not Raman active, but they become Raman active in the tetragonal and ferroelectric phase. By measuring the temperature where the first-order phonon intensity becomes zero one can determine  $T_c$  accurately.

Multiferroicity is also a focus of the program. Multiferroics is an area of much active research with an abundance of basic science to be studied and novel applications to be explored. A ferromagnetic material has a switchable spontaneous magnetization arising from the ordering of the magnetic dipoles. A ferroelectric material has a switchable spontaneous polarization arising from the ordering of the electric dipoles. A ferroelastic material has a switchable spontaneous deformation. In a multiferroic material, at least two of the ferroic properties (ferroelectricity, ferromagnetism, and ferroelasticity) occur in the same phase. The possibility that these orders can couple with each other opens up opportunities for novel electronic devices.

## **Recent Progress**

1. Nanoscale ferroelectricity in BaTiO<sub>3</sub>/SrTiO<sub>3</sub> superlattices probed by UV Raman spectroscopy. We demonstrated that UV Raman spectroscopy is an effective technique to measure  $T_c$  in ferroelectric ultrathin films and superlattices. We showed that one-unit-cell-thick BaTiO<sub>3</sub> layers in BaTiO<sub>3</sub>/SrTiO<sub>3</sub> superlattices are not only ferroelectric (with  $T_c$  as high as 250 K) but also polarize the quantum paraelectric SrTiO<sub>3</sub> layers adjacent to them.  $T_c$  was tuned by ~500 K by varying the thicknesses of the BaTiO<sub>3</sub> and SrTiO<sub>3</sub> layers, revealing the essential roles of electrical and mechanical boundary conditions for nanoscale ferroelectricity. The higher-than-bulk  $T_c$  in superlattices with thicker BaTiO<sub>3</sub> illustrates the effects of strain on the ferroelectricity in nanoscale BaTiO<sub>3</sub> layers.

2. We have applied UV Raman spectroscopy to the investigations of acoustic properties of BaTiO<sub>3</sub>/SrTiO<sub>3</sub> superlattices. The superlattices made of piezoelectric oxides are proposed to

be used as acoustic Bragg mirrors and cavities with superior acoustic performance and potential applications in electronic and optical terahertz modulators. The phonon mirrors consisting of BaTiO<sub>3</sub>/SrTiO<sub>3</sub> superlattices on SrTiO<sub>3</sub> substrates were synthesized by reactive molecular-beam epitaxy and studied by UV Raman spectroscopy. The observation of folded acoustic phonons at the frequencies predicted by elastic continuum model demonstrates the feasibility to design, fabricate, and characterize oxide piezoelectric acoustic devices.

3. We have studied asymmetric SrTiO<sub>3</sub>/BaTiO<sub>3</sub>/CaTiO<sub>3</sub> superlattices prepared by Dr. Ho Nyung Lee of Oak Ridge National Lab. For the sample STO1/BTO1/CTO1, which has only one-unit-cell-thick layers of SrTiO<sub>3</sub>, BaTiO<sub>3</sub>, and CaTiO<sub>3</sub> in one period, we found that the ferroelectric  $T_c$  is 283 K. This is consistent with the observation of Dr. Lee of polarization hysteresis at room temperature. We have also measured  $T_c$  in samples STO2/BTO6/CTO2, STO2/BTO4/CTO2, CTO2/BTO4/STO2, and STO2CTO2BTO4STO2. The precise determination of  $T_c$  in these asymmetric superlattices is important for nanoscale ferroelectricity.

4. We have grown epitaxial and c-axis oriented thermoelectric Bi<sub>2</sub>Sr<sub>2</sub>Co<sub>2</sub>O<sub>y</sub> thin films using pulsed laser deposition. Strongly correlated layered cobalt oxides have attracted great attention as a promising thermoelectric material due to their high Seebeck coefficient, low electric resistivity, low thermal conductivity and stability in air at high temperature. The structure of Bi<sub>2</sub>Sr<sub>2</sub>Co<sub>2</sub>O<sub>y</sub> contains two subsystems: the CdI<sub>2</sub>-type CoO<sub>2</sub> nanosheet, which possesses strongly correlated electron system and serves as electric transport layers to achieve large Seebeck coefficient and low electric resistivity, and the distorted rock salt-type Bi<sub>2</sub>Sr<sub>2</sub>O<sub>4</sub> block which serves as phonon scattering regions to achieve low thermal conductivity. The films we have obtained exhibit large Seebeck coefficient and low resistivity at room temperature. A large negative in-plane magnetoresistance and nonlinear resistivity are also observed in the films at low temperature. Growing on the *n*-type Nb-doped SrTiO<sub>3</sub> substrate, thermoelectric *p-n* junctions are produced.

5. We have grown thin films of double perovskite Bi<sub>2</sub>FeCrO<sub>6</sub> (one half of the B positions in the ABO<sub>3</sub> structure are occupied by a B' ion). Bi<sub>2</sub>FeCrO<sub>6</sub> has been predicted by first-principles calculations to be a multiferroic material with large polarization and magnetization. Reports of Bi<sub>2</sub>FeCrO<sub>6</sub> thin films grown by pulsed laser deposition have proven the existence of multiferroicity, but the values of polarization and magnetization are much smaller than the theoretical predictions. Understanding of this discrepancy is important for the discovery of multiferroic materials with large polarization and magnetization and spin-charge coupling. We have grown epitaxial Bi<sub>2</sub>FeCrO<sub>6</sub> films on (001) SrTiO<sub>3</sub> substrate by pulsed laser deposition, and x-ray diffraction scan has shown ordering of the B-site in these films. This provides an ideal platform for the Raman spectroscopic study of multiferroicity.

## Future Plan

The objectives of future research are to advance the knowledge of ferroelectricity at nanoscale using UV Raman spectroscopy, and to probe spin-charge-lattice coupling with magneto-Raman spectroscopy in nanoscale multiferroic thin films.

Ferroelectric films and superlattices with their thickness being only several nanometers are interesting for basic sciences and important for devices. The PI has previously done ground breaking research using UV Raman spectroscopy to study nanoscale ferroelectric films and superlattices. This powerful new technique allowed his team to reveal how the ferroelectric phase transition depends on the thickness and boundary conditions of the nanoscale ferroelectric layers. In this project, the PI's group will continue working in this area to fully develop this technique and use it to its full potential. He plans to focus on single layer nanoscale ferroelectric films, ferroelectric layer under different epitaxial strain, and thin films and superlattices of various ferroelectric materials.

Multiferroics are materials in which different ferroic properties - ferroelectricity, ferromagnetism, and ferroelasticity - simultaneously exist and couple between each other. They present rich new physics and open doors for various novel devices. When the multiferroic film dimension is at the nanoscale, their ferroelectric and magnetic properties and the spin-charge-lattice coupling can be very different from those in the bulk materials. In this project, the PI will use magneto-Raman spectroscopy (Raman scattering in magnetic field) to investigate central issues of multiferroics, including the mechanisms of ferroelectricity and magnetism, the coupling between ferroelectric and magnetic orders, magnons and their strong coupling with phonons, the interfacial magnetoelectric effects, and the magnetization switching behavior by ferroelectric polarization through strain. The PI plans to investigate double perovskite multiferroic films, vertical heterostructures, strain-enabled multiferroics, ferroelectric/ferromagnet superlattices, as well as various multiferroic films from collaborators.

The proposed research activities will have significant impact on the understanding of nanoscale ferroelectricity and nanoscale multiferroicity. In particular, the combination of magnetic field with lattice dynamic study will be a powerful tool to probe the coupling among spin, charge, and lattice orders in multiferroic materials.

#### **Publications of DOE sponsored research (2005-2007)**

1. D. A. Tenne, X. X. Xi, A. V. Pogrebnikov, and J. M. Redwing, Raman scattering in pure and carbon-doped  $\text{MgB}_2$  films, *Phys. Rev. B* 71, 132512 (2005).
2. A. Venimadhav, A. Soukiassian, D. A. Tenne, Qi Li, X. X. Xi, D. G. Schlom, R. Arroyave, Z. K. Liu, H. P. Sun, Xiaoqing Pan, Minhyea Lee, and N. P. Ong, Structural and transport properties of epitaxial  $\text{Na}_x\text{CoO}_2$  thin films, *Appl. Phys. Lett.* 87, 172104 (2005).
3. D. A. Tenne, A. Bruchhausen, N. D. Lanzillotti-Kimura, A. Fainstein, R. S. Katiyar, A. Cantarero, A. Soukiassian, V. Vaithyanathan, J. H. Haeni, W. Tian, D. G. Schlom, K. J. Choi, D. M. Kim, C. B. Eom, H. P. Sun, X. Q. Pan, Y. L. Li, L. Q. Chen, Q. X. Jia, S. M. Nakhmanson, K. M. Rabe, X. X. Xi, Probing Nanoscale Ferroelectricity by Ultraviolet Raman Spectroscopy, *Science* 313, 1614 (2006).
4. A. Soukiassian, W. Tian, D. A. Tenne, X. X. Xi, D. G. Schlom, N. D. Lanzillotti-Kimura, A. Bruchhausen, A. Fainstein, H. P. Sun, X. Q. Pan, A. Cros, and A. Cantarero, Acoustic Bragg mirrors and cavities made using piezoelectric oxides, *Appl. Phys. Lett.* 90, 042909 (2007).

5. D. A. Tenne, I. E. Gonenli, A. Soukiassian, D. G. Schlom, S. M. Nakhmanson, K. M. Rabe, and X. X. Xi, Raman study of oxygen reduced and re-oxidized strontium titanate, *Phys. Rev. B* 76, 024303 (2007).
6. Y. L. Li, S. Y. Hu, D. Tenne, A. Soukiassian, D. G. Schlom, X. X. Xi, K. J. Choi, C. B. Eom, A. Saxena, T. Lookman, Q. X. Jia, and L. Q. Chen, Prediction of ferroelectricity in  $\text{BaTiO}_3/\text{SrTiO}_3$  superlattices with domains, *Appl. Phys. Lett.* 91, 112914 (2007).
7. Y. L. Li, S. Y. Hu, D. Tenne, A. Soukiassian, D. G. Schlom, L. Q. Chen, X. X. Xi, K. J. Choi, C. B. Eom, A. Saxena, T. Lookman, and Q. X. Jia, Interfacial coherency and ferroelectricity of  $\text{BaTiO}_3/\text{SrTiO}_3$  superlattice films, *Appl. Phys. Lett.* 91, 252904 (2007).

## Nanowire for Photonics and Energy Conversion

Peidong Yang

Department of Chemistry, University of California, Berkeley, CA 94720  
Materials Sciences Division, Lawrence Berkeley National Laboratory, Berkeley, CA 94720. Email: [p\\_yang@berkeley.edu](mailto:p_yang@berkeley.edu)

Semiconductor nanowires have witnessed an explosion of interest in the last several years due to advances in synthesis and the unique thermal, optoelectronic, chemical, and mechanical properties of these materials. The potential applications of single-crystalline nanowires are truly impressive, including computational technology, communications, spectroscopic sensing, alternative energy, and the biological sciences. While lithographic silicon processes are rapidly approaching their physical size limits, optical information processing promises to be a low-power, high-bandwidth alternative for the continuation of Moore's Law. In the context of global energy needs, low-cost solution-phase nanowire synthesis has also sparked interest in novel solar cell architectures which may play a significant role in the renewable energy sector. Additionally, the use of compact, integrated optical sensors can be envisioned for the detection of pathogenic molecules in the arena of national security or for the diagnosis and study of human disease. This breadth of application naturally requires a multidisciplinary community, including but not limited to materials scientists, chemists, engineers, physicists, and microbiologists, all converging to solve challenging problems at nanometer length scales. However, *sine qua non*, the materials must be synthesized and characterized before the exploration of their properties and applications can take place.

Semiconductor systems with photon, phonon and/or electron confinement in two dimensions offer a distinct way to study electrical, thermal, mechanical, and optical phenomena as a function of dimensionality and size reduction. These structures have cross-sectional dimensions that can be tuned from 5 to 500 nm, with lengths spanning hundreds of nanometers to millimeters. The vapor-liquid-solid crystal growth mechanism has been utilized for the general synthesis of nanowires of different compositions, sizes, and orientation.<sup>1</sup> Precise size control of the nanowires can be readily achieved using metal nanocrystals as the catalysts. Epitaxial growth plays a significant role in making such nanowire heterostructures and their arrays.<sup>2</sup> To this end, we have successfully synthesized superlattice nanowires<sup>3</sup> and core-sheath nanostructures. Achieving such high level of synthetic control over nanowire growth allows us to explore some of their very unique physical properties. For example, semiconductor nanowires can function as self-contained nanoscale lasers,<sup>4</sup> sub-wavelength optical waveguides,<sup>5</sup> photodetector and efficient nonlinear optical mixer.<sup>6</sup> It was also discovered that the thermoconductivity of the silicon nanowires can be significantly reduced when the nanowire size in the 20 nm region, pointing to a very promising approach to design better thermoelectrical materials.<sup>7</sup> In addition, semiconductor nanowire arrays can be used as potential substrates to achieve high energy conversion efficiency in photovoltaics.<sup>8</sup>

The rapid pace of research in the field of one-dimensional nanostructures is driven by the very exciting scientific challenges and technological potential of mesoscopic systems. Our synthetic capabilities continue to expand quickly, while progress with the difficult tasks of precision property control and assembly inches forward. There are several outstanding scientific challenges in the field that need to be addressed urgently, the most significant of which is the integration and interfacing problem. The ability to create high-density arrays is not enough: how to address individual elements in a high-density array and how to achieve precise layer-to-layer registration for vertical integration are just two of the many challenges still ahead.<sup>9,10</sup> To achieve reproducible nanostructural interfaces, semiconductor-semiconductor and metal-semiconductor alike, requires careful examination and understanding of the chemistry and physics occurring at the interface. Equally important is the very precise control of the size uniformity, dimensionality, growth direction, and dopant distribution within semiconductor nanostructures, as these structural parameters will ultimately dictate the functionality of the nanostructures. In particular, the physical significance of the dopant distribution and the interfacial junction, and their implications in device operation and performance, will likely require careful re-examination and/or re-definition at the nanometer length scale. Lastly, accurate theoretical simulations appropriate to the above-mentioned mesoscopic regime are becoming feasible with the enhanced computing power available, and should assist our understanding of many of these size- and dimensionality-controlled phenomena.

## Reference

---

<sup>1</sup> T. Kuykendall, P. Ulrich, S. Aloni, P. Yang, *Nature Materials*, 6, 951, 2007.

<sup>2</sup> T. Kuykendall, P. J. Pauzauskie, Y. Zhang, J. Goldberger, D. Sirbuly, J. Denlinger, P. Yang, *Nature Materials*, 3, 528, 2004.

<sup>3</sup> Y. Wu, R. Fan, P. Yang, *Nano. Lett.*, 2, 83, 2002.

<sup>4</sup> M. Huang, S. Mao, H. Feick, H. Yan, Y. Wu, H. Kind, E. Weber, R. Russo, P. Yang, *Science*, 292, 1897, 2001.

<sup>5</sup> M. Law, D. Sirbuly, J. Johnson, J. Goldberger, R. Saykally, P. Yang, *Science*, 305, 1269, 2004.

<sup>6</sup> Y. Nakayama, P. J. Pauzauskie, A. Radenovic, R. M. Onorato, R. J. Saykally, J. Liphardt, P. Yang, *Nature*, 447, 1908, 2007.

<sup>7</sup> A. I. Hochbaum, R. Chen, R. D. Delgado, W. Liang, E. C. Garnett, M. Najarian, A. Majumdar, P. Yang, *Nature*, 451, 163, 2008

<sup>8</sup> M. Law, L. E. Greene, J. C. Johnson, R. Saykally, P. Yang, *Nature Materials*, 4, 455, 2005.

<sup>9</sup> A. Jamshidi, P. J. Pauzauskie, P. J. Schuck, A. T. Ohta, P. Chiou, J. Chou, P. Yang, M. C. Wu, *Nature Photonics*, 2, 85, 2008.

<sup>10</sup> P. Pauzauskie, A. Radenovic, E. Trepagnier, H. Shroff, P. Yang, J. Liphardt, *Nature Mater.* 5, 97, 2006.

## **Session II: Novel Electronic Materials**

## Atomic Processes and Defects in Wide-Bandgap Semiconductors

Andrew M. Armstrong, Robert M. Fleming, Sam M. Myers, Alan F. Wright (PI)

Email contact: [afwrigh@sandia.gov](mailto:afwrigh@sandia.gov)

Sandia National Laboratories, Albuquerque, NM 87185

### Program Scope

The attainable optoelectronic properties of AlGaInN semiconductors are seriously constrained by defect, impurity, and doping effects whose atomistic origins are poorly or incompletely understood. Further progress in the application of these materials will be greatly facilitated by a fundamental understanding of the properties and behaviors of solutes and defects. This is the objective of this research.

To achieve this objective, electrical, optical, spectroscopic, and compositional analyses are carried out under a variety of experimental conditions and the results are interpreted through modeling which utilizes atomic configurations and energies obtained from density-functional-theory (DFT). This multifaceted approach yields a unified, predictive description of solute and defect behavior that, in certain respects, goes beyond what has heretofore been achieved for semiconductors. Under study are the most consequential impurities (H, C, O), dopants (Mg, Si), and point defects (vacancies and self-interstitials), with investigated properties including atomic configurations, equilibrium state populations, energy levels in the gap, diffusion, solute-defect reactions, uptake and release at the surface, and the effects of electron and ion irradiation. The most extensive research to date has focused on the important behaviors of H and point defects and their detrimental impact on electrical conductivity in *p*-type GaN(Mg).

### Recent Progress

#### Defects produced during proton irradiation of *p*-type GaN(Mg,H)

We observed that when *p*-type Mg-doped GaN containing H or  $^2\text{H}$  was irradiated with 1-MeV protons and then isochronally annealed at a succession of increasing temperatures, the IR absorption by the MgH complex was replaced with an upwardly shifted peak ( $+12\text{ cm}^{-1}$  for  $^1\text{H}$  and  $+9\text{ cm}^{-1}$  for  $^2\text{H}$ ) in a stage near  $300^\circ\text{C}$  [1]. The modest size of this shift strongly suggests that the MgH complex remains intact but is modified by the approach of a mobile point defect created by the irradiation. Based on indications that Ga Frenkel pairs recombine near room temperature and density-functional-theory (DFT) results indicating that the activation energy for N vacancy diffusion is large [2], we hypothesized that the mobile species is the N interstitial ( $\text{N}_i$ ) [1]. In support of this hypothesis, DFT calculations identified a stable  $\text{MgHN}_i$  complex for which the perturbation of the H stretch-mode vibration frequency is small and upward relative to the MgH complex [3]. Fig. 1 shows IR absorption spectra of the GaN(Mg, $^2\text{H}$ ) samples before and after irradiation and anneals. Also shown are the atomic configurations obtained from DFT calculations and believed to be responsible for the two IR absorption peaks shown in the spectra. We performed additional experiments to extract the diffusion activation energy of the mobile species [4] and DFT calculations to obtain the activation energy for  $\text{N}_i$  diffusion in *p*-type GaN [5]. Experimental data were obtained by first irradiating GaN(Mg, $^2\text{H}$ ) with 1 MeV protons to create a uniform distribution of  $\text{N}_i$  and  $\text{V}_\text{N}$ , and then monitoring the  $^2\text{H}$ -stretch vibration modes of the  $\text{Mg}^2\text{H}$  center and of the center identified as  $\text{Mg}^2\text{HN}_i$  during anneal treatments. Analysis of data from a sequence of isothermal anneals yielded an activation energy of 1.99 eV for diffusion of the mobile species. DFT calculations [5] were performed to identify diffusion paths for  $\text{N}_i$  in *p*-type GaN and obtain the activation energies along these paths. The calculations were performed for the +1, +2, and +3 charge states, which are expected to be dominant in *p*-type GaN. Two paths were identified: one yields  $\text{N}_i$  movement perpendicular to the GaN *c*-axis and the other yields movement both perpendicular and parallel to the *c*-axis. The activation energies along the latter path are 1.98 eV for the +3 charge state, 2.12 eV for the +2 charge state, and 1.79 eV for the +1 charge state. These results agree well with the value obtained from the experiments, providing support for the hypothesis that  $\text{N}_i$  is the mobile species observed in proton irradiated *p*-type GaN(Mg,H).

### Theory and modeling of the nitrogen vacancy in $p$ -type GaN(Mg,H)

The N vacancy ( $V_N$ ) is widely believed to compensate Mg acceptors in GaN and thereby contribute to the difficulty of  $p$ -type doping. However, experimental evidence for this is largely indirect, and heretofore there has not been a theoretical basis for prediction. To advance understanding of the GaN(Mg,H) system, we performed a multifaceted theoretical study to describe the reactions and thermodynamics of  $V_N$  at the elevated temperatures relevant to growth and processing. First, DFT was used to obtain the configurations and formation energies of the multiple charge states of  $V_N$ , its binary complexes with Mg and H, and the ternary complex  $MgV_NH^{+1}$  [6]. Then, the phonon modes of GaN containing  $V_N$  were calculated using DFT [6], thereby allowing the finite temperature contribution to the incremental free energies of the defects to be quantified for the first time.

The above results, together with our prior DFT calculations for the stable and metastable states of interstitial  $H^+$  and the MgH complex [7], were incorporated into a detailed analysis of the elevated-temperature thermodynamics of  $V_N$  and its complexes. The number of distinct species involved was 19 including multiple charge states. Key results from the thermodynamic modeling are shown in Fig. 2, which presents a series of calculations for different Mg concentrations. The  $p$ -type GaN(Mg,H) was assumed first to equilibrate in  $H_2$  gas at  $1000^\circ\text{C}$ , corresponding to representative growth conditions, and then to undergo cooling to  $25^\circ\text{C}$ , accompanied by H outgassing but no change in the number of vacancies whose diffusion is much slower. The combined concentration of all  $V_N$ -related species is seen to rise rapidly with Mg concentration, leading to a pronounced reduction in the room-temperature hole concentration, due to compensation above about  $10^{19}$  Mg/cm $^3$ . The predicted maximum in hole concentration as a function of Mg concentration has in fact been observed by a number of investigators, including us. Our findings thus indicate that  $V_N$  figures importantly in the difficulty of  $p$ -doping at high Mg concentrations.

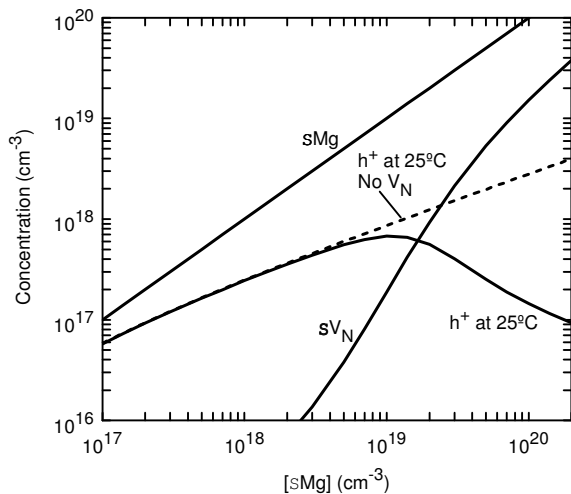


**Fig. 2.** Predicted concentrations of  $V_N$  and holes, plotted as a function of Mg concentration.

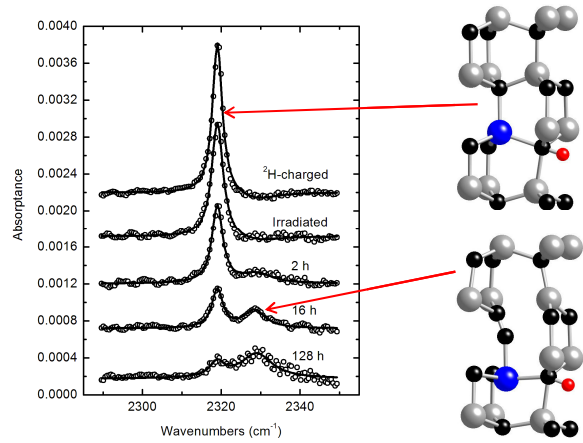


**Fig. 1.** Left: IR absorption spectra of GaN(Mg, $^2\text{H}$ ) before and after 1 MeV proton irradiation and anneals at  $250^\circ\text{C}$ . Right: Configurations from DFT calculations for MgH (upper) and  $MgHN_1$  (lower). Grey spheres denote Ga, black spheres denote N, blue spheres denote Mg, and red spheres denote H. Arrows indicate the atomic configurations believed to be responsible for the IR absorption peaks.

### $p$ -type doping of InGaN

Achieving large hole concentrations remains difficult because of the depth of the Mg acceptor level ( $\sim 170$  meV). As a result, large Mg concentrations ( $\sim 5 \times 10^{19}$  cm $^{-3}$ ) are required to obtain even modest hole concentrations ( $\sim 5 \times 10^{17}$  cm $^{-3}$ ). Alloying GaN(Mg) with InN can lower the Mg acceptor level ( $\sim 80$  meV in  $\text{In}_{0.20}\text{Ga}_{0.80}\text{N}$ ) and correspondingly increase the hole concentration. The origin of the decrease in the Mg acceptor level is not currently understood and in an effort to understand this property we recently began an investigation of  $p$ -type InGaN(Mg).

We grew  $p$ -type GaN and  $\text{In}_{0.05}\text{Ga}_{0.95}\text{N}$  using MOCVD. The In content was determined using x-ray diffraction and the electrical properties were characterized from Hall measurements. In GaN(Mg),

the maximum hole concentration was found to be  $\sim 4 \times 10^{17} \text{ cm}^{-3}$  while in InGaN(Mg) the maximum hole concentration was  $\sim 8 \times 10^{17} \text{ cm}^{-3}$ . To examine the possible role of hydrogen in InGaN(Mg), H was introduced during MOCVD growth of GaN(Mg) in attempt to form MgH centers. A post-growth anneal is required to remove the H and activate the *p*-type Mg doping. In GaN(Mg,H), the concentration of the MgH centers before and after the anneal might be determined by measuring the IR absorption of the H stretch-mode vibration associated with the MgH center. To determine if H is also present in as-grown InGaN(Mg), a 1.5  $\mu\text{m}$  thick InGaN(Mg) region was grown on a thick GaN layer and FTIR measurements were performed. These measurements showed no peak associated with an MgH center, and Hall measurements yielded a hole concentration about a factor of 10 lower than for a thinner InGaN film. In order to make sense of these results, we performed SIMS measurements of the Mg, H, C, O, and Si concentrations. From these results it is seen that the Mg concentration increases at a depth of  $\sim 1.5 \mu\text{m}$ , which is where the InGaN growth begins and the concentration of H is near its background level ( $\sim 2 \times 10^{17} \text{ cm}^{-3}$ ). As the InGaN thickness increases, the film begins to roughen, and impurity concentrations (H, C, O, and Si) increase substantially. The increase in these impurity concentrations is thought to occur due to more facile incorporation on the roughened surface. The increase in the *n*-type impurities (O and Si) may explain the lower than expected hole concentration in this InGaN as compared with the results for thinner samples. The results to date seem to indicate that unlike GaN(Mg), H is not incorporated into InGaN(Mg) and Mg thus is likely activated in the as-grown material.

## **Future Plans**

### Addition of DLTS and DLOS capabilities

We propose to add deep level transient spectroscopy (DLTS) and deep level optical spectroscopy (DLOS) to our suite of experimental capabilities. Both will be used to determine quantitative defect signatures such as the thermal and optical activation energy  $E_a$  and the corresponding defect concentration  $N_t$ . Similar to photocapacitance, DLOS can optically probe deep levels ranging from  $\sim 0.5 - 5 \text{ eV}$ , so a complimentary application of DLTS and DLOS can survey the entire bandgap of nitride alloy system. DLOS and DLTS are quantitative in both  $E_a$  and  $N_t$ . These experimental values will be compared to DFT values calculated for candidate defect states, thus providing a way to identify the defect responsible for the observed bandgap states, or at least allow us to rule out certain candidates.

Specifically, we propose to first apply DLOS/DLTS to study defects in *p*-type GaN(Mg) grown at Sandia using MOCVD. Most previous studies of *p*-type GaN(Mg) employed DLTS to study majority carrier traps and thus were limited to observing traps within  $\sim 1 \text{ eV}$  of the valence band edge, leaving much of the bandgap uninvestigated. A technique such as DLOS is required for comprehensive investigations of electrically active defects throughout the entire bandgap of *p*-type GaN(Mg). Our intent is to use both DLTS and DLOS to perform a complete survey of electrically active defects in *p*-type GaN(Mg) as a function of Mg concentration to determine the mechanism responsible for hole saturation. The experimental results will be correlated with DFT results described in the previous section and provide a means to validate the calculations.

### Enhancement of DFT capabilities

We propose to begin using a Sandia-developed DFT code [8] for our group-III nitride defect studies to permit greater supercell size. This is an important advance because the reliability of DFT calculations increases with the size of the supercell. The Sandia code (Socorro) is highly parallelized and can efficiently utilize hundreds of processors in a calculation. Moreover, this code can perform projector-augmented wave (PAW) calculations and thereby efficiently treat the *N* *p* electrons and the highest-energy Ga and In *d* electrons. Our first task will be to generate and test PAW functions for Ga, N, Mg, and H. The tests will include selected calculations for defects examined previously by us and comparison of the results with our prior results obtained using the VASP code. We will then proceed to examine the supercell size dependence of the results obtained for defects in GaN(Mg) and refine our model parameters based on the results.

We also propose to implement in Socorro the capability to compute the dynamical matrix of defect supercells. The phonon frequencies obtained from these dynamical matrices will be used to obtain finite temperature contributions to defect free energies within the harmonic approximation. These contributions will enable us to improve our modeling results, including our estimates of equilibrium

defect concentrations at elevated temperatures. Comparison of these concentrations with values obtained from DLTS or DLOS measurements will help us to identify the defects responsible for the DLTS or DLOS signals, or at least allow us to rule out certain candidates.

### Studies of $p$ -type doping in InGaN

To make progress in understanding  $p$ -type doping in InGaN, we will first address the undesired roughening that occurs when growing samples more than 0.5 mm thick. To prevent the roughening observed in thicker films, the InGaN may need to be structured differently by either strain relaxing the InGaN layer earlier on by or building the  $p$ -type InGaN film using a superlattice approach with high temperature GaN grown between thick InGaN layers. Because no MgH FTIR peak is observed in the existing InGaN(Mg) sample, it will be intentionally loaded with deuterium (D) and we will search for a MgD FTIR peak, similar to what we did in our earlier studies of GaN(Mg,D) [1]. If this peak is found, we will then perform annealing studies to obtain a better understanding of D in InGaN(Mg,D). We may also attempt to perform FTIR measurements of MgD on thinner samples since the sensitivity of FTIR for the MgD peak is greater than for the MgH peak. Depending on the outcome of the FTIR measurements, DFT may be used to determine the configurations and associated formation energies of H in bulk  $p$ -type InGaN and the configuration and binding energy of the MgH center in InGaN(Mg,H).

### **References**

---

- [1] S. M. Myers and C. H. Seager, J. Appl. Phys. 97, 093517 (2005).
- [2] A. F. Wright and T. R. Mattsson, J. Appl. Phys. 96, 2015 (2004).
- [3] R. R. Wixom and A. F. Wright, Phys. Rev. B 72, 024114 (2005).
- [4] R. M. Fleming and S. M. Myers, J. Appl. Phys. 100, 043513 (2006).
- [5] R. R. Wixom and A. F. Wright, J. Appl. Phys. 100, 123108 (2006).
- [6] S. M. Myers, A. F. Wright, M. Sanati, and S. K. Estreicher, J. Appl. Phys. 99, 113506 (2006).
- [7] A. F. Wright, C. H. Seager, S. M. Myers, D. D. Koleske, and A. A. Allerman, J. Appl. Phys. 94, 2311 (2003).
- [8] See <http://dft.sandia.gov/socorro>.

### **DOE Sponsored Publications 2005-2007**

1. *Density functional theory investigation of N interstitial migration in GaN*, R. R. Wixom and A. F. Wright, J. Appl. Phys. 100, 123108 (2006).
2. *Measurement of temperature-dependent defect diffusion in proton-irradiated GaN(Mg,H)*, R. M. Fleming and S. M. Myers, J. Appl. Phys. 100, 043513 (2006).
3. *Theoretical properties of the N vacancy in p-type GaN(Mg,H) at elevated temperatures*, S. M. Myers, A. F. Wright, M. Sanati, and S. K. Estreicher, J. Appl. Phys. 99, 113506 (2006).
4. *N interstitial and its interaction with substitutional Mg in p-type GaN*, J. Appl. Phys. 98, 033704 (2005).
5. *Binding of the N interstitial with neutral MgH in p-type GaN investigated with density functional theory*, R. R. Wixom and A. F. Wright, Phys. Rev. B 72, 024114 (2005).
6. *H enhancement of N vacancy migration in GaN*, Appl. Phys. Lett. 87, 201901 (2005).
7. *Substitutional and interstitial oxygen in wurtzite GaN*, A. F. Wright, J. Appl. Phys. 98, 010353 (2005).
8. *Interaction of defects and H in proton-irradiated GaN(Mg,H)*, S. M. Myers and C. H. Seager, J. Appl. Phys. 97, 093517 (2005).

## Doped Semiconductor Nanomaterials for Solid State Lighting Applications

PI: Frank Bridges<sup>a</sup>, Co-PI's: Sue Carter<sup>a</sup>, and Jin Z. Zhang<sup>b</sup>,

e-mail addresses: [bridges@physics.ucsc.edu](mailto:bridges@physics.ucsc.edu); [sacarter@ucsc.edu](mailto:sacarter@ucsc.edu); [zhang@chemistry.ucsc.edu](mailto:zhang@chemistry.ucsc.edu)

a) Department of Physics, University of California Santa Cruz

b) Department of Chemistry and Biochemistry, University of California Santa Cruz

The electroluminescent (EL) material ZnS :Cu, Cl and similar phosphors have the unusual property that under AC excitation they exhibit bright blue-green electroluminescence at electric fields 100 times smaller than for DC driven devices. Because these materials have high external quantum efficiencies (> 50%), long device lifetimes combined with low operating voltages would result in low cost, high power efficiency devices, providing a breakthrough in next generation solid state lighting. A crucial aspect of the low voltage operation is the formation of Cu<sub>x</sub>S precipitates, even at low Cu concentrations (0.15%), where it is assumed that holes and electrons are injected into the ZnS from opposite ends of the Cu<sub>x</sub>S precipitates each time the voltage is reversed. A fundamental unsolved challenge is understanding how the charge injection, transport and recombination are affected by this novel nanostructure and the implications of this structure for device efficiency and lifetime. For example, changes in the local atomic structure induced by high AC electric fields results in a decrease in EL over time; this aging effect has previously been shown to progress faster for smaller ZnS particle sizes.

In a preliminary study (Warkentin, PRB **75**, 075301, 2007), we showed that the main Cu precipitate looks like CuS at the nearest neighbor level (from EXAFS), and more importantly that the EL degradation could be significantly reversed by an anneal at 200C. Building upon these results, we are studying how this degradation/rejuvenation is affected for a wider range of temperatures, for which we expected, but did not observe, changes in the CuS precipitates; we have also extended our studies to samples containing orange-emitting Mn dopants to understand the role of the emissive sites. Typically, a 100V square wave at 100 kHz was used to degrade the EL in 20 hours to about 20% of initial intensity, an affect that is largely independent of doping type. Using a 2 hour annealing time, the optimum annealing temperature is 180C as shown in Fig. 1. At this temperature the rejuvenation can approach 70%, with most of the rejuvenation occurring in the first 10 minutes as shown in Fig. 2. We also found that annealing as-prepared samples at the slightly higher temperature of 240C strongly degrades the AC EL, such that no significant rejuvenation ever occurs after a 240 anneal. Finally we have shown that this degradation/rejuvenation cycle can be repeated several times but each time the rejuvenated emission is decreased; after 5-6 cycles the rejuvenation is small. Similar results were observed for the Mn-doped samples, with annealing resulting in recovery for both the orange and blue emitting sites, indicating that the nature of the emissive site is not critical to the degradation mechanism. The strong sensitivity of the rejuvenation with minor changes in temperatures suggest that local diffusion effects are important.

Another means of monitoring the EL intensity under degradation and rejuvenation is to image one of the 20 μm ZnS particles; the EL emission emanates from many bright points as shown in Fig. 3. During degradation, many of these points “disappear” (intensity falls below the CCD camera threshold), and the number of emission spots slowly decreases with time as shown in Fig. 4. Upon annealing, most of the spots that disappeared reappear and no new emission sites are formed within our spatial resolution. For the Mn-doped samples, we observed both blue and orange emissive centers which exhibited similar decay dynamics based on our preliminary data. Our next step will be to perform a systematic study of as a function of doping and particle size.

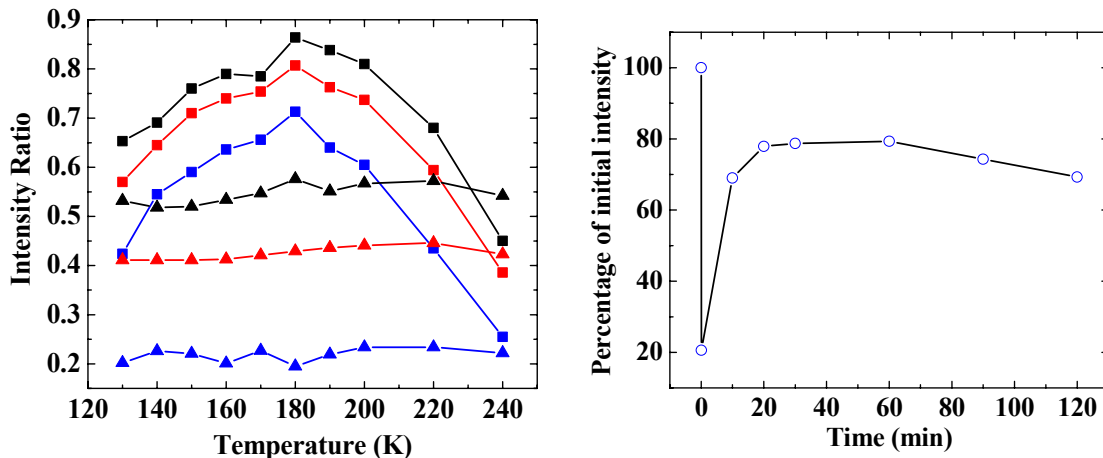


Figure 1 (Left) Lower curves: degraded intensities after 20 hours operation - 1 kHz (black triangle), 5 kHz (red triangle), 100 kHz (blue triangle). Top 3 curves: ratio of EL intensity after annealing to initial intensity for 1kHz (black square), 5 kHz (red square), 100 kHz (blue square).

Figure 2 (Right) Plot of increased EL intensity after several consecutive short (~10-20 min) anneals. Most of the rejuvenation occurs in the first 10 minutes with a peak at one hour. Annealing temperature 200C. Points at zero time – initial intensity and degraded intensity (20%).

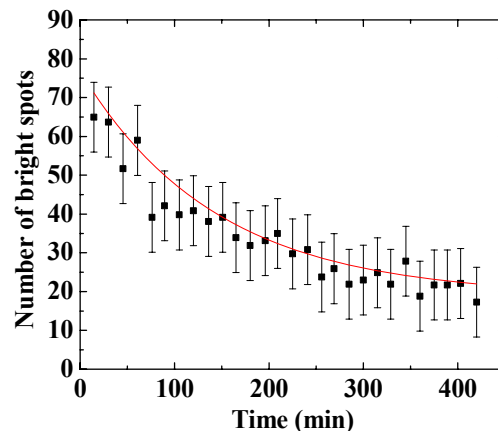
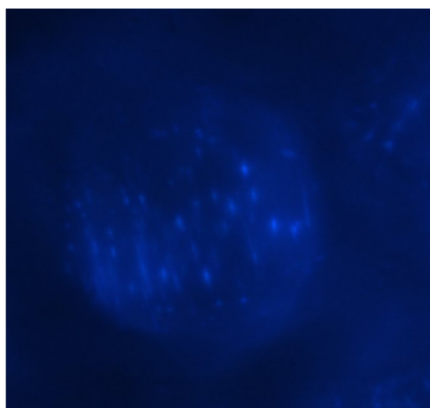


Figure 3 (Left) Microscope image of 20µm particle showing many points of light emission.

Figure 4 (Right) Plot of the number of visible spots as a function of time during degradation.

To probe for changes in the local atomic structure about the Cu sites, we collected Extended X-ray Absorption Fine Structure (EXAFS) data at the Cu K-edge EXAFS data for several as-made, thermally degraded (240C anneal), and (EL) degraded powders.

After data reduction, the EXAFS k-space data were Fourier transformed to r-space (k range, 3-11.5  $\text{\AA}^{-1}$ ; window Gaussian broadened by 0.3  $\text{\AA}^{-1}$ ). In Fig. 3 we show the EXAFS r-space data measured at 3 K for all the samples – See caption for details. It is obvious that, within errors, the local structure around Cu atoms for each sample is almost identical out to 8 $\text{\AA}$ , particularly between as-made and EL degraded or thermally degraded (240C anneal) samples for the first (Cu-S) peak. The main CuS-like nano-precipitates are not significantly changed by thermal anneals or AC voltages that degrade the EL. This indicates that at most the CuS-like nano-precipitates change shape slightly – e.g. possibly sharp points/edges become rounded.

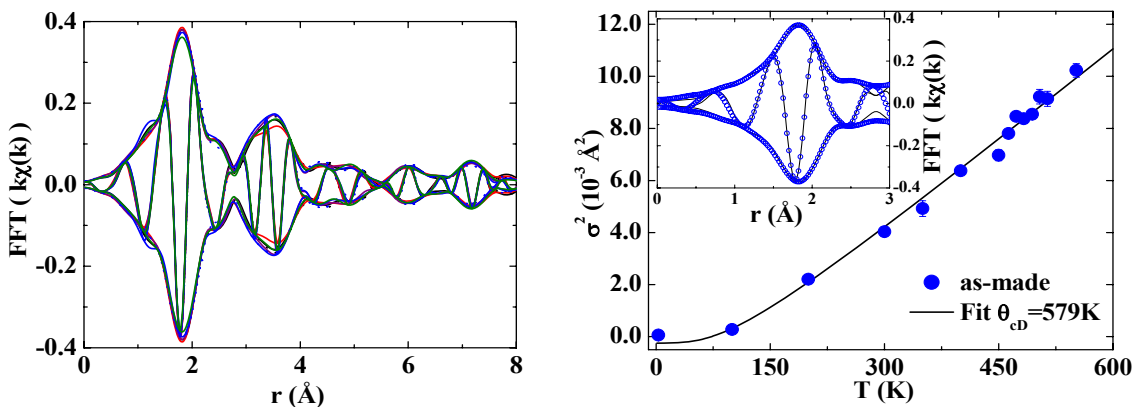


Figure 3 (Left) Overlay of the Fourier transformed EXAFS data for six samples at 3K: as-made ZnS:Cu (solid black), thermally degraded at 240C (black dotted), ZnS:Cu #2 (red), ZnS:Cu #3 (green), Cu,Mn co-doped (blue), Cu,Mn co-doped and degraded (blue-dot) ZnS:Cu #4 -green emission (purple); k-range 3-11.5Å.

Figure 4 (Right) Plot of  $\sigma^2$  vs T for an as-made ZnS:Cu,Cl sample (blue dots); correlated Debye fit (solid black line) gives a correlated Debye temperature of 579K. Inset shows a fit to the first peak using a CuS reference –fit range 1.1-2.5Å

To further investigate possible structural differences (particularly for the temperature range 200-240C over which the effect of thermal annealing changes from rejuvenation to degradation) we collected EXAFS data as a function of T from 3-550K. Based on our earlier work we again fit the first peak (1.1-2.5Å) using an experimental CuS standard and again obtained an excellent fit - see inset of Fig. 4. The main figure is a plot  $\sigma^2$  vs temperature for the as-made sample; the correlated Debye fit is shown as a solid line (Debye temperature - 579 K). For the first neighbor peak there is no indication of a significant change in coordination or bond length between 200 and 240C (473-513K) and  $\sigma^2(T)$  is a smooth function of T. Thus most of the CuS-like nano-crystals in ZnS have the same structure as bulk CuS up to 3 Å. The EL or thermal degradation does not strongly affect the CuS precipitates, except possibly the shape. Future EXAFS work will include a detailed study of CuS (function of T), studies of the ground samples with various dopants now being prepared for EL studies, and studies of the doped nano-particles to help gain deeper fundamental insight into the local structure changes that lead to degradation.

To explore size effects, we will grind the larger particles to produce particle sizes down to 100 nm, and have started to synthesize nano-particles to build up particles. Synthesis of ZnS doped with copper and chloride has been attempted through various methods including aqueous, organic, open air, inert atmosphere, hydrothermal, and inverse microemulsion. Fluorescent ZnS nanoparticles have been synthesized by some of these methods, and characterized using fluorescence, UV-Vis, EPR (Electron Paramagnetic Resonance), and XRD (X-ray Diffraction). While fluorescence data indicate doping of ZnS nanoparticles, further confirmation using other techniques such as XPS (X-ray Photoelectron Spectroscopy) and EXAFS are still needed.

Recently, we have made progress in synthesizing Cu-doped and undoped ZnS nanoparticles using different methods. For example, ZnS quantum dots have been synthesized using an organometallic route (Zhong, J. Mater. Chem. **14**, 2790, 2004), which traditionally produces a product with high crystallinity and strong fluorescence. The inert atmosphere synthesis of ZnS in TOPO (trioctyl phosphine oxide) and HDA (hexadecylamine) produced bright-blue fluorescent ZnS nanoparticles. Addition of 1-10 mol % copper was added to the synthesis, but signs of doping were not observed through fluorescence or EPR.

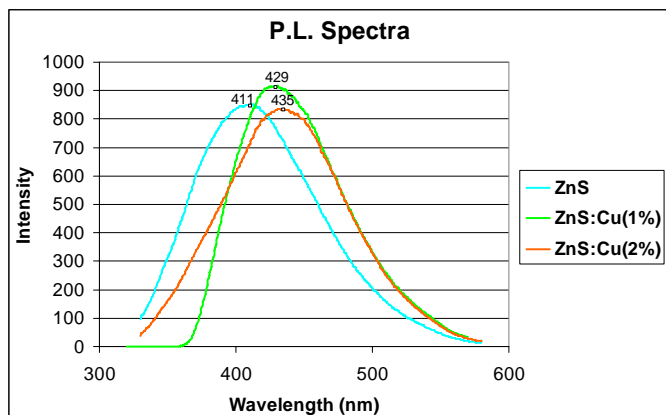


Figure 7: Fluorescence of ZnS, ZnS:1%Cu, and ZnS:2%Cu

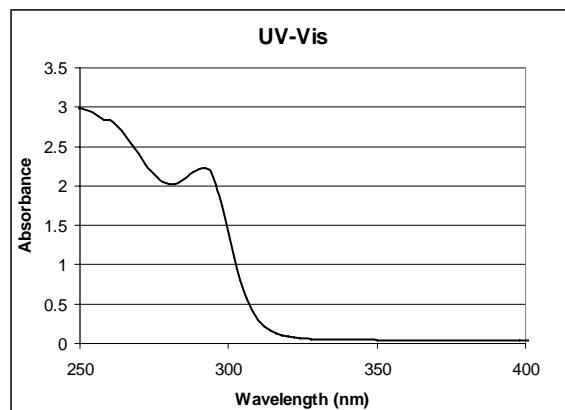


Figure 8: UV-Vis of ZnS:Cu nanoparticles.

Water-soluble particles were synthesized, that exhibited bright blue luminescence under UV-lamp excitation (Li, *Nanotechnology* **18**, 205604, 2007). Three samples were compared: ZnS, ZnS:1%Cu, ZnS:2%Cu. A red-shift in the emission peak was observed, as shown in figure 7. With an excitation wavelength of 310nm, the emission peak is red-shifted with the increasing concentration of copper added to the synthesis. This red-shift is an indication of doping of copper into ZnS nanoparticles. The states that copper introduces to the ZnS bandgap lead to the lower energy emission of the photoluminescence. These particles exhibited an interesting characteristic that their fluorescence increased with time significantly, until the particles flocculated and then lost their fluorescence after one day, likely due to insufficient surface passivation. Improvement of quantum yield with aging of nanoparticles in oxygen has been observed and attributed to formation of a protective oxide layer. Further investigation is under way to improve the surface passivation and long-term stability of the particles.

A similar system of aqueous precipitation of copper-doped ZnS nanoparticles capped with MPA was investigated under different reaction conditions (Zhuang, *J. Mater. Chem.* **13**, 1853, 2003). Soluble particles that exhibited a sharp excitonic peak in UV-Vis, as shown in figure 8, were obtained. The narrow width of this peak is characteristic of a narrow size distribution. The absorbance is blue-shifted from 340nm absorption of bulk ZnS, signaling quantum confined nanoparticles. At the end of the air-free synthesis (occurring after purge with nitrogen), the fluorescence of the nanoparticles was negligible. After aging in open-air conditions, a fluorescence peak developed, and was further increased with reflux. This peak was red-shifted in the copper-doped sample when irradiated with a UV-lamp which is an indication of Cu-doping. Confirmation of doping with XPS, ESR, and XAFS will need to be conducted.

The next steps in ZnS:Cu and Cl synthesis and characterization is to examine the particle size under HRTEM, determine their crystal structure using XRD, and confirm doping. The particles will then be purified and the ACEL properties determined for different thicknesses of power. Further investigations will be made to achieve highly uniform particles, controllable parameters (of size, emission wavelength), and maximum quantum yield. Both modifications to the current synthesis as well as continued investigations into the very high quantum yield routes of organic and inverse micro-emulsion syntheses will be explored. The long-term stability of the nano-particles (or aggregates of them), with respect to the local structure changes that lead to degradation under AC applied electric fields, will be investigated as well.

# First Principles Prediction of Structure and Thermodynamics of Complex Oxides

Professor Gerbrand Ceder  
Department of Materials Science and Engineering  
Massachusetts Institute of Technology

## Ground State Structure Prediction

The objective of our research program is to develop first principles approaches to predict the structure of materials at zero and non-zero temperature. First principles methods, in which the properties of a material are computed from quantum mechanics have shown to be capable of predicting many materials properties, but without a knowledge of the structure of the material, these predictions are likely to be irrelevant. Hence, structure prediction forms the platform on which rational materials design can be performed. Finding structure by traditional optimization methods on quantum mechanical energy models is not possible due to the complexity and high dimensionality of the coordinate space. As a result searches for the lowest energy crystal structure have been either very incomplete, or have been performed on over simplified Hamiltonians. An unusual, but efficient solution to this problem can be obtained by merging ideas from heuristic and ab initio methods. In a departure from previous computational approaches, we show that significant progress can be made by merging the ideas of empirical structure prediction methods with the predictive power of high-throughput quantum mechanical calculations.

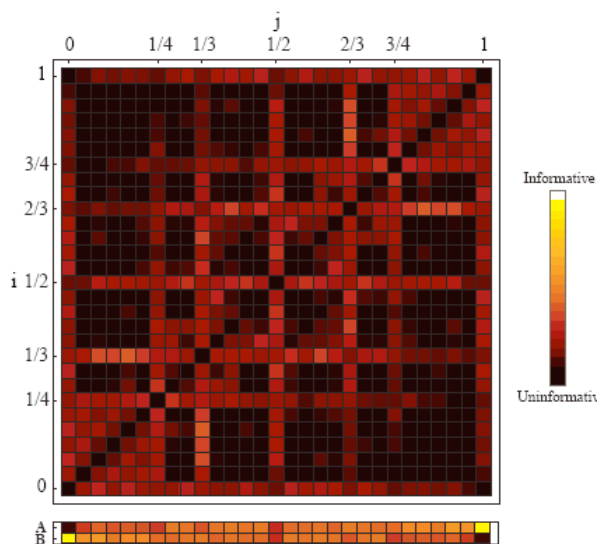


**Figure 1:** Structure correlation present in a database of binary alloys. Bright (dark) points indicate that the crystal structure appearing at  $c_i$  and  $c_j$  are more (less) correlated.

We have used quantitative knowledge methods, such as neural nets and Bayesian probability approaches to extract knowledge from large amounts of experimental information and a database of over 15,000 first principles computations. This then allows one to suggest a shortlist of structures for a new system, each of which can be computed with ab-initio methods. We show that this approach is highly efficient in finding the ground states of binary metallic alloys and can be easily generalized to more complex systems.

In our approach a general probability function is constructed in the space of ground state.

Composition space is discretized into a finite set  $\{c_1, c_2, \dots, c_k\}$  of  $k$  compositions of interest, each at which  $X_i$  is a variable denoting the structure appearing at  $c_i$ , or the value "no information" if nothing is known. In addition, the variables  $X_A, X_B, X_C, \dots$  designate

the chemical constituents A, B, C, and so on. Let  $\mathbf{X}$  denote the set of variables ( $X_A, X_B, \dots, X_1, X_2, \dots, X_k$ ). The probability function  $p(\mathbf{X})$ , if it were known exactly, would encode knowledge about the stable structures in all alloys. Our approach has been to determine  $p(\mathbf{X})$  in part by making it consistent with known experimental data. Unlike other structure suggestion methods, this probabilistic approach provides a simple, rigorous mechanism for incorporating degrees of *partial knowledge* through the process of *conditioning* and *marginalization* of the probability density. For a particular system the task of making predictions consists of calculating the conditional probability,  $p(\mathbf{X} | \mathbf{e})$ , where  $\mathbf{e}$  represents known information about a system. At a minimum, the information  $\mathbf{e}$  consists of the elements present and their respective crystal structures. Naturally, as more information becomes available, particularly if compounds are formed at intermediate compositions,  $p(\mathbf{X} | \mathbf{e})$  will become more strongly peaked around the most likely set of candidate ground states.

### Novel Electronic Entropic Effects

An important consequence of charge localization in mixed-valence materials is the entropy that can be generated from the valence distribution. Apart from the intra-ionic entropy (which does not contribute to phase stability as it is linear in composition) localized charges can contribute configurational electronic entropy to the system, which can be as large as the configurational entropy of the ions. Hence, in a system such as  $\text{Li}_x\text{FePO}_4$  entropy is generated by the Li/vacancy disorder and by the  $\text{Fe}^{2+}/\text{Fe}^{3+}$  disorder. Both disorder problems can not be treated independently as strong coupling exists between the  $\text{Fe}^{2+}$

and Li (or between the vacancy and  $\text{Fe}^{3+}$ ). To study the finite temperature behavior of this system without bias we used a coupled cluster expansion approach developed by us in a previous DOE contract to study coupled cation/anion disorder in doped oxides.

Fig. 2 shows the experimental and calculated temperature-composition phase diagram of  $\text{Li}_x\text{FePO}_4$ . The experiments feature a two-phase region at low temperature (H + T phase) and a remarkable eutectoid transition at around 450 K. Such a eutectoid is surprising as most immiscible systems form a miscibility gap in which the highest temperature for disordering is near the 0.5 composition. In this system, surprisingly, the disorder transition temperature is depressed for concentrated alloys. The calculated phase

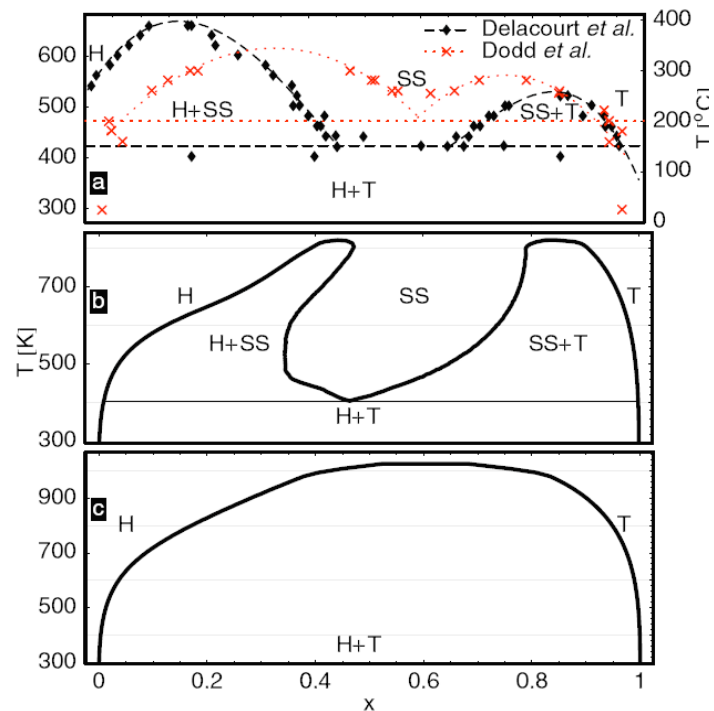


Figure 2:  $\text{Li}_x\text{FePO}_4$  phase diagram. (a) Experimental phase boundary data taken from Delacourt *et al.* and from Dodd *et al.*; (b) calculated with both Li and electron degrees of freedom and (c) with explicit Li only.

diagram in Fig 2b is in very good agreement with experiment when both electronic and ionic entropy are included. To investigate the particular role of the electronic entropy we removed it by variationally optimizing (rather than sampling) the electronic configuration for each ionic state (effectively removing electronic entropy). A simple miscibility gap is found in this case, without the eutectoid point, in disagreement with experiment. *Therefore electronic entropy is crucial to account for the phase diagram of a mixed valence system such as  $Li_xFePO_4$ .*

## Theoretical and Experimental Studies of Ion Beam Synthesized Nanocrystals

Daryl C. Chrzan,<sup>†</sup> Joel W. Ager III, and Eugene E. Haller, Electronic Materials Program, Materials Sciences Division, Lawrence Berkeley National Laboratory, Berkeley, CA 94720

<sup>†</sup>dcchrzan@berkeley.edu.

### *Program Scope*

In 1909, Pawlaw predicted that the melting points of small particles would be suppressed relative to their bulk counterparts. His continuum thermodynamics based argument rested on the fact that for small particles, the interfaces make a significant contribution to the free energy of the particle. Pawlaw's predictions have proven correct, and studies of the melting behavior of nanoparticles are now common.

Many studies, however, are limited in scope by the constraints of typical experiments. For example, one can readily study the melting behavior of free standing nanoparticles. However, study of the solidification of the same nanoparticles can be confounded by liquid droplet mobility that leads to coalescence. Further, it is desirable to extend thermodynamic studies beyond the examination of melting and solidification of pure materials to consider the effects of alloying.

For bulk materials, study of the relevant phase diagrams forms the first step in the development of any materials processing route. The thermodynamics of nanocrystal alloying is properly represented within a nanoscale alloy phase diagram, and one goal of our research is to determine accurately the structure of such diagrams. Nanoscale phase diagrams will enable the development of processing routes leading to interesting nanostructures, for example core/shell or bi-lobe nanoparticles. These phase diagrams, when coupled with convenient and broadly applicable fabrication tools will enable the discovery of new scientific phenomena, and exploitation of that phenomena within technological applications.

Ion beam synthesis (IBS) provides a fabrication tool that enables study of a broad range of nanoscale alloys. Specifically, ion implantation can be used to fabricate nanoparticles of varying composition embedded in a wide variety of host materials. As examples, our group has synthesized Ge nanocrystals in both silica and alumina, Ge/Sn nanocrystals in silica, and Ge/Au nanocrystals in silica. Proper choice of matrix material enables direct characterization of thermodynamic phase transformations using transmission electron microscopy (TEM), Raman scattering, and atomic force microscopy (AFM), amongst other techniques. Consequently, we have chosen to employ ion beam synthesis as our primary means of nanoparticle fabrication.

Our research, then, has three facets. First, we wish to understand and thereby improve control of IBS of nanoparticles. Thus we have developed and continue to improve theories for IBS. Second, we wish to characterize the thermodynamic behavior of our synthesized nanoparticles. We have consequently applied TEM, AFM, Raman spectroscopy and other characterization tools to understand the properties of our nanoparticles as a function of temperature and nanoparticle size. Here, too, we have applied available theoretical tools to understand and predict the results of experiments. The third facet of our work revolves around exploitation. To wit, we have

developed processing routes to alter the structure of binary alloy nanocrystals from homogeneously mixed, to completely segregated bi-lobed nanocrystals. Such structural changes might find applications in new technology, for example the phase change might form the basis for the next generation of static RAM and/or optical storage devices.

## Recent Progress

### Theory of Ion Beam Synthesis

Through a combination of kinetic Monte Carlo and rate equations methods, we have developed a theory for IBS of nanoparticles that predicts quantitatively the shape of the nanoparticle size distributions as a function of implantation conditions.

Under typical IBS conditions, nanoparticle size distributions reach a steady state. Our theoretical studies indicate that there are two parameters that control the steady state island size distribution. The first is the ratio of the implantation rate,  $F$ , to the effective diffusion rate for ions within the matrix,  $D$ . Implantations with smaller values of  $F/D$  lead to wider nanoparticle size distributions. The second parameter is the interface energy between the nanoparticles and the matrix. The primary effect of an increase in interface energy is to increase the critical size for nanoparticle nucleation. Thus larger interface energies lead to larger nanoparticles. Remarkably, the interface energy has little, if any, effect on the shape of the nanoparticle size distribution.

Size distributions predicted from our theories agree *quantitatively* with those observed experimentally (Fig. 1) for Ge implantation into silica. Given that the only adjustable parameter in our theory is the ratio  $F/D$ , we consider this striking confirmation of the appropriateness and power of our theoretical approach.

### Phase Transformations of Confined Nanoparticles

Confinement of the nanoparticles within a matrix expands considerably the range of melting/solidification behaviors that one might observe. To establish this point, we considered the melting and solidification of Ge nanocrystals embedded in amorphous silica.

We used a heating stage to perform *in situ* transmission electron microscopy (TEM) studies

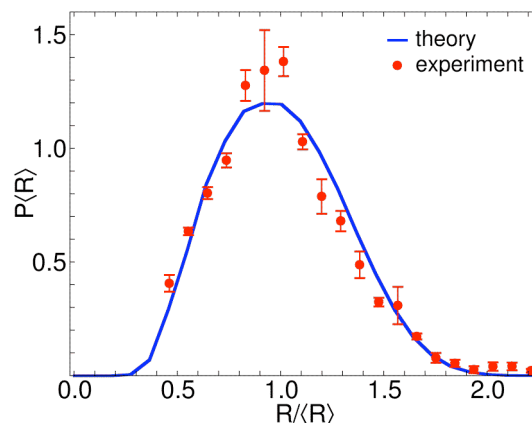


Figure 1. A comparison of the shape of the island size distribution predicted from theory as compared to the experiment.  $R$  is the nanoparticle radius,  $\langle R \rangle$  is the average radius, and  $P$  is the probability density for the nanoparticle sizes.

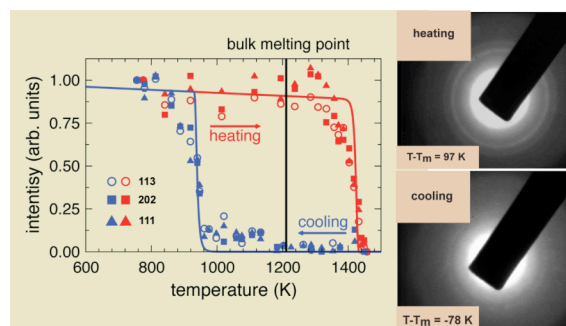


Fig. 2 Diffracted intensity from *in situ* TEM studies of the melting and solidification of Ge nanocrystals embedded in silica. The inset shows typical diffraction patterns. The lines are the diffracted intensity expected from classical nucleation theory.

of the melting and solidification of these Ge nanocrystals. Surprisingly, the melting/solidification cycle showed a large hysteresis, *nearly centered* on the melting point of bulk Ge (Fig. 2). This behavior is in striking contrast to the behavior of bulk materials that can, with great care, be substantially supercooled, but not superheated. Prior observations of superheating for embedded nanocrystals have been explained via lattice registry effects. However, the amorphous structure of the silica matrix rules out this common explanation.

Perhaps surprisingly, classical continuum thermodynamic nucleation theory provides a quantitatively accurate explanation. We developed a theoretical model for the melting and solidification pathways, and computation of the free energy associated with these pathways revealed the origin of the barriers to both melting and solidification: The Ge(liquid)/silica and Ge(solid)/silica interface energies are nearly identical. After convoluting the nucleation theory with the experimentally observed nanoparticle size distributions, and assuming a kinetic diffraction process, we obtain the hysteresis loop shown by the solid lines in Fig. 2. Again, the agreement between theory and experiment is striking.

### ***Future Plans***

The experiments and theories described briefly above establish that properties of the nanocrystal/matrix interface can expand substantially the range of observed physical behaviors. We are now turning our attention to the study of alloy phase stability. Our first task is to develop of theory for the equilibrium structure of binary alloy nanocrystals. A “zeroth-order” theory, in which the nanoparticles are restricted to be spherical, and in which segregation is perfect leads to the predictions shown in Fig. 3.

We are in the process of developing a more broadly applicable theory for the structure of alloy nanoparticles. To complement the theoretical studies, we have begun experimental studies of confined Ge/Sn nanoparticles. Thus far we have established that these nanoparticles grow in a two-lobe structure, with one lobe crystalline, mostly Ge, the other mostly Sn. We have also demonstrated that we can homogenize the composition of the nanoparticles using pulsed laser melting (Fig. 4). Subsequent rapid thermal annealing restores the crystalline structure of the Ge.

### ***Journal Publications 2005-2007***

I.D. Sharp, Q. Xu, C.Y. Liao, D.O. Yi, J.W. Beeman, Z. Liliental-Weber, K.M. Yu, D.N. Zakharov, J.W. Ager, D.C. Chrzan and E.E. Haller. Stable, freestanding Ge nanocrystals. *Journal of Applied Physics* **97**, 124316 (2005).

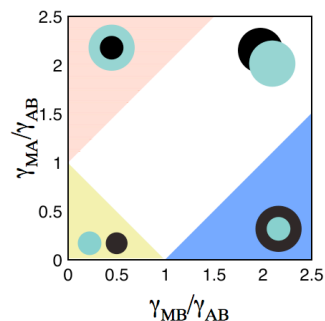


Figure 3. Equilibrium structures expected for a perfectly segregating A/B alloy confined to partial spherical cavities. The symbols,  $\gamma_{XY}$ , refer to interface energies between materials  $X$  and  $Y$ . Here,  $M$  stands for matrix. The stable structures for each of the regions are shown.

I.D. Sharp, D.O. Yi, Q. Xu, C.Y. Liao, J.W. Beeman, Z. Liliental-Weber, K.M. Yu, D. Zakharov, J.W. Ager III, D.C. Chrzan and E.E. Haller. Mechanism of stress relaxation in Ge nanocrystals embedded in SiO<sub>2</sub>. *Applied Physics Letters* **86**, 063107 (2005).

Q. Xu, I. D. Sharp, C. W. Yuan, D. O. Yi, C. Y. Liao, A. M. Glaeser, A. M. Minor, J. W. Beeman, M. C. Ridgeway, P. Knuth, J. W. Ager III, D. C. Chrzan and E. E. Haller. Large melting-point hysteresis of Ge nanocrystals embedded in SiO<sub>2</sub>. *Physical Review Letters* **97**, 155701 (2006).

D. Sharp, Q. Xu, D. O. Yi, C. W. Yuan, J. W. Beeman, K. M. Yu, J. W. Ager III, D. C. Chrzan and E. E. Haller. Structural Properties of Ge nanocrystals embedded in sapphire. *Journal of Applied Physics* **100**, 114317 (2006).

D. Sharp, Q. Xu, C. W. Yuan, J. W. Beeman, J. W. Ager, D. C. Chrzan and E. E. Haller. Kinetics of visible light photo-oxidation of Ge nanocrystals: Theory and in situ measurement. *Applied Physics Letters* **90**, 163118 (2007).

Q. Xu, I. D. Sharp, C. W. Yuan, D. O. Yi, C. Y. Liao, A. M. Glaeser, A. M. Minor, J. W. Beeman, M. C. Ridgeway, P. Knuth, J. W. Ager III, D. C. Chrzan and E. E. Haller. Comment on "Large melting-point hysteresis of Ge nanocrystals embedded in SiO<sub>2</sub>" – Reply, *Physical Review Letters* **99**, 079602 (2007).

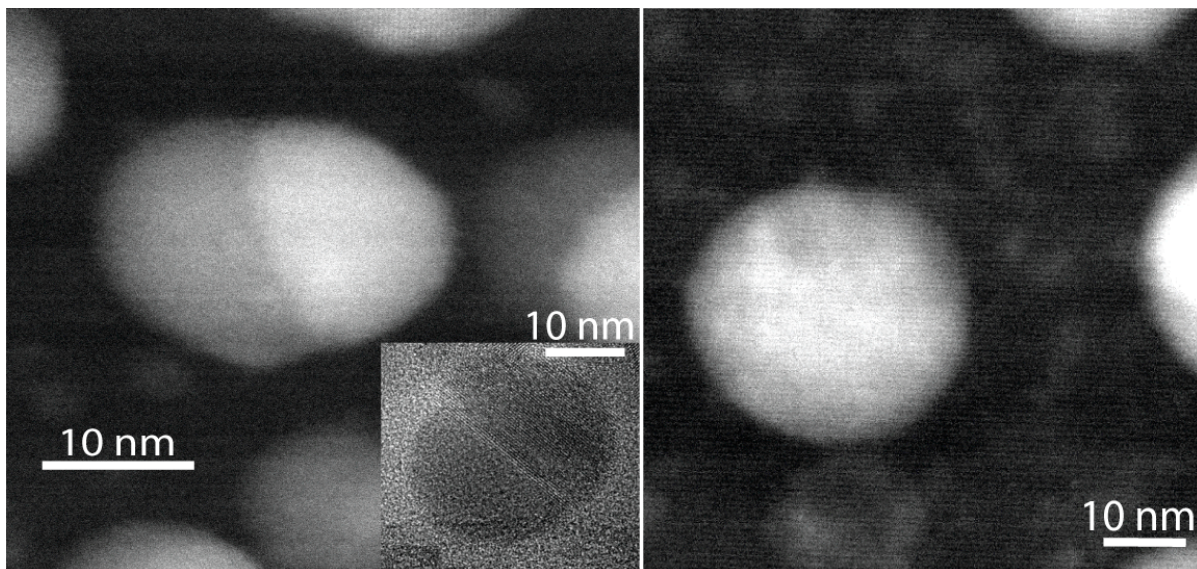


Figure 4. Z-contrast TEM images of Ge/Sn nanocrystals fabricated using IBS. The image on the left shows clearly the bi-lobe structure, and spectroscopy confirms that half of the nanocrystal is mostly Ge, the other half mostly Sn. The inset on the right is a high-resolution image of a bi-lobe nanocrystals. The image on the right is a typical Ge/Sn nanocrystal after pulsed laser melting. The laser energy is absorbed by the Ge half of the bi-lobed structure, and the entire nanocrystal melts. When the laser is turned off, the nanoparticle cools rapidly, preventing the thermodynamically favored segregation. Raman studies suggest that subsequent annealing returns the structure to a state similar to that shown on the left.

## The Electronic Materials Program at LBNL

E. E. Haller, PI, J. W. Ager III, Co-PI, D. C. Chrzan, Co-PI, O. D. Dubón, Co-PI,  
Z. Liliental-Weber, Co-PI, W. Walukiewicz, Co-PI, K. M. Yu, Co-PI

Lawrence Berkeley National Laboratory, Materials Sciences Division, MS 2R0200,  
1 Cyclotron Road, Berkeley, CA 94720

The Electronic Materials Program advances the fundamental understanding of the materials science of semiconductors. The research focuses on the relationships between synthesis and processing conditions and the structure, properties, and stability of semiconductor materials systems. Progress in these areas is essential for the performance and reliability of technologies that lie at the heart of the DOE mission, including solar power conversion devices, solid state sources of visible light, visual displays, and a large variety of sensors and power control systems for energy generation, conservation, and distribution.

### New Materials for High-Efficiency Solar Cells.

“Traditional” semiconductor alloying (as in  $\text{Al}_x\text{Ga}_{1-x}\text{As}$ ) continuously changes electronic properties such as valence and conduction band edges and the bandgap between the endpoint compounds. But it has been known experimentally since the mid-1990’s that alloys such as  $\text{GaAs}_{1-x}\text{N}_x$  do not follow this trend; in this case, a few % of N drastically reduces the bandgap, rather than increasing it in the direction of GaN. Beginning in 1999, our combined experimental and theoretical work have established that  $\text{GaAs}_{1-x}\text{N}_x$  is an important member of a large family of “highly mismatched” alloys (HMAs) formed by isoelectronic substitution of elements with very different atomic sizes and/or electronegativities. In HMAs, band-anticrossing (BAC) between the localized level of the alloying element and the extended states of the host lead to a rich variety of new phenomena.

We have demonstrated that anti-crossing effects can be used to “move” either the valence band or the conduction band edge up or down in energy without affecting the other bands in a wide range of III-V and II-VI compound semiconductors. The case in which a new level is created in the gap is of special interest for high efficiency solar cells (Fig. 1). We have developed both III-V and II-VI (ZnTeO) HMAs which have the requisite intermediate band and have demonstrated the direct nature of the transition from the valence band to the intermediate band. This work led to a 2006 R&D 100 Award for two of our investigators (Walukiewicz and Yu).

In the future, we will control carriers, light, and spin using the unique band tuning capabilities found in HMAs. The valence band BAC effect can be used to fabricate materials for efficient solar water splitting. For example, adding As to GaN to form  $\text{GaAs}_x\text{N}_{1-x}$  produces an

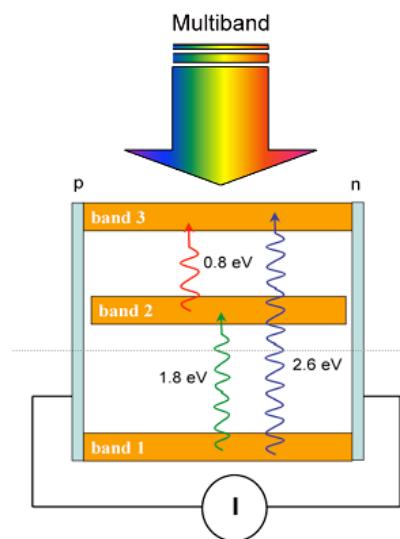


**Fig. 1.** Schematic depiction of an intermediate band solar cell. In addition to the usual absorption from the valence to conduction band (1→3), light can also be absorbed (and converted to electrical energy) by the 2-photon process, 1→2 and 2→3, with the intermediate band 2 functioning as a “stepping stone.” In this sense, an intermediate band solar cell is equivalent to two-junction tandem cell but with a much simpler design and higher ultimate thermodynamic efficiency (63.2% vs. 55%).

arsenic-localized level 0.6 eV above the valence band edge of GaN. As the As concentration is increased, the localized level forms a new, higher valence band. This effect can be used to narrow the gap (which increases efficiency) while maintaining the straddling of the water redox potential. The localized levels created in the gap in, for example, GaAsPN, can be used as conducting pathways. We will investigate whether the intermediate band can be used to make *energy selective* contacts to other semiconductors. Such contacts are a required element of theoretically predicted high-efficiency hot-electron solar cells

The energy tuning range of the group III-nitrides (AlN, GaN, and InN) was greatly expanded by our discovery in 2002 that the band gap ( $E_g$ ) of InN is 0.7 eV as opposed to 2 eV, as previously believed. Thus, the  $E_g$  tuning range of  $\text{In}_x\text{Ga}_{1-x}\text{N}$  goes from 0.65 eV ( $x=1$ , InN) to 3.4 eV ( $x=0$ , GaN), which encompasses most of the useful part of the solar spectrum. While the large electron affinity of InN (5.8 eV) and of In-rich alloys leads to a propensity for native donor defect formation and surface electron accumulation, our recent work has shown that Mg is an acceptor in InN, and can be used to make p-type InN and InGaN over the entire composition range. Our future work in this area will focus on controlling the surface properties to enable contacts to p-InGaN and on making pn junctions. Based on our discovery the conduction band of certain InGaN alloys is well-aligned with a number of conducting oxides, we are developing InGaN/oxide layered structures as conducting and corrosion resistant photocathodes for solar fuel generation.

### Thermodynamics and Kinetics at the Nanoscale.

While it is well-known that decreasing the particle size decreases the melting point, confinement of nanoparticles within a solid matrix expands considerably the range of melting/solidification behaviors. We used *in situ* transmission electron microscopy (TEM) to study the melting and solidification of Ge nanocrystals embedded in amorphous silica. Surprisingly, the nanocrystals melted at a temperature far above the bulk value and the melting/solidification cycle showed a large hysteresis. This behavior is in striking contrast to the behavior of bulk materials that can, with care, be substantially supercooled but not superheated. A new continuum thermodynamic nucleation theory provides a straightforward and quantitative accurate explanation: The Ge(liquid) and Ge(solid) interface energies are nearly identical, which leads to a situation in which *both* solidification and melting require nucleation.

We are exploring the phase diagrams of strongly segregating binary alloys, concentrating on how the interface(s) with the matrix affect the segregation transition. Our ultimate aim is to develop phase diagrams for nanoscale systems and to use these to generate homogeneous alloy, bi-lobed and core/shell nanocrystals. Our initial studies of bi-lobed Ge-Sn nanocrystals are promising. Using pulsed-laser-melting, we have been able to homogenize the nanocrystals. Subsequent annealing appears to regenerate a segregated structure, suggesting that such phase-change nanocrystals might form the basis for a new type of static RAM.

**Isotopically Controlled Semiconductor Structures.** Most semiconductors contain at least one element that consists of more than one stable isotope: silicon is composed of the three isotopes:

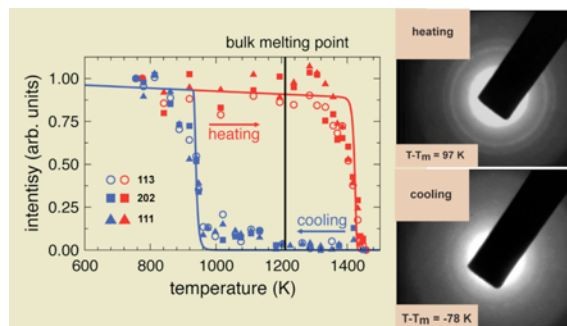


**Fig. 2** Diffracted intensity from *in situ* TEM studies of the melting and solidification of Ge nanocrystals embedded in silica. The inset shows typical diffraction patterns. The lines are the diffracted intensity expected from classical nucleation theory.

$^{28}\text{Si}$  (92.23%),  $^{29}\text{Si}$  (4.67%), and  $^{30}\text{Si}$  (3.10%). A number of physical properties of semiconductors depends on isotopic composition, including those due to atomic mass differences and nuclear spin differences. To investigate these effects, we grew high-purity bulk crystals and thin-film structures using Si enriched in all 3 of its stable isotopes. Isotope composition affects the electronic structure through electron-phonon coupling and through the change of volume with isotopic mass. As shown in Fig. 3, by comparing the energies of indirect transitions in absorption and photoluminescence that are assisted by the same phonon, the mass dependence of Si's indirect and higher energy direct gaps were determined precisely.

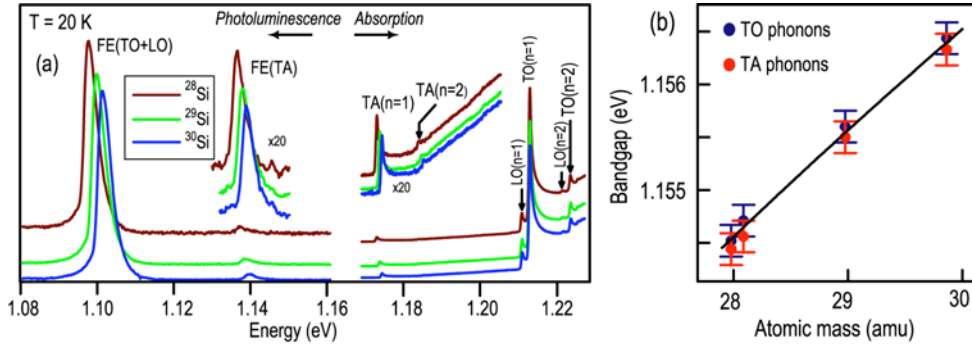


**Fig. 3.** (a) Optical absorption and photoluminescence (PL) across the indirect gap of silicon occur with assistance from phonons (TA, LO, and TO). Absorption peaks are observed at the band gap plus the phonon energy; PL peaks are at the band gap minus the phonon energy. By matching transitions assisted by the same phonons the precise value of the band gap as a function of mass is obtained by interpolation. (b) The excitonic bandgap of Si as a function of atomic mass; the line is the  $M^{-1/2}$  dependence. The purely electronic Si bandgap, in the absence of all electron-phonon interaction and volume change effects, is obtained by extrapolating to  $M \rightarrow \infty$  and is 1.2138 eV.

There is increasing interest in the properties of spins in the solid state driven, in part, by the possibility of realizing quantum computing schemes, and the decoherence time ( $T_2$ ) of an isolated spin is a key figure of merit. It has been known since the invention of electron spin resonance spectroscopy that the  $T_2$  of the electron bound to  $^{31}\text{P}$  is increased in  $^{28}\text{Si}$  enriched material due to derichment of  $^{29}\text{Si}$  with its odd spin nucleus. In this context, pulsed ESR measurements on a  $^{28}\text{Si}$  LBNL single crystal are the current “world record” with a  $T_2$  at 10 K of 5 ms. Also, in a collaborative study using highly  $^{28}\text{Si}$  enriched single crystals provided by LBNL, the hyperfine coupling of the electronic nuclear donor spins for the  $^{31}\text{P}$  donor were observed optically for the first time. The optical detection of the nuclear spin state and selective pumping and ionization of donors in specific electronic and nuclear spin states suggest a number of new possibilities that may be useful for the realization of silicon-based quantum computers.

We will continue world-wide collaborative efforts on the spectroscopy of these unique materials, based on both optical and spin-based measurements. We have recently lowered the impurity concentration in our  $^{28}\text{Si}$ -enriched material by zone-refining. The spin decoherence time observed in electron spin resonance (ESR) for the electron bound to  $^{31}\text{P}$  is expected to be longer than our existing “world record” and may define the upper limit for maintaining quantum coherence in this system. We also note that while the 150 neV linewidths observed optically for the hyperfine interaction of the  $^{31}\text{P}$  electron and nuclear spins are the narrowest ever measured, they are not yet at the limit predicted by the photoluminescence lifetime, showing that inhomogeneous effects are still present. This indicates a clear role for advanced synthesis of isotopically controlled structures with even higher chemical and structural purity.

**Semiconductor Spintronics.** Because of their potential as both injection sources and filters for spin-polarized carriers, ferromagnetic semiconductors have attracted much attention for spin-

based electronics, or *spintronics*. In the prototypical ferromagnetic semiconductor  $\text{Ga}_{1-x}\text{Mn}_x\text{As}$ , inter-Mn exchange is known to be mediated by holes in extended or weakly localized states; however, the fundamental nature of inter-Mn exchange remains unclear. Our studies have shown that in  $\text{Ga}_{1-x}\text{Mn}_x\text{As}$  thin films Mn atoms occupying interstitial position are the crucial defects affecting the ferromagnetism in this alloy system. We have also demonstrated that the upper limit of Curie temperature  $T_C$  of  $\text{Ga}_{1-x}\text{Mn}_x\text{As}$  is caused by the Fermi-level-induced saturation of free holes in the crystal. Other noteworthy milestones include the first demonstration of ferromagnetism in single-crystalline  $\text{Ga}_{1-x}\text{Mn}_x\text{P}$ . Our future efforts will include the exploration of new materials that may display room-temperature ferromagnetism, including group IV-based ferromagnetic semiconductors, and the local control of ferromagnetism by nanopatterning and defect engineering. Figure 4 presents recent results on the laser activation of ferromagnetism in hydrogenated  $\text{Ga}_{1-x}\text{Mn}_x\text{As}$ .

### Selected references

- Ager III, J. W., J. W. Beeman, W. L. Hansen, E. E. Haller, I. D. Sharp, C. Liao, A. Yang, M. L. W. Thewalt, and H. Riemann, "High-purity, isotopically enriched bulk silicon," *J. Electrochem. Soc.* **152**, G448-G451 (2005).
- Alberi, K., J. Wu, W. Walukiewicz, K.M. Yu, O.D. Dubon, S.P. Watkins, C.X. Wang, X. Liu, Y.-J. Cho, and J.K. Furdyna, "Valence band anticrossing in mismatched III-V semiconductor alloys," *Phys. Rev. B* **75** 045203 (2007).
- Farshchi, R., O. S. Dubón, D. J. Hwang, N. Misra, C. P. Grigoropoulos, and P. D. Ashby, "Laser activation of ferromagnetism in hydrogenated  $\text{Ga}_{1-x}\text{Mn}_x\text{As}$ ," *Appl. Phys. Lett.* **92**, 012517 (2008).
- Jones, R. E., K. M. Yu, S. X. Li, W. Walukiewicz, J. W. Ager III, E. E. Haller, H. Lu, and W.J. Schaff, "Evidence for p-type doping of InN," *Phys. Rev. Lett.* **96**, 125505 (2006).
- Jones, R. E., H. C. M. van Genuchten, K. M. Yu, W. Walukiewicz, S. X. Li, J. W. Ager III, Z. Liliental-Weber, E.E. Haller, H. Lu, and W. J. Schaff, "High Electron Mobility InN by Irradiation and Thermal Annealing," *Appl. Phys. Lett.* **90**, 162103 (2007).
- Scarpulla, M. A., B. L. Cardozo, R. Farshchi, W. M. Hlaing Oo, M. D. McCluskey, K. M. Yu, and O. D. Dubon, "Ferromagnetism in  $\text{Ga}_{1-x}\text{Mn}_x\text{P}$ : evidence for inter-Mn exchange mediated by localized holes within a detached impurity band," *Phys. Rev. Lett.* **95**, 207204 (2005).
- Tyryshkin, A. M., J. J. L. Morton, S. C. Benjamin, A. Ardavan, G. A. D. Briggs, J. W. Ager III, and S. A. Lyon, "Coherence of Spin Qubits in Silicon," *J. Phys. Cond. Mat.* **18** S783-S794 (2006).
- Walukiewicz, W., J. W. Ager III, K. M. Yu, Z. Liliental-Weber, J. Wu, S. X. Li, R. E. Jones, and J. D. Denlinger, "Structure and Electronic Properties of InN and In-rich Group III-Nitride Alloys," *J. Phys. D* **39** R83 (2006).
- Xu, Q., I. D. Sharp, C. W. Yuan, D. O. Yi, C. Y. Liao, A. M. Glaeser, A. M. Minor, J. W. Beeman, M. C. Ridgway, P. Kluth, J. W. Ager III, D. C. Chrzan, and E. E. Haller, "Large melting point hysteresis of Ge nanocrystals embedded in  $\text{SiO}_2$ ," *Phys Rev. Lett.* **97**, 155701 (2006); comment reply **99**, 079602 (2007).
- Yang, A., M. Steger, D. Karaiskaj, M. L. W. Thewalt, M. Cardona, K. M. Itoh, H. Riemann, N. V. Abrosimov, A. V. Gusev, A. D. Bulanov, A. K. Kaliteevskii, O. N. Godisov, P. Becker, H.-J. Pohl, J. W. Ager III, and E. E. Haller, "Optical detection and ionization of donors in specific electronic and nuclear spin states," *Phys. Rev. Lett.* **97**, 227401 (2006).
- Yim, J. W., R. E. Jones, K. M. Yu, J. W. Ager, W. Walukiewicz, W. J. Schaff, and J. Wu, "Effects of surface states on electrical characteristics of InN and  $\text{In}_{1-x}\text{Ga}_x\text{N}$ ," *Phys. Rev. B* **76**, R041303 (2007).

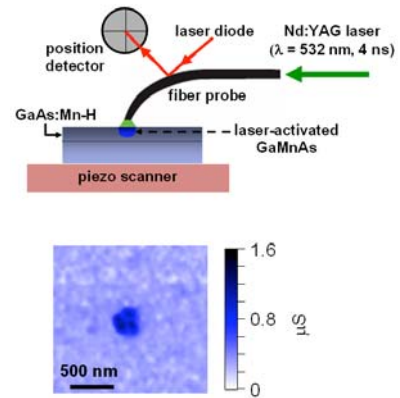


**Fig. 4.** Top: Schematic of the optical near-field configuration used for the irradiation of hydrogenated  $\text{Ga}_{1-x}\text{Mn}_x\text{As}$ . Bottom: Conductance atomic force microscopy image of a laser-irradiated spot. Annealing with the focused laser results in local electrical and ferromagnetic activation of Mn acceptors.

## Interfaces of Polymer Electronic Devices DOE (DE-FG02-04ER46165)

**Antoine Kahn**, Princeton University; **Jean-Luc Brédas**, Georgia Institute of Technology;  
**Anil Duggal**, General Electric Global Research; **George Malliaras**, Cornell University

The field of organic molecular thin films and devices is developing extremely fast, driven by the enormous potential that small molecule and polymer semiconductors have for applications in large-scale electronic and optoelectronic devices, using basic devices such as the organic light emitting diodes (OLED), the field effect transistors (FET) and the photovoltaic cell. The endless choice of molecules and the wide range of organic thin film processing techniques (from vacuum deposition to printing from solvent solutions) allow a degree of originality that cannot be matched with inorganic semiconductor technology. In the same time, the multiplicity of compounds and processing techniques places considerable demands on our ability to understand and control the structural and electronic properties of these materials and their interfaces. Interfaces of organic materials with inorganic and organic solids play a central role in charge injection and transport, and are exceedingly important for device performance and lifetime. Thin film multi-layer architectures of organic devices place active layers within nanometers of metal-organic (MO) or organic-organic (OO) interfaces, enhancing the impact of their structural and chemical properties on the device performance. Most technologically important organic semiconductors have large energy gaps ( $\geq 2$  eV), making injection barriers potentially large. The central part of the work supported by DOE focuses on achieving a detailed understanding of the mechanisms that control interface energetics and chemistry, of the impact of the electronic structure on the injection process, and of methods to modify the electrical behavior of these interfaces.

Using a unique combination of state-of-the-art experimental and theoretical tools, expertise and experience in organic materials, thin films and devices, and a small number of model polymers and their interfaces, we investigated: (i) The connection between theoretical and measured electronic levels; (ii) The electron and hole transport levels and injection barriers for different

polymers and metal contacts; (iii) The connection between injection currents and energy barriers; (iv) The dependence of barriers and injected currents on the processing and structure of the polymer films. (v) The performance, i.e. injection efficiency and stability, of these interfaces.

We performed in-depth experimental and theoretical investigations of the electronic structure of model polymers F8 and TFB. We achieved excellent agreement between computed densities of occupied and unoccupied states and spectroscopic data obtained via ultra-violet and inverse photoemission spectroscopies (UPS, IPES) (Fig. 1), allowing a clear determination of the full electronic structure of these compounds. The theoretical description of the unoccupied states, and agreement with corresponding IPES data, were the first reported for polymer semiconductors. This investigation led to the determination of the single-particle gap ( $E_i$ ) and positions of the electron and hole transport levels in these materials, and their ionization energy (IE) and electron affinity (EA) [1], which

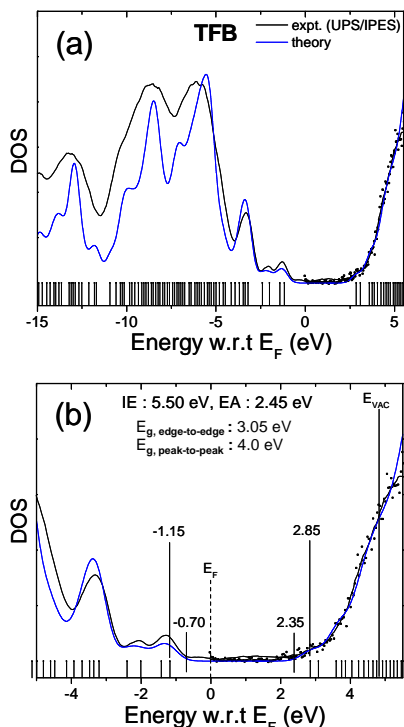


Fig. 1: Measured DOS (black line) vs. calculated DOS (blue line) of TFB: (a) broad spectra of occupied and unoccupied states and (b) an enlarged view of the energy region close to  $E_F$  (HOMO and LUMO)

are key parameters to understand the energetics of organic/organic and organic/inorganic interfaces. In particular, the larger IE value obtained for F8 than for TFB was found to be consistent with easier hole injection measured in the latter [2].

Computations of the intra-chain band structure and reorganization energy revealed interesting differences between F8 and TFB; the valence band of F8 is more dispersive than that of TFB whereas the reorganization energy of TFB is somewhat larger than that of F8, suggesting a higher intra-chain hole mobility in F8 than in TFB [3]. Experimental proof of the contrary (see below) stresses the paramount importance of inter-chain hopping in limiting transport in these materials.

We performed time-of-flight (TOF) measurements of carrier drift mobility as a function of electric field and temperature. Hole mobilities were measured in both F8 and TFB by applying a bias across the sample and photo-generating holes at the electrode/polymer interface with a nanosecond pulse nitrogen laser. Typical TOF traces, obtained for both TFB and F8, showed the well-defined plateau corresponding to non-dispersive hole transport. The mobilities showed a Pool-Frenkel (PF)-like behavior, with a field dependence that could be described by  $\mu(E) = \mu_0 \cdot \exp(\beta \cdot \sqrt{E})$ , where  $\mu_0$  is the (extrapolated) zero field mobility,  $\beta$  is the so-called PF factor, and  $E$  is the applied electric field (Fig. 2). The PF factors are between 0.2 and  $2.3 \times 10^{-3} \text{ (cm/V)}^{1/2}$  for these polymer films [4]. At a field of 100 kV/cm, which is near the onset of OLED operation, the room temperature mobility of TFB is  $0.01 \text{ cm}^2\text{V}^{-1}\text{s}^{-1}$ , which is remarkably high. The hole mobility in F8 was an order of magnitude lower.

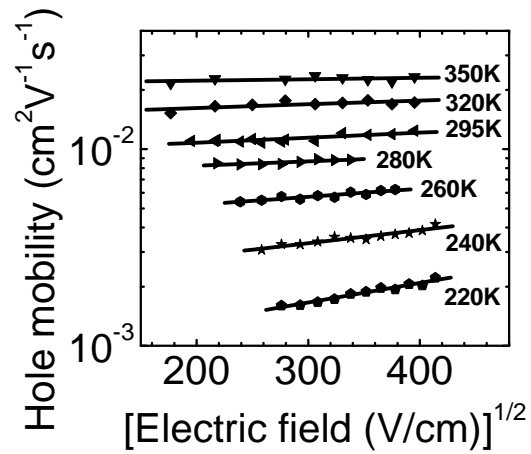


Fig. 2: Electric field dependence of hole mobility in TFB for various temperatures.

Additional information about transport in TFB was obtained by analyzing the temperature dependence of the mobility. According to the Gaussian Disorder Model [5], transport in organic materials takes place by hopping in a manifold of localized states. The latter is considered to be a Gaussian characterized by its standard deviation  $\sigma$ , which reflects the width of the transport manifold and is also known as the energetic disorder parameter. Accordingly, the temperature dependence of the zero field mobility is given

by  $\mu_0(T) = \mu_\infty \cdot \exp\left[-\left(\frac{2 \cdot \sigma}{3 \cdot k \cdot T}\right)^2\right]$ , where  $\mu_\infty$  is the high temperature limit of the zero field

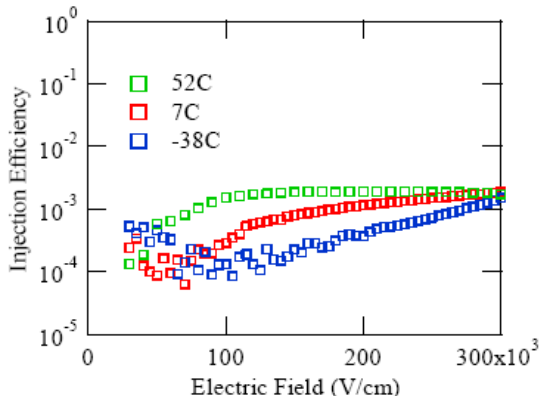


Fig. 3: Injection efficiency from PEDOT:PSS into TFB

mobility,  $k$  is the Boltzmann constant, and  $T$  is the absolute temperature. The data agree with this equation, and for TFB,  $\sigma = 65.9 \pm 0.5 \text{ meV}$  and  $\mu_\infty = 0.19 \text{ cm}^2\text{V}^{-1}\text{s}^{-1}$  [4]. In addition to energetic disorder, there is disorder in the position of the hopping sites, characterized by the positional disorder parameter  $\Sigma$ . [5] The latter was extracted from the plot of  $\beta$  versus  $(\sigma/kT)^2$ , and was found to be equal to 2.2 for TFB [4]. These transport measurements show that TFB is a model organic semiconductor and is ideally suited for a study of injection.

Knowledge of mobility allows an estimation of the space charge limited hole current,  $J_{SCL}$ , *i.e.*, the highest unipolar current that can flow through an organic semiconductor film and thus of the *injection efficiency*, the ratio between measured injected current and  $J_{SCL}$ . We found injection efficiencies with PEDOT:PSS on the order of  $10^{-5}$  for F8 and  $10^{-3}$  for TFB (Fig. 3), in spite of the low hole injection barriers with this electrode (see below) [2]. Au and indium tin oxide (ITO) anodes yielded even lower injection efficiencies, in agreement with the higher barrier heights measured by photoelectron spectroscopy.

TOF requires preparation of relatively thick ( $\sim 1 \mu\text{m}$ ) and trap-free films in order to observe transients with well-defined transit time, and it has remained very difficult to measure device relevant films (thicknesses  $\sim 10\text{-}100 \text{ nm}$ ). One promising technique for measuring mobility, Dark Injection Transient Current (DITC), can in principle measure the mobility of films with thickness relevant to OLEDs. However, the approach to date has been limited to transit times greater than  $\sim 1 \mu\text{sec}$  due to circuit architecture. DITC is thus typically limited to either thick films or films which have poor mobility. Nevertheless, we were successful in identifying a model system which could be probed and showed that the technique could be utilized to separate the sources of device degradation which currently plague industrial applications [6]. Furthermore, our team recently developed a new circuit architecture that is capable of measuring transit times 10 times faster than reported previously. With this breakthrough, DITC can now be used to measure the mobility of films 10 times thinner or mobilities 10 times higher than possible before and so is now appropriate for basic physics measurements for industrially relevant materials and device designs.

We used UPS and X-ray photoemission spectroscopy (XPS) to investigate molecular level alignment and injection barriers at polymer-on-electrode and electrode-on-polymer interfaces. Electrodes ranged from low work function (WF) Al and Sm to high WF Au, Pt and PEDOT:PSS. Fig. 4 shows the evolution of the interface barrier  $\phi_h$  as a function of the electrode WF, *i.e.*, the

$$\text{interface parameter } S = \frac{d\phi_h}{dW}$$

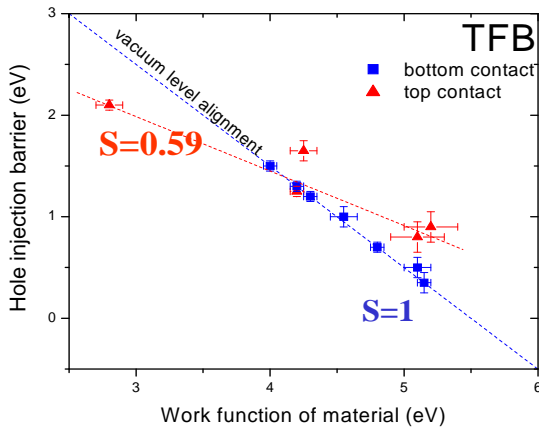


Fig. 4: Evolution of interface barrier as a function of electrode work function. Blue: polymer-on-electrode interfaces; Red: electrode-on-polymer interfaces

*Polymer-on-electrode* interfaces were investigated for polymer (F8 and TFB) thicknesses down to 3 nm, to insure proper measurement of the “interface” molecular level position. It was found that all interfaces obeyed vacuum-level alignment (Schottky-Mott limit, with an interface parameter  $S=1$ ; Fig. 4), although small interface barriers ( $\leq 0.6 \text{ eV}$ ) were accompanied by some “band bending” away from the interface, to raise the Fermi level position to about 0.6 eV above (or below) the band edge in the bulk of the material [1].

*Electrode-on-polymer* interfaces were investigated for metal layers evaporated in vacuum and metal thicknesses ranging from 0.1 to 10 nm. Unlike in the previous case, these interfaces were found to deviate from the vacuum level alignment (Schottky-Mott) rule, and exhibit an interface parameter  $S$  significantly smaller than unity (Fig. 4) [1]. Chemistry and induced density of interface states are bound to play a more significant role at intimate metal-on-top polymer interfaces than at interfaces formed by spinning the polymer film from solution on an already fully-formed and likely contaminated electrode surface.

A comprehensive summary of Fermi level positions at F8 and TFB interfaces with various electrodes (both polymer-on and electrode-on) is given in Fig. 5. Remarkable on this graph is the small hole injection barrier provided by PEDOT:PSS on TFB ( $\sim 0.35$  eV), although this system appears to still be injection-limited, as discussed above.

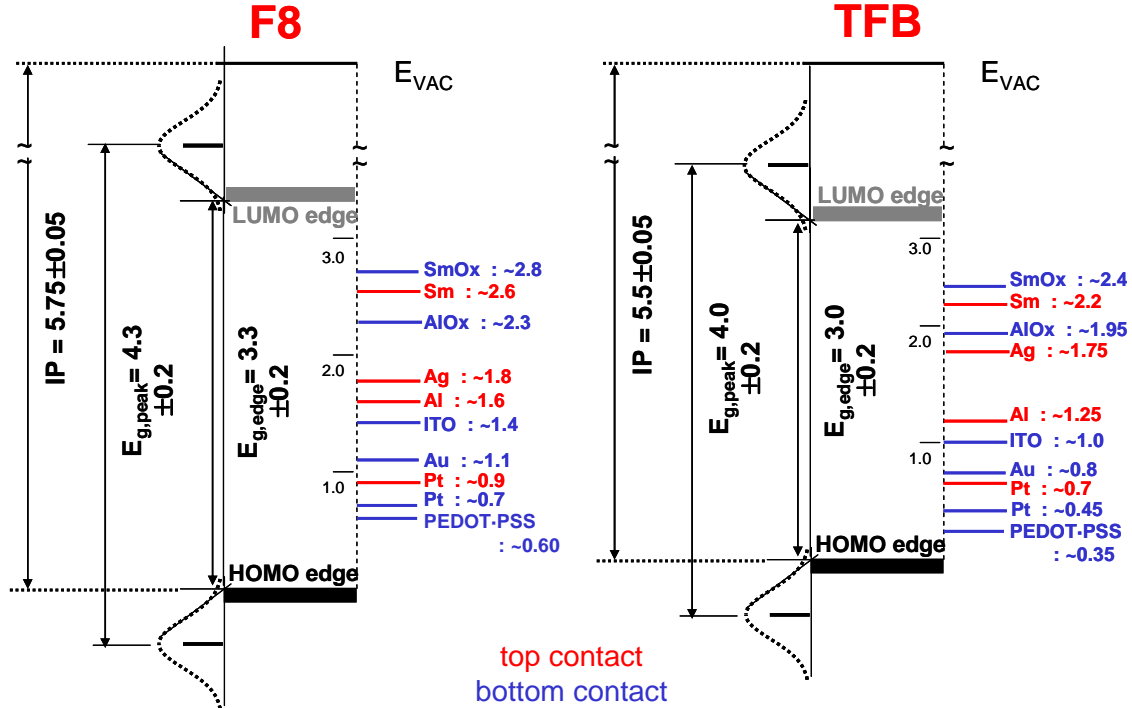


Fig. 5: Summary of Fermi level position in the gap of F8 and TFB as a function of electrode material. Numbers on the right of electrode elements indicate the Fermi level – to – HOMO energy difference. Blue entries are for polymer-on-electrode interfaces, and red entries for electrode-on-polymer interfaces

We finally initiated DFT computations on the electronic structure of, and interaction at, the TFB/PEDOT:PSS interface. The polymer was modeled by a monolayer of an oligomer consisting of one fluorene (F) and one triarylamine (T) monomeric unit (denoted as FT) and a slab of PEDOT:Tos (Tos = tosylate). These calculations, which we believe are the first for this type of organic-organic heterojunction, are providing considerable insight in the phenomenon of charge transfer and interface dipole formation.

1. J. Hwang, E.-G. Kim, J. Liu, J.-L. Brédas, A. Duggal and A. Kahn, *Photoelectron Spectroscopic Study of the Electronic Band Structure of Polyfluorene and Fluorene-Arylamine Copolymers at Interfaces*, J. Phys. Chem. C **111**, 1378 (2007)
2. H.H. Fong, A. Papadimitratos, J. Hwang, A. Kahn, and G.G. Malliaras, *Hole injection in a model polyfluorene*, in preparation.
3. E.-G. Kim, V. Coropceanu, and J.-L. Brédas, *Transport mechanism in fluorene-triarylamine copolymers*, in preparation
4. H.H. Fong, A. Papadimitratos, and G.G. Malliaras, *Non-dispersive hole transport in a polyfluorene copolymer with a mobility of 0.01 cm<sup>2</sup>/Vs*, *Appl. Phys. Lett.* **89**, 172116 (2006).
5. H. Bässler, *Phys. Status Solidi B* **175**, 15 (1993).
6. A. Papadimitratos, H.H. Fong, G.G. Malliaras, A. Yakimov, and A. Duggal, *Degradation of hole injection at the contact between a conducting polymer and a fluorine copolymer*, *Appl. Phys. Lett.* **91**, 042116 (2007).

Abstract

**Defect Chemistry Study of Nitrogen Doped ZnO Thin Films**

June 2007-May 2010

*Dr. Lei L. Kerr<sup>a</sup> (PD/PI), and Dr. Andre Sommer<sup>b</sup> (Co-PI)*

<sup>a</sup>Department of Paper and Chemical Engineering, <sup>b</sup>Department of Chemistry and BioChemistry,  
Miami University of Ohio, Oxford, OH 45056

*Dr. David C. Look (PI), and Mr. Zhaoqiang Fang (Co-PI),*

Semiconductor Research Center, Wright State University, Dayton, OH 45435

*Dr. Xiaonan Li (PI), and Dr. Timothy J. Coutts (Co-PI)*

National Renewable Energy Laboratory, 1617 Cole Blvd., Golden, CO 80104

Email: kerrll@muohio.edu

**Program Scope**

A full realization of the optoelectronic potential of ZnO in high efficiency tandem solar cells and blue/UV light emitting diodes requires high quality *p*-type ZnO and a robust control of the *p*-type doping. Nitrogen is the most promising candidate for *p*-type doping in ZnO. However, it has been very challenging to prepare *p*-type nitrogen doped ZnO (ZnO:N), and most attempts, even successful ones, produce low hole concentrations and mobilities, and sometimes even instabilities. At this time, there is no technology or process for making good *p*-type ZnO in a reproducible manner. The physical properties and stability of ZnO are closely linked to its defect chemistry. The objective of this project is to investigate the defect chemistry in nitrogen doped ZnO thin films and produce reliable *p*-type ZnO. The approach we take is to correlate the results from *in-situ* Raman, deep level transient spectroscopy (DLTS), and Hall-effect experiments, in conjunction with electron irradiation, to enhance the understanding of the nitrogen doping mechanism in ZnO. This knowledge should provide fundamental insights into the control of defect formation and thus establish a foundation for the design of future high performance and reliable *p*-ZnO films.

**Recent Progress**

1. DLTS

Electron and hole traps in N-doped ZnO were investigated using a structure of n<sup>+</sup>-ZnO:Al/i-ZnO/ZnO:N grown on a p-Si substrate by metal-organic chemical vapor deposition. Current-voltage and capacitance-voltage characteristics measured at temperatures from 200 to 400 K show that the structure is an abrupt n<sup>+</sup>-p diode with very low leakage currents. By using deep level transient spectroscopy, two hole traps, H3 (0.35 eV) and H4 (0.48 eV), are found in the p-Si substrate, while one electron trap E3 (0.29 eV) and one hole trap H5 (0.9 eV) are observed in the thin ZnO:N layer. The originality of these defects is not clear and is under investigation.

2. Ex-situ Raman

In addition to DLTS, we have demonstrated that Raman characterization is a potentially powerful tool to study the mechanism of nitrogen doping. We have observed new Raman features near 280, 510, 570, 642, 773, 1360 and 1565 cm<sup>-1</sup> shift in nitrogen doped ZnO (ZnO:N) thin films compared with undoped ZnO films. Peaks at 280, 510, 570, 642, and 773 cm<sup>-1</sup> are attributed to the nitrogen related defect complex. The Raman peaks at 1360 cm<sup>-1</sup> and 1565 cm<sup>-1</sup> shift are assigned to D- (disordered) and G- (Graphitic) bands associated with the carbon-related defect complex, respectively. The intensity and the intensity ratio of peaks at 1360 cm<sup>-1</sup> and 1565

$\text{cm}^{-1}$  have been found to be sensitive parameters that reflect the conductivity type of ZnO:N. Explanations are presented which correlate the Raman features to the electric conductivity of the films. From this analysis, we found that at temperature lower than or at  $400^\circ\text{C}$ , nitrogen incorporation will form the nitrogen or possible nitrogen carbon related defect complex. As the growth temperature increases to  $500^\circ\text{C}$ , the features associated with nitrogen are difficult to distinguish and the features associated to carbon begin to emerge. This observation possibly indicates the decrease of the nitrogen content and the increase of the carbon content in the ZnO:N film. The increase of carbon content may affect the donor behavior of the film. This observation suggests that growth conditions should be controlled to avoid carbon into the film. To obtain real-time evolution of the defects, an in-situ analysis is needed. In fact, no *in-situ* Raman study to investigate the kinetic aspects of nitrogen doping has ever been reported in the literature.

### 3. In-situ Raman Reactor Fabrication

The Raman reactor is designed and fabricated. The drawing of the reactor is shown in Figure 1. This reactor features the flexibility in gas introduction, vacuum, heating and cooling.

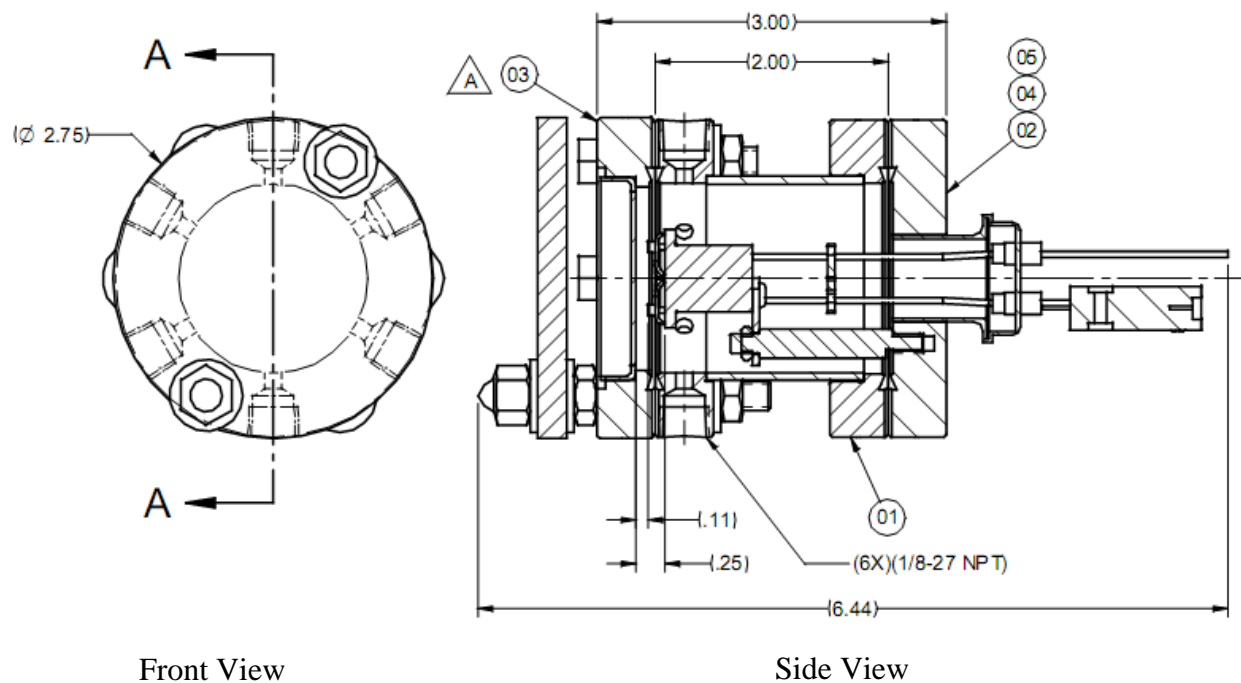


Figure 1. Schematic Drawing of In-Situ Raman Reactor

### 4. ZnO:N Deposition Reactor Set-up

The common method in the synthesis of ZnO:N is doping nitrogen into the lattice during the formation of ZnO. For example, in the CVD method, Diethylzinc is used as a zinc precursor to generate Zn radical and then react with O to form ZnO. Even though the decomposition of Diethylzinc is at low temperature, this process introduces its product, carbon into the film. In our previous ex-situ Raman experiments, we have found that carbon content may affect the donor behavior of the film. This observation suggests that growth conditions should be controlled to avoid carbon into the film. The solubility of nitrogen in ZnO:N is limited by this process. We designed two synthesis routes for ZnO:N to overcome the problem encountered in the traditional

CVD method. We have finished the experiments set-up for physical vapor deposition of ZnO:N. A tube furnace is purchased from MTI Co. Modification was made to avoid the tube cracking and enforce the process reproducibility and safety. The set-up features vacuum, precise gas flow control, temperature control and ramping, wide range deposition temperatures (from 200~1200 °C). The experimental set-up is shown in Figure 2.



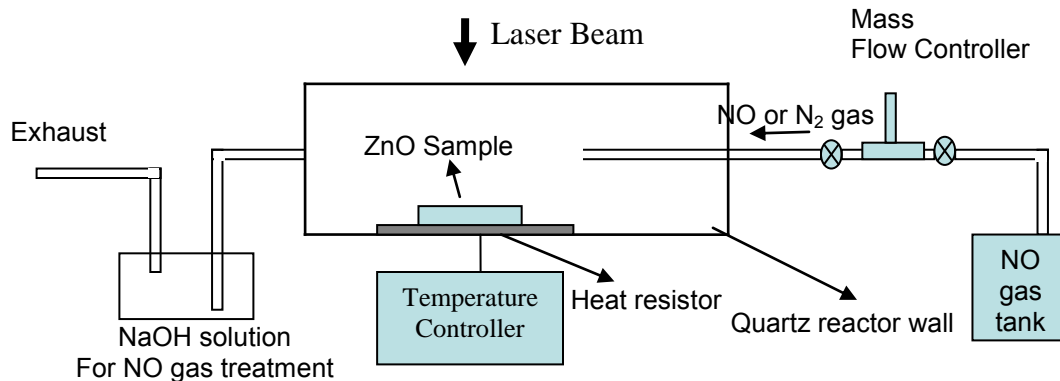
Figure 2. Reactor for ZnO:N Deposition

### Future Plans

Our future plans will be

- (1) ZnO:N will be synthesized and characterized. A homogenous device will be made.
- (2) Perform the In-situ Raman Experiments

The aim of the *in-situ* Raman is to investigate substrate temperature, NO flow rate, and different nitrogen precursor effects on the electrical properties of nitrogen doped ZnO through an *in-situ* Raman study. Investigating the correlations between growth conditions and film properties will reveal new insights into controlling the electrical properties of ZnO:N, and will provide significant guidelines for *p*-type ZnO:N growth.



- (3) Both room temperature and temperature dependent Hall effect measurements will be used to identify film conductivity type, shallow level defect and free carrier concentrations and mobilities.
- (4) DLTS will be used investigate the deep level defects that are related to residual impurities or point defects.
- (5) The electron irradiation is used to investigate the origin of the traps in ZnO:N by creating defects with high-energy electron irradiation.

# Luminescence, Structure, and Growth of Wide-Bandgap InGaN Semiconductors

S. R. Lee, D. D. Koleske, M. H. Crawford, G. Thaler, D. M. Follstaedt, and N. A. Missert  
Sandia National Laboratories, P. O. Box 5800, Albuquerque, NM 87185-1086

Email contact: srlee@sandia.gov

## Program Scope

Wurtzite-structure III-nitride alloys of InN, GaN, and AlN exhibit unusual optoelectronic and structural properties unlike those of well-known cubic-structure semiconducting alloys such as SiGe, InGaAs, and InGaP. Chief among these properties is the unique ability of InGaAlN alloys to span an unprecedented range of direct bandgaps that reach from the infrared (InN), to the visible (InGaN), upwards into the ultraviolet (AlN). These wide-bandgap alloys enable diverse new technologies important to solid-state lighting, remote sensing of chemical and biological agents, and perhaps even quantum computing. Yet, the high lattice mismatch, the immiscibility, and the widely varying thermal stability of the III-nitride alloys make their synthesis almost as challenging as their promise.

Because their synthesis is in fact demanding, as-grown III-nitride materials often contain extended defects like dislocations or *v*-defects, as well as various point defects or impurity complexes, not to mention possible carrier-localizing compositional inhomogeneities. This complex microstructure strongly alters the underlying intrinsic properties of these materials. Then again, these intrinsic properties are in themselves distinctive. For example, the wurtzite structure, the large piezoelectric coefficients, and the high lattice mismatch of III-nitride heterostructures combine to produce enormous piezoelectric fields that fundamentally alter bandstructure via the quantum-confined Stark effect (QCSE). Moreover, compared to cubic alloys, the wurtzite structure of the III-nitrides modifies both the elastic properties and the dislocation slip systems available for relaxation of the high-lattice-mismatch strains.

Against this remarkable backdrop, we seek improved understanding of the luminescence mechanisms that operate in InGaN alloys. Our approach combines complementary optical and structural characterization studies with unique experimental designs based on novel heterostructures and tailored materials growth. This approach attempts to isolate specific processes, structures, or defects in order to improve our understanding of the mechanisms that link epitaxial growth, materials structure, and luminescence pathways in these alloys. These studies help to provide the fundamental knowledge needed to make energy-efficient solid-state white lighting a practical reality. Such a reality could ultimately reduce American energy expenditures for lighting by as much as \$30 billion/year.

## Recent Progress

### Mechanisms for Enhanced Quantum Efficiency of InGaN Quantum Wells Grown on InGaN Underlayers

The luminescence efficiency of InGaN multi-quantum well (MQW) structures has been found to depend on a number of factors and is, to date, not well understood. Recently, a striking phenomenon has been observed, namely a greater than 3X enhancement of internal quantum efficiency of InGaN MQWs with the addition of a lower-growth-temperature InGaN epilayer between the MQWs and the higher growth temperature GaN template layer.<sup>1,2</sup> This deceptively simple structural change has the potential to remotely influence a number of properties that are thought to impact QW luminescence including compositional fluctuations, point and extended defect populations, and materials microstructure. In addition, these low-growth-temperature layers have been shown to nucleate *v*-defects that have been proposed to play a significant role in avoiding non-radiative recombination by producing a potential-energy barrier around threading dislocations.<sup>3,4</sup> The present work seeks to clarify the mechanisms that enable luminescence enhancement in InGaN QW-on-underlayer structures. Our studies go beyond previous reports to include analysis of underlayers over a range of indium compositions and layer thicknesses, as well as underlayers grown at different temperatures to directly control the formation of *v*-defects.

Our spectroscopic and structural studies focused on InGaN MQW heterostructures emitting at ~450 nm and grown by metal-organic vapor phase epitaxy (MOVPE) on two types of underlayers: (a) 200-nm-thick InGaN underlayers ( $T_g = 790^\circ\text{C}$ ) with indium compositions ranging from 0 to 9% and (b) 200-nm-thick underlayers with indium composition fixed at 2% but grown at either  $790^\circ\text{C}$  or  $880^\circ\text{C}$  to enable direct comparisons of samples with or without *v*-defects. In the underlayer composition study, we further included “hybrid” underlayers composed of GaN/InGaN bilayer structures. Transmission electron microscopy (TEM) and high-angle annular detector dark-field STEM were employed to evaluate dislocation types at *v*-defects and to characterize QWs on the sidewalls of the *v*-defects. Time-resolved and temperature-dependent photoluminescence (PL) studies were conducted to evaluate radiative and non-radiative recombination processes and internal quantum efficiencies. Scanning

cathodoluminescence (CL) enabled direct spatial imaging of luminescence with  $\sim 50$  nm resolution, and these luminescence maps were correlated with secondary-electron and atomic-force-microscopy (AFM) images.

Our studies reveal the critical importance that underlayer composition has for producing intense light emission. In Figure 1, we show internal quantum efficiencies (IQE) of InGaN QWs as a function of underlayer indium composition. Here, the IQE is determined from the ratio of PL intensity at 300K versus 4K under “resonant” excitation conditions (415 nm) where the QWs are selectively pumped. We see that the addition of only 2.5% indium enables almost 7X enhancement of IQE over low-temperature GaN underlayers, with relatively little change for higher indium compositions. Notably, even a very thin InGaN underlayer (20 nm) on a GaN underlayer (“Hybrid UL” in Fig. 1) promotes significant IQE improvements. Results of Arrhenius modeling will be presented to elucidate PL quenching mechanisms as a function of underlayer composition and thickness.

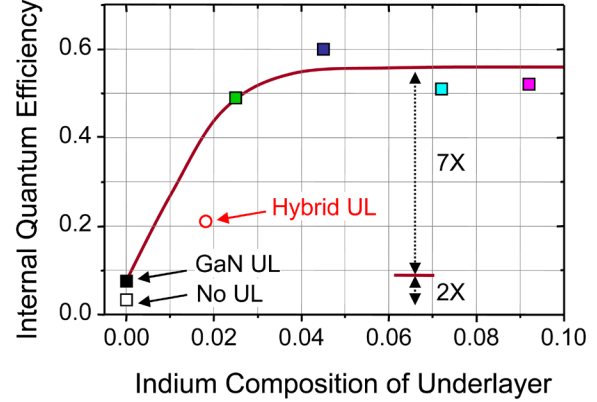


**Figure 1.** Internal quantum efficiency for InGaN QWs with different composition underlayers (ULs). The hybrid underlayer is a bilayer that includes 20 nm of  $\text{In}_{0.018}\text{Ga}_{0.982}\text{N}$  on top of 180 nm of low-temperature GaN.

In further studies, temperature-dependent PL of structures with different underlayer growth temperatures demonstrated that *equal IQE enhancement can be achieved with and without v-defects*. These results are significant because they indicate that the decoration of threading dislocations by v-defects is not the dominant mechanism for PL enhancement, contrary to recent prominent claims.<sup>4</sup> CL images will be presented to further reveal submicron-scale modifications to luminescence in the presence of v-defects and as a function of underlayer composition. Analysis of these and other data will be presented to support our hypothesis that alteration of point-defect populations is a likely mechanism for PL enhancement in InGaN QW-on-underlayer samples.

### AFM Studies of the Surface-Step Morphology of InGaN/GaN Heterostructures

Despite the high density of dislocations in GaN epitaxial layers grown on sapphire, InGaN-based light-emitting devices (LEDs) grown on these GaN layers are surprisingly bright and efficient. Several theories have been proposed to explain this efficient light emission.<sup>4-8</sup> While important details of these theories vary, a unifying theme is the existence of carrier localization or potential barriers that prevent non-radiative recombination at dislocations or other defects. One theory of growing interest proposes that small fluctuations in the thickness of InGaN QWs may interact with the large piezoelectric field of the highly strained QW to produce bandgap fluctuations strong enough to localize carriers at room temperature.<sup>7</sup> This idea seems compelling considering both the tendency for InGaN surface roughening during growth on GaN,<sup>8</sup> and the recent TEM observation of monolayer thickness fluctuations in InGaN/GaN MQWs,<sup>7</sup> which appear to arise from irregular surface steps formed during growth of the InGaN QW.

On the other hand, QW-thickness fluctuations might instead lower radiative efficiency by a competing effect whereby altered piezoelectric fields in the QWs concomitantly reduce the overlap of electron-hole wavefunctions. This reduced overlap in regions where the QWs are thicker may be one reason why smoother interfaces may be necessary for improving green-LED efficiency, as demonstrated by Wetzel.<sup>9</sup> To improve understanding of the interaction between surface morphology, QW-thickness fluctuations, and these luminescence mechanisms, further studies of surface-step structure and surface morphology in InGaN/GaN heterostructures are needed.

For this study, InGaN films were grown on GaN templates using MOVPE. The GaN template films were on c-plane sapphire oriented  $0.2^\circ$  toward the m-plane direction. The surfaces of GaN templates grown on this sapphire orientation are dominated by single-monolayer step arrays oriented along the a-plane direction. The change in this initial step morphology upon addition of indium to the heterolayer was studied by growing a series of green-emitting MQWs comprised of 3.3-nm-thick  $\text{In}_{0.20}\text{Ga}_{0.80}\text{N}$  QWs separated by 11-nm-thick GaN barrier layers, where the parameter varied in the series was the number of QWs in the heterostructure. Following growth, the step morphology of the InGaN-terminated surface of each sample was measured by AFM. Subsequent analysis of the AFM images yielded step positions, step heights, and the relative frequency of occurrence for steps of different heights. The observed step heights cluster around integer multiples of  $c/2$ , where  $c$  is the wurtzite unit-cell height, and  $c/2$  is the height change caused by adding one III-V compound monolayer to the surface.

The resulting frequency distributions for the observed step-heights are shown in Fig. 2 for the initial GaN template and for heterostructures comprised of 1, 2, 3 and 7 pairs of GaN barrier layers and InGaN QW layers. Note that as the number of QWs increases, the frequency of single-layer steps decreases and the frequency of multiple-

layer steps increases, indicating an increased tendency to form step bunches upon the addition of InGaN QW layers. Note also that for heterostructures with more than 2 QWs, changes in the frequency distribution saturates, suggesting that the mechanisms that roughen and smooth the heterostructure's surface are balanced by each other as further GaN-barrier/InGaN-QW layer pairs are added. Motivated by this observation, further experiments were performed where the growth temperature of the GaN-barrier layers was varied to investigate the competing influences of roughening, smoothing, and intermixing during MQW growth. From yet other AFM studies of single QWs where indium composition was varied, we found that InGaN step bunching also tends to increase with indium composition, or equivalently, heterolayer strain.

### Future Plans

In the near-term, we plan to continue ongoing studies of both the enhanced luminescence produced by InGaN underlayers and the surface-step morphology of InGaN/GaN heterostructures. For our continuing underlayer work, we will seek to clarify the method by which a remote InGaN layer might alter the defect population and/or compositional uniformity of the QWs. We specifically seek to identify whether the underlayer alters the growth mode, which could substantially modify the structural quality of overlying QW layers. Alternatively, the underlayer might act as a trap or barrier to defect diffusion. Specific sample designs to delineate these possibilities will include “overlayer” structures, where the low-growth-temperature InGaN layer is grown above (and subsequent to) the QWs and therefore does not alter the QW growth mode or create v-defects that interact with the QWs but still may enable defect trapping. Additionally, buried underlayer structures, where the InGaN underlayer is followed by a low temperature or high temperature GaN layer before the standard QW structure, will be grown and studied. These structures will serve to examine the extent to which the “remoteness” of these layers is a factor, potentially clarifying how the location of the InGaN underlayers may be altering the growth mode as well as compositional and defect properties of the QWs.

For our continuing work on InGaN step morphology, we will compare our observed InGaN and GaN step-height distributions to various existing theories<sup>10-13</sup> describing step-bunching and morphological instabilities. The dependence of these theories on the growth rate, the surface-diffusion rate, and the magnitude and sign of the film stress may offer further opportunities to design experiments that test these theories for applicability to the step behavior found on wide-bandgap InAlGaIn-alloy growth surfaces. Further work will also examine the connection between observed step distributions and the optical properties of InGaN/GaN heterostructures, with an emphasis on possible linkages to resulting QW thickness fluctuations that may localize carriers.

Recently, we have also begun new experiments in two additional areas. The first of these two areas is the influence of growth temperature on luminescence efficiency. Our interest in this topic stems from the fact that higher-indium-content  $\text{In}_x\text{Ga}_{1-x}\text{N}$  alloys ( $x > 20\%$ ) that emit at green and longer wavelengths suffer from very low light-emission efficiency. A challenge that limits present understanding of mechanisms behind this low internal quantum efficiency is the fact that lower growth temperatures ( $\leq 740^\circ\text{C}$ ) must be employed to achieve the higher indium incorporation needed for light emission at these longer wavelengths. It has also been shown for GaN and InGaN heterostructures that reduced growth temperatures alone may impair materials properties by promoting impurity incorporation and point-defect formation,<sup>14</sup> indium compositional instability,<sup>15</sup> indium-metal condensation,<sup>16</sup> and transitions in the heteroepitaxial growth mode.<sup>17</sup> These growth-temperature-induced effects are therefore likely to compete with the intrinsic properties of higher-indium-content alloys that might otherwise dominate the recombination processes, such as strain-induced piezoelectric fields in InGaN/GaN QW structures grown on the polar basal plane of GaN. The goal of these emerging experiments is to develop materials-synthesis strategies, heterostructure designs, and characterization methods that isolate growth-temperature-related defectivity in InGaN alloys from separate intrinsic effects arising solely from concomitant variations in alloy composition.

The second new area of study is the thermal stability of InGaN. Our interest here stems from the inherent limitations placed on heterostructure growth and processing by the intrinsic thermal instability of InGaN alloys, which thermodynamically prefer to revert to indium metal and  $\text{N}_2$  gas at the elevated temperatures and near-

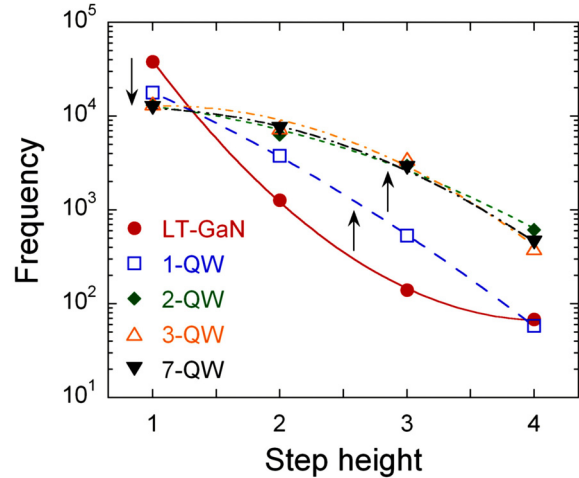


**Figure 2.** Step-height frequency distributions for various  $\text{In}_{0.20}\text{Ga}_{0.80}\text{N}/\text{GaN}$  QW heterostructures. The step height is expressed as integer multiples of  $c/2$ . The legend indicates the number of barrier-QW periods present in each heterostructure.

atmospheric pressures typically used to process InGaN alloys. In these studies we plan to grow by MOVPE both InGaN quantum wells and thicker InGaN single heterolayers of various compositions. The as-grown samples will be subjected to both isochronal and isothermal annealing studies where evolution of the structural and optical properties will be characterized as a function of the annealing conditions. Subsequent analysis of the resultant annealing data will allow us to extract both the activation energy and the order of the reaction-rate kinetics, thereby providing insight into the basic mechanisms underlying decomposition of these alloys at high temperature.

In the longer term, additional studies may turn to strain-limited indium incorporation and related strain-relaxation processes in InGaN/GaN heterostructures, as well as alternative methods for characterizing threading dislocations in III-nitride heterostructures. Plans for these longer-term possibilities, along with more detailed plans regarding the ongoing and newly started studies summarized above, are documented in our regular FWP submittals to BES/DOE.

## DOE Sponsored Publications for 2005 to Present

- *Characterization of Minority-Carrier Hole Transport in Nitride-Based Light-Emitting Diodes with Optical and Electrical Time-Resolved Techniques*, R. J. Kaplar, S. R. Kurtz, D. D. Koleske, A. A. Allerman, A. J. Fischer, and M. H. Crawford, Mater. Res. Soc. Symp. Proc. Vol. **831**, E10.9 (2005).
- *Novel Optical Probes of InGaN/GaN Light-Emitting Diodes: 1. Electroreflectance Stark Spectroscopy, and 2. Time-Resolved Emission*, R. J. Kaplar, S. R. Kurtz, and D. D. Koleske, Phys. Stat. Sol. (c) **2**, 2866 (2005).
- *Effect of Threading Dislocations on the Bragg Peakwidths of GaN, AlGaIn, and AlN Heterolayers*, S. R. Lee, A. M. West, A. A. Allerman, K. E. Waldrip, D. M. Follstaedt, P. P. Provencio, D. D. Koleske, and C. R. Abernathy, Appl. Phys. Lett. **86**, 241904 (2005).
- *Quantum-Confined Stark Effect and Polarization Field in Single Quantum Well InGaN/GaN LEDs*, R. J. Kaplar, S. R. Kurtz, and D. D. Koleske, Mater. Res. Soc. Symp. Proc. Vol. **892**, FF32.1 (2006). This article received a Best-Paper Award, Symposium FF, 2005 Fall Meeting of the Materials Research Society.
- *Research Challenges to Ultra-Efficient Inorganic Solid-State Lighting*, Julia M. Phillips, Michael E. Coltrin, Mary H. Crawford, Arthur J. Fischer, Michael R. Krames, Regina Mueller-Mach, Gerd O. Mueller, Yoshi Ohno, Lauren E. S. Rohwer, Jerry A. Simmons, and Jeffrey Y. Tsao, Laser & Photon. Rev. **1**, 307 (2007).
- *Effect of Dislocation Density on Efficiency Droop in GaInN/GaN Light-Emitting Diodes*, Martin F. Schubert, Sameer Chhajed, Jong Kyu Kim, E. Fred Schubert, Daniel D. Koleske, Mary H. Crawford, Stephen R. Lee, Arthur J. Fischer, Gerald Thaler, and Michael A. Banas, Appl. Phys. Lett. **91**, 231114 (2007).
- *Dislocation Reduction in AlGaIn Grown on Patterned GaN*, D. M. Follstaedt, A. A. Allerman, S. R. Lee, J. R. Michael, K. H. A. Bogart, M. H. Crawford, and N. A. Missert, J. Crystal Growth **310**, 310 (2008).

## Online Publications

- *Basic Research Needs for Solid State Lighting*, Chaired by Julia M. Phillips and Paul E. Burrows, BES Workshop on Solid-State Lighting, May 22-24, 2006, Bethesda, MA; available on the web at [http://www.er.doe.gov/bes/reports/files/SSL\\_rpt.pdf](http://www.er.doe.gov/bes/reports/files/SSL_rpt.pdf).
- *2006 Fundamental Research Underlying Solid-State Lighting Contractors Meeting*, pp. 67-70, 2006 DOE Solid-State Lighting Workshop, Feb. 1-3, 2006, Lake Buena Vista, FL; available on the web at [http://www.netl.doe.gov/ssl/PDFs/2006\\_Solid\\_State\\_Abstract\\_Book\\_FINAL.pdf](http://www.netl.doe.gov/ssl/PDFs/2006_Solid_State_Abstract_Book_FINAL.pdf).

## Literature Cited

1. T. Akasaka, *et al.*, Appl. Phys. Lett. **89**, 101110 (2006) and references therein.
2. J. K. Son, *et al.*, J. Cryst. Growth **287**, 558 (2006).
3. H. Takahashi, *et al.*, Jpn. J. Appl. Phys. **39**, L569 (2000).
4. A. Hangleiter, *et al.*, Phys. Rev. Lett. **95**, 127402 (2005).
5. S. Chichibu, *et al.*, Appl. Phys. Lett. **71**, 2346 (1997).
6. S. Chichibu, *et al.* Nat. Mat. **5**, 810 (2006).
7. D. M. Graham, *et al.*, J. Appl. Phys. **97**, 103508 (2005).
8. S. Sonderegger, *et al.*, Appl. Phys. Lett. **89**, 232109 (2006).
9. C. Wetzel, *et al.*, Appl. Phys. Lett. **85**, 866 (2004).
10. Y. H. Xie, *et al.*, Phys. Rev. Lett. **73**, 3006 (1994).
11. J. Tersoff, *et al.*, Phys. Rev. Lett. **75**, 2730 (1995).
12. R. V. Kukta and K. Bhattacharya, Thin Solid Films **357**, 35 (1999).
13. A. C. Schindler, *et al.*, Phys. Rev. B **67**, 075316 (2003).
14. D. D. Koleske, *et al.*, J. Cryst. Growth **242**, 55 (2002).
15. I. Ho and G. B. Stringfellow, Appl. Phys. Lett. **69**, 2701 (1996).
16. F. Jiang, *et al.*, Appl. Phys. Lett. **89**, 161915 (2006).
17. R. A. Oliver, *et al.*, J. Appl. Phys. **97**, 013707 (2005).

This work is supported by the Division of Materials Sciences and Engineering, Office of Basic Energy Sciences, U. S. Department of Energy. Sandia is a multiprogram laboratory operated by Sandia Corporation, a Lockheed Martin Company, for the U. S. Department of Energy's National Nuclear Security Administration under contract DE-AC04-94AL85000.

# Superconducting Materials

Qiang Li (Principal Investigator, qiangli@bnl.gov), A. Moodenbaugh, and W. Si  
Condensed Matter Physics and Materials Science Department  
Brookhaven National Laboratory, Upton, NY 11973-5000

## Program Scope

This program studies the basic relationships between structure and properties of superconductors to provide understanding of fundamental materials science and physics required for their energy applications. It encompasses investigations of physical properties, nanostructure, basic mechanisms, and electronic states. Correlated electronic materials, which have a wide range of superconducting, magnetic, and emergent high thermoelectric behavior, are being made to understand the effect of competing orders, chemical doping, interface, and structure defects on superconducting properties. Both equilibrium and non-equilibrium synthesis route are used to explore a broad phase space of superconductors and to enhance the properties of superconducting materials.

## Introduction

Superconductors offer powerful opportunities for restoring the reliability of the power grid and increasing its capacity and efficiency. Superconductivity itself is a profound example of correlated electron behavior. The basic understanding of superconductivity and superconducting materials has contributed to the growth of knowledge in other basic energy research areas, such as high thermoelectric power in complex oxides[1][2], spin transport, electronic behavior in low dimensions. Although present high temperature superconductor (HTS) technology can be deployed for some of the grid functions, significant barriers remain to achieving the full potential of superconductivity for transforming the power grid. Bridging the gaps in performance improvement of superconductors and identifying the limiting factors requires a fundamental understanding of the microscopic origin of superconducting behavior.

The two most important superconducting properties are transition temperature (critical temperature  $T_c$ ) and current-carrying capability measured by critical current density  $J_c$ , because they determine the limits to practical applications.  $T_c$  is related to the mechanism of superconductivity. Significant progress has been made in the past two decades. However, an acceptable understanding of the underlying principles of high-temperature superconductivity is still lacking. The grand challenge here is the need to understand the mechanism of HTS, which is the ultimate driving force in our attempt to discover new superconductors by design, rather than by serendipity. In contrast to the quantity  $T_c$ ,  $J_c$  is governed by vortex pinning strength, which is determined by the ability of defects in superconductors to pin the superconducting vortices carrying the magnetic flux. Although several recently proposed strategies have shown progress in enhancing flux pinning, the fundamental flux pinning mechanism in HTS remains controversial.

This research program emphasizes improvement in both the critical temperature  $T_c$  and the critical current density  $J_c$  by capitalizing on advanced synthesis and characterization capabilities, and unique opportunities for synergistic collaborations at Brookhaven National Laboratory. Our research activities seek advancement by achieving a broad understanding (1) the response of high temperature superconductivity to competing order parameters, doping, and interfaces, and (2) the response and control of  $J_c$  in HTS by defect tuning.

## Recent Progress (primary accomplishments in 2005-2007)

The measurements of anisotropic transport and magnetization properties of  $\text{La}_{2-x}\text{Ba}_x\text{CuO}_4$  (LBCO) for  $x = 1/8$  revealed dynamic layer decoupling of the  $\text{CuO}_2$  planes, as shown in Fig. 1. A state of 2D fluctuating superconductivity (SC) with enhanced  $T_c$  was observed for the first time. We found compelling evidence that the dominant impact of the stripe ordering is to electronically decouple the  $\text{CuO}_2$  planes. The charge-ordering transition, at  $T_{co}$ , is correlated with a rapid increase in the anisotropy

between the resistivity along the  $c$ -axis,  $\rho_c$ , and that parallel to the  $\text{CuO}_2$  planes,  $\rho_{ab}$ . At the spin-ordering temperature,  $T_{\text{so}}$ , there is a sharp drop in  $\rho_{ab}$  by an order of magnitude; we label the latter magnetic-field-dependent transition as  $T_c^{2\text{D}}$ . Below  $T_c^{2\text{D}}$ ,  $\rho_{ab}(T)$  follows the temperature dependence predicted for a 2D superconductor above the Berezinskii-Kosterlitz-Thouless (BKT) transition temperature  $T_{\text{BKT}}$ . This state also exhibits weak, anisotropic diamagnetism and a thermopower very close to zero. Below the nominal  $T_{\text{BKT}}$  ( $\sim 16$  K), we observed nonlinear voltage-current ( $V$ - $I$ ) behavior consistent with expectations for a 2D superconductor. We concluded that charge inhomogeneity and 1D correlations are good for pairing in the  $\text{CuO}_2$  planes. It appears that the stripe order in  $\text{La}_{1.875}\text{Ba}_{0.125}\text{CuO}_4$  frustrates 3D superconducting phase order, but is fully compatible with 2D superconductivity and an enhanced  $T_c$  [3].

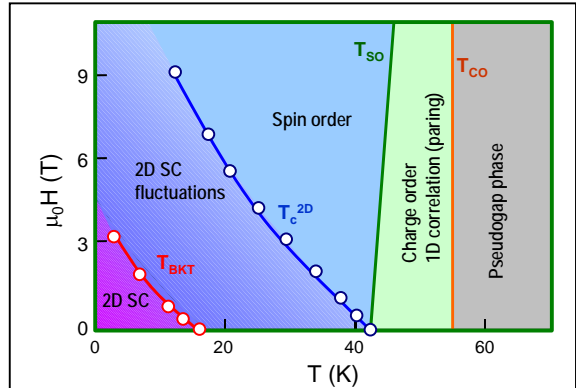


Fig. 1. Experimental phase diagram for  $\text{La}_{1.875}\text{Ba}_{0.125}\text{CuO}_4$ . The transition lines for charge order, spin order, and the boundaries labeled  $T_c^{2\text{D}}$  and  $T_{\text{BKT}}$  are described in the text.

Measurements of the electrical resistivity of single crystal  $\text{La}_{2-x}\text{Ba}_x\text{CuO}_4$   $x = 1/8$  were coordinated with measurements over a wide frequency and temperature range of the  $ab$ -plane optical properties of a cleaved single crystal. We found that the dc and low-frequency conductivity is Drude-like and shows a metallic response with decreasing temperature. However, below  $\sim 60$  K, corresponding to the onset of charge-stripe order, there is a rapid loss of spectral weight below about 40 meV, resulting in a major reduction in the number of free carriers. This suggests a partial gapping of the Fermi surface. Surprisingly, the sample is still metallic and becomes a superconductor at low temperature. This is a striking example of how charge and spin stripe order, metallic behavior and superconductivity can exist in the same material [4].

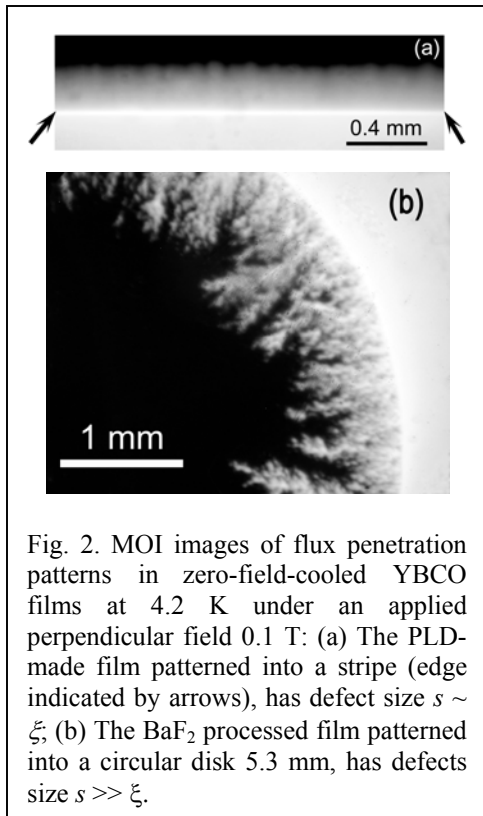


Fig. 2. MOI images of flux penetration patterns in zero-field-cooled YBCO films at 4.2 K under an applied perpendicular field 0.1 T: (a) The PLD-made film patterned into a stripe (edge indicated by arrows), has defect size  $s \sim \xi$ ; (b) The  $\text{BaF}_2$  processed film patterned into a circular disk 5.3 mm, has defects size  $s \gg \xi$ .

Magnetic flux front and induction contours in superconducting YBCO films with defect size  $s \sim \xi$  (superconducting coherence length) and  $s \gg \xi$  were studied by the magneto-optical imaging (MOI) technique[5]. They exhibit remarkably different patterns (Fig. 2). Robust self-affine spatial correlation was observed using scaling analysis in the small pinning-dominated ( $s \sim \xi$ ) disordered films prepared by pulsed laser deposition (PLD). The roughness exponent  $\alpha$  was determined to be  $\sim 0.66$ , independent of the number of defects (or film thickness). When the disorder landscape also included a distribution of large defects ( $s \gg \xi$ ) as in the  $\text{BaF}_2$  ex-situ processed films, the flux front and induction contours exhibited self-similarity, with a fractal dimension  $D$  determined to be  $\sim 1.33$  using the box-counting method. This study suggests that different fractal behavior manifests the multiple aspects of the self-organized criticality at different length scales in flux pattern formation. Through tuning the relative disorder length scale, flux pattern formation offers a new way to explore the nature of flux pinning in superconductors, as well as the general self-organized criticality in quenched disordered systems [6][7].

Effects of stacking and of magnetic substrates on ac (hysteresis) losses of octagonal disks of a  $\text{YBa}_2\text{Cu}_3\text{O}_7$  (YBCO)

layer on Ni-5 at.% W substrate were measured as a function of perpendicular ac magnetic fields at 20 Hz in liquid nitrogen. The losses varied inversely proportional to the number of the disks. Magnetic substrates sandwiching the YBCO film reduced the losses of a disk at low magnetic fields. At low fields, the losses depended on the ac magnetic field amplitude  $B$  and film thickness  $t$  as  $\sim B^3/t$  rather than the  $\sim B^4/t^3$  expected for a superconducting film on a nonmagnetic substrate. At high fields, the losses were independent of the stacking and of the magnetic substrate. The basic principle for the loss reduction is a decrease in the curvature of the flux lines [8].

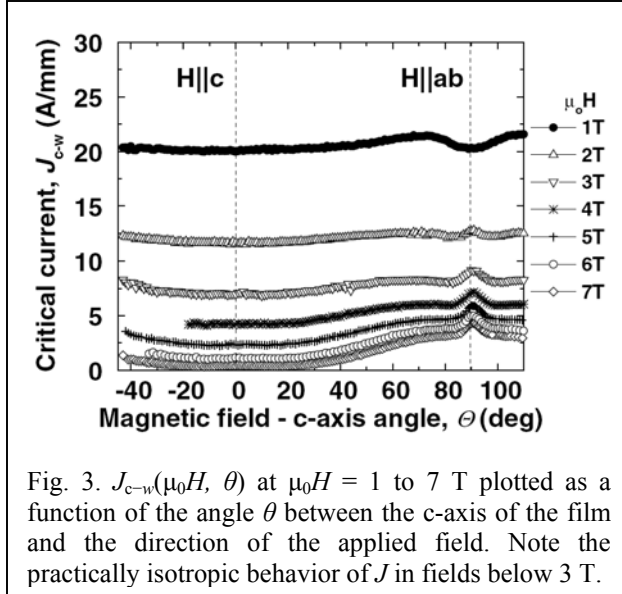


Fig. 3.  $J_{c-w}(\mu_0 H, \theta)$  at  $\mu_0 H = 1$  to 7 T plotted as a function of the angle  $\theta$  between the c-axis of the film and the direction of the applied field. Note the practically isotropic behavior of  $J$  in fields below 3 T.

We observed a record high  $J_{c-w}(H)$  by combining strong, isotropic flux pinning with high  $T_c$  in a 3- $\mu\text{m}$ -thick YBCO film. Strong isotropic flux pinning was observed for the first time in strong anisotropic HTS at liquid nitrogen temperature. We found that, at  $H < 3\text{T}$ ,  $J_c(H)$  was nearly independent of the angle  $\theta$  between the field direction and the normal to the tape plane, indicating the presence of not only strong but also isotropic magnetic-flux pinning centers in the film (Fig. 3). The very weak angular dependence of  $J_c$  around c-axis indicates that the pinning centers in record high- $J_c$  YBCO thick films are nearly isotropic and are not correlated to a particular direction or alignment. Key features of these improved samples are meandering grain boundaries and a very high number of defects. Interestingly,  $T_c$  is also higher in these films than in other films with strong pinning [9][10].

Studies of structure, heat capacity, and transmission electron microscopy with electron energy loss spectroscopy (EELS) were coordinated to probe the changes in superconductivity in  $\text{MgB}_2$  when the Mg atoms are progressively replaced by Al. We obtained the first direct evidence for the filling of the hole states in the planar  $\sigma$  band, crucial for the high  $T_c$  in pure  $\text{MgB}_2$ , by the extra electrons donated by Al. Yet, other property measurements indicated that superconductivity was not destroyed when there was sufficient Al to fill all of the hole states, but it persisted to much higher levels of Al doping. Using a two-band model of superconductivity, fits to the heat capacity data indicated that it is the  $\pi$  band that survives in the heavily doped regime, which is an inversion of the hierarchy of the bands in pure  $\text{MgB}_2$  [11][12].

## Future Plans

The future research activities will include performing the synthesis and characterization of superconducting property within our group, and extending the work in collaboration with other groups in the Condensed Matter Physics and Materials Science Department to provide spectroscopic studies of the electronic states, magnetic correlations, and analytical TEM studies of the *local* electronic states and nanostructure. Such a multi-pronged experimental approach will allow us to address the key science issues ranging from the macroscopic to the atomic level. The response of the electronic structure and transport properties to the competing orders, doping, structural defects and interface will be the main focus of our program. The followings are several key science issues that will be addressed directly.

### *Interplay of superconductivity and diluted stripes*

The superconducting phase in HTS is just one of several competing electronic phases (e.g., magnetically ordered insulating phase and pseudo-gap phase) that may be used as new “knobs” to “tune” the performance of superconductors. Here, we propose to extend our current LBCO work to compositions  $x \neq 1/8$  and investigate the impact of the diluted stripes on superconductivity. For  $x \neq 1/8$ , there is a

tendency to develop discommensurations in stripe order, which, in turn, produce regions of enhanced (or depressed) superconducting order. As long as the stripes are dilute, the energy depends weakly on the precise spacing. Thus, to gain interlayer condensation energy, the system can self-organize. This leads to a rapid suppression of the 2D regime and a dramatic increase of the 3D superconducting  $T_c$ . We will perform systematic transport measurements, which will be augmented by measurements of the electronic state using techniques such as angular resolved photoemission spectroscopy (APRES) and scanning tunneling microscopy (STM), and measurements of magnetic correlations with neutron scattering.

### ***Tuning the electronic anisotropy***

The early 2000s saw a paradigm shift to second generation (2G) wires based on YBCO that has several significant advantages over the 1G wire in current use. One of the primary advantages of YBCO is the possibility of in-field operation at 77 K. These advantages are inherent properties of the YBCO superconducting material, which, among all the HTS cuprates, shows the lowest intrinsic electronic anisotropy. Lower intrinsic anisotropy strengthens pinning, reduces vortex creep, and increase the vortex lattice shear rigidity. We propose to investigate how the electronic anisotropy of superconductors responds to the cation doping, such as Ca-doping in YBCO. An important question to be answered here is how Ca-doping changes the local electronic structure of the  $\text{CuO}_2$  planes and  $\text{CuO}$  chains through coordinated measurements by direct transport and the EELS in an aberration-corrected scanning transmission electron microscope (STEM). With a probe size of  $\sim 1 \text{ \AA}$ , such an instrument is able to provide “column-by-column” spectroscopy.

### ***Interface induced superconductivity and thermoelectricity***

The perovskite oxide interface exhibits a plethora of exceptional properties, providing the basis for novel concepts for designing new types of superconductors, or enhancing the  $T_c$  of known superconducting materials. The proposed work will explore oxide heterostructures to understand materials interface aspects that control their superconducting behavior, as well as its relation to thermoelectricity.

### ***Vortex pinning and $J_c$ in YBCO films***

In 2G YBCO coated conductors, the principal defects responsible for flux pinning are not understood, although many possible candidates have been suggested so far. Given the complexity of HTS, it is desirable to reduce the problem to the quantitative study of the effectiveness of specific defect types. Incorporating a second non-superconducting phase together with YBCO to increase flux pinning could be a path to higher current-carrying capacity. However, our recent studies [9] show single-phase films deposited at high growth rates also achieve record high  $J_c > 3 \text{ MA/cm}^2$ , indicating that the baseline YBCO itself can support a high population of defects for good flux pinning. The goal of this part of the proposed research is to identify the defects that are the dominant pinning centers in these films, and the development of model systems in which a specific defect type can be introduced in a controlled way to enhance  $J_c$ .

### **References (publications of this program sponsored by DOE/BES in 2005-07, a partial list)**

- [1] Y. F. Hu, *et. al.* Appl. Phys. Lett., **87** 171912 (2005)
- [2] Y. F. Hu, *et. al.* Appl. Phys. Lett., **86** 082103 (2005)
- [3] Q. Li, *et. al.* Phys. Rev. Lett., **99**, 067001 (2007)
- [4] C. C. Homes, *et. al.* Phys. Rev. Lett., **96**, 257002 (2006)
- [5] Q. Li and Z. Ye, Journal of Electronic Materials, **36**(10), 1288 (2007)
- [6] Z. Ye, *et. al.* Phys. Rev. B **72** 134514 (2005)
- [7] Z. Ye, *et. al.* Appl. Phys. Lett., **87** 122502 (2005)
- [8] M. Suenaga and Q. Li, Appl. Phys. Lett., **88**, 262501 (2006)
- [9] V F Solovyov, *et.al.*, Supercond. Sci. Technol., **20** L20–L23 (2007)
- [10] V. F. Solovyov, *et. al.* J. Appl. Phys., **99** 013902 (2006)
- [11] R. F. Klie, *et.al.*, Physical Review B **73**, 014513 (2006)
- [12] L. D. Cooley, *et. al.* Phys. Rev. Lett., **95**, 267002-5 (2005)

**Program Title:** Novel Ordered semiconductor Alloys

**Principle Investigators:** A. Mascarenhas, W.E. McMahon, S.-H. Wei

**Mailing address:** NREL 1617 Cole Blvd., Golden, CO 80401

**e-mail:** [angelo\\_mascarenhas@nrel.gov](mailto:angelo_mascarenhas@nrel.gov)

### Program Scope:

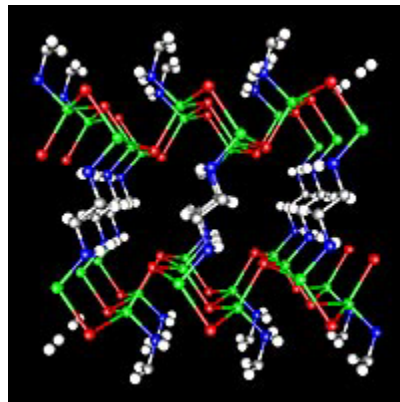
This research is directed at investigating the causes and consequences of ordering in semiconductor alloys. The understanding provided by research on semiconductor growth related instabilities such as spontaneous ordering and their optoelectronic consequences, serves to promote and advance the areas of fundamental materials science related to surface physics, epitaxial growth, and semiconductor materials physics. Uses of this phenomenon range from the ability to tune bandgap for a given lattice constant for multijunction solar cell applications, LEDs for solid-state lighting applications, to slowing down and storage of light. The research is multidisciplinary, combining experimental and theoretical efforts and involves collaborations with several universities and national laboratories. Additionally, it utilizes the DOE National Synchrotron facilities and the supercomputer resources at the NERSC facility.

### Recent Progress: Major Achievements

#### *1) Zero Thermal Expansion using Hybrid semiconductors*

Although inorganic-organic hybrid materials have been studied for decades, most previously studied hybrid materials, with few exceptions do not have long-range order but have weak bonds between the organic and inorganic components. Recently, a new family of crystalline hybrid materials has been synthesized by our collaborators at Rutgers University. These hybrid structures which are based on conventional II-VI semiconductors (e.g., ZnTe and CdS) are spontaneously ordered nanostructures of inorganic slabs or wires interconnected or coordinated by organic molecules.

Our early experimental investigations on a prototype system  $\text{ZnTe}(\text{en})_{0.5}$  (en = ethylenediamine) which has a 3-D structure resembling well-known inorganic monolayer superlattices like  $(\text{GaP})_1/(\text{InP})_1$  revealed a few unique properties, e.g. a giant band gap tunability, with a range greater than 1.5 eV, and a strongly enhanced band edge free excitonic absorption. We have now demonstrated that this hybrid material which does not exhibit the typical “interlayer mixing” found in inorganic superlattices, shows uniaxial zero-thermal-expansion (ZTE) in a very broad temperature range (4K – 400K), and concurrently possesses superior electronic and optical properties (see ref. 1). The ZTE behavior is a result of compensation of contraction and expansion of different segments along the inorganic-organic stacking axis. This research suggests an alternative route to designing materials on a nanoscopic scale with ZTE or any desired positive or negative thermal expansion by assembling nano-



$\text{ZnTe}(\text{en})_{0.5}$  hybrid semiconductor

scale units in an ordered manner, and may play a role in the design of future generations of electronics and optoelectronics that can withstand a wide range of temperatures.

This work involved collaborations with multiple institutions: Rutgers University, Argonne's Advanced Photon Source, University of Arkansas and the University of Colorado at Boulder.

## *2) Self assembled quantum coaxial cables for solar energy harvesting*

The recent surge in interest in self-assembled semiconductor nanowires is driven by the need to satisfy the critical requirement that for many practical applications the electron and hole conductivity should be retained for at least one dimension in order to inject or extract the carriers into or out from the nanostructures, while still being able to take advantage of novel physics phenomena associated with reduced dimensionality. This is achievable with nanowires but not dots. Although a large variety of group IV, III-V, and II-VI nanowires have been grown or synthesized and investigated, most efforts on core-shell wires have focused on structures consisting of core and shell materials with type I band alignments (e.g., GaP-Ga<sub>2</sub>O<sub>3</sub>, GaN/AlGa<sub>3</sub>N, CdSe/ZnS), where the shell provides either the conventional quantum confinement effect for both electrons and holes in the core) or the role of a protective cladding to reduce sensitivity to the core's environment. In a conventional semiconductor, electrons and holes typically stay in the same region after photoexcitation, which is very desirable for certain applications e.g. light-emitting devices, where a maximized wavefunction overlap of the electron and hole yields a high radiative recombination rate. However, for a number of key renewable energy applications, including hydrogen generation via photoelectrochemical water splitting and dye-sensitized solar cells, efficient charge separation of the electron and hole after photoexcitation is instead highly preferred, but not readily available in the existing repertory of materials. We have now shown that "quantum coaxial cables", core-shell semiconductor nanowires with large type II band alignments can be designed to provide this feature, together with a superior electronic conductivity, another critical feature for photoconversion devices to reach their ultimate efficiency limits (see ref. 3). In such nanowires, the electron and hole wavefunctions are naturally confined in the core and shell region, respectively, without the need for a barrier layer (the spacer) in between. Specifically, these core-shell nanowires (1) offer materials with optimized band structure and much better stability for water splitting, (2) enable solid-state dye sensitized solar cells (as opposed to the current liquid based cells), and (3) minimize the radiative recombination loss in the conventional solar cell as well as cover nearly the entire usable solar spectrum in one single ternary system (e.g., from <0.5 eV to >3.0 eV with GaN-GaP).

## **Work in progress and future plans**

### *1) Surfactant control of spontaneous ordering*

Surfactants are often used during the growth of semiconductor materials to improve the quality and characteristics of the resulting materials, but the exact mechanism is often unknown. Because the ordering of GaInP is driven by a surface reconstruction with a two-atom periodicity, any surfactant which alters the surface construction can alter the ordering of the final GaInP film (which, in turn, alters its band gap). Both Sb and Bi are known to disrupt the ordering process, and we have demonstrated theoretically how this can be explained for Sb by Sb adatom attachment at step edges. Similar structures are

expected for Bi. We are currently testing this theory experimentally by imaging surface Sb and Bi using an STM (scanning tunneling microscope) attached to our growth chambers. A complementary study will investigate the role of hydrogen on the same surfaces. GaInP is known to order when grown by MOCVD (metalorganic chemical vapor deposition), but not when grown by MBE (molecular beam epitaxy). The current explanation is that the surface reconstruction which promotes ordering requires surface passivation by hydrogen atoms, and these hydrogen atoms are prevalent in MOCVD growth but absent in MBE growth. To better understand the role of hydrogen in GaInP ordering, we therefore plan to artificially introduce atomic hydrogen into an MBE chamber during growth using a hydrogen cracker. Because of their value for III-V solar cell growth, these studies are being done in collaboration with the National Center for Photovoltaics III-V high-efficiency team. The immediate practical interest in this work is that many existing and proposed III-V solar cell structures depend critically on tailoring the band gap of key layers by controlling the degree of ordering.

### *2) Orientational ordering of ferroelastic domain twins*

Our earlier experimental and theoretical investigations on the electronic and optical properties of a 1-D superlattice of ordered domain twins of GaInP<sub>2</sub> had shown that at the interface of a single uniaxial domain twin (e.g., as formed in ordered GaInP alloys) ballistic electrons exhibit an interesting phenomenon of “total and negative refraction” (see ref. 2). Besides the linear stacking arrangement of domain twins into a 1-D superlattice, ordered domain twins can also be arranged into a 2-D lattice. Depending on the material parameters (e.g., the degree of anisotropy in dielectric constants or effective masses), the propagation of light or electrons in such 2-D orientationally ordered structures can be shown to form either spirals or closed loops. It is thus possible to use such material for significantly slowing down the propagation of light. We plan on using ferroelectric liquid crystals as a prototype model for experimentally designing such orientationally ordered lattices, and to experimentally measure the optical properties of these structures.

### *3) Ferroelastic ordered domains: New materials for superlenses*

There has recently been a great deal of interest in metamaterials that exhibit negative refractive index, due to predictions that such materials will enable design of a ‘superlens’ that has no aberrations. However, no such materials have been demonstrated in the optical frequency range, and the physical possibility of transparent negative-index materials has been seriously questioned. Previously we demonstrated (see ref. 2) that negative refraction is also possible in a birefringent crystal twin of the type that occurs in an ordered GaInP orientational boundary. Our current work shows that in two dimensions this refraction is accompanied by aberration-free imaging for the far-field, an implicit requirement of any superlens. Our currently ongoing research suggests the use of birefringent ordered twin domain materials for some novel two-dimensional optical lenses with the potential of loss-less aberration-free imaging.

**PUBLICATIONS emanating from this project during the period (2005-2007)**

1. "Zero Thermal Expansion in Hybrid Organic-Inorganic semiconductors," Y. Zhang, A. Mascarenhas, et al, *Phys. Rev. Lett.*, **99**, 215901 (2007).
2. "Negative Refraction of Electromagnetic and Electronic waves in Uniform Media," Y. Zhang and A. Mascarenhas, Book Chapter, *Physics of Negative Refraction and Negative Index Materials, Springer Series in Materials Science*, Vol. **98**, 1-18 (2007).
3. "Quantum coaxial cables for solar energy harvesting," Y. Zhang, L.W Wang, and A. Mascarenhas, *Nanoletters* **7** (5), 1264 (2007).
4. "Physics of Negative Refraction and Negative Index Materials", *Springer Series in Materials Science*, Vol. 98, Book Editors: C. Krowne and Y. Zhang. Springer, Berlin Heidelberg New York (2007).
5. "Ordering induced direct and indirect transitions in semiconductor alloys," C.Y. Moon, J.B. Li, S.-H. Wei, et al. *Phys. Rev. B*, **74** (20), art. no. 205203 Nov (2006).
6. "5-7-5 line defects on As/Si(100): A general stress-relief mechanism for V/IV surfaces," W.E. McMahon, G. Batyrev, T. Hannappel, J.M. Olson, and S.B. Zhang, *Phys. Rev. B* **74**, 033304 (2006).
7. "Band gap of Hg chalcogenides: Symmetry-reduction-induced band-gap opening of materials with inverted band structures," C.Y. Moon and S.-H. Wei, *Phys. Rev. B* **74**, 045205 Jul (2006).
8. "Carrier-mediated stabilization of ferromagnetism in semiconductors: holes and electrons," G.M. Dalpian and S.-H. Wei, *Physica Status Solidi B*, **243** (9), 2170-2187 Jul (2006).
9. "Impurity-induced phase stabilization of semiconductors," G.M. Dalpian, Y.F. Yan and S.-H. Wei, *Appl. Phys. Lett.*, **89** (1), 011907 (2006).
10. "Study of phase selectivity of organic-inorganic hybrid semiconductors," C.Y. Moon, G.M. Dalpian, Y. Zhang; et al., *Chem. Mats.*, **18** (12), 2805-2809 Jun 13 (2006).
11. "Electron-mediated ferromagnetism and negative s-d exchange splitting in semiconductors," G.M. Dalpian and S.-H. Wei, *Phys. Rev. B* **73**, 245204 Jun (2006).
12. "Novel Approach to Tuning the Physical Properties of Organic-Inorganic Hybrid Semiconductors," Y. Zhang and A. Mascarenhas; et al. *Phys. Rev. Lett.*, **96** (2): 026405 Jan 20 (2006).
13. "Phenomenological band structure model of magnetic coupling in semiconductors," G.A. Dalpian, S.-H. Wei, X.G. Gong, et al., *Sol. State Comm.*, **138** (7), 353-358 (2006).
14. "Impurity-stabilized zinc-blende phase of wurtzite compounds," G.M. Dalpian and S.-H. Wei, *J. Phys. Chem. Solids*, **66** (11), 2008-2010 Nov (2005).
15. "Transition from ferromagnetism to antiferromagnetism in  $Ga_{1-x}Mn_xN$ " G.M. Dalpian and S.-H. Wei, *J. Appl. Phys.* **98** (8), 83905 Oct 15 2005.
16. "Electron-induced stabilization of ferromagnetism in  $Ga_{1-x}Gd_xN$ ," G.M. Dalpian and S.-H. Wei, *Phys. Rev. B* **72**, 115201 Sep (2005).
17. "Spontaneous lateral modulation in short-period superlattices investigated by grazing-incidence X-ray diffraction," O. Caha, P. Mikulik, J. Novak, V. Holy, S.C. Moss, A. Norman; A.Mascarenhas, J.L. Reno, and B. Krause; *Phys. Rev. B*, **72** (3), 035313 Jul (2005).
18. "X-ray characterization of atomic-layer superlattices," J.H. Li, S.C. Moss, Y. Zhang, A. Mascarenhas, and J. Bai, *J. Phys. D-Appl. Phys.*, **38** (10A), A147-A153 Sp. Iss. May 21 (2005).
19. "Step structures on III-V phosphide (001) surfaces: How do steps and Sb affect CuPt ordering of  $GaInP_2$ ?" I.G. Batyrev, W.E. McMahon, S.B. Zhang; et al. *Phys. Rev. Lett.*, **94** (9), art. no. 096101 Mar 11 (2005).
20. "Total and negative refraction of electromagnetic waves," Y. Zhang and A. Mascarenhas, *Mod. Phys. Lett. B*, **19**, 21 (2005). (Invited review paper)
21. "X-Ray Characterization of Atomic-Layer Superlattices," J.H. Li, S.C. Moss, Y. Zhang, A. Mascarenhas, and J. Bai, *J. Phys. D: Applied Phys.*, **38**, A147-A153 (2005).
22. "Step structures on MOVCD grown III-V phosphide (001) surfaces: How do steps and Sb affect CuPt ordering of  $GaInP_2$ ?" I.G. Batyrev, W.E. McMahon, S.B. Zhang, J.M. Olson, and S.-H. Wei, *Phys. Rev. Lett.*, **94**, 096101 (2005).
23. "Atomic ordering induced bandgap reductions in  $GaAsSb$  epilayers grown by MBE," B.P. Gorman, A.G. Norman, R Lukic-Zrnic, C.L. Littler, H.R. Moutinho, T.D. Golding, and A.G. Birdwell, *J. Appl. Phys.*, **97**, 063701 (2005).

## Magnetic and Optical Properties of Ferromagnetic ZnO Nanoparticles

### Principal Investigator (PI)

Matthew D. McCluskey  
Department of Physics and Astronomy  
Washington State University  
Pullman, WA 99164-2814  
E-mail: mattmcc@wsu.edu

### Co-PIs

Leah Bergman  
Department of Physics  
University of Idaho  
Moscow, ID 83844  
E-mail: lbergman@uidaho.edu

You Qiang  
Department of Physics  
University of Idaho  
Moscow, ID 83844  
E-mail: youqiang@uidaho.edu

### Program Scope

This research is focused on developing a fundamental understanding of magnetic and optical phenomena in ferromagnetic zinc oxide (ZnO) nanoparticles. Ferromagnetic semiconductors have emerged as important materials for spintronic applications.<sup>1,2</sup> In quantum computing devices, the spin states would be used to construct “qubits,” theoretically enabling the manipulation of huge amounts of data.<sup>3</sup> For non-volatile memory storage applications, ferromagnetism is used to store data for extended periods of time.<sup>4</sup> By manipulating spins, rather than charge, it is anticipated that more energy-efficient memory storage will be developed.<sup>5</sup> Recent discoveries of ferromagnetic behavior in certain dilute magnetic semiconductors (DMSs) have led to increased interest in the development and studies of these materials.<sup>6</sup> Semiconductors offer the possibility of optical devices such as spin light emitting diodes (spin-LEDs),<sup>7,8,9,10</sup> spin-polarized solar cells,<sup>11</sup> and magneto-optical switches.<sup>12</sup> The development of *room-temperature* ferromagnetic materials will be essential for the practical realization of these technologies.

The use of *nanoscale* semiconductors provides several advantages over bulk materials. First, the electronic and optical properties can be tuned by varying the size of the nanocluster.<sup>13,14</sup> Second, nanoclusters can be embedded in a matrix, which can be made into fibers or other technologically useful forms.<sup>15</sup> Finally, by reducing the dimensions to the nanoscale, high storage densities may be achieved by addressing the spin states of single quantum dots.<sup>16</sup> From a fundamental point of view, the study of nanoclusters provides insight into the mesoscopic regime between single molecules and bulk crystals.

ZnO is a wide-bandgap semiconductor<sup>17</sup> that has attracted tremendous interest as a blue light emitting material,<sup>18</sup> a buffer layer for GaN-based devices,<sup>19</sup> and a transparent conductor<sup>20</sup> in solar cells.<sup>21</sup> Theoretical work has predicted ferromagnetism above room temperature for Mn-doped ZnO (given a large hole concentration),<sup>22</sup> an important requirement for spintronic devices. Spurred by that prediction, research into ZnO crystals for spintronic applications is an active area

of experimental research.<sup>23</sup> In addition to the potentially high Curie temperature ( $T_c$ ), ZnO has numerous properties that are desirable for device applications, including low cost, environmental friendliness, and efficient light output.

The experimental approach involves the following:

- Synthesis of ZnO nanoparticles with well-defined magnetic and structural properties.
- Investigation of optical processes in ferromagnetic ZnO nanoparticles.
- Characterization of defects in ZnO nanoparticles, in the bulk and on the surface.

## Recent Progress

### *Synthesis of ZnO nanoparticles*

Nanoparticles were produced by the reaction of zinc acetate dihydrate [ $\text{Zn}(\text{CH}_3\text{COO})_2 \cdot 2\text{H}_2\text{O}$ ] with sodium hydrogen carbonate ( $\text{NaHCO}_3$ ) at 200 °C for 3 hours. X-ray diffraction and transmission electron microscopy (TEM) results showed that the particles are 15-20 nm diameter with the hexagonal wurtzite structure (Fig. 1). The particles were pressed into 7 mm diameter pellets with a thickness of 0.25 mm. In our preliminary studies, Cu was used as a dopant because it is well characterized and is easy to incorporate substitutionally into the ZnO lattice. For Cu-doped ZnO, a similar growth procedure was used as for undoped ZnO, except that the zinc acetate precursor was doped with copper acetate (~1% wt). Some of the pellets were sealed in a quartz ampoule filled with 2/3 atm hydrogen and annealed at 350 °C for 1 hour.

Nanoparticles with diameters of ~5 nm were produced by a new kind of cluster beam source that combines improved magnetron sputtering with a gas aggregation tube, the so called *sputtering-gas-aggregation* source. In our preliminary work, oxygen gas was introduced into the aggregation chamber during processing. Zn atoms from a pure Zn target were oxidized, and uniform ZnO nanoparticles were formed. ZnO nanoparticle films with a thickness of ~1  $\mu\text{m}$  were deposited onto Si substrates.

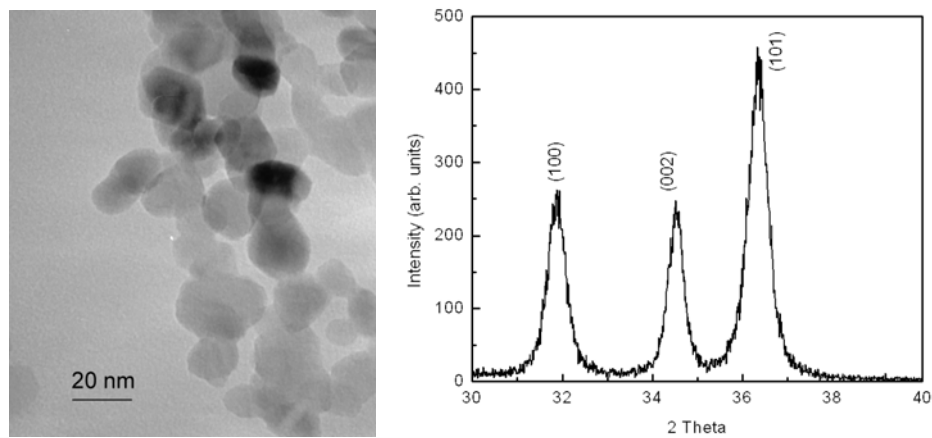


Fig. 1. TEM image and X-ray diffraction pattern of ZnO nanoparticles.

### Hydrogen in ZnO nanoparticles

The effect of hydrogen on the conductivity of ZnO nanoparticles has implications for nanoscale optoelectronic devices. In this study, infrared (IR) reflectance spectra of as-grown and hydrogen-annealed ZnO nanoparticles were measured at near-normal incidence. The as-grown particles were electrically semi-insulating, and show reflectance spectra characteristic of insulating ionic crystals. Samples annealed in hydrogen showed a significant increase in electrical conductivity and free-carrier absorption. A difference was observed in the *reststrahlen* line shape of the conductive sample compared to that of the as-grown sample. The effective medium approximation was applied to model the reflectance and absorption spectra. The agreement between experimental results and the model suggests that the nanoparticles have inhomogeneous carrier concentrations.

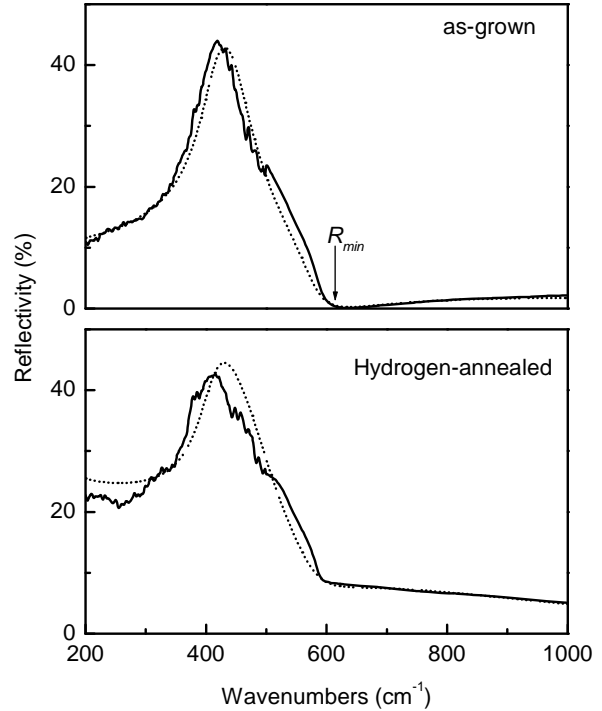


Fig. 2. IR reflectance spectra of ZnO nanoparticles. The dotted lines denote the calculated spectra.

IR reflectance spectra are shown in Fig. 2 for an as-grown sample and a sample annealed in hydrogen. The reflectivity of the as-grown sample shows a sharp decrease in reflectivity ( $R_{min} \approx 0$ ) near the longitudinal optical phonon frequency  $\omega_{LO}$ . This feature is a typical *reststrahlen* band reflection of semi-insulating ZnO.<sup>7</sup> The hydrogen annealed sample exhibits a change in the *reststrahlen* line shape, and the disappearance of  $R_{min}$  was observed. The reflectance change is consistent with an increase in the free carrier concentration. To model the reflectance spectra, the dielectric function of ZnO was calculated by a classical Lorentz-Drude model.<sup>16</sup> To obtain fits to the data (dotted lines), we had to assume an inhomogeneous distribution of doping among the nanoparticles. Some nanoparticles were heavily doped ( $n \sim 10^{19} \text{ cm}^{-3}$ ) while others were lightly doped ( $n \sim 10^{17} \text{ cm}^{-3}$ ).

### Copper-doped ZnO nanoparticles

To probe the electronic transitions of  $\text{Cu}^{2+}$  impurities in ZnO nanoparticles, IR transmission spectra were taken at liquid-helium temperatures. Two absorption peaks were observed at energies of 5781 and 5821  $\text{cm}^{-1}$  (Fig. 3). These

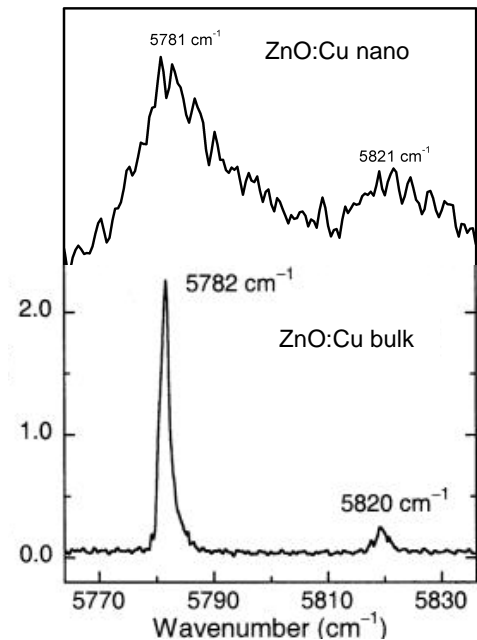


Fig. 3. IR spectra of ZnO:Cu nanoparticles (this work) and bulk crystal (Ref. 24).

absorption peaks arise from internal transitions of  $\text{Cu}^{2+}$  ions between the  $^2\text{T}$  level and two sublevels of the  $^2\text{E}$  state. Similar absorption lines were observed in bulk ZnO.<sup>24</sup> However, the width of the absorption peaks in our nanoparticles is broader than that of bulk crystals, perhaps due to inhomogeneous strains and/or electric fields.

## Future Plans

- Determine the origin of the broadening of  $\text{Cu}^{2+}$  electronic transitions in ZnO nanoparticles and investigate the  $\text{Cu}^{1+}$  lines.
- Investigate Cu-H complexes by hydrogenating ZnO nanoparticles. Investigate local vibrational modes due to O-H bonding.
- Extend our studies to other transition-metal dopants such as Co and Mn.
- Systematically investigate the effect of quantum confinement on doped ZnO nanoparticles.

## Publications of DOE-sponsored research

- W.M. Hlaing Oo, M.D. McCluskey, J. Huso, and L. Bergman, "Infrared and Raman spectroscopy," *J. Appl. Phys.* **102**, 043529:1-5 (2007).

---

<sup>1</sup> G.A. Prinz, *Science* **282**, 1660 (1998).

<sup>2</sup> T. Dietl and H. Ohno, *MRS Bulletin* **28** (10), 714 (2003).

<sup>3</sup> A. Steane, *Reports on Progress in Physics* **61**, 117 (1998).

<sup>4</sup> S. Parkin, X. Jiang, C. Kaiser, A. Panchula, K. Roche, and M. Samant, *Proceedings of the IEEE* **91**, 661 (2003).

<sup>5</sup> B. Pimentel, "Stanford, IBM team to explore 'spintronics'," *San Francisco Chronicle* (April 26, 2004).

<sup>6</sup> S.K. Kamilla and S. Basu, *Bull. Mater. Sci.* **25**, 541 (2002).

<sup>7</sup> B.T. Jonker, Y.D. Park, B.R. Bennett, H.D. Cheong, G. Kiosoglou, and A. Petrou, *Phys. Rev. B* **62**, 8180 (2000).

<sup>8</sup> Y. Ohno, D.K. Young, B. Beschoten, F. Matsukura, H. Ohno, and D.D. Awschalom, *Nature* **402**, 790 (1999).

<sup>9</sup> J.M. Kikkawa and D.D. Awschalom, *Nature* **397**, 139 (1999).

<sup>10</sup> R. Fiederling, M. Keim, G. Reuscher, W. Ossau, G. Schmidt, A. Waag, and L.W. Molenkamp, *Nature* **402**, 787 (1999).

<sup>11</sup> I. Zutic, J. Fabian, and S. Das Sarma, *Phys. Rev. B* **64**, 121201 (2001).

<sup>12</sup> Y.S. Didosyan, H. Hauser, G.A. Reider, and W. Toriser, *J. Appl. Phys.* **95**, 7339 (2004).

<sup>13</sup> D. Loss and D.P. DiVincenzo, *Phys. Rev. A* **57**, 120 (1998).

<sup>14</sup> J.A. Gupta, D.D. Awschalom, X. Peng, and A.P. Alivisatos, *Phys. Rev. B* **59**, R10421 (1999).

<sup>15</sup> P. Mulvaney, *Glass Science and Technology* **75**, 310, Suppl. C1 (2002).

<sup>16</sup> J.M. Elzerman, R. Hanson, L.H. Willems van Beveren, B. Witkamp, L.M.K. Vandersypen, and L.P. Kouwenhoven, *Nature* **430**, 431 (2004).

<sup>17</sup> Ü. Özgür, Ya. I. Alivov, C. Liu, A. Teke, M.A. Reshchikov, S. Dogan, V. Avrutin, S.-J. Cho, and H. Morkoç, *J. Appl. Phys.* **98**, 041301 (2005).

<sup>18</sup> D.C. Look, *Mater. Sci. Engin. B* **80**, 383 (2001).

<sup>19</sup> R.J. Molnar, in *Semiconductors and Semimetals* **57** (Academic Press, New York, 1999), pp. 1-31.

<sup>20</sup> T. Minami, *MRS Bulletin* **25** (8), 38 (2000).

<sup>21</sup> A. Nuruddin and J.R. Abelson, *Thin Solid Films* **394**, 49 (2001).

<sup>22</sup> T. Dietl, H. Ohno, F. Matsukura, J. Cibert, and D. Ferrand, *Science* **287**, 1019 (2000).

<sup>23</sup> P. Sharma, A. Gupta, K.V. Rao, F.J. Owens, R. Sharma, R.Ahuja, J.M. Osorio Guillen, Börje Johansson, and G.A. Gehring, *Nature Materials* **2**, 673 (2003).

<sup>24</sup> N.Y. Garces, L. Wang, L. Bai, N.C. Giles, L.E. Halliburton, and G. Cantwell, *Appl. Phys. Lett.* **81**, 622 (2002).

# “Hybrid Inorganic Nitride/Organic Semiconductor Heterostructures”

**Principal Investigator:** Arto V. Nurmikko

Brown University, Division of Engineering, Providence, RI 02912

[Arto\\_Nurmikko@brown.edu](mailto:Arto_Nurmikko@brown.edu)

**Co-investigator:** Jung Han

Department of Electrical Engineering, Yale University, New Haven, CT

[Jung.Han@Yale.edu](mailto:Jung.Han@Yale.edu)

## Program Scope and Definition:

We seek to explore hybrid inorganic-organic semiconductor media with an internal organization on the nanometer scale, as composite material structures which physically integrate crystalline III-nitrides and II-VI compounds, respectively, with selected organic semiconductors. The two approaches in this proposal include (1) layer-by-layer synthesis of colloidal II-VI quantum dot/organic structures by wet chemistry and, (2) the conformal UHV deposition of conjugated organic semiconductors onto the nitride nanostructures. The application tasks include facilitating electrical interconnects to nanostructures, as well as modifying the coupling between electronic and electromagnetic states. Scientific interest and promise arises from the fact that some of the basic physical attributes of III-nitride and (opto)electronically important organic materials are qualitatively as well as quantitatively quite different, such as carrier mobility which may differ by several orders of magnitude. Yet, the III-nitrides, II-VI compounds and selected organic semiconductors have large optical oscillator strengths, though a fundamental difference exists between the physical nature of the corresponding electronic excitations (extended Wannier and molecular Frenkel excitons, respectively). The contrasts, attributes, as well as limitations of each material system drive our intention to explore the basic science and physical properties of III-nitride/organic and II-VI/organic semiconductor heterostructures. The key question we wish to answer in the affirmative is: does material integration of inorganic and organic semiconductors, on the nanoscale, yield material synergy which leads into higher (opto)electronic performance of the joint “intercalated” material than the simple sum of its parts?

## Recent Progress: 1. Highly Efficient Resonance Energy Transfer in Ultrathin Organic-Inorganic Semiconductor Hybrid Films

**1(a) Introduction.** The possibility to grow tailored systems incorporating both inorganic and organic materials has implications in manipulating excitation transfer and exchange. In the strong coupling regime, the hybridization of the Frenkel exciton in organic materials and the Wannier-Mott excitons in inorganic materials could lead to some exciting linear and nonlinear optical properties of the hybrid material [1]; In the weak coupling regime, the efficient incoherent energy transfer between the organic and inorganic materials could facilitate the development of new optoelectronic devices with improved performance, in application areas such as light emitting devices [2], solar cells [3] and sensors [4], etc. Semiconductor colloidal II-VI quantum dots (QDs) with superior photostability and wavelength tunability as well as J-aggregate of specific molecular dyes with large absorption oscillator strength and delocalized Frenkel exciton states are two good examples in each category.

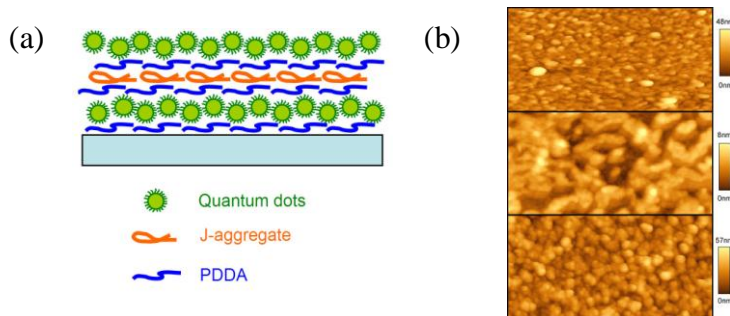


Figure 1: (a) Schematics of the hybrid film layer structures (b) AFM images of a monolayer of QDs, a monolayer of J-aggregate, and the hybrid film II, respectively.

We report the study of efficient resonant energy transfer in organic-inorganic hybrid thin films, in which alternating mono layers of QDs and J-aggregate of cyanine dyes are deposited by layer-by-layer (LBL) assembly.

Furthermore, by properly choosing the size of the QDs, in turn their spectral emission wavelength, the donor/acceptor role of each species can be practically altered.

**1(b) Synthesis and morphological characterization of the hybrid films.** The schematics of the LBL deposited hybrid thin film structure used in this study is illustrated in Fig 1(a). A monolayer J-aggregate of (5,6-dichloro-2-[3-[5,6-dichloro-1-ethyl-3-(3-sulfopropyl)-2(3H)-benzimidazolide]-1-propenyl]-1-ethyl-3-(3-sulfopropyl) benzimidazolium hydroxide, inner salt, sodium salt (TDBC) was sandwiched between two layers of CdSe-ZnS core/shell structured QDs of the chosen emission wavelengths. Monolayers of poly-(diallyldimethylammonium chloride) (PDDA) were used as the polyelectrolyte adhesion layer. The hybrid film was deposited by immersing a glass substrate into the aqueous solutions of each species in a dip-coating fashion, monolayer at a time. Two types of hybrid films were synthesized, one with QD emission wavelength centered at 548nm (referred to as film I) and the other with QD emission wavelength at 653nm (referred to as film II), with respect to the J-aggregate emission at 594nm.

AFM characterization results of the completed hybrid film (e.g. film II) are shown in Fig 1(b). Two additional LBL films containing a monolayer of QD and J-aggregate, respectively, were also characterized. As seen in Fig1(b), the LBL process was optimized so that the QD and J-aggregate could form a nearly complete monolayer while retaining a low surface roughness.

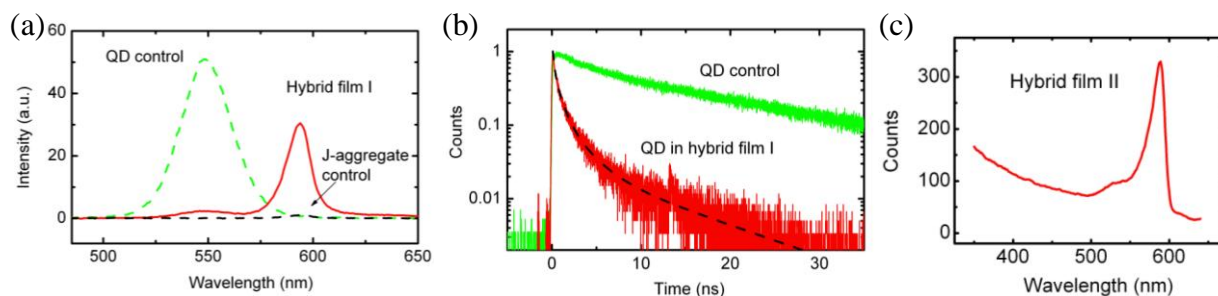


Figure 2 (a) PL spectra of hybrid film I, QD control and J-aggregate control films when excited at 350nm (b) Time-resolved PL traces of QDs in hybrid film I and control film (c) PLE spectrum of the hybrid film II probing at the QD emission peak wavelength of 653nm.

**1(c) Optical characterization.** Steady-state photoluminescence (PL) spectroscopy characterizations of film I show that the QD emission was significantly quenched, with a simultaneous boost of the J-aggregate emission (Fig 2a). Time-resolved PL study probing at the QD emission wavelength confirmed the activation of a highly efficient nonradiative decay channel by energy transfer from QD to J-aggregate (Fig 2b). The overall energy transfer efficiency was calculated to be over 90%.

In the case of film II, QD emission was enhanced by nearly 10 times upon excitation at the peak of J-aggregate absorption. Further characterization was carried out by photoluminescence excitation spectroscopy (PLE), in which a pronounced feature resemble the J-aggregate absorption band appeared on top of the QD PLE background (Figure 2c). Quantitative analysis on PLE and absorption data of film II yielded energy transfer efficiency from J-aggregate to QD to be as much as >30%, despite the short radiative lifetime of J-aggregate.

**1(d) Conclusions.** Highly efficient excitation energy transfer has been observed in semiconductor organic-inorganic hybrid thin film, enclosing colloidal QDs and cyanine dye J-aggregates. The energy transfer mechanism was found to be Förster-type in nature. These findings suggested the possibility of realizing a strongly coupled organic-inorganic hybrid material in such a film structure upon further material improvement.

[1] V.M. Agranovich, D.M. Basko, G.C. La Rocca and F. Bassani, "Excitons and optical nonlinearities in hybrid organic-inorganic nanostructures", *J. Phys.: Condens. Matter* **10**, 9369 (1998)

[2] Seth Coe, Wing-Keung Woo, Mounqi Bawendi and Vladimir Bulovic, "Electroluminescence from single monolayers of nanocrystals in molecular organic devices", *Nature* **420**, 800 (2002)

[3] Wendy U. Huynh, Janke J. Dittmer, A. Paul Alivisatos, "Hybrid Nanorod-Polymer Solar Cells", *Science* **295**, 2425 (2002)

[4] Igor L. Medintz, Aaron R. Clapp, Hedi Mattoussi, Ellen R. Goldman, Brent Fisher and J. Matthew Mauro, "Self-assembled nanoscale biosensors based on quantum dot FRET donors", *Nature Materials* **2**, 630 (2003)

## 2. Nitride /Organic Hybrid Heterostructures for Photosensor Devices

**2(a) Introduction.** As part of ongoing efforts to explore novel semiconductor materials and to improve the performance of GaN-based optoelectronic devices, n-GaN/organic semiconductor hybrid heterojunction devices have been investigated [1][2][3]. For nano-structured or nano-textured heterogeneous materials, such as high density arrays of InGaN crystalline nanowires, one key challenge is the implementation of electrical interfaces. Soft organic semiconductors which can be deposited conformally onto the underlying structures can be useful. We have studied the planar heterojunction composed of n-GaN and small molecule organics (Fig.3) to gain insight into the charge transport across these hybrid “nitride/organic” junctions.

### 2(b). Photovoltaic effects in n-GaN/CuPc Heterostructures.

We employed an n-type GaN film, within which a single InGaN quantum well inserted as a spectroscopic marker was separated from the film surface by a 6nm thin GaN cap layer (Si doped,  $n \sim 1 \times 10^{18}/\text{cm}^3$  grown by MOCVD). On top of the pristine nitride surface, small molecule organic thin films typically less than 100nm thick were deposited using UHV thermal evaporation. These organic materials were carefully chosen so that ideally their LUMO-HOMO bands should line up approximately with the conduction and valence bands of GaN (Fig.4a). For solar-cell-type of application, CuPc(copper phthalocyanine), a widely used donor material for organic photovoltaic devices, was used as the organic component in our hybrid device. Fig.4.(b) shows the I-V characteristics of a fabricated Au/CuPc/n-GaN/Ti/Al device structure with and without laser light illumination at 390nm wavelength. We see strong

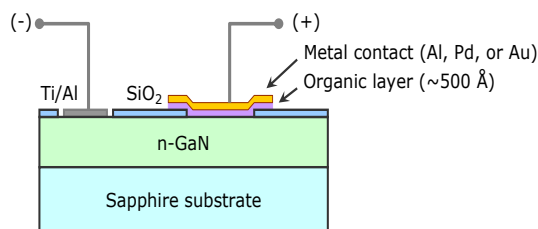


Fig. 3 Schematic of n-InGaN/organic planar junction test “device” structure (typical active area : 0.4 mm<sup>2</sup>)

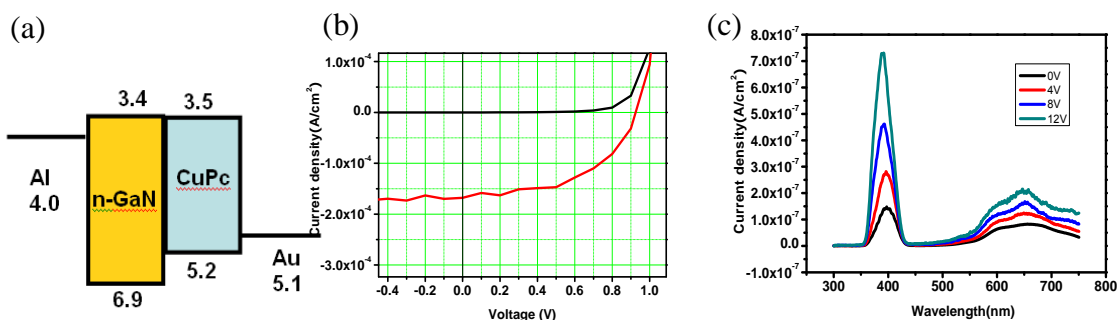


Fig.4. (a) Possible energy band lineup (b) Current density vs. voltage characteristics of an Al/n-GaN/CuPc/Au photovoltaic cell under 18mW/cm<sup>2</sup> laser at 390nm. (c) Photocurrent spectrum response under halogen lamp/monochromator illumination

rectification characteristics with a relatively low turn-on voltage of 0.8V. The photocurrent spectrum under various reverse bias is shown in Fig.4(c). The spectra show photocurrent response at 390nm which corresponds to onset of the InGaN QW absorption wavelength, and broad photocurrent response centered around 650nm, due to absorption

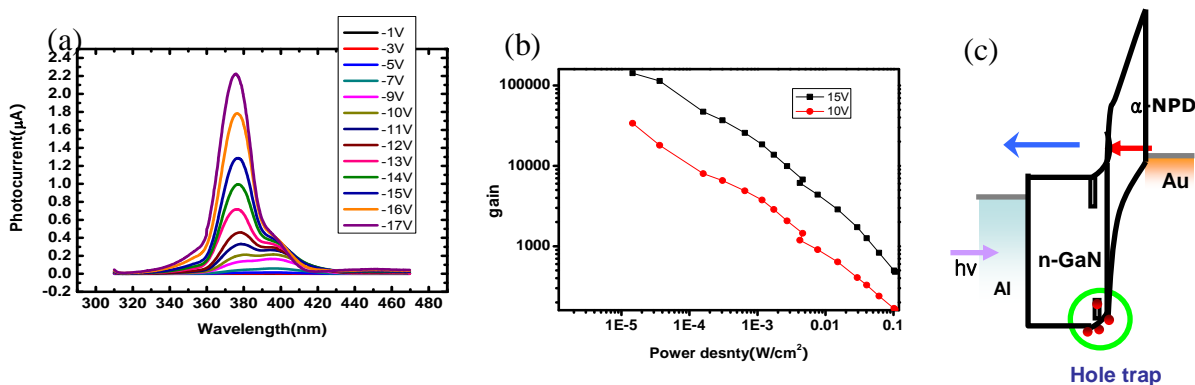


Fig3.(a) Photocurrent spectrum of InGaN/NPD device (b) Photocurrent multiplication gain with different light intensity with laser at 390nm (c) Illumination of hole trap mechanism and deep energy band bending schematics.

band of CuPc. Robust photocurrent response implies that e-h pairs generated in InGaN QW and Frenkel excitons generated in CuPc are able to transport to and across the heterojunction interface effectively.  $V_{oc}$  was measured to be 0.93V and  $I_{sc}$  to be 0.2 A/cm<sup>2</sup> with 390nm laser illumination at 18mW/cm<sup>2</sup> power density. Estimated internal quantum efficiency at 390nm is around 50% and is approaching 100% with increasing reverse bias.

**2(c). Photoconductivity gain in n-GaN/NPD Heterostructures** In a different photodetector configuration for the hybrid device, CuPc was replaced by  $\alpha$ -NPD(N,N'-diphenyl-N,N'-bis(1-naphthyl)-1,1'-biphenyl-4,4''-diamine), which is a common hole-transport material in OLED devices. IV characteristics show strong rectification characteristics and higher series resistance attributed to the lower carrier mobility in  $\alpha$ -NPD. Strong photocurrent response was detected at 380nm, corresponding to the onset of the InGaN absorption and there is no observable contribution from the  $\alpha$ -NPD. Particularly, photocurrent gain was observed when the device is under reverse bias, which is strongly dependent on the optical power density (Gain=Power<sup>-0.65</sup>). This can be explained by trap-like states existing at the interface, possibly originated from imperfect Van der Waals bonding, and surface defects associated with the GaN/ $\alpha$ -NPD interface. As a result, holes generated at InGaN QW driven toward  $\alpha$ -NPD by the external field are trapped at the interface, leading to reinforcement of the electric field in  $\alpha$ -NPD. Electron tunneling from the HOMO band of  $\alpha$ -NPD to the conduction band of GaN is likely to occur after the band bending reached certain threshold. Electron current flow persists while holes are trapped at the interface, i.e. the photocarrier gain effect. A hole-trapping picture is further supported by the slow transient optical response time (10ms at room temperature).

**2(d). Conclusion** Charge and exciton transport mechanisms in GaN/ $\alpha$ -NPD and GaN/CuPc hybrid heterojunctions demonstrations were studied and show useful and contrasting behavior dependency on the organic materials used. GaN/CuPc devices enjoy evident ease in electron and hole transport across the interface and show robust photovoltaic response at both InGaN and CuPc absorption wavelength. On the other hand, GaN/ $\alpha$ -NPD device exhibits large photocurrent gain phenomenon likely due to hole trapping at the interface, indicating that the nitride/organic electronic interface is very sensitive to the type of organic material in use. These results may suggest the utility of organic/inorganic hybrid heterojunction device in novel photosensor applications.

[1] Seth Coe, Wing-Keung Woo, Mounji Bawendi and Vladimir Bulovic, "Electroluminescence from single monolayers of nanocrystals in molecular organic devices", *Nature* **420**, 800 (2002)

[2] Wendy U. Huynh, Janke J. Dittmer, A. Paul Alivisatos, "Hybrid Nanorod-Polymer Solar Cells", *Science* **295**, 2425 (2002)

[3] Hyunjin Kim, Cuong Dang, Yoon-Kyu Song, Qiang Zhang, William Patterson, A.V. Nurmikko K-K. Kim, S-Y. Song, and Jung Han, *Phys. Stat.Sol (c)* **4**, 2411-2414 (2007)

### **Future Plans:**

Our longer term aspirations include exploiting the hybrid properties for applications, both such established areas as solid state lighting and photovoltaics, but also for entirely new innovative device concepts that might arise from the combination of joint electronic and optoelectronic properties from such material synergy.

### **Publications:**

"Highly Efficient Resonance Energy Transfer in Ultrathin Organic-Inorganic Quantum Dot Semiconductor Hybrid Films", Q. Zhang, T. Atay, H. Urabe, and A.V. Nurmikko, J. Tischler, Scott Bradley, and V. Bulovic, *Nature Nanotechnology* **2**, 555 (2007)

"Nitride-Organic Semiconductor Hybrid Heterostructures for Optoelectronic Devices", H. Kim, C. Dang, Y.-K. Song, Q. Zhang, W. Patterson, A.V. Nurmikko, K-K. Kim, S-Y. Song, and J. Han, *Phys. Stat.Sol (c)* **4**, 2411-2414 (2007)

## Addressing Fundamental Questions for Graphene Films Synthesized on Silicon-Carbide

Principal Investigator: Taisuke Ohta  
Mailing Address: Sandia National Laboratories  
Surface & Interface Sciences Department  
PO Box 5800, MS-1415  
Albuquerque NM 87185, USA  
E-mail: tohta@sandia.gov  
Presented works in collaboration with:  
Dr. Eli Rotenberg (E. O. Lawrence Berkeley National Laboratory)  
Prof. Karsten Horn (Fritz Haber Institute, Berlin, Germany)  
Dr. Thomas Seyller (Universität Erlangen-Nürnberg, Erlangen, Germany)  
Dr. Andreas K. Schmid (E. O. Lawrence Berkeley National Laboratory)

### **Program Scope**

Much recent attention has been given to the physical properties of graphene for its exotic electron transport<sup>1, 2, 3</sup> and potential technological advantages for high-speed electronics and gas sensor applications.<sup>4, 5</sup> Graphene is a single planar sheet of  $sp^2$ -bonded carbon atoms densely packed in a honeycomb crystal lattice, and is the building block of graphite, carbon nanotubes,  $C_{60}$ , and other mesoscopic forms of carbon.<sup>6</sup> In order to successfully understand the fundamental properties of graphene-based structures and potentially implement graphene for various novel device applications, significant efforts have been devoted for developing methods to reliably synthesize ultrathin graphene films (1-5 ML) supported on a solid substrate.<sup>7, 8, 9, 10</sup> Our project addresses key fundamental questions for graphene films synthesized on silicon-carbide (SiC) substrates. This synthesis method is based on removing the Si atoms from the surface of SiC through annealing, thereby leaving behind a graphene film (graphitization),<sup>3, 8, 9, 11, 12</sup> and has a potential advantage of reliably synthesizing graphene films supported on semiconductor substrates that are also technologically-scalable. Currently, there is much scientific debate on the fundamental properties of the SiC-supported graphene films: the influence of the underlying substrate to their electronic structure<sup>13, 14, 15, 16, 17</sup> and the film morphology to the carrier mobility.<sup>18</sup> Through a thorough understanding of the synthesis process, thin film structures as well as the defects therein, and the transport properties, we plan to address these fundamental questions.

### **Past Research Results and Recent Progress**

Our research effort has been focusing on the fundamental properties of graphene films synthesized on SiC, particularly the electronic band structure and the film morphology. Here we present some of our recent accomplishments.

#### ***Layer-dependent electronic structures of single layer and multilayer graphene***

The dispersion relation of electrons (electronic band structure) is one of the fundamental aspects that determine the electronic properties of a material. We have studied the electronic band structure using angle resolved photoemission spectroscopy (ARPES), which is a direct probe to determine the valence band (occupied electronic structure) by simultaneously measuring the electron energy and momentum excited by photoemission process, thus determining the dispersion relation. This research provides invaluable insights into the electronic properties of graphene films.

As an aromatic molecule made of  $sp^2$  hybridized carbon atoms, the electronic structure of graphene is comprised of  $\sigma$  and  $\pi$  bonding orbitals and  $\sigma^*$  and  $\pi^*$  anti-bonding orbitals. Because of the unique crystal structure of graphene with two equivalent sublattices,  $\pi$  and  $\pi^*$  bands, the highest occupied and the lowest unoccupied electronic states, respectively, converge to a point (called the Dirac-point,  $E_D$ ) at K and K' points in the Brillouin zone. The unique structure of the  $\pi$  bands is reflected in their photoemission intensity patterns as a function of  $k_{\parallel}$  displayed in Fig. 1, which exhibits linear dispersion near  $E_D$ .

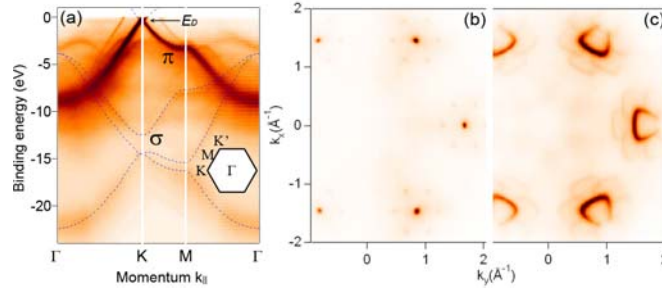


Fig. 1 (a) Photoemission images revealing the bandstructure of single layer graphene along high symmetry directions,  $\Gamma$ -K-M- $\Gamma$ .<sup>19</sup> The blue dashed lines are scaled DFT bandstructure of a freestanding film.<sup>20</sup> Inset shows the 2D Brillouin zone (BZ) of graphene. (b) and (c) Constant energy contours of graphene's bandstructure at  $E_D$  ( $E_F - 0.45\text{eV}$ ) and below  $E_D$  ( $E_F - 2\text{eV}$ ), respectively, plotted as a function of the two parallel momentum directions,  $k_x$  and  $k_y$ .<sup>21</sup>  $\pi$  and  $\pi^*$  bands converge to a point at the corner of BZ at  $E_D$  (b), and have finite size away from  $E_D$  (c). The replica bands are due to scattering from  $6\sqrt{3}\times 6\sqrt{3}$  periodicity of the interface carbon-rich layer underneath the graphene layer.

The influence of the interlayer interaction to the graphene's band structure is manifested in  $\pi$  and  $\pi^*$  bands near  $E_D$ . A systematic increase of the graphene film thickness by controlling the annealing condition for the graphitization process has revealed the layer-dependent electronic structures from single layer to multilayer graphene (Fig. 2). The number of  $\pi$  bands increases with the number of layers due to interlayer interaction, clearly seen away from  $E_D$ , where the Coulomb potential of each layer does not play a major role.

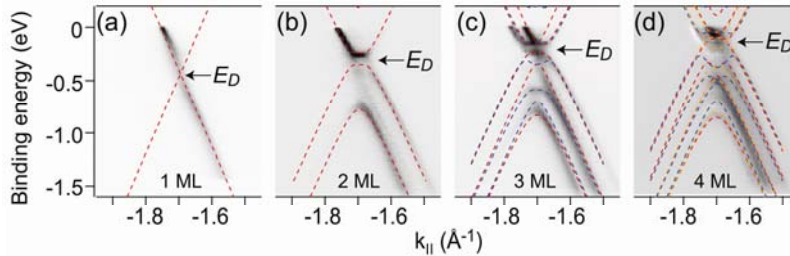


Fig. 2 (a-d) The  $\pi$  and  $\pi^*$  bands near  $E_F$  for 1 to 4 graphene layers, respectively.  $k_{\parallel} = -1.703 \text{ \AA}^{-1}$  corresponds to the K point, the corner of the hexagonal Brillouin zone.<sup>19</sup> The  $\Gamma$  point is at  $k_{\parallel} = 0 \text{ \AA}^{-1}$ , while the M point is at  $-2.555 \text{ \AA}^{-1}$ . The dashed lines are from a calculated tight binding bandstructure, with band parameters adjusted to reproduce measured bands. Red and orange lines are for Bernal-type (ABAB and ABAC) stackings, while blue lines are for rhombohedral-type stackings. The measured  $\pi$  bands are suppressed on one side of the BZ due to interference effects between the two equivalent sublattices.<sup>22</sup>

### Morphology of graphene films

We studied the growth morphology of graphene films using low energy electron microscopy (LEEM). Shown in Fig. 3 (a) is the morphology of a graphene film of  $\sim 2$  layer thickness. The local distribution of the number of graphene layers can be identified by the image contrast and the electron reflectivity spectra shown in (b). To date, LEEM<sup>23,24</sup> and Raman microscopy<sup>25</sup> are the only reliable techniques reported that can determine the thickness of graphene films. We also demonstrated that the interface carbon-layer, which turns into graphene upon further annealing (see below), can be identified using LEEM. LEEM studies of the growth morphology of the graphene film and the interface carbon-layer are expected to play key role in our future research on understanding of the graphitization process.

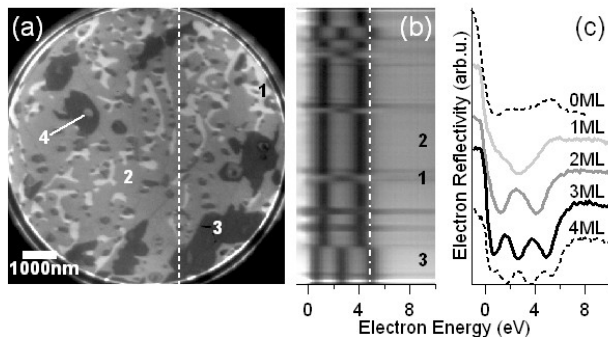


Fig. 3 (a) LEEM image of a graphene film on SiC(0001), recorded with the electron energy of  $E_{vac} + 4.88$  eV and  $8 \mu\text{m}$  field of view. (b) Image intensity as a function of electron energy (electron reflectivity spectra) for a section along the white dashed line in (a) is represented on a grey-scale, revealing features associated with areas of different reflectivity (brightness) in the image (a). The electron energy of (a) is indicated as the white dash-dot-dash line. The numbers superimposed in (a) and (b) correspond to the number of graphene layers. (c) Electron reflectivity spectra of five representative regions with corresponding number of layers, where 0ML denotes the interface carbon-layer.<sup>23</sup>

### Future Plans

Building upon our previous graphene materials research experiences, we plan to develop a synergistic experimental/theory graphene research effort at Sandia National Labs focusing on the fundamental questions for the synthesis process, thin film structures as well as the defects therein, and the transport properties. The formation of graphene films on SiC is illustrated in Fig. 4. Prior to graphene formation, a SiC surface is initially covered with an interface carbon-layer through annealing as shown in the first step. By further annealing, this interface carbon layer is converted to graphene by forming a new interface carbon-layer underneath. It was recently shown that the surface roughening during the formation of the interface carbon-layer is responsible for the resulting morphology of graphene films.<sup>26</sup> Furthermore, a transport study of graphene films synthesized by the graphitization process attributed the limited mobility to their rough morphology.<sup>18</sup> A detailed understanding of the graphitization process including nucleation and growth of the interface carbon-layer is needed for synthesizing the large-area graphene films. The availability of improved ultrathin graphene films and graphene nanostructures, such as nanoribbons, will help Sandia further the understanding of graphene’s fundamental electronic properties based upon the Dirac formulation of quantum mechanics, rather than the more typical Schrodinger formulation useful for understanding other semiconductor materials systems. These efforts will also help provide a better understanding for understanding graphene’s potentially high mobility ( $\sim 200,000 \text{ cm}^2/\text{Vs}$ ), its relatively temperature insensitive Quantum Hall Effect characteristics, the controllable manipulation of the band structure of more complex graphene-based systems, and the potential exploitation of graphene as a useful condensed matter testing ground for interesting aspects of QED.

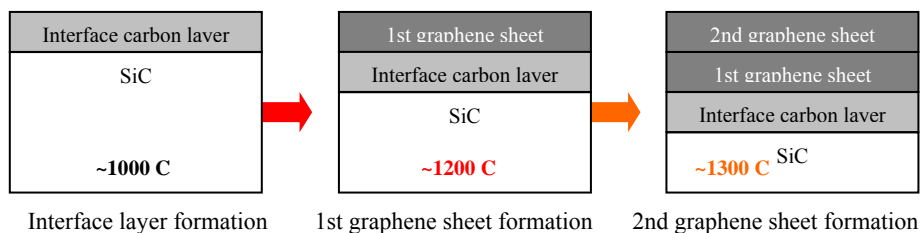


Fig. 4 Schematic illustrations of the sequence of graphene formation on SiC(0001) (Si-face).

Upon successful development of the synthesis of graphene films, we plan to explore fundamental properties of graphene films on SiC, specifically atomic and electronic structures at point defects, edges, and molecular adsorption sites. We will investigate the feasibility of novel hybrid characterization approaches vital for supporting fundamental studies of the graphene system, as well as other electronic

nanomaterials. A unique nature of graphene's defects has been predicted and explored.<sup>27</sup> Exploiting the microfabrication capabilities at Sandia Labs, the influence of defects and molecular adsorption on the electron transport of nanostructured graphene films will be studied. The fundamental understanding of the defects and molecular adsorption will provide important insights towards the development of graphene-based, high-speed electronics and gas sensors applications.

- 
- <sup>1</sup> K. S. Novoselov *et al.*, Two-dimensional gas of massless Dirac fermions in graphene, *Nature* 438, 192 (2005).
- <sup>2</sup> Y. Zhang, Y. W. Tan, H. L. Stormer, P. Kim, Experimental observation of the quantum Hall effect and Berry's phase in graphene, *Nature* 438, 201 (2005).
- <sup>3</sup> C. Berger *et al.*, Electronic Confinement and Coherence in Patterned Epitaxial Graphene, *Science* 312, 1191 (2006).
- <sup>4</sup> F. Schedin *et al.*, Detection of Individual Gas Molecules Absorbed on Graphene, *Nature Materials* 6, 652 (2007).
- <sup>5</sup> A. K. Geim, K. S. Novoselov, The rise of graphene, *Nature Materials*, 6, 183 (2007).
- <sup>6</sup> R. Saito, G. Dresselhaus, and M. S. Dresselhaus, *Physical Properties of Carbon Nanotubes* (Imperial College Press, 1998).
- <sup>7</sup> K. S. Novoselov *et al.*, Electric Field Effect in Atomically Thin Carbon Films, *Science* 306, 666 (2004).
- <sup>8</sup> I. Forbeaux, J. M. Themlin, and J. M. Debever, Heteroepitaxial graphite on 6H-SiC(0001): Interface formation through conduction-band electronic structure, *Phys. Rev. B* 58, 16 396 (1998).
- <sup>9</sup> C. Berger *et al.*, Ultrathin Epitaxial Graphite: 2D Electron Gas Properties and a Route toward Graphene-based Nanoelectronics, *J. Phys. Chem. B* 108, 19 912 (2004).
- <sup>10</sup> D. A. Dikin *et al.*, Preparation and characterization of graphene oxide paper, *Nature* 448, 457 (2007)
- <sup>11</sup> T. Ohta, B. Bostwick, T. Seyller, K. Horn, and E. Rotenberg, Controlling the Electronic Structure of Bilayer Graphene, *Science* 313, 951 (2006).
- <sup>12</sup> A. Bostwick, Taisuke Ohta, T. Seyller, K. Horn, E. Rotenberg, Quasiparticle dynamics in graphene, *Nature Physics*, 3, 36 (2007).
- <sup>13</sup> K. Emtsev *et al.*, Initial Stages of the Graphite-SiC(0001) Interface Formation Studied by Photoemission Spectroscopy, *Mat. Sci. Forum* 556, 525 (2007).
- <sup>14</sup> F. Varchon *et al.*, Electronic structure of epitaxial graphene layers on SiC: effect of the substrate, *Phys. Rev. Lett.* 99, 126805 (2007).
- <sup>15</sup> A. Matusch and O. Pankratov, Ab Initio Study of Graphene on SiC, *Phys. Rev. Lett.* 99, 076802 (2007).
- <sup>16</sup> A. Bostwick *et al.*, Symmetry Breaking in Few Layer Graphene Films, *New J. Phys.* 9, 385 (2007).
- <sup>17</sup> S. Y. Zhou *et al.*, Substrate-induced bandgap opening in epitaxial graphene, *Nature Materials* 6, 770 - 775 (2007).
- <sup>18</sup> G. G. G. *et al.*, Field effect in epitaxial graphene on a silicon carbide substrate, *Appl. Phys. Lett* 90, 253507 (2007).
- <sup>19</sup> T. Ohta, A. Bostwick, J.L. McChesney, Th. Seyller, K.Horn, E.Rotenberg, Interlayer interaction and electron screening in multilayer graphene, *Phys. Rev. Lett.* 98, 206802 (2007).
- <sup>20</sup> S. Latil and L. Henrard, Charge Carriers in Few-Layer Graphene Films, *Phys. Rev. Lett.* 97, 036803 (2006).
- <sup>21</sup> T. Ohta *et al.*, On the electronic structure of single and multilayer graphene films, accepted to Hoshako (Journal of the Japanese Society for Synchrotron Radiation Research (2008).
- <sup>22</sup> E. L. Shirley, L. J. Terminello, A. Santoni, F. J. Himpsel, Brillouin-zone-selection effects in graphite photoelectron angular distributions, *Phys. Rev. B* 51, 13614 (1995).
- <sup>23</sup> T. Ohta *et al.*, Morphology of graphene thin film growth on SiC(0001), accepted to *New J. Physics* (2008).
- <sup>24</sup> H. Hibino, H. Kagashima, F. Maeda, M. Nagase, Y. Kobayashi, H. Yamaguchi, Microscopic thickness determination of thin graphite films formed on SiC from quantized oscillation in reflectivity of low-energy electrons, private communication (2008).
- <sup>25</sup> A. C. Ferrari *et al.*, Raman Spectrum of Graphene and Graphene Layers, *Phys. Rev. Lett.* 97, 187401 (2006).
- <sup>26</sup> C. Riedl, U. Starke, J. Bernhardt, M. Franke, K. Heinz, Structural properties of the graphene-SiC(0001) interface as a key for the preparation of homogeneous large-terrace graphene surfaces, *Phys. Rev. B* 76, 245406 (2007).
- <sup>27</sup> G. M. Rutter, J. N. Crain, N. P. Guisinger, T. Li, P. N. First, J. A. Stroscio, Scattering and Interference in Epitaxial Graphene, *Science*, 317, 219 (2007).

# Hetero-junctions of Boron Nitride and Carbon Nanotubes: Synthesis and Characterization

Yoke Khin Yap

*Department Physics*  
*Michigan Technological University*  
*118 Fisher Hall, 1400 Townsend Drive, Houghton, MI 49931*  
*E-mail: [ykyap@mtu.edu](mailto:ykyap@mtu.edu)*  
*URL: <http://www.phy.mtu.edu/yap/index.html>*

## Program Scope

Hetero-junctions of boron nitride nanotubes (BNNTs) and carbon nanotubes (CNTs) are expected to have appealing properties that are not available from pure BNNTs and CNTs. The growth of BNNT/CNT junctions was hindered by the absent of a common growth technique for both types of nanotubes. Recently, we have succeeded for the first time to grow pure BNNTs directly on substrates by plasma-enhance pulsed-laser deposition (PE-PLD) and thermal chemical vapor deposition (CVD). Since we have previously reported on the growth of CNTs by these techniques, a common route for growing BNNTs and CNTs on substrates is thus obtained. Based on this unique capability, a thorough research plan is proposed here for exploring the basic growth mechanism and fundamental physical properties of BNNT/CNT junctions.

We aim to establish basic knowledge for growing these hetero-junctions with desired segments of BNNTs and CNTs and thus tunable band structures and properties. Their structural, compositional, electronic, photonic/optical, magnetic, and spintronic properties will be characterized. Isolated and superlattices of these BNNT/CNT junctions are expected to have multiple functions, which is important for energy efficient device fabrications and applications. Every device fabricated from these junctions will be potentially useful for more than one type of application at a nanoscale. This project will also strengthen our collaboration with DOE Nanoscale Science Research Centers including the Center for Nanophase Materials Sciences (CNMS) at Oak Ridge National Laboratory, and the Center for Integrated Nanotechnologies (CINT) at Sandia National Laboratories and Los Alamos National Laboratory.

## Motivation

Theoretical studies indicate that BNNTs/CNTs junctions [1, 2] and h-BN/graphite sheets [3, 4] are energetically stable. Calculation shown that energy required for an N atom (or B atom) to exchange with a C atom at a BNNT/CNT junction is rather large (2.1 and 2.0 eV, respectively). Such a large “inter-diffusion” energy indicates that abrupt interfaces are energetically favored. Various configurations of such BNNT/CNT nanotubular junctions have been evaluated. Some of the conclusions are summarized as follows:

1. BNNT/CNT junctions are energetically stable either in the armchair or the zigzag configurations as shown in Figure 1.
2. Zigzag BNNT/CNT junctions (Figure 1a) are junctions of insulators/semiconductors. They possess flat band structures and tunable direct band gaps (~0.5 to 2.0 eV). Thus these BNNT/CNT junctions can be used as nanoferrromagnetic materials, spintronic and

tunable photonic/optical devices etc.. This is applicable only for single wall BNNT/CNT junctions since multiwalled CNTs is not semiconductors.

3. Armchair BNNT/CNT junctions (Figure 1b) are insulator/semimetal junctions with direct band gap and can form Schottky barrier devices, diodes, and quantum dots etc. [1]. This will be applicable for both single and multiwalled BNNT/CNT junctions that have the semimetallic CNT segments.

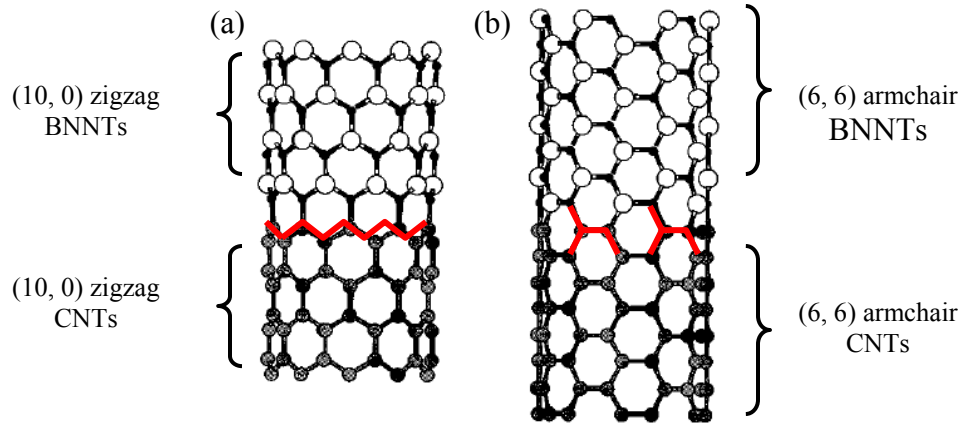


Figure 1. Schematic representations of (a) Zigzag (10, 0) and (b) armchair (6,6) BNNT/CNT junctions (modified from reference 1). The zigzag and armchair patterns are schematically drawn at the junctions in red. Carbon atoms are in gray circles (bottom sections). Large white and small black circles are, respectively, B and N atoms (top sections).

### Recent Progress

We have established the capability in controlling the number of graphene shells on CNTs by thermal CVD. These CNTs can be grown vertically aligned with multiwalled [5, 6], single- and double- walled [7] structures as shown in Figure 2. This capability will enable our attempts in growing single wall BNNT/CNT junctions.

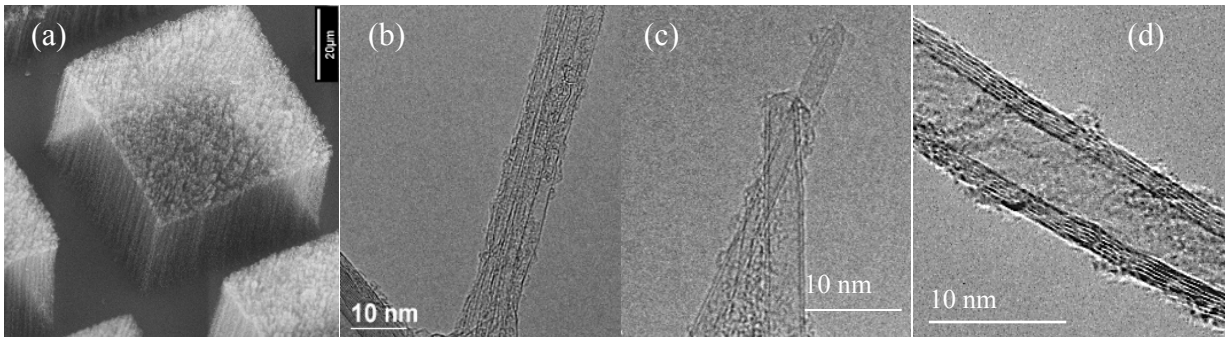


Figure 2. (a) Vertical arrays of carbon nanotubes can be grown as (b) single-, (c) double-, and (d) multi- walled structures at MTU.

We have previously succeeded for the first time in growing BNNTs on substrates at desired locations and orientations by PE-PLD at significantly low temperatures (600 °C) [8]. We

have also achieved effective growth of BNNTs by thermal CVD [9]. As shown in Figure 3a, clean and long BNNTs with diameters 20-100 nm can be obtained. Raman spectra (Figure 3b) and electron energy loss spectroscopy (EELS, not shown) indicate that these are pure BNNTs with high structural order as confirmed by transmission electron microscopy (Figure 3c).

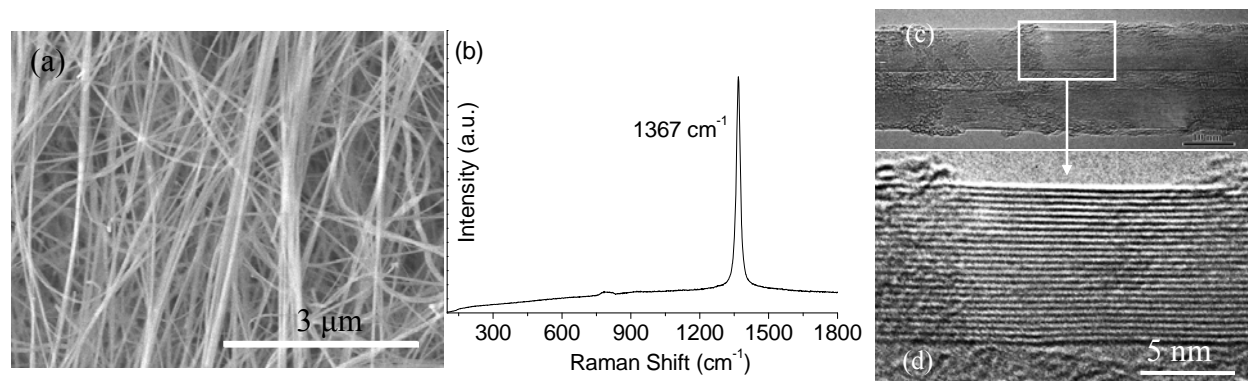


Figure 3. (a) SEM images, (b) Raman spectra, and (c and d) TEM images of BNNTs grown by Thermal CVD at MTU.

By combining our capabilities in growth both CNTs and BNNTs, we have succeeded for the first time in growing BNNT/CNT junctions as shown in Figure 4. This was achieved during the first year of the project. As shown, two types of BNNT/CNT junctions were obtained, i) branching junctions (Figure 4a), and ii) co-axial junctions (Figure 4b). For the branching structures, CNTs are branching out from a BNNT. On the other hand, the junctions of the co-axial structures are highlighted in circles. This is the first success on the growth of these novel BNNT/CNT junctions. All these junctions are having multiwalled structures.

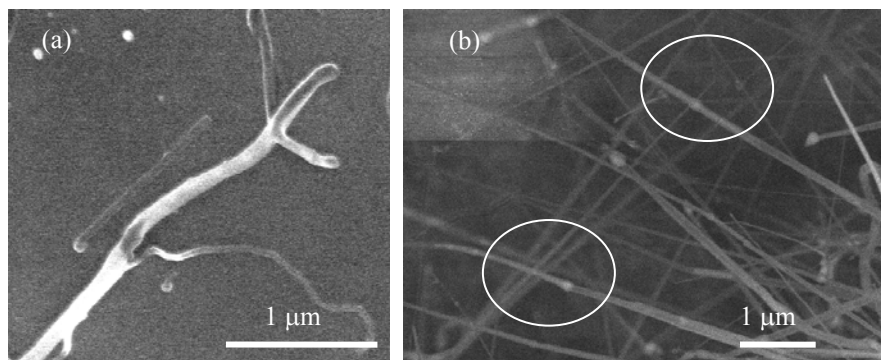


Figure 4. SEM images of (a) branching, and (b) co-axial BNNT/CNT junctions grown at Michigan Tech.

### Summary and Future Plans

Promising preliminary data were obtained on the growth of novel BNNT/CNT junctions during the first year of the project. We will continue to understand the growth mechanism of these BNNT/CNT junctions. We are currently exploring the growth of BNNT/CNT junctions with controllable diameters, which will lead toward the formation of single wall junctions. The structural and electronic properties of these junctions are currently under investigation.

## Acknowledgement

This project is supported by the U. S. Department of Energy, the Office of Basic Energy Sciences (Grant No. DE-FG02-06ER46294 managed by Dr. Refik Kortan in the Division of Materials Sciences and Engineering). Our work on carbon nanotubes is supported by Defense Advanced Research Agency (Contract Number DAAD17-03-C-0115, through Army Research Laboratory), and in part, performed at the Center for Nanophase Materials Sciences sponsored by the U.S. Department of Energy (Contract No DE-AC05-00OR22725 with UT-Battelle, LLC.). The results on boron nitride nanotubes are generated with the support from National Science Foundation CAREER award (DMR 0447555), and partly performed at the Center for Integrated Nanotechnologies at Sandia National Laboratories (SNL). SNL is a multi-program laboratory operated by Sandia Corporation, a Lockheed-Martin Company, for the U. S. Department of Energy under Contract No. DE-AC04-94AL85000.

## References

- [1]. X. Blase, J.-C. Charlier, A. De Vita, R. Car, "Theory of composite  $B_xC_yN_z$  nanotubes heterojunctions," *Appl. Phys. Lett.* **70**, 197 (1997).
- [2]. J. Choi, Y-H Kim, K. J. Chang, D. Tománek, "Theory of composite  $B_xC_yN_z$  nanotubes heterojunctions," *Phys. Rev.* **B 67**, 125421 (2003).
- [3]. S. Okada, M. Igami, K. Nakada, A. Oshiyama, "Border states in heterosheets with hexagonal symmetry," *Phy. Rev.* **B 62**, 9896 (2000).
- [4]. S. Okada, A. Oshiyama, "Magnetic ordering in hexagonally bonded sheets with first-row elements," *Phy. Rev. Lett.* **87**, 146803 (2001).
- [5]. V. Kayastha, Y. K. Yap, S. Dimovski, and Y. Gogotsi, "Controlling dissociative adsorption for effective growth of carbon nanotubes," *Appl. Phys. Lett.* **85**, 3265 (2004).
- [6]. V. K. Kayastha, Y. K. Yap, Z. Pan, I. N. Ivanov, A. A. Puretzky, D. B. Geohegan, "High-density vertically aligned multiwalled carbon nanotubes with tubular structures," *Appl. Phys. Lett.* **86**, 253105 (2005).
- [7]. V. K. Kayastha, S. Wu, J. Moscatello, Y. K. Yap, "Synthesis of vertically aligned single- and double- walled carbon nanotubes without etching agents," *J. Phys. Chem. C (Letter)* **111**, 10158 (2007).
- [8]. J. Wang, V. Kayastha, Y. K. Yap, Z. Fan, J. G. Lu, Z. Pan, I. Ivanov, A. A. Purezky, D. B. Geohegan, "Low temperature growth of boron nitride nanotubes on substrates," *Nano Letters*.**5**, 2528 (2005).
- [9]. C. H. Lee, J. Wang, V. K. Kayatha, J. Y. Huang, Y. K. Yap (in preparation).

## **Publications**

We have acknowledged the supports from DOE in the following presentations during the first year of this project:

- 1) Yoke Khin Yap, “Controlled Growth of Carbon, Boron Nitride, and ZnO Nanotubes,” in the DOE Basic Energy Science Peer Review of the Center for Nanophase Materials Sciences at Oak Ridge National Laboratory, Dec 4, 2006.
- 2) Yoke Khin Yap, “Growth of Carbon, Boron Nitride and ZnO Nanotubes for Biological Applications,” in Symposium E6 - Bioelectronics, Biointerfaces, and Biomedical Applications 2, Electrochemical Society 2006 Joint International Meeting in Cancun, Mexico (Oct. 29 to Nov. 3, 2006) Abstract 1168.
- 3) Yoke Khin Yap, “Nanomaterials and Nanocomputers: Promises and Challenges,” in the Indo-US Shared Vision Workshop on Soft, Quantum & Nano Computing (SQUAN-2007), Agra, India, Feb 22-25, 2007. This workshop was sponsored by the Indo-US Science and Technology Forum (IUSSTF, <http://www.indoustf.org/>).
- 4) Yoke Khin Yap, “Prospective Nanomaterials for Biological and Chemical Sensing,” in the Center for Fire, Explosives & Environment Safety, Defense Research & Development Organization, New Delhi, India on Feb. 26, 2007.

## **Session III: Interfaces / Surfaces**

## Proximity Effects in Conducting Oxide Heterostructures

J.A. Eastman, D.D. Fong, P.H. Fuoss, P. Zapol, A. Bhattacharya, and G.B. Stephenson

Materials Science Division, Argonne National Laboratory, Argonne, Illinois, USA

### Program Scope

This program strives to create, characterize, and understand thin film oxide heterostructures that exhibit novel ionic, electronic, or mixed conduction properties. By exploiting *proximity effects* induced by heterointerfaces through *space charge*, *elastic strain*, and *interfacial atomic structure*, we are creating new materials with properties currently unattainable in bulk structures. These proximity effects are systematically varied by judiciously selecting cation species with desired size and valence for *each atomic plane*, and are amplified in heterostructures when, as shown in Fig. 1, layer spacings are reduced below distances where electronic charges strongly interact or strain-fields overlap.

Our emphasis is on two-phase nanocomposite heterostructures that phase-separate during growth to form single-crystal epitaxially-strained nanolamellae, nanopillars, or nanodots. These nanostructures, which have specific size distributions, dimensionalities, and morphologies, are embedded in single-crystal thin film matrices. The complex oxide materials that form the building blocks of these heterostructures include combinations of fast ion conductors such as fluorite-structured oxides (e.g., cubic-ZrO<sub>2</sub>) and pyrochlores (e.g.,

Nd<sub>2</sub>Zr<sub>2</sub>O<sub>7</sub>), good electronic conductors, including ZnO and bixbyite-structured oxides (e.g., Sn-doped In<sub>2</sub>O<sub>3</sub>), and bulk insulators such as MgO and oxide spinels (e.g., MgAl<sub>2</sub>O<sub>4</sub>). We will also investigate layered oxide systems, such as Ca<sub>3</sub>Co<sub>4</sub>O<sub>9</sub>, that are comprised of naturally formed nanoblocks, each with their own unique conduction properties.

We employ in-situ x-ray scattering and spectroscopy during oxide heterostructure synthesis to improve deposition control and better understand the growth process. Our synthetically engineered heterostructures are assembled by atomic layer deposition (ALD), metal-organic chemical vapor deposition (MOCVD), sputter deposition, and molecular beam epitaxy (MBE), all techniques with the potential to provide precise control of each atomic plane in a growing heterostructure. We are exploiting the unique capability of in-situ synchrotron x-ray techniques to determine depth-resolved atomic-level structure and film composition in *real-time*, in the near-atmospheric pressure, elevated temperature environments that are integral to growth and transport behavior.

The experimental studies are closely coupled with simulation and theory efforts. Multi-scale simulations provide insight into the factors that control strain, composition, and structure during growth, and are playing a key role in identifying and elucidating charge transport mechanisms. This approach combining experimental results with theory facilitates the development of predictive models for the design of oxide heterostructures with emergent properties.

### Recent Progress

#### *Self-assembled ZrO<sub>2</sub>/In<sub>2</sub>O<sub>3</sub> heterostructures*

We recently initiated studies of the synthesis and properties of ZrO<sub>2</sub>/In<sub>2</sub>O<sub>3</sub> heterostructures and have demonstrated that this is a promising materials system for observing proximity-induced conduction behavior. Since ZrO<sub>2</sub> is known to exhibit high ionic conductivity (fast oxygen diffusion) but is an electronic insulator, while doped In<sub>2</sub>O<sub>3</sub> is a good electronic conductor but a poor ionic conductor, our expectation is that the interfaces between these materials will exhibit novel mixed conduction behavior. Initial samples have been grown by sputter deposition onto yttria-stabilized zirconia (YSZ) (001) substrates at 700°C. As seen in Fig. 2(a), we have succeeded in creating thin film heterostructures consisting of In<sub>2</sub>O<sub>3</sub> lamellae dispersed in a YSZ matrix. Synchrotron x-ray observations of these samples indicate that the In<sub>2</sub>O<sub>3</sub> lamellae extend through the

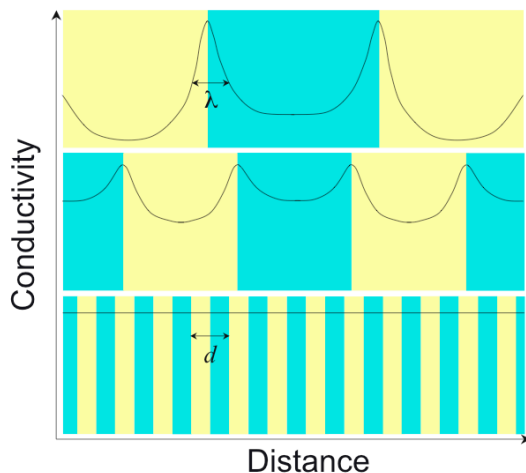


**Fig. 1** Schematic representation of conductivity (or other properties) vs. distance in a two-phase oxide heterostructure for different interfacial spacings,  $d$ . Emergent behavior occurs when  $d$  approaches a characteristic length,  $\lambda$ , which, e.g., could be the width of a space charge region or the extent of an interfacial strain field. As shown, the conductivity near the interface can differ substantially from the bulk properties of the two materials.

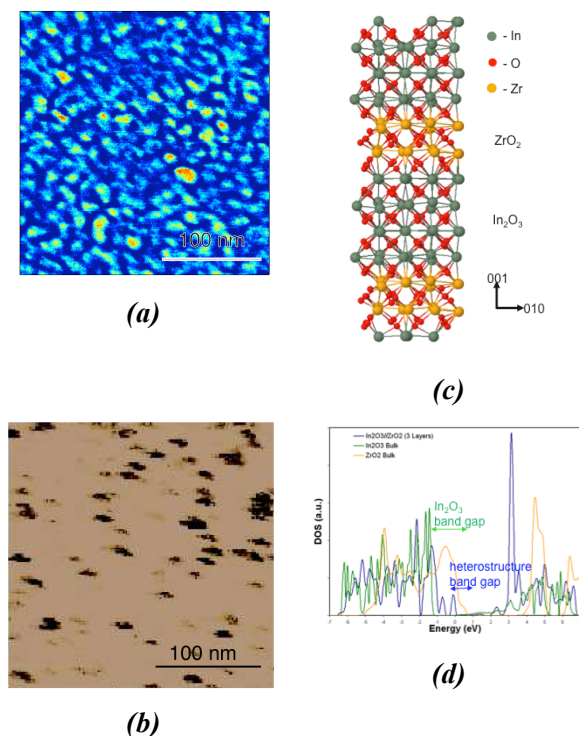


**Fig. 2:** Epitaxially-strained YSZ/ $\text{In}_2\text{O}_3$  films have been grown by simultaneously sputter-depositing  $\text{In}_2\text{O}_3$  and YSZ. Phase contrast AFM images (a) show that, for one particular choice of growth conditions, the resulting heterostructure consists of lighter contrast  $\text{In}_2\text{O}_3$  lamellae randomly distributed in a YSZ matrix. The lateral spacing between the lamella is approximately 10 nm. Topographical images (not shown) indicate that films such as this are extremely smooth, with height variations of less than 0.4 nm across the field of view. (b) Conductive AFM image from an epitaxially-strained YSZ/ $\text{In}_2\text{O}_3$  film on a YSZ (001) substrate with a Sn-doped  $\text{In}_2\text{O}_3$  bottom electrode. Dark colors indicate regions of higher conductivity. (c) DFT energy minimization of a heterostructure consisting of two-layers of cubic (100)  $\text{ZrO}_2$  lattice-matched to four layers of (100)  $\text{In}_2\text{O}_3$  resulted in significant buckling of the initially flat  $\text{ZrO}_2$  oxygen planes due to the symmetry reduction caused by the interface. (d) The calculated density of states (DOS) for this heterostructure shows significant differences compared with the DOS of  $\text{ZrO}_2$  and  $\text{In}_2\text{O}_3$  alone. In particular, the heterostructure is predicted to have a smaller band gap and hence be more conductive than either  $\text{In}_2\text{O}_3$  or  $\text{ZrO}_2$  alone, while still exhibiting optical transparency.

entire film thickness and are fully lattice-matched, producing both in- and out-of-plane misfit strain. To our knowledge, this is the first experimental demonstration of 3D misfit strain in an oxide nanocomposite film. The unusual strain state and close proximity of interfaces in such heterostructures is expected to affect the concentrations and mobilities of both ionic and electronic charge carriers. We are currently correlating in-film and through-film transport properties with the interface

spacing, strain state, and dopant distribution in both the  $\text{ZrO}_2$  and  $\text{In}_2\text{O}_3$  phases. Figure 2(b) shows a conductive-AFM image taken by our collaborator, S. Hong, from a YSZ- $\text{In}_2\text{O}_3$  nanocomposite film grown on YSZ (001) with a bottom Sn-doped  $\text{In}_2\text{O}_3$  electrode. As seen, the film contains regions of both high and low electrical conductivity, the high conductivity regions being only  $\sim 10$  nm wide. The correlation between conductivity and oxide phase/structure is now under investigation.

Growth and characterization of multilayer films helps to elucidate the mechanisms governing interfacial proximity effects. We have recently performed first-principles simulations to characterize the structure and conduction behavior of  $\text{ZrO}_2/\text{In}_2\text{O}_3$  (001) multilayers (Fig. 2(c) and are also synthesizing and creating similar multilayers experimentally. The (001) planes of both  $\text{ZrO}_2$  and  $\text{In}_2\text{O}_3$  are polar, consisting of alternating oxygen and cation planes. To maintain overall charge neutrality the interfacial oxygen planes in a heterostructure must have occupancy intermediate between that of the oxygen planes in either bulk material. This in turn results in non-bulk coordination of the cations on either side of the interface. Our calculations indicate that this structure results in significant changes in the heterostructure density of states (and hence also changes in electrical conductivity), as seen in Fig. 2(d). These preliminary studies illustrate the potential for creating improved transparent conducting oxides through heterostructure design.

#### *In-situ observations of oxide ALD*

Optimal control over conduction behavior in oxide heterostructures requires full understanding of the growth process, a requirement that necessitates in-situ studies that can provide insight into the many phenomena that control the structure and chemistry of heterostructure interfaces. Atomic layer deposition has well-recognized potential for independently controlling the growth of each monolayer of material in a heterostructure. However, in part due to the lack of previous in-situ studies, many important questions remain unanswered regarding the atomic scale mechanisms that control morphology, strain development, and phase stability during ALD. We recently initiated the first in-situ synchrotron x-ray studies of ZnO and  $\text{ZrO}_2$  ALD, two materials that are of great scientific and technological interest.

Our in-situ x-ray observations have begun to elucidate the effects of substrate temperature, substrate material and surface orientation, and the characteristics of various precursor chemicals on ALD growth behavior. For example, x-ray fluorescence observations reveal that  $\text{ZrO}_2$  ALD onto YSZ (001) substrates under conditions typically used by others is not self-limiting; rather the film thickness depends on ZTB exposure time. In the case of ZnO ALD, however, we find that the growth behavior depends strongly on the choice of substrate. Growth onto  $\alpha\text{-Al}_2\text{O}_3$  (0001) substrates (Fig. 3(a)) results in particle formation rather than growth of a coalesced film. In contrast, ZnO

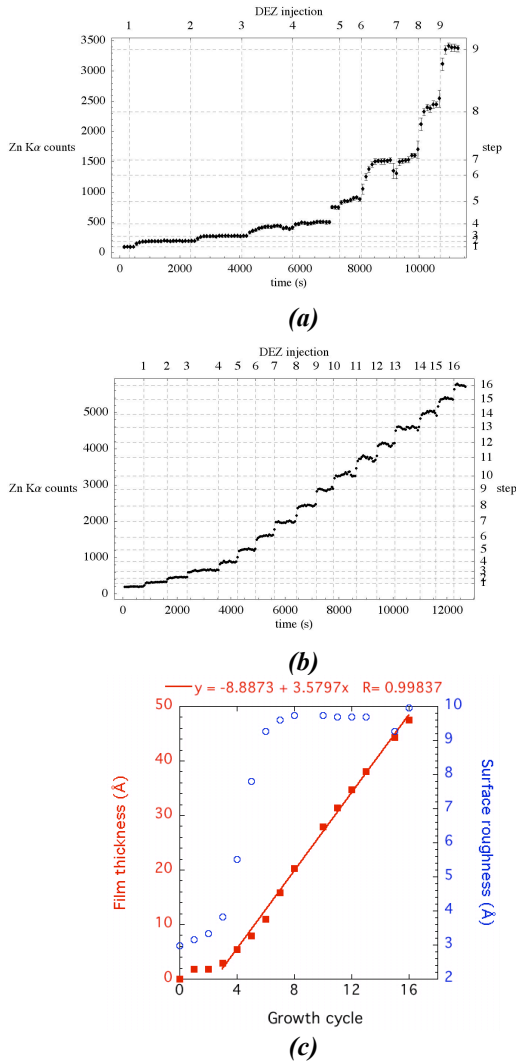


**Fig. 3:** ALD growth of ZnO on  $\alpha$ -Al<sub>2</sub>O<sub>3</sub> (0001) and Si (001) substrates. (a) Evolution of the Zn K $\alpha$  integrated intensity with time for ZnO growth on  $\alpha$ -Al<sub>2</sub>O<sub>3</sub> (0001). The moment of each 10-second DEZ injection is shown by the vertical lines (purges and H<sub>2</sub>O injection times are not indicated). (b) Evolution of the Zn K  $\alpha$  integrated intensity with time for ZnO growth on Si (001). (c) Film thickness (left axis, red symbols) and surface roughness (right axis, blue symbols) as measured by in-situ x-ray reflectivity.

growth onto Si (001) substrates under identical deposition conditions is self-limiting and shows a constant increase in film thickness with each diethyl zinc (DEZ) exposure after the first few growth cycles (Fig. 3(b)). The reasons for this substrate-dependent behavior are not yet understood. Future theoretical and experimental studies will examine the effects of substrate polarity and surface chemistry on initial growth characteristics.

The in-situ fluorescence measurements are complemented with in-situ x-ray reflectivity to study the evolution of film thickness, density, and surface and buried interface

roughness during ALD. During the ZnO on Si (001) deposition described above, we find that the increase in film thickness with each DEZ exposure becomes constant after the second growth cycle (Fig. 3(c)). In contrast, the film surface roughness continues to increase for several more growth cycles, but then stabilizes.

## Future Directions

### *Interfacially-dominated heterostructures*

We will continue to design and create oxide heterostructures that exhibit controllable proximity-enhanced conduction behavior, using the concepts of space charge, strain, and interfacial structure as guiding principles. Simulations will play a leading role in guiding the choice of materials systems for experimental study, in modeling their assembly during synthesis, and in providing the needed understanding of the interplay between interfacial structure, chemistry, and properties.

We will extend our initial studies from mixed conduction systems such as ZrO<sub>2</sub>/In<sub>2</sub>O<sub>3</sub> to other systems where both materials are insulators, but where conduction may still be induced due to the effects of charge discontinuities at polar interfaces. This possibility has attracted much attention recently because such charge discontinuities have been reported to give rise to so-called 2D electron gas (2DEG) behavior in perovskite heterostructures, particularly SrTiO<sub>3</sub>/LaAlO<sub>3</sub><sup>1</sup>. However, the formation of a thin interfacial reaction layer of La<sub>1-x</sub>Sr<sub>x</sub>TiO<sub>3</sub>, which is a bulk metal, has been reported recently<sup>2</sup> to be the origin of 2DEG behavior in that system. Since this calls into question whether 2DEG interfacial conduction in oxide heterostructures exists in the absence of a bulk-conducting phase, it is important to synthesize and characterize other materials combinations where polar discontinuities exist but possible artifacts due to interfacial reactions are avoided. One such materials system we will investigate is MgO/MgAl<sub>2</sub>O<sub>4</sub>, a system in which phase separation is expected, lattice mismatch is small (enabling epitaxial growth), and, perhaps most importantly, no known bulk conducting phases exist that involve only combinations of the constituents in these materials. Both conductive-AFM (in collaboration with S. Hong) and transmission electron holography (in collaboration with A. Petford-Long and N. Zaluzec) studies are being undertaken to elucidate interfacial conduction behavior.

### *Oxide heterostructure growth science and interfacial characterization*

We will continue to tune proximity effects through manipulation of the interfacial spacing and secondary phase morphology in oxide nanocomposites and multilayers. State-of-the-art in-situ monitoring techniques will be used to enable the construction of specially designed interfaces.

<sup>1</sup> A. Ohtomo and H.Y. Hwang, *Nature*, **427**, 423 (2004)

<sup>2</sup> P.R. Wilmott et al., *Phys. Rev. Lett.*, **99**, 155502 (2007)

Since interfacial composition can have profound effects on oxide heterostructure conduction behavior, it is important to fully understand how cation segregation and space charge behavior at both surfaces and buried interfaces depends on conditions such as temperature, oxygen partial pressure, polarity, and strain state. As a first step in this process, we have recently initiated studies of yttria segregation behavior in YSZ. Interestingly, we observe that the polar (001) surface is unsegregated (i.e., has the bulk composition) when heated to 800°C in oxygen, while significant yttria-depletion is observed when samples with the neutral (111) surface are exposed to the same conditions. DFT calculations of surface and interface structures coupled with ab initio thermodynamics will help to understand segregation phenomena. In the future we will extend these studies to investigate segregation behavior in other polar and non-polar materials and to determine segregation profiles at buried interfaces in oxide heterostructures.

While we have previously had much success in using in-situ x-ray techniques to provide insight into oxide film growth by MOCVD (and have recently initiated in-situ studies of oxide ALD), in-situ x-ray techniques have not yet been used during oxide MBE. We are very interested in pursuing such studies since in-situ x-ray scattering and spectroscopy techniques have great potential to provide valuable real-time information on composition and structure (including strain state) during growth. While a technique such as high-pressure RHEED helps in determining surface symmetry and relative surface roughness during growth, it does not provide the quantitative information on surface structure and composition that can be obtained with x-ray scattering and spectroscopy. The large penetration depth of high-energy x-rays also allows structure determination throughout the film thickness, including that of the buried interface.

Studies on the layered cobaltite,  $\text{Ca}_3\text{Co}_4\text{O}_9$ , will emphasize both the interesting growth science involved in depositing

hexagonal  $\text{CoO}_2$  nanoblocks onto cubic  $\text{Ca}_2\text{CoO}_3$  layers by oxide MBE, as well as the effects of elastic strain and the substrate interface ( $\alpha\text{-Al}_2\text{O}_3$  or rutile- $\text{TiO}_2$ ) on in-plane electrical and thermal transport. As the  $\text{CoO}_2$  nanoblocks are excellent electrical conductors and the  $\text{Ca}_2\text{CoO}_3$  planes have poor thermal conductivity, these layered oxides have considerable potential as high temperature thermoelectrics. Epitaxial nanocomposites of  $\text{Ca}_3\text{Co}_4\text{O}_9$  with  $\alpha\text{-Al}_2\text{O}_3$  and rutile- $\text{TiO}_2$  will also be synthesized, leading to studies of heterophase boundaries on thermoelectric behavior.

#### **Proximity-enhanced conduction behavior**

We will investigate the effects of space charge, strain, and interfacial structure on ionic and electronic conduction. A key experimental and theoretical focus will be determination of the relevant characteristic length(s). In-situ and ex-situ transport measurements, the former utilizing x-ray, electron, and substrate curvature techniques, will be complemented with DFT calculations of electronic properties and ion transport barriers to provide insight into how interfacial proximity can affect carrier concentrations and mobilities. As indicated previously, many proximity effects are expected; some magnified by nanoscale interfacial spacing and quantum confinement effects. The coupling between conduction and other proximity-influenced properties will also be investigated, emphasizing studies of optical transparency and thermoelectric properties. Ionic and electronic transport properties will be characterized both ex-situ and during in-situ measurements of structure, stress, and chemistry under elevated temperature, controlled  $\text{pO}_2$  conditions. In-situ characterization of samples will provide direct observations of defect evolution under applied electric fields.

Work supported by the U. S. Department of Energy, Office of Science (BES), under Contract No. DE-AC02-06CH11357. Contributing author: Jeffrey A. Eastman, [jeastman@anl.gov](mailto:jeastman@anl.gov)

#### **Publications 2005 to present:**

- 1) J.A. Eastman et al., *Appl. Phys. Lett.* **87**, 51914 (2005).
- 2) P.H. Fuoss, et al., *APS Science 2004*, ANL-05/04, 119(2005).
- 3) D.D. Fong et al., *Phys. Rev. B* **71**, 144112 (2005).
- 4) D.D. Fong et al., *J. Synchr. Rad.* **12**, 163 (2005).
- 5) P.H. Fuoss et al., *J. Taiwan Vac. Soc.*, **18**, 69 (2005).
- 6) S.K. Streiffer et al., *Proc. 12th US-Japan Seminar on Dielectric and Piezoelectric Ceramics*, Annapolis, MD, Nov. 6-9, (2005).
- 7) S.K. Streiffer et al., *Proc. of Internat. Workshop on Dielectric Thin Films*, Tokyo, Japan (2005).
- 8) D.D. Fong et al., *Phys. Rev. Lett.* **96**, 127601 (2006).
- 9) D.D. Fong, Carol Thompson, *Annu. Rev. Mater. Res.*, **36**, 431 (2006).
- 10) G.-W. Zhou et al., *Phys. Rev. Lett.*, **96**, 226108 (2006).
- 11) F. Jiang et al., *Appl. Phys. Lett.* **89**, 161915 (2006).
- 12) P. Zapol et al., *Phys. Rev. B* **74**, 235434 (2006).
- 13) R.-V. Wang et al., *Appl. Phys. Lett.* **89**, 221914 (2006).
- 14) L. Wang et al., *Surf. Sci.*, **600**, 2372 (2006).
- 15) H. Iddir et al., *Phys. Rev. B* **75**, 073203 (2007).
- 16) R.-V. Wang et al., *Thin Solid Films* **515**, 5593 (2007).
- 17) M.A. Zurbuchen et al., *J. Mater. Res.*, **22**, 1439 (2007).
- 18) S. Erdin et al., *J. Electroanalytic Chem.* **607**, 147 (2007).
- 19) G.-W. Zhou et al., *J. Appl. Phys.*, **101**, 033521 (2007).
- 20) H. Iddir et al., *Phys. Rev. B*, **76**, 241404 (2007).

## Adhesion and Wetting

**PI:** J. E. Houston

jehoust@sandia.gov

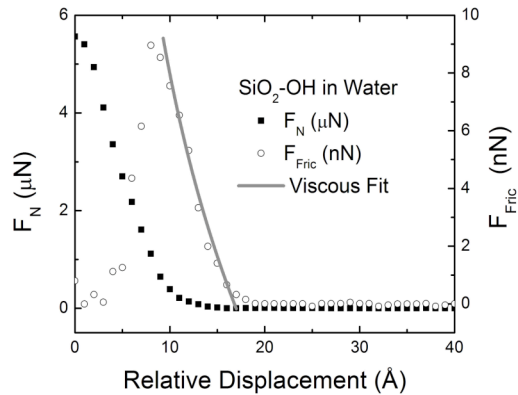
Dept. 1114, Sandia National Laboratories, PO Box 5800-1415 Albuquerque, NM 87185

This subtask exploits the unique capabilities of the Interfacial Force Microscope (IFM). The IFM was developed at Sandia under DOE/BES support to exploit its unique capabilities in applications to important problems in adhesion and wetting. Since both of these phenomena are so closely tied to interfacial mechanical properties, the technique has also found broad applications dealing with the nanomechanical properties of interfacial materials. The instrumentation, which is now commercially available on a small scale, has been adopted by several universities in the US and Canada. Sandia's original instrument is ten years old and suffers from antiquated electronics and computer-control instrumentation. In spite of its age, it is still able to produce data not obtainable by any other instrument and has received the Material Science Award for significant implications for DOE related technologies in Metallurgy and Ceramics and an R&D100 award. In addition, its scientific impact has ranged over a very broad spectrum of material science, which include the first measurements of the initial nucleation of dislocations in single-crystal Au showing theoretical strength and the first demonstration of a quantitative relaxation analysis for an extreme viscoelastic material (sometimes referred to as a solid liquid). We have recently designed and prototyped a significantly improved system based upon a dual, laser-interferometer controlled sensor (US Patent No. 6,627,048). The sensor represents the first self-calibrating force-probe technique capable of the independent measurement of both normal and lateral interfacial forces and promises even greater sensitivity, stability, ease of operation and breadth of application.

### Recent Progress:

**Interfacial water:** Recent IFM studies include a continuation of work dealing with a fascinating phenomenon that we first observed in a study of the interaction of alkanethiol molecules on a Au sample and tip terminated by five oligoethylene glycol units in water Kim. The original motivation was to determine why these surfaces were so lyophobic for many protein molecules. However, it was discovered in “draining” experiments, i.e., the force of interaction as the tip approached the surface at various speeds, that the force increased with tip speed at interfacial separations of a few nm. This phenomenon was interpreted as being due to the viscosity of interfacial-water layers on both the tip and sample. Surprisingly, the values obtained from a draining analysis *indicated a viscosity for this interfacial water 10<sup>6</sup> larger than that of bulk water*. In an attempt to verify these surprising results, we have continued the investigation with variations of the chemical nature of the surfaces, as well as their environment, including both bulk water and high humidity. The results, which have required the development of a specific set of characterization tools by P. J. Feibelman, were consistent in findings of the viscous interfacial water layer and the viscosity values were always in the range from 1 to 20 million times that of bulk water. The one common factor required was that both surfaces must be very hydrophilic and that the interfacial water must be confined between the tip

and sample surfaces to within a couple of nm. This work was done in collaboration with Professor X.-Y. Zhu, PostDoc R. C. Major and grad student M. Goertz in the Chemistry Department at the University of Minnesota. An example, involving a W tip and a Si(001) surface terminated by –OH groups, both of which were highly hydrophilic, is shown in Fig 1. Here, the friction force can be seen to begin to rise at about a nm before the nominal surface contact point, indicated by the onset of



significant repulsive normal-force values. The Feibelman analysis of the initial friction rise yielded an interfacial-water viscosity value of 2.4 KPa-sec, compared to the value of bulk water (0.89 mPa-sec), again revealing a ratio of more than million.

Figure 1, The normal (filled squares) and friction (open circles) forces plotted against the tip displacement for a Si(001) terminated by hydrophylic –OH groups interacting with a W tip in bulk water.

In our most recent studies, we have turned to one of the more fascinating examples of interfacial water, i.e., the “liquid-like layer” at the surface of bulk ice. The debate concerning the question as to just why ice is so slippery has been ongoing for more than a century and a half and, while a considerable amount is now known, the question remains largely unanswered and hotly debated. Although the behavior of the layer thickness with temperature has been measured by a broad range of experimental techniques, the results have shown a considerable range of thickness values. We have used the IFM to investigate not only the thickness of this layer, but also its viscoelastic behavior as a function of temperature. The data consists of measurements of both the normal force and lateral “friction” force as a function of temperature, a compilation of the former is illustrated in Fig. 2. The negative force values indicate a liquid-like behavior creating an attractive force on the tip due to the meniscus formed between the tip and the ice surface by the LL-like water layer. Contact with the more

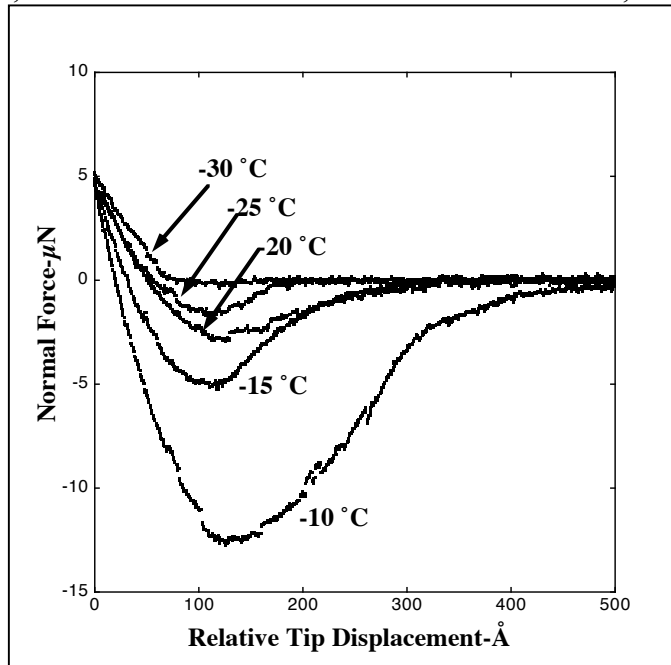


Fig. 2, The normal force vs. tip displacement for ice at various temperatures. The LL-layer is indicated by the meniscus behavior of the attractive forces (negative values).

solid-like ice substrate is indicated by the normal forces turn toward repulsive at the bottom of the attractive well. Plotting the nominal thickness of the meniscus versus temperature, compared to the predicted theoretical behavior is shown in Fig. 3, indicating a reasonable agreement.

Results for the nominal modulus for the solid-ice substrate and lateral-force “friction” data have also been obtained, but as yet have not been fully analyzed. However, we can say that the modulus values are all smaller than those tabulated for bulk ice. In addition, there is clear evidence of a viscous LL-like layer near the solid surface. However, the details of the implications of this data have not yet been fully appreciated.

**Instrument development:**

The Interfacial Force Microscope is, at present, *the only experimental technique available for stable and quantitative measurements of adhesive and mechanical properties at the micro- and nano-scales.* However, the current IFM is strictly a “research instrument” neither widely available nor “user friendly”. In addition, the sensors are difficult to fabricate and assemble and often fail due to particulate incursion. We are presently in the final stages of the development of a laser-interferometer version of the IFM. Both the 1D retrofit and the full 2D systems have been fully prototyped and the electronics and software packages are presently in the final stages of being assembled. The heart of the new system is a unique laser-interferometer IFM sensor (U.S. Patent No. 6,627,048). In this system, the capacitor gaps are used as two independent interferometer cavities and each capacitor gap is locked at a certain interferometer position by independent feedback loops, which apply the necessary voltages to the capacitor pads in order to balance forces (both normal and lateral) applied to the tip. Normal forces are proportional to the sum of the two applied voltages, while lateral forces are proportional to the voltage difference. In addition to producing the first scanning force-probe technique capable of independent normal and lateral-force sensing, this scheme dramatically increases the sensitivity, stability and ease of operation of the IFM system. In addition, the sensor configuration has been simplified to include a fixed substrate and removable top plate, which is magnetically held in place. Thus, the top plate is easily removed for tip replacement and overall sensor cleaning. This scheme dramatically reduces the cost and complexity of sensor fabrication and significantly increases its overall reliability.

**MEMS rheology demonstration:**

A serious problem facing all MEMS-device development is the lack of an instrument to accurately measure the forces and displacements for individual sub-units in actual operating devices. Such forces and displacements, which are always lateral to the device

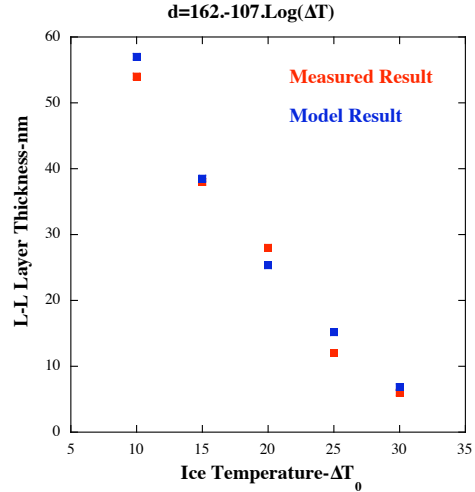


Fig. 3, A comparison of the LL-layer thickness vs. T with a model of the expected behavior.

layout, are presently only available from device modeling, which is often inadequate because of the difficulty of establishing dimensions and material properties at the micro-, or even, nano-meter level. The situation is made even more difficult if the device is mechanically unstable, for example ones that are specifically designed to be bistable. Such devices are the basis of many useful applications, for example the air-bag accelerometer, but most of these require an accurate knowledge of forces and displacements present at the points of instability. No instrument is presently available to provide such measurements. However, in concept, the IFM is ideally suited for just this kind of application, since analyzing the device requires a stable sensor. In fact, we have recently demonstrated this capability on actual Sandia-developed MEMS devices. These initial demonstration measurements already have allowed component designers to adjust design parameters in order compensate for differences in the measured performance and design predictions

Although the present IFM system is by no means ideal for performing such an analysis, coupling the new 2D laser-interferometer sensor with commercial metrology-based xyz manipulators, along with top-down IFM head-mount, displaced optical microscopy and adaptive IFM imaging for fine location, *will produce a totally unique instrument capable of the rapid characterization of MEMS-level force and displacement metrology*. Such a facility will not only allow rapid qualification of component design and fabrication, but will also provide the first instrument capable of analyzing the distribution of chip-generated forces throughout the string of down-stream elements in order to locate problem components in a failure-analysis setting.

### **Publications (2005-2007)**

The following is a list of publications resulting from research conducted during the last three-year performance period of this project.

“Hydrophilicity and the Viscosity of Interfacial Water,” M. P. Goertz, J. E. Houston, and X.-Y. Zhu, *Langmuir* (in press).

“Bridging the Gap-Observation of Ultra Long Range Hydrophobic Interactions, S. Singh, J. E. Houston, J. C. Brinker, and F. B. Van Swol, *Nature* 442, 536 (2006).

“Viscous Water Meniscus under Nanoconfinement,” R. C. Major, J. E. Houston, M. J. McGrath, J. I. Siepmann, and X.-Y. Zhu, *Phys. Rev. Lett.* 96, 177803 (2006).

“Does exceptional viscous drag impede flow through a nano-sieve’s pores?”  
P. J. Feibelman and J. E. Houston, *Mater. Res. Soc. Symp. Proc.* 930, JJ04 (2006).

“A Local-Probe Analysis of the Rheology of a "Solid Liquid," J. E. Houston, *J. Poly Sci. B: Polymer Physics* 21, 2992 (2005).

“A Comparative Study of Adhesion, Friction and Mechanical Properties of CF<sub>3</sub> and CH<sub>3</sub>-Terminated Alkanethiol Monolayers,” J. E. Houston, C. Doelling, T. K. Vanderlick, Y. Hu, G. Scoles, I. Wenzl. And T. R. Lee, *Langmuir*, 21, 3926 (2005).

## Atomic Scale Surface Phenomena

Program Coordinator:  
Gary L. Kellogg  
Mail Stop 1415  
Sandia National laboratories  
Albuquerque, NM 87185  
Email: glkello@sandia.gov

### Program Scope

The purpose of this program is to develop an atomic-scale understanding of technologically important processes occurring at solid surfaces, material interfaces and solid-liquid interfaces. The program has three major thrust areas (subtasks): (1) adhesion and wetting (2) localized corrosion, and (3) surface nanostructure formation. The adhesion and wetting subtask exploits the unique capabilities of the Interfacial Force Microscope (IFM). This instrument was developed at Sandia under DOE/BES support to exploit its unique capabilities in applications to important problems in the general field of adhesion and wetting. The goal of the localized corrosion subtask is to develop a quantitative understanding of the mechanisms of localized corrosion initiation in passive metals. Here, our approach is based on the novel and unique application of nanofabrication techniques to produce tailored oxides and to simulate specific defect types on controlled substrates in well-defined locations. The goal of surface nanostructure formation subtask is to establish the scientific principles governing the formation and stability of nanostructures on surfaces. Current efforts focus on understanding how atomic-scale, kinetic processes control collective phenomena on surfaces such as domain pattern formation (self-assembly) in two-phase, two-dimensional systems and surface alloy formation in metal-metal and semiconductor-semiconductor epitaxy.

The Subtask PIs, and their areas of expertise are as follows:

Adhesion and Wetting, Jack Houston, PI – *Experimental studies using the Interfacial Force Microscope (IFM)*. The R&D 100 award-winning IFM was invented by Dr. Houston, who continues to lead its further development and application to interphase material research. This tool is unmatched in its ability to simultaneously measure normal and lateral forces at well-characterized nanoscale interfaces with extraordinary sensitivity. Under this project, Dr. Houston has used the IFM to study the nano-mechanical and nano-tribological properties of solids and composite materials, self-assembled monolayers, and confined fluids at solid interfaces.

Localized Corrosion, Nancy Missert, PI – *Detailed understanding of corrosion mechanisms through investigation of pit initiation in tailored oxides and at nanoengineered defects*. The ability to correlate nanostructure evolution and pit initiation in passive metals is essential for the development of predictive aging models. Dr. Missert and her collaborators use well-characterized, engineered oxide/substrate systems and systematically separate out oxide property/response relationships in large sample

population sets, using state-of-the-art characterization techniques. This deterministic approach allows quantitative information regarding initiation mechanisms to be obtained, beyond the purely statistical analyses previously applied to bulk oxides and alloys.

Surface Nanostructure Formation, Gary Kellogg, PI – *Direct observations of collective surface phenomena at the nanoscale using low energy electron microscopy (LEEM)*. Success in linking atomistic processes to nanoscale structural changes requires the ability to observe dynamic processes at length scales where collective behavior manifests itself. Dr. Kellogg and his collaborators use the LEEM to investigate a wide range of surface phenomena including impurity induced nanostructure formation on Si, chemical etching of Si surfaces, surface phase transitions, surface faceting, and two-dimensional self-assembly – at length scales from tens of nanometers to microns.

**Note:** There will be poster presentations and separate abstracts provided on the Adhesion/Wetting and Localized Corrosion Subtasks by Jack Houston and Kevin Zavadil, respectively. The remainder of this abstract focuses on Subtask 3: Surface Nanostructure Formation.

### **Recent Progress (Subtask 3)**

- The potential use of self-assembled domain patterns as templates for the fabrication of surface nanostructures has generated considerable interest in understanding the physics that underlies two-dimensional pattern formation. Previously, we discovered that two phases of lead atoms on copper surfaces spontaneously order into stable domain patterns having dimensions of tens of nanometers. We showed that the pattern formation was driven by surface strain, but the large-scale motion required to achieve thermodynamically stable patterns was not understood. In recent LEEM investigations, we identified the mechanism leading to this large-scale motion. The high mobility of lead-overlayer islands results from the fast transport of lead atoms across the surface and, surprisingly, of copper atoms through the lead overlayer. A high lead vacancy concentration, predicted by our first-principles calculations, facilitates the latter. This new insight is important because, without the large-scale cooperative motion of tens of thousands of atoms, pattern formation would not take place on observable timescales. This study also represents one of the few examples where an atomistic understanding of mass transfer in complex, multi-component, multi-phase systems has been achieved.
- We developed a new experimental technique (with Jim Hannon, IBM, Yorktown Heights and Karsten Pohl, U. New Hampshire), which allows us to obtain three-dimensional maps of surface chemical composition with a lateral resolution of 8 nm. In our **LEEM-IV** analysis, we carry out intensity vs. electron energy (so-called “current-voltage” or simply IV) measurements pixel-by-pixel for an entire LEEM image. We then analyze the reflectivity data using multiple-scattering low energy electron diffraction (LEED) calculations (in analogy with conventional LEED-IV analysis).
- With our new LEEM-IV procedure, we identified the atomic origins of the chemical heterogeneity that develops during the deposition of Pd on Cu(001). Pd is a candidate

metal to inhibit the detrimental effects of electromigration in copper interconnects, but little is known about how, and at what temperature, Pd intermixes with Cu. Based on the chemical information provided by LEEM-IV analysis, we showed that the interesting intensity variations observed in LEEM images of Pd/Cu(001) can be explained with a conceptually simple “step-overgrowth” model. Although the model was developed in relation to the specific system of Pd on Cu(001), step overgrowth requires only fast surface diffusion (or equivalently low growth rate) and relatively slow bulk diffusion. This state of affairs is quite common in growth, and the same mechanism should be operative generally.

- The initial stages of Ge and Si growth on *pure* Si(001) are well understood. However, at growth conditions where devices are made, the deposition of Ge leads to the formation of a Ge/Si alloy in the first few atomic layers. It is thus important to determine if the atomic processes active on this alloy surface differ from that on the pure silicon surface. Accordingly, we have used STM to study the initial growth of Ge on the Ge/Si(001) alloy. We measured the time constant of the evolution of precursor Ge chain-like structures into compact islands as a function of temperature on the Ge/Si(001) surface alloy. We also measured the relative configurational free energy of kinked versus straight segments of the chain-like structures. This energy reflects a second-nearest-neighbor interaction mediated by the alloy substrate. These results, along with those reported last year concerning the formation and migration of adatom pairs, show unequivocally that nucleation and diffusion processes active on the pure silicon surface (and the models used to describe them) are not valid on the Ge/Si alloy.

### **Future Plans (Subtask 3)**

- We will measure the effect of subsurface (alloyed) Pd on the mobility of Cu adatoms on Cu(001). A quantitative measure of this effect is important in determining the extent to which Pd/Cu surface alloys can inhibit the detrimental effects of electromigration on Cu interconnects. We will also examine the thermal stability of the surface alloy.
- We will investigate the atomistic processes underlying Ge/Si surface alloying using our entire arsenal of experimental techniques. A main focus will be on determining the critical role of surface steps in the alloying of Ge into Si(001). Our novel LEEM-IV analysis will be used to determine the three-dimensional Ge concentration profile in the region around spontaneously formed steps. We will also use scanning tunneling spectroscopy (STS) to distinguish the atomic species in the surface alloy and the composition of the adsorbed species. We will measure the relative formation free energies of deposited Ge as a function of the underlying alloy composition.
- Following the discovery (Michely group, Aachen, Germany) that a very regular array of Ir islands grows on a single graphene sheet adsorbed on Ir(111), we will study the energetics of this self-organizing system. Using first-principles, Density Functional Theory calculations, we will first investigate the breaking of pi-bonds needed for graphene to bind to the underlying precious metal. Then we will develop an understanding of the potential energy surface that biases the diffusion of Ir adatoms on top of the graphene layer.

In the longer-term we plan to initiate a theoretical and experimental effort to understand diffusion in “fluid-like” systems. At elevated temperatures and in multicomponent systems many different types of thermal defects can exist simultaneously and have been found to interact in complex ways. Similarly, the nature of diffusing thermal defects in weakly bound systems such as organic thin films is a completely open question. In these situations, the energies of atomic processes cannot be simply extracted from Arrhenius plots. While there exists extensive theoretical formalisms for understanding diffusion in such complex systems, there has been very little quantitative comparison with experiment. We will attack this problem by measuring the temperature dependence of the evolution of surface morphology on metals at high temperature in sufficient detail to characterize the expected non-Arrhenius behavior. We will then develop the theoretical framework needed to interpret these results in terms of the complex behavior known to occur on such surfaces at the atomic scale. The same procedure will then be applied to organic films (e. g., self-assembled monolayers on Au).

**References to publications of DOE sponsored research that have appeared in 2005-2007 or that have been accepted for publication. (Subtask 3).**

- “How Pb-overlayer Islands Move Fast Enough to Self-Assemble on Pb-Cu Surface Alloys,” M.L. Anderson, N.C. Bartelt, P.J. Feibelman, and G. L. Kellogg, *Phys. Rev. Lett.* **98**, 096106 (2007).
- “Local Structural and Compositional Determination via Electron Scattering: Heterogeneous Cu(001)-Pd Surface Alloy,” J. Sun, J. B. Hannon, G. L. Kellogg, and K. Pohl, *Phys. Rev. B* **76**, 205414 (2007).
- “Addimer Chain Structures: Metastable Precursors to Island Formation on Ge-Si(001)-(2x1) Alloyed Surface,” Kyle J. Solis, Lance R. Williams, B.S. Swartzentruber, and Sang M. Han, *Surface Sci.* **601**, 172 (2007).
- “Origins of Nanoscale Heterogeneity in Ultra-thin Films,” J. B. Hannon, J. Sun, K. Pohl, and G. L. Kellogg, *Phys. Rev. Lett.* **96**, 246103 (2006).
- “Two-Dimensional Ir Cluster Lattice on a Graphene Moiré on Ir(111),” Alpha T. N'Diaye, Sebastian Bleikamp, Peter J. Feibelman, and Thomas Michely, *Phys. Rev. Lett.* **97**, 215501 (2006).
- “Reversible Shape Transition of Pb Islands on Cu(111),” R. van Gastel, N. C. Bartelt, and G. L. Kellogg, *Phys. Rev. Lett.* **96**, 36106 (2006).
- “The Effect of Embedded Pb on Cu Diffusion on Pb/Cu(111) Surface Alloys,” M. L. Anderson, N. C. Bartelt, P. J. Feibelman, B. S. Swartzentruber, and G. L. Kellogg, *Surface Sci.* **600**, 1901 (2006).
- “Effects of Elastic Anisotropy on the Periodicity and Orientation of Striped Stress Domain Patterns at Solid Surfaces,” François Léonard, N. C. Bartelt, and G. L. Kellogg, *Phys. Rev. B*, **71**, 045416 (2005).
- “Surface-Diffusion-Limited Island Decay on Rh(001),” G. L. Kellogg and N. C. Bartelt, *Surface Sci.* **577**, 151 (2005).
- “Oscillatory Interaction between O Impurities and Al Adatoms on Al(111) and Its Effect on Nucleation and Growth,” C. Polop, H. Hansen, W. Langenkamp, Z. Zhong, C. Busse, U. Linke, M. Kotrla, P. J. Feibelman, and T. Michely, *Surf. Sci.* **575**, 89 (2005).

# Towards Quantitative Understanding of Strain Induced Nano-scale Self-assembly from Atomic-scale Surface Energetics and Kinetics

Feng Liu (fliu@eng.utah.edu)  
Department of Materials Science & Engineering  
University of Utah, Salt Lake City, UT 84112

## Program Scope

Strain engineered self-assembly in heteroepitaxial growth of thin films has been recognized as an attractive *natural* route for fabrication of nanostructures [1]. The nanoscale thin-film structures and morphologies are fundamentally linked to the atomic-scale surface/interface energetics and kinetics. However, the atomic-scale quantities, especially their dependence on strain, are generally unknown for most systems. This has limited our understanding to a qualitative macroscopic level. The objective of this program is to take a multiscale theoretical and computational approach in an effort to achieve quantitative microscopic understanding of strain induced nanoscale self-assembly. We will combine several state-of-the-art techniques, including first-principles calculation, continuum-theory modeling, kinetic Monte Carlo simulation, and step dynamics simulation, to make quantitative analysis of nucleation, growth, and stability of quantum dots (QDs, strained islands), focusing on the growth of Ge and SiGe alloy on Si. The approach we develop will be generally applicable to other systems. Our studies will significantly further our fundamental understanding of QD growth to a quantitative microscopic level and provide useful guidelines for future experimental efforts in strain engineering of QD self-assembly. They will have a significant impact on advancing thin-film based device technology for energy applications, to help fulfill the mission of the Department of Energy.

## Recent Progress

Extensive experimental and theoretical work has been attempted in the last decade to stimulate, guide, and control the self-assembly processes to improve the uniformity of QDs by manipulating the thermodynamics and kinetics of epitaxial growth [1]. Qualitatively, it is known the formation of QDs, or strained islands in general, is driven by relaxation of strain energy at the expense of increase of surface energy, but the quantitative knowledge of these two energy terms, especially their dependence on strain, remains unknown for most systems. Recently, by combining first-principles calculation with continuum modeling, we have made an important breakthrough in performing, for the first time, quantitative theoretical analyses and predictions for growth of Ge and SiGe QDs on Si substrate. These include critical size for Ge and SiGe QD

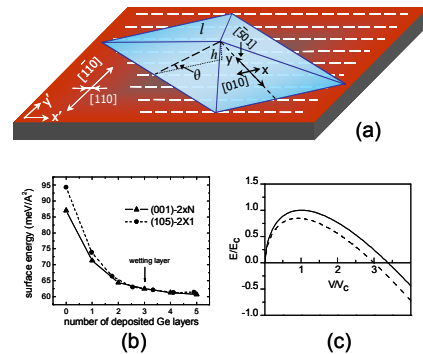


Fig. 1. (a) Schematics of a Ge(105) hut on Si(001). (b) Surface energies of Ge/Si(105) and Ge/Si(001) surfaces vs. the deposited Ge layers. (c) The hut formation energy vs. hut volume. The solid and dashed line shows respectively the results without and with edge stress effect.

nucleation/formation, stability for self-assembly, and distribution of SiGe alloy concentration in QDs versus in wetting layer [2-4].

One special feature of QDs is that they are usually bound by faceted surfaces [such as (105) facets on Ge hut islands (Fig. 1a)] that are often stabilized by strain. We have performed extensive first-principles calculations of surface energies and their strain dependence of substrate, wetting layer, and QD surfaces, for the Ge hut on Si(001) (Fig. 1b) [2,3]. The comparison of the relative stability of these surfaces under strain conditions have allowed us to obtain a much better understanding of the physical origin of QD formation [2]. Using these surface energies as input parameters for continuum modeling, we further obtained quantitative estimates of the “critical” size of nucleation/formation for both pure Ge and SiGe alloy QDs (Fig. 1c) [2], in very good agreement with experiments.

We have also calculated surface stress tensors of QDs and wetting layers to assess the stability of QDs for self-assembly. The QD formation contains two major contributions: the strain relaxation energy proportional to QD volume and the cost of surface energy proportional to QD surface area. If only these two terms were present, there would be no stable QD size [5]. However, the surface stress of the QD is generally different from that of the substrate, which gives rise to an additional term of elastic edge energy. If the edge energy were large enough, it would introduce a stable QD size against coarsening [6]. The significance of such surface stress-induced edge relaxation on QD stability has been a subject of long-standing controversy. Our calculations revealed that for Ge hut on Si(001), this edge term is too small to induce a stable size (Fig. 1c) [2].

In addition to thermodynamic properties of surface energies and surface stresses, we performed also quantitative studies of kinetic properties, in particular the surface diffusion energy barriers. A few years ago, we developed a generic method for predicting how an external strain will change surface diffusion barrier, by first-principles calculation of adatom induced surface stress along the diffusion pathways on the unstrained surface [7,8]. Applying this method, we recently showed that on a compressive Ge(001) surface, Ge diffuses  $10^2$ - $10^3$  times faster than Si in the temperature range of 300 to 900 K; while on a tensile surface, the Ge and Si diffusivities are comparable (Fig. 2) [4]. Consequently, growth of a compressive SiGe film is kinetically different from that of a tensile film, although thermodynamically the two systems have the same strain energy. The diffusion disparity between Si and Ge was shown to be greatly enhanced on the strained Ge islands compared to that on the Ge wetting layer on Si(001), which explained several experimental observations, such as the Si enrichment in the wetting layer relative to that in the islands [4].

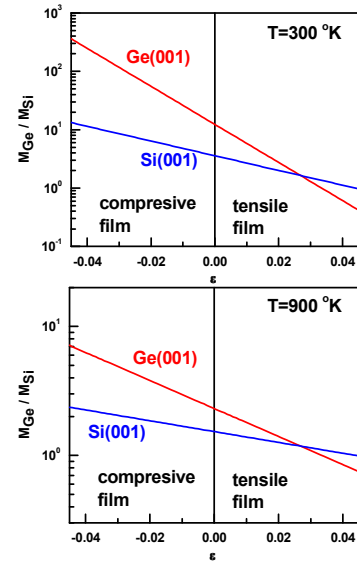


Fig. 2. Semi-log plot of the Ge/Si surface mobility ratio as a function of in-plane strain on Si(001) or Ge(001), at 300 K and 900 K. The left panel shows results for a compressive SiGe alloy film on a Si substrate and the right panel for a tensile SiGe alloy film on a Ge substrate.

## Future Plans

We will continue to expand our studies to explore the atomic-scale thermodynamics and kinetics that underlie the nanoscale self-assembly in growth of strained thin films, focusing on the QDs and quantum wires (QWs) in Ge/Si(001) systems. These include extension to QDs of different shapes, such as Ge domes (Fig. 3), SiGe alloy QDs, QD molecules, Ge and SiGe QWs, and to the effect of strain on Ehrlich-Schwoebel (ES) step-edge barriers. These studies will involve first-principles calculations with much larger and complex supercells, so the use of DOE-NERSC supercomputers will be critically helpful.

One interesting topic we plan to undertake is on shape transformation of QDs. It is known that Ge QD grows initially in the pyramidal shape of hut (Fig. 1a). It will then transform into either an elongated pyramidal shape (as a QW) or a shape of dome (Fig. 3) with steeper side facets. However, it remains unclear how would these two types of shape transformations compete with each other and which shape transformation has a thermodynamic or kinetic origin. Similar to our study of Ge hut [2], we will perform quantitative analysis of the elongated “hut” and dome islands, to compare their relative stability with the hut. These studies not only are of great scientific interests in understating strain induced island shape instability, but also have important technological implications in controlling the growth of QDs vs. QWs.

We plan also to extend our study of the effect of strain on adatom surface diffusion to adatom diffusion over a surface step, by examining how the ES step-edge barrier would be affected by external strain. Most importantly, we will determine whether the generic model we developed for adatom surface diffusion barrier [7] is applicable to ES barrier. The situation at step edge is much more complex than on surface, because the ES barrier often involves complex atomic-scale processes of concerted motion of multiple atoms. It is interesting as well as useful to know whether the simple linear stress-strain relationship established for adatom jumping on the surface [7,8] is still valid for adatom crossing (ascending or descending) a step involving motion of multiple atoms. It is expected that strain will have a different effect on different diffusion pathways. This implies that strain may not only change diffusion or step-crossing energy barriers, but even change the diffusion mechanisms and pathways, converting from one scenario of single atom rolling to another of concerted motion of multiple atoms, and vice versa.

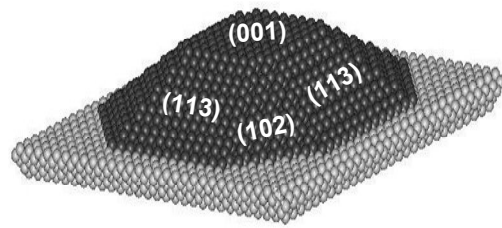


Fig. 3. Schematics of a Ge dome bounded with (113) and (102) facets.

## References

1. Feng Liu, in “*Handbook of Theoretical and Computational Nanotechnology*”, eds. M. Rieth and W. Schommers, **4**, Chapter 10, 577-625(2006).
2. G.H. Lu and Feng Liu, *Phys. Rev. Lett* **94**, 176103 (2005).
3. G.H. Lu, Martin Cuma, and Feng Liu, *Phys. Rev. B* **72**, 125415 (2005).
4. L. Huang, Feng Liu, G.H. Lu and X.G. Gong, *Phys. Rev. Lett* **96**, 016103 (2006).
5. J. Tersoff and F.K. LeGoues, *Phys. Rev. Lett* **72**, 3570 (1994).
6. V.A. Shchukin *et al.*, *Phys. Rev. Lett* **75**, 2968 (1995).
7. D.J. Shu, Feng Liu, and X.G. Gong, *Phys. Rev. B*, **64**, 245410 (2001).
8. L. Huang, Feng Liu, G.H. Lu and X. G. Gong, *Phys. Rev. B* **70**, 155320 (2004).

## DOE Sponsored Publications in 2005-2007

1. “Directed Self-assembly of Quantum Dots by Local-Chemical-Potential control via Strain Engineering on Patterned Substrates”, H. Wang, Feng Liu, and M. Lagally, in “Lateral Alignment of Epitaxial Quantum Dots”, Ed., O. Schmidt, Springer, Chapter 20, page 524 (2007) (**invited book chapter**).
2. “MD simulation of structural and mechanical transformation of single-walled carbon nanotubes under pressure”, J. Zang, O. Aldás-Palacios and Feng Liu, *Commun. Comput. Phys.* **2**, 451 (2007) (**invited review**).
3. “Modeling and Simulation of Strain-Mediated Nanostructure Formation on Surface”, Feng Liu, in “*Handbook of Theoretical and Computational Nanotechnology*”, eds. M. Rieth and W. Schommers, **4**, Chapter 10, 577 (2006) (**invited book chapter**).
4. “Quantitative Prediction of Critical Size for the Formation of Semiconductor Quantum Dots”, G.H. Lu and Feng Liu, in “*J. Chinese Phys. Association*”, **35**, 447 (2006) (**invited review**).
5. “Computational R&D for Industrial Applications”, Feng Liu, News Article of Center for High-Performance Computing, University of Utah, Fall issue, p. 1 (2005) (**invited review**).
6. “Intrinsic current-voltage characteristics of graphene nanoribbon transistors and effect of edge doping”, Q. Yan, B. Huang, J. Yu, F. Zheng, J. Zang, J. Wu, B. Gu, Feng Liu, W. Duan, *Nano Lett.* **7**, 1469, (2007).
7. “Making a field effect transistor on a single graphene nanoribbon by selective doping”, Bing Huang, Qimin Yan, Gang Zhou, Jian Wu, Bing-Lin Gu, Wenhui Duan, and Feng Liu, *Appl. Phys. Lett.* **91**, 253122 (2007).
8. “First-Principles Study of Adsorption and Diffusion on Ge/Si(001)-(2X8) and Ge/Si(105)-(1X2) Surfaces”, L. Huang, G.H. Lu, Feng Liu, and X. G. Gong, *Surf. Sci.* **601**, 3067 (2007).
9. “Impurity mediated absorption continuum in single-walled carbon nanotubes”, C. Zhang, J.C. Chao, X.G. Guo and Feng Liu, *Appl. Phys. Lett.* **90**, 023106 (2007).
10. “Nucleation-Mediated Lateral Growth on Foreign Substrate”, D.J. Shu, M. Wang, Feng Liu, Z. Zhang, R.W. Peng, R. Zhang, N.B. Ming, *J. Phys. Chem. C*, **111**, 1071 (2007).
11. “Surface Mobility Difference between Si and Ge and its Effect on Growth of SiGe Alloy Films and Islands”, L. Huang, Feng Liu, G.H. Lu and X. G. Gong, *Phys. Rev. Lett* **96**, 016103 (2006).
12. “Pressure-Induced Transition in Magnetoresistance of Single-walled Carbon Nanotubes”, J. Z. Cai, L. Lu, H. W. Zhu, C. Zhang, B. Q. Wei, D. H. Wu, and Feng Liu, *Phys. Rev. Lett* **97**, 026402 (2006).
13. “Critical Epi-Nucleation on Reconstructed Surfaces and a Model Study of Si(001) Homoepitaxy”, R.S. Pala and Feng Liu, *Phys. Rev. Lett* **95**, 136106 (2005).
14. “Nanomechanical Architecture of Strained Bilayer Thin Films: from design principles to experimental fabrication”, M. Huang, C. Boone, M. Roberts, D.E. Savage, M. Lagally, N. Shaji, H. Qin, R. Blick, J. A. Nairn and Feng Liu, *Adv. Mater.* **17**, 2860(2005).
15. “Self-organization of Semiconductor Nanocrystals by Selective Surface Faceting”, B. Yang, P. Zhang, D.E. Savage, M. Lagally, G.H. Lu, M. Huang, and Feng Liu, *Phys. Rev. B* **72**, 235413 (2005).
16. “Bending of Nanoscale Ultrathin Substrates by Growth of Strained Thin Films and Islands”, M.H. Huang, P. Rugheimer, M. Lagally, and Feng Liu, *Phys. Rev. B* **72**, 085450 (2005).
17. “Towards Quantitative Understanding of Formation and Stability of Ge Hut Island on Si(001)”, G.H. Lu, M. Huang, and Feng Liu, *Phys. Rev. Lett* **94**, 176103 (2005).
18. “First-principles study of strain stabilization of Ge(105) facet on Si(001)”, G.H. Lu, M. Cuma, and Feng Liu, *Phys. Rev. B* **72**, 125415 (2005).
19. “Relative stability of Si surfaces: a first-principles study”, G.H. Lu, M. Huang, M. Cuma, and Feng Liu, *Surf. Sci.* **588**, 61 (2005).

# Surface Engineering by Simultaneous Action of Multiple External Fields

Principal Investigator: **Dimitrios Maroudas**, Professor  
University of Massachusetts, Amherst  
Department of Chemical Engineering,  
157B Goessmann Laboratory, 686 North Pleasant Street, Amherst, MA 01003-3110  
E-mail: [maroudas@ecs.umass.edu](mailto:maroudas@ecs.umass.edu); Telephone: (413) 545-3617; FAX: (413) 545-1647

Co-Principal Investigator: **M. Rauf Gungor**, Research Associate Professor  
Department of Chemical Engineering, University of Massachusetts, Amherst

## Program Scope

This theoretical and computational research program started on 8/1/2007. It aims at enabling surface engineering strategies based on the fundamental understanding and predictive modeling of the surface morphological response of solid materials subjected to the combined action of multiple external forces. The research focuses on the surface morphological evolution and stability of electrically conducting (metallic) and semiconducting solids under the simultaneous application of mechanical stresses and electric fields. Special emphasis is placed on identifying the conditions under which the multiply driven surface morphology is stable and exploring the complexity of the corresponding various morphologically stable surface patterns. In addition, we emphasize on the driven evolution of nanoscale features aiming at stabilizing and controlling nanoscale patterns on surfaces by their manipulation through simultaneously applied multiple external forces. Specifically, we address systematically the morphological response to the combined action of electric fields and mechanical stresses of bulk solid surfaces, surfaces of thin films grown epitaxially on thick or thin substrates, as well as nanoscale surface features such as coherently strained islands grown heteroepitaxially on substrate surfaces. The research is based on a modeling approach that combines theoretical analyses of surface morphological stability with self-consistent dynamical simulations of surface evolution based on properly parameterized continuum surface transport models and with molecular-dynamics simulations for atomic-scale analysis of strain relaxation mechanisms.

In terms of materials chemical composition, the study focuses on Cu (primarily) and Si systems (bulk solids or substrates on which films or small islands can be grown epitaxially). In terms of studying surface morphological response, the scope of the program is broad and includes the following research tasks:

- Continuum-scale analysis of morphological evolution and stability under surface electromigration conditions of: (a) surfaces of stressed elastic solids; (b) surfaces of coherently strained thin films grown heteroepitaxially on solid substrates; and (c) coherently strained islands grown heteroepitaxially on solid substrate surfaces.
- Atomic-scale analysis of surface morphological evolution, focusing on the role of strain relaxation mechanisms, such as plastic deformation dynamics, in: (a) solids stressed beyond the linear elastic regime and up to their limit of strength; and (b) heteroepitaxial films/islands with thicknesses/sizes greater than the critical ones for misfit dislocation generation.
- Systematic studies of the effects of electromechanical conditions (varied over a broad range of material and operating parameters) on surface morphological response.

## Recent Progress

During the first five months of this program, we have made substantial progress in our studies of surface morphological response of stressed elastic solids under electromigration conditions, as well as atomic-scale studies of strain relaxation mechanisms and plastic deformation dynamics toward enabling rigorous studies of surface morphological response beyond the linear elastic regime. In addition, we have made progress in (i) development of computational models for analyzing morphological evolution of heteroepitaxially grown islands

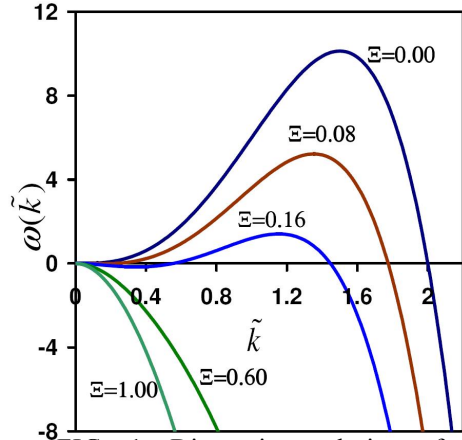


FIG. 1. Dispersion relations for various  $\Xi$  values giving the dependence of the characteristic dimensionless frequency,  $\omega$ , for the growth ( $\omega > 0$ ) or decay ( $\omega < 0$ ) rate of a shape perturbation from a planar surface morphology on the dimensionless wavenumber of the perturbation for certain surface diffusional anisotropy parameters [1].

stabilization of materials morphology and/or structure by simultaneous application of multiple external forces.

on substrate surfaces under surface electromigration conditions; (ii) analysis of complex asymptotic states in surface morphological evolution, including oscillatory states and chaotic attractors, and (iii) extension of surface morphological evolution modeling from 2D to 3D. Here, we summarize some of our most important findings to date.

### ***Current-induced Stabilization of Surface Morphology in Stressed Solids***

– We have examined the surface morphological evolution of an electrically conducting, single-crystalline elastic solid under the simultaneous action of an electric field and mechanical stress based on a fully nonlinear model and combining linear stability theory (LST) with self-consistent dynamical simulations [1]. We have demonstrated that electric current, through surface electromigration, can stabilize the surface morphology of the stressed solid against crack-like surface instabilities. It should be mentioned that analogous surface morphological stability analyses can be conducted over a broad class of materials, such as magnetic and optical materials, under various external fields, leading to more general conclusions regarding the

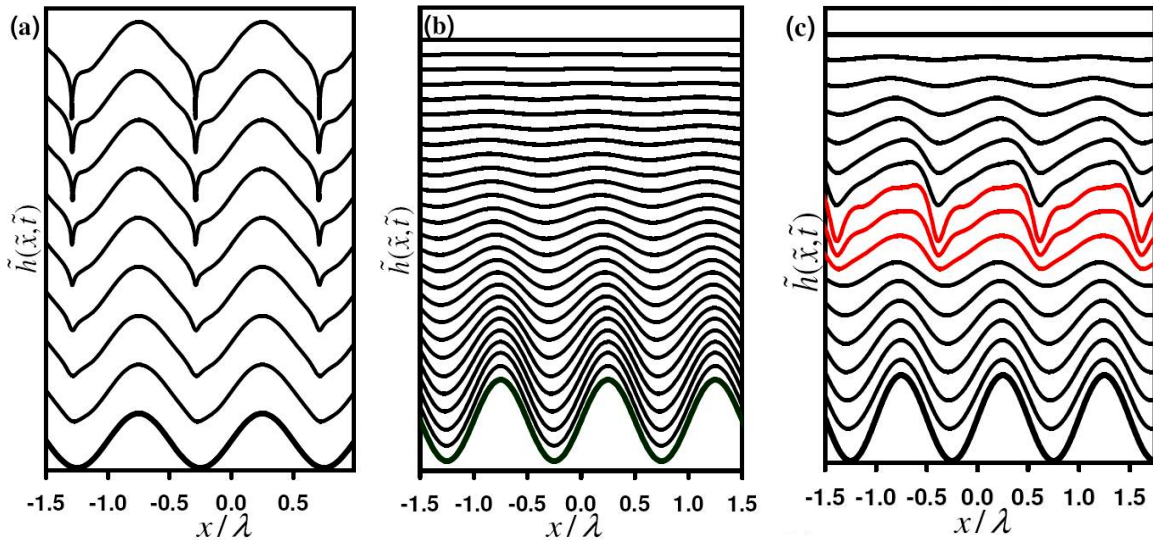


FIG. 2. Surface morphological evolution, starting with a low-amplitude sinusoidal shape perturbation at (a)  $\Xi = 0.0$  and (b)  $\Xi = 0.60$ . (c) Same shape perturbation and  $\Xi$  value as in (b) but the electric current is turned off for a period of time and then it is turned back on. The anisotropy parameters are the same with those that yielded the dispersion curves of Fig. 1. The evolution sequences are from the bottom to the top, the electric field is applied from right to left, and the stress is tensile and applied uniaxially along  $x$  [1].

Figure 1 shows the LST results for the surface morphological response as the governing dimensionless parameter,  $\Xi$ , increases for certain surface diffusional anisotropy parameters [1];  $\Xi$  expresses the relative strength of the two externally applied forces, electric field and stress, scaled with the capillary force. The most important implication of Fig. 1 is that application of a sufficiently strong electric field ( $\Xi > \Xi_c$ ) stabilizes fully the surface morphological response against any shape perturbation wavelength. This finding implies that *electric current can stabilize surfaces of stressed solids that are otherwise vulnerable to cracking through the so-*

called Asaro-Tiller or Grinfeld (ATG) instability. We have confirmed the LST findings through dynamical simulations of surface morphological response to the simultaneous action of electric field and stress. Representative simulation results are shown in Fig. 2. Surface cracking due to an ATG instability is shown in Fig. 2(a). The inhibition of such a stress-induced morphological instability due to the proper action of an electric field is shown in Figs. 2(b) and 2(c).

**Texture Effects on the Surface Morphological Stability of Metallic Thin Films** – Using the same model of driven surface morphological evolution and combining linear stability analysis with self-consistent dynamical simulations, we have analyzed the effects of surface crystallographic orientation of a metallic thin film on its surface morphological response to the simultaneous action of an electric field and mechanical stress [2]. The analysis maps surface morphological stability as a function of surface crystallographic orientation in stressed elastic and electrically conducting solids under surface electromigration conditions. The results have provided a fundamental understanding of and an interpretation for the well-known longer electromigration lifetime of thin films of face-centered cubic (fcc) metals with  $\{111\}$  texture.

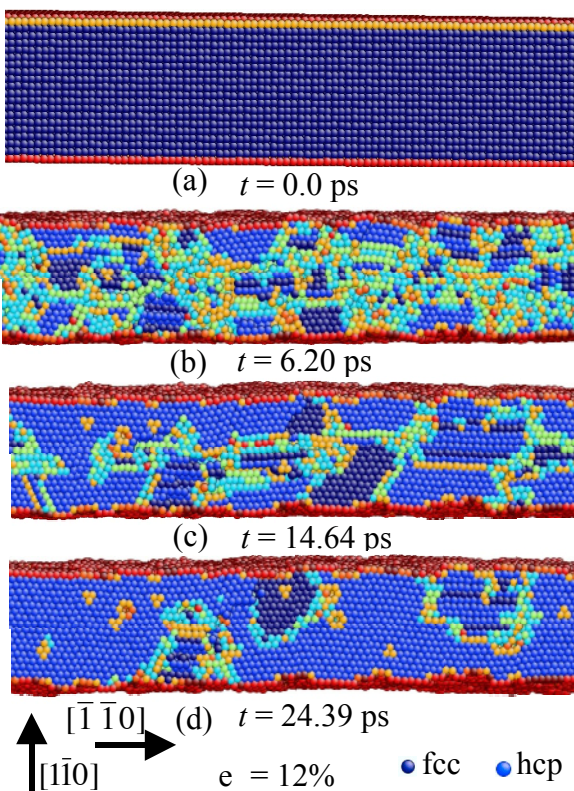


FIG. 3. (a)-(d) A cross-sectional view of a biaxially strained (to  $\epsilon = 12\%$ ) Cu thin film showing the evolution of the film structure as it undergoes structural transition from an initial fcc lattice [(a)]; the plane shown is the (001) fcc lattice plane. The hcp phase nucleates at the film's surface [(b)] and propagates into the bulk of the film [(c), (d)]. Dark and light blue atoms are in perfect fcc and hcp lattice arrangements, respectively. Maroon atoms are surface atoms and other colored atoms are inside dislocation cores. The three subdomains embedded in the hcp-martensite phase in (d) are faulted hcp (middle) and fcc regions. The corresponding time,  $t$ , in the MD simulation is recorded starting from the film at its unstrained state [4].

**Atomic-Scale Analysis of Defect Dynamics and Strain Relaxation Mechanisms in Biaxially Strained Ultra-thin Films of FCC Metals** – We have conducted a detailed systematic computational analysis of strain relaxation mechanisms and the associated defect dynamics in ultra-thin, i.e., a few nanometers thick, Cu films subjected to biaxial tensile strain [3].

The analysis is based on isothermal-isostrain molecular-dynamics (MD) simulations of the response of Cu films that are oriented normal to the  $[111]$  crystallographic direction using an embedded-atom-method parameterization for Cu and multi-million-atom slab supercells. Our analysis reveals five regimes in the thin film's mechanical response with increasing strain. Within the considered strain range, after an elastic response up to a biaxial strain level  $\epsilon = 5.5\%$ , the strain in the metallic thin film is relaxed by plastic deformation. At low levels of the applied biaxial strain above the yield strain ( $\epsilon \sim 6\%$ ), threading dislocation nucleation at the surface of the thin film in conjunction with vacancy cluster formation in the film lead eventually to formation of voids that extend across the thickness of the film. For  $6\% < \epsilon < 8\%$ , dislocations are emitted uniformly from the thin-film surface, inhibiting the nucleation of voids. For  $\epsilon \geq 8\%$ , in addition to nucleation of dislocations from the film surface, dislocation loops are generated in the bulk of the film and grow to intersect the thin-film surface. For  $\epsilon \geq 10\%$ , a high density of point defects in the film leads to nucleation of Frank partial dislocations that dissociate to form stacking fault tetrahedra. In addition, dislocation-dislocation interactions due to the high dislocation density lead to formation of Lomer-Cottrell dislocation locks

and complex stable dislocation junctions that act as obstacles to dislocation glide. As a result of these defect mechanisms, nano-scale domains are formed in the crystalline film with an average domain size of 1.5 nm and low-angle misorientations.

We are currently conducting MD-based analyses of the structural response of ultra-thin metallic films to biaxial straining as a function of surface crystallographic orientation. In addition to the isothermal-isostrain simulations, we are also simulating dynamic deformation experiments (at constant strain rate) and probing the atomic-scale mechanisms that govern the thin-film mechanical behavior. Among our most interesting recent results is the observation of martensitic fcc→hcp phase transformations in biaxially strained Cu films with [110] surface crystallographic orientation [4]. We have found that martensites nucleate at the surface and grow into the bulk of the film due to dislocation glide; in this process, the magnitudes of the relative atomic slip displacements are identical to those proposed for Bain transformations. Mechanical stability analysis shows that the phase transformation onset is consistent with the onset of a shearing instability of the thin film. Figure 3 shows a cross-sectional view of the structural evolution during strain relaxation of the thin film that has been strained biaxially to  $\varepsilon = 12\%$ . This evolution sequence shows the film as it undergoes structural transition from its initial fcc lattice.

### Future Plans

Our future plans address the research tasks outlined in the program scope. Short-term plans (substantial progress expected within the next year) include: (1) continuation of the 2D continuum-level analysis of surface morphological stability and evolution of stressed elastic solids under surface electromigration conditions and exploration of surface orientation and anisotropy effects; (2) continuation of the MD simulation work toward analysis of strain relaxation phenomena beyond elastic response; (3) analysis of complex asymptotic states (oscillatory states including chaotic attractors) in driven surface morphological evolution; (4) preliminary analysis of driven morphological evolution of strained islands on substrates; (5) targeted atomistic calculations toward parameterizing surface anisotropies; (6) extension of 2D continuum-level modeling to 3D; and (7) development of careful experimental protocols (in collaboration with expert experimentalists) to test the modeling predictions.

Longer-term plans (substantial progress expected within the three-year period) include: (1) completion of the 2D continuum-level analysis of surface morphological stability and evolution of stressed elastic solids under surface electromigration conditions; (2) completion of the MD simulations for analysis of strain relaxation phenomena and development of constitutive equations for continuum-level modeling; (3) completion of the analysis of complex asymptotic states toward understanding formation of patterns in the morphology of driven surfaces and surface features; (4) 3D continuum-level modeling and analysis of surface morphological stability and pattern formation; (5) parameterization of surface anisotropies and incorporation into the continuum-level modeling; (6) modeling of driven morphological evolution of surfaces of strained layers on substrates and of heteroepitaxial islands on substrates; and (7) collaborative effort with experimental partners to establish effects on surface morphological response of the simultaneous action of multiple external forces.

### References

1. V. Tomar, M. R. Gungor, and D. Maroudas, "Current-induced Stabilization of Surface Morphology in Stressed Solids," *Physical Review Letters* **100**, Article No. 036106, 4 pages (2008).
2. V. Tomar, M. R. Gungor, and D. Maroudas, "Theoretical Analysis of Texture Effects on the Surface Morphological Stability of Metallic Thin Films," submitted to *Applied Physics Letters*; preprint available.
3. K. Kolluri, M. R. Gungor, and D. Maroudas, "Atomic-Scale Analysis of Defect Dynamics and Strain Relaxation Mechanisms in Biaxially Strained Ultra-thin Films of Face-Centered Cubic Metals," submitted to *Journal of Applied Physics*; preprint available.
4. K. Kolluri, M. R. Gungor, and D. Maroudas, "Martensitic fcc→hcp Phase Transformations in Strained Ultra-thin Metallic Films," submitted to *Physical Review Letters*; preprint available.

# Interfaces in Electronic and Structural Materials

Y. Mishin\*

Department of Physics, MSN 3F3, George Mason University, 4400 University Drive, Fairfax, VA 22030

## 1. Program scope

The goal of this project is to achieve a deeper fundamental understanding of atomic structure, solute segregation, phase transformations, mechanical response and dynamics of interfaces in metallic materials. The specific phase transformations studied here include the flat-to-faceted transition at grain boundaries (GBs), the interface disordering transition, and the surface and GB melting and pre-melting transitions in pure metals and alloys. GB sliding and migration in response to applied shear stresses will be investigated to understand the complex relationships between the critical stresses of these processes, the crystal symmetry and temperature. The dynamics of GB motion coupled to shear deformation will be studied over a wide range of velocities, temperatures and stresses. As model systems we use pure metals (Cu, Ag, Ni, Al and Ta), binary alloys (Cu-Ag, Cu-Ta) and intermetallic compounds (Ni-Al).

This project employs state-of-the art atomistic simulations methods, including regular and accelerated molecular dynamics (MD) and Monte Carlo, as well as development of theoretical models of the relevant processes. It also involves the development of new interatomic potentials for the systems of interest, including the systems Cu-Ag and Cu-Ta.

## 2. Recent Progress

### 2.1 Phase transitions at interfaces

Significant progress has been achieved in understanding the structural phase transitions at interfaces [1-4,7-9,11,12,14]:

**Faceting transitions at GBs [11].** Energies and atomic structures of asymmetrical  $\Sigma 11$   $90^\circ$  [110] tilt GBs in Cu have been studied by MD simulations. Two interesting transitions have been found: (1) The boundaries dissociate into a low-angle and a high-angle boundary separated by a layer of an FCC-based long-period structure containing intrinsic stacking faults, and (2) the high-energy boundary breaks into nanometer-size facets, some of which are not  $\Sigma 11$  and do not even belong to any particular coincident-site lattice (CSL). Thus, asymmetrical tilt boundaries locally deviate from the CSL and from the average plane imposed by the macroscopic geometry, demonstrating a limitation of the CSL model of GBs. The results are consistent with high-resolution transmission electron microscopy observations available in the literature.

**Order-disorder transitions at APBs [4,13].** Using semi-grand canonical Monte-Carlo simulations, we have shown that (111) anti-phase boundaries (APBs) in the  $\text{Ni}_3\text{Al}$ -based  $\gamma'$  phase can undergo a “pre-wetting” transition as the APB region disorders and eventually transforms into a metastable  $\gamma$ -phase layer. To understand the nature of this transition, we performed detailed thermodynamic, compositional, and structural analyses of the APBs for different bulk composition at a fixed temperature of 700 K. The “pre-wetting” composition was identified and the APB thickness was shown to remain finite as the bulk composition approaches the  $\gamma/\gamma'$  transition point. The latter finding is important as it indicates that the APB transformation at this temperature is first order, not second order as was thought before.

---

\* Email address: [ymishin@gmu.edu](mailto:ymishin@gmu.edu)

**Melting and pre-melting transitions [2,7,12,14].** Cu GBs were found to accumulate significant disorder and eventually form a liquid-like layer about 10-20 K below the bulk melting point  $T_m$ . In this pre-melting temperature range, the local structure factor in the GBs tends to zero while GB diffusion rapidly accelerates and approaches the diffusivity of bulk liquid. The GB diffusion mechanism involves collective displacements of atomic chains. An interesting finding is that the thickness of the  $\Sigma 5$  (210) GB rapidly increases with temperature when approaching  $T_m$  from below but remains *finite* at  $T_m$ . Furthermore, this boundary can be slightly overheated above  $T_m$ , suggesting that its melting is a first-order transition. Likewise, the (111) surface of Cu does not pre-melt and remains metastable over a certain temperature range above  $T_m$ . By contrast, the (110) surface melts continuously and its thickness diverges to infinity when temperature approaches  $T_m$  from below. The pre-melting process is preceded by a surface order-disorder transition at about  $0.65T_m$ . The latter is manifested in a break in the temperature dependence of the structure factor and surface stress, whereas the surface free energy remains fairly smooth. These investigations shed light on the mechanisms and thermodynamic nature of surface pre-melting in pure metals.

To study pre-melting in alloys, a new embedded-atom potential has been developed for the Cu-Ag system, which predicts the phase diagram in good agreement with experiment [7]. Monte Carlo simulations of the Cu  $\Sigma 5$  (210) GB revealed the formation of a liquid-like GB layer when approaching the solidus line from below. The chemical composition of the layer approaches the liquidus composition at the respective temperature. The composition and thickness of the liquid layer are continuous functions of temperature and grain composition. The boundary can be readily overheated above the solidus line in agreement with the expected first order of the transition.

**Surface wetting and dewetting [12,14]** were studied in the Cu-Ta system. The latter presents significant interest for microelectronics applications. First-principles calculations of thermodynamic and mechanical properties of interfaces between Cu thin films and a (110) BCC-Ta substrate predicted their high stability (low excess energy, high work of separation) [12]. It was also predicted that a monolayer coverage must be very stable while a multi-layer coverage unstable, leading to the formation of Cu islands. To test this prediction by large-scale MD simulations, a new angular-dependent interatomic potential was constructed for the Cu-Ta system by fitting to first-principles data. The MD simulations revealed that a Cu film placed on the Ta (110) surface indeed dewets from it, forming a Cu droplet on top of a stable monolayer. Furthermore, a droplet of liquid Cu placed on a clean Ta (110) surface spreads over it as a stable monolayer while the extra Cu atoms remain in the droplet. The close agreement between the first-principles and atomistic data verifies our methodology and leads to the important conclusion that the failure of Cu/Ta contacts must occur inside the Cu film and not along the interface.

## 2.2 Interface dynamics

A major area of this project is GB motion coupled to shear deformation [5,6,9,10,15]. We have proposed a geometric theory of the coupling effect for tilt GBs and linked the multivalued character of the coupling factor  $\beta$  to crystal symmetry. The coupled motion of [001] and [211] tilt GBs has been studied by MD over the entire misorientation range and a wide range of temperatures. The coupling factor was found to be multivalued, can be positive or negative, and shows abrupt switches between the branches. At high temperatures, the response of high-angle GBs to shear stresses changes from coupling to sliding until coupling disappears. The coupling factors determined by the MD simulations are in excellent agreement with our geometric model. The temperature–misorientation diagram of mechanical responses of GBs proposed in our work can be used for the interpretation of mechanical behavior of nanocrystalline materials.

Atomic mechanisms of coupled GB motion have been identified. This motion does not require atomic diffusion and is typically implemented by distortion and rotation of structural units forming the GB. The unit transformations occur by the nucleation and growth mechanism

in which the transformed GB area is bounded by a disconnection loop and grows by the loop extension.

Significant efforts were dedicated to understanding the dynamics of stress-driven GB motion. At low temperatures and relatively large velocities, the GB motion exhibits stick-slip dynamics characterized by a saw-tooth behavior of stress and stop-and-go character of the boundary motion. The peak stress increases with the GB velocity but decreases with temperature. The stress-velocity-temperature relations established by our MD simulations are consistent with existing theoretical models of stick-slip dynamics [15]. At high temperatures and/or slow velocities, the GB begins to make occasional backward jumps, the stress behavior becomes noisy, and the stick-slip dynamics eventually transform to driven Brownian motion. The latter regime is characterized by a linear stress-velocity relation known experimentally.

When this work started, a major problem in this field was the huge gap between the experimental GB velocities and the extremely high velocities implemented in MD simulations due to the time-scale limitation of the method. To solve this problem, we collaborated with Dr. A.F. Voter's group at LANL to push the minimum accessible velocity down by means of accelerated MD methods. The parallel-replica MD method has allowed us to greatly expand the velocity range and finally approach the experimental velocities [10]. Besides closing the gap between simulations and experiment, this study has pointed to a close analogy between couple GB motion in crystals and other known cases of stick-slip dynamics, including the tip movements in atomic friction microscopy.

### 3. Future plans

We intend to continue the study of the APB “pre-wetting” transition in  $\text{Ni}_3\text{Al}$ , extending it to a wide temperature range and constricting the transition line on the Ni-Al phase diagram. We will also examine other APB orientations, particularly the (100) orientation involved in the dislocation dissociation in this material. A phase-field model of this transition will be developed and compared with the atomistic simulation results.

The effect of the interface pre-melting transition on physical and mechanical properties will be examined, including interface diffusion and interface sliding.

In the area of interface dynamics, we are planning to extend the MD studies of the coupling effect to asymmetrical tilt and later general mixed GBs. We are currently working on a generalized geometric model of coupling that should be applicable to mixed GBs. The model will have the capability to predict the complete set of geometrically possible coupling modes of any arbitrary GB given one of its crystallographic descriptions and the point-symmetry group of the crystal. Preliminary results for a  $\Sigma 7$  GB in Al indicate that multiple symmetry-related geometric descriptions of the same GB do actually give rise to multiple coupling modes and that they can be activated by MD simulations by adjusting the direction of the applied shear. These findings are important for the understanding of mechanical responses of interfaces to applied loads during fabrication and service of materials.

We will continue to study the stress-velocity-temperature relations for GB migration and sliding using regular and accelerated MD. This work will be extended to incommensurate interfaces and will later include solute effects. Simultaneously, we are planning to develop theoretical models to explain the regime changes in interface dynamics. Presently, the stick-slip models treat the interface sliding as a spatially uniform process. They thus ignore its nucleation and growth nature and are completely decoupled from nucleation theory. We intend to examine this process within a simple model, probably in the spirit of the driven 2D Frenkel-Kontorova-Tomlinson model, and connect the stick slip and other dynamic regimes with the classical and diffuse-interface theories of phase nucleation.

#### 4. Publications of DOE sponsored research (2005-2007)

1. J. A. Brown and Y. Mishin: Segregation and structural transformations at  $\Sigma 3$  grain boundaries in NiAl: A Monte-Carlo study, *Acta Materialia* **53**, 2149-2156 (2005).
2. A. Suzuki and Y. Mishin: Atomic mechanisms of grain boundary diffusion: Low versus high temperatures, *Journal of Materials Science* **40**, 3155-3161 (2005).
3. Y. Amouyal E. Rabkin and Y. Mishin: Correlation between grain boundary energy and geometry in Ni-rich NiAl, *Acta Materialia* **53**, 3795-3805 (2005).
4. A. Suzuki and Y. Mishin: Atomistic modeling of intermetallic alloys, *Materials Science Forum* **502**, 21-26 (2005).
5. Y. Mishin: Atomistic mechanisms of grain boundary migration, *Materials Science Forum* **502**, 157-162 (2005).
6. J. W. Cahn, Y. Mishin and A. Suzuki: Duality of dislocation content of grain boundaries, *Philosophical Magazine* **86**, 3965-3980 (2006).
7. P. L. Williams, Y. Mishin and J. C. Hamilton: An embedded-atom potential for the Cu-Ag system, *Modelling and Simulation in Materials Science and Engineering* **14**, 817-833 (2006).
8. Y. Mishin and A. Y. Lozovoi: Angular-dependent interatomic potential for tantalum, *Acta Materialia* **54**, 5013-5026 (2006).
9. J. W. Cahn, Y. Mishin and A. Suzuki: Coupling grain boundary motion to shear deformation, *Acta Materialia* **54**, 4953-4975 (2006).
10. Y. Mishin, A. Suzuki, B. P. Uberuaga and A. F. Voter: Stick-slip behavior of grain boundaries studied by accelerated molecular dynamics, *Physical Review B* **75**, 224101 (2007).
11. J. A. Brown and Y. Mishin: Dissociation and faceting of asymmetrical tilt grain boundaries: Molecular dynamics simulations of copper, *Physical Review B* **76**, 134118 (2007).
12. A. Hashibon, C. Elsasser, Y. Mishin and P. Gumbsch: First-principles study of thermodynamical and mechanical stabilities of thin copper film on tantalum, *Physical Review B* **76**, 245434 (2007).
13. C. A. Becker, Y. Mishin and W. J. Boettinger: The pre-wetting transition at anti-phase boundaries: an atomistic modeling study of Ni<sub>3</sub>Al, *Journal of Materials Science* (accepted).
14. A. Hashibon, A. Y. Lozovoi, Y. Mishin, C. Elsasser and P. Gumbsch: Interatomic potential for the Cu-Ta system and its application to surface wetting and dewetting, *Physical Review B* (accepted).
15. V. A. Ivanov and Y. Mishin: Dynamics of grain boundary motion coupled to shear deformation, *Physical Review B* (submitted).

## Interfacial Materials Program (FWP 58307)

A K Petford-Long, O Auciello, S Hong and S Nakhmanson  
Materials Science Division, Argonne National Laboratory, 9700 S Cass Avenue, Argonne, IL 60439.  
Petford.long@anl.gov; auciello@anl.gov; hong@anl.gov; nakhmanson@anl.gov

### Program Scope

This program combines advanced materials synthesis, complementary *in situ* and *ex situ* characterization and property measurement techniques with computer simulations to elucidate the interfacial contributions to novel phenomena exhibited by oxide thin film heterostructures. The program is structured around three themes: interface control through understanding growth dynamics in complex oxide films, the contribution of interfaces when oxide films are incorporated in heterostructures and developing an understanding of domain behavior in ferroic nanostructures as a function of microstructure and composition. The complementary strengths of simulation and experiment provide fundamental insights into the mechanisms and interfacial driving forces that control composition and microstructure and thus overall film properties.

### Recent Progress

***In situ studies of ferroelectric thin films:*** Research on this topic focused on *in situ* film synthesis and characterization of film growth and interface processes using two unique systems. An integrated sputter-deposition/ion mass spectroscopy/x-ray photoelectron spectroscopy system has been used to obtain initial information on the nature of the interface between novel multiferroic BiFeO<sub>3</sub> films and the Pt electrode layers. In addition, an integrated MOCVD film growth, x-ray scattering and fluorescence facility at the Advanced Photon Source (collaboration with ANL FWP 58926) has provided the first insights into domain wall structure and energetics in ferroelectric thin films. This system also led to the first demonstration of the existence of spontaneous polarization in epitaxial three unit cell thick PbTiO<sub>3</sub> (PTO)-films and to results showing that interface and surface environment control domain behavior in PTO films.

***Atomistic simulation of ferroelectric perovskites:*** The first interatomic potentials capturing ferroelectricity in perovskites, including the full phase diagram, were developed and used to study solid solutions and heterostructures. The influence of epitaxial strain on polar properties of thin films and superlattices was investigated with first-principles computational techniques, showing for the first time that strong coupling between polarization and strain is not a universal feature of all perovskite-oxide ferroelectrics.

***Studies of novel complex oxide phenomena at the micro and nanoscale:*** In collaboration with L. Ocola (CNM), we are investigating photovoltaic phenomena in transparent ITO/LaNiO<sub>3</sub>/Pb(Zr<sub>x</sub>,Ti<sub>1-x</sub>)O<sub>3</sub>/LaNiO<sub>3</sub>/ITO capacitors grown on glass. Our interest in these materials stems from the novel concept that high electric fields in the ferroelectric layer can provide a much more efficient separation of electron-hole pairs generated by UV radiation than in conventional semiconductor materials like Si. First measurements have confirmed this effect, and have shown up to three orders of magnitude higher current out of the device upon sunlight illumination, with respect to the current measured without illumination.

***Integration and patterning of oxide/carbon heterostructures:*** We have applied our knowledge of the growth mechanisms and interfacial characteristics of oxide thin films to the development of novel layered heterostructures comprised of two dissimilar materials such as piezoelectric Pb(Zr<sub>x</sub>,Ti<sub>1-x</sub>)O<sub>3</sub> (PZT) and ultrananocrystalline diamond (UNCD) integrated using a novel oxygen diffusion barrier layer (see cross-section TEM image in Figure 1), We demonstrated the 1<sup>st</sup> piezoactuated diamond-based micro/nano electromechanical structures using the hybrid PZT/UNCD heterostructure (Fig. 1 insert), opening new avenues for fundamental studies of mechanical properties of hybrid MEMS.

***In situ transport studies of tunnel junction structures at the nanoscale:*** We have developed a unique system for making nanoscale transport measurements on cross-section samples whilst simultaneously imaging the same region in-situ in the TEM. Using this integrated imaging/transport measurement approach we have been able to determine the structural and chemical origins of local changes to the transport properties in magnetic tunnel junctions (Fig. 2).

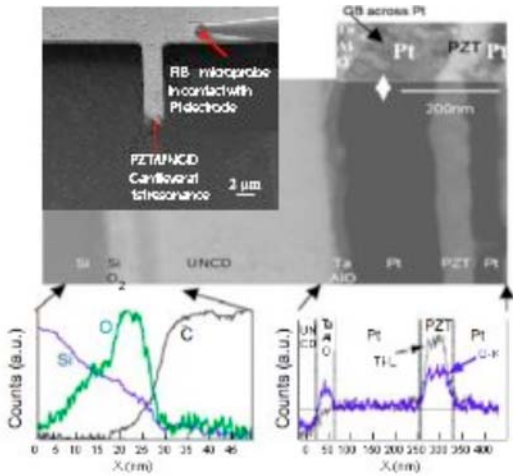


Figure 1. Cross-section TEM showing integrated PZT/UNCd layers enabled by a new TiAl or TiAlO<sub>x</sub> diffusion barrier layer; Insert: first demonstration of low power piezoelectrically actuated diamond MEMS resonator based on a hybrid PZT/UNCd cantilever.

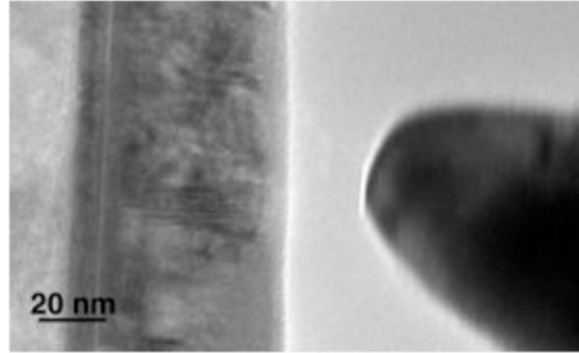


Figure 2. Cross-section TEM sample of a magnetic tunnel junction. Local I-V curves taken from the region immediately under the Au tip can be correlated with the local microstructure. The MgO tunnel barrier is the line of pale contrast between the two crystalline CoFe electrodes. The Au tip (diameter ~40 nm) can be moved in 3-D with nm accuracy to pinpoint specific regions for making transport measurements.

### Future directions

Our research efforts aimed at understanding growth dynamics and domain formation in ferroic complex oxide films continue. As an example, we intend to undertake a comprehensive study of polarization stability and dynamics under conditions where the environmental charge balance is disturbed, in order to gain quantitative insight into the timescales and processes by which a ferroelectric surface can interact with external species. Our experimental efforts will be coupled with theory/simulation aimed at creating atomistic models of ferroelectric surfaces and examining their polar properties with a particular emphasis on elucidating the nature of the depolarizing-field compensation mechanism in such systems.

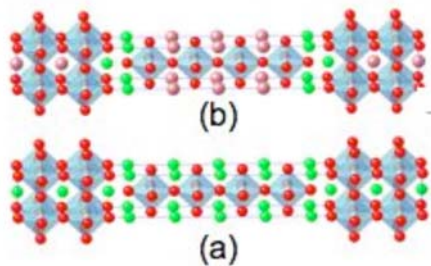


Figure 3. (a) A Sr<sub>5</sub>Ti<sub>4</sub>O<sub>13</sub> layered perovskite, which can be grown using molecular-beam epitaxy but does not possess any ferroelectric properties.

(b) An X<sub>3</sub>Sr<sub>2</sub>Ti<sub>4</sub>O<sub>13</sub> layered-perovskite superlattice based on Sr<sub>5</sub>Ti<sub>4</sub>O<sub>13</sub>, with X (atoms shown in pink) being, e.g., either Ba or Pb. Depending on the atomic species involved, the material could exhibit ferroelectric or antiferroelectric structural instabilities.

We also have a strong effort devoted to understanding the way in which interfacial effects control electronic phenomena in laterally confined nanostructures. We intend to examine a number of novel layered-perovskite-superlattice heterostructures (See Fig. 3.) based on homologous series (e.g. Ruddlesden-Popper series) for various “classical” perovskite ferroelectrics. The properties of such structures are strongly dependent on choice of superlattice components as well as the thickness of the perovskite-type layers. We will use first-principles-based computer modeling to identify systems with the most interesting

electroactive properties, which will then be synthesized and characterized experimentally. Our studies of dissimilar material heterostructures will continue, and we intend to incorporate materials such as Bi-based ferrite into these structures.

We are extending our studies of the nanoscale features that control transport phenomena in heterostructures, to include transparent ferroelectric/conductive oxide heterostructures and multiferroic tunnel junction structures comprising ferromagnetic and ferroelectric layers. We are doing this via a combination of local transport measurements at the nanometer scale, high spatial resolution structural and chemical analysis and band structure calculations. The ferroelectric effect in thin films is strongly dependent on layer thickness as well as on the specific electrostatic interactions at the ferroelectric layer/electrodes/substrate interfaces. A further layer of complexity is introduced when the ferroelectric structure is patterned laterally at the nanoscale. We plan to combine first-principles-based computer modeling and experimental characterization to investigate the polar properties of ultra-thin ferroelectric films grown on various substrates (to control the structure's stress state) and interfaced with various electrode materials (to control the electrostatics). The behavior of such confined nanostructures is currently poorly understood and we believe that we are in a strong position to make a major contribution in this area. We are utilizing our unique combination of experimental and theoretical tools to focus on oxide thin films that exhibit electrical resistance change triggered by collective electronic processes. For example: local measurements to determine the nature of transport such as the quantity and polarity of majority carriers when resistive switching takes place, and to pinpoint the exact location where the nanoscale conduction channel changes its nature by electric pulses. This will provide a global picture regarding the resistive switching mechanism and contribute to the device design and enhancement of its reliability.

The grand challenge in ferroic nanostructures is to develop an understanding of their domain behavior and we are actively pursuing this for thin films and nanopatterned structures. Figure 4 shows preliminary AFM and piezo force microscopy (PFM) images of a 36 nm thick BiFeO<sub>3</sub> film grown by rf magnetron sputtering on SrRuO<sub>3</sub>-coated (001) single crystal SrTiO<sub>3</sub> (SRO/STO). We were able to polarize domains in both positive and negative directions without affecting the topography. The next step will be to use the tip as the moving top electrode to characterize the size and shape dependence of the switching and piezoelectric properties of patterned nanostructures.

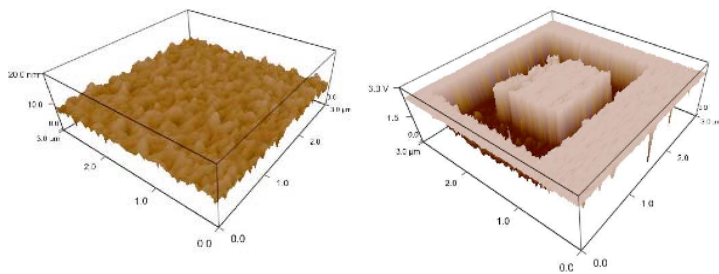


Figure 4. Topography (left) and PFM phase (right) image of the same BFO layer on SRO/STO showing artificially poled regions. The 1  $\mu\text{m} \times 1 \mu\text{m}$  center region was polarized with top-to-bottom orientation, whereas the 2  $\mu\text{m} \times 2 \mu\text{m}$  peripheral region was polarized in the bottom-to-top direction.

Imaging domain wall motion as a function of applied field, in a configuration in which we can also image the microstructure of the film, will allow us to measure domain wall velocities and to visualize effects such as pinning at defects. Our studies of the nanomagnetic behavior of arrays of patterned thin film oxide heterostructures is continuing and is being extended to artificial multiferroic heterostructures, including investigation of the effect of the ferroelectric field on magnetic phenomena and vice versa.

#### References to publications of DOE-sponsored research (2005–2007)

- “Vanadium-Al<sub>2</sub>O<sub>3</sub> nanostructured thin films prepared by pulsed laser deposition: optical switching”, S Nuñez-Sanchez, R Serna, M Jiménez de Castro, J Garcia López, A K Petford-Long and J F Morhange, *Appl. Surf. Sci.* **253**, 8136–8140 (2007).
- “High resolution structural characterization of giant magnetoresistive structures containing a nano-oxide layer”, C Y You, A Cerezo, P H Clifton, L Folks, M J Carey and A K Petford-Long, *Appl. Phys. Lett.* **91**, 011905 (2007).

- “Micromagnetic modelling of spin-wave dynamics in exchange-biased Permalloy disk”, O Heinonen, D K Schreiber and A K Petford-Long, *Phys. Rev. B* **76**, 144407 (2007).
- “In-situ structure and transport correlations in magnetic tunnel junctions”, A.N. Chiaramonti, D K Schreiber, B. Kabius, W.F. Egelhoff Jr. and A.K. Petford-Long, *Microsc. And Microanal.* **13** (Suppl. 2), CD626 (2007).
- “Comparison of the chemical heterogeneities and microstructure between CoFeB/MgO/CoFeB and CoFeB/Al-O/CoFeB magnetic tunnel junctions”, C.K. Sudbrack, A.N. Chiaramonti, J.M. Hiller, W.F. Egelhoff Jr and A.K. Petford-Long, *Microsc. And Microanal.* **13** (Suppl. 2), CD620 (2007).
- “Transmission electron microscopy of multilayer thin films”, A K Petford-Long and A N Chiaramonti, *Ann. Rev. Mater. Res.* (In Press, 2007).
- “Electric and magnetic phenomena studied by in-situ transmission electron microscopy”, J Cumings, E Olsson, A K Petford-Long and Y Zhu, *Mat. Res. Bull.* (in Press, 2007).
- “Science and technology of integrated ultrananocrystalline diamond/multifunctional materials for fabrication of high performance RF MEMS/NEMS devices” **(Invited)**, O. Auciello, S. Pacheco, A.V. Sumant, C. Gudeman, S. Sampath, A. Datta, R.W. Carpick, V.P. Adiga, P. Zurcher, Z. Ma, H.C. Yuan, J.A. Carlisle, B. Kabius, J. Hiller, S. Srinivasan, **IEEE Microwave Magazine**, (Dec 2007).
- “Preface: Science of Ferroelectric Thin Films and Application to Devices”, S. Baik, N. Setter, O. Auciello (Eds.), *J. Appl. Phys. Special Issue on Advances in the Science and Technology of Ferroelectric Thin Films and Devices*, vol. 100 (2006), 05101.
- “Science and Technology of Thin Films and Interfacial Layers in Ferroelectric and High-Dielectric Constant Heterostructures and Application to Devices” **(Invited)**, O. Auciello, - *J. Appl. Phys. Special Issue on Advances in the Science and Technology of Ferroelectric Thin Films and Devices*, 100 (2006) 051614.
- “Science and Technology of Piezoelectric/Diamond Hybrid Heterostructures for High Performance MEMS/NEMS Devices”, O. Auciello, A.V. Sumant, J. Hiller, B. Kabius, and S. Srinivasan, *MRS Proceedings* (in press, 2008).
- “Growth and Characterization of Transparent Pb(Zi,Ti)O<sub>3</sub> Capacitor on Glass Substrate”, K. K. Uprety, L. E. Ocola and O. Auciello, *J. Appl. Phys.* **102** (2007) 084107.
- “Piezoelectric/Ultrananocrystalline Diamond Heterostructures for High-Performance Multifunctional Micro/Nanoelectromechanical Systems”, S. Sudarsan, J. Hiller, B. Kabius, O. Auciello, *Appl. Phys. Lett.* **90** (2007) 134101.
- “Design and fabrication of a multi-layer micro/nanofluidic device with an electrically driven nanovalve”, H. Li, L. E. Ocola, O. Auciello, M. Firestone, Abstract 794, program number MN-MoA6, 54th AVS Symposium, Seattle, WA, October 2007.
- “Science and Technology of Piezoelectric/Diamond Heterostructures for Monolithically Integrated High Performance MEMS/NEMS/CMOS Devices”, O. Auciello, A.V. Sumant, J. Hiller, B. Kabius, Z Ma, M.B. Pisani, G. Piazza, G.E Wabiszewski, R.W. Carpick, and S. Srinivasan, *IEEE Journal* (in press).
- “Identification of Peptides for the Surface Functionalization of Perovskite Ferroelectrics”, B. D. Reiss, G.-R. Bai, O. Auciello, L. E. Ocola, and M. A. Firestone, *Appl. Phys. Lett.* **88** (2006) 083903
- “Local surface potential distribution in oriented ferroelectric thin films,” Y. Kim, S. Bühlmann, J. Kim, M. Park, K. No, Y. K. Kim, and S. Hong, *Appl. Phys. Lett.* **91**, 052906 (3 pages) (2007)
- “Screen charge transfer by grounded tip on ferroelectric surfaces,” Y. Kim, J. Kim, S. Bühlmann, S. Hong, Y. K. Kim, S.-H. Kim and K. No, *Phys. Stat. Sol. (RRL)* **2**(2), 74–76 (2008)
- “Atomic scale design of nanostructures”, J. Bernholc, W. Lu, S. M. Nakhmanson, P. H. Hahn, V. Meunier, M. Buongiorno Nardelli, W. G. Schmidt, *Mol. Phys.* **105**, 147 (2007).
- “Suppressed Dependence of Polarization on Epitaxial Strain in Highly Polar Ferroelectrics”, H. N. Lee, S. M. Nakhmanson, M. F. Chisholm, H. M. Christen, K. M. Rabe, and D. Vanderbilt, *Phys. Rev. Lett.* **98**, 217602 (2007).
- “Raman study of oxygen reduced and re-oxidized strontium titanate”, D. A. Tenne, I. E. Gonenli, A. Soukiassian, D. G. Schlom, S. M. Nakhmanson, K. M. Rabe, X. X. Xi, *Phys. Rev. B* **76**, 024303 (2007).

## Electronic Processes in Solid State Organic Electronic Materials

Darryl L. Smith  
T-11, MS B262  
Los Alamos National Laboratory  
Los Alamos, NM 87545  
dsmith@lanl.gov

### Program Scope:

Organic electronic materials are of great intrinsic scientific interest because strong competing interactions produce a rich spectrum of tunable ground and excited states that make them an ideal vehicle for the study of flexible strongly correlated material systems. These materials are also technologically important for a broad class of applications because of the tunability of their electronic properties, facile thin film and heterostructure fabrication, and the possibility of creating nanoscale structures and devices through molecular assembly techniques. Because of the very large material and device structure phase space, there is a critical need for basic scientific research on the fundamental physical properties of organic electronic materials. The goal of this project is to provide an understanding of the fundamental physical processes that are important in determining the electrical and optical properties of organic electronic materials. We are focusing on representative materials, including both conjugated polymers and small molecules, which serve as model systems to understand these fundamental physical processes. We are using a closely coupled theory/fabrication/measurement approach. The project consists of four basic classes of tasks: 1) electronic structure of condensed phases of organic electronic materials and its effect on electrical and optical properties; 2) spin dependent optical properties of organic semiconductors containing metal atoms and the use of magnetic fields to probe these properties; 3) spin dependent electrical transport and spin injection from ferromagnetic metals into organic semiconductors; and 4) modeling of novel electrical and opto-electronic devices based on these organic semiconductors.

### Recent Progress:

*Organic Semiconductor Electronic Structure Calculations:* We established a new

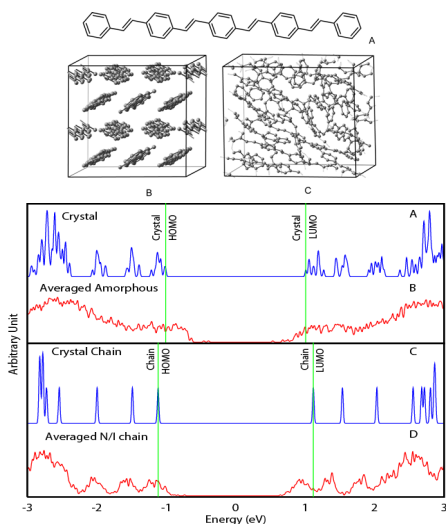


Fig. 1) Top: molecular structure of a five ring oligomer of PPV. Middle: left; crystal structure and right; disordered structure of PPV oligomers. Bottom: calculated density of states for: A), crystal; B), disordered cluster; C), isolated ordered oligomer; and D) ensemble of isolated disordered oligomers. From Ref. 1)

theoretical tool for studying disordered organic semiconductors based on a combination of classical molecular dynamics, to determine probable molecular geometries, and first-principle density functional theory (DFT) calculations, to determine the electronic structure for that geometry. Our initial studies focused on the role

of intra-molecular conformational disorder and inter-molecular electronic interactions on the electronic structure of disordered clusters of PPV [1] oligomers. We found that in PPV electron trap states are induced primarily by intra molecular configuration disorder, while the hole trap states are generated primarily from inter molecular electronic interactions. The PPV calculations considered clusters of five-ring PPV oligomers, in order to isolate the effect of configurational disorder. The unit cell used for the MD simulations and DFT calculations consisted of 12 five-ring oligomers, a total of 816 atoms. Figure 1) shows an example of the PPV calculations that were recently published in Physical Review.

*Magnetic Field Effects on the Optical Properties of Metal-Organic Compounds:* We studied the optical properties of metal-organic compounds in strong magnetic fields to understand their spin dependent electronic structure [2]. We measured photoluminescence (PL) of dilute concentrations of Pt porphyrin (PtP) and a substituted Pt porphyrin (PtOEP) in strongly and weakly interacting hosts as a function of magnetic field and temperature. The origin of the strong temperature and magnetic field dependence that we observed in the PL spectrum was found to result from a combination of the spin-orbit interaction and the Jahn-Teller (JT) effect. The calculated excited state potential surface for PtP has four equivalent energy minima for distortions that are linear combinations of  $b_{1g}$  and  $b_{2g}$  vibrational modes. In the lower symmetry PtOEP the energy minima are distorted from the symmetric positions in PtP. Traversal about the energy surface is accompanied by a Berry phase that introduces a new selection rule for the optical transitions. Because of the symmetry differences, there are qualitatively behaviors in PtP and PtOEP. These results show that the spin-orbit interaction can determine optical selection rules in these metal-organic compounds and show much promise for establishing optical spin generation/detection approaches in organic semiconductors.

*Device Considerations for Spin Based Organic Devices:* Electron spin based devices often use a ferromagnetic (FM) metal as an electrode since they are capable of spin polarized electrical injection and detection. Recently there has been major progress in understanding electron spin transport at ferromagnetic metal/inorganic semiconductor interfaces. There is strong synergy between research into the spin dependent properties of organic and inorganic semiconductors and we are exploring these two areas in parallel. We completed a first principles electronic structure calculation of spin dependent tunneling in inorganic systems that explained a major experimental mystery [3] involving a sign change of the spin polarization of the tunneling current at Fe/GaAs contacts. We have also completed a theoretical study of the effect of the voltage bias dependence of tunnel barrier shape at a Schottky contact on spin injection properties of ferromagnetic metal/inorganic semiconductor interfaces [4]. We experimentally investigated ferromagnetic metal/polymer Schottky energy barriers and hole injection from these contacts [5]. These results will form the basis of future spin injection studies at ferromagnetic metal/organic semiconductor contacts. We studied device structures, both theoretically and experimentally, fabricated from organic semiconductors [6,7,8] comparing charge and spin transport properties.

*Device Model of Light Emitting Field Effect Transistors:* Recent experiments at UC Santa Barbara and Cambridge demonstrated ambipolar channel conduction and light emission in conjugated polymer field effect transistors (FETs). Electrons are injected from a low work-function metal contact and holes from a high work-function contact. The injected

charge carriers propagate along the FET channel and recombine in regions where both types of carriers are present. We established a device model for these ambipolar organic field effect transistors based on the gradual channel approximation [9,10,11]. The model includes the effect of charge carrier trapping at the gate insulator/organic semiconductor interface through density dependent mobilities. In collaboration with the experimental group at Cambridge, we made detailed comparisons between the predictions of the device model and experimental observations [12].

### **Future Plans:**

We will extend our studies of the effects of disorder on organic semiconductor electronic structure to the following: 1) *Oligomer length*. In amorphous systems the oligomers do not remain planar. Effective conjugation lengths governed by kinks and twists in the oligomer associated with intra-molecular disorder may override the tendency to close the energy gap with increasing length. These issues are important to understand in order to develop realistic hopping models of charge mobility. 2) *Intra-molecular conformational constraints*. A combination of intra-molecular torsional motion in the vinylene unit, coupled with bond length alternation, is a dominant mechanism for introducing trap states and electron-hole asymmetry in PPV. We will study PFO and other organic semiconductors with specific bonding patterns chosen to enhance or constrain important internal motions and contrast the results with those for PPV. 3) *Influence of side chains on inter-molecular interactions*. Many organic semiconductor devices rely on derivative materials in which a side chain is introduced to improve solubility. These side chains typically involve saturated hydrocarbon units and are therefore not expected to directly introduce electronic states near the energy gap, but they can affect the electronic structure indirectly through steric interactions. We will study these steric effects as a function of the length of the side chain using models based on PPV.

Organic semiconductors are of interest for the active layer in spintronic devices because they are composed of light elements with weak spin-orbit interactions and thus have long spin lifetimes. Recently there has been dramatic progress in exploiting spin-based phenomena in inorganic semiconductors. Due to the spin-orbit interaction inherent in these materials, right- and left-circularly polarized light couples differently to spin-up or spin-down electrons. As a result, spin-polarized electrons can be generated and detected using circularly polarized optical probes. In organic materials the corresponding optical selection rules do not apply. It is, however, possible to introduce heavy elements into organic semiconductors and thereby locally introduce a spin-orbit interaction using metal-organic (MO) compounds. The ability to spatially pattern the strength of spin-orbit coupling in a structure is unique to organic semiconductors. The wide range of organic semiconductors and MO compounds available permits us to combine them in ways to allow either optical spin injection, by absorbing on a MO molecule and transferring spin polarized carriers to an organic semiconductor, or optical spin detection by transferring spin polarized carriers from an organic semiconductor to a MO molecule. We will use a combined experimental and theoretical approach, building upon our work with PtP and PtOEP, to find and understand metal-organic molecules suitable for injection and detection of spin polarized electrons in organic semiconductors.

Electrical spin injection from ferromagnetic contacts has been demonstrated in inorganic semiconductors. We have developed a model for electrical spin injection in

organic semiconductors. The essential feature of this theory is that electrical spin injection from a magnetic contact into a nonmagnetic semiconductor requires that the two are not in quasi-equilibrium. This can be accomplished by introducing Schottky barriers or tunnel barriers. Schottky barrier formation on conjugated organic semiconductors differs from that on inorganic semiconductors inasmuch as contacts made to organic semiconductors often follow near-ideal Schottky behavior, thus permitting the energy barrier to electrical injection to be varied over a wide range by using metals with different work functions. In addition, insulating tunnel barriers to organic semiconductors based on organic molecules can be conveniently fabricated using self-assembly techniques. Our measurements of the effective work functions of a variety of FM metals on organics show that suitably processed FM metals can have appropriate Schottky barriers for spin polarized hole injection into most organic semiconductors.

### **Publications:**

- 1) P. Yang, E. R. Batista, S. Tretiak, A. Saxena, R. L. Martin and D. L. Smith, "Effect of Intra-molecular Disorder and Inter-molecular Electronic Interactions on the Electronic Structure of Poly-*p*-Phenylene Vinylene (PPV)", *Phys. Rev. B* **76**, 241201R (2007).
- 2) C. V. Diaconu, R. L. Martin, E. R. Batista, D. L. Smith, B. K. Crone, I. H. Campbell, and S. A. Crooker, "Coupling of Geometric Phase and Spin-Orbit Effects in the Excited States of Platinum II Porphine", *J. Chem. Phys.* (submitted).
- 3) A. N. Chantis, K. D. Belashchenko, D. L. Smith, E. Y. Tsymbal, M. van Schilfgaarde and R. C. Albers, "Reversal of Spin Polarization in Fe/GaAs (001) Driven by Resonant Surface States: First-principles Calculations", *Phys. Rev. Lett.* **99**, 196603 (2007).
- 4) D. L. Smith and P. P. Ruden "Spin-polarized Tunneling Through Potential Barriers in Ferromagnetic Metal/Semiconductor Schottky Contacts", *Phys. Rev.* (submitted).
- 5) I. H. Campbell and B. K. Crone, "Energy Barriers from Ferromagnetic Contacts to Semiconducting Polymers", *Appl. Phys. Lett.* **90**, 242107 (2007).
- 6) M. Yunus, P. P. Ruden, and D. L. Smith, "Spin Injection Effects on Exciton Formations in Conjugated Organic Semiconductors", *J. Appl. Phys.* (submitted).
- 7) A. C. Niemayer, I. H. Campbell, F. So and B. K. Crone, "High Quantum Efficiency Polymer Photoconductors Using Interdigitated Electrodes", *Appl. Phys. Lett.* **91**, 103504 (2007).
- 8) I. H. Campbell and B. K. Crone, "Bulk Photoconductive Gain in Poly(Phenylene Vinylene) Based Diodes", *J. Appl. Phys.* **101**, 024502 (2007).
- 9) D. L. Smith and P. P. Ruden, "Analytic Device Model for Light-Emitting Ambipolar Organic Semiconductor Field-Effect Transistors", *Appl. Phys. Lett.* **89**, 233519 (2006).
- 10) D. L. Smith and P. P. Ruden, "Device Modeling of Light-Emitting Ambipolar Organic Semiconductor Field-Effect Transistors", *J. Appl. Phys.* **101**, 084503 (2007).
- 11) P. P. Ruden and D. L. Smith, "Device Model for Light-Emitting Field-Effect Transistors with Organic Semiconductor Channel", *Materials, Processes, and Applications*, edited by A.C. Arias, J.D. MacKenzie, A. Salleo, N. Tessler (Mater. Res. Soc. Symp. Proc. Volume 1003E, Warrendale, PA, 2007), 1003-O04-08.
- 12) J. Zaumseil, C. R. McNeill, M. Bird, D. L. Smith, P. P. Ruden, M. Roberts, M. J. McKiernan, R. H. Friend and H. Sirringhaus, "Quantum Efficiency of Ambipolar Light-Emitting Polymer Field-Effect Transistors" *J. Appl. Phys.* (accepted).

## Atomic Scale Surface Phenomena

### Subtask: Localized Corrosion

K.R. Zavadil, N.A. Missert, P.J. Feibelman, P.G. Kotula, and N. Vasiljevic  
Sandia National Laboratories, PO Box 5800, Albuquerque, NM 87185-0888  
[krzavad@sandia.gov](mailto:krzavad@sandia.gov)

#### Program Scope:

This subtask research effort seeks to provide a detailed understanding of corrosion mechanisms in passive metals and alloys through the investigation of passivity breakdown and pit initiation in tailored oxides and at nanoengineered defects. The ability to correlate nanostructure evolution and pit initiation in passive metals is essential for the development of predictive aging models for materials and device reliability science and engineering. Aluminum and its alloys are of particular focus because of their widespread use throughout the DOE complex ranging from microelectronic interconnects to transportation applications. The objective of this research is to gain new insight into the initiation stage of localized corrosion. Our approach is to precisely create and control defects and nanoscale structures, such as model passive oxides, so as to isolate, identify, and elucidate their role in corrosion initiation.

#### Recent Progress:

Recent work has focused on establishing causal links between discovered nanoscale phenomena and pit initiation. We have documented the formation of interfacial voids at the aluminum:passive oxide interface (1). These structures could represent early precursors to eventual pit nucleation events given the fact that these voids grow to eventually form nanoscopic pores (2). Our work in this specific area of this subtask is to map accessible regions of a pitting reaction coordinate that describes the nanoscopic evolution of the passive oxide toward a progressively less stable barrier layer as the native environment becomes more electrochemically aggressive. Figure 1 provides a general view of structures that we believe contribute to this overall trend toward

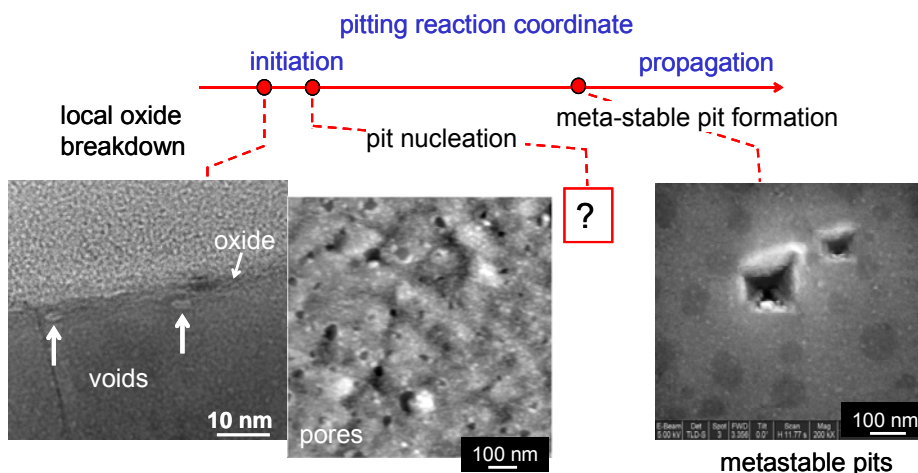


Figure 1. Generalized scheme for a pitting reaction coordinate instability. The specific work described in this abstract highlights our attempt to clarify causal relationships and mechanisms and provide relevant input to computational efforts in reliability assessments and life extension efforts.

*Electrolyte and Ion Effects on the Formation of Nanoscale Structure in Aluminum's Passive Oxide Prior to Pit Initiation*

The impact of pH, chloride concentration, and the presence of an alternate, adsorbing anion on interfacial void formation in the passive oxide of aluminum have been explored (3). Constant current, anodic polarization of a model passive oxide on Al(111) oriented thin films exhibits a characteristic signature involving a local maxima in the potential as a function of time (Fig. 2a). We have shown that this maxima corresponds to a threshold for interfacial void formation and the corresponding charge density is a measure of the efficiency for void nucleation and growth. Efficiency is found

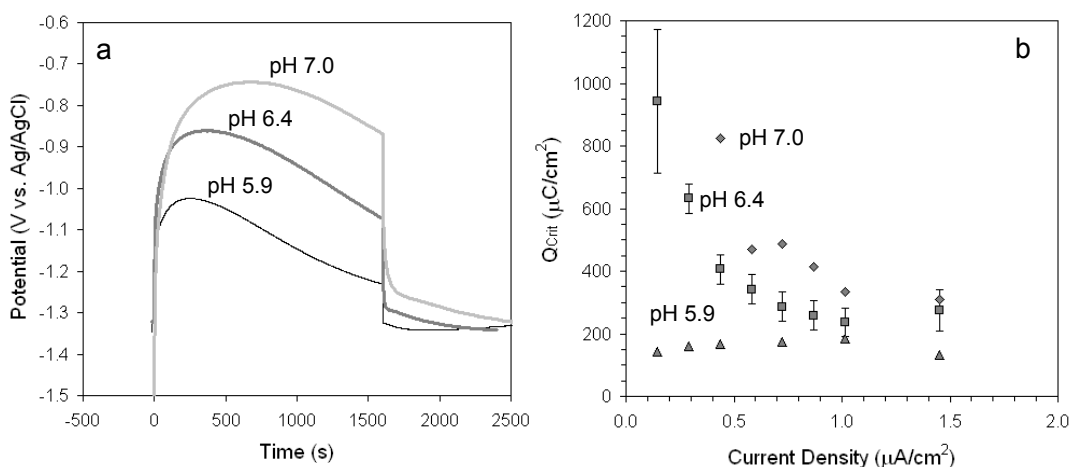
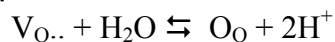


Figure 2. a) Variation in the chronopotentiometric response for a  $0.7 \mu\text{A}\cdot\text{cm}^{-2}$  anodic step in 50 mM NaCl as a function of pH. b) Dependence of the charge density required to produce a potential maximum as a function of pH and applied anodic current density ( $\blacktriangle$  pH 5.9,  $\blacksquare$  pH 6.4,  $\blacklozenge$  pH 7.0).

to be sensitive to primarily pH (Fig. 2b) and the presence of alternate anions. The pH sensitivity can be understood in terms of the competition between a vacancy pairing reaction that forms voids and a vacancy filling reaction that leads to oxide growth. Proton concentration enters into the vacancy pairing reaction through the generation of excess oxygen vacancies, according to:



where  $\text{O}_{\text{O}}$  represents an O anion on the conceptual oxygen sub-lattice of the passive oxide. This excess concentration leads to vacancy saturation within the inner anhydrous barrier oxide layer (primarily responsible for passivity), followed by void formation from the pairing reaction with cation vacancies. Equally interesting is the fact that chloride concentration variation at low to moderate levels exhibits minimal impact on void formation, arguing for a concerted proton-chloride interaction where a critical chloride concentration (estimated to be  $3 \times 10^{19} \text{ cm}^{-3}$  based on competitive borate anion adsorption measurements) is sufficient to drive void formation.

### *Inducing and Imaging Localized Passivity Breakdown in Aluminum Using an AFM Approach*

The physical and chemical scales of and spatial relationships for pit nucleation and latter stage metastable pitting events are of particular interest in establishing structure – activity correlations. Where these events can be detected through electrochemical means, a description of scale and location is generally not possible because no *a priori* knowledge exists for where to look for such an event. We have combined electrochemical atomic force microscopy and the concept of electrochemical machining to determine whether local polarization can be used as probe for local sensitivity to pit initiation (4). Localized polarization is produced using fast potential pulses between a conductive nanoelectrode (i.e. an AFM tip) and the surface at time scales required for interfacial charging. Our initial attempts are not particularly fast (millisecond), but do show promise in constraining the location of pitting to the proximity of the AFM tip (see Fig. 3). Additionally, this approach has proven to provide high resolution imaging of

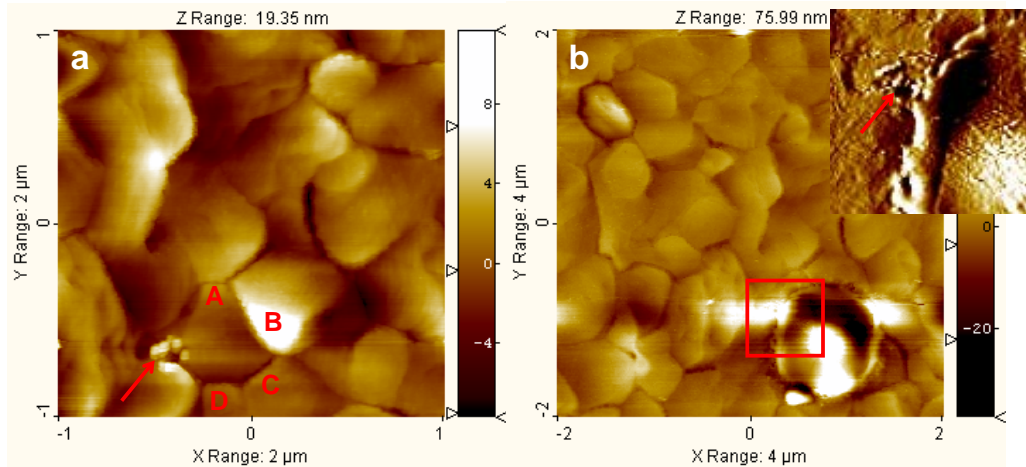


Figure 3. a) *in situ* AM-AFM image of an Al:0.5 wt% Cu film surface prior to localized polarization in 50 mM NaCl – arrow designates site of possible hard tapping by tip, and b) *in situ* image after applying a 0 mV, 1 ms pulse at a tip-film distance of 400 nm - highlighted square corresponds to the region of letter designated grains in panel a. The inset shows site detail.

transformational changes in the passive oxide not previously reported for aluminum. These directly imaged changes include the transition of oxide platelets on the surface to oxide nodules as well as the formation nanopores. High fidelity imaging and localized polarization can be combined with a variety of other preconditioning techniques, including void nucleation and growth, to directly image the sensitivity of a known nanostructure population to a local stimulant for passivity breakdown. Causal relationships between nanostructure and passivity loss could be established using this stimulus – response mapping approach.

#### Future Plans:

Our plans include the further development of the fast pulse AFM experiment to operate in a more realistic time frame for interfacial charging (10 to 100 nanosecond). Experiments will be extended to include both large grained Al, Al-xCu and other solid

solution systems where the added constitute is believed to facilitate transition from pit nucleation to propagation. We will incorporate analytical TEM measurements to understand the role that solute additives play in local oxide stability. Specifically, we are interested in the probability that segregated solute may serve as void nucleation sites within the passive oxide.

We seek to better understand the role that metal:oxide interfacial structure plays in passivity. First principles calculations are employed to discover structural motifs that correspond to weak oxide – metal bonding. Experimental exploration of such structures is planned through the use of single crystal substrates, vacuum processing techniques, and vacuum AFM to create interfaces of known step density. Electrochemical measurements followed by analytical electron microscopy will be used to determine relationships between the initial interfacial structure, the extent to which nanostructure evolves, and the overall activity. Control of pH is a particularly potent tool in these studies as computationally-derived models that predict weak Al – O bonding argue for defect sites that may exhibit strong affinity for H. Recall that these model anhydrous oxides show a strong sensitivity toward pH, possibly indicating a chemical path for probing the role of atomic scale defects.

Our direct imaging will be complimented by conducting microcapillary-based statistical studies. Preliminary work has shown that pit nucleation event frequencies could be related to electrochemical preconditioning (5). The possibility exists for statistically linking the characteristics of programmed void populations with pit nucleation frequency. We have developed a microcapillary capability based on 20  $\mu\text{m}$  diameter electrochemical cells. Event transients in the 100 femtoamp range (pit radii of  $< 7$  nm) can be detected by operating in this cell size regime. Plans exist for the acquisition of a 300 attoamp noise limit potentiostat to improve sensitivity. We have established a collaboration with D. Krouse (Industrial Research Ltd, NZ) and J. Soltis (Quest Reliability, NZ) to conduct automated data analysis for large data sets.

#### References:

1. K.R. Zavadil, J.A. Ohlhausen, and P.G. Kotula, “Nanoscale Void Nucleation and Growth in the Passive Oxide on Aluminum as a Pre-pitting Process,” *J. Electrochem. Soc.* **153**(8), B296-303 (2006).
2. K.R. Zavadil, P.G. Kotula, and J.A. Ohlhausen, “Interfacial Structure and Composition as Controlling Factors in Void Formation at the Passive Oxide – Aluminum Interface,” *ECS Trans.* **1**(4), 139 (2006).
3. K.R. Zavadil, “Inducing and Imaging Localized Passivity Breakdown in Aluminum using an AFM Approach,” accepted *ECS Trans.* (2008).
4. K.R. Zavadil, P.G. Kotula, and J.A. Ohlhausen, “Electrolyte and Ion Effects on the Formation of Nanosacle Structure in Aluminum’s Passive Oxide Prior to Pit Initiation,” accepted *ECS Trans.* (2008).
5. K.R. Zavadil P.G. Kotula, J. Soltis, and D. Krouse, “Programming Void Populations in the Passive Oxide of Aluminum in an Attempt to Correlate Evolving Nanostructure with Passivity Loss,” *ECS Trans.* **3**(31), 207 (2007).

## **Session IV: Hydrogen / Fuel Cells**

## The State of Water in Proton Conducting Membranes

Harry R. Allcock<sup>1</sup>, Digby D. Macdonald,<sup>2</sup> Alan J. Benesi,<sup>1</sup> David Lee<sup>1</sup>

<sup>1</sup>Department of Chemistry

<sup>2</sup>Center for Electrochemical Science and Technology

Department of Materials Science and Engineering

The Pennsylvania State University

University Park, PA 16802

hra@chem.psu.edu

### ABSTRACT

#### SCOPE AND OBJECTIVES

This research is to define more exactly the state of water in proton conducting membranes. The objective is to establish the relationship between the state of water and proton conductivity, and to understand more completely the mechanism of proton conduction. Once the role of water in proton conduction has been elucidated, we will develop methods and protocols for controlling the membrane structures at the molecular level to optimize their properties for use in advanced Proton Exchange Membrane Fuel Cells (PEMFCs). In particular, we seek to extend the maximum operating temperature of PEMF's to values well above 100°C in non-pressurized systems. Higher operating temperatures give rise to higher conductivities and hence to reduced IR potential drop across the membrane, thereby enhancing the power density of the cell. Higher temperatures also lead to faster reaction rates, which implies lower catalyst loading, particularly at the air electrode, and significantly reduced catalyst poisoning by carbon monoxide at the anode. A closely related goal is to develop membrane and electrode systems that will enhance low humidity operation. This can be accomplished by utilizing knowledge of the state of water and the mechanism of proton conduction to design membranes with chemical and structural features that mimic the behavior of water. Our work will employ Nafion® and polyphosphazene membranes; the former to ensure continuity with our previous work on this subject, and the latter because, in our opinion, they offer the greatest possibilities of achieving our goals. A wide range of skills are being focused on this challenge including membrane design and synthesis, NMR techniques, dielectric relaxation studies, and electrochemistry (including electrochemical impedance spectroscopy).

The work involves four tightly coupled tasks as follows: **Task 1.** Membrane Design and Synthesis (Department of Chemistry); **Task 2.** NMR Relaxation Studies (Department of Chemistry); **Task 3.** Dielectric Relaxation Studies (Department of Materials Science and Engineering); and **Task 4.** Electrochemical Evaluation (Department of Materials Science and Engineering). The proposed work combines novel membrane synthesis and characterization with systematic formulation to deliberately reveal the effects of several synthesis variables on membrane function. These variables include the impact of hydrophobic and hydrophilic moieties, ion exchange capacity, and membrane morphology on the state of the water in the membrane, the membrane conductivity, the performance at high temperature, and the operation at low humidity.

The working hypothesis of this study is that proton conduction occurs via the Grotthus chain mechanism, in which a proton is passed between adjacent water molecules through a cooperative rotation/proton transfer process. Water availability for this cooperative rotation/proton transfer process in existing membranes is probably limited by water evaporation. We are addressing this situation through altering the density of the acid groups, and placing them in strategic proximity to each other, thus producing membranes that experience the cooperative rotation/proton transfer process without encountering the performance reduction caused by evaporation. Thus, this study is designed to ascertain the impact of the membrane composition and structure on the membrane function for high temperature PEMFCs. Each group of membranes we synthesize will be characterized in a similar manner. The purity of the starting materials and synthesized polymers will be assessed. The total water uptake, heat of hydration and glass transition temperatures will be determined. Translational diffusion coefficients and angular reorientation will be characterized by NMR. The effect of hydrophobic and hydrophilic domain size on the state of water and conductivity will be studied by using scanning electron microscopy (SEM) and transmission electron microscopy (TEM) techniques to probe the morphology of both dry and hydrated membranes. The information is being collected and correlated with conductivity data. The baseline temperature for all experiments will be 80°C. As the most promising direction for membrane synthesis is revealed, the experiments will include incremental increases in operating temperature.

## RECENT PROGRESS

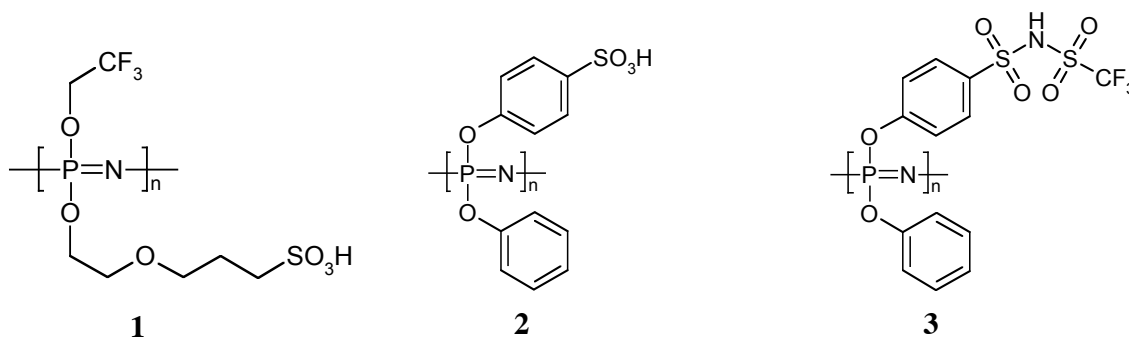
The initial experimental work has been focused on two aspects. These are 1) an examination of the NMR spectra of water in commercial Nafion 117 membranes, and 2) synthesis of new polymers that are analogues of Nafion, but are based on an inorganic backbone rather than the carbon backbone of conventional macromolecules.

**NMR Spectra of Water in Nafion.** Nafion is a proton conductor because it contains sulfonic acid functional groups, which supply protons, and because the polymer is swollen by water, which provides a vehicle for proton transmission across the membrane. The characteristics of Nafion are enhanced by the presence of hydrophobic fluorocarbon domains which provide physical and chemical stability and promote the segregation of the structure into hydrophobic and hydrophilic domains. It is believed that two types of water exist in Nafion-type membranes - structured water that resembles water in ice, and non-structured water that may be the principal vehicle for proton transmission. Solid-state deuterium NMR spectroscopy has been used to investigate this possibility.

At the start of this phase of the investigation a major hurdle was encountered. This was the fact that commercial Nafion is contaminated by transition metal species, such as iron, that broaden the NMR line width, shortening the  $T_1$  relaxation. The use of ESR spectroscopy proved to be an inadequate measure of transition metal content, and elemental analysis was employed to estimate iron content. Literature methods to purify Nafion proved to be only partly effective to remove these contaminants, and alternative methods were devised. The main modification involved treatment with ethanol and water followed by the use of nitric acid in place of hydrochloric acid. After this purification, experiments were conducted to establish the

level of iron contamination below which the NMR results would not be compromised. This level appears to be below 1100 ppm. After purification, our membranes showed only 11 ppm of iron. Experiments were then initiated to monitor the change of proton conductivity as a function of water content of the membrane and to correlate these results with the state of the water. Nafion was hydrated in a humidification chamber of which the humidity was controlled by a saturated salt solution. Dry Nafion was suspended above the saturated salt solution in a sealed chamber for 5 days to attain equilibrium. The NMR results confirm that two types of water are present in Nafion, and we attribute this to the presence of both structured water molecules and bulk water molecules.

**Synthesis of New Proton-Conductive Polymers.** A polyphosphazene with the structure shown in **1** has been synthesized in a first attempt to obtain an analogue of Nafion, but with a more regular distribution of sulfonic acid and hydrophobic units. The alkyl ether sulfonic acid units are hydrophilic, while the trifluoroethoxy groups are highly hydrophobic and are the counterparts of the fluorocarbon component of Nafion. The synthesis protocol involved the polymerization of the cyclic monomer, hexachlorocyclotriphosphazene, to poly(dichlorophosphazene), followed by sequential replacement of the chlorine atoms in this polymer by trifluoroethoxy and the vinyl ethyleneoxy units. The vinyl groups were then employed as reaction sites for conversion to sulfonic acid sites by treatment with sodium sulfite. Two other polymers have been synthesized, with the structures shown in **2** and **3**. Here, the phenoxy groups in **2** and **3** are hydrophobic components, and the aryloxy sulfonic acid or moieties are both hydrophilic units and proton sources. The functional sites in **3** are both proton sources and amphiphilic units. These three polymers are currently being analyzed by solid-state NMR methods and impedance spectroscopy.



## FUTURE PLANS

NMR  $T_1$  relaxation experiments will continue with Nafion with the objective of further defining the state of water in this material. More data at different hydration levels are still required with use of the 300 MHz spectrometer. These data will be compared with the  $T_1$  relaxations obtained from a 500 MHz spectrometer. We expect that  $T_1$  relaxations will be lengthened by 5 – 10 milliseconds, which would indicate the presence of solid state water.

The phosphazene polymers will then be subjected to the same NMR analysis as Nafion, and all the polymers in this project will be analyzed by impedance spectroscopy, and dielectric spectroscopy. Ultimately it is anticipated that the results will point to a preferred polyphosphazene structure that provides the means for maximizing the solid state water content of a membrane and allowing proton conduction at elevated temperatures.

# High Performance Nano-Crystalline Oxide Fuel Cell Materials: Defects, Structures, Interfaces, Transport, and Electrochemistry

*S.A. Barnett, D. Ellis, L.D. Marks, T.O. Mason, K. Poepfelmeier, P.W. Voorhees*

Northwestern University

2220 Campus Drive

Evanston, IL 60208

Phone: 847 491 2447; FAX: 847 491 7820

s-barnett@northwestern.edu

DOE Program Officer: Refik Kortan

301/903-3308; refik.kortan@science.doe.gov

## Program Scope

Solid oxide fuel cells (SOFCs) are an important technology for efficient utilization of hydrogen, and the closely related technologies steam electrolysis<sup>1,2</sup> and ceramic membranes<sup>3</sup> are important for efficient production of hydrogen. Important fundamental challenges remain in SOFCs, including reducing operating temperature and improving the stability and fuel flexibility of the anode. Operating temperature is important not only for making the technology viable – reducing the cost of high-temperature components, improving the stability of metallic interconnects, and easing high-temperature seal issues – but for enabling new SOFC applications such as transportation and portable generation. Anode alternatives to metallic Ni are needed to improve stability during redox cycling and during electrolysis at high steam contents, and for enabling highly efficient hydrogen production from natural gas.<sup>4,6</sup>

The main aim of this project is to investigate nano-scale materials with applications for fuel-flexible low-temperature solid oxide fuel cells (SOFCs), integrating fundamental studies done from the atomic scale (point defects) to extended defects (interfaces, grain boundaries, and surfaces) to the morphological scale (typically 50 – 1000 nm in SOFC electrodes). New approaches are being employed to characterize and understand transport and oxygen exchange properties of nano-scale materials needed to make fuel cell membrane/electrolytes that can operate effectively over a wide range of conditions. New fabrication methods have been developed to produce nano-scale materials. Given the obvious questions regarding the stability of nano-materials, even at reduced SOFC operating temperatures, nano-material stability is being studied both experimentally and via modeling. Overall, this work aims to provide a scientific basis for engineering high efficiency nano-composite materials for SOFC applications.

## Recent Progress

Highlights from the three strongly inter-related research thrusts are briefly described in the following paragraphs.

### Transport properties of nano-scale ionic conductors

A “nano-Grain Composite Model” was developed and used for analyzing the complex impedance behavior of nanocrystalline SOFC electrolyte materials. AC-impedance spectroscopy data for nanocrystalline 8 mol% YSZ was analyzed using the model to separate the grain-boundary and grain-core components. The electrical conductivity results for two grain sizes—10 nm and 41 nm—are shown in Fig. 1

alongside data for microcrystalline YSZ of comparable composition. The grain core conductivities of nano-YSZ are only slightly decreased from that of microcrystalline YSZ. In contrast, the grain boundary conductivities are significantly higher (by 5-10 times) than for microcrystalline YSZ. Thus, the slightly enhanced ionic conductivity in grain boundaries is mitigated by increased grain boundary density and also by reduced grain core conductivities in nano-ionic conductors, such that there are no large enhancements overall. On the other hand, large enhancements are present in mixed conducting materials.

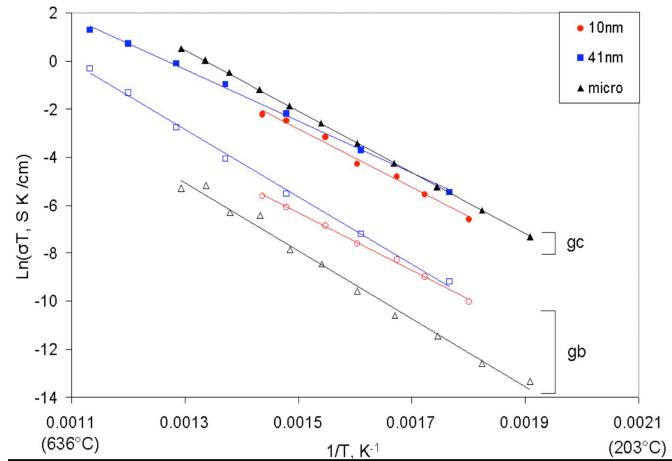


Figure 1. Local grain core (gc) and grain boundary (gb) conductivities for microcrystalline (“micro”) vs. nanocrystalline YSZ. Microcrystalline data are taken from Ref. 7.

#### Nano-electrode processes and stability

Two-phase anode nano-structures have been produced by a new method where nano-clusters precipitate onto the surfaces of a supersaturated oxide phase. Figure 2 illustrates Ru nano-clusters < 5 nm in diameter on (La,Sr)(Cr,Ru)O<sub>3</sub> surfaces, produced using this method. The nano-clusters form during anode operation, avoiding the coarsening that would normally occur during ceramic processing. Figure 2 also shows the substantial polarization resistance reduction that occurs when the nano-clusters appear. Interestingly, the Ru clusters do to coarsen substantially over 1000 h at 800°C.

The group has also employed infiltration methods to study nano-cathode materials. (La,Sr)(Co,Fe)O<sub>3</sub> mixed conductor has been infiltrated into Gd-doped Ceria porous structures. The ability to separately control the morphology of the two phases, via their separate processing/firing conditions, allows relatively low polarization resistances

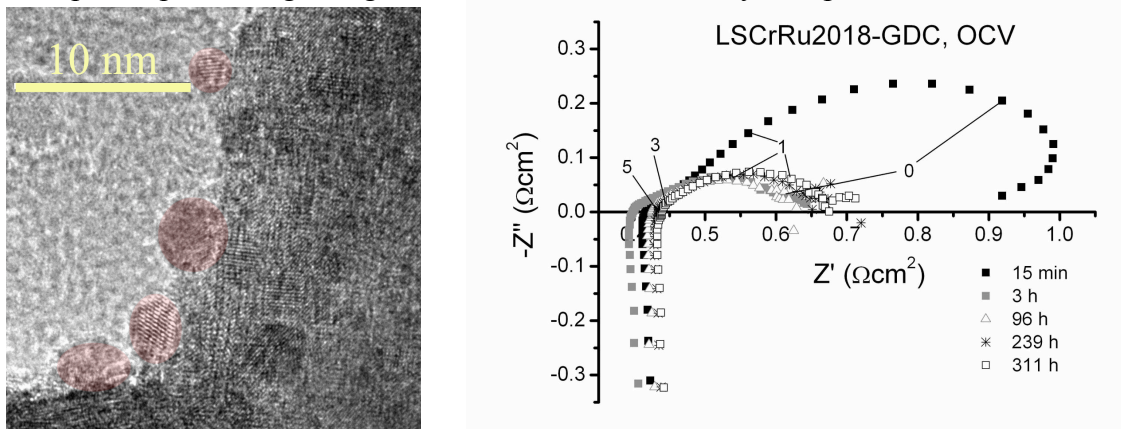


Figure 2. (a) High-resolution electron microscope image showing a portion of a  $La_{0.8}Sr_{0.2}Cr_{0.82}Ru_{0.18}O_3$  particle with Ru nano-clusters that nucleated upon reduction in  $H_2$  at 800°C for 45 h. (b) Electrochemical impedance spectra obtained at various times from a SOFC with LSCrRu-GDC anode at 800°C, showing a rapid decrease in polarization resistance that coincided with the nucleation of Ru nano-clusters.

down to  $0.27 \Omega \text{ cm}^2$  at  $600^\circ\text{C}$ . For example, the lowest resistances were obtained with a nano-scale LSCF structure obtained by firing at  $800^\circ\text{C}$  (Figure 3), whereas the GDC phase required a firing temperature of  $1000\text{-}1100^\circ\text{C}$  in order to attain a well-necked microstructure.

#### Novel mixed-conducting anode materials

A new class of mixed-conducting anode materials, based on the composition  $(\text{La,Sr})(\text{Cr,Fe})\text{O}_3$ , was shown to provide good stability and low polarization resistance. In addition, the anodes show excellent tolerance to sulfur impurities present in real fuels. Figure 4 shows an example of a sulfur tolerance test carried out in hydrogen fuel with 150 ppm  $\text{H}_2\text{S}$ . These levels of sulfur normally result in catastrophic failure of conventional Ni-based SOFC anodes.

#### **Future Plans**

Much of the work described above will be continued in the short term. In the longer term, we plan to emphasize two main directions: effect of nano-structure on intrinsic transport properties and manipulation of micro/nano-structure to improve low-temperature electrode kinetics. The bulk transport studies will emphasize nano-structured mixed conductors. More emphasis will be placed on 3D reconstruction of electrode structure, which will be used in finite-element electrochemical models to correlate nano/microstructure with performance. Coarsening models are being applied to predict the change in size and shape of nano-clusters during SOFC operation.

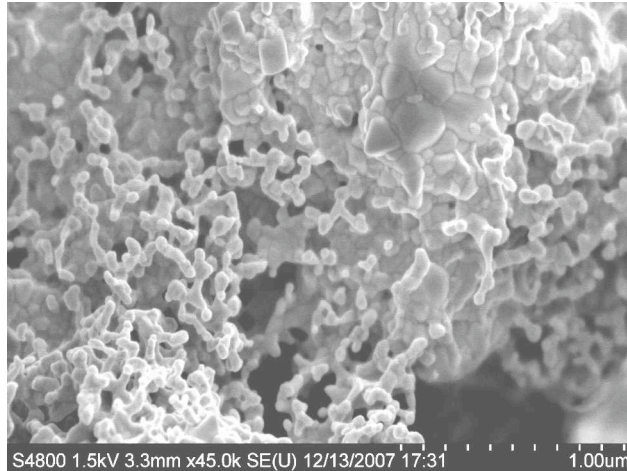


Figure 3. Fracture cross-sectional SEM image of a cathode fabricated by infiltrating LSCF (12.5 vol% loading, fired at  $800^\circ\text{C}$ ) into a GDC scaffold that had been fired at  $1100^\circ\text{C}$ . The LSCF particle widths were 50-100 nm, and the infiltration decrease the cathode area-specific resistance by more than 10 times, to  $0.27 \Omega \text{ cm}^2$  at  $600^\circ\text{C}$ .

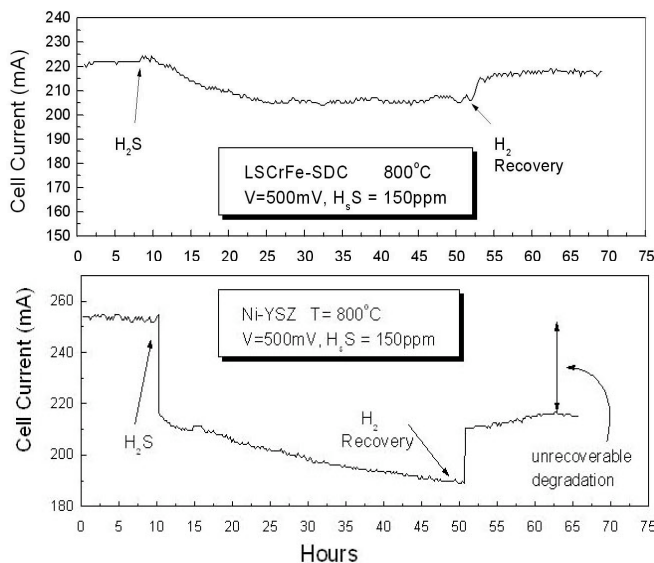


Figure 4. Stability of an SOFC with the  $(\text{La,Sr})(\text{Cr,Fe})\text{O}_3$  anode operated in 150 ppm  $\text{H}_2\text{S}$  (top), compared with that for a SOFC with a conventional Ni-YSZ anode (bottom).

## References

- <sup>1</sup> M. Mogensen, S. H. Jensen, A. Hauch, I. Chorkendorff, and T. Jacobsen, in *7th European Solid Oxide Fuel Cell Forum*, edited by U. Bossel (European Fuel Cell Forum, Lucerne, Switzerland, 2006), p. P0301.
- <sup>2</sup> U. Balachandran, T. H. Lee, S. Wang, and S. E. Dorris, *International Journal of Hydrogen Energy* **29**, 291-296 (2004).
- <sup>3</sup> P. N. Dyer, R. E. Richards, S. L. Russek, and D. M. Taylor, *Solid State Ionics* **134**, 21-33 (2000).
- <sup>4</sup> Z. Zhan, Y. Lin, M. Pillai, I. Kim, and S. A. Barnett, *Journal of Power Sources* **161**, 460-465 (2006).
- <sup>5</sup> H. J. M. Bouwmeester, *Catalysis Today* **82**, 141-150 (2003).
- <sup>6</sup> J. Martinez-Frias, A.-Q. Pham, and S. M. Aceves, *International Journal of Hydrogen Energy* **28**, 483-490 (2003).
- <sup>7</sup> X. Guo and J. Maier, *J. Electrochem. Soc.* **148**, E121-E126 (2001).

## Publications of DoE-Sponsored Research

- Axel van de Walle and Don Ellis, "First-principles thermodynamics of coherent interfaces in samarium-doped ceria nanoscale superlattices," *Phys. Rev. Lett.* **98**, 266101 (2007).
- Yu. F. Zhukhovskii, E.A. Kotomin, and D.E. Ellis, "A Comparative *ab initio* Study of Ca/BaTiO<sub>3</sub>(001) and Cu/MgO(001) Overlayers," *Phys. Stat. Solidi B* (2008, in press)
- E.A. Kotomink, Yu. F. Zhukovskii, S. Piskunov, and D.E. Ellis, "Hybrid DFT Calculations of the F Centers in Cubic ABO<sub>3</sub> Perovskites," *J. Phys. Conf. Ser. C* (2008, in press).
- N Perry and T.O. Mason "Local Electrical and Dielectric Properties of Nanocrystalline YSZ," *Journal of Materials Science*, in press.
- N.J. Kidner, N.H. Perry, T.O. Mason, and E.J. Garboczi, "The Brick Layer Model Revisited: Introducing the nano-Grain Composite Model (n-GCM)," *J. Am. Ceram. Soc.* (2008).
- Madsen, B.D., Kobsiriphat, M., Marks, L.D., Wang, Y., Barnett, S.A. "SOFC Anode Performance Enhancement through Precipitation of Nanoscale Catalysts," in *SOFC X* (ed. S.C. Singhal) (Electrochemical Society, 2007), p 1339-1348.
- Madsen, B.D., Kobsiriphat, W., Wang, Y., Marks, L.D. & Barnett, S.A., Nucleation of nanometer-scale electrocatalyst particles in solid oxide fuel cell anodes. *Journal of Power Sources* **166**(1), 64-67 (2007).
- Madsen, B.D. & Barnett, S.A., La<sub>0.8</sub>Sr<sub>0.2</sub>Cr<sub>0.98</sub>V<sub>0.02</sub>O<sub>3-δ</sub> - Ce<sub>0.9</sub>Gd<sub>0.1</sub>O<sub>1.95</sub> - Ni Anodes for Solid Oxide Fuel Cells. *J. Electrochem. Soc.* **154**(6), B501-B507 (2007).
- Yuanbo Lin and Scott A. Barnett, La<sub>0.9</sub>Sr<sub>0.1</sub>Ga<sub>0.8</sub>Mg<sub>0.2</sub>O<sub>3-δ</sub>-La<sub>0.6</sub>Sr<sub>0.4</sub>Co<sub>0.2</sub>Fe<sub>0.8</sub>O<sub>3-θ</sub> Composite Cathodes For Intermediate-Temperature Solid Oxide Fuel Cells, *Solid State Ionics*, in press.
- Jacob M. Haag, Brian D. Madsen, Scott A. Barnett, and Kenneth R. Poeppelmeier, Application of LaSr<sub>2</sub>Fe<sub>2</sub>CrO<sub>9-δ</sub> In Solid Oxide Fuel Cell Anodes, *Electrochemical and Solid State Letters*, in press
- Patent application: Formation of a Nano-Scale Catalyst Phase in SOFC Anodes Via Controlled Precipitation, B.D. Madsen, W. Kobsiriphat, Y. Wang, L.D. Marks, S.A. Barnett

## NMR Characterization of Complex Metal Hydrides

Robert C. Bowman, Jr., Son-Jong Hwang, and Chul Kim

**Program Title:** Development and Evaluation of Advanced Hydride Systems for Reversible Hydrogen Storage  
DOE/EERE Metal Hydride Center of Excellence (MHCoe) Project DE-AI01-06EE11105

### Principal Investigators:

Robert C. Bowman, Jr.  
Jet Propulsion Laboratory (JPL)  
Mail Stop 79-24  
California Institute of Technology,  
Pasadena, CA 91109-8099  
Robert.C.Bowman-Jr@jpl.nasa.gov

Son-Jong Hwang  
Division of Chemistry and Chemical Engineering  
Mail Code 210-41  
California Institute of Technology (Caltech)  
Pasadena, CA 91125  
sonjong@cheme.caltech.edu

**Program Scope:** JPL and Caltech are applying advanced NMR methods to investigate and characterize the structures and phase compositions of borohydrides, alanates, amides, and other novel light element hydrides produced by their MHCoe partners to clarify the roles that catalysts, dopants, and processing have on phase transformations and degradation of these materials. These studies focus on chemical pathways that affect the reversible formation and decomposition of hydride phases. They also support development and validation of hydride destabilization strategies for light metal hydrides containing Li and Mg by characterizing all reactant and product phases. This Task is supplemented with support via Caltech from the DOE/BES Project “In Situ NMR Studies of Hydrogen Storage Systems” awarded to Prof. Mark Conradi (Washington U., St. Louis, MO). The objective of these BES-funded experiments at Caltech is to monitor for changes in hydride compositions and structures following the high-temperature and *in situ* NMR experiments of the hydrogen and metal diffusion processes to help identify fundamental mechanisms of the kinetics for hydrogen absorption and desorption reactions.

**Recent Progress:** Multinuclear nuclear magnetic resonance (NMR) spectroscopy provides novel insights on the compositions, chemical bonding, and structures of complex metal hydrides. By implementing advanced solid-state NMR techniques such as Magic Angle Spinning (MAS), cross-polarization (CP) MAS, and multi-quantum (MQ) MAS; these NMR measurements give very detailed information on the complicated relationships involving these hydride phases. Because short-range interactions dominate NMR parameters, highly disordered as well as amorphous materials can be more thoroughly evaluated via solid state NMR than is typically possible with x-ray or neutron diffraction studies since the latter usually require good crystallinity as well as sufficiently large domain sizes. Taking examples from some of our recent investigations on high-capacity hydrogen storage candidates, we illustrate how these high-resolution NMR techniques can address and often resolve diverse issues on the phase formation and decomposition processes.

The discovery that Ti and certain other metals (e.g., Sc) greatly enhanced the reversible hydrogen absorption rates of NaAlH<sub>4</sub> stimulated the intense interest of complex hydrides as high performance storage materials. In spite of extensive theoretical and experimental studies, the actual catalytic mechanisms in Ti-doped alanates still remain unresolved and very controversial. Since the <sup>45</sup>Sc nucleus possesses excellent NMR sensitivity with large chemical/Knight shifts as well as being a very effective catalyst with NaAlH<sub>4</sub>, MAS-NMR studies have been performed on Sc-doped NaAlH<sub>4</sub> samples when prepared by ball milling and after hydrogen desorption/absorption cycles. The <sup>23</sup>Na, <sup>27</sup>Al, and <sup>45</sup>Sc spectra are shown in Figure 1 where different phases are identified. As previously seen in NaAlH<sub>4</sub> ball milled with TiCl<sub>3</sub>; Al metal, Na<sub>3</sub>AlH<sub>6</sub>, and NaCl phases were formed during similar processing with ScCl<sub>3</sub> according to the following reaction equation:



Generic metallic Sc phases are denoted by “Sc”. The Na<sub>3</sub>AlH<sub>6</sub> is present from enhancement of desorption by Sc-doping. While the fate of ScCl<sub>3</sub> after ball milling and hydrogen reactions was invisible via x-ray diffraction, which is similar to behavior of Ti-doped alanates, the peaks in the <sup>45</sup>Sc MAS-NMR spectra revealed various changes including formation of amorphous/nanophase ScCl<sub>3</sub>, Al<sub>1-x</sub>Sc<sub>x</sub> alloys, ScH<sub>x</sub>, ScAl<sub>3</sub> intermetallic, as well of one or more currently unidentified phases. Additional MAS-NMR studies are in progress on samples with different

amounts of  $\text{ScCl}_3$  as well as performing more cycling experiments to understand better the role of the Sc additive on the reaction paths for the sodium alanate phases. These results will be reported in the future.

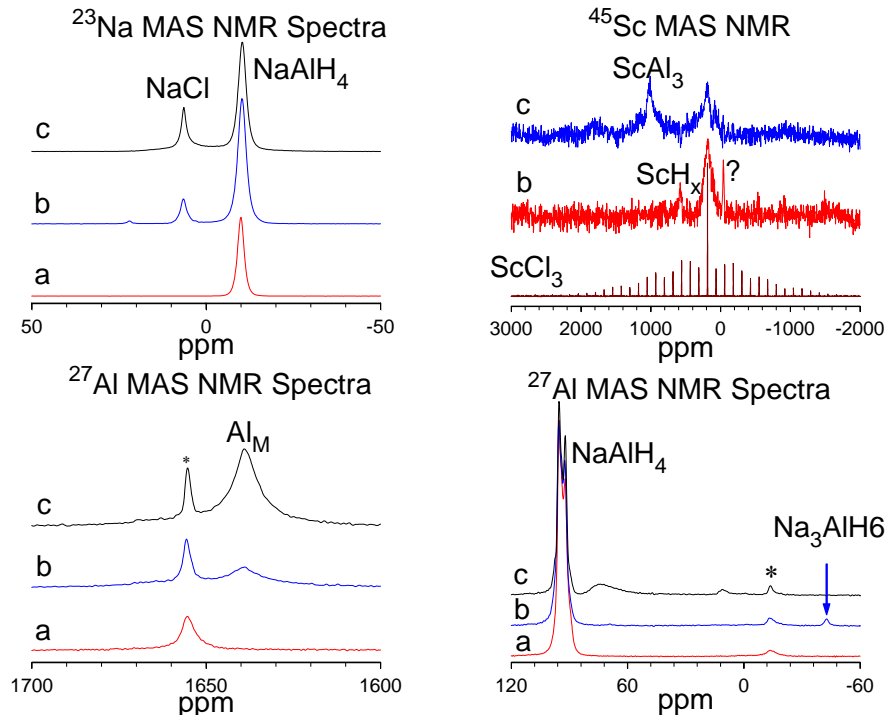
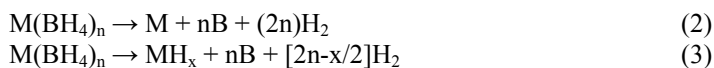


**Figure 1.** Multinuclear MAS NMR spectra for a)  $\text{NaAlH}_4$ , b) ball milled with 4 mol%  $\text{ScCl}_3$ , c) after two  $\text{H}_2$  desorb-adsorb cycles compared to pure  $\text{NaAlH}_4$  and  $\text{ScCl}_3$ . Two regions for  $^{27}\text{Al}$  spectra are for peaks from Al metal near 1640 ppm and  $\text{NaAlH}_4$  and  $\text{Na}_3\text{AlH}_6$  phases at 92 ppm and -42 ppm, respectively. Spinning side bands (rate=14.5 kHz) are marked with \* while those of  $\text{ScCl}_3$  were left unmarked.

Metal borohydrides  $\text{M}(\text{BH}_4)_n$  have among the highest theoretical hydrogen storage capacities when compared to most traditional metal hydrides and other complex hydrides such as alanates or amides. The generic maximum release of hydrogen from  $\text{M}(\text{BH}_4)_n$  during thermal desorption is thought typically to follow the reaction paths



depending on whether a stable binary hydride (i.e.,  $\text{MH}_x$ ) or elemental metal (M) is the final product. In either case, B is presumed to be in an amorphous state since it is not detected by X-ray diffraction. The regeneration of borohydrides following desorption remains a challenge. Several groups have found that  $\text{LiBH}_4$  usually decomposes in two or more stages rather than the single transitions suggested by reactions (2) or (3). Sequential formation of several hypothetical phases “ $\text{LiBH}_3$ ”, “ $\text{LiBH}_2$ ”, and “ $\text{LiBH}$ ” have been suggested to occur but with little or no experimental verification since identification of these substoichiometric borohydrides is severely hampered by the absence of clearly discernable X-ray or neutron diffraction peaks from reacted (or dehydrogenated) samples. In our studies, solid state NMR methods are employed to characterize/identify the amorphous intermediates formed during decomposition reactions of various metal borohydride  $\text{M}(\text{BH}_4)_n$  systems. The most probable intermediate candidates contain the  $[\text{B}_{12}\text{H}_{12}]^{2-}$  anion, which is a hydrolytically stable polyhedral borane complex with the closo-structure shown in Figure 2. Its structure is a regular icosahedron of boron atoms with terminal B-H bonds. Considering the fact that some of elemental boron polymorphs (which should be the final product of the decomposition reaction from reactions 2 and 3) also contain icosahedral boron frameworks, the formation of  $[\text{B}_{12}\text{H}_{12}]^{2-}$  anions seems as likely choice as an intermediate during the decomposition to elemental boron. Our high resolution MAS NMR methods have provided clear evidence that a  $[\text{B}_{12}\text{H}_{12}]^{2-}$  species is a major intermediate when  $\text{LiBH}_4$  is dehydrogenated. The stable nature of the closo-borane compound ( $\text{B}_n\text{H}_n$ ) in an aqueous environment allowed us to further confirm its structural identity by use of solution phase NMR. Formation of the same intermediate was observed for several

borohydride phases based on Li, Mg, and Sc, highlighting the universality of reaction pathway regardless of the accompanying metal element. These results shed new insight into the hydrogen storage behavior and reversibility potential for borohydrides. Volumetric measurements provided the composition changes during the absorption and desorption reactions where MAS-NMR spectra give clear indications of the phases formed that are independent of their crystalline or amorphous structures. In particular,  $^{11}\text{B}$  MQ-MAS and CPMAS measurements established the creation of highly stable intermediate polyboranes (i.e.,  $\text{B}_{12}\text{H}_{12}$  anionic species) in the amorphous decomposition products that severely impact the ability of most borohydrides to reform the initial phases following hydrogen desorption. Correlations between the volumetric and NMR results suggest these polyborane species will limit reversibility for most borohydrides unless alternative means can be developed to enhance their reactivity.

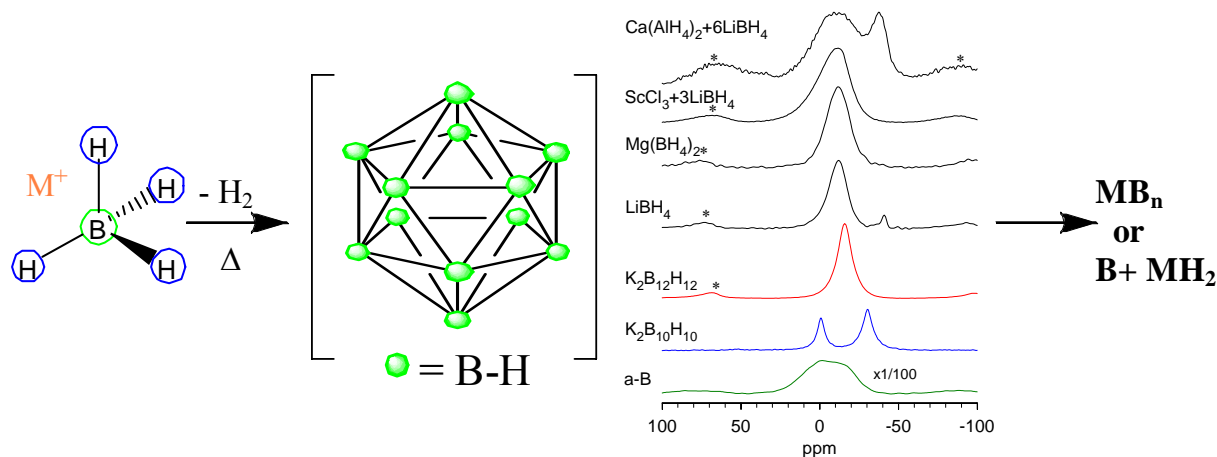


**Figure 2.** Solid state  $^{11}\text{B}$  NMR studies identify the formation of  $\text{M}_{2/n}\text{B}_{12}\text{H}_{12}$  phases as major intermediate species in hydrogen desorption reaction of various  $\text{M}(\text{BH}_4)_n$  systems before further conversion to either  $\text{MB}_n$  or  $\text{B}+\text{MH}_n$ . Solid-state  $^{11}\text{B}$  NMR characteristics of  $\text{M}_{2/n}\text{B}_{12}\text{H}_{12}$  in the amorphous phase of these reactions are consistent with the model compound  $\text{K}_2\text{B}_{12}\text{H}_{12}$ . Formation of  $\text{M}_{2/n}\text{B}_{12}\text{H}_{12}$  complexes is observed in the decomposition of  $\text{M}(\text{BH}_4)_n$  with various metals including Li, Mg, Sc, in addition to a coupled system involving  $\text{Ca}(\text{AlH}_4)_2+\text{LiBH}_4$ .

#### Future Plans:

Within the MHCoe and Washington U. Projects, we are continuing our systematic studies on the behavior of the following metal hydrides systems:

- Complete work on the destabilization behavior of the  $\text{Ca}(\text{AlH}_4)_2/\text{LiBH}_4$  and  $\text{LiBH}_4/\text{MgH}_2$  using volumetric and NMR measurements.
- Perform MAS-NMR measurements on  $\text{Mg}(\text{BH}_4)_2(\text{NH}_3)_2$ ,  $\text{Zn}(\text{BH}_4)_2(\text{NH}_3)_2$  and  $\text{Zr}(\text{BH}_4)_4(\text{NH}_3)_4$  to assess structures and decomposition products to go beyond recent work on the  $\text{Mg}(\text{BH}_4)_2$  phases.
- Continue NMR and volumetric characterization studies of desorption and reversibility of  $\text{Ca}(\text{BH}_4)_2$ .
- Complete evaluations of the phase compositions of  $\text{LiBH}_4/\text{MgH}_2/\text{TiCl}_3$  mixtures with ball milling and temperature cycling in collaboration with our MHCoe partners U. Hawaii and HRL.
- Continue collaborative NMR measurements with Washington U. of Sc and Ti doped alanes from U. Hawaii and IFE (Norway) to assess catalytic effects, etc.
- In collaboration with Washington U, continue to characterize the local structure, chemical bonding, and hydrogen diffusion parameters of  $\text{NaMgH}_3$  samples prepared at SRNL for comparison with the binary hydrides  $\text{MgH}_2$  and  $\text{NaH}$ .
- Continue  $^1\text{H}$ ,  $^6\text{Li}$ ,  $^{15}\text{N}$ , and  $^{27}\text{Al}$  MAS-NMR measurements of the Li-Mg-Al-N-H phases to assess their destabilization and reversibility behavior.
- Assess the phase compositions, local chemical bonding parameters, desorption properties of the various  $\text{AlH}_3/\text{AlD}_3$  phases using MAS-NMR on samples being provided by various MHCoe partners and IFE (Norway).

### DOE Supported Publications:

1. S.-J. Hwang, R. C. Bowman, Jr., J. Graetz and J. J. Reilly, "NMR Studies of the Aluminum Hydride Phases and their Stabilities", *Mater. Res. Soc. Symp. Proc. Vol. 927* (2006), Paper 0927-EE03-03.
2. H. Wu, M. R. Hartman, T. J. Udovic, J. J. Rush, W. Zhou, R. C. Bowman, Jr. and J. J. Vajo, "Crystal Structure of the novel ternary hydrides  $\text{Li}_4\text{Tt}_2\text{D}$  (Tt = Si and Ge)", *Acta Cryst. B* **63** (2007) 63-68.
3. M. R. Hartman, J. J. Rush, T. J. Udovic, R. C. Bowman, Jr., and S.-J. Hwang, "Structure and Vibrational Dynamics of Isotopically Labeled Lithium Borohydride Using Neutron Diffraction and Spectroscopy", *J. Solid State Chem.* **180** (2007) 1298-1305.
4. J. Graetz, J.J. Reilly, J. G. Kulleck, and R. C. Bowman, Jr., "Kinetics and Thermodynamics of the Aluminum Hydride Polymorphs", *J. Alloys Compounds* **446-447** (2007) 271-275.
5. S.-J. Hwang, R. C. Bowman, Jr., J. Graetz, J. J. Reilly, W. Langley, and C.M. Jensen, "NMR Studies of the Aluminum Hydride Phases and their Stabilities", *J. Alloys Compounds* **446-447** (2007) 290-295.
6. H. Kabbour, C. C. Ahn, S.-J. Hwang, R. C. Bowman, Jr., and J. Graetz, "Direct Synthesis and NMR Characterization of Calcium Alanate", *J. Alloys Compounds* **446-447** (2007) 264-266.
7. M. S. Conradi, M. P. Mendenhall, T. M. Ivancic, E. A. Carl, C. D. Browning, P. H. L. Notten, W. P. Kalisvaart, P. C. M. M. Magusin, R. C. Bowman, Jr., S.-J. Hwang, and N. L. Adolphi, "NMR to Determine Rates of Motion and Structures in Metal-Hydrides", *J. Alloys Compounds* **446-447** (2007) 499-503.
8. R. C. Bowman, Jr. and S.-J. Hwang, "Nuclear Magnetic Resonance Studies of Hydrogen Storage Materials" *Materials Matters* **2**(No. 2) (2007) 29-31.
9. H. Wu, W. Zhou, T. J. Udovic, J. J. Rush, T. Yildirim, M. R. Hartman, R.C. Bowman, Jr., J. J. Vajo, "Neutron Vibrational Spectroscopy and First-principles Study of Novel Ternary Hydrides:  $\text{Li}_4\text{Si}_2\text{H(D)}$  and  $\text{Li}_4\text{Ge}_2\text{H(D)}$ ", *Phys. Rev. B* **76** (2007) 224301.
10. J. Lu, Z. Z. Fang, H. Y. Sohn, R. C. Bowman Jr., and S.-J. Hwang, "Potential and Reaction Mechanism of Li-Mg-Al-N-H System for Reversible Hydrogen Storage" *J. Phys. Chem. C* **111** (2007) 16686-16692.
11. L. Senadheera, E. A. Carl, T. M. Ivancic, M. S. Conradi, R. C. Bowman, Jr., S.-J. Hwang, and T. J. Udovic, "Molecular  $\text{H}_2$  Trapped in  $\text{AlH}_3$  Solid", *J. Alloys Compounds* (2008). (in press)  
doi:10.1016/j.jallcom.2007.08.071.
12. S.-J. Hwang, R. C. Bowman, Jr., J. W. Reiter, J. Rijssenbeek, G. L. Soloveichik, J.-C. Zhao, H. Kabbour, and C. C. Ahn, "NMR Confirmation for Formation of  $[\text{B}_{12}\text{H}_{12}]_2$ -Complexes during Hydrogen Desorption from Metal Borohydrides", *J. Phys. Chem. C* (In Press).

# **An ab-initio study of the low-temperature phases of lithium imide**

*Gerbrand Ceder\**

Massachusetts Institute of Technology

77 Massachusetts Avenue, Building 13-5056, Cambridge, MA 02139

Lithium imide ( $\text{Li}_2\text{NH}$ ), a potentially important material for hydrogen storage, has presented researchers with a challenging problem in structural determination. Early x-ray diffraction studies suggested that the structure of lithium imide was antiferite, with a simple cubic sublattice of tetrahedral lithium cations and an FCC sublattice of octahedral nitrogen anions. The position of the hydrogen nuclei was not determined, but in recent years several studies have presented evidence that the hydrogen is tightly bound to the nitrogen, forming imide groups. Despite extensive recent investigation of the structure of lithium imide, there is no consensus on the locations of the lithium nuclei or the orientations of the imide groups below approximately 360 K. Computational and experimental analyses have arrived at no fewer than six different proposed crystal structures. In this work, we have used *ab-initio* calculations along with analysis of previously reported experimental results to propose a structural model for lithium imide that is consistent with both experiments and calculated energies, and significantly more complicated than initially thought. Our result points at a unique and unexpected structural prototype for  $\text{Li}_2\text{NH}$  that may be of importance for other materials containing NH groups or other heteronuclear diatomic ions. We find that well ordered vacancies on 1/6 of the tetrahedral sites are part of the structure, which may be relevant for the kinetics of dehydrogenation of this material.

## NMR of Hydrogen Motion in Ionic Hydrides

Mark S. Conradi

**Program Title:** In situ NMR studies of hydrogen storage systems

**P.I.:** Mark S. Conradi

Washington University, Dept. of Physics–1105

One Brookings Drive

St. Louis, MO 63130

msc@wuphys.wustl.edu

**Program scope:** The goal of the project is to characterize and understand the mobility of hydrogen and metal atoms in ionic and complex hydrides, and to improve our knowledge of their dehydrogenating and rehydrogenating reactions.

**Recent progress:**  $\text{MgH}_2$ : The H kinetics (diffusion) in  $\text{MgH}_2$  are notoriously slow in the absence of ball-milling or additives like  $\text{Nb}_2\text{O}_5$ . We find that the rate  $\omega_H$  of hydrogen hopping in  $\text{MgH}_2$  remains too slow to narrow the hydrogen NMR line ( $\omega_H < 10^5 \text{ s}^{-1}$ ) up to 400C. Such slow motion rates are also too slow for measurement by quasielastic neutron scattering. Going to higher temperature is not practical, because of the excessive  $\text{H}_2$  equilibrium pressure (20 bar already at 400C). Thus, we turned to NMR slow-motion methods.

In the slow-motion technique, one prepares dipolar spin order, allows this to decay during a variable waiting time  $\tau$ , and then inspects the amount of remaining dipole order. Dipole order describes a state in which nuclear spins are preferentially aligned along their local fields (from neighboring nuclear spins), and thus represents a correlation between the orientations of the spins and the local fields they see. The correlation of spin and local field directions is essentially destroyed by a single jump. Hence, the time constant  $T_{1D}$  is, to within a factor of 2, the mean time for the typical atom in the solid to jump once; equivalently, the rate  $T_{1D}^{-1}$  is nearly equal to the rate of atomic jumps,  $\omega_H$ .

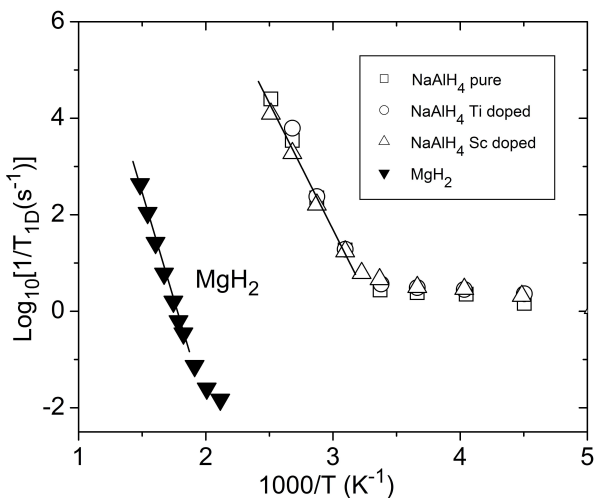


Figure 1:

Also presented in Figure 1 are  $T_{1D}^{-1}$  data from  $\text{NaAlH}_4$  samples, undoped and with 4 mol% Ti and Sc added catalyst. The thermally activated region is fit well by the line corresponding to an

The decay rate  $T_{1D}^{-1}$  is presented in Figure 1 as a function of reciprocal temperature for  $\text{MgH}_2$ . The data at higher temperatures and decay rates represent the first direct measurements of H hopping in  $\text{MgH}_2$ . The line through this data corresponds to an activation energy of 1.86eV. We note this region of rates  $T_{1D}^{-1}$  or  $\omega_H$  extends from a high of  $400\text{s}^{-1}$  down to one per 10 seconds, slow hopping indeed. The lower temperature  $T_{1D}^{-1}$  data have a weaker temperature dependence. We believe that quadrupolar relaxation of the low-gamma and low abundance  $^{25}\text{Mg}$  provides a parallel route for decay of the dipolar order. This route becomes dominant at low temperatures, where the contribution to  $T_{1D}^{-1}$  from atomic jumps becomes small.

activation energy of 1.0 eV. The data in this region are independent of the catalyst, in accord with our identification of the relevant motion as jump reorientations of the tetrahedral  $\text{AlH}_4^-$  anions (but also in accord with the view that the catalysts do not enter the alanate lattice). Our activation energy is about 20% higher than a previous estimate by Tarasov from the temperature dependence of the deuterium quadrupole frequency in  $\text{NaAlD}_4$ . We note that his measurement estimates the potential barrier from the curvature of the bottom of the well, based on the simplest form of potential (e.g.  $\sin 2\theta$ ) commensurate with the tetrahedral symmetry. At low temperatures, the contribution to  $T_{1D}^{-1}$  in  $\text{NaAlH}_4$  is greater than in  $\text{MgH}_2$  (see Figure 1), because of the 100% abundance of  $^{23}\text{Na}$  and  $^{27}\text{Al}$ .

**NaMgH<sub>3</sub>:** This material is made by ball-milling equal molar quantities of NaH and MgH<sub>2</sub>. It decomposes in two steps,  $\text{NaMgH}_3 \rightarrow \text{NaH} + \text{Mg} + \text{H}_2$  and  $2\text{NaH} \rightarrow 2\text{Na} + \text{H}_2$ . The first step has an equilibrium pressure of about 1.8 bar at 400C, so NaMgH<sub>3</sub> is somewhat more stable than MgH<sub>2</sub> (20 bar at 400C). We obtained NaMgH<sub>3</sub> through our collaborator Ragaiy Zidan at Savannah River National Laboratory; x-ray diffraction found only NaMgH<sub>3</sub> with no residual crystalline NaH or MgH<sub>2</sub> evident.

Hydrogen NMR lineshapes are presented in Figure 2. The unexpected features are (i) some line narrowing appears already at 126C, and (ii) the narrowing is inhomogeneous. That is, at any temperature a fraction *f* of the spins are mobile and gives rise to a narrowed resonance and fraction 1-*f* remains immobile and yields the broad line. The fraction *f* increases smoothly with temperature, from ~20% at 125C to essentially 100% at 275C. Thus, one can not identify the mobile spins with the two different sites of hydrogen (1/3 and 2/3 of all H) in the Perovskite structure. We note that the onset of line narrowing requires  $\omega_H$  to be greater than  $10^5 \text{ s}^{-1}$ , so the motions in NaMgH<sub>3</sub> are much faster than in MgH<sub>2</sub>, as shown in Figure 1.

Our measurements of  $T_1$  in NaMgH<sub>3</sub> find the same relaxation rates for both components, narrow and broad. Thus the mobile and immobile spins are either physically close enough (~50nm) so that spin diffusion can equalize their spin temperatures, or the mobile and immobile regions are dynamic and can exchange with each other. In either case, the mobile and immobile spins are physically close together.

We have performed similar measurements on NaMgH<sub>3</sub> intentionally doped by ball-milling with (separately) NaOH and Mg(OH)<sub>2</sub>, because we regard hydroxides/oxides as the likeliest impurities (hydroxide yields oxide if water is driven off). These samples behave similarly to the undoped material. In fact the changes upon hydroxide doping at the 5 mol% level are no larger than the batch-batch variation between undoped samples.

To try to understand the H motion in MgH<sub>2</sub> and NaMgH<sub>3</sub>, and especially why they are so different, we have examined NaH by hydrogen NMR. Ball-milled (bm) NaH from Savannah River (the same material used to prepare NaMgH<sub>3</sub>) and coarse-grained NaH from Aldrich Chemical were compared. We note that the ionic hydrides (NaH, MgH<sub>2</sub>, LiH) are generally available only in low purity, with unreacted metal and oxide/hydroxide impurities. The spectra are presented in Figure 3 at several temperatures. Both materials exhibit substantial line narrowing by 300C. We note that the

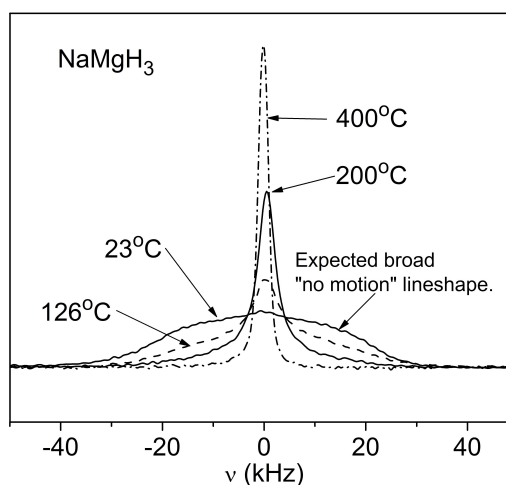


Figure 2:

ball-milled NaH behaves much like the ball-milled NaMgH<sub>3</sub> in Figure 2, with coexistence of broad and narrow resonance components. The coarse-grained Aldrich material, on the other hand, shows a homogeneous line narrowing in which essentially only a single component appears, as expected for a nominally uniform material.

A more quantitative measure of the rate  $\omega_H$  of H hopping can be obtained from  $T_{1\rho}$  measurements. In particular,  $T_{1\rho}$  passes through a minimum when  $\omega_H$  is approximately  $2\omega_1$ , or  $3 \times 10^5 \text{ s}^{-1}$  in the present experiments. Data from ball-milled samples of NaMgH<sub>3</sub> and NaH are displayed in Figure 4. The data are remarkably similar and hint at a common mechanism in the two materials. We note the comparatively weak temperature dependences of the  $T_{1\rho}$  values, suggesting that these systems may have broad distributions of H hopping rates.

**Future plans:** We will focus on the ionic hydrides MgH<sub>2</sub>, NaMgH<sub>3</sub>, and NaH. In MgH<sub>2</sub> with no additives, the H motion is extremely slow (Figure 1) while the motions are much faster in NaH and NaMgH<sub>3</sub>. Much of our research will use hydrogen NMR to determine the rate  $\omega_H$  of H hopping, using line narrowing,  $T_{1\rho}$ , and  $T_{1D}$  measurements. We plan systematic investigations into the effects on atomic mobility of ball milling, additives like Nb<sub>2</sub>O<sub>5</sub>, chemical defects like oxide ions, and the effects of hydrogen depletion and overpressure.

Despite years of intensive study, the mechanism by which spent Na<sub>3</sub>AlH<sub>6</sub> and NaAlH<sub>4</sub> with titanium catalyst are rehydrided remains unclear. Clearly, to reverse either reaction requires transport of Al and/or Na atoms during the rehydriding. There is a growing opinion that some Al-bearing species which is mobile on the surface of aluminum must be involved. Molecular AlH<sub>3</sub> and/or polymers thereof have been specifically mentioned in this regard.

We propose to detect the mobile Al-bearing species, whatever it is, by in-situ NMR. That is, we will acquire <sup>27</sup>Al NMR signals from a sample during rehydriding. Thus, we will start with spent titanium

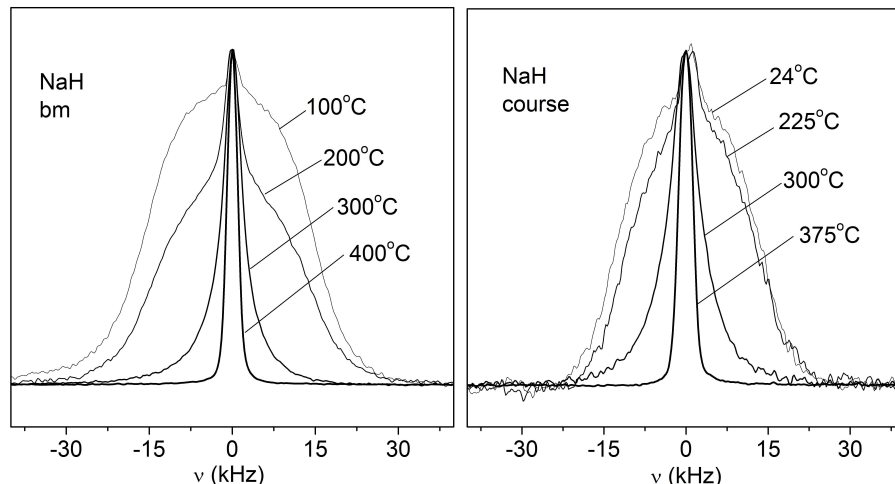


Figure 3:

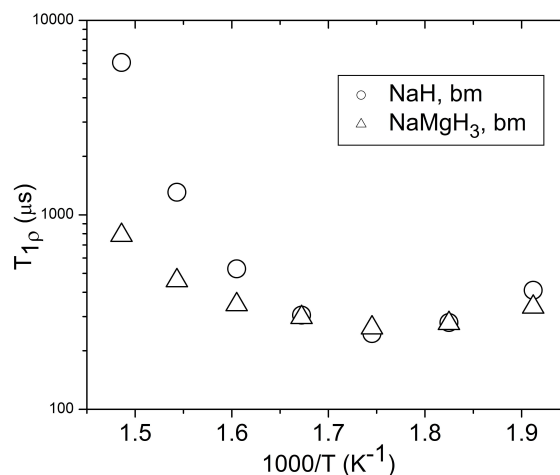


Figure 4:

or scandium catalyzed NaAlH<sub>4</sub> (NaH plus Al metal) and apply 100 bar of H<sub>2</sub> gas, at the typical rehydriding temperature of 100-120C.

1. "Rotation and Diffusion of H<sub>2</sub> in Hydrogen-Ice Clathrate by NMR", L. Senadheera and M.S. Conradi, *J. Phys. Chem. B* **111**, 12097-12102 (2007).
2. "NMR to Determine Rates of Motion and Structures in Metal-Hydrides", M. S. Conradi, M. P. Mendenhall, T. M. Ivancic, E. A. Carl, C. D. Browning, P. H. L. Notten, W. P. Kalisvaart, P. C. M. M. Magusin, R. C. Bowman, Jr., S.-J. Hwang, and N. L. Adolphi, *J. Alloys Compounds* **446-447**, 499-503 (2007).
3. "Molecular H<sub>2</sub> Trapped in AlH<sub>3</sub> Solid", L. Senadheera, E. A. Carl, T. M. Ivancic, M. S. Conradi, R. C. Bowman, Jr., S.-J. Hwang, and T. J. Udovic, *J. Alloys Compounds* (2007). (in press) doi:10.1016/j.jallcom.2007.08.071.
4. "Rate of Hydrogen Motion in Ni-Substituted LaNi<sub>5</sub>H<sub>x</sub> from NMR", M. P. Mendenhall, R. C. Bowman, Jr., T. M. Ivancic, and M. S. Conradi, *J. Alloys Compounds* **446-447**, 495-498 (2007).
5. "Spin Sorting: Apparent Longitudinal Relaxation without Spin Transitions", Y. V. Chang, S. E. Haywood, J. C. Woods, and M. S. Conradi, *Chem. Phys. Lett.* **437**, 126-131 (2007).
6. "Comparison of Spin Relaxation in the Metal-Hydrogen Systems ZrNiH<sub>x</sub> and ZrNiD<sub>x</sub>", C. D. Browning, T. M. Ivancic, R. C. Bowman, Jr., and Mark S. Conradi, *Phys. Rev. B* **73**, 134113 (2006).
7. "The evolution of Structural Changes in Ettringite during Thermal Decomposition", M. R. Hartman, S. K. Brady, R. Berliner, and Mark S. Conradi, *J. Solid State Chem.* **179**, 1259-1272 (2006).
8. "Proton Magnetic Resonance Spectra of YH<sub>3</sub> and LuH<sub>3</sub>", S. K. Brady, Mark S. Conradi, G. Majer, and R. G. Barnes, *Phys. Rev. B* **72**, 214111 (2005).
9. "Apparatus for High Temperatures and Intermediate Pressures for In Situ NMR of Hydrogen Storage Systems", D. B. Baker and Mark S. Conradi, *Rev. Sci. Instrum.* **76**, 073906 (2005).
10. "Nuclear Magnetic Resonance Studies of Hydrogen Storage Material", R. C. Bowman, Jr. and S.-J. Hwang, *Materials Matter* **2**, 29-34 (2007).
11. "NMR Relaxation times in H<sub>2</sub>-D<sub>2</sub>O Clathrate", L. Senadheera and M.S. Conradi, (in preparation).

## Nanocomposite proton conductors

Lutgard C. De Jonghe (PI), Jeffrey A. Reimer(Co-PI), Philip N. Ross (Co-PI)

Materials Sciences Division  
Lawrence Berkeley National Laboratory  
1 Cyclotron Road  
Berkeley CA 94720

The program designs, synthesizes and tests rare earth phosphate materials for proton conducting applications in the temperature region of 300-450 degrees Celsius. The program relies on three major approaches: a theoretical understanding of proton conduction in Rare Earth-Phosphates (REPs) employing quantum computation and molecular simulation; the chemical design, synthesis, and proton conductivity measurement of nanocomposite materials; and the structural and dynamical characterization of the nanocomposite materials using a range of advanced characterization methods including nuclear magnetic resonance (NMR), high resolution TEM, vibrational spectroscopy, as well as computational methods. Aliovalently-substituted REPs, rare earth phosphate glasses and nanocomposites derived from these are synthesized, and evaluated for proton conduction. A comparison of theoretical predictions and observed conductivities provides an insight into the microscopic nature of conduction and directs the synthesis of novel nanocomposite rare earth phosphates. Basic processes and materials compatibilities of novel anodes and cathode composite electrodes are studied.

### Progress

#### *Computational Efforts.*

Based on the density functional calculations, the proton transfer mechanism in  $\text{LaPO}_4$  has been investigated at the atomic scale within the transition state theory. Using the nudged elastic band method, the minimum energy paths of typical proton transfer processes were computed, including intra-tetrahedral transfer, inter-tetrahedral transfer, proton rotation around  $\text{PO}_4$  tetrahedra, and the oscillatory transfer between adjacent tetrahedra. Because the  $\text{PO}_4$  tetrahedra in  $\text{LaPO}_4$  are separated, proton transfer between different tetrahedra is required for continuous proton conduction. The energy barriers for these processes are shown to be around 0.8 eV, very close to experimentally measured activation energies. The intra-tetrahedral transfer on the phosphate groups presents a high energy barrier, and is very unlikely to occur. Proton conductivity of  $\text{LaPO}_4$  was also calculated by considering the vibration frequencies of the system within the harmonic approximation.

#### *CeO<sub>2</sub>/CePO<sub>4</sub> Composites.*

Cerium phosphate nanoparticles with diameters of 10-180nm were synthesized by a variety of solution techniques. X-Ray Diffraction (XRD) determined the crystalline phase(s) present in each sample. Population, shift, and spin-lattice relaxation  $^{31}\text{P}$  solid state Nuclear Magnetic Resonance (NMR) measurements accounted for all the  $^{31}\text{P}$  nuclei expected in each sample, and were able to distinguish between phosphorous nuclei in different environments and phases. Transmission Electron Microscopy (TEM) characterized the morphology and crystallinity of the powder samples as well as of the sintered compacts of the powders. In conjunction with TEM, Energy-Dispersive Spectroscopy (EDS) provided a measure of the composition of the bulk intergranular regions within each  $\text{CePO}_4$  sample. The presence of an amorphous, phosphate-rich intergranular phase was found in those samples prepared by dissolution of ceria in  $\text{H}_3\text{PO}_4$  under various conditions.

#### *Lanthanum Phosphates with Highly Conductive Grain Boundary Phase*

Previously unrecognized amorphous grain boundary films are shown to provide rapid proton conduction paths in polycrystalline lanthanum phosphates. Experiments reveal the amorphous phosphorus-rich grain boundary films to be stable in air at 773 K, with conductivity upwards of  $2.5 \times 10^{-3}$  S/cm at 773 K, many orders of magnitude higher than in the crystalline bulk. The results indicate the possibility of forming

stable, high proton-conductivity nano-composites of RE-phosphate glasses and crystalline ceramics for intermediate temperature (573 K to 773 K) fuel cells.

Variable temperature  $^1\text{H}$  MAS NMR in these lanthanum phosphates revealed the impact of microscopic structure control on proton dynamics. The formation of the hygroscopic P-rich boundary facilitates  $\text{H}_2\text{O}$ -assisted dynamics at temperatures below  $150^\circ\text{C}$ , as manifested in the narrowing of  $^1\text{H}$  spectra. The computed activation energy of proton dynamics at these lower temperatures, 0.134 eV, confirms the assisted nature of proton transport and is consistent with previous first-principles calculations that show the energy barrier to oscillatory proton transfer between  $\text{PO}_4$  tetrahedra to be  $\sim 0.15\text{eV}$ . Proton transport may be enhanced by the presence of mobile water and/or a network of P-OH groups, which facilitate low temperature dynamics along the intergranular boundaries of the crystalline  $\text{LaPO}_4$  grains.

These results have prompted us to focus on RE- phosphate glass and RE-phosphate glass ceramic nanocomposites.

#### *Lanthanum-Calcium Phosphate Glass -Ceramic*

A dual phase glass-ceramic composite is produced by heating a  $\text{CaLa}(\text{PO}_3)_5$  glass at  $800^\circ\text{C}$  for 20 h. The glass-ceramic consists of intertwined crystalline  $\text{La}(\text{PO}_3)_3$  and amorphous  $\text{Ca}(\text{PO}_3)_2$  with an overall conductivity around  $1.52 \times 10^{-5} \text{ S/cm}^{-1}$  at  $550^\circ\text{C}$  in humidified air. For the water vapor treated glass-ceramic, the vibration modes of the incorporated water as well as of P-OH groups are detected by infrared spectroscopy in the range  $3440\text{-}1660 \text{ cm}^{-1}$ , suggesting that glass-ceramic  $\text{La}(\text{PO}_3)_3\text{-Ca}(\text{PO}_3)_2$  is a proton conductor. As expected from infrared spectroscopy, the conductivity of the glass-ceramic is higher in humidified air than in dry air, consistent with proton conduction.

The  $^{31}\text{P}$  NMR MAS spectra revealed the various chemical environments for phosphorus in the  $\text{La}_2\text{O}_3\text{-}2\text{CaO-}5\text{P}_2\text{O}_5$  composite. As a result of the heat treatment, the otherwise disordered glass separates into regions of lanthanum phosphate and calcium phosphate rich phases, where the chemical shift values of the heat-treated composite match well with the individual heat treated lanthanum phosphate and calcium phosphate components from the literature.

#### *Modified La- metaphosphate Glasses*

The structure of La based metaphosphate glasses modified with aliovalent alkaline earth elements (Ba, Ca, Sr) so that the P:(M+La) ratio of 3 is constant were analyzed using optical techniques. Increasing the  $\text{M}^{2+}:\text{La}$  ratio smoothly decreased the density and glass transition temperature, and shifted the vibrational modes by as much as 40 wavenumbers. The ionic radii of the alkaline earth minimally affected the P-O-P and P=O vibrations, though significantly affected the symmetric  $\text{PO}_2$  vibration. The average cation-oxygen coordination number remained near  $\sim 7$  except for Ca where it became closer to 6. The POP: $\text{PO}_2$  ratio increased with increasing alkaline earth additions, though the addition of divalent elements into a trivalent metaphosphate structure is partially accommodated by incorporation of protons as charge compensating defects. Protons incorporated are found on phosphate tetrahedra in direct relationship to the divalent cation.

#### *La-Sr-Al Ultraphosphates*

Recent results on La-Sr- ultraphosphates have shown quite intriguing results. Glasses of these compositions were prepared, quenched, and thermally treated to effect glass-ceramic transformations. The resulting samples showed phase separation at the nanoscale, as well as remarkable conductivity increases upon transformation. Preliminary results on Al-doped La-Sr ultraphosphate glasses indicated the stability of the resulting glasses could be increased by the presence of Al, suppressing the microstructural transformations.

### *Fuel cell concepts*

We have recently developed the capability to produce uniform thin films of our most conductive phosphate glasses. An example of a  $\sim 2\mu$  -thick free-standing glass film are shown. It will be attempted to apply such films to supporting metallic anodes, to produce novel fuel cell architectures. Methods will be developed to assure chemical compatibility of the REPs with the substrate anodes, and with low-temperature perovskite cathodes such as Sr-doped  $\text{PrMnO}_3$ .

### **Future work**

The objective of the work is to generate novel proton conductors, based on Rare Earth Phosphates (REPs) that can serve reliably as hydrogen fuel cell membranes in the temperature range between 300 and 500°C. The target proton conductivities at  $\sim 450^\circ\text{C}$  are put at  $5 \cdot 10^{-3} (\Omega\text{cm})^{-1}$ , sufficient to this purpose when used as supported thin films less than about 10 micrometers thick. The work is expected to develop an understanding of the fundamental aspects of proton conduction mechanisms in such systems, and how these are affected by structure and composition. Such understanding can guide the syntheses, and is expected to be of significance to proton conduction not only in REPs, but also in other inorganic polymer systems.

Work performed in the past program period has demonstrated that aliovalent cation-substituted REPs can be promising proton conductors below 500°C. High-conductivity grain boundary phosphate phases were produced in polycrystalline Lanthanum phosphates synthesized by powder methods. However, true nanocomposites could not be produced by these routes, due the unavoidable grain growth that accompanies the necessary densification of powder compacts, and made grain sizes below 1 micrometer unattainable at full density. Glass drawing methods and glass transformation synthesis routes proved far more productive, and are therefore pursued. Present work found that stability of doped (La,Sr)- phosphates in humid environments could be significantly enhanced by the addition of Al. Further modifications and particularly the formation of nanocomposites resulting from controlled transformation of REP glasses can be expected to lead to conductivity enhancements, as would follow from the known theories of conduction in dual-phase nano-ionics. The generation of controlled nanostructures by glass- ceramic processing routes is particularly attractive, not only because they are technologically advantageous, but also because they allow for the rapid preparation of thin, dense membranes in which the desired nanostructures can be manipulated through thermal treatments that control nucleation and growth of dispersed nanophases. The syntheses of REPs by melt processing and glass-ceramic transformation will therefore be further exploited.

While the syntheses efforts have yielded encouraging conductivity results, the fundamental processes that produced these results are not sufficiently understood. Conductivity measurements and IR spectroscopy carried out in the previous program period have, for the first time, given strong indications that proton trapping at aliovalent doping sites may play an important role in doped RE-glasses and their crystalline counterparts. This will be examined by detailed vibrational spectroscopy and particularly by the application of heteronuclear correlation NMR. These and other NMR methods, including pulsed gradient NMR, coupled with first principle calculations, are expected to provide the necessary clarification of the fundamental aspects of proton transport in the modified REPs, and establish the principles by which stable, highly conductive REP proton conductors are to be developed.

It is only through the close integration of the interdisciplinary approach incorporated in this project that the complex REPs can be understood and developed, to yield useful proton conductors for the intended operation below 500°C.

#### *Proton Diffusometry: STRAFI*

Quantitative determination of diffusive motion of protons in the membrane materials, including their motion under driving forces in an actual electro-active device, is an important goal of the present work and will be established in this program period. Field-gradient NMR, being one of the few methods that provide a measurement of the local diffusivities of multiple types of protons present in a single material, will yield insight into this protonic motion. In the materials under investigation, the characteristic spin-spin relaxation time is so short that an enormous field gradient is required. The proposed strategy, therefore, is to design an apparatus that uses the stray field of a superconducting magnet to create magnetic field gradients on the order of tens of tesla-per-meter to make diffusometry measurements (*i.e.*, Stray Field NMR or STRAFI). The construction of a high temperature  $^1\text{H}$  NMR probe will be completed in the next few

months. This will provide, both one-dimensional  $^1\text{H}$  NMR spectra and proton diffusivity measurements at elevated temperatures (300-500°C), bringing our proton NMR studies into the same temperature range as the AC impedance methods. Should the relative time scales of signal attenuation due to  $T_2$  relaxation and diffusion prove to be more favorable than anticipated, the probe may be altered to include anti-parallel Helmholtz coils to perform pulsed field-gradient (PFG) NMR, which would likely provide improved proton peak resolution during diffusion measurements. In addition to characterizing bulk diffusion, our first efforts will spectroscopically assess the extent to which all proton bonding environments are participating in bulk diffusion; while we expect the proton lineshape to be a motionally-averaged single peak, we are fully capable of spectroscopic resolution of the protons in STRAFI for thin samples, or *via* pulsed field-gradients which will be amenable given higher diffusivities at temperatures above 300°C.

The most significant conclusion from these measurements will be the ability to correlate microscopic proton dynamics with structural regions of the phosphate material and, and by comparison with AC impedance spectroscopy measurements, provide insight into the mechanism of protonic transport through these materials. Such information will provide guidance in the design of new materials that exhibit higher proton conductivity.

### Publications

L. Karpowich, S. Wilcke, Rong Yu, G. Harley, J.A. Reimer, and L. C. De Jonghe, "Synthesis and characterization of mixed-morphology  $\text{CePO}_4$  nanoparticles", *Journal of Solid State Chemistry*, **180** (2007) 840–846

Gabriel Harley, Rong Yu, and Lutgard C. De Jonghe, "Proton Transport Paths in Lanthanum Phosphate Electrolytes", *Solid State Ionics* **178** (2007) 769–773

R. Yu, Q. Zhan, L.C. De Jonghe, "Crystal structures and displacive transition in noble metal nitrides", *Angew. Chem. Int.*, **46**, (2007) 1136–1140

Rong Yu and Lutgard C. De Jonghe, "Proton-Transfer Mechanism in  $\text{LaPO}_4$ ", *J. Phys. Chem. C*, **111**(2007) 11003-11007.

Guojing Zhang, Rong Yu, Shashi Vyas, Joel Stettler, Jeffrey A. Reimer, Gabriel Harley, and Lutgard C. De Jonghe, "Proton conduction and characterization of an  $\text{La}(\text{PO}_3)_3\text{-Ca}(\text{PO}_3)_2$  glass-ceramic," *LBNL-63603*(2007) in press, *Solid State Ionics* 2008.

Theses: Lindsey Karpowich, *Synthesis and Conductivity of cerium Phosphates*, M.S. Thesis, U.C. Berkeley, 2007. L. De Jonghe, Advisor.

Gabriel Harley, *Synthesis and Proton conduction in Lanthanum Phosphates*, M.S. Thesis, UC. Berkeley, 2006, L. De Jonghe, Advisor.

## **A Surface Stress Paradigm for Studying Catalyst and Storage Materials Relevant to the Hydrogen Economy**

Cody Friesen  
Assistant Professor  
School of Materials  
P.O. Box 878706  
Arizona State University  
Tempe, AZ 85287-8706  
cfriesen@asu.edu

### **Program Scope**

This program is focused on the understanding and development of materials relevant to the future hydrogen economy utilizing a surface stress paradigm. This BES program is the *first* time that surface stress measurements have been used to look at phenomena such as oxygen reduction, catalyst poisoning, and hydrogen-storage. In this context, these measurements have proven to be a powerful tool for studying catalysts and hydrogen storage materials in both vacuum and electrochemical environments.

The adsorption of species and the associated interaction always leads to a modification of the thermodynamic surface stress. This fact can be exploited as a spectroscopic method for studying existing and potential catalysts and hydrogen storage materials. Prior to obtaining the first round of funding on this program, we showed how in-situ, real-time stress measurements were used to directly measure the elastic component of atom-surface interaction during homoepitaxial growth of several transition-metals in an ultra-high vacuum (UHV) environment (this work resulted in two *Physical Review Letters* and a publication in the *Journal of Applied Physics*). That work was made possible through the development of an ultra-high sensitivity cantilever-based stress monitor that to our knowledge is the most sensitive in existence. The temporal and surface stress resolution of the device coupled with our parallel understanding of the electronic structure details associated with transition-metal catalysts and hydrogen storage materials suggested an exciting new approach focused on measuring, understanding, and augmenting properties via the nanomechanical response of surfaces to catalytic and storage processes.

We are examining, in the UHV environment, the adsorbate-surface interaction, interaction between like and unlike adsorbates, reaction thermodynamics, and reaction kinetics for both single-component and bi-functional catalysts; all obtained through surface stress measurements and supporting electronic structure calculations. We are also looking at poison tolerance and electro-oxidation at alloy catalyst electrodes in electrochemical environments. As a minor component of the work, the efficacy and mechanical degradation of H-storage materials studied during electrochemical loading/unloading cycles are being studied. Finally, we have made substantial progress in understanding the constitutive connection between surface stress, d-band depth, and catalytic activity. This constitutive relation may extend to variations in Eigenstrain; developing our understanding of this connection may lead to a new direction for the development of catalysts.

In the “Recent Progress” section two main efforts are highlighted: Surface stress measurements of CO adsorption on Pt surfaces and a theoretical/experimental examination of the connection between transition-metal intrinsic surface stress and catalytic activity.

### **Recent Progress**

#### *Surface Stress Changes during Carbon Monoxide Adsorption and Oxidative Stripping on Pt {111}*

Before low-temperature hydrogen fuel cells become a viable energy solution numerous hurdles must be overcome. One of the hurdles is to prevent or limit the poisoning of the anode catalyst. Fuel cell anodes are poisoned by carbon monoxide (CO) impurities in the fuel which adsorb onto the catalyst, blocking catalytically active sites. The adsorption of CO is a displacive, non-Faradaic reaction. It is displacive in that the double layer is displaced (i.e. adsorbed water molecules, cations and/or anions are displaced from the electrode/electrolyte interface as CO is adsorbed) and non-Faradaic in that no free charge is transferred from the CO molecule to electrode. Charge transients measured during the adsorption of CO are due to the removal of the double layer, allowing for accurate measurements of the potential of zero total charge. CO can be stripped from the electrode by oxidizing it to CO<sub>2</sub>. The charge associated with the oxidation of CO and the concomitant reformation of the double layer allows for calculation of CO coverage. Previous work on CO displacement experiments at Pt surfaces has resulted in accurate measurements of both the pzc and CO coverage.

Our in-situ, ultra-high resolution surface stress measurements during both adsorption and electrochemical stripping of CO have been compared to UHV results as a function of coverage and structure. Our work in UHV has shown that in-situ surface-stress measurements during CO adsorption can resolve structural changes in the adsorbate layer. The difference between the UHV adsorption of CO and its adsorption in an electrolyte is predominantly associated with double layer effects. By measuring the surface stress of CO adsorption at the pzc it is possible to quantitatively compare the UHV work with the electrochemical work. The kinetics of both the adsorption (which are extremely fast in UHV and much slower in an electrolyte) and stripping of CO have also been examined in detail.

#### *The Surface Stress of fcc Transition-Metals and the Connection to Catalytic Activity*

The surface free energy and surface stress of *sp*-metals are both determined by a single parameter: the bulk charge density. The surface represents the truncation of the electronic structure, an associated electrostatic dipole, and the resulting Friedel oscillations that decay monotonically into the bulk over distances of order ~10 monolayers. Both the surface free energy and surface stress of all simple metals are in the range of 0.075 to 1.5 J/m<sup>2</sup>. However, in transition-metals surface energies can exceed 3 J/m<sup>2</sup> and the surface stress can exceed 4 J/m<sup>2</sup>. Additionally, there is no correlation between the surface stress of transition-metals and bulk charge density. It has previously been observed that the presence of *d*-electrons tend to screen the Friedel oscillations resulting in a significantly shorter decay distance. Another interesting observation is that the most catalytically active metals are also those with the largest surface stresses.

This work has centered on an ab-initio investigation of the origins of surface stress in transition-metals. Specifically, we set out to find a single parameter, like bulk charge density for *sp*-metals, that correlates to the surface stress of transition-metals. We examined a number of features related to the characteristics of the *d*-electrons in this study. We have found strong correlation between the

surface stress and the difference in  $d$ -band depth going from an infinite solid to one with (111) surfaces across all fcc transition-metals (Rh, Ir, Ni, Pd, Pt, Cu, Ag, and Au). Explicitly, we examined the up-shift in  $d$ -band position at the  $\Gamma$ -point, where the  $e_g$  and  $t_{2g}$  bands are exact and no  $s$ - $d$  interaction occurs. The strength of the correlation is shown to depend on both element group and row.

Where these findings become particularly interesting from an electrochemical standpoint is in the context of catalytic activity. There has been a recent surge in interest in tuning catalytic activity by applying strain to transition-metal catalysts. The phenomenon follows from the fact that the  $d$ -bands in late-stage transition-metals are up(down)-shifted by a tensile (compressive) strain, which enhances (diminishes) the hybridization of the  $d$ -states and the electronic states of adsorbed species. Since surface stress is constitutively related to strain, it is not surprising that metals with the largest surface stress are also those that are naturally more catalytically active. The preceding two points also imply a constitutive relation between catalytic activity and surface stress; suggesting a new direction for the design of catalysts. Our experimental work using surface stress changes to study catalysts is highlighted to show how the above concepts are being studied in the laboratory frame.

### **Future Plans**

-We've solved a substantial issue associated with our high-resolution stress measurements of species adsorption in the ultra-high vacuum environment. We are now confirming our results for the system CO/Pt{111} and will be submitting that for publication soon.

-The CO/Pt{111} work that we've performed in electrochemical environments is now being extended to Pt/Ru alloy surfaces. We showed with the CO/Pt{111} system that surface stress measurements allow for the observation of details of non-faradaic processes that otherwise are not-experimentally observable.

-We are continuing to build our understanding of the constitutive connection between  $d$ -band depth - intrinsic surface stress - catalytic activity. We are also in the process of developing a system in which this connection can be shown experimentally.

### **Publications and Talks Attributable to this Program**

-Th. Heaton and C. Friesen, "Pt{111} and Au{111} Electrocapillarity: Interphase Structure, the pzc, and Oxygen Reduction", *J. Phys. Chem. C*, **111**, 14433 (2007).

-C. Friesen, "Thermodynamic Separability of Ultra-Thin Film Surfaces and Interfaces" *Surf. Sci.* **600**, 1012 (2006).

-L. Mickelson, Th. Heaton, C. Friesen, "Surface Stress Observations during the Adsorption and Electrochemical Oxidation of CO on Pt{111}", *J. Phys. Chem. C*, *In Press*.

-T. Heaton, R. Zeller, E. Engstrom, J.R. Hayes, C. Friesen, "Hydrogen UPD and Uptake in Pd{111}: a Gravimetric and Stress Evolution Study", In Preparation.

-J.K. Kennedy, T. Trimble, C. Friesen, "Surface Stress and Direct Elastic Observations of Structural Change in the Adsorption System CO/Pt{111}", In Preparation.

### Talks

"The Surface Stress of fcc Transition-Metals and the Connection to Catalytic Activity" C. Friesen, Electrochemical Society, Washington DC. October, 2007. (Invited)

L. Mickelson, Th. Heaton, and C. Friesen, "Surface Stress Changes during Carbon Monoxide Adsorption and Oxidative Stripping on Pt {111}" Electrochemical Society Meeting, Washington DC, October, 2007.

Th. Heaton and C. Friesen, "A Surface Stress Study of the Metal Electrode-Electrolyte Interphase Region" Electrochemical Society Meeting, Washington DC, October, 2007.

"Pt{111} Electrocapillarity: A Direct Measure of the pzc and its Application to Oxygen Reduction" C. Friesen and T. Heaton, Electrochemical Society Meeting, Cancun Mexico, October, 2006.

## Issues and Challenges in Hydrogen Storage

P. Jena

Physics Department, Virginia Commonwealth University  
Richmond, VA 23284-2000

The success of a hydrogen economy depends critically on our ability to find materials that can store hydrogen with large gravimetric (9 wt %) and volumetric (0.081 kg/L) density and operate under ambient thermodynamic conditions. The conventional storage of hydrogen in the form of liquids and compressed gas does not meet industry requirements not only because the energy density of stored hydrogen is substantially lower than that in gasoline, but there are significant costs in compressing or liquefying at cryogenic temperatures. Thus, storage of hydrogen in solid materials is the only option. However, materials that can store hydrogen with high gravimetric densities have to be lighter than aluminum. Unfortunately in these materials hydrogen is either bonded weakly as in graphite and carbon nanotubes or strongly as in light metal hydrides and organic molecules. Thus, hydrogen either desorbs at very low temperatures or very high temperatures. Ideal bonding of hydrogen suitable for room temperature has to be intermediate between physisorption and chemisorption. This can be achieved by fundamentally altering the chemistry of hydrogen bonding in light materials either through the use of catalysts or through nano-structuring.

This talk deals with theoretical calculations aimed at a fundamental understanding of how hydrogen interacts with light elements and how the use of catalysts and/or nanostructured materials can alter these interactions. The motivation for these calculations is not only to understand existing experiments, but also guide experimentalists in the search and discovery of new hydrogen storage materials. I will concentrate both role of catalysts in hydrogen desorption in sodium alanate and  $\text{MgH}_2$  as well as storage of hydrogen in nanostructured materials such as metal doped carbon fullerenes, nanotubes, and organic complexes. The calculations are done using density functional theory with generalized gradient approximation for exchange and correlation. A multi-scale approach involving atomic orbital theory and supercell band structure techniques is used for studying systems ranging from clusters to crystal. Effect of temperature is studied using molecular dynamics simulation. In the following, I outline briefly these two separate approaches.

**Role of Catalysts:** In light metal hydrides such as  $\text{NaAlH}_4$  and  $\text{MgH}_2$ , hydrogen is bonded covalently and its desorption requires high temperatures. An understanding of the electronic structure of these hydrides can be achieved even at the level of clusters. For example, earlier studies by us had shown that in  $\text{AlH}_n$  clusters, the binding energy steadily increases from  $n=1$  to 3 and reaches a peak at  $n=3$ . For  $n=4$ , the cluster is unstable and dissociates into  $\text{AlH}_2 + \text{H}_2$ . The situation is completely different when one considers the stability of its anion counterpart, i.e.  $\text{AlH}_n^-$ . Here the binding energy continues to increase until  $n=4$  and indeed is the highest at  $n=4$ . This clearly illustrates why  $\text{NaAlH}_4$  is so stable and it can be thought of as  $\text{Na}^+ + \text{AlH}_4^-$ . It is the charge transfer from Na to  $\text{AlH}_4$  that stabilizes the system. Thus, any catalysts that can reduce this charge transfer will weaken the Al-H bond strength and hence lower the hydrogen desorption temperature. This is accomplished by Ti and other transition metal atoms. A systematic study of the role of 3d transition metal atoms in the hydrogen bonding in sodium

alanate will be presented. The above analysis also suggests that vacancies created at the Al and/or Na sites can also lower the hydrogen desorption temperature and demonstrates the importance of studying the role of defects. These results are consistent with experiments where ball milling of the samples with out the addition of catalysts lead to improved thermodynamic behavior. Since it is experimentally difficult to quantify the defects produced in ball milled samples, a proper understanding of the role of catalysts by synergy between theory and experiment has been difficult.

This difficulty can be alleviated by focusing on the interaction of  $\text{NaAlH}_4$  with carbon nanotubes, fullerenes, and graphite surface where novel experimental techniques have been used without using ball milling. We have carried out a systematic study of the interaction of a single  $\text{NaAlH}_4$  cluster with a graphene layer, fullerene, and carbon nanotubes of varying diameters (see Fig. 1).

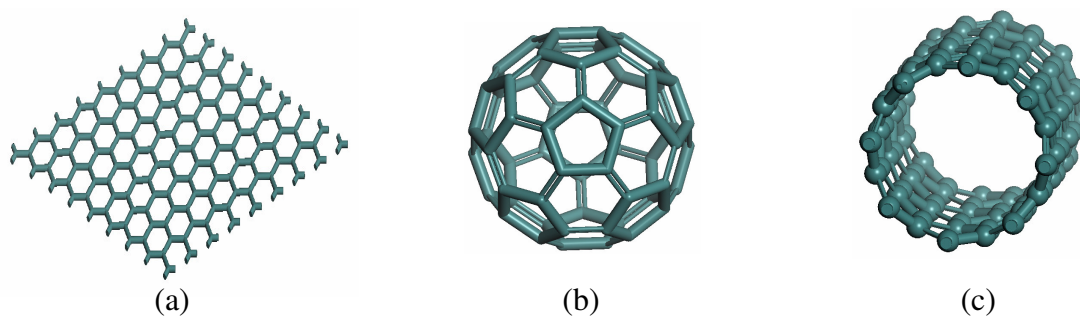


**Fig. 1: Carbon based structures: (a) a graphene layer, (b) zero-dimensional carbon fullerene, and (c) one-dimensional carbon nanotube.**

Note that in these systems, the curvature can be varied and one can study how this curvature affects the nature of bonding between H and Al. We show that this bonding becomes weaker as the curvature of the carbon frame increases and a carbon nanotube with large curvature can be as effective in desorbing hydrogen at lower temperatures and  $\text{TiCl}_3$ . We also show that this lowering is directly related to the electron affinity of these systems which increases as curvature increases. This is consistent with the above picture that the charge transfer of Na to the  $\text{AlH}_4$  unit becomes less with the curvature of the supporting carbon nanotube simple because the Na atom now has to share its electron with the carbon nanotube and the  $\text{AlH}_4$  unit. These results agree with recent experiments and provide an unambiguous understanding of the hydrogen desorption mechanism in light metal hydrides. Similar studies have also been carried out using Fe and NbO as catalysts in the dehydrogenation of  $\text{MgH}_2$ .

**Role of Nano-structures:** Studies have been carried out to understand the interaction of hydrogen with pure as well as metal coated carbon fullerenes and nanotubes and polyacetylenes. We demonstrated that while the bonding of hydrogen in pure carbon nanostructures is very weak, it can be significantly enhanced if they are decorated with metal atoms. The mechanism that is responsible for this binding was illustrated by Kubas and the author more than a decade ago where the bonding of hydrogen is intermediate between physisorption and chemisorption and the binding energies lie in the range of  $0.5 - 0.8 \text{ eV/H}_2$  which is ideal for room temperature applications. Hydrogen remains in a quasi-molecular state with its molecular bond slightly stretched to about  $0.9 \text{ \AA}$ . It was found by earlier authors that a uniformly transition metal coated carbon fullerene or nanotube can store up to 8 wt % hydrogen under ambient conditions. We,

however, showed that transition metals cluster on a carbon fullerene (see Fig. 2) and this clustering severely limits the amount of hydrogen that can be stored.

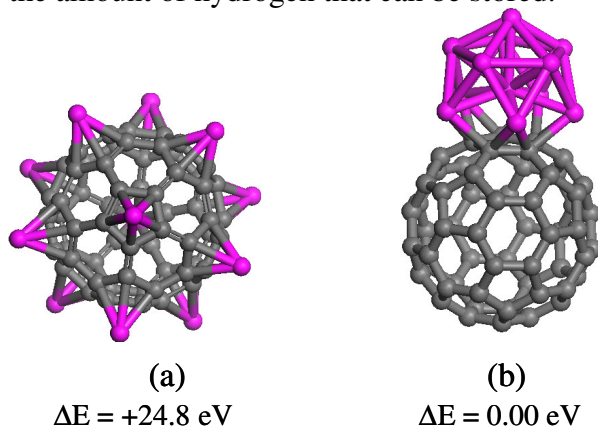


**Fig. 2:** Two configurations of  $\text{Ti}_{12}\text{C}_{60}$  where (a) Ti atoms (red) remain isolated and (b) when they cluster. The relative energy  $\Delta E$  is evaluated referring to configuration (b).

Clustering of metal atoms can be prevented if the metal atoms are Li instead of transition metals. Unfortunately, here the binding of hydrogen is weak and cryogenic temperatures are needed. We also studied some novel molecular complexes such as silsesquioxanes where transition metal atoms can be attached to ligand sites and are naturally prohibited from clustering (see Fig. 3). Such systems can store hydrogen with gravimetric density approaching 5 wt % and with hydrogen binding energies in the range suitable for room temperatures applications.

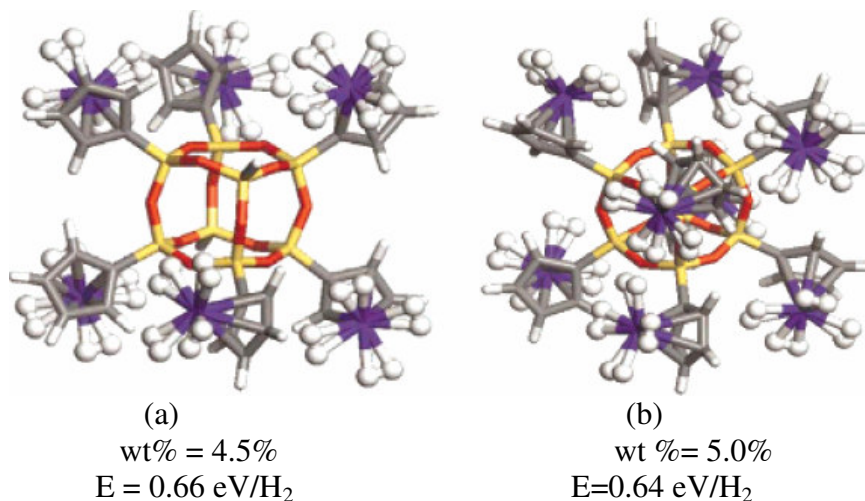


**Fig. 3:** Hydrogen adsorption in six- (a), and eight- (b) Sc-Cp-grafted structures.  $E$  is the average adsorption energy.

These calculations were further extended to study systematically the nature of hydrogen bonding in metal organic complexes involving Ti supported on  $\text{C}_4\text{H}_4$ ,  $\text{C}_5\text{H}_5$ , and  $\text{C}_8\text{H}_8$ . Hydrogen molecules were sequentially added to see how the binding energies vary as a function of number of hydrogen molecules and whether they remain molecular or dissociated. We showed that the maximum number of hydrogen molecules that can be attached to Ti decorated organic molecules

can be simply predicted by the 18-electron rule and that the hydrogen gravimetric density can reach as high as 9 wt % (see Fig. 4) with average bonding energy of about 0.55 eV/H<sub>2</sub>. The stability of multi-decker complexes of these metal organic systems has also been investigated by sequential addition of hydrogen molecules. Experimental studies are under way to verify some of our predicted results.

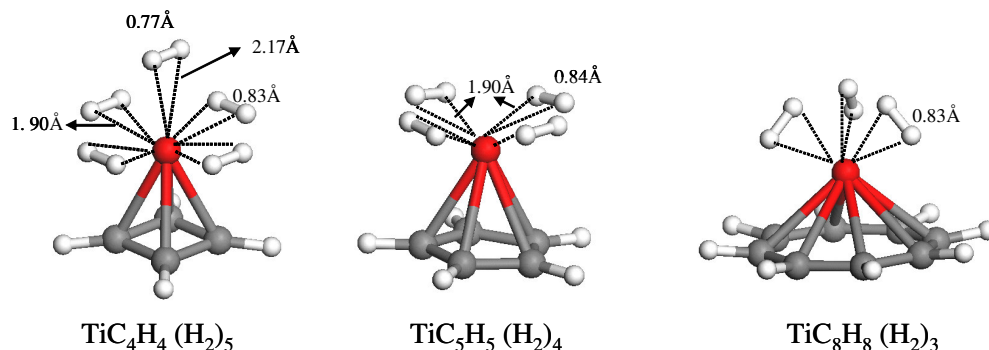


Fig. 4: Optimized geometries of  $\text{TiC}_m\text{H}_m(\text{H}_2)_n$ , ( $m=4,5,8$ , and  $n=3-5$ ) along with important bond lengths (Å).

**Achievements:** The above outline describes only a very small fraction of our accomplishments resulting from the Department of Energy Funding. We received two grants-one on Coated and Supported Metal Clusters (2005-2008) and the other to organize the International Symposium on Materials Issues in a Hydrogen Economy (2007). The goal of the project funded in 2005 was to provide a theoretical understanding of cluster-support interaction by focusing on 3d transition metal atoms adsorbed on organic molecular templates such as coronene and iron and silica clusters coated with noble metals such as gold. We not only completed much of what was proposed, but also embarked on new projects motivated by exciting experiments.

The highlights of our published research can be divided into seven different areas: (1) Evolution of the geometry and electronic structure of elemental clusters, (2) Gold-based hetero-atomic clusters, (3) Transition metal clusters supported on organic molecules, (4) Novel chemistry of Al-H clusters, (5) Clusters for hydrogen storage, (6) Defects in semiconductors, and (7) Clusters as a bridge across disciplines. We showed that properties of clusters evolve non-monotonically and their convergence toward bulk behavior depends upon the property and cluster composition. Gold coating of iron and iron oxide clusters not only preserves the magnetic properties of core shell structures but also allow them to resist corrosion, thus making them ideal for biomedical applications. Fe and Co decorated coronene show very different structural properties although they remain ferromagnetic. We discovered that Al-H clusters exhibit novel chemistry analogous to boranes and prescribed rules of magicity that enabled us to search and discover a large class of Al-H clusters with novel bonding characteristics. We demonstrated that metal coated carbon nanostructures bind hydrogen in quasi-molecular form and have the potential as hydrogen storage materials, provided they can be prevented from clustering. We showed that some of the discrepancies between experiments on dilute magnetic semiconductors are due to clustering of transition metal atoms. We also demonstrated that clusters can be viewed not only as a field intermediate between atoms and bulk, but also as a bridge across disciplines where complex phenomena can be explained by using them as models.

A summary of our achievements are highlighted in the following.

- 51 papers published /in press in refereed journals (including 2 in Science, 2 in Nano Letters, 3 in Physical Review Letters, 5 in Applied Physics Letters, 1 in Journal of the American Chemical Society Communication, 3 in Proceedings of the National Academy of Sciences, 5 in refereed conference proceedings, and the rest in journals such as Journal of Chemical Physics, Journal of Physical Chemistry, Physical Review, and Journal of the American Chemical Society). Of the above, 43 papers acknowledge support of the DOE grant.
- 8 papers published jointly with experimentalists
- Edited two conference proceedings
- Work featured on the cover of Proceedings of the National Academy of Sciences
- 9 papers reproduced in the Virtual Journal of Nanotechnology
- One of the papers covered by 15 news organizations and reported on 91 websites. Another paper has also received media coverage.
- Organized 3 International Conferences.
- Gave 27 invited talks at national/international conferences and 18 seminars/colloquia in institutions around the world.
- Graduated one student with a Ph. D. in 2006.

## **Complex hydrides – A new frontier for future energy applications Towards reversibility through mechanochemistry and nanostructuring**

V.K. Pecharsky (presenting), M. Pruski, L.S. Chumbley, V.S.-Y. Lin  
Ames Laboratory, Iowa State University, Ames, IA 50011-3020; e-mail [vitkp@ameslab.gov](mailto:vitkp@ameslab.gov)  
and

P. Jena, Virginia Commonwealth University, Richmond, VA 23284-2000

### **Program Scope**

Every energy-related application of hydrogen requires a safe and efficient storage, especially in transportation where there are severe weight and volume constraints. Even though large scale commercial applications of hydrogen are at least 10 to 15 years, and possibly, as far as 25 to 40 years away, real progress in solving hydrogen storage problems is required now. We achieve this through basic knowledge of transformation mechanisms in complex hydrides-hydrogen systems, thus precipitating discoveries needed for future transition to hydrogen – a renewable, clean, and safe energy carrier. The specific objectives of the multidisciplinary team effort are to address issues that have the potential to advance basic science of complex hydrides and open up possibilities for their future use by drawing on the experience and expertise of principal investigators in materials science, physics and chemistry of complex hydrides, X-ray diffraction, high resolution solid-state NMR, electron microscopy, catalysis, nanostructuring, and first principles theory and modeling. Our goals are i) examining both thermal energy- and mechanical energy-driven phase transformations in selected model hydride systems at and away from thermodynamic equilibrium; ii) establishing the nature and structure of the products and intermediaries; iii) identifying events critical to achieving reversibility of hydrogen in model systems under mild conditions; iv) creating a knowledge base relating composition, structure and properties of model hydrides; v) refining and extending the current understanding of the mechanisms of solid-state transformations from a few known hydrides to complex hydride-hydrogen systems; vi) exploring the potential of nanoscale for improving behaviors of chosen complex hydride-hydrogen systems; vii) integrating experiment with modeling and first principles theory to provide a fundamental understanding of the nature of hydrogen bonding, the structure and stability of the model systems, the effects of mechanical energy, temperature, and pressure in altering the nature of hydrogen-metal bond, and the role of nanostructuring on the absorption and desorption properties of hydrogen; viii) developing predictive tools suitable to guide the discovery of materials at the atomic scale and tuning processing strategies to control the nano-, meso- and microscopic structures.

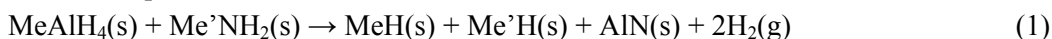
### **Recent Progress**

We built upon our early experiments, in which we pioneered the idea that ball milling (mechanochemical processing) is an excellent tool to rapidly destabilize  $\text{TiCl}_4/\text{LiAlH}_4$  system, explained the mechanism of Ti catalysis by formation of active  $\text{TiAl}_3$  species, extended the applicability of mechanochemical synthesis beyond that proposed by I. Zaluski *et al.*, *J Alloys Comp.* **290**, 71 (1999), and suggested that mechanisms of mechanochemical transformations may be different from those induced by temperature. As a result of this work, we established that mechanochemistry adds a new dimension to the destabilization by chemical substitutions, which is a well-known technique that can be traced back to the studies of J.J. Reilly and R.H. Wiswall, *Inorg. Chem.* **7**, 2254 (1968). In the realm of complex hydrides, most of the current research employs milling only to homogenize chemically doped system, and then equilibrium dehydrogenation-hydrogenation events are triggered by controlling temperature and hydrogen pressure. Our approach, on the other hand, benefits from a stochastic and often nonequilibrium nature of ball milling events, during which the supplied kinetic energy may promote nonequilibrium dehydrogenation (when

performed in inert or low  $P_{\text{H}_2}$  atmosphere) and hydrogenation (in high  $P_{\text{H}_2}$  atmosphere) transformations. The power of mechanochemistry is derived from a combination of the following possible processes: global heating, local melting, reduction of particle size, increase in surface area, generation of fresh surface, formation of defects and dislocations, nonequilibrium phase changes, deformations and strains accompanied by local bond stretching, and mass transport. Some, but not all of these effects may be achieved by controlled nanostructuring, such as self assembly or supporting nanoparticles on rigid mesoporous structures. Indeed, reaching our goals requires a basic understanding of the mechanisms of dehydrogenation-hydrogenation phase transformations occurring in the ball milling vial and in nanostructures, and differences between the mechanically and temperature induced transformations. Alanates, amides and magnesium hydride have been chosen as suitable model systems.

In order to gain insights on the mechanisms of equilibrium dehydrogenation, we led the theoretical effort to explain the site preference of Ti, and clarified that the improved hydrogenation thermodynamics of sodium alanate, which was observed experimentally, originates from the weakening of the Al-H bond. We also demonstrated that defects, which are easily created in a milling vial, such as Na and Al vacancies, have a profound influence on the hydrogen desorption energies and that the vacancies lead to the formation of  $\text{AlH}_3$  clusters. We established that both the nature of the dopant and ball milling time are important parameters that should be optimized in order to achieve a nearly ideal destabilization in a particular system. Similar studies on the dehydrogenation mechanism in the Nb doped  $\text{MgH}_2$  showed that the likely pathway is the substitution of Nb at the Mg sites and the clustering of hydrogen around Nb. Although dehydrogenation from the vicinity of Mg vacancies is exothermic, vacancies are likely to play a lesser role in hydrogen desorption here due to their high formation energies. Density functional calculations also led to the conclusion that the  $\alpha$ -phase of  $\text{Li}_2\text{Mg}(\text{NH})_2$  detected in both X-ray and neutron diffraction data is the ground state. Even though the N-H bond in  $\text{Li}_2\text{Mg}(\text{NH})_2$  is stronger than that in  $\text{Li}_2\text{NH}$ , dehydrogenation of the  $\text{Li}_2\text{Mg}(\text{NH})_2 - \text{LiH}$  system is more favorable thermodynamically than that of the  $\text{Li}_2\text{NH} - \text{LiH}$  system. This counterintuitive result forms a foundation for future discoveries of promising destabilized complex hydrides for hydrogen storage.

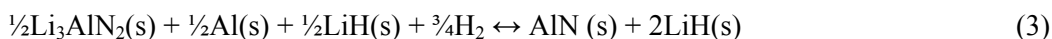
Mechanochemical and thermochemical transformations of  $\text{LiAlH}_4\text{-LiNH}_2$ ,  $\text{LiAlH}_4\text{-NaNH}_2$ ,  $\text{NaAlH}_4\text{-LiNH}_2$ , and  $\text{NaAlH}_4\text{-NaNH}_2$  have been carried out. The overall mechanochemical transformations proceed as follows



(Me = Li, Na) yielding 4.3 to 6.6 wt.% hydrogen, but the actual transformation mechanisms include multiple stages and intermediaries. Unlike mechanochemical reactions, thermochemical transformations proceed differently, considering both the intermediaries and the final products of the reactions. For example, when both Me and Me' are Li, the overall transformation is



Yielding a total of 9 wt.% hydrogen by weight. The products (Eq. 2) were partially rehydrogenated at  $P_{\text{H}_2} = 170$  bar between 230°C and 280°C, and the potential mechanism is shown in Eq. 3. Even though the amount of reabsorbed hydrogen is small (2.6 wt.%), the transformation described by Eq. 3 is reversible.



In addition to the alanate-amide systems described above, several other mixed systems containing Mg have been tested. These include imides and magnesium hydride or magnesium, magnesium hydrides and magnesium nitride, and other.

A recent discovery of non equilibrium synthesis of a number of Al-H clusters, which are analogous to boranes, and a theoretical prediction of their stability supports the idea that direct synthesis of alane is possible under reasonably low hydrogen pressures if a process is carried far

from thermodynamic equilibrium of the overall ( $\text{Al} + 1\frac{1}{2}\text{H}_2 = \text{AlH}_3$ ) hydrogenation reaction. Mechanochemical processing is a nonequilibrium process and it was obvious that direct synthesis of alane in a high pressure ball milling vial needed to be attempted. As a result, we were able to detect formation of as much as 2.4 % of  $\text{AlH}_3$  according to the solid-state NMR and gas volumetric analyses. In addition to showing the feasibility of the direct synthesis of alane, in another experiment we found that mechanochemical solid-state reaction between stoichiometric amounts of  $\text{LiAlH}_4$  and  $\text{FeCl}_2$  (20 min at room temperature) results in the formation of  $\text{LiCl}$ ,  $\text{Fe}$ , X-ray amorphous  $\text{AlH}_3$ , and hydrogen. In this process,  $\text{AlH}_3$  forms in a 96 % yield, which was confirmed by thermogravimetric and gas-volumetric analyses.

Reducing the length scale of a material, i.e. forming a nanostructure, is of special importance in hydrogen research. This occurs because first, the surface energy may become a decisive factor in shifting thermodynamic equilibrium, and second, lowering the size of particles to a few nanometers considerably reduces the distances over which the mass transport must be realized, thus improving the kinetics of complex hydride-hydrogen systems. Various mesoporous carbon structures have been synthesized and 10 to 20% loading of mesoporous carbon with complex hydrides has been demonstrated. The  $^1\text{H}$ - $^{27}\text{Al}$  cross polarization (CP) magic angle spinning NMR of a material impregnated with 10 wt.% of  $\text{LiAlH}_4$  yields a resonance around 70 ppm (99 ppm in a pure  $\text{LiAlH}_4$ ), pointing to a slow dynamics ( $\tau_{\text{CP}} = 600 \mu\text{s}$ ) and modified Al-H bonding. We believe that mesoporous carbons will make model templates (scaffolds) superior to carbon aerogels. The former have well defined structures leading to well defined and controllable geometry of the pores. This makes modeling effort meaningful because the size of the complex hydride cluster may be varied systematically in one, two, or three dimensions, thus guiding the selection of the most beneficial template structures.

### Future Plans

We will continue to rely upon integrating innovative synthetic approaches with state-of-the-art characterization and theoretical modeling. Whereas our general objectives and strategy will remain essentially the same as in the past, several new research directions will be pursued. Our main objectives can be summarized as follows: i) the studies of mechanochemical and temperature induced transformations of mixed systems containing magnesium will be completed by establishing relevant details of their mechanisms; ii) the effort toward direct synthesis of  $\text{AlH}_3$  with higher yields will continue; iii) mechano- and thermo-chemical studies will be extended to include several new systems; iv) the effectiveness of using mechanical energy to create nonequilibrium rehydrogenation pathways under low hydrogen pressures and temperatures will be thoroughly studied; v) we will continue to employ and improve characterization methods, such as gas-volumetric analyses, solid-state NMR spectroscopy, x-ray diffraction, and electron microscopy to determine to the best extent possible the structure and properties of all materials developed in this project; vi) the theoretical modeling will emphasize multi-scale techniques based on density functional theory.

As our knowledge advances, there will be increased emphasis on integrating experiment with theory. We expect that these efforts will guide us toward the discovery of hydrogen-containing solids that would be unattainable using conventional synthetic methods. They will also lead to understanding of thermodynamics and kinetics of dehydrogenation and hydrogenation transformations in these materials.

Systems, which have been studied only preliminarily, will be thoroughly examined in order to establish detailed mechanisms of dehydrogenation transformations and assess their potential for reversibility of hydrogen. Since mechanochemical and thermochemical phase transformations in complex hydride systems progress differently, both will be analyzed in detail using protocols developed in the past. Unlike thermally-induced transformations of pure or doped complex hydrides, ball milling is likely to follow nonequilibrium pathways; details of both are only known

for a few closely related alanate-amide systems, and for others they will be systematically studied experimentally in concert with relevant modeling effort. As our understanding improves, additional binary and ternary model systems containing  $\text{MAlH}_4$ ,  $\text{M}_3\text{AlH}_6$ ,  $\text{MNH}_2$ ,  $\text{M}_2\text{NH}$ ,  $\text{MH}$ , where  $\text{M} = \text{Li, Na, or K}$ ,  $\text{MgH}_2$ ,  $\text{CaH}_2$ ,  $\text{AlH}_3$ , and mixed ionic complex hydrides such as  $\text{Li}_2\text{Mg}(\text{NH})_2$  and  $\text{Na}_{3-x}\text{Li}_x\text{AlH}_6$  will be selected and examined with the purpose of testing the validity of our conclusions and expanding their generality. The pool of systems will be extended to include  $\text{MMgH}_3$  and  $\text{MBH}_4$ , where  $\text{M} = \text{Li and Na}$  as our work progresses. Of particular interest is the observed reversibility of chemically stable  $\text{AlN}$  in the presence of  $\text{LiH}$ . We will, therefore, examine systems containing  $\text{BN}$ ,  $\text{AlN}$ ,  $\text{GaN}$ ,  $\text{LiH}$ , and  $\text{NaH}$  in order to gain a better insight on the mechanisms involved.

Although thermodynamics enables the hydrogenation of complex hydrides, this has generally been achieved in the past mostly *via* solvent-based processes at high hydrogen pressures (sometimes as high as  $10^4$  -  $10^5$  bar). Overcoming high hydrogenation pressures is a critical issue, which requires considerable basic research. The poor kinetics of reactions in complex metal hydride – hydrogen systems is often another limiting step. To overcome kinetic limitations, conventional wisdom calls for increasing the temperature, which, however, requires a further increase of hydrogenation pressure. We will, therefore, use mechanical energy to exploit benefits of nonequilibrium states, facilitate improved kinetics, and provide mass transport required to hydrogenate either partially or fully dehydrogenated complex hydride solids. Results of our research support a vision that non-thermal processing of complex hydrides is a feasible way to achieve acceptable parameters of the hydrogenation stage. Dehydrogenated model systems or appropriate mixtures of known intermediary or final products of dehydrogenation will be subjected to high pressure ball milling experiments that will be carried at and below ambient temperature at  $P_{\text{H}_2}$  reaching 350 bar. Lowering the temperature should shift the equilibrium towards the hydrogenation transformations, and unlike in an autoclave, lowering the temperature in a ball mill does not lead to diminished mass transport due to a suppressed diffusion.

## References

1. S. Li, P. Jena, and R. Ahuja, Effect of Ti and metal vacancies on the electronic structure, stability, and dehydrogenation of  $\text{Na}_3\text{AlH}_6$ : Supercell band-structure formalism and gradient-corrected density-functional theory, *Phys. Rev. B* **73**, 214107 (2006).
2. S. Li, P. Jena, and R. Ahuja, Dehydrogenation mechanism in catalyst-activated  $\text{MgH}_2$ , *Phys. Rev. B* **74**, 132106 (2006).
3. A. Blomqvist, C.M. Araujo, R. Ahuja, and P. Jena, Dehydrogenation from 3d-transition metal doped  $\text{NaAlH}_4$ : Prediction of new catalysts, *Appl. Phys. Lett.* **90**, 141904 (2007).
4. Ya. Mudryk, Y. Lee, T. Vogt, K. A. Gschneidner, Jr., and V. K. Pecharsky, "Polymorphism of  $\text{Gd}_5\text{Si}_2\text{Ge}_2$  – the equivalence of temperature, magnetic field, and chemical and hydrostatic pressures", *Phys. Rev. B* **71**, 174104 (2005).
5. C.M. Araujo, R.H. Scheicher, P. Jena, and R. Ahuja, On the structural and energetic properties of the hydrogen absorber  $\text{Li}_2\text{Mg}(\text{NH})_2$ , *Appl. Phys. Lett.* **91**, 091924 (2007).
6. O. Dolotko, H. Zhang, O. Ugurlu, J.W. Wiench, M. Pruski, L.S. Chumbley, and V.K. Pecharsky, Mechanochemical transformations in  $\text{Li}(\text{Na})\text{AlH}_4$ - $\text{Li}(\text{Na})\text{NH}_2$  systems, *Acta Mater.* **55**, 3121 (2007).
7. O. Dolotko, H. Zhang, Z. Qin, J. Wiench, M. Pruski, L.S. Chumbley, and V.K. Pecharsky, Mechanochemistry of the  $\text{MNH}_2$  –  $\text{MgH}_2$  systems ( $\text{M} = \text{Li or Na}$ ), *Acta Mater.* Submitted.
8. X. Li, A. Grubisic, S.T. Stokes, G.F. Gantefor, K.H. Bowen, K. Boggavarapu, M. Willis, P. Jena, R. Burgert, and H. Schnockel, Unexpected stability of  $\text{Al}_4\text{H}_6$ : A borane analog?, *Science* **315**, 356 (2007).
9. B. Kiran, P. Jena, X. Li, A. Grubisic, S.T. Stokes, G.F. Gantefor, K. Bowen, R. Burgert, and H. Schnokel, A magic rule for  $\text{Al}_n\text{H}_m$  magic clusters, *Phys. Rev. Lett.* **98**, 256802 (2007).
10. A. Grubisic, X. Li, S.T. Stokes, J. Cordes, G.F. Gantefor, K. Bowen, B. Kiran, P. Jena, R. Burgert, and H. Schnokel, Closo-alanes ( $\text{Al}_4\text{H}_6$ ,  $\text{Al}_n\text{H}_{n+2}$  ( $4 \leq n \leq 8$ )): A new chapter in aluminum hydride chemistry", *J. Am. Chem. Soc.* **129**, 5969 (2007).

## **THERMODYNAMIC AND KINETIC STUDIES ON HIGH TEMPERATURE PROTON CONDUCTORS USING THIN FILMS AND POROUS BODIES**

DOE Grant Number: DE-FG02-06ER46086

Prof. Anil V. Virkar  
Department of Materials Science & Engineering  
122 S. Central Campus Drive  
University of Utah  
Salt Lake City, UT 84112  
Phone: (801) 581-5396  
Email: [anil.virkar@m.cc.utah.edu](mailto:anil.virkar@m.cc.utah.edu)

Graduate Students Currently Supported on the Project: Hyung-Tae Lim, Ravikanth Abbaraju, and James Wright.

**Program Scope:** The principal objective of this work is to investigate thermodynamic and kinetic properties of complex oxides having multiple mobile species, with principal emphasis on high temperature proton conductors (HTPC). Typical HTPC materials are alkaline earth containing perovskites doped to create oxygen vacancies. When heated in atmospheres containing water vapor, some of the oxygen vacancies are filled up by absorbing water vapor and releasing mobile protons into the structure. Such materials thus can transport three electrically charged species; namely oxygen ions ( $O^{2-}$ ) by a vacancy mechanism, protons ( $H^+$ ) by a hopping mechanism and electron holes (h). Depending upon externally imposed conditions (atmospheres, electrical load), net transport of charged species (electrical current) as well as transport of neutral species ( $H_2$ ,  $O_2$ , and  $H_2O$ ) can occur through such materials. The reported studies on such materials have usually been on bulk samples, typically several millimeters in thickness. The applications of these materials for such as electrochemical devices as fuel cells, hydrogen and oxygen separation membranes, electrolyzers, etc., however, involve the use of thin films (a few microns in thickness) to minimize the internal resistance. Measurements made on bulk samples often are not representative for applications in a thin film form since slow kinetics prevents the measurement of properties under thermodynamically equilibrated conditions on thick samples. Lack of the attainment of thermodynamic equilibrium can lead to large errors making it difficult to measure ‘true’ properties. For example, diffusion coefficients measured on bulk samples are often orders of magnitude different from ‘true’ values measured under thermodynamically equilibrated conditions. One aspect of the current work is on the measurement of properties under thermodynamically equilibrated conditions. This is achieved by making measurements on porous bodies and/or thin films. It is shown, for example, that in cases wherein the sample exchanges certain species with the gas phase (e.g. oxygen, water vapor, hydrogen), the measurement of physical properties on porous samples gives true values. A case in point is the thermoelectric power. Our experiments/analysis have shown that reliable measurements of thermoelectric power are often difficult to make on dense bulk samples of oxides. However, this can be readily achieved using porous samples. Since

many properties depend upon sample stoichiometry, this conclusion is general and applicable to many other properties.

Measurement of transport properties and the attainment of equilibrium in thin films and membranes, as used for many devices, must also include the role of interfaces. Measurement of transport properties on bulk samples, as has been the practice, makes it difficult (and often impossible) to account for the role of surfaces and interfaces. A case in point is a thin film fuel cell in which often the performance characteristics are almost completely dictated by interfaces. Thus, the measurement of transport properties of interfaces is important. Also, what occurs at the interfaces dictates the fundamental stability of the membrane. Techniques such as impedance spectroscopy are insufficient to address many transport-related issues as they cannot resolve effects of parallel transport of minority defects. Thus, while many reports on the measurement of surface and interfacial properties have been published, often it is not possible to draw reliable conclusions when the same materials are used in a thin film form in electrochemical devices. This necessitates the development of measurement techniques and analysis which allow a study of thin films in actual electrochemical devices, while also addressing the fundamental stability of the membrane. The measurement of properties in solid state electrochemical devices also presents particular challenges since unlike typical electronic devices in which the only moving species are electrons (and/or holes), in electrochemical devices the principal mobile species are ionic. Associated with their movement are changes in volume, especially when electrochemical reactions occur. One aspect of the work is on the investigation of thermodynamic and kinetic properties using thin films. This has necessitated the development of embedded reference electrodes, which allow the measurement of chemical potentials of neutral species. Using this technique, it has now become possible to measure, for example, oxygen chemical potential in thin film solid oxide fuel cells.

**Recent Progress:** Our recent progress in four areas is briefly described in what follows.

**a) Theoretical Analysis of A Fuel Cell Based on Mixed Proton, Oxygen Ion, and Electron Hole Conductors:** Theoretical analysis of a fuel cell using an HTPC with three mobile species is underway. The analysis is based on the usual assumption of local thermodynamic equilibrium. It is shown that local thermodynamic equilibrium, the fundamental assumption made in all reported studies to date, suggests that it is more convenient to use internal EMFs in the representative equivalent circuit rather than capacitors. Using this model, an equivalent circuit is developed which includes multiple internal EMFs, uniquely related to the respective local thermodynamic equilibria. The interfacial regions are also described in terms of internal EMFs and resistances. Eventual experimental work will involve the use of embedded electrodes to measure chemical potentials of neutral species. This work is being performed by the PI, Anil Virkar.

**b) Measurement of Chemical Potential of Oxygen in Thin Film Solid Oxide Fuel Cells:** Externally measured current through a fuel cell is primarily due to the ionic flux that occurs through the electrolyte, which is related to ionic conductivity of the electrolyte and gradient in oxygen ion electrochemical potential. The magnitude of the current or the

gradient in electrochemical potential of oxygen has no direct relationship to the stability of the electrolyte. Virtually all published work on fuel cells is on performance measurements and on degradation but only as judged on the basis of performance loss. Our work has shown that a fundamental source of degradation is related to local thermodynamic instabilities, which are actually transport-induced. These in principle can be investigated using embedded reference electrodes, which facilitate the measurement of oxygen chemical potential. We have recently developed techniques to embed reference electrodes in electrolyte films on the order of 20 to 40 microns in thickness. Using this approach, actual measurements of oxygen chemical potential are made during cell operation. The measurements show that there are situations in which the chemical potential can lie outside the stability range of the membrane leading to local thermodynamic instability and cell degradation. This work has profound implications concerning degradation of fuel cell stacks. This work is being performed by Mr. Hyung-Tae Lim, a graduate student working towards a Ph.D.

c) Measurement of Stoichiometry-Thermodynamic Properties using an Electrochemical Technique: Most complex oxides exhibit deviation from stoichiometry, which is a function of temperature and oxygen partial pressure. Often the changes are minute and difficult to measure gravimetrically. Also, measurements on bulk samples are generally inaccurate due to sluggish transport kinetics. In order to circumvent these difficulties, a new electrochemical cell is being devised. It consists of an enclosed chamber made of an oxygen ion conductor such as yttria-stabilized zirconia (YSZ). The desired sample, as a porous body, is placed inside the chamber. Two sets of electrodes are placed on the chamber walls; one set for electrochemical pumping and the other set for potentiometric sensing. The experimental procedure consists of electrochemically pumping oxygen in or out, measuring the net coulombs passed through the external circuit, and measuring the oxygen partial pressure in the chamber. These measurements allow experimental determination of the relationship between oxygen non-stoichiometry and oxygen partial pressure (or oxygen chemical potential). Current work is on rare earth oxide-doped ceria and will be expanded to include perovskites. This work is being performed by Mr. James Wright, a graduate student working towards a Ph.D.

d) Ceramic-Polymer Composite Membranes for Fuel Cells: Considerable work has been reported on the development of membranes for low temperature fuel cells. Nafion-based membranes are excellent proton conductors, but undergo dehydration above about 100°C. HTPC membranes are not conductive enough, and must be heated to about 500°C (or higher) to be effective. In the case of polymeric membranes, the challenge is to develop membranes that are stable at high enough temperatures (over 150°C, and preferably as high as 200°C) and retain moisture. In HTPC membranes, the challenge is to develop materials with sufficient protonic conductivity at low enough temperatures. Several researchers have demonstrated that the addition of inorganic fillers to Nafion (or other proton conducting polymeric materials) increases high temperature stability and performance. The inorganic fillers increase the water retention capability, while Nafion provides pathways for proton conduction. That is, a combination of inorganic fillers and Nafion leads to a synergetic effect. We are investigating the effect of nanosize oxide additions to Nafion and other polymeric proton conductors on transport. The focus is on

surface chemistry and defect chemistry of the oxides and their effect on transport. This work is being performed by Mr. Ravakanth Abbaraju, a graduate student working towards a Ph.D.

**Future Plans:** (1) Theoretical work on mixed proton, oxygen ion, and electron hole conductors will be extended to general theory of multi-species transport including the role of interfaces. Main emphasis will be on determining the conditions of stability. (2) Measurement of oxygen chemical potential in anode-supported fuel cells using multi-layer electrolytes. Extension of the work to determine the conditions of instability, and their implications to fuel cell stack degradation. (3) Investigation of thermodynamic and kinetic properties of complex oxides using porous samples. (4) Investigation of the role of nanosize oxides on the transport properties of composite proton conductors.

**List of Publications:**

- 1) W. Wang and A. V. Virkar, "Ionic and Electron-Hole Conduction in  $\text{BaZr}_{0.93}\text{Y}_{0.07}\text{O}_{3-\delta}$  by 4-Probe DC Measurements", *J. Power Sources*, **142** 1-9 (2005).
- 2) A. S. Patnaik and A. V. Virkar, "Transport Properties of Potassium-Doped  $\text{BaZrO}_3$  in Oxygen and Water Vapor Containing Atmospheres", *J. Electrochem. Soc.*, **153** (7) A1397-A1405 (2006).
- 3) R. Ganeshanathan and A. V. Virkar, "Measurement of Transport Properties by Conductivity Relaxation on Dense  $\text{La}_{0.6}\text{Sr}_{0.4}\text{CoO}_{3-\delta}$ : With and Without Porous Surface Layers", *J. Electrochem. Soc.*, **153** (12) A2181-A2187 (2006).
- 4) H-T. Lim and A. V. Virkar, "Thermoelectric Power of Gd-doped  $\text{CeO}_2$  ( $\text{Gd}_{0.1}\text{Ce}_{0.9}\text{O}_{2-\delta}$ ) (GDC10): Measurements on Porous Bodies", *J. Power Sources*, **161** 676-684 (2006).
- 5) H-T. Lim and A. V. Virkar, "Thermoelectric Power of Silver and a Proton Conductor: Measurements on Dense and Porous Samples", *J. Electrochem. Soc.*, **154** (1) B25-B31 (2007).
- 6) A. V. Virkar and Y. Zhou, "Mechanism of Catalyst Degradation in Proton Exchange Membrane Fuel Cells (PEMFC)", *J. Electrochem. Soc.*, **154** (6) B540-B547 (2007).
- 7) A. V. Virkar, "A Model for Solid Oxide Fuel Cell (SOFC) Stack Degradation", *J. Power Sources*, **172** 713-724 (2007).
- 8) H-T. Lim and A. V. Virkar, "Measurement of Oxygen Chemical Potential in Thin Electrolyte Film, Anode-Supported Solid Oxide Fuel Cells", Accepted for Publication, *J. Power Sources*, (2008).

## Elucidation of Hydrogen Interaction Mechanisms with Metal-Doped Carbon Nanostructures

Ragaiy Zidan, Polly Berseth, Ashley Stowe  
Savannah River National Laboratory  
Aiken, South Carolina 29808 USA

E. mail: [ragaiy.zidan@srnl.doe.gov](mailto:ragaiy.zidan@srnl.doe.gov)

Our work was planned and performed to support the Hydrogen Fuel Initiative along two independent paths; the first was to investigate hydrogen interaction with carbon nanostructures and in particular metal doped carbon nanotubes, the second path was to develop a fundamental understanding of the mechanistic aspects of the formation and decomposition of complex hydrides.

The research work was aimed at obtaining a fundamental understanding at the nanoscale level of hydrogen sorption behavior with Carbon Nanostructures. The experimental work is closely linked to relevant modeling studies of these materials. Our effort was focused on understanding the hydrogen interaction mechanisms such as physisorption, weak covalent bonding, and chemisorption in these nano-carbon systems.

The program involved investigating the thermodynamics governing formation of complex metal hydrides via ball milling and molten state processing techniques. Synthesized materials— $M(\text{AlH}_4)_x$ ;  $MM'H_3$ ;  $M_xM'_{3-x}\text{AlH}_6$ — have been investigated by spectroscopic tools including nuclear magnetic resonance (NMR), neutron scattering, and X-ray diffraction. Phonon vibrations and the effect of the catalyst on the local lattice structure were investigated by incoherent inelastic neutron scattering (IINS) spectroscopy. Pressure effects on the structure of metal hydride materials were analyzed with high pressure XRD and Raman instrumentation.

Although our research work was conducted as two independent efforts during our research activities we recognized that these nanostructure carbon systems are ideal systems for investigating the catalytic effect of metallic dopants on the formation and decomposition of complex hydride materials. Our work led to the finding that certain graphitic systems can catalyze the formation and decomposition of sodium aluminum hydride. We have shown that nano graphitic systems (e.g.  $\text{C}_{60}$  and carbon nanotubes) can be very efficient catalysts that cause  $\text{NaAlH}_4$  to be reversible even when a metal dopant was not detectable.

### Studying H<sub>2</sub>/CNT interactions

- We hypothesized that H<sub>2</sub>/carbon nanostructures interactions are diameter dependent
- Challenging to verify because CNT are synthesized with a large diameter dispersion
- Collaboration with A. Rao and Dr. J. Gaillard at Clemson University; we developed a method of attaching a single carbon nanotube, or a small array of nanotubes to act as a cantilever for harmonic detection of resonance (HDR). See Fig. 1.
- This array is used to distinguish between possible interaction such as H<sub>2</sub>, D<sub>2</sub> and H-D

### Single Carbon Nanotube (CNT) Cantilever

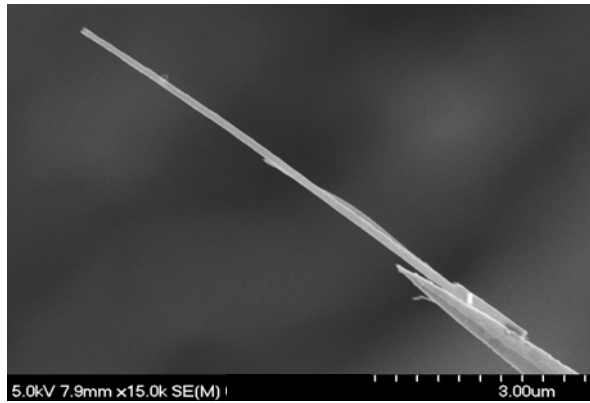


Fig.1

### Preliminary results on catalyzing the Reversibility of NaAlH<sub>4</sub> with Carbon

- NaAlH<sub>4</sub> is the most studied complex hydride material for vehicle applications
- CNT were reported to improve the properties of NaAlH<sub>4</sub>
- Details and mechanism of this improvement are not known
- We've been examining various diameter CNT, graphite and C<sub>60</sub>
- Graphite additive aids hydrogenation, but less than the curved graphitic carbon (e.g. C<sub>60</sub> and CNT)
- Exciting results as CNT production involves nano-particles of metals, which could also be adding to catalyzing reaction and producing reversible complex hydrides- future work on this aspect is planned- See Fig.2

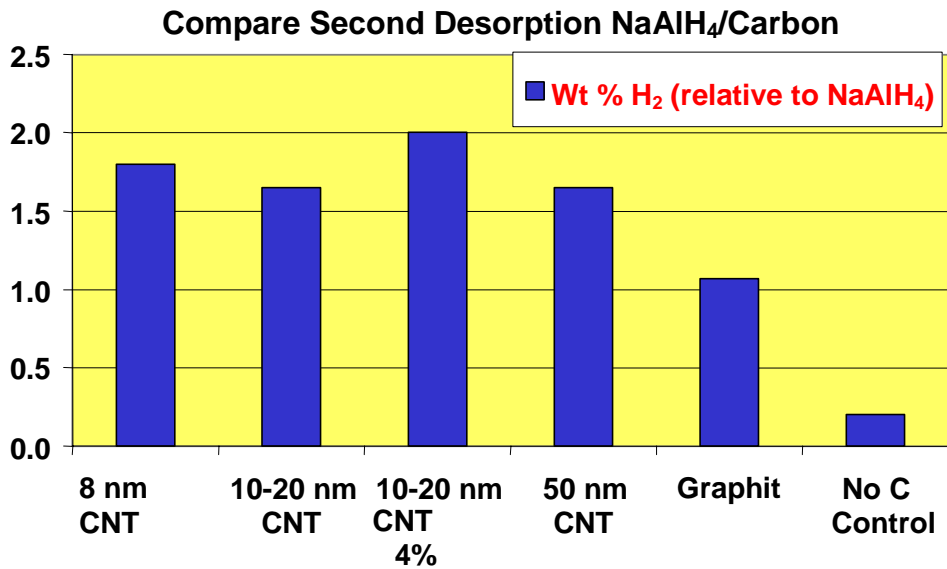


Fig.2

Developing a fundamental understanding of these catalytic effects can have a tremendous impact on the basic understanding of the role of catalysts in enhancing the kinetics of complex hydrides, the formation of intermediates and explain what facilitates their mass transport to form these hydrides. Based on our recent results we believe that further studies are needed to explain the uniqueness of hydrogen interaction with carbon nanostructures and utilize this understanding to explain the role of nano-catalysts in the formation and decompositions of complex hydrides. Our effort was also supported by atomistic modeling *ab initio* calculations to explain the mechanism of these kinetic enhancements.

### Mechanistic Aspects of the Formation and Decomposition of Complex Hydrides

NaMgH<sub>3</sub> was used as model compound to understand the formation of novel complex hydrides. IINS vibrational spectrum study at 10 K indicated new finding that two phases coexist with disorder and two distinct hydrogen sites within the material see Fig 3. NMR studies discovered a captivating and unexpected phenomenon where the proton motion in NaMgH<sub>3</sub> is much faster than in either of the binary constituents. Structural studies of NaAlH<sub>4</sub> have also been conducted at elevated pressures in collaboration with FIU a high pressure phase transition was discovered in unmilled NaAlH<sub>4</sub> at 6.35 GPa followed by amorphization at 13 GPa.

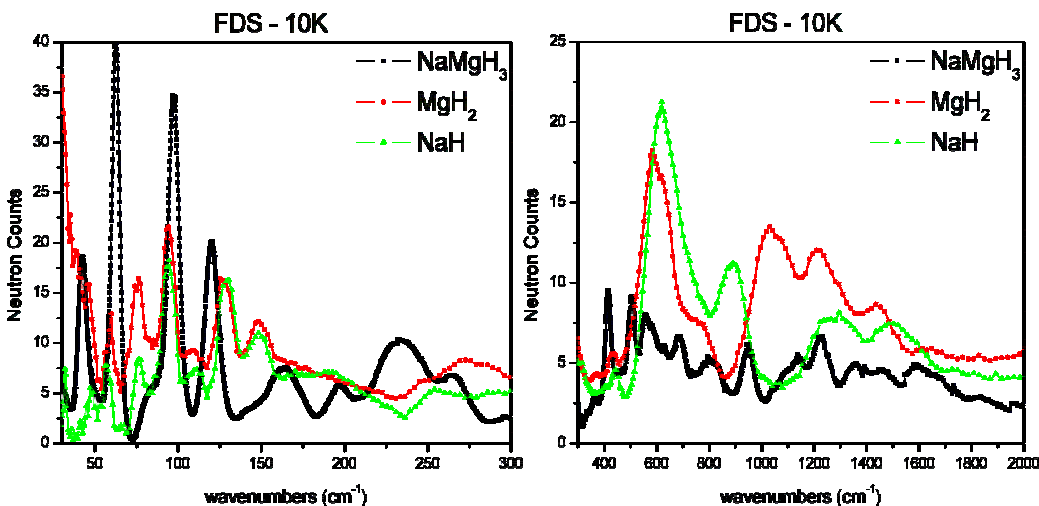


Fig. 3

### Future Work:

Our future work will continue to support the Hydrogen Fuel Initiative through the development of a basic understanding of the formation and decomposition of complex hydride materials. The study will be the first comprehensive study of its kind that is aimed at understating the nature of hydrogen bonding with Carbon Nanostructure and their role as catalysts. Carbon nanostructures (e.g. Metal Doped Carbon Nanotubes and fullerenes) will be studied to for their catalytic effect that we recently realized and they will be also utilized in investigating the role catalysts play in enhancing both hydrogenation and dehydrogenation in complex hydrides. Our goal is to determine the basic mechanism of formation, phase transition and decomposition of these hydrides and the role of catalysts/dopant on enhancing hydrogen release and more importantly making it possible to reverse some of these hydrides.

We expect that a steady stream of results will be generated from this work. Hydrogen storage in carbon system and complex hydrides offers promising materials for energy applications due to their high capacity, the potential of reduced heats of adsorption/desorption.

## Publications

1. G. E. Keskar, Bevan; Gaillard, Jay; Skove, Malcolm J. ; Serkiz, S. M.; Rao, A. M., *Sensors and Actuators A* (submitted)
2. C. Stowe, P. A. Berseth, T. P. Farrell, L. Laughlin, D. Anton, and R. Zidan, *Journal of Alloys and Compounds, In Press, Accepted Manuscript* (2007)
3. Jun Wang, Armin D. Ebner, Tanya Prozorov, Ragaiy Zidan and James A. Ritter *Journal of Alloys and Compounds*, Volume 395, Issues 1-2, 31 May 2005, Pages 252-262
4. Vennila, Drozd, V., George, L., Saxena, S., Liermann, P., Liu, H., Stowe, A. C., Anton, D., Zidan, R., *Journal of Alloys and Compounds* (submitted)
5. Kiran, A. K. Kandalam, and P. Jena, *The Journal of Chemical Physics* 124, 224703-6 (2006)
6. Q. Sun, P. Jena, Q. Wang, and M. Marquez, *J. Am. Chem. Soc.* 128, 9741-9745 (2006)
7. Q. Sun, Q. Wang, P. Jena, and Y. Kawazoe, *J. Am. Chem. Soc.* 127, 14582-14583 (2005)
8. Q. Sun, Q. Wang, P. Jena, B. V. Reddy, and M. Marquez, *Chem. Mater.* 19, 3074-3078 (2007)
9. S. J. Li, P., *Physical Review Letters* 97, 209601 (2006).

**Session V: Magnetism / Spintronics**

# Extraordinary Responsive Magnetic Rare Earth Materials

## Bonding, crystallography and magnetism in complex intermetallic compounds

K.A. Gschneidner, Jr. (presenting), V.K. Pecharsky, L.S. Chumbley, T.A. Lograsso, G.J. Miller, A.I. Goldman, B.N. Harmon, and R.J. McQueeney

Ames Laboratory, Iowa State University, Ames, IA 50011-3020; e-mail [cagey@ameslab.gov](mailto:cagey@ameslab.gov)

### Program Scope

A major goal of this program is to uncover the underlying electronic, atomic and microscopic interactions that result in an extraordinarily strong coupling between the magnetic and crystal lattices, and remarkable responsiveness to both strong (temperature and pressure) and weak (magnetic field) triggers in selected model rare earth intermetallic material systems. We focus on the state-of-the-art synthesis, processing and characterization, combined with theory, modeling and computations gauged and refined against reliable experimental data. The model systems include GdNi and other equiatomic RM compounds (R is a rare earth metal and M is a 3d transition metal or a main Group 14 element),  $RAI_2$ ,  $RCo_2$ ,  $La(Fe_{1-x}Si_x)_{13}$  and its hydrides  $La(Fe_{1-x}Si_x)_{13}H_y$ , and  $R_5T_4$  compounds (T is a main Group 14 element). These materials exhibit a number of diverse and unique properties associated with magnetic ordering alone, magneto-volume effect, itinerant electron metamagnetic, and magnetic-martensitic transformations, respectively, which may or may not be driven by a reversible breaking and reforming of specific chemical bonds. Development and validation of phenomenological models of transformations that range from magneto-volume to magnetic-martensitic is another goal, thus guiding future discoveries of material systems exhibiting strong reactions to small changes of magnetic field, with temperature and pressure providing additional sources of stimulation.

### Recent Progress

Composition and structure are critical factors determining the physical properties of intermetallic compounds, but the dominance of metallic bonding often leads to close packed or related structures with no directionality in the chemical bonding. Identifying critical pair-wise interatomic interactions, therefore, is a major challenge and one needs sophisticated and computationally accurate electronic structure methods to relate structure and properties. Despite crystallographic complexity, peculiar structural features of the  $R_5T_4$  family have been connected to systematic variations of physical properties. Once identified, structure-property relationships have predictive powder providing a foundation towards future discoveries in this and other model systems. Below, we describe only a few examples that are related to our recent progress in understanding of the relationships between chemical bonding, crystallography and magnetism of complex intermetallic compounds.

All  $R_5T_4$  compounds are self-assembled multi-layers, formed by subnanometer-thick, remarkably robust two-dimensional slabs, the stacking of which varies with composition (R, T), temperature ( $T$ ), pressure ( $P$ ), and magnetic field ( $H$ ), thus defining their most interesting and unique physics. In the orthorhombic  $Gd_5Si_4$ -type, also known as O(I), the T-atoms located on the surfaces of the slabs form short (2.6 Å), covalent-like  $T_2$  dimers, thus enabling strong interslab interactions propagating along the  $b$ -axis. The “long” T-T distances, are ~5.4 Å. Next, is the monoclinic  $Gd_5Si_2Ge_2$ -type (M), in which the interslab interactions are nonuniform. The short  $T_2$  dimers are only found between every other slab, and therefore, strong interactions are limited to pairs of neighboring slabs. The weakly interacting pairs have better balanced T-T distances, i.e. ~3.5 and 4.5 Å vs. ~2.6 and 5.4 Å for the short and long T-T contacts, respectively. The third is the orthorhombic  $Sm_5Ge_4$ -type variant, also known as O(II). The uniformity of the interslab

interactions is restored, but strongly bonded interslab  $T_2$  dimers are no longer present. Finally, in the  $Tm_5Si_2Sb_2$ -type – O(III) – all interslab interactions and all the T-T distances are identical.

By coupling the electronic structure with magnetothermodynamic models for finite temperature we have studied the magnetostructural transition of  $Gd_5Si_2Ge_2$ . This approach leads to a good agreement with already established experimental results of the magnetostructural transition. Our analysis shows that the electronic structure method which takes into account strong Coulomb correlations within the framework of scalar relativistic (no spin orbit coupling) band theory works reasonably well for this system. The use of a nonlocal exchange correlation functional with the electronic structure LSDA+U method works better as compared to the local exchange correlation functional, giving a better estimate of the magnetostructural transition temperature and other magnetic properties of  $Gd_5Si_2Ge_2$ . Our study shows lower value of total energy in the O(I) phase compared to the M phase, which confirms stability of the orthorhombic phase at low temperature. The calculated magnetic moments of the Gd atoms in this compound are larger in the orthorhombic phase than in the monoclinic phase. The variability of the magnetic moments of different Gd atoms within same phase or different phases is mostly due to the changing contribution from  $5d$  electrons of Gd atoms. The magnetic exchange coupling energy of the orthorhombic phase is higher than that of the monoclinic phase.

A collaboration between Ames and Argonne National Laboratories has revealed key atomic-level information about  $Gd_5(Si_xGe_{4-x})$  materials. In addition to the expected strong magnetization of gadolinium ions, a significant induced magnetization of the germanium ions has been detected experimentally and confirmed theoretically. This discovery is counterintuitive, yet it explains the origin of the unprecedented magneto-responsiveness by (dis)appearance of magnetic Gd-Ge-Ge-Gd bridges that cause magnetic (dis)ordering during the field induced structural transition. It also opens up a range of new opportunities for the design of novel magnetic materials due to the potential for enhancing magnetic interactions between the rare-earth metals by employing nominally nonmagnetic elements. The discovery has been made possible by using the ultra-pure materials prepared in Ames and high-brilliance, circularly-polarized X-rays at the Advanced Photon Source to probe the magnetism of gadolinium and germanium ions.

An unexpected feature has been found in  $Er_5Si_4$ , where a structural transition in the true paramagnetic (PM) state is affected by  $H$ . Both the heat capacity peak and the underlying crystallographic transformation at  $\sim 220$  K between the low temperature M- $Er_5Si_4$  and high temperature O(I)- $Er_5Si_4$  are suppressed nearly linearly by  $H > 40$  kOe at the rate  $dT_{M \rightarrow O(I)}/dH = -0.058$  K/kOe. To the best of our knowledge, to date there have been no reports that a relatively weak  $H$  is able to measurably affect the temperature of a crystallographic transition in the PM state, i.e.  $\sim 200$  K above the spontaneous magnetic ordering temperature.

DC magnetization studies on the  $Er_{0.75}Dy_{0.25}Al_2$  compound reveal a ferromagnetic ordering at 25 K followed by a transition at 10 K, which is marked by a strong thermal hysteresis in low fields. In the PM state, just above the  $T_C$ , a Griffiths-like phase is observed. The ac magnetic susceptibility and the magnetic relaxation data bear signatures of a glassy state below  $T_C$  which is attributed to the presence of competing single ion anisotropies of  $Er^{3+}$  and  $Dy^{3+}$  randomly distributed in the crystalline lattice. The X-ray diffraction studies on  $Er_{0.75}Dy_{0.25}Al_2$  confirm that there is no structural transition over the temperature range 5-300 K. Thus, the peak at 10 K has no structural origin. This has further been ascertained by the lack of thermal hysteresis the electrical resistivity. These results are consistent with the assumption that strong quadrupolar interactions play an important role in the formation of the first order phase transition at 10 K in  $Er_{0.75}Dy_{0.25}Al_2$ .

## Future Plans

Described above is the only study that we are aware of indicating that peculiar structural and bonding changes between nonmagnetic atoms may play a role in defining magnetism of the rare

earth sublattice by inducing measurable magnetic moments on conventionally non-magnetic sites. Much more experimental data need to be collected and analyzed, including other representatives of the  $R_5T_4$  family, especially  $Tb_5Si_{1.8}Ge_{2.2}$ ,  $Dy_5SiGe_3$  and  $Er_5Ge_4$ . An interesting question also arises about the role of a single 5d electron of La in influencing magnetism of  $Fe_{12}$  clusters in  $La(Fe_xSi_{1-x})_{13}$ , which will be answered through a combined experimental and theoretical XMCD study. We believe that our expertise in coupling XMCD experiments with first principles theory positions us well for a rapid progress in understanding the broader role, traditionally nonmagnetic atoms are playing in rare earth magnetism.

At present we do not have sufficient data to fully understand the mechanism of field effect on the crystal structure of paramagnetic  $Er_5Si_4$ , yet we believe that it may be related to both the large magnetic moment of Er and strong spin-orbit coupling influenced by crystalline electric field effects. Thermal expansion studies carried under hydrostatic pressure indicate that the structural-only transformation has an extraordinary high pressure dependence, i.e.  $dT_{M \rightarrow O(I)}/dP = -30$  K/kbar, and therefore, supports an assumption that even a minuscule field-induced strain in the paramagnetic state may be sufficient to measurably affect the structural-only transformation. We also believe that the effect of the magnetic field on this polymorphic transformation that does not involve magnetic order should be highly anisotropic. We have initiated a thorough investigation of recently prepared single crystals (only polycrystalline samples have been studied to date). A different, yet potentially related issue is an extreme sensitivity of the  $Er_5Si_4$  structures to small concentrations of interstitial impurities (none of the  $Er_5Si_4$  compounds prepared using commercial grade 99.9% pure Er metal adopts the M allotrope). Controlled impurity additions (e.g. hydrogen or carbon) will be initiated to determine the role of phase volume change on the stability of O(I) and M modifications of  $Er_5Si_4$ .

Theory and modeling will be fully incorporated with experimental results employing both theoretical solid state physics and quantum chemistry as two essential parts. The first part is an analysis of electronic structure and magnetic properties at absolute zero temperature from first principles theory and the second part is for analyzing the chemical bonding factors influencing structure-property relationships. Our experience with  $Gd_5Si_2Ge_2$  proves that  $R_5T_4$ , RM and  $RCO_2$  systems are challenging for a standard approach such as the local spin density approximation (LSDA) due to the presence of highly localized 4f-electrons, and therefore, the inclusion of onsite Coulomb parameter, U, on R atoms is a must. Thus, employing LSDA+U in  $Gd_5Si_2Ge_2$  leads to a remarkable improvement in the predicted electronic structure and magnetic properties. Simultaneous application of improved first principles methods and quantum chemical approaches therefore should provide consistent insights enabling basic understanding of the complex interplay between crystal structure, magnetic interactions, and chemical bonding in a diverse pool of systems.

## References

1. Y. Mozharivskyj, A.O. Pecharsky, V.K. Pecharsky, and G.J. Miller, "On the high-temperature phase transition of  $Gd_5Si_2Ge_2$ ," J. Am. Chem. Soc. **127**, 317 (2005).
2. A.L. Lima, A.O. Pecharsky, K.A. Gschneidner, Jr., V.K. Pecharsky, T.A. Lograsso, and D.L. Schlagel, "Magnetic properties of single crystal  $DyAl_2$ ", Phys. Rev. B. **72**, 024403 (2005).
3. Ya. Mudryk, Y. Lee, T. Vogt, K. A. Gschneidner, Jr., and V. K. Pecharsky, "Polymorphism of  $Gd_5Si_2Ge_2$  – the equivalence of temperature, magnetic field, and chemical and hydrostatic pressures", Phys. Rev. B **71**, 174104 (2005).
4. K. Ahn, A.O. Tsokol, Yu. Mozharivskyj, K. A. Gschneidner, Jr., and V. K. Pecharsky, "Phase relationships, and structural, magnetic and thermodynamic properties of the  $Yb_5Si_4 - Yb_5Ge_4$  pseudobinary system", Phys. Rev. B **72**, 054404 (2005)
5. Ya. Mudryk, A. P. Holm, K. A. Gschneidner, Jr., and V. K. Pecharsky, "Crystal structure – magnetic property relationships of  $Gd_5Ge_4$  examined by *in situ* x-ray powder diffraction", Phys. Rev. B **72**, 064442 (2005).

6. T. A. Lograsso, D. L. Schlagel and A. O. Pecharsky, "Synthesis and characterization of single crystalline  $Gd_5(Si_xGe_{1-x})_4$  by the Bridgman method," *J. Alloys Compd.* **393**, 141 (2005).
7. W. Wu, A.O. Tsokol, K.A. Gschneidner, Jr., and J.A. Sampaio, "Influence of oxygen on the giant magnetocaloric effect of  $Gd_5Si_{1.95}Ge_{2.05}$ ," *J. Alloys Compd.* **403**, 118 (2005).
8. O. Ugurlu, L.S. Chumbley, D. L. Schlagel, T. A. Lograsso, and A.O. Tsokol, "Identification of thin plates seen in  $R_5(Si_xGe_{1-x})_4$  alloys, where R is Gd, Tb, Dy, and Er," *Scr. Mater.* **53**, 373 (2005).
9. O. Ugurlu, L.S. Chumbley, D. L. Schlagel, and T. A. Lograsso, "Characterization of an atypical Widmanstätten structure in  $Gd_5Si_2Ge_2$  alloys," *Acta Mater.* **53**, 3525 (2005).
10. O. Ugurlu, L. S. Chumbley, D. L. Schlagel, T. A. Lograsso, and A. O. Pecharsky, "Characterization of  $R_5(Si_xGe_{1-x})_4$  Alloys, where R is Gd, Tb, Dy, and Er," *Light Metals 2005*, H. Kvande, Ed. (The Minerals, Metals & Materials Society, TMS, Warrendale, PA 2005) p. 1181.
11. D. L. Schlagel, T. A. Lograsso, A. O. Pecharsky, and J. Sampaio, "Crystal growth of RE-Si-Ge magnetocaloric materials," *Light Metals 2005*, H. Kvande, Ed. (The Minerals, Metals & Materials Society, TMS, Warrendale, PA 2005) p. 1177.
12. D. Paudyal, V.K. Pecharsky, K.A. Gschneidner, Jr., and B.N. Harmon, "Electron correlation effects on magnetostructural transition and magnetocaloric effect in  $Gd_5Si_2Ge_2$ ," *Phys. Rev. B* **73**, 144406 (2006).
13. C. Ritter, C. Magen, L. Morellon, P.A. Algarabel, M.R. Ibarra, V.K. Pecharsky, A.O. Tsokol, and K.A. Gschneidner, Jr., "Magnetic and crystallographic structures of  $Er_5(Si_xGe_{1-x})_4$ ," *J. Phys.: Condens. Matter* **18**, 3937 (2006).
14. A. Chernyshov, Ya. Mudryk, V.K. Pecharsky, and K.A. Gschneidner, Jr., "Structural and magnetothermal properties of the  $Gd_5Sb_xGe_{4-x}$  system," *J. Appl. Phys.* **99**, 08Q102 (2006).
15. C. Magen, L. Morellon, Z. Arnold, P.A. Algarabel, C. Ritter, M.R. Ibarra, J. Kamarad, A.O. Tsokol, K.A. Gschneidner, Jr., and V.K. Pecharsky, "Effects of pressure on the magnetic and crystallographic structure of  $Er_5Si_4$ ," *Phys. Rev. B* **74**, 134427 (2006).
16. C. Magen, C. Ritter, L. Morellon, P.A. Algarabel, M.R. Ibarra, A.O. Tsokol, K.A. Gschneidner, Jr., and V.K. Pecharsky, "Magnetic-field-induced structural transformations in  $Er_5Si_4$ ," *Phys. Rev. B* **74**, 174413 (2006).
17. O. Ugurlu, L. S. Chumbley, D. L. Schlagel, and T. A. Lograsso, "Orientation and formation of atypical Widmanstätten plates in the  $Gd_5(Si_xGe_{1-x})_4$  system," *J. Phys.: Condens. Matter* **18**, 3937 (2006).
18. Y. Mozharivskij, A.O. Tsokol and G.J. Miller, "Structural variations in  $Gd_5Si_{4-x}Sn_x$ : size vs. electronic effects," *Z. Kristallogr.* **221**, 493 (2006).
19. S. Misra and G.J. Miller, "On the distribution of tetrelide atoms (Si,Ge) in  $Gd_5(Si_xGe_{1-x})_4$ ," *J. Solid State Chem.* **179**, 2290 (2006).
20. D. Paudyal, V.K. Pecharsky, K.A. Gschneidner, Jr., and B.N. Harmon, "Magnetism of  $Gd_5Ge_4$ : A first principles study," *Phys. Rev. B* **75**, 094427 (2007).
21. F. Bondino, A. Brinkman, M. Zangrando, F. Carbone, D. van der Marel, D.L. Schlagel, T.A. Lograsso, K.A. Gschneidner, Jr., V.K. Pecharsky, and F. Parmigiani, "Experimental investigation of the electronic structure of  $Gd_5Si_2Ge_2$  by photoemission and x-ray absorption spectroscopy," *Phys.: Condens. Matter* **19**, 186219 (2007).
22. D. Haskel, Y.B. Lee, B.N. Harmon, Z. Islam, J.C. Lang, G.Srajer, Ya. Mudryk, K.A. Gschneidner, Jr., and V.K. Pecharsky, "Role of Ge in bridging ferromagnetism in the giant magnetocaloric  $Gd_5(Ge_{1-x}Si_x)_4$  alloys," *Phys. Rev. Lett.* **98**, 247205 (2007).
23. R. Nirmala, Ya. Mudryk, V.K. Pecharsky, and K.A. Gschneidner, Jr., "Unusual magnetism of  $Er_{0.75}Dy_{0.25}Al_2$ ," *Phys. Rev. B* **76**, 014407 (2007).
24. V. Franko, A. Conde, V.K. Pecharsky and K.A. Gschneidner, Jr., "Field dependence of the magnetocaloric effect in Gd and  $(Er_{1-x}Dy_x)Al_2$ : Does a universal curve exist?" *Europ. Phys. Lett.* **79**, 47009 (2007).
25. Kyunghan Ahn, V.K. Pecharsky and K.A. Gschneidner, Jr., "Phase relationships, and the structural, magnetic and thermodynamic properties in the  $Sm_5Si_xGe_{4-x}$  pseudobinary system," *Phys. Rev. B* **76**, 014415 (2007).
26. R. Nirmala, Ya. Mudryk, V.K. Pecharsky, and K.A. Gschneidner, Jr., "Magnetic and structural transitions in  $Dy_5Si_3Ge$ ," *Phys. Rev. B* **76**, 104417 (2007).
27. V.K. Pecharsky, Ya. Mudryk, and K.A. Gschneidner, Jr., "In-situ powder diffraction in high magnetic fields," *Z. Kristallogr. Suppl.* **26**, 139 (2007).

## **Exchange anisotropy, engineered coercivity and spin transport in atomically engineered L1<sub>0</sub> heterostructures.**

Principal Investigator: Kannan M. Krishnan

Department of Materials Science, Box 352120  
University of Washington, Seattle, WA 98195-2120  
e-mail: kannanmk@u.washington.edu

**Program Scope:** We are investigating some of the scientific and technically challenging issues in thin film magnetism focusing on epitaxially grown layers of specific L1<sub>0</sub> ordered, intermetallic, heterostructures with well-controlled crystallography and interface structure. Specifically, we are addressing antiferromagnetic/ferromagnetic systems, exhibiting exchange bias (EB) in both in-plane (MnPd/Fe) and perpendicular (IrMn/(Co/Pt)<sub>n</sub>) geometries, and ferromagnetic/ferrimagnetic (Co/Y<sub>3</sub>Fe<sub>5</sub>O<sub>12</sub>) bilayers with strong interlayer exchange coupling and exhibiting spin reorientation transitions. In the former case, the work includes experimental and theoretical studies to gain more fundamental insight into the origin and magnitude of EB, as well as to address important aspects of EB such as the asymmetry in the magnetic reversal mechanism, the role of interfacial structure, including compensated or uncompensated spins, AF domains and competing anisotropies. Size effects, particularly in structures with lateral dimension of the order of their domain sizes, are studied by soft lithography/patterning, and their time/temperature behavior by studies of magnetic viscosity, anomalous Hall effect and ultra fast magnetometry. These fundamental magnetic studies also determine the distribution of anisotropies, long-term thermal stability, high precessional switching and magnetic damping. In the latter case of the metal/oxide heterostructures, the domain structure of the metal is carefully modulated by that of the underlying oxide, opening the possibility of carrying out novel experiments to study spin-dependent domain-wall scattering and quantify domain wall resistance in mesoscopic geometries. Ongoing work, utilizing state-of-the-art characterization methods to address the critical role of all aspects of the microstructure, at relevant length scales, in determining these specific magnetic properties, includes domain imaging by photoemission electron microscopy (PEEM), element-specific X-ray magnetic reflectivity and x-ray resonant scattering at the ALS and BESSE II. Collaborative work with Prof. R. Stamps (UWA) in modeling and analysis of slow-dynamics, using an inductive ferromagnetic resonance technique, as well as efforts to study spin-transfer torque in these perpendicular anisotropy systems, including a novel fabrication technique, has also been initiated. The ultimate goal of this research is to gain a deeper understanding of the range of related magnetic phenomena, including spin transport, and establish pathways for potential technological applications of these thin film and patterned heterostructures.

**Recent Results:** We have made a coordinated effort in all aspects of this program [1]. Some of the highlights, including recent results are discussed below:

*Direct Imaging of the Asymmetric Magnetic Reversal Mechanism in Exchange-biased Heterostructures* [2]: X-ray photoemission electron microscopy at the ALS was used to probe the remnant magnetic domain structure in high-quality, single-crystalline, exchange-biased Fe/MnPd bilayers. It was found that the induced unidirectional

anisotropy strongly affects the overall magnetic domain structure. Real space images of the ferromagnetic domains provide, for the first time, direct evidence for an asymmetric magnetization reversal process after saturation along the ferromagnetic hard direction. The magnetization reversal occurs by moment rotation for decreasing fields while it proceeds by domain nucleation and growth for increasing fields. The observed domains are consistent with the crystallography of the bilayers and favor a configuration that minimizes the overall magnetostatic energy of the ferromagnetic layer. This work has also been highlighted at the Advanced Light Source [3].

*Perpendicularly Anisotropy and Exchange-bias: Competing Anisotropies and Interactions*

[4]: Following the successful synthesis of perpendicularly exchange-biased (IrMn/ or FeMn/(Co/Pt)<sub>n</sub>) heterostructures [5], we have investigated the role of competing magnetic interactions [6] and probed their asymmetric magnetic reversal mechanism by magnetic force microscopy and magnetoresistance measurements [7]. Perpendicular exchange bias in multilayers arise from a complex interplay between unidirectional anisotropy at the terminating ferromagnet(FM)/antiferromagnet(AFM) interface, the perpendicular anisotropy of the FM/nonmagnet(NM) multilayer stack and the overall magnetostatic energy of the structure. Exchange bias field ( $H_{eb}$ ) and coercivity ( $H_c$ ) of [Co/Pt]<sub>y</sub>/FeMn with perpendicular anisotropy have been investigated by varying the thickness of top Co layer in direct contact with the FeMn or number of Co/Pt bilayers. An unusual dependence of  $H_{eb}$  and  $H_c$  on these parameters has been observed. As the top Co layer thickness of [Co/Pt]<sub>y</sub>/FeMn multilayer varies, both  $H_{eb}$  and coercivity  $H_c$  show a peak in values and decrease when the top Co is too thin or too thick.  $H_{eb}$  of [Co/Pt]<sub>y</sub>/FeMn is inversely proportional to the number of Co/Pt bilayer,  $y$  for  $2 \leq y \leq 5$ , while  $H_c$  increases. For  $y > 5$ ,  $H_{eb}$  increases and  $H_c$  decreases with  $y$  until both of them reach constant values. These observations have been attributed to the role of the effective perpendicular anisotropy of the FM multilayer, especially the FM layer adjacent to AFM layer, in maintaining the perpendicular exchange bias. In addition to the above, magnetoresistance (MR) and magnetic force microscopy (MFM) measurements were used to probe the magnetic reversal mechanism of perpendicular exchange bias systems since the transport properties of electron in FM thin films can be greatly affected by the spin structures. The magnetoresistance is asymmetric along the ascending and descending branches of the hysteresis loops, which can be explained by the difference of domain wall density in the two reversal branches. The latter follows from the analyses of the MFM images and fractal geometry of the domain walls. Both the MR and MFM data are consistent with the reported data on x-ray small angle scattering and time-resolved Kerr microscope data in that the magnetic reversal is due to domain nucleation and growth in both the descending and ascending branches, in contrast to most in-plane exchange bias system.

*Spin reorientation transitions in perpendicularly exchange-coupled, ferromagnetic, ultra-thin films studied using element specific imaging* [8]:

As part of a recent doctoral dissertation [9] at MSE/UW on "Domain wall stability and resistance in perpendicularly-coupled metal/oxide bilayers", we have studied the spatial variations in the spin-reorientation transition of an exchange-coupled Co-wedge/YIG ( $Y_3Fe_5O_{12}$ ) bilayer, from perpendicular to in-plane domain structure, using magnetic force microscopy (MFM) and photo-emission electron microscopy (PEEM). Even though MFM measurements of the YIG film showed perpendicular stripe domains, it was not possible to unambiguously resolve the domain structure of only the top ferromagnetic metal layer because of complications arising from the stray fields of the much thicker YIG underlayer. Hence, using element-specific, x-ray magnetic circular dichroism (XMCD) of the transition metal  $L_{3,2}$  edges (Co and Fe, respectively) for magnetic contrast, PEEM measurements were

carried out to resolve the domain structure of the individual Co and YIG layers. The two were identical up to a Co thickness of 4.5nm, confirming that the Co layer was exchange coupled with the YIG underlayer; however, a transition of the Co domains, from perpendicular to in-plane, was observed at thickness of 4.5 ~ 6nm. For thicker regions of the Co film (> 6nm), a sizeable portion of the Co layer showed in-plane domains; their spins were perpendicular to the domain walls of the stripe domains with Co XMCD values in the range of -5% to +5% -- a value smaller than that of the perpendicular domains.

*XRMR/XMCD investigations of the interface spin-lattice in epitaxially grown Fe/MnPd*

*exchange bias samples*: X-ray magnetic reflectometry (XRMR) is a powerful technique to probe nanomagnetic structures with special sensitivity to the spin lattice at FM/AFM interfaces [10]. In our investigations, we focus on finding evidence for pinned moments in MnPd/Fe, with emphasis on the Mn sites. By using XRMR, both *a*-axis (spin uncompensated interface) and *c*-axis (spin compensated) MnPd were investigated with the ultimate goal of obtaining high-resolution magnetic depth profiles of the samples. From these profiles, the origin of exchange bias, namely the magnetic configuration at the ferromagnet/antiferromagnet interface was probed. The investigation of *a*- and *c*-axis MnPd is also motivated by the different amount of exchange bias found in these systems. The detailed analysis of the *a*-axis MnPd has just been completed and the origin of the pinned Mn moments have been identified [11]. Further, a decrease in the helical asymmetry with  $H_{EB}$  for the *c*-axis samples has been observed. Detailed analysis of the data is in progress.

**Work in Progress and Future Plans:** In addition to pursuing the above measurements to completion, the following experiments are either being planned or in progress:

1. Local effective fields created in Fe by MnPd through exchange anisotropy are studied using an inductive, strip-line, ferromagnetic resonance technique. Our first set of measurements, in collaboration with Prof. R. Stamps on Univ. of Western Australia, show anomalies in the frequency as a function of field which have been interpreted as a distribution in unidirectional anisotropy field orientation and strengths [12].
2. We are using soft lithography methods, in general, and solvent-assisted microcontact molding (SAMIM), in particular, for making nano-patterned (Co/Pt)<sub>5</sub>/IrMn elements to investigate the size and shape effects on perpendicular exchange bias. The aim is to confine the elements to the typical size of the AFM domains. Moreover, it is known that such patterning results in a distribution of anisotropies and our goal is to study this using temperature-dependent torque magnetometry for both in-plane and perpendicular exchange-bias systems.
3. Measurement of the domain wall resistance in (Co/Y<sub>3</sub>Fe<sub>5</sub>O<sub>12</sub>) bilayers where the domains in the metallic (Co) layer can be modulated by the underlying oxide layer.
4. Recent work suggests that a major contribution to the phenomena of exchange bias arises from a thermally activated reorientation of the antiferromagnetic layer. However, all this work has been done on polycrystalline samples. In collaboration with Prof. K. O'Grady, of the University of York, we are developing measurement protocols to study thermal activation process in epitaxial films with crystallographically well-defined interfaces.

5. Building on our expertise in synthesizing perpendicular exchange bias heterostructures, we are building spin valves with perpendicular anisotropy for spin torque experiments. However, unlike traditional approaches involving complex multi-step lithography, we are proposing to deposit the heterostructure into a pre-fabricated via in an insulating support film. The fabrication will be carried out at the EMSL facilities at PNNL using the newly installed focused ion-beam machine followed by deposition and transport measurements in our laboratory.

### Publications (2005-2007)

- [1] Kannan M. Krishnan, et al, "Nanomagnetism and spin electronics: materials, microstructure and novel properties", *Jour. Mat. Sci.* **41**, 793–815 (2006)
- [2] P. Blomqvist, Kannan. M. Krishnan and H. Ohldag, "Direct imaging of asymmetric magnetization reversal in exchange-biased Fe/MnPd bilayers by x-ray photoemission electron microscopy", *Phys. Rev. Lett.*, **94**, 107203 (2005)
- [3] [http://www.als.lbl.gov/als/science/sci\\_archive/107exchange\\_bias.html](http://www.als.lbl.gov/als/science/sci_archive/107exchange_bias.html)
- [4] Xiaosong Ji (Dual Ph.D. in Materials Science and Engineering and Nanotechnology, UW) "Perpendicular anisotropy and exchange bias in magnetic thin film heterostructures", 2007.
- [5] X. Ji, Honglyou Ju, David E. McCready and Kannan M. Krishnan, "Perpendicular exchange bias in ion-beam sputtered (Co/Pt)<sub>n</sub>/FeMn multilayers", *Jour. Appl. Phys.* **98**, 116101 (2005)
- [6] X. Ji and Kannan M. Krishnan "Competing magnetic interactions in perpendicular exchange-biased (Co/Pt)<sub>x</sub>/FeMn multilayers", *Jour. Appl. Phys.* **99**, 08C105 (2006)
- [7] X. Ji, A. B. Pakhomov and Kannan M. Krishnan, "Asymmetry magnetic reversal of perpendicular exchange-biased (Co/Pt)<sub>5</sub>/IrMn probed by magnetoresistance and magnetic force microscopy", *Jour. Appl. Phys.*, **101**, 09E507 (2007)
- [8] Y.S. Chun, H. Ohldag and Kannan M. Krishnan "Spin reorientation transitions in perpendicularly exchange-coupled, ferromagnetic, ultra-thin films studied using element specific imaging", *IEEE Trans. Mag.*, **43**, 3004 (2007).
- [9] Yonsoo Chun (Ph.D. in Materials Science and Engineering, UW) "Domain wall stability and resistance in perpendicularly-coupled metal/oxide bilayers", 2007
- [10] G. Srajer, L. H. Lewis, S.D. Bader, ... Kannan M. Krishnan ...J.Z. Sun, "Advances in nanomagnetism via x-ray techniques", *Jour. Mag. Mag. Mat.*, **307**, 1 (2006)
- [11] S. Bruck, X. Ji, E. Goering and Kannan M. Krishnan, in preparation
- [12] K. J. Kennewell, Xiaosong Ji, J-G Hu, R. C. Woodward, K. M. Krishnan, R. L. Stamps, "Measuring exchange anisotropy in Fe/MnPd using inductive magnetometry", *Jour. Appl. Phys.*, **101**, 09E518 (2007).

# Field-Structured Composites

J. E. Martin, D. Read, G. Venturini, R. Anderson Sandia National Labs

## CURRENT RESEARCH

**Field-Structured Composites.** We are interested in developing particle composites structured by electric or magnetic fields as scientifically interesting and useful materials. Such field-structured composites (FSCs) are made by dispersing dielectric or magnetic particles into a pre-polymer liquid and polymerizing while subjecting the dispersion to structuring electric or magnetic fields. As discussed below, these fields can be quite complex, and can be used to create a wide variety of composite structures.

The motivation for this work is that the properties of a composite depend strongly on the structure of the particle agglomerates. [1-3] For example, through theory, simulation, and experiment we have shown that the magnetic susceptibility of a composite can be significantly enhanced along one direction, and slightly suppressed along the other two, if the particles are organized into chains by a uniaxial field. [4] Likewise, we have discovered that the susceptibility can be significantly enhanced in two directions (and strongly suppressed in the third direction) by organizing the particles into sheets with a biaxial ac field. [4] More surprising is our discovery that triaxial ac magnetic fields can be used to organize particles into various foam-like structures with an enhanced susceptibility in all directions. [5, 6] These enhancements are factors of 2-4 for composites of multi-domain particles, [7] but we have shown through simulation and experiment that these can be a factor of 50 or more for nanocomposites of single-domain iron nanoparticles. [8]

Triaxial fields. A few years ago we designed and built an ac triaxial Helmholtz coil that can generate magnetic fields in the frequency range of 75-2500Hz. Each coil is in series resonance with fractal capacitor banks that enable us to create a resonance at essentially any frequency in this range. Because the frequency and amplitude of each coil are individually selected, a wide variety of particle structures can be produced. This work has led to several patents, most significantly on the use of triaxial magnetic fields for optimizing the properties of particle composites. [6] Dipolar interactions in triaxial magnetic fields are a truly fascinating topic, because they give rise to purely many-body interactions: the pair-wise additive part of the dipole interaction actually vanishes in a balanced triaxial field. Molecular-like clusterings of particles are stable, so in a sense we have discovered a method of creating quantum chemical effects with classical fields. On a more practical note, we have discovered that heterodyned triaxial fields can be used to athermally attain the thermodynamic ground state in a magnetic field, simultaneously cheating statistical mechanics and fully optimizing the composites. [7]

Actuators. We have also shown theoretically that the magnetostriction of particle composites is quadratic in the permeability, [9] so field-structuring has a pronounced effect on this property. In this case the magnetostriction is due to dipolar interactions between particles, not the magnetostriction of the particles themselves. Our experimental measurements confirm this, showing that field-structuring can easily increase magnetostriction by 10X over unstructured controls. [10] In fact, we have demonstrated magnetostrictive strains as large as 10,000ppm, which is 5X larger than terfenol C– the next best material.

Sensors. The effect of field-structuring on electrical and thermal transport is extremely large. Field-structuring can increase the electrical conductivity of a composite by more than 12 decades. When such materials are cast as thin films we have found them to be excellent chemical sensors, with fully reversible responses as great as 10 decades, and sensitivities in the ppb range for volatile organic compounds. [11, 12] Transduction is due to the change in the composite conductivity as the VOC swells the polymer. We have demonstrated that the sensitivities of these sensors can be varied over a 100-fold range by controlling the stress in the polymer, and our most sensitive sensors are 100 times more sensitive than conventional carbon black chemiresistors. We have received two patents on our chemical sensors, and a third is pending. [13-15] These materials also function as strain sensors, and have gauge factors that are 11 decades larger than competing technologies. [11]

**Magnetoresistance.** The large magnetostriction and strain gauge factor of FSCs combine to create extremely large magnetoresistance at low applied fields. [16] We have measured a 6 decade resistivity change in a field of only 0.06T. This effect, which is many orders of magnitude greater than observed for other magnetoresistance mechanisms, may be useful in tuning the response of our chemical sensors.

**Magnetic Mixing.** During our work on synthesizing composites in triaxial magnetic fields we discovered that certain types of triaxial magnetic fields, which call vortex fields, create extremely strong mixing in suspensions of magnetic particles. Our measurements of the mixing torque show a number of surprising features: the torque is quadratic in the applied field, independent of the field frequency, and independent of the liquid viscosity. [17] These effects are quite contrary to the behavior of a stir bar. We believe the mixing effects are due to the formation of particle chains, and a theoretical development of this mechanism gives all of the expected behaviors. [18] This theory also shows that the mixing torque is independent of particle size, which means that it can be scaled for microfluidics without a loss of efficiency. In fact, we have observed mixing with Fe nanoparticles. A patent application is being prepared on this new technology.

**Quantum Dots.** In the last few years some effort has been focused on the light conversion approach to Solid-State Lighting. In this approach a phosphor is used to down convert the light emitted by an LED. Our interest is in the use of II-VI semiconductor quantum dots to convert UV LED light to visible light. This project has centered on synthesizing CdS QDs in inverse micelles and measuring their optical properties. [19] These materials have very broad emission and upon aging can even emit white light, even though they are uniform in size. Our work has centered on understanding this emission. We have found that the photoluminescence decay can be characterized as a stretched exponential, [20] with a lifetime that is proportional to the quantum yield. [21] We have also discovered that purifying, photolyzing, and functionalizing the surface with certain ligands can increase the quantum yield to nearly 40%, which is roughly four times better than the value reported in the literature. [22] At this time our work is focused on understanding why certain samples age to give white emission, whereas others do not.

## FUTURE DIRECTIONS

**Field-Structured Composites.** To date essentially all of our experimental and theoretical work on field-structured composites has focused on spherical particles. The magnetic properties of such composites is ultimately limited by the low effective susceptibility of the spherical shape, which cannot exceed 3 in the MKS system. Due to their much weaker demagnetization fields, highly anisotropic particles can have much larger effective susceptibilities along their long axes. Composites of aligned anisotropic particles will therefore exhibit significantly enhanced magnetic properties, and greatly improved transport properties.

We now have available to us two sources of anisotropic particles: platelets and rods. Preliminary experiments show that field-structured composites of platelets have 11x greater susceptibility than we have ever achieved for spherical multi-domain particles. Similar or greater enhancements are expected for the nanorods now available to us. These nanorods are 350 nm in diameter and of tailorable, and uniform, length. They can be made of any magnetic element, or even of a sequence of magnetic and non-magnetic elements. We expect composites made of these anisotropic particles to have much greater magnetostriction, magnetoresistance, and magnetochemiresistance than our previous materials, and improved performance as sensors and as thermally conductive composites. Understanding the physical properties of these composites will require working with vector pair correlation functions that also include particle orientation. This will present interesting new computational and theoretical challenges.

**Magnetic Mixing and Magnetohydrodynamic Instabilities.** We now wish to extend our magnetic mixing work to suspensions of platelets and rods. Preliminary theoretical calculations

show the behavior should be quite different, due to the tendency of anisotropic particles to align with a long axis along the field. We are especially interested in determining if the torque density is greater than that achieved with spherical particle. This effort will also include fundamental studies of the magnetohydrodynamics of these suspensions in complex applied fields. In early experimental work we have discovered remarkable pattern formation phenomena that are critically dependent on the field frequencies and phase relations. These magnetohydrodynamic instabilities are exciting and we are working hard to try to understand their formation.

#### ACKNOWLEDGEMENTS

Sandia is a multiprogram laboratory operated by Sandia Corporation, a Lockheed Martin Company, for the United States Department of Energy's National Nuclear Security Administration under Contract DE-AC04-94AL85000.

#### REFERENCES

1. *Simulation of the Athermal Coarsening of Composites Structured by a Uniaxial Field.* Martin J E, Anderson R A and Tigges C P, 1998 J. Chem. Phys. **108** 3765.
2. *Simulation of the Athermal Coarsening of Composites Structured by a Biaxial Field.* Martin J E, Anderson R A and Tigges C P, 1998 J. Chem. Phys. **108** 7887.
3. *Thermal Coarsening of Uniaxial and Biaxial Field-Structured Composites.* Martin J E, Anderson R A, Tigges C P, 1999 J. Chem. Phys. **110** 4854.
4. *Anisotropic Magnetism in Field-Structured Composites.* Martin J E, Venturini E, Odinek J, and Anderson R A, 2000 Phys. Rev. E. **61** 2818.
5. *Generating Strange Magnetic and Dielectric Interactions in Particle Suspensions: Classical Molecules and Particle Foams.* Martin J E Anderson R A, and Williamson R L, 2003 J. Chem. Phys. **118** 1557-1570.
6. United States Patent #6.844,378 "Method of Using Triaxial Magnetic Fields for Making Particle Structures," James E. Martin, Robert A. Anderson, and Rodney L. Williamson, January 18, 2005.
7. *Using Triaxial Magnetic Fields to Create High Susceptibility Particle Composites.* Martin J E, Venturini E, Gulley G, Williamson J, 2004 Phys. Rev. E **69** 21508-1 to 15.
8. *Giant Magnetic Susceptibility in Field-Structured Dipolar Nanocomposites.* Venturini E, Martin J E, Odinek J and Huber D, submitted to J. Magnetism and Mag. Mat.
9. *Electrostriction in Field-Structured Composites: Basis for an Artificial Muscle?* Martin J E, Anderson R A, 1999 J. Chem. Phys. **111** 4273.
10. *Magnetostriction of Field-Structured Magnetoelastomers.* Martin J E, Anderson R A, Read D, Gulley G, 2006 Phys. Rev. E **74** (5) 051607-051624.
11. *Controlling Percolation in Field-Structured Particle Composites: Observations of Giant Thermoresistance, Piezoresistance, and Chemiresistance.* Martin J E, Anderson R A, Odinek J, Adolf D and Williamson J, 2003 Phys. Rev. B **67** 94207-1 to 11.
12. *Field-Structured Chemiresistors.* Martin J E, Read D, Williamson R, Butler, preprint.

13. United States Patent #6,194,769 BI Issued "*Sensor devices comprising field structured composites*," J. E. Martin, R. C. Hughes, and R. A. Anderson, Feb. 27, 2001.
14. United States Patent #6,290,868 "*Field-Structured Material Media and Methods for Synthesis Thereof*," J. E. Martin, R. C. Hughes, and R. A. Anderson, Sept. 18, 2001.
15. United States Patent Application "*Stress-Tuned Particle Composite for Use in Sensors*," James E. Martin, Douglas H. Read
16. *Extreme Magnetoresistance of Field-Structured Composites*. Martin J E, Read D, Williamson R., Submitted to J. Appl. Phys.
17. *Strong Intrinsic Magnetic Mixing in Vortex Magnetic Fields*. Martin J E, Shea-Martin L, Anderson R A, submitted to Nature Mat.
18. *Theory of Strong Intrinsic Mixing of Particle Suspensions in Vortex Magnetic Fields*. Martin J E, submitted to Phys. Rev. E.
19. *Measuring the Absolute Quantum Efficiency of Luminescent Materials*. Shea-Rohwer L, Martin J E, 2005 J. Lumin. **115** 77-90.
20. *Lifetime Determination of Materials that Exhibit a Stretched Exponential Luminescent Decay*. Shea-Rohwer L, Martin J E, 2006 J. Lumin. **121** 573-587.
21. *Luminescence Decay of Broad-Band Emission from CdS Quantum Dots*. Shea-Rohwer L E, Martin J E, 2007 J. Lumin. Vol 127 (2) 499-507.
22. *Increasing the Quantum Yield of Broad-Band Emission from CdS Quantum Dots by Surface Modification*. Shea-Rohwer L E, Martin J E, submitted to Chem. Mat.

# Spin-Dependent Effects in Ferromagnetic Semiconductor and Manganite Thin Films

Jing Shi, Department of Physics and Astronomy, University of California, Riverside

We have investigated spin-dependent transport effects in two types of material systems: ferromagnetic semiconductors, e.g. Mn-doped GaAs, and manganite thin films and superlattices, e.g.  $\text{La}_{1-x}\text{Sr}_x\text{MnO}_3$  and  $\text{La}_{1-x}\text{Ba}_x\text{MnO}_3$ . Both material systems are very important for potential spintronics applications.

In the first material system,  $\text{Ga}_{1-x}\text{Mn}_x\text{As}$  as a prototypical spintronic material has been relatively well studied. It is known that the holes in this p-type material experience strong spin-orbit interaction in addition to the strong scattering from random impurities, leading to a strong anomalous Hall effect. However, just as in other ferromagnets, the nature of the anomalous Hall effect has not been completely known and competing theoretical models still exist. In most previous experiments, the anomalous Hall effect was measured at high magnetic fields in order to fully saturate and align the in-plane magnetization along the out-of-plane applied magnetic field. As also found by other researchers, when the magnetic field is applied or varied, both  $\rho_{xx}$  and  $\rho_{xy}$  change, but the

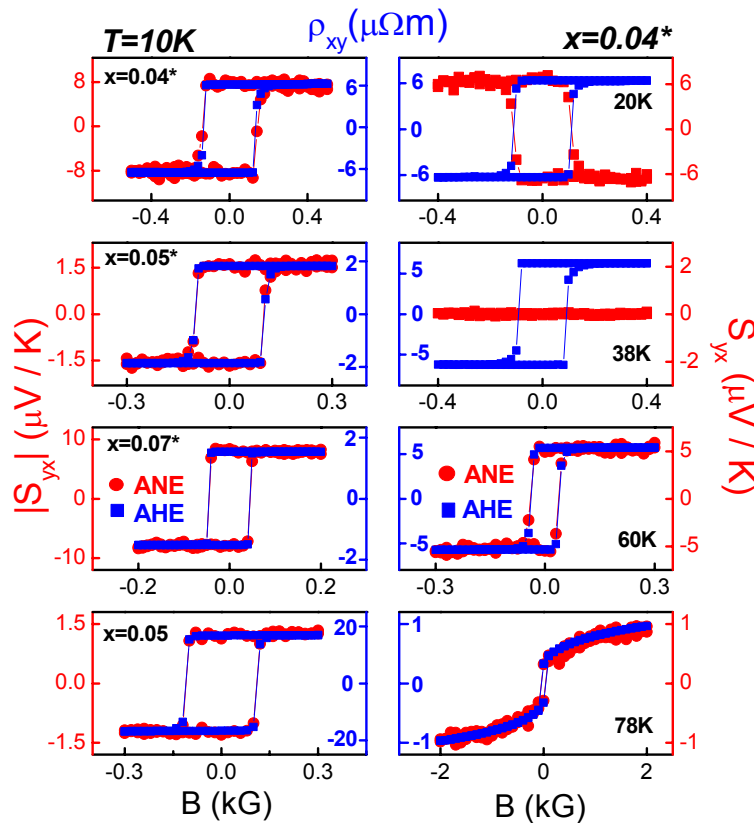


Fig. 1. (Left) Anomalous Hall effect (AHE) and anomalous Nernst effect (ANE) in four GaMnAs samples with perpendicular anisotropy. (Right) Temperature dependence of both AHE and ANE for the sample with 4% Mn concentration. Note that there is a sign change at  $T=38$  K.

exponent  $n$  of the power-law  $\rho_{xy} \sim \rho_{xx}^n$  is found to clearly depart from 1 or 2, which was predicted for extrinsic or intrinsic mechanism respectively. To address the origin of the

anomalous Hall effect, we have specially designed the GaMnAs thin films with perpendicular magnetic anisotropy so that the zero-field transport properties can be measured and analyzed. For this work, we have collaborated with Dr. Hideo Ohno at Tohoku University who pioneered this sub-field. In our laboratory, we have systematically conducted both electrical transport and thermoelectric transport measurements simultaneously on same samples. In our work, we have found a usually large spontaneous or anomalous Nernst effect ( $\sim 1\mu\text{V/K}$ ) in all GaMnAs thin film samples. This anomalous Nernst effect scales with the anomalous Hall effect as the magnetic field is swept (Fig. 1). In fact, both curves are reminiscent of the magnetic hysteresis loop in samples with perfect perpendicular anisotropy. The spontaneous Nernst signal ( $H=0$ ) was taken as a function of the temperature. The anomalous Hall signal does not change sign over the entire temperature range, however, the anomalous Nernst signal does change sign at some intermediate temperature. In ordinary transport, the thermoelectric transport coefficients are connected to the electrical transport coefficients by the well-known Mott relation. For the intrinsic spin-orbit origin, it is not clear that the Mott relation still holds until it was theoretically shown recently. We have analyzed the temperature-dependent zero-field off-diagonal transport coefficients and found that the both effects are indeed related by the Mott relation. In the meantime, by fitting our experimental data, we concluded that the exponent of the power-law is very close to two, which confirms the intrinsic nature of the observed effects. Therefore, we have experimentally validated the Mott relation for the intrinsic mechanism in ferromagnetic semiconductors for the first time.

In the second material system, we aimed to study the interfacial magnetism in manganite films and its consequence in magnetic tunneling characteristics. The main attractiveness of using manganites in spintronic devices is its high spin polarization, as demonstrated in our previous organic spin valve devices. In addition, the interfacial properties are very well preserved after device fabrication. We have grown high-quality thin manganite thin films and superlattices using our new laser molecular beam epitaxy system. Due to the difference in layering sequence for films grown in different crystallographic directions, we expect different interfacial properties such as the magnetism (ferromagnetism vs. antiferromagnetism, or paramagnetism) and electronic properties (insulating vs. conducting). This is exemplified in films grown in  $[100]$  and  $[110]$  directions. In the former, the sequence is  $\text{LaSrO/MnO}_2/\text{LaSrO}/\dots$ , but in the latter, it is  $\text{O/LaSrMnO/O}/\dots$ . The double exchange strength between Mn-Mn is likely to be different in these two films. We have employed both magnetic tunnel junction devices such as  $\text{LSMO/STO/LSMO}$  and second-harmonic generation technique to investigate the interfacial electronic and magnetic properties. First of all, we have achieved very high Curie temperature ( $\sim 350\text{ C}$ ) in epitaxial  $\text{LSMO}$  films without any post-growth annealing. In addition, in the superlattices of  $[\text{LSMO/STO}]_n$  on  $(110)$  with  $\text{LSMO}$  thickness ranging from 3 to 20 monolayers, we have found that the ferromagnetism exists in the thinnest  $\text{LSMO}$ , i.e. down to 3ML. In addition, the interface layer of  $\text{LSMO}$  is clearly ferromagnetic. This result is significantly better than what was reported earlier by Kawasaki et al. in their structures grown on  $(100)$ . With the second-harmonic generation and magneto-optics, we are able to probe the bulk and interfacial contributions independently (Fig. 2). By measuring the temperature dependence of both linear and non-linear magneto-optic responses, we can obtain the Curie temperatures of the two

components. The interfacial electronic properties are closely related to the tunneling characteristics such as the current-voltage characteristics and tunneling magnetoresistance. We are currently fabricating magnetic tunnel junction devices using photo- and electron beam lithography techniques. We are able to directly correlate the temperature dependence of the second-harmonic response with that of the tunneling magnetoresistance of the same film structures.

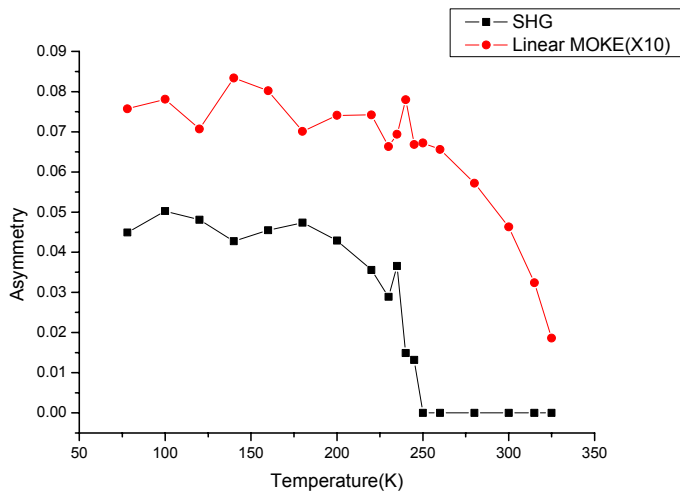


Fig. 2. Linear magneto-optic Kerr effect signal (red) and second harmonic generation – SHG- signal (black) vs. temperature in 100 ML LSMO. The interfacial magnetism precipitously drops to zero at about 250 K, at least 80 K below the Curie temperature of the bulk component.

We are currently focusing on the understanding and controlling of the interfaces in manganite films. In the near future, we wish to more systematically explore the effect on the interfaces from other factors such as strain, doping profile, and etc. In addition, we also wish to study the spin polarization of manganite films and superlattices.

## **Project Title: Magnetization Dynamics and Cooperative Phenomena in Spin and Charge Frustrated Correlated Electron Materials**

**Principal Investigator: Dr. Hariharan Srikanth**

University of South Florida, Department of Physics, PHY 114

4202 East Fowler Ave, Tampa, FL 33620

E-mail: [sharihar@cas.usf.edu](mailto:sharihar@cas.usf.edu)

**Project Participants (USF): Dr. M.H. Phan (Postdoctoral Associate), Ms. Natalie Frey (Ph.D student), Mr. James Gass (Ph.D student)**

**Project Collaborators (ORNL): Dr. Manuel Angst, Dr. Brian Sales and Dr. David Mandrus (Group Leader –Correlated Electron Materials)**

**Other Collaborators (Northeastern University): Dr. C. N. Chinnasamy, Prof. Vincent Harris**

### **Program Scope:**

Transition-metal and rare-earth based oxides exhibit rich complexity in their fundamental physical properties determined by the intricate interplay between structural, electronic and magnetic degrees of freedom. Of particular current interest are systems that inherently favor charge and spin frustration due to the arrangement of transition-metal or rare-earth atoms on a triangular lattice. Research on geometrically frustrated materials has continued to yield new surprises in terms of cooperative phenomena such as the coexistence of ferrimagnetism, ferroelectricity and superconductivity. This project is focused on fundamental studies of such phenomena through systematic experimental investigations of static and dynamic magnetic susceptibility along with magnetocaloric effect (MCE) in correlated oxides. Our present focus in the first few months of the project is on two complex oxide systems –LuFe<sub>2</sub>O<sub>4</sub> which is a multiferroic material with the ground state properties still not well understood and GdFe<sub>3</sub>O<sub>12</sub> garnet nanoparticles that potentially exhibit interplay of intrinsic spin frustration and particle blocking effects.

### **Recent Progress: (LuFe<sub>2</sub>O<sub>4</sub> multiferroic oxides)**

The family of RFe<sub>2</sub>O<sub>4</sub> ( $R = Y, Er, Yb, Tm, \text{ and } Lu$ ) compounds, which exhibit charge and magnetic order on a geometrically frustrated lattice, have received growing attention from the scientific community, owing to their extraordinarily interesting physical properties [1,2]. In particular in LuFe<sub>2</sub>O<sub>4</sub>, the observation of an electric polarization possibly originating from charge order [3] and the subsequent discovery of a giant room-temperature magnetocapacitance [4] has created a lot of attention [5]. Multiferroic properties along with the intrinsic geometric spin frustration in LuFe<sub>2</sub>O<sub>4</sub> make it a very promising candidate material for magnetic refrigeration and other technologies. While recent magnetization and neutron results suggest a three-dimensional magnetic structure with additional transitions, understanding the unusual magnetic properties of LuFe<sub>2</sub>O<sub>4</sub> still remains incomplete, partially due to the complex phase diagram [6,7]. The very complexity makes it attractive for magnetocaloric applications and we propose LuFe<sub>2</sub>O<sub>4</sub> to be a good candidate material as it

can show large magnetic field-induced magnetic entropy change over a wide temperature range due to the occurrence of multiple successive metamagnetic transitions.

We have completed a systematic study of the DC and AC magnetic properties and the first study of the magnetocaloric effect (MCE) in LuFe<sub>2</sub>O<sub>4</sub>. Correlation between the magnetism and MCE is established and the influence of the magnetic field on the metamagnetic transitions and MCE have been analyzed. We have observed striking new magnetic features in high quality single crystals of LuFe<sub>2</sub>O<sub>4</sub> that appear to suggest that the magnetism at low temperature is due to cluster glass behavior resulting from interacting ferrimagnetic clusters. Our results are providing new insights into the ground state of LuFe<sub>2</sub>O<sub>4</sub> which is a topical issue under intense investigation by several groups. Two manuscripts are under preparation based on these results and are targeted for submission in the March/April 2008 time frame to Physical Review Letters and Applied Physics Letters. In addition, an abstract based on this work has been accepted for oral presentation at the INTERMAG conference to be held in May 2008 in Madrid, Spain. The PI will attend the conference and present the paper.

We now provide a brief summary of the magnetocaloric effect (MCE) studies on these materials which is being reported for the first time. LuFe<sub>2</sub>O<sub>4</sub> crystals were grown in an image furnace at Oak Ridge in Dr. Mandrus' laboratory and studied using neutron diffraction[6,7]. DC and AC magnetization measurements were performed in the PI's lab at USF using a Physical Property Measurement System from Quantum Design in the temperature range of 5 – 300 K at applied fields up to 70kOe. The magnetic entropy change ( $\Delta S_M$ ) was numerically extracted using the Maxwell relation from a large family of M-H curves collected at different fixed temperatures.

Our magnetization data reveal unusual magnetic behavior only in fields applied parallel to the c-axis of the crystal, in agreement with previous studies [1,6,7]. Zero-field-cooled (ZFC) magnetization curves at applied field ~100 Oe show the two transitions around 240K and 170K also indicated by neutron scattering [6]. Field-cooled (FC) magnetization curves at the same field exhibit three broad cusps, two of which coincide with the above transitions. The magnetic entropy changes  $\Delta S_M(T)$  at these features were calculated from a family of M-H curves at fixed temperatures using the Maxwell relation:

$$\Delta S_M = \int_0^H \left( \frac{\partial M}{\partial T} \right)_H dH.$$

Fig. 1 shows magnetization M(T) curves extracted from these measurements with the inset showing the MCE.  $\Delta S_M(T)$  curves show three peaks at temperatures which correspond to the cusps in the FC magnetization. As the magnetic field is increased, the positions of MCE peaks at ~170 and 240 K tend to remain unchanged, whereas the one at ~65 K significantly shifts to a lower value. Noticeably, the MCE peak temperature of ~65 K for  $\Delta H = 3$  kOe decreases to ~55 K

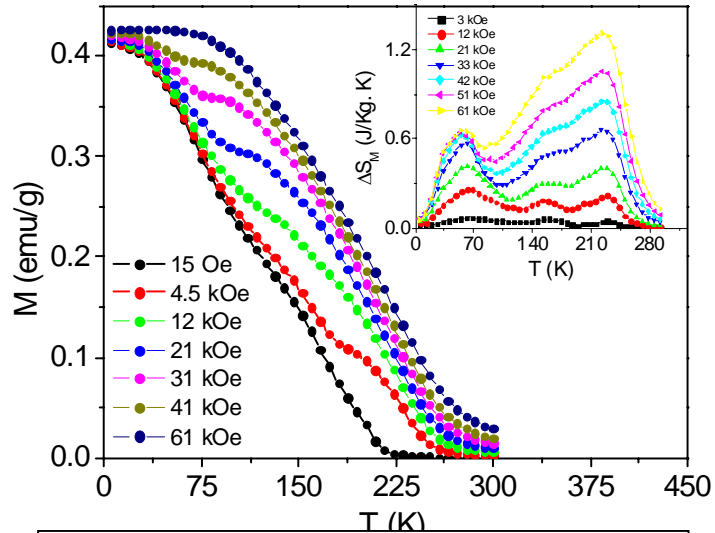


**Fig. 1** Field-cooled magnetization M vs T extracted from isothermal magnetization data. Inset: magnetocaloric effect  $\Delta S_M(T)$ .

which remains almost unchanged for  $\Delta H \geq 42$  kOe. This is consistent with the observation that this low temperature metamagnetic transition in  $\text{LuFe}_2\text{O}_4$  is kinetically arrested below  $\sim 55$  K [7]. The magnitude of  $\Delta S_M(T)$  at the peak temperatures varies differently as the applied magnetic field is increased (see the inset of Fig. 1). For  $\Delta H \leq 21$  kOe, the magnitude of  $\Delta S_M(T)$  is obviously larger for the case at  $\sim 55$  K than for those at  $\sim 170$  and  $240$  K, while the opposite trend is observed for  $\Delta H > 21$  kOe. This suggests different mechanisms for AF-FM couplings/correlations for the metamagnetic transitions. An important conclusion is that enhanced spin entropy (at the kinetically arrested transition) yields large MCE at lower applied fields which is desirable for applications. From the practical magnetic cooling perspective, it is worth noting from the inset of Fig. 1 that the application of magnetic field leads to a broadening of the metamagnetic transitions and hence a broadened  $\Delta S_M(T)$  curve over very wide temperature range. As a result, the magnetic cooling power – which is proportional to the width of the  $\Delta S_M(T)$  curve – is greatly enhanced. This opens up new opportunities for the developments of a new class of material with multiple successive metamagnetic transitions for magnetic refrigeration.

**Nanoscale garnets ( $\text{Gd}_3\text{Fe}_5\text{O}_{12}$ ):**

Iron garnets have been studied in the bulk phase by several groups over the years and are known to be promising candidates for microwave device applications. Very recently, we have initiated a collaboration with Prof. Vince Harris at Northeastern University and obtained nanoscale garnets synthesized by them with mean particle size ranging from 30nm to 50nm. Our goal is to address a fundamental question in these systems –in the nanoscale size range when the particles are below the single domain limit, what happens to the spin glass nature associated with the intrinsic geometric frustration due to the three different interpenetrating sublattices (Gd ions,  $\text{Fe}^{2+}$  and  $\text{Fe}^{3+}$  ions)? Our preliminary experiments have thrown up important clues to answer this question.

While the overall behavior (i.e. blocking temperature, irreversibility of ZFC and FC curves) looks similar to other ferrite nanoparticle systems we have studied, there are deviations at low temperature that suggests that spin frustration persists in the blocked state. Fig. 2 shows the ZFC and FC magnetization at an applied field of 100 Oe for 30 nm garnet nanoparticles. The inset shows the particle size dependence of blocking and irreversibility

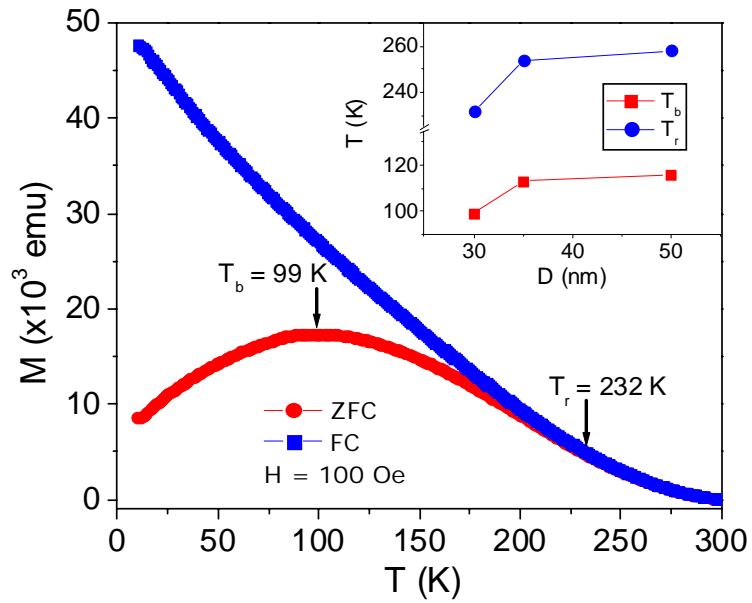


Fig. 2 Zero-field cooled and field-cooled magnetization of 30 nm garnet nanoparticles. Inset: Particle size dependence of blocking and irreversibility temperatures

temperatures. We will present and discuss DC, AC and RF susceptibility measurements on garnet nanoparticles and provide evidence that clearly allows one to decouple the blocked state from a spin glass state at low temperatures.

Overall, we present DC, AC magnetization and magnetocaloric effect studies in different classes of spin frustrated oxide systems. Our results reveal new phenomena and glass characteristics that can be correlated to the geometric frustration in these materials. Future work will continue to explore the ground state in these oxides through systematic magnetic susceptibility experiments at frequencies from DC to 20 MHz.

**Work at USF supported by DOE through grant number DE-FG02-07ER46438.**

#### REFERENCES

- [1] J. Iida, Y. Nakagawa, N. Kimizuka, J. Phys. Soc. Jpn. 55, 1434 (1986).
- [2] Y. Yamada et al., Phys. Rev. B 62, 12167 (2000).
- [3] N. Ikeda et al., Nature 436, 1136 (2005).
- [4] M. A. Subramanian, T. He, J. Chen, N.S. Rogado, T.G. Calvarese, A.W. Sleight, Adv. Mater. 18, 1737 (2006).
- [5] H.J. Xiang, M.-H. Whangbo, Phys. Rev. Lett. 98, 246403 (2007); Y. Zhang et al., ibid. 98, 247602 (2007); A. Nagano et al., ibid. 99, 217202 (2007).
- [6] A. D. Christianson et al., Phys. Rev. Lett. accepted, (2008)

# Spin Polarized Functionality Through Complex Oxide Heteroepitaxy

PI: Yuri Suzuki

Lawrence Berkeley National Laboratory / UC Berkeley

210 Hearst Memorial Mining Building MC1760

Department of Materials Science & Engineering

UC Berkeley

Berkeley, CA 94720-1760

[ysuzuki@berkeley.edu](mailto:ysuzuki@berkeley.edu)

## PROGRAM SCOPE

The *main research objective* of the program is to develop novel complex oxide thin films and heterostructures that will lead to an understanding of the role of surfaces and interfaces in spin polarized transport. Control of interface strain, roughness, chemical mixing, and magnetism will not only enable control of spin transport across interfaces, but also can be used to devise entirely new materials with properties distinct from their bulk counterparts. In particular, complex spin polarized oxide materials provide a rich playground for the exploration of novel magnetic properties not found in the bulk constituents and enable the development of functional interfaces to be incorporated into energy efficient technological applications.

Our current focus is on two classes of complex oxide materials where interfaces play a key role:

(i) new interface and thin film materials whose properties are inaccessible in bulk form

(ii) novel magnetic junction devices based on highly spin polarized complex oxide materials that exploit complex oxide interfaces

## RECENT PROGRESS

Highlights of recent work include (i) spin polarization at the surfaces of half metallic oxides  $\text{La}_{0.7}\text{Sr}_{0.3}\text{MnO}_3$  and  $\text{Fe}_3\text{O}_4$ , (ii) the development of a new type of hybrid magnetic tunnel junction/spin filter devices that exploits oxide interfaces, (iii) double barrier  $\text{LaAlO}_3/\text{SrTiO}_3$  junctions and (iv) tunable conductivity in  $\text{LaTiO}_3$  thin films.

We find that spin polarization depends on the crystal orientation of the surface. When juxtaposed with paramagnets or ferromagnets, we are able to demonstrate strong magnetic coupling for isostructural and no magnetic coupling for non-isostructural interfaces. We have exploited these interfacial phenomena in a new type of hybrid spin filter/ magnetic tunnel junction. Our hybrid spin-filter/magnetic-tunnel junction devices are epitaxial oxide junctions of highly spin polarized  $\text{La}_{0.7}\text{Sr}_{0.3}\text{MnO}_3$  and  $\text{Fe}_3\text{O}_4$  electrodes with magnetic  $\text{NiMn}_2\text{O}_4$  insulating barrier layers. These devices are composed of two kinds of interfaces: a non-isostructural perovskite-spinel interface with very little magnetic coupling and an isostructural spinel-spinel interface with strong magnetic coupling. These contrasting behaviors are confirmed by surface sensitive, element specific X-ray magnetic circular dichroism combined with X-ray absorption spectroscopy. Depending on whether the barrier is in a paramagnetic or ferromagnetic state, the junction exhibits magnetic tunnel junction behavior where the spin polarized conduction is dominated by the electrode-barrier interface or spin filter behavior where conduction is dominated by barrier layer magnetism.

We have also developed another type of device called the double barrier junction. It is composed of SrRuO<sub>3</sub> electrodes and a double barrier layer of LaAlO<sub>3</sub>/SrTiO<sub>3</sub> bilayers that enables us to probe the extent of the metallic interface between the two band insulators LaAlO<sub>3</sub> and SrTiO<sub>3</sub> observed by many groups. Scanning transmission electron microscopy and electron energy loss spectroscopy indicate that the interdiffusion of cations at the LaAlO<sub>3</sub>/SrTiO<sub>3</sub> interface is half a unit cell or less and that the oxygen content of the SrTiO<sub>3</sub> does not differ from that of bulk SrTiO<sub>3</sub> substrates. Control tunnel junctions with just a single layer of either SrTiO<sub>3</sub> or LaAlO<sub>3</sub> show typical tunneling conductance curves while double barrier junctions consistently show ohmic behavior for total barrier thickness on the order of 5nm. These results suggest that the metallic reconstruction at the LaAlO<sub>3</sub>/SrTiO<sub>3</sub> interface is at least 2.5nm thick.

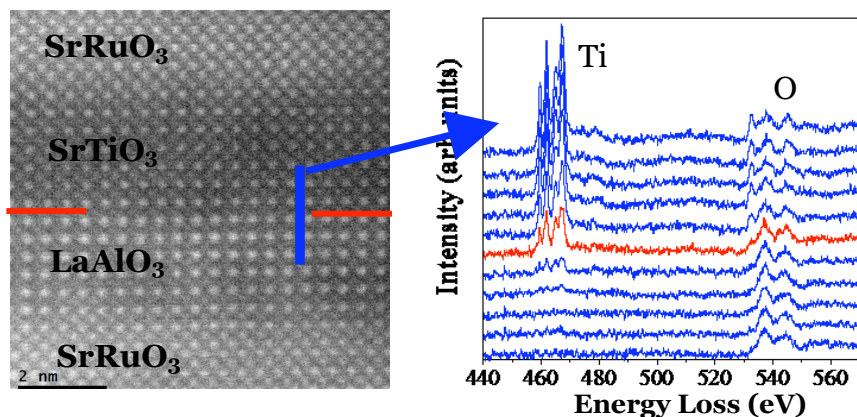


Figure 1. Scanning transmission electron microscopy image (left) and electron energy loss spectroscopy shows the atomically abrupt interface of a double barrier SrRuO<sub>3</sub>/LaAlO<sub>3</sub>/SrTiO<sub>3</sub>/SrRuO<sub>3</sub> junction (right) in collaboration with Chi and Browning.

Finally, strong electron-electron and electron-lattice correlations play critical roles in metal-insulator transitions of complex oxide materials. LaTiO<sub>3</sub> (LTO) is a correlated Mott insulator in the bulk, but metallicity can be induced by alkaline earth doping of the La site, cation deficiency, or charge transfer from a nearby interface. However, hydrostatic pressure has not been shown to induce metallicity in bulk LaTiO<sub>3</sub>. We have recently demonstrated electrical transport characteristics, ranging from metallic to insulating, in LaTiO<sub>3</sub> thin films tetragonally deformed by (001) SrTiO<sub>3</sub> (STO), (LaAlO<sub>3</sub>)<sub>0.3</sub>(Sr<sub>2</sub>AlTaO<sub>6</sub>)<sub>0.7</sub> (LSAT), and LaAlO<sub>3</sub> (LAO) substrates. Structural distortions are induced by epitaxial in-plane (IP) biaxial compressive strain, and the lower symmetry lifts the degeneracy of electronic bands, creating anisotropy that cannot be routinely attained in the bulk. We have proposed a model that explains how electronic anisotropy, resulting from reduced lattice symmetry, plays a crucial role in the metal-insulator transition (MIT) in LTO thin films. From our studies, the effects of epitaxial strain in LTO films must be considered in conjunction with any interfacial electronic reconstruction phenomena in order to explain metallicity in LTO/STO heterostructures.

## FUTURE PLANS

In each highlighted area above as well as our additional projects in magnetic nanostructures and other complex oxide thin film materials, we plan to focus on some of the big challenges in the areas of oxide interfaces and spin based devices. We will tackle the role of interface electronic reconstruction versus defects in the observed metallicity and magnetism observed at SrTiO<sub>3</sub>/LaAlO<sub>3</sub> interfaces via lateral and junction heterostructures. One of the big challenges in the development of spin-based devices has been to develop ferromagnetic materials as spin filter barrier layers and spin polarized electrodes. We will develop spinel structure thin film materials

to this end; oxide spinels represent a class of materials whose properties can be tuned by cation distribution and valence as well as oxygen content.

## REFERENCES (2005-present)

1. Yayoi Takamura, Jostein K. Grepstad, Rajesh V. Chopdekar, Ann F. Marshall, Hong Zheng, John F. Mitchell, and Yuri Suzuki, Structural, Magnetic and Electronic Properties of (110)-Oriented Epitaxial Thin Films of the Bilayer Magnanite  $\text{La}_{1.2}\text{Sr}_{1.8}\text{Mn}_2\text{O}_7$ , *Applied Physics Letters* **87** 142508 (2005).
2. Jostein Grepstad, Yayoi Takamura, Andreas Scholl, Ingebrigt Hole, Yuri Suzuki, Thomas Tybell, "Effects of Thermal Annealing in Oxygen on the Antiferromagnetic Order and Domain Structure of Epitaxial  $\text{LaFeO}_3$  Thin Films," *Thin Solid Films* **486** 108-112 (2005).
3. Yayoi Takamura, Jostein K. Grepstad, Rajesh V. Chopdekar, Ann F. Marshall, Hong Zheng, John F. Mitchell, and Yuri Suzuki, "Thickness Dependent Properties of (110)-Oriented  $\text{La}_{1.2}\text{Sr}_{1.8}\text{Mn}_2\text{O}_7$  films," *Journal of Applied Physics* **99** 8S902 (2006).
4. L.M.B. Alldredge, R.V. Chopdekar, B.B. Nelson-Cheeseman, Y. Suzuki, "Complex oxide based magnetic tunnel junctions with nonmagnetic insulating barriers," *Journal of Applied Physics* **99** 8K303 (2006).
5. Yayoi Takamura, Rajesh V. Chopdekar, Andreas Scholl, Andrew Doran, J. Alexander Liddle, Bruce Harteneck, and Yuri Suzuki, "Tuning magnetic domain structure in  $\text{La}_{0.7}\text{Sr}_{0.3}\text{MnO}_3$  islands by matrix and substrate strain," *Nano Letters* **6** 1287 (2006).
6. L.M.B. Alldredge, R.V. Chopdekar, B.B. Nelson-Cheeseman, Y. Suzuki, "Spin-polarized conduction in oxide magnetic tunnel junctions with spinel/perovskite interfaces," *Applied Physics Letters* **89** 182504 (2006).
7. Elke Arenholz, Gerrit van der Laan, Rajesh V. Chopdekar, Y. Suzuki, "Anisotropic X-ray magnetic linear dichroism at the L<sub>2,3</sub> edges of  $\text{Fe}_3\text{O}_4$ ," *Physical Review B* **74** 094407 (2006).
8. R. Farshchi, R. V. Chopdekar, Y. Suzuki, P. D. Ashby, I. D. Sharp, J. W. Beeman, E. E. Haller, and O.D. Dubon, "2D-patterned ferromagnetic III-Mn-V semiconductors: towards planar spintronics," *Physica Status Solidi C* **4** 1755 (2007).
9. Lane W. Martin, Qian Zhan, Yuri Suzuki, R.Ramesh, Miaofang Chi, N. Browning, Teruyasu Mizoguchi, Jens Kreisel, "Growth and Structure of  $\text{PbVO}_3$  Thin Films," *Applied Physics Letters* **90** 062903 (2007).
10. Amit Kumar, Lane Martin, Sava Denev, Jeffery B. Kortright, Yuri Suzuki, R. Ramesh, Venkatraman Gopalan, "Polar and Magnetic Properties of  $\text{PbVO}_3$  Thin Films," *Physical Review B* **75** 060101 (2007).

11. Elke Arenholz, Gerrit van der Laan, Rajesh Chopdekar, Yuri Suzuki, "Angle Dependent Ni<sup>2+</sup> X-ray Magnetic Linear Dichroism: Interfacial Coupling Revisited," *Physical Review Letters* **98** 197201 (2007).
12. R. Farshchi, P. D. Ashby, D. J. Hwang, C. P. Grigoropoulos, R. V. Chopdekar, Y. Suzuki, and O. D. Dubon, "Hydrogen patterning of Ga<sub>1-x</sub>Mn<sub>x</sub>As for planar spintronics," *Physica B: Condensed Matter* **401-402** 447 (2007).
13. B.B. Nelson-Cheeseman, R.V. Chopdekar, L.M.B. Alldredge, J.S. Bettinger, E. Arenholz, Yuri Suzuki, "Spin Transport Tuned by Interfacial and Barrier Layer Magnetism in Magnetic Tunnel Junctions," *Rapid Communications Physical Review B* **76** R220410 (2007).
14. Matthew T. Corbo, Florian Straub, Haimei Zheng, Maria de la Paz, Yuri Suzuki, "Magneto-Optical Kerr Effect in Multiferroic Nanostructures," *Proceedings of the Materials Research Society Meeting* **966E** T14.02 (2007).
15. Gerrit van der Laan, Elke Arenholz, Rajesh Chopdekar, Yuri Suzuki, "Influence of Crystal Field on Anisotropic X-ray Magnetic Linear Dichroism at the Co L<sub>2,3</sub> Edges," *Physical Review B* **77** 64407 (2008).
16. B.B. Nelson-Cheeseman, R.V. Chopdekar, J.S. Bettinger, E. Arenholz, A. Scholl, A. Doran, and Y. Suzuki, "Magnetism and Chemical Structure at Spinel-Spinel Interfaces," to be published in *Journal of Applied Physics*.

# Coupled Phenomena in Magnetoelectric Multiferroics

Xiaoli Tan

*Dept. of Materials Science and Engineering, Iowa State University, Ames, IA 50011*  
*xtan@iastate.edu*

R. William McCallum

*Materials and Engineering Physics, Ames Laboratory, U.S.-DOE, Ames, IA 50011*  
*mccallum@ameslab.gov*

Vladimir Antropov

*Condensed Matter Physics, Ames Laboratory, U.S.-DOE, Ames, IA 50011*  
*antropov@ameslab.gov*

## ***Program Scope***

Magnetic and electronic materials are deeply rooted into every aspect of modern technology. Trends toward device miniaturization have generated tremendous interest in combining electronic and magnetic properties into multifunctional materials, so that a single device component can perform multiple tasks. The magnetoelectric effect, induction of electric polarization by a magnetic field and conversely, of magnetization by an electric field, provides an interaction between magnetic and electric properties. These so called *multiferroics* may be divided into two broad classes of materials. In the first class, ferroelectricity is associated with a distortion of the crystal lattice which breaks spatial inversion symmetry at one temperature. At a second temperature, usually lower, some type of simple magnetic order occurs. Due to the seemingly uncoupled nature of the two transitions, the influences of applied magnetic fields on electrical polarization in the magnetically ordered state are usually limited. In the second type of material, the ferroelectric transition occurs at a single combined transition temperature with a long range sinusoidal magnetic order. These materials depend on the modulated magnetic order to break the spatial inversion symmetry so that ferroelectricity can exist. Therefore, the spontaneous polarization is highly dependent on the exact nature of the magnetic order. As a consequence, external magnetic fields control the ferroelectric polarization through their influences on the magnetic order.

This program focuses on the  $\text{RMn}_2\text{O}_5$  (R is a rare earth element, La, and Bi) oxide family which belongs to the second type. In this family, the exact nature of the exchange interactions and ferroelectricity and their coupling is still open to debate. For instance, both  $\text{Mn}^{3+}$  ionic displacement and spin-density waves have been offered as the primary mechanism for ferroelectricity. Also, the factors influencing the strength of the magnetoelectric coupling and possibly defining a theoretical maximum coupling are essentially unknown in realistic systems. At the present time, even qualitative studies of the quite complex quantum theory of phase transitions to describe multiferroics have not been performed. A quantitative study of the electronic structure, magnetic interactions and the way these interactions are directly or indirectly affected by applied electric field is required to fully understand these materials and produce a recipe to obtain the optimal balance of the competing interactions to define a maximum of the multiferroic effects.

This program takes an integrated “materials-experiment-theory” approach to address the fundamental questions in the  $\text{RMn}_2\text{O}_5$  family of compounds. These complex oxides are

improper ferroelectrics where the symmetry breaking necessary for ferroelectricity results from the magnetic order. We are studying these technologically promising compounds through definitive experiments supported by detailed theoretical calculations. While there has been a large amount of experimental work on multiferroic materials in the recent past, there is limited understanding of the fundamental origins of the complex properties that are exhibited. We are producing high quality single crystals and polycrystalline ceramics and perform a unique combination of complementary diffraction experiments with electron, x-ray, and neutron beams. DOE-sponsored national user facilities will be intensively utilized to carry out the critical diffraction studies.

### ***Recent Progress***

Our initial efforts on materials preparation have focused on  $\text{YMn}_2\text{O}_5$ ,  $\text{TbMn}_2\text{O}_5$ , and  $\text{GdMn}_2\text{O}_5$ . The complex kinetics of formation of these compounds leads to the claim by many authors that they cannot be prepared using solid state synthesis techniques. However by manipulating the driving force for formation using oxygen partial pressure we have rapidly obtained phase pure powders and bulk pellets. Furthermore, by exploring the wet chemistry method, we have prepared phase pure nanoparticles with controlled size. Figure 1 shows the transmission electron microscopy (TEM) image of the 50nm particles. With regard to the single crystal growth, it should be noted that the  $\text{RMn}_2\text{O}_5$  compounds form on cooling by a peritectoid reaction of two solid compounds. Hence, they are never in equilibrium with a melt in their own system. Previously, single crystals have been grown using a  $\text{PbO-PbF}_2\text{-B}_2\text{O}_3$  flux but these crystals were found to contain Pb. We are pursuing several methods of crystal production and have produced the millimeter-sized crystals of  $\text{YMn}_2\text{O}_5$  for the first time by the molten salt electrolysis method. Initial x-ray diffraction of powdered samples indicates they are free of second phase.

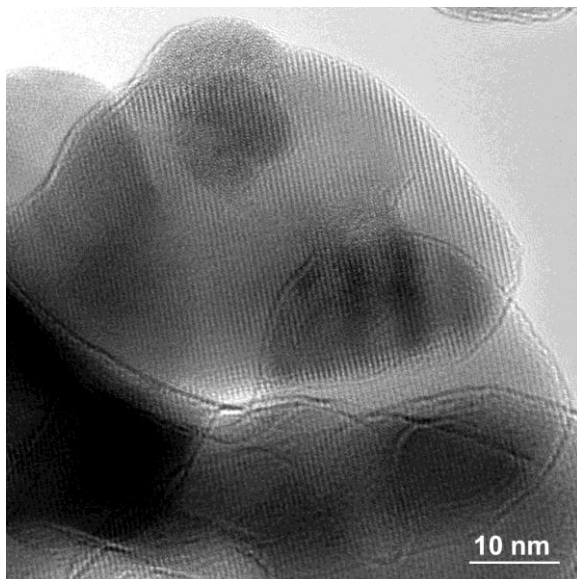


Fig. 1. TEM image of  $\text{YMn}_2\text{O}_5$  nanoparticles.



Fig. 2. High quality  $\text{YMn}_2\text{O}_5$  single crystals.

In situ TEM experiments with applied electric fields at low temperatures are critical to this project. We have demonstrated our ability to image ferroelectric domains under applied electric fields at liquid nitrogen temperature in ferroelectric ceramic samples using a specially

constructed specimen holder in MEP's newly acquired FEI Tecnai G2 F20 TEM. The same microscope and sample holder have been used to image magnetic domains in a  $\text{Pb}(\text{Fe}_{2/3}\text{W}_{1/3})\text{O}_3$ -based multiferroic ceramic specimens at low temperatures ( $\text{LN}_2$  cooling) using the Lorentz lens on the microscope. TEM observation of the  $\text{YMn}_2\text{O}_5$  ceramic specimens at 20K with a liquid helium cryogenic holder has been demonstrated at the Electron Microscopy Center at the Argonne National Lab, as shown in Fig. 3.

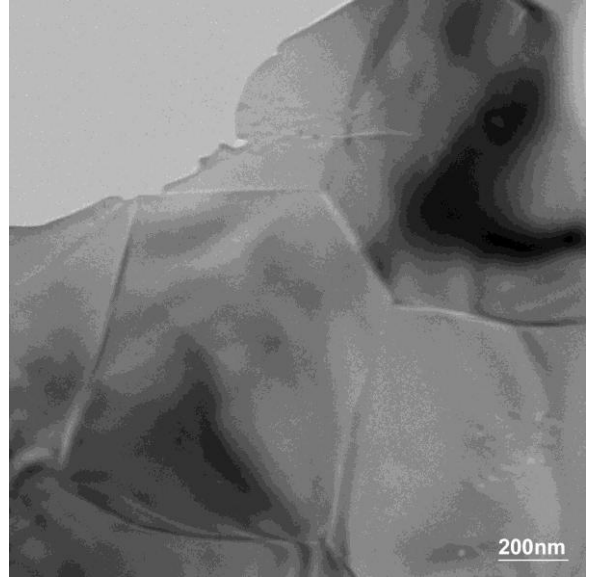


Fig. 3. TEM bright field image of the  $\text{YMn}_2\text{O}_5$  ceramic specimen at 20K.

Magnetic measurements have been performed on a series of  $\text{YMn}_2\text{O}_5$  nanopowders with different sizes prepared under different oxygen pressures. Fig. 4(a) shows the  $\chi$  vs. T under zero-field-cool and field-cool (100Oe) of the nanopowder obtained at 1000°C under 10 bar oxygen pressure. For comparison, results for another powder with about the same size prepared at 1000°C under 1 bar oxygen pressure are shown in Fig. 4(b). Obvious differences are seen: (1) the  $\chi$  at 10K is 0.017emu/Oe/mol for the powder calcined under 1 bar  $\text{O}_2$  pressure while 0.066emu/Oe/mol for the powder calcined under 10 bar  $\text{O}_2$ . (2) For the powder prepared under 1 bar  $\text{O}_2$ , there's only one transition temperature at 40~45K. While for the powder obtained under 10 bar  $\text{O}_2$ , there's another transition occurring at 10~15K and this transition dominates the magnetic behavior of the material. The magnetic transition at 40~45K still exists but becomes very obscure because of the strong magnetization of the 10~15K ordering. The significant oxygen pressure effect we observed experimentally has been predicted by our theoretical calculations.

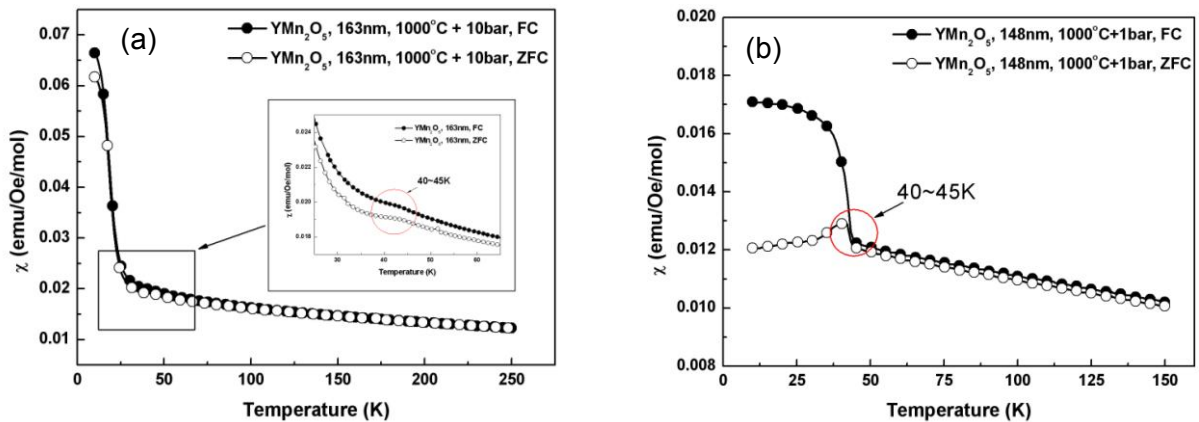


Fig. 4. Magnetic susceptibility  $\chi$  vs. temperature T of  $\text{YMn}_2\text{O}_5$  nanopowder prepared under different oxygen pressure: (a) 10 bar  $\text{O}_2$ ; and (b) 1 bar  $\text{O}_2$ .

Theoretical calculations are initially being performed on the related, but simpler, compound  $\text{YMnO}_3$  where there are previous theoretical results for comparison. These calculations will identify which computational techniques are appropriate for this class of materials. The critical feature of the calculations is that they predict an energy gap for these insulating materials. As with previous results in other systems, our calculations for this system

demonstrate that the LDA technique does not produce a gap while LDA+U and SIC techniques do. The magnetic moment at Mn site was found to be 3.2  $\mu\text{B}$ . However, our most interesting result is a LDA calculation for a material which contain oxygen vacancies, a possibility which has not been previously addressed theoretically. We performed a calculation for the structure with the in-plane O atom at the 2a position removed. This resulted in the formation of a small gap  $\sim 0.2$  eV. Thus, both the standard Coulomb correlations and a high concentration of oxygen defects can produce an energy gap in these materials. While the oxygen defect concentration used in the calculation is much higher than that is expected in the materials shown in Fig. 4, these calculations predict that oxygen defects may play a role in determining the energy gap.

### Future Plans

The family of  $\text{RMe}_2\text{O}_5$  compounds offers the opportunity to systematically vary both crystallographic and electronic properties of a class of multiferroic materials while preserving the same space group. Using this generic family we will investigate: (i) the chemical substitution both on rare-earth and 3d-sites, (ii) the dependence on volume and distortion, and, as a consequence, the origin of striction mechanisms, (iii) the character of the various exchange mechanisms, (iv) the influence of 4f electrons on multiferroics properties and their interaction with 3d magnetic electrons, and (v) additional interactions as they are observed. The planned experiments for materials preparation and characterization are summarized in Fig. 5.

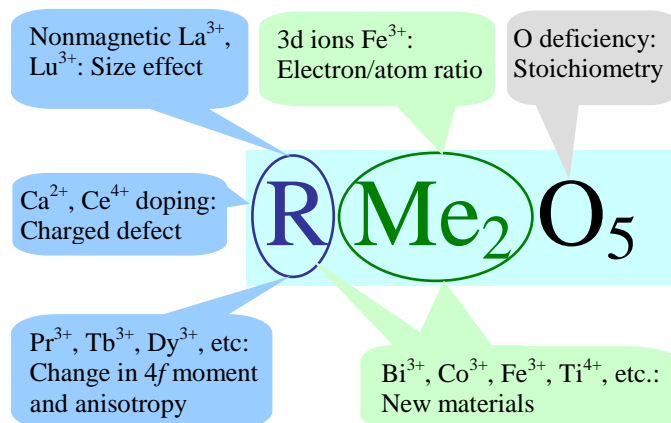


Fig. 5. Schematic diagram for the proposed systematic trend study.

Experimental determination of systematic variations of the properties of the materials as a function of lattice parameter, transition element electron/atom ratios, and rare earth moment will provide validation for extensive first principles calculations with the goal of establishing a quantitative understanding of the fundamental questions in these multiferroic compounds. The validated models are expected to help predict critical figure-of-merit parameters, such as Curie/Neel temperature, saturation magnetization, spontaneous polarization, etc. as a function of materials parameters. The theoretical results will be used to guide experiment, measurement, and materials preparation.

### List of Publications

- J. Pulikkotil and V. Antropov, “Influence of oxygen defects on the energy gap formation and magnetic properties of multiferroic materials,” presented at the 52nd Magnetism and Magnetic Materials Conference in Tampa, November 2007 and will be published in *Journal of Applied Physics* in 2008.
- We are in the process of preparing one manuscript on  $\text{YMn}_2\text{O}_5$  nanoparticles.

Title: “Structure and Magnetism in Novel Group IV Element-Based Magnetic Materials”

Principal Investigator: Frank Tsui ([ftsui@physics.unc.edu](mailto:ftsui@physics.unc.edu)), Physics and Astronomy, University of North Carolina, CB#3255, Phillips Hall, Chapel Hill, NC 27599

## I. Program Scope

The program is to investigate structure, magnetism and spin polarization of novel group IV element-based magnetic materials as a function of composition and epitaxial constraints. Systematic structural, magnetic, and electrical measurements on epitaxial films and heterostructures of Si/Ge-based magnetic ternary alloys containing two transition metal elements grown by non-equilibrium MBE techniques are carried out, using x-ray microbeam diffraction and spectroscopy, and x-ray magnetic circular dichroism, scanning probe microscopy, and tunneling spectroscopy. The work is aimed at elucidating the nature and interplay between structure, magnetism, and spin-polarization in this novel class of ternary alloys that exhibit promises for high temperature magnetic semiconductors and half-metallic compounds, and exploring fundamental processes that stabilize epitaxial growth of Si-compatible magnetic materials and control the electronic and magnetic properties in these complex materials. Combinatorial approach provides the means for the systematic studies, and the complex nature of the work necessitates this approach.

The research is a collaborative team effort between researchers and students at universities and national labs. It is leveraged against significant advances and resources in MBE synthesis of novel Ge-based magnetic materials (funded by NSF). Students are trained at many levels in areas of critical importance. The work promises to make significant impact on Si/Ge compatible spin-polarized materials by exploring and elucidating the fundamental processes that control structure, magnetism and spin-polarization and by enhancing our ability to manipulate and tailor electronic and magnetic structures through atomic scale synthesis.

## II. Recent Progress

### II.a. Stability of Transition Metal Dopants in a Ge Magnetic Semiconductor

Our study on epitaxial films of Co and Mn co-doped Ge magnetic semiconductor (DMS) has provided the first direct evidence of enhanced transition metal dopant stability, and an atomistic mechanism for significantly increasing doping level in a DMS [manuscript submitted]. Systematic investigation of structural and chemical properties using x-ray microbeam techniques at the Advanced Photon Source (APS) and dynamic secondary ion mass-spectrometry reveals that co-doping with Co can dramatically reduce phase separation and diffusion of Mn within Ge lattice, and that substitutional Co with its strong tendency to dimerize with interstitial Mn plays a critical role in controlling the energetics and kinetics of the system and thus the coherent epitaxial growth process. Our magnetic and magnetotransport measurements further show that Co as a co-dopant complements Mn in Ge magnetically and electronically, such that by enhancing the total doping level, the magnetic properties can be significantly enhanced. The work demonstrates feasibility for tailored DMS materials and provides the impetus for developing atomistic approaches to elucidate group IV-based DMS and to realize room temperature ferromagnetism.

As shown in Fig. 1, the epitaxial phase diagram of Co and Mn co-doped Ge (001) exhibits 4 different regions: coherent epitaxy in regions I and II, where the film strains with respect to Ge obey the Vegard's law and the film is free of detectable disorders, region III with Mn surface aggregation (blue contours around the binary Mn-Ge), which is suppressed by Co co-doping, and in region IV rough epitaxial growth with stacking faults (green contours and gray area) but without detectable secondary phases.

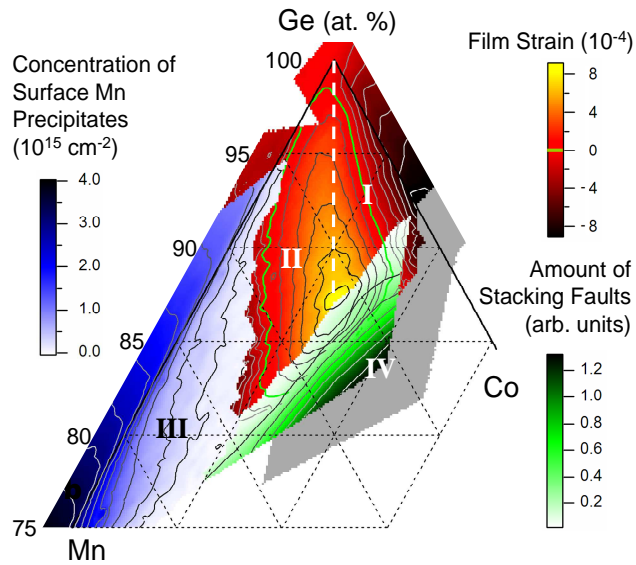


**Fig. 1** Phase diagram and strain states of Co and Mn co-doped Ge (001) epitaxial thin film.

The measured film strains within the two regions of coherent epitaxy (I and II in Fig. 1) and the corresponding linear (planar)

dependences on concentrations (the Vegard's law) reveal the critical role played by substitutional Co with its strong tendency to dimerize with interstitial Mn in controlling the energetics and kinetics of the system. This mechanism and the quantitative values of atomic radii associated with the dimers and access monomers, obtained from fitting the measured strains, show excellent agreement with recent first principle calculations.

In order to study heterostructures of DMS and undoped semiconductors, growth and properties of superlattices containing highly doped Ge DMS and undoped Ge have been investigated [preprint].

As shown in Fig. 2, smooth layer-by-layer epitaxial growth has been observed during the growth of Ge DMS (blue) with co-dopants of Co and Mn at 5 at. % each and that of undoped Ge (red). In-situ real time reflection high energy electron diffraction (RHEED) experiments show persistent (atomic) bilayer oscillations in both intensity and width that are identical to the behavior of low temperature homoepitaxial growth of Ge (001), demonstrating the ability for controlled

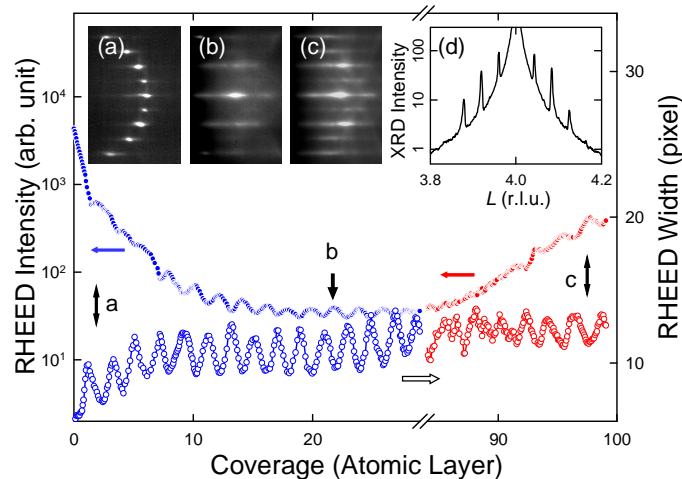


**Fig. 2** Layer-by-layer epitaxial growth of superlattices containing Ge DMS and Ge. RHEED patterns (a-c) and RHEED intensity (close symbols) and width (open symbols) oscillations during growth of Co and Mn co-doped Ge (blue) and Ge (red). (d) XRD pattern of the superlattice.

synthesis on atomic scale. Ex-situ x-ray diffraction (XRD) experiments on the completed superlattice show that the XRD pattern [see Fig. 2(d)] exhibits many orders of superlattice side bands on both sides of the Bragg reflection, indicating high crystalline quality with sharp interfaces between DMS and Ge.

When optimally doped, the Ge-based DMS exhibit ferromagnetism near room temperature and *p*-type semiconductivity with high mobility. The total doping concentration can be increased to beyond 15 at. %, where ferromagnetism is enhanced correspondingly. The nature of magnetism and spin dependent states at the high doping levels are being examined using complementary techniques. In a recent work on a II-VI compound [Dietl and co-workers 2007], co-doping with N and I is shown to alter morphology of dopant-rich clusters, via a different mechanism, but reducing the dopant-rich cluster is shown to suppress ferromagnetism. Evidently it is still an open question whether in general heterogeneous clusters are essential for ferromagnetism in DMS. These advances demonstrate feasibility for tailored DMS materials, and provide the impetus for developing atomistic approaches and analysis, in order to elucidate the nature of dopants and their correlations in DMS.

## II.b. Structural and Chemical Order in the Heusler Alloy $\text{Co}_2\text{MnGe}$ .

Full spin polarization at the Fermi level has been predicted for this Heusler compound, but experimentally it has been proven to be extremely illusive, owing to the presence of a variety of potential disorders. Using microbeam anomalous diffraction (at APS) and combinatorial MBE techniques, we have examined and identified these disorders for the first time, including elemental site swapping and sublattice vacancies, and their composition dependence. A comprehensive model has been developed for quantitative analyses. Our results show that the structural and chemical ordering is very stable over a narrow region of composition with Co to Mn atomic ratio of 2:1, as shown in Fig. 3, illustrating that the structural quality of the film near the Heusler compound depends sensitively on composition.

Our results show that the x-ray techniques are sufficiently sensitive and quantitative to probe the various amounts of disorders, including Co-Mn, Co-Ge, and Mn-Ge site swapping, and Co sublattice vacancies. The analysis thus far does not include solid-state effects that give rise to the fine structures below the elemental edge. Full analysis that includes these effects and the experiments are being developed in collaboration with beamline scientists at the APS, including x-ray absorption near edge structure and x-ray absorption fine structure, which will allow us to probe the chemical environment around each atom.

Our abilities to synthesize high quality materials, to fine-tune epitaxial constraints using heteroepitaxial strained buffer layers, and to detect and quantify structural and chemical order make it possible to investigate the interplay between atomic scale ordering and magnetism

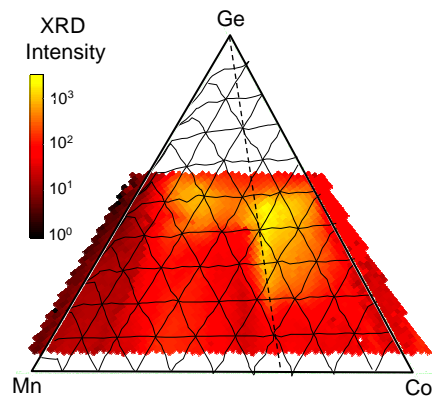


**Fig. 3** Crystalline quality versus composition for  $\text{Co}_x\text{Mn}_y\text{Ge}_{1-x-y}$  (111) epitaxial film: integrated XRD intensity at (022) reflection. The dashed line indicates a constant Co to Mn atomic ratio of 2:1.

and spin dependent states as functions of composition and epitaxial constraints, and to probe the processes that control spin polarization in these systems, as they are outlined in the next section.

### III. Future Plans

We plan to use energy dependent x-ray microbeam techniques at the APS to investigate impurity states of transition metal dopants and their local environment in DMS, and structural and chemical ordering in epitaxial films of Heusler alloys. We plan to examine local density of states and spin polarization near the Fermi level in these materials, using tunneling and point contact spectroscopy, and to probe the interplay between these and structural and chemical ordering, as a function of composition and epitaxial constraints.

We plan to investigate carrier mediated ferromagnetism and active control of magnetization states in group IV based DMS using an insulating field effect structure. We also plan to use both types of coherent epitaxial films to explore spin dependent transport phenomena in strained SiGe structures.

Critical complementary experiments are being developed to probe atomic scale local states in these materials, including impurity states, distribution and correlation, in collaboration with DOE funded groups and national labs. They include

- local electrode atom probe (LEAP) tomography
- analytical scanning transmission electron microscopy (STEM) and spectroscopy
- focused ion beam (FIB) based sample preparation for LEAP and STEM
- electron spin resonance (ESR) spectroscopy

### IV. References

1. *Anomalous X-Ray Diffraction Study of Disorders in Epitaxial Films of the Heusler Alloy  $Co_2MnGe$* , B. A. Collins, Y. Zhong, Y. S. Chu, L. He, and F. Tsui, *J. Vac. Sci. Tech. B* **25**, 999-1003 (2007).
2. *Epitaxial Growth of  $(FeCo)_xGe_{1-x}(001)$* , L. He, B. A. Collins, F. Tsui, Y. Zhong, S. Vogt, Y. S. Chu, *J. Vac. Sci. Tech. B* **25**, 1217-1220 (2007).
3. *Combinatorial Synthesis and Characterization of Epitaxial Films of Co and Mn Doped Ge (001)*, F. Tsui, B. A. Collins, L. He, A. Mellnik, Y. Zhong, S. Vogt, Y. S. Chu, *Appl. Surf. Sci.* **254**, 709-713 (2007).
4. *High-Resolution X-ray Diffraction Studies on Combinatorial Epitaxial Ge (001) Thin Films on Ge(001) Substrates*, Y. Zhong, Y. S. Chu, B. A. Collins and F. Tsui, *Appl. Surf. Sci.* **254**, 714-719 (2007).

# Understanding the Spin-Lattice Coupling in Multiferroic Oxides

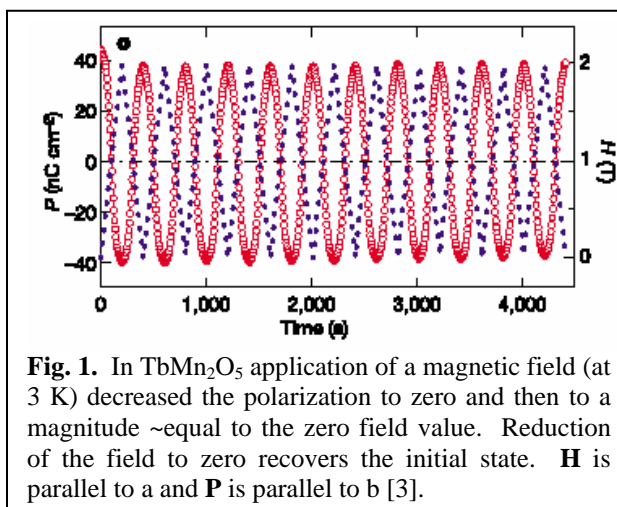
Trevor A. Tyson, New Jersey Institute of Technology

**Abstract:** Multiferroic oxides (such as  $\text{RMnO}_3$  and  $\text{RMn}_2\text{O}_5$  ( $\text{R}=\text{rare earth}$ )) are a class of materials which are simultaneously ferroelectric and ferromagnetic. The possibility of coupling the magnetic and electric properties will enable new functions. These capabilities will possibly lead to devices in which ferroelectric memory can be written with magnetic fields or magnetic bits can be written by an electric field. However, the detailed mechanism behind the coupling of the spin and atomic degrees of freedom in these materials is not well understood. In this proposal we will conduct structural measurements on multiple length scales in the presence of magnetic and electrical fields in order to ascertain the mechanism behind the spin-lattice coupling. Building on pilot study results, we will conduct temperature and magnetic field dependent x-ray absorption measurements to determine changes (with respect to the rare earth and transition metal sites) in atomic structure accompanying transition into the magnetic state and to explore the magneto-structural coupling. Coupling of longer range local distortions will be probed by x-ray diffuse scattering. The long-range structure will be examined by high resolution wide angle x-ray diffraction measurements. Exploration of the effect of substrate induced strain on films of these materials may lead to new systems with enhanced electric polarization. This effect will be first explored by hydrostatic high-pressure optical and structural measurements on bulk samples. The multiple length scale synchrotron-based measurements may assist in developing more detailed models of these materials and possibly lead to device applications. An important contribution of this work will be the training of graduate students and postdoctoral researchers in materials synthesis and synchrotron based spectroscopy and x-ray scattering techniques.

## I. Introduction and Motivation

Magneto-electric multiferroics are a class of materials which are simultaneously ferroelectric and ferromagnetic [1, 2]. The possibility of coupling of the magnetic and electric properties will enable new functions. These include the ability to store data as both magnetic and electrical bits and the ability to write ferroelectric bits with magnetic fields. Although broad classes of ferromagnetic materials and ferroelectric materials exist, not many multiferroelectric systems have been observed. It has been suggested in by Spalding [1] that while the 3d occupancy on  $\text{ABO}_3$  systems creates unpaired electrons needed for magnetism, it also stabilizes inversion center preserving Jahn-Teller distortions. Magnetoelectric effects have also been explored in systems such as  $\text{Ti}_2\text{O}_3$ ,  $\text{GaFeO}_3$ , boracite,  $\text{TbPO}_4$ ,  $\text{BiFeO}_3$  and  $\text{BiMnO}_3$  [2]. The characteristic feature of these systems was the weak coupling between the magnetic and electric components.

Recently, Kimura *et al.* [3] discovered a large magnetoelectric and magnetocapacitance effects induced by magnetic fields in the simple perovskite system  $\text{TbMnO}_3$ . The application of a magnetic field along the



b-axis suppresses the polarization along the b-axis but enhances it along the a-axis. The low temperature (below 40K) spontaneous polarization approaches  $\sim 80\text{nC/cm}^2$ . This is approximately two orders of magnitude lower than the room temperature polarization of  $\text{BaTiO}_3$ . More recently, Hur *et al.* [4] discovered reversible switching in the system  $\text{TbMn}_2\text{O}_5$  (composed of c-axis  $\text{MnO}_6$  polyhedral chains cross linked by  $\text{MnO}_5$  pyramids). By sweeping the magnetic field from zero to two Tesla the polarization passes through zero and attains a value with magnitude  $\sim$ equal to the zero field value (Fig. 1). Reducing the field to zero recovers the initial state. The magnitude of the polarization in zero field is  $\sim 40\text{nC/cm}^2$ . Measurement of the thermal expansivity ( $\alpha$ ) along the a, b and c axes reveal jump at the magnetic and electric ordering temperatures [5]. The change in crystal dimensions by this bulk measurement on crossing the transitions is  $\Delta L/L \sim 10^{-6}$ . Indeed, anomalous changes have been found in the thermal displacement factors by neutron diffraction [6]. However, no significant changes in the lattice parameters have been found in the  $\text{ReMn}_2\text{O}_5$  (Re= Rare earth ion) system by high resolution x-ray diffraction methods [7].

A hexagonal phase ( $P6_3cm$ ) of  $\text{AMnO}_3$  is found for small radius ions (A=Ho, Er, Tm Yb, Lu Y and Sc) [1,8,9, 10], although the orthorhombic phase can be stabilized under soft chemistry conditions [11]. The region of hexagonal stability can be extended or reduced by deposition of  $\text{RMnO}_3$  films on strain inducing substrates [12]. The hexagonal manganites exhibit coupled ferromagnetism and ferroelectricity and large polarizations with high transition temperatures. Hence these materials fall into the class of multiferroic systems. Specifically, ferroelectric thin films have attracted much attention for use in nonvolatile random access memory (See Refs. [13] and references therein). Ferroelectric memories which utilize ferroelectric gate oxides based field effect transistors (metal/ferroelectric/semiconductor field effect transistors, MFS-FETs) are scaleable and exhibit nondestructive readout. In real devices problems such as polarization fatigue, retention and depolarization have been observed with the well known ferroelectrics such as lead zirconate titanate (PZT,  $\epsilon = 1700$ ). The properties of the hexagonal manganites in relation to their atomic and electronic structure are not well understood. A deep understanding is required to optimize these materials for data storage use.

In this proposal we focus on the  $\text{AMnO}_3$  and  $\text{ReMn}_2\text{O}_5$  systems and extend the results to the more general class of multiferroic complex oxides. Building on pilot study results, we will conduct temperature and magnetic field dependent x-ray absorption measurements to determine changes (with respect to the rare earth and transition metal site) in atomic structure accompanying transition into the magnetic state and to explore the magneto-structural coupling. Coupling of longer range local distortions will be probed by x-ray diffuse scattering. The long-range structure will be examined by high-resolution wide angle x-ray diffraction measurements. Exploration of the effect of external pressure will be carried out by diamond anvil cell based IR and x-ray diffraction (XRD) measurement. Substrate induced strain on films will also be studied. The experiments will be complemented by first principle density functional calculations.

## II. Research Team

### NJIT Members

Prof. T. A. Tyson (PI)  
Dr. Y. Qin (Postdoctoral Researcher)  
Mr. P. Gao (Graduate Student)  
Mr. Z. Chen (Graduate Student)

### Collaborators

Dr. J. Bai, University of Tennessee and Oak Ridge Nat. Lab. (NSLS X14A) – Collaboration on High resolution XRD  
Prof. S.-W. Cheong (Rutgers University) – Collaboration on single crystal and powder sample Synthesis  
Dr. C. Dubourdieu (CNRS) – Collaboration on thin film growth  
Dr. Z. Liu (Carnegie Institute, Washington, NSLS U2A) –collaboration on IR measurements  
Dr. Z. Zhong (Brookhaven National Laboratory, NSLS X17B1) – collaboration on hard x-ray diffuse scattering

### III. Preliminary Results

#### ReMn<sub>2</sub>O<sub>5</sub> System

Our initial measurement of the temperature dependent (3 K to 500 K) local structure of TbMn<sub>2</sub>O<sub>5</sub> showed that (1) the Tb-O bond distribution contributed significantly to the observed low temperature polarization and (2) that significant structural changes in the Tb-O distribution occur when the Tb ions order magnetically at low temperature. We have now conducted a series of measurement of the local structure of DyMn<sub>2</sub>O<sub>5</sub>. These magnetic field dependent local structural measurements were conducted at 3 K in magnetic fields varying from 0 to 9 T. A very weak but reproducible variation of the Dy-O distribution with magnetic field was observed. These results indicate that in this system, the Re site is central to the observed spin lattice coupling. The weak variation of the Dy-O distribution with magnetic field is consistent with the low polarization observed. The results indicate that theoretical models of these materials must properly treat the spin ordering on the Re sites (and not just the Mn sites).

#### Hexagonal AMnO<sub>3</sub> System

Detailed temperature dependent measurements were conducted on the hexagonal HoMnO<sub>3</sub> system. Previous heat capacity measurements revealed second order transitions at ~70 K, ~33 K and ~5 K. Neutron diffraction measurements associated these features with the Neel temperature and the spin reorientation temperatures of the triangular Mn lattice. The lowest temperature feature corresponds to the Ho site magnetic ordering temperature. The nature of the crystal structure enable us to extract information on the out-of plane Mn-O bonds and both the in plane Mn-O and Mn-Mn bonds. In Fig. 2(a) we see that no changes are observable in the out-of-plane (along c) Mn-O distribution. However, the in-plane Mn-O distribution shows second order  $\lambda$ -type features at all three magnetic ordering temperatures. The in-plane Mn-Mn bond distances reveal the same effect. This system thus possesses very strong spin-lattice coupling which may be tuned by in-plane strain. Experiments on strained films are in progress.

High pressure infrared and high pressure x-ray diffraction measurements have been conducted on a broad range of hexagonal ReMnO<sub>3</sub> systems. We have found large anisotropies in the compressibility of the a and c lattice parameters. The a-axis is significantly more compressible than the c axis. Also, we have observed the creation of a new phase in the LuMnO<sub>3</sub> system at ~10 GPa shown in Figs. 3 and 4. Structural refinements and the development of a method for measuring the polarization of a system at high pressures are in progress. The possibility of stabilizing this phase in the form of a film is being explored. Detailed first principles density

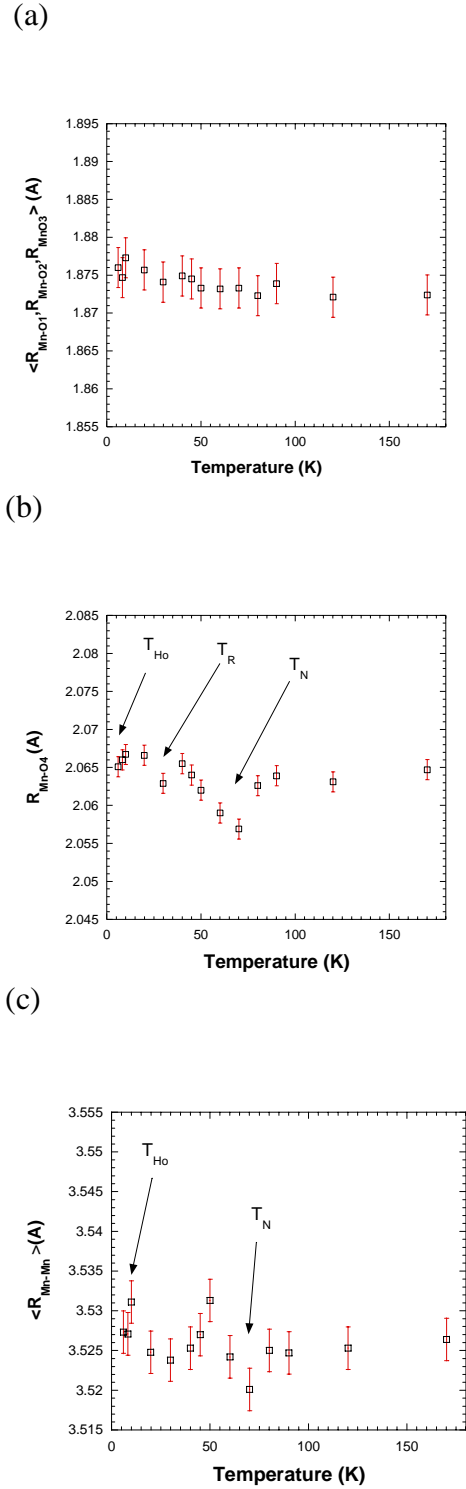


**Fig. 2.** The (a) out-of-plane Mn-O, (b) in-plane Mn-O and (c) in-plane Mn-Mn bond distances as a function of temperature. Note the  $\lambda$ -type (second order) anomalies occurring in the Mn-O4 (in-plane bond distance) which coincide with the Neel ( $T_N$ ), spin rotation ( $T_R$ ) and Ho ordering ( $T_{Ho}$ ) temperatures. Measurements were conducted at NSLS beam line X23B.

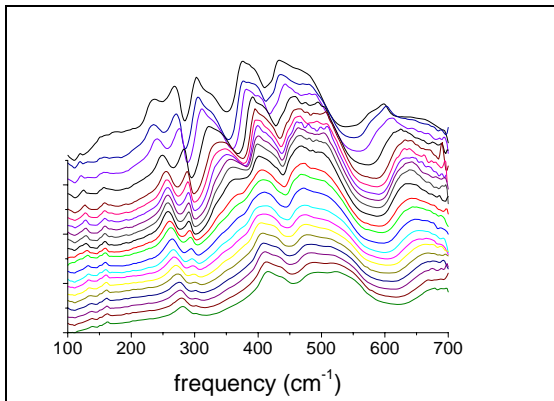


**Fig. 3.** Pressure-dependent infrared spectra for hexagonal LuMnO<sub>3</sub> at room temperature. The top curve is at 1 atm while lower curve is at ~20 GPa (~1 GPa steps). Note the pressure dependent changes in the region near 300 cm<sup>-1</sup>. XRD scans reveal a first-order phase transition. The pressure dependence of the polarization in bulk and in strained films is being explored. Methods for determining the polarization of samples in diamond anvil cell measurements are being explored. The IR spectra were measured at NSLS beamline U2A. .

functional (DFT) calculations are being conducted to determine the stable phases as a function of pressure and to predict the magnetic ground states.

#### IV. Challenges

Some challenges are being encountered. (1) An adequate beamline for routine hard x-ray diffuse scattering measurements is essential. A beamline which covers the energy range 60 to 100 KeV and has the ability to cool samples down to 3 K is being sought. (2) Access to a facility for conducting neutron pair distribution function analysis will significantly strengthen our local structural measurement capability and complement and constrain our XAFS models. (3) The acquisition of a small computer cluster for DFT calculations will be quite helpful for predicting which systems will be most promising to study.

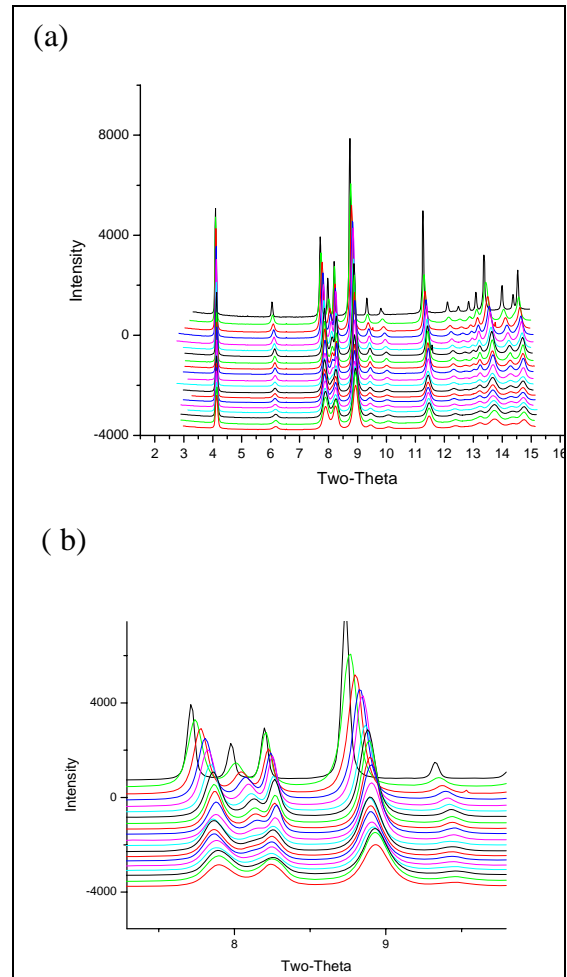


**Fig. 4.** Pressure-dependent x-ray diffraction pattern for LuMnO<sub>3</sub> on (a) extended and (b) limited angular ranges. The peaks near 8° (in (b)) changes above ~10 GPa and exhibits hysteresis but recover the starting structure on pressure release. The nature of the structural transition and its ferroelectric properties are being explored. The top curve is at 1 atm and lower curve is at 21 GPa. The measurements were conducted at NSLS X17C at a wavelength of 0.4066 Å.

## References

- [1] N. A. Spaldin, "Why are there so Few Magnetic Ferroelectrics", *J. Phys. Chem.* **104**, 6694 (2000).
- [2] (a) M. Fiebig, "Revival of the Magnetoelectric Effect", *J. Phys. D* **38**, R123 (2005).  
(b) N. Spaldin and M. Fiebig, "The Renaissance of Magnetoelectric Multiferroics", *Science* **309**, 391 (2005)  
(b) W. Prellier, M. Singh, P. Murugavel, "The Single-Phase Multiferroic Oxides: from Bulk to Thin Films", *J. Phys. Cond. Matt.* **17**, R803 (2005).
- [3] T. Kimura, T. Goto, H. Shintani, K. Ishizaka, T. A. Armita, Y. Tokura, "Magnetic Control of Ferroelectric Polarization", *Nature* **426**, 55 (2003).
- [4] N. Hur, S. Park, P. A. Sharma, J. S. Ahn, S. Guha and S.-W. Cheong, "Electric Polarization Reversal and Memory in a Multiferroic Material Induced by Magnetic Fields", *Nature* **429**, 392 (2004)
- [5] C. R. dela Cruz, F. Yen, B. Lorenz, M. M. Gospodinov, C. W. Chu, W. Ratcliff and J. W. Lynn, "Structural Anomalies at the Magnetic and Ferroelectric Transitions in  $\text{RMn}_2\text{O}_5$  (R=Tb, Dy, Ho)", *Phys. Rev. B* **73**, 100406 (2006).
- [6] L. C. Chapon, G. R. Blake, M. J. Gutmann, S. Park, N. Hur, P. G. Radaelli, and S. W. Cheong, "Structural Anomalies and Multiferroic Behavior in Magnetically Frustrated  $\text{TbMn}_2\text{O}_5$ ", *Physical Review Letters* **93**, 177402/1 (2004).
- [7] I. Kagomiya, S. Matsumoto, K. Kohn, Y. Fukuda, T. Shoubu, H. Kimura, Y. Noda and N. Ikeda, "Lattice Distortion at the Ferroelectric Transition of  $\text{YMn}_2\text{O}_5$ ", *Ferroelectrics* **286**, 167 (2002).
- [8] T. Katsufuji, S. Mori, M. Masaki, Y. Moritomo, N. Yamamoto, and H. Takagi, "Dielectric and magnetic anomalies and spin frustration in hexagonal  $\text{RMnO}_3$  (R=Y, Yb, and Lu)", *Phys. Rev. B* **64**, 104419 (2001).
- [9] H. L. Yakel Jr, W. C. Koehler, E. F. Bertaut and E. F. Forrat, "On the crystal structure of the manganese(III) trioxides of the heavy lanthanides and yttrium", *Acta Cryst.* **16**, 957 (1963).
- [10] S. Lee, I. A. Pirogov, Jung Hoon Han, J.-G. Park, A. Hoshikawa, and T. Kamiyama, "Direct observation of a coupling between spin, lattice and electric dipole moment in multiferroic  $\text{YMnO}_3$ ", *Phys. Rev. B* **71**, 180414 (2005).
- [11] (a) J. A. Alonso, M. J. Martinez-Lope, M. T. Casais, M. T. Fernandez-Diaz, "Evolution of the Jahn-Teller Distortion of  $\text{MnO}_6$  Octahedra in  $\text{RMnO}_3$  Perovskites (R=Pr, Nd, Dy, Tb, Ho, Er, Y): A Neutron Diffraction Study", *Inorg. Chem.* **39**, 917 (2000).  
(b) H. W. Binks, H. Fjellvag and A. Kjekshus, "Synthesis of Metastable Perovskite-type  $\text{YMnO}_3$  and  $\text{HoMnO}_3$ ", *J. Sol. St. Chem* **129**, 334 (1997).
- [12] (a) A. A. Bosak, C. Dubourdieu, J. P. Senateur, O. Y. Gorbenko, and A. R. Kaul, "Epitaxial stabilization of hexagonal  $\text{RMnO}_3$  (R = Eu-Dy) manganites", *Journal of Materials Chemistry* **12**, 800 (2002).  
(b) A. A. Bosak, A. A. Kamenev, I. E. Graboy, S. V. Antonov, O. Y. Gorbenko, A. R. Kaul, C. Dubourdieu, J. P. Senateur, V. L. Svechnikov, H. W. Zandbergen, and B. Hollander, "Epitaxial phase stabilization phenomena in rare earth manganites", *Thin Solid Films* **400**, 149 (2001).
- [13] (a) D. Kim, D. Killingsmith, D. Dalton, V. Olariu, F. Gnadinger, M. Rahman, A. Mahmud, and T. S. Kalkur, "Ferroelectric properties of  $\text{YMnO}_3$  films deposited by metalorganic chemical vapor deposition on Pt/Ti/SiO<sub>2</sub>/Si substrates", *Materials Letters* **60**, 295 (2006).  
(b) H. N. Lee, Y. T. Kim, and S. H. Choh, "Comparison of memory effect between  $\text{YMnO}_3$  and  $\text{SrBi}_2\text{Ta}_2\text{O}_9$  ferroelectric thin films deposited on Si substrates", *Applied Physics Letters* **76**, 1066 (2000).  
(c) T. Yoshimura, N. Fujimura, and T. Ito, "Ferroelectric properties of c-oriented  $\text{YMnO}_3$  films deposited on Si substrates", *Applied Physics Letters* **73**, 414 (1998).  
(d) N. Fujimura, T. Ishida, T. Yoshimura, and T. Ito, "Epitaxially grown  $\text{YMnO}_3$  film: new candidate for nonvolatile memory devices", *Applied Physics Letters* **69**, 1011 (1996).  
(e) N. Fujimura, S.-i. Azuma, N. Aoki, T. Yoshimura, and T. Ito, "Growth mechanism of  $\text{YMnO}_3$  film as a new candidate for nonvolatile memory devices", *Journal of Applied Physics* **80**, 7084 (1996).

**Session VI: Thermoelectrics / Structural Properties**

# Understanding compound phase transitions in new Heusler alloy magnetocaloric materials

(Grant No. USDOE-DE-FG02-06ER46291)

Naushad Ali and Shane Stadler  
 Southern Illinois University, Department of Physics, Carbondale, IL 62901  
[nail@physics.siu.edu](mailto:nail@physics.siu.edu) [sstadler@physics.siu.edu](mailto:sstadler@physics.siu.edu)

## SCOPE/DEFINITION

This project originated with the observation of a giant magnetocaloric effect (MCE) in the Heusler alloy  $\text{Ni}_2\text{Mn}_{1-x}\text{Cu}_x\text{Ga}$ .<sup>1,2</sup> The measured entropy change for this system is about  $-64 \text{ J}\cdot\text{K}^{-1}\cdot\text{kg}^{-1}$  ( $-532 \text{ mJ}\cdot\text{cm}^{-3}\cdot\text{K}^{-1}$ ) (in an applied field of 5 T) at room temperature, i.e., more than double the largest value reported at that time (Fig. 1, upper). This material also has a significant MCE effect ( $-27 \text{ J}\cdot\text{K}^{-1}\cdot\text{kg}^{-1}$ ) in fields at or below 2 T, making it a strong candidate for employment in magnetocaloric refrigeration devices based on *permanent* magnets rather than on high-maintenance superconducting magnets. The parent alloy  $\text{Ni}_2\text{MnGa}$  undergoes two transitions: A second order paramagnetic/ferromagnetic transition at 376 K ( $T_C$ ), and a first order martensitic (structural) transition at 202 K ( $T_M$ ). Varying the stoichiometry by substitution has the effect of changing the transition temperatures  $T_M$  and  $T_C$  and, in the case where Mn is substituted with Cu ( $x = 0.25$ ), the two transitions coincide (Fig. 2, lower). It is at this “compound transition” that the large MCE is observed. It is therefore of great importance to understand the underlying physics of these phenomena.

Our goal is to gain insight into the **fundamental physics** at the atomic level. We are currently conducting a systematic study on the effects of atomic substitutions in  $\text{Ni}_2\text{MnGa}$ -based alloys, and also exploring related full- and half-Heusler alloys, for example Ni-Mn-X ( $X=\text{In}, \text{Sn}, \text{Sb}$ ), that exhibit a wide variety of interesting and potentially useful physical phenomena. This research includes investigating magnetocaloric effects (including *inverse* effects), bulk exchange bias properties, and large magnetoresistance phenomena in these materials. The initial work involves sample preparation and conventional measurements of average bulk properties (magnetometry, x-ray diffraction, resistance, thermal expansion, etc.). Additionally, we are beginning to employ x-ray magnetic circular dichroism (XMCD), a synchrotron-based technique, in order to determine the element-specific magnetic moments of each magnetic atomic species in a given alloy. XMCD and x-ray absorption spectroscopy (XAS) will be used to study the magnetic and electronic structures, respectively, with a strong emphasis on the temperature dependence near transition regions.

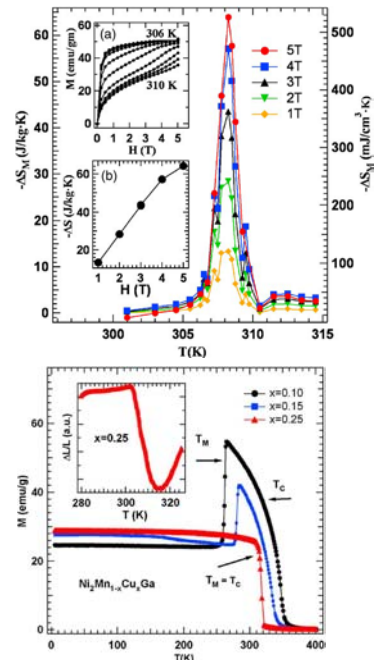


**Fig. 1.** (Upper)  $\Delta S_M$  calculated from magnetization isotherms. (Lower)  $M$  vs.  $T$  for various concentrations  $x$ . (inset) Thermal expansion for  $x=0.25$ .

## RECENT PROGRESS

Since the onset of this project, we have systematically studied a variety of Ni-Mn-X full- and half-Heusler alloys. In addition to magnetocaloric effects, we have observed many other interesting and potentially useful properties including: Inverse magnetocaloric effects, magnetocaloric effects at second order phase transitions, intermartensitic transitions, field-induced transitions, large magnetoresistance, and bulk exchange bias.

Starting with  $\text{Ni}_2\text{Mn}_{1-x}\text{Cu}_x\text{Ga}$  as the parent material, we have systematically studied this system by substituting with Fe, Co, and Ge, i.e.,  $\text{Ni}_2\text{Mn}_{1-x}(\text{Cu-Fe})_x\text{Ga}$ ,  $\text{Ni}_2\text{Mn}_{0.75}\text{Cu}_{0.25-x}\text{Co}_x\text{Ga}$ , and  $\text{Ni}_2\text{Mn}_{1-x}\text{Cu}_x\text{Ga}_{1-y}\text{Ge}_y$ , respectively.<sup>3,4</sup> In all cases, we have studied the structural and magnetic properties, and the substitutions had the effect of changing the temperature of the maximum magnetic entropy change while preserving its magnitude (see Fig. 2 for example). In this particular case, changing the Co concentration from  $x = 0.0$  to  $x = 0.05$  corresponded to a shift of 25 C°.

Second-order transitions are interesting because they do not possess some problems associated with first-order transitions such as hysteretic losses; this is particularly important in magnetocaloric applications. We have studied the gradual overlap of the first- and second-order phase transitions in  $\text{Ni}_{2+x}\text{Mn}_{1-x}\text{Ga}$  alloys through magnetization and thermal expansion measurements.<sup>5</sup> Similar to the behavior observed in  $\text{Ni}_2\text{Mn}_{1-x}\text{Cu}_x\text{Ga}$ , the overlap of the first- and second-order transitions resulted in a large magnetic entropy change  $\Delta S_M \approx -66 \text{ J}\cdot\text{K}^{-1}\cdot\text{kg}^{-1}$  ( $x=0.19$ ) for a magnetic field change of 5 T. This compound showed significant entropy changes with  $0.16 \leq x \leq 0.20$ , and spanned a temperature range of about 325 to 365K. We have also investigated the magnetic (and magnetocaloric) properties of the half-Heusler alloy  $\text{Ni}_{50}\text{Mn}_{50-x}\text{In}_x$  in the vicinity of the second-order transition.<sup>6</sup> The maximum entropy change was significant ( $-6.8 \text{ J}\cdot\text{K}^{-1}\cdot\text{kg}^{-1}$ ) for a field change of 5 T, which is comparable to the largest values reported near room temperature for second-order transitions.

Exchange bias behavior was observed in bulk Ni-Mn-Sb and Ni-Mn-Sn alloys.<sup>7,8</sup> Shifts in the hysteresis loops (up to 250 Oe) were observed in field-cooled samples at 5 K (see Fig. 3). In these systems, the exchange bias behavior was attributed to antiferromagnetic (AFM)/ferromagnetic (FM) interfaces resulting from the coexistence of AFM/FM exchange interactions within the material. Interestingly, the alloy  $\text{Ni}_{50}\text{Mn}_{37+x}\text{Sb}_{13-x}$  ( $0 \leq x \leq 1$ ) also exhibits an *inverse* magnetocaloric effect near the martensitic transition ( $T \approx 297 \text{ K}$ ).<sup>9</sup> The

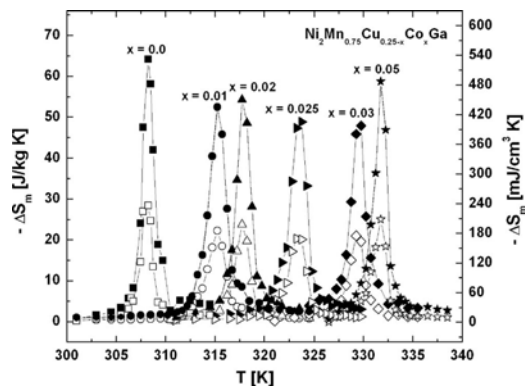


Fig. 2.  $\Delta S_M$  as a function of temperature and Co concentration.

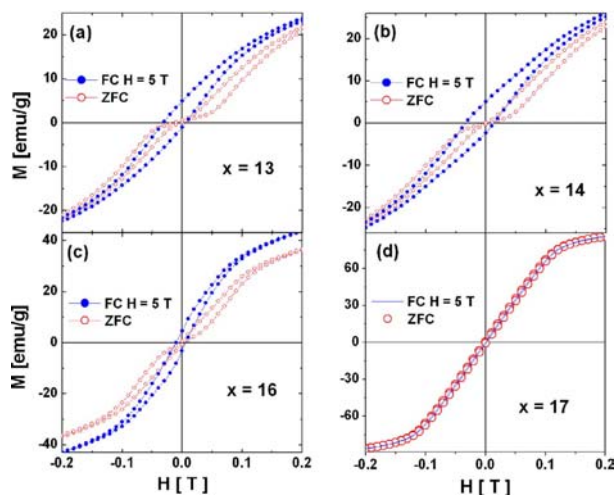


Fig. 3. Field cooled (FC) and zero field cooled (ZFC) hysteresis loops for  $\text{Ni}_{50}\text{Mn}_{50-x}\text{Sn}_x$  at  $T=5 \text{ K}$ .

entropy change is substantial ( $\Delta S_M = +19 \text{ J}\cdot\text{K}^{-1}\cdot\text{kg}^{-1}$ ) for a field change of  $\Delta H = 5 \text{ T}$ . We plan to explore these types of systems in more detail in the future.

Large magnetoresistance (MR) and field-induced structural transitions have been observed in  $\text{Ni}_{50}\text{Mn}_{50-x}\text{Sn}_x$  alloys for concentrations  $13 \leq x \leq 16$ .<sup>10</sup> The effects occur at the respective martensitic transition temperatures ( $T_M$ ), which can be tuned in temperature by varying the Sn concentration. The largest observed values of the MR ( $\Delta\rho/\rho_0$ ) were  $-42\%$  for  $x = 14$  at  $T = 250\text{K}$ , and  $-23\%$  above room temperature ( $T \approx 320 \text{ K}$ ) for  $x = 13$ , where the magnetic field change was  $\Delta H = 5 \text{ T}$  (see Fig. 4). The magnetization and x-ray diffraction measurements indicated that the origin of the observed magnetoresistance is a magnetically induced magnetostructural transition from a complex 10M modulated orthorhombic phase containing some antiferromagnetic coupling to a ferromagnetic cubic  $L2_1$  structure.

In general, it is interesting to note that many of these Heusler alloy systems possess more than one interesting and useful property simultaneously. For instance, the last system we discussed ( $\text{Ni}_{50}\text{Mn}_{50-x}\text{Sn}_x$ ) exhibits both ferromagnetic shape memory and giant magnetoresistance effects, it therefore should attract interest as a potential multifunctional material.

## FUTURE PLANS

There are a number of topics that we plan to add to the current project:

**I. Inverse magnetocaloric effects:** Some materials that we have studied exhibit these properties (e.g.,  $\text{Ni}_{50}\text{Mn}_{37+x}\text{Sb}_{13-x}$ ), and others exhibit *both* negative and positive (inverse) effects in the same systems but at different temperatures (e.g.,  $\text{Ni}_{50}\text{Mn}_{50-x}\text{In}_x$ ).

**II. Strain measurements:** We are currently conducting strain measurements as a function of magnetic field and temperature on systems that exhibit both ferromagnetic shape memory and magnetocaloric effects (Fig. 5).

**III. Ni-Mn-Ga based films grown by pulsed laser deposition (PLD):**  $\text{Ni}_2\text{MnGa}$  films have been grown on various substrates ( $\text{SrTiO}_3$ , Si, GaAs, glass). Magnetization (SQUID and MOKE) and AC susceptibility (MOKE method) measurements show evidence of a martensitic transition in these films.

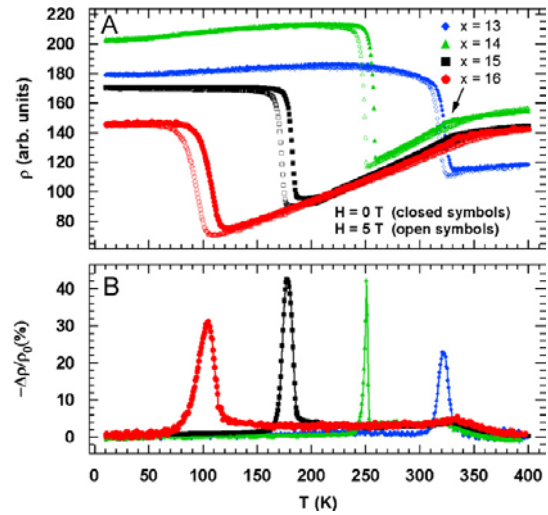


**Fig. 4.**  $\text{Ni}_{50}\text{Mn}_{50-x}\text{Sn}_x$ : (A) Resistivity ( $\rho$ ) as a function of temperature ( $T$ ) in 0 and 5 T applied magnetic fields. (B)  $\Delta\rho/\rho_0$  (%) as a function of  $T$  for all samples.

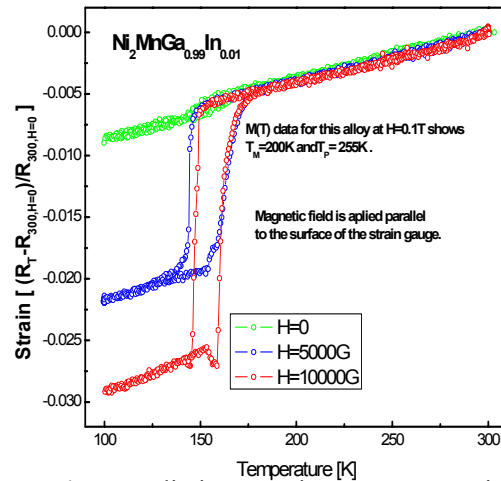


**Fig. 5.** Preliminary strain measurements in In-doped  $\text{Ni}_2\text{MnGa}$ .

**IV. X-ray Magnetic Circular Dichroism (XMCD).** Preliminary measurements have already been carried out on bulk  $Ni_2Mn_{1-x}Cu_xGa$  in collaboration with Dr. Sujoy Roy at LBNL. These measurements will help us to understand the change in electronic and magnetic structures as a function of temperature near various transitions.

## REFERENCES

- <sup>1</sup>*Magnetocaloric properties of  $Ni_2Mn_{1-x}Cu_xGa$* , Shane Stadler, Mahmud Khan, Joseph Mitchell, Naushad Ali, Angelo M. Gomes, Igor Dubenko, Armando Y. Takeuchi, and Alberto P. Guimarães, *Appl. Phys. Lett.* **88**, 192511 (2006).
- <sup>2</sup>*Magnetocaloric properties of the  $Ni_2Mn_{1-x}(Cu,Co)_xGa$  Heusler alloys*, A. M. Gomes, M. Khan, S. Stadler, N. Ali, I. Dubenko, A. Y. Takeuchi, and A. P. Guimarães, *J. Appl. Phys* **99**, 08Q106 (2006).
- <sup>3</sup>*Magneocaloric properties of Fe and Ge doped  $Ni_2Mn_{1-x}Cu_xGa$* , Mahmud Khan, Shane Stadler, and Naushad Ali, *J. Appl. Phys* **101**, 09C515 (2007).
- <sup>4</sup>*Phase transitions and corresponding magnetic entropy changes in  $Ni_2Mn_{0.75}Cu_{0.25-x}Co_xGa$* , Mahmud Khan, Igor Dubenko, Shane Stadler, and Naushad Ali, *J. Appl. Phys* **102**, 023901 (2007).
- <sup>5</sup>*The Overlap of First\_ and Second-Order Phase transitions and Related Magnetic Entropy Changes in  $Ni_{2+x}Mn_{1-x}Ga$  Heusler Alloys*, Mahmud Khan, Shane Stadler, Jonathan Craig, Joseph Mitchell, and Naushad Ali, *IEEE Trans. Mag.* **42**, 3108 (2006).
- <sup>6</sup>*Large magnetic entropy change in  $Ni_{50}Mn_{50-x}In_x$* , Arjun Kumar Pathak, Mahmud Khan, Igor Dubenko, Shane Stadler, and Naushad Ali, *Appl. Phys. Lett.* **90**, 262504 (2007).
- <sup>7</sup>*Exchange bias behavior in Ni-Mn-Sb Heusler alloys*, Mahmud Khan, Igor Dubenko, Shane Stadler, and Naushad Ali, *Appl. Phys. Lett.* **91**, 072510 (2007).
- <sup>8</sup>*Exchange bias behavior in Mn rich Ni-Mn-Sn Heusler alloys*, Mahmud Khan, Igor Dubenko, Shane Stadler, and Naushad Ali, *J. Appl. Phys* **102**, 113914 (2007).
- <sup>9</sup>*Inverse Magnetocaloric effect in ferromagnetic  $Ni_{50}Mn_{37-x}Sb_{13-x}$  Heusler alloys*, M. Khan, S. Stadler, and N. Ali, *J. Appl. Phys.* **101**, 053919 (2007).
- <sup>10</sup>*Magnetoresistance and field-induced structural phase transitions in  $Ni_{50}Mn_{50-x}Sn_x$  Heusler alloys*, Mahmud Khan, Arjun K. Pathak, Moti R. Paudel, Igor Dubenko, Shane Stadler, and Naushad Ali, *J. Magn. Magn. Mater.* **320**, L21 (2008).

## ADDITIONAL REFERENCES (with acknowledgment to DOE)

- Intermartensitic transformations in  $Ni_2Mn_{1-x}Co_xGa$  Heusler alloys*, M. Khan, S. Stadler, and N. Ali, *J. Appl. Phys.* **99**, 08M705 (2006).
- Exchange Bias in Bulk Ni-Mn-In Based Heusler Alloy*, Igor Dubenko, Mahmud Khan, Arjun Pathak, Bhoj Gautam, Shane Stadler, and Naushad Ali (*J. Magn. Magn. Mater.*, Accepted for Publication).
- Intermartensitic transformations in Fe doped Ni-Mn-Cu-Ga Heusler alloys*, Mahmud Khan, Bhoj Gautam, Arjun Pathak, Igor Dubenko, Shane Stadler, and Naushad Ali (*J. Appl. Phys.*, Submitted for Publication).
- The structural and magnetic properties of  $Ni_2Mn_{1-x}B_xGa$  Heusler alloys*, Bhoj Gautam, Mahmud Khan, Arjun Pathak, Igor Dubenko, Shane Stadler, and Naushad Ali (In preparation).
- Effect of small changes in Mn concentration on phase transition temperatures and magnetic entropy variation of  $Ni_2Mn_{0.75}Cu_{0.25}Ga$  Heusler Alloys*, Bhoj Gautam, Mahmud Khan, Arjun Pathak, Igor Dubenko, Shane Stadler, and Naushad Ali (In preparation).

# Surface Wave Mediated Near-Field Heat Transfer

Principal Investigator: Gang Chen

Mechanical Engineering Department  
Massachusetts Institute of Technology  
77 Massachusetts Avenue, 3-260  
Cambridge, MA 02139  
Email: gchen2@mit.edu

## Program Scope

Phonon-polaritons are special electromagnetic modes existing in polar materials that result from the hybridization of photons and transverse optical phonons. Figure 1 shows the dispersion of phonon polaritons. Inside the bulk material, two branches of phonon-polaritons exist: the lower branch is more phonon-like while the upper branch is more photon-like. In between the transverse and optical phonons, no bulk phonon-polaritons are allowed as the dielectric constant is negative, but a surface electromagnetic wave forms that decays exponentially on both sides of the surface. Based on this figure, the following observation can be made on surface phonon polaritons (SPPs).

(1) The dispersion is on the right-hand side of the light line and hence light cannot escape the surface. Reciprocally, light cannot be coupled from outside through the medium in the surface-phonon polariton resonance range.

(2) In the large wavevector limit, the dispersion is flat, suggesting that a high density-of-states (DOS) exists near the surface phonon polaritons resonance. This high DOS means that a large energy density is stored by the SPPs near the surface.

This high energy density suggests interesting heat transfer phenomena can happen with SPPs. Our project explores the energy transport mediated by SPPs. We have carried out experimental and theoretical studies on surface wave mediated energy transport. Major results obtained so far include: (1) theoretical and experimental studies of surface phonon polariton heat transfer along thin film, (2) theoretical and experimental studies of surface phonon polariton heat transfer across nanogaps, and (3) continued development of investigation of thermal/mechanical properties of nanowires/nanotubes. Here we will focus progresses on surface phonon-polariton mediated heat transfer.

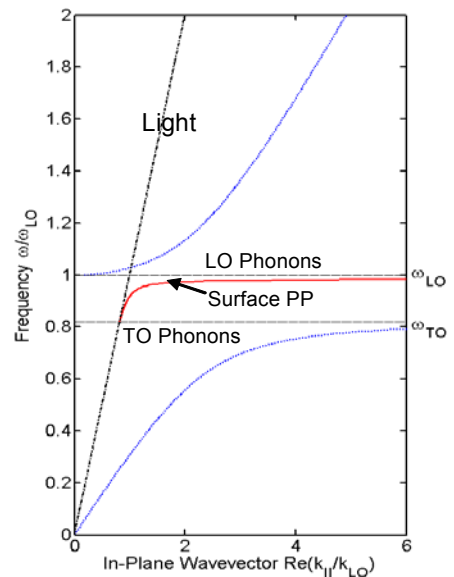


Figure 1 Dispersion showing that surface phonon polaritons lie between transverse and longitudinal optical phonons.

# Recent Progress

## 2.1 Investigation of Phonon Polariton Heat Conduction Along Films

We examined SPP mediated heat conduction along thin films such as amorphous SiO<sub>2</sub> and found that for a 50 nm thick film of amorphous silicon dioxide, the contribution to the thermal conductivity due to surface polaritons can exceed that due to the bulk phonons. We further identified that the source of this increase is the very long propagation length of the anti-symmetric surface polariton mode. These results were obtained based on a kinetic theory approach (P5, P11). We have recently carried out computation starting from fluctuation-dissipation electrodynamics, and obtained results that are consistent with the kinetic theory approach.

Our modeling shows that the enhanced energy transport due to surface waves along the film plane direction arises mainly from the increased propagation length. We carried out experimental studies to measure the propagation length of surface phonon polaritons using attenuated total internal reflection (P19). In this experiment, radiation from a light source is launched into a ZnSe crystal that is in close proximity to the film of interests. The wave propagating inside the ZnSe crystal evanescently couples to the SPP wave on SiO<sub>2</sub> surface. From the attenuation of the propagating wave, the damping of the SPP wave on the SiO<sub>2</sub> surface can be determined. Our measurements are in reasonable agreement with modeling results.

## 2.2 Investigation of Phonon Polariton Heat Transfer Across Nanogaps

Originally, we anticipated that the high density-of-states of the surface waves should contribute to the increased heat conduction along the film. However, our modeling and experiments further identified that the benefit for heat transfer along the film comes mainly from the long propagation length. On the other hand, our previous modeling and other existing work had suggested that the high density of states can lead to near-field radiation heat transfer between two surfaces that is significantly higher than that between two blackbodies. Experimental work in this area, however, is scarce and there is no experimental data regarding radiation heat transfer between two surfaces that both support phonon-polaritons. We developed two experimental configurations to measure near-field radiation heat transfer between SPPs, as explained below.

**Parallel Plate Experiments.** We first carried out an experiment between two parallel plates using quartz optical flats. Glass spheres with a nominal diameter of 1 μm are used as spacer. These glass spheres are diluted and sparsely placed at three places on one optical flat, and a second flat is placed on top of the spheres. We have carried out a calculation that shows conduction from the

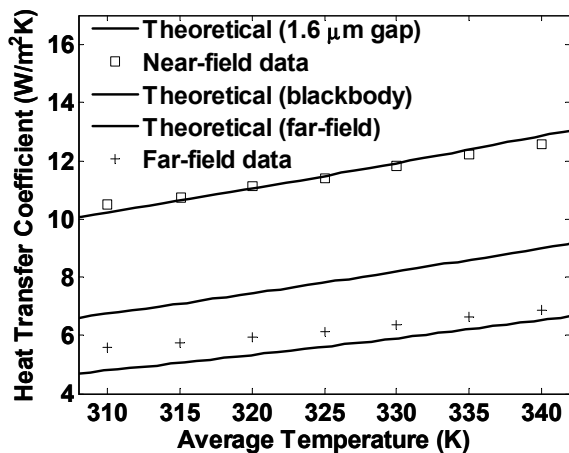


Figure 2 Temperature dependent heat transfer coefficient between two parallel quartz plates. Experimental results at 1.6 μm surpasses that of blackbody radiation.

spheres are not important. Figure 2 shows the experimental results between the two plates are above that of blackbody radiation.

**Sphere-Plate Experiments.** It is difficult, however, to push the parallel-plate configuration to nanometer regime because submicron particulates residual on the surface can create thermal shorts and prevent closer separation. We subsequently developed a technique to measure near-field radiation heat transfer between a sphere and a flat plate (P4). To estimate experimental sensitivity required, we first carried out a full-vector wave fluctuation-dissipation electrostatics simulation for radiation heat transfer between two spheres (P4). The simulation tells us that we need an experimental technique that can measure thermal conductance  $10^{-11}$ - $10^{-8}$  W/K range. To meet the sensitivity requirements, we adopted a unique heat flux sensing method: bi-layer cantilevers that are sometimes used in atomic force microscopes. This technique is based on the factor that the two layers have different thermal expansion coefficient, and a temperature change can lead to the deflection of the cantilever (P22). This technique has a power resolution of around  $\sim 10$  pW and a temperature sensitivity of  $10^{-5}$ K, while to measure a thermal conductance of  $10^{-11}$  W/K at a temperature difference of 10 K, the power transferred is 100 pW. Hence, this technique has the potential to meet our requirements. Figure 4 shows experimental results that are in reasonable agreement with our theory.

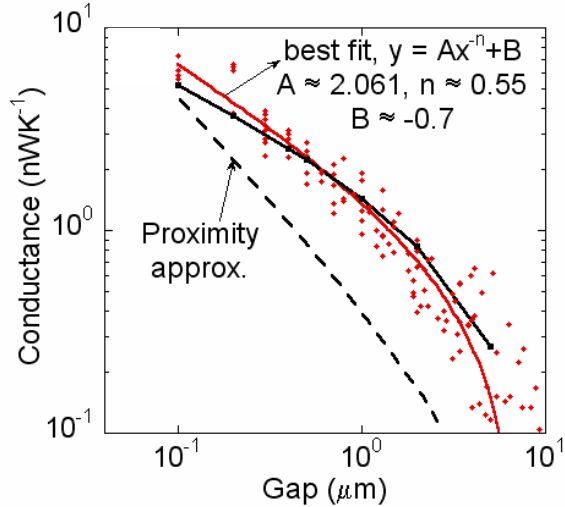


Figure 3 Experimental data (diamonds) from 13 heat transfer-distance measurements for heat transfer between a glass sphere and a glass flat plate.

## Future Plans

We plan to continue our experimental and theoretical studies of near-field radiation heat transfer, building on the sphere/flat-plate experimental configuration. Our tasks in experimental studies include (1) improve the experimental techniques, (2) investigate near field radiation heat transfer between a sphere and a flat plate, and (3) investigate near field radiation heat transfer between two spheres. Concurrently, we will carry out modeling based on Rytov's fluctuating electrostatics theory, and extend this approach to match experimental configurations. Our goals are to directly compare theory and experiments, and to use modeling determining interesting experimental configurations (materials, temperature, distance, etc.).

## Publications

- P1. G. Chen, *Nanoscale Energy Transfer and Conversion*, Oxford Press, ISBN 019515942X, 2005.
- P2. C. Dames and G. Chen "Thermal Conductivity of Nanostructured Thermoelectric Materials," CRC Handbook, edited by M. Rowe, pp.42-1 to 42-16, 2006, Taylor and Francis, Boca Raton.
- P3. Christopher Dames, "Thermal Properties of Nanowires," Ph.D. Thesis, Mechanical Engineering Department, MIT, May, 2006.
- P4. Arvind Narayanaswamy, "Investigation of Nanoscale Thermal Radiation: Theory and Experiments," Ph.D. Thesis, Mechanical Engineering Department, MIT, May, 2007.
- P5. Dye-Zone A. Chen, "Energy Transmission Through and Along Thin-Films Mediated by Surface Phonon-Polaritons," Ph.D. Thesis, Mechanical Engineering Department, MIT, July, 2007.

- P6. R.G. Yang, G. Chen, M. Laroche, and Y. Taur, "Simulation of Nanoscale Multidimensional Transient Heat Conduction Problems using Ballistic-Diffusive Equations and Phonon Boltzmann Equation," *Journal of Heat Transfer*, Vol. 127, pp. 298-306, 2005.
- P7. R.G. Yang, G. Chen, and M.S. Dresselhaus, "Thermal Conductivity of Core-Shell and Tubular Nanowires," *Nano Letters*, Vol. 5, pp. 1111-1115, 2005.
- P8. J. Y. Huang, S. Chen, S. H. Jo, Z. Wang, G. Chen, M.S. Dresselhaus, and Z. F. Ren, "Atomic-Scale Imaging of Wall-by-Wall Breakdown and Concurrent Transport Measurements in Multiwall Carbon Nanotubes," *Physical Review Letters*, Vol. 94, 236802, 2005.
- P9. B. Poudel, W.Z. Wang, C. Dames, J.Y. Huang, S. Kumar, D.Z. Wang, D. Banerjee, G. Chen, and Z.F. Ren, "Formation of Crystallized Titania Nanotubes and Their Transformation into Nanowires," *Nanotechnology*, Vol. 16, pp. 1935-1940, 2005.
- P10. C. Dames, G. Chen, B. Poudel, W. Wang, J. Huang, Z. Ren, Y. Sun, J.I. Oh, C. Opeil, and M.J. Naughton, "Low-Dimensional Phonon Specific Heat of Titanium Dioxide Nanotubes," *Applied Physics Letters*, Vol. 87, 031901, 2005.
- P11. D. A. Chen, Arvind Narayanaswamy, and Gang Chen, "Surface Phonon-Polariton Mediated Thermal Conductivity Enhancement of Amorphous Thin Films," *Physical Review B*, Vol. 72, 155435, 2005.
- P12. J. Y. Huang, S. Chen, Z.Q. Wang, K. Kempa, Y. M. Wang, S. H. Jo, G. Chen, M.S. Dresselhaus, and Z. F. Ren, "Superplastic Single-Walled Carbon Nanotubes," *Nature*, Vol. 439, p. 281, 2006.
- P13. S. Chen, J.Y. Huang, Z. Wang, K. Kempa, G. Chen, and Z.F. Ren, "High-Bias-Induced Structure and the Corresponding Electronic Property Change in Carbon Nanotubes," *Applied Physics Letters*, Vol. 87, 263701, 2005.
- P14. G. Chen, "Nanoscale Heat Transfer and Nanostructured Thermoelectrics," *IEEE Transactions on Components and Packaging Technology*, Vol. 29, pp. 238-246, 2006.
- P15. J.Y. Huang, S. Chen, Z. F. Ren, Z. Q. Wang, D. Z. Wang, M. Vaziri, Z.G. Suo, G. Chen, and M.S. Dresselhaus, "Kink Formation and Motion in Carbon Nanotubes at High Temperatures," *Physical Review Letters*, August 18, Vol. 97, 075501, 2006.
- P16. J.Y. Huang, S. Chen, Z.F. Ren, G. Chen, and M.S. Dresselhaus, "Real Time Observation of Tubule Formation from Amorphous Carbon Nanowires under High-Bias Resistive Heating," *Nano Letters*, Vol. 6, pp. 1699-1705, 2006.
- P17. J.Y. Huang, S. Chen, Z.F. Ren, Z. Wang, K. Kempa, M.J. Naughton, G. Chen, M.S. Dresselhaus, "Enhanced Ductile Behavior of Tensile-Elongated Individual Double- and Triple-Walled Carbon Nanotubes at High Temperatures," *Physical Review Letters*, Vol. 98, 185501, 2007.
- P18. D.-Z. A. Chen, R. Hamam, M. Soljagic, J. D. Jannopoulos, and G. Chen, "Extraordinary Optical Transmission Through Sub-Wavelength Holes in A Silicon Dioxide Film via Surface Phonon-Polaritons," *Applied Physics Letters*, Vol. 90, 181921, 2007.
- P19. D.-Z. A. Chen and G. Chen, "Measurement of Silicon Dioxide Surface Phonon-Polariton Propagation Length by Attenuated Total Reflection," *Applied Physics Letters*, V. 91, 121906 (1-3), 2007.
- P20. C. Dames, S. Chen, C. T. Harris, J. Y. Huang, Z. F. Ren, M. S. Dresselhaus, and G. Chen, "A Hot Wire Probe for Thermal Measurements of Nanowires and Nanotubes Inside a Transmission Electron Microscope," *Review of Scientific Instruments*, Vol. 78, 104903 (1-13), 2007.
- P21. A. Narayanaswamy and G. Chen, "Thermal Near-Field Radiative Transfer between Two Spheres," *Physical Review B*, accepted.
- P22. S. Sheng, A. Narayanaswamy, S. Goh, and G. Chen, "Thermal Conductance of AFM Bi-Material Cantilevers," *Applied Physics Letters*, Vol. 92, 063509 (1-3), 2008.
- P23. L. Hu and G. Chen, "Analysis of Optical Absorption in Silicon Nanowire Arrays for Photovoltaic Applications," *Nano Letters*, v. 7, No. 11, November, pp. 3249-3252, 2007.

# Atomistic and Mesoscopic Study of Metallic Glasses (ERKCM40)

P.I.: Takeshi Egami, Co-P.I.: Easo George and Jamie R. Morris  
Oak Ridge National Laboratory and University of Tennessee at Knoxville

## Scope of the Program:

The goal of this project is to develop fundamental understanding of the structure, dynamics and deformation mechanisms of metallic glasses over multiple length scales, from the atomistic to the mesoscopic. At the atomistic level, analytical theory, molecular dynamics simulations and first-principle calculations are used to investigate atomic dynamics, the energy landscape crossover and mode-coupling behavior in the liquid state, the glass transition, atomic transport, structural relaxation and glass formability. We focus on the dynamic fluctuation in the local topology of the atom connectivity network, represented by the novel concept of atomic-level stresses. Local atomic dynamics in the liquid is studied by neutron inelastic scattering, while local atomic rearrangements in the glass that occur during deformation and annealing are probed using synchrotron x-ray and pulsed neutron scattering. At the mesoscopic level strain localization in nano-scale samples is investigated to determine the origins of brittleness. Constrained plastic deformation in multiphase glasses and their composites across multiple length scales are investigated with a view to understand how to prevent catastrophic shear localization. The eventual goal is to develop broad scientific principles for the alloy design of new materials for energy applications in a prescriptive manner.

## Recent Progress:

### *Development of the Topological Fluctuation Theory*

A major difficulty that have hampered the development of theories of liquids and glasses is the absence of the physically meaningful and yet concise description of the atomic structure. Our novel approach is to use the atomic-level stresses (T. Egami, *et al.*, *Phil. Mag. A*, **41**, 883 (1980)) to describe the local topology and distortion of the atomic structure. We developed a novel theory of glass transition based on the concept of topological instability and thermal fluctuations in the atomic-level stresses. As shown in Fig. 1 the theory can predict the glass transition temperature virtually without an adjustable parameter with high accuracy. This represents the first quantitative theory of the glass transition.

### *Molecular Dynamics Simulation of Liquid Dynamics*

Using molecular dynamics (MD) simulations we succeeded in identifying the temperature,  $T_{CO}$ , much above the glass transition temperature, at which the structure and dynamics of the liquid changes significantly. For instance, the Stokes-Einstein relationship holds above  $T_{CO}$ , but fails below. The shear stress correlation function is isotropic above  $T_{CO}$ , but becomes anisotropic and shows the size effect below. The second peak of the atomic pair-distribution function splits into two below  $T_{CO}$ . The bond fluctuation statistics also shows deviations below  $T_{CO}$ . These anomalies indicate that below this temperature atoms form local network that lives longer than the Debye time, the time for atomic vibration. We plan to calculate the dependence of these temperatures on the Poisson's ratio, using the many-body potential with variable Poisson's ratio that we recently developed.  $T_{CO}$  corresponds to the so-called crossover temperature in the energy landscape theory.

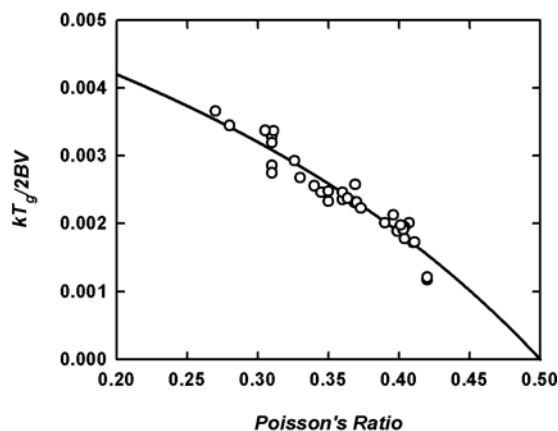


Fig. 1 Experimental value of  $kT_g/2BV$  plotted against the Poisson's ratio for a number of metallic glasses. The solid line is the theory [T. Egami, *et al.*, *Phys. Rev. B* **76**, 024203 (2007)].

It is usually defined by the temperature dependence of the inherent structure, the structure obtained by rapid cooling to  $T = 0\text{K}$ . We have shown the crossover temperature can be identified in the real structure, without reference to the inherent structure. This is important because the inherent structure is not unique, and slightly dependent on the rapid cooling process to  $T = 0\text{K}$ . We have also shown that the equipartition law for the local elastic energy of the atomic-level stresses (each of the six components proportional to  $kT/4$ ) was shown to be valid for various highly unequal potential, proving its generality. This demonstration forms an important basis for general validity of our theories based on the atomic-level stresses.

#### *Experimental Works:*

Neutron and x-ray elastic scattering measurements were made on BMGs to characterize their changes in the structure due to mechanical deformation, for the first time on heavily deformed BMG. The results suggest that at the initial stage of deformation the bond-orientational anisotropy that explained the uniform creep deformation occurs in heavily deformed sample, but later the structural change opposite to the structural relaxation takes place. Compositional inhomogeneity induced by the Soret effect was studied in two Zr-based bulk metallic glasses (BMGs),  $\text{Zr}_{50}\text{Cu}_{50}$  and  $\text{Zr}_{50}\text{Cu}_{40}\text{Al}_{10}$ , and one Cu-based BMG,  $\text{Cu}_{60}\text{Zr}_{30}\text{Ti}_{10}$ , prepared by rapid solidification. The concentration of Cu increases from the surface to the interior, whereas the concentrations of Zr, Ti and Al all decrease. The magnitude of the Soret effect is found to be highly dependent on the sample size and interactions between the diffusing atoms in BMGs. Demonstrated that there is near-surface softening in a  $\text{Zr}_{50}\text{Cu}_{50}$  BMG, i.e., hardness decreases with increasing cooling rate. This change in mechanical behavior may be related to the Soret (compositional) effect seen in the same BMG. However, additional experiments are needed to determine the relative effects of structural and compositional changes on mechanical properties.

#### **Future Plans:**

The topological fluctuation theory (TFT) of the glass, expressed in terms of the atomic-level stresses, will be generalized for the many-body potential with variable Poisson's ratio with MD simulations. In particular, we will verify the dependence of the glass transition temperature on Poisson's ratio. TFT will be extended to account for the rapid increase in viscosity in the supercooled liquid. Further effort will be made to make contacts with the energy landscape theory and the mode-coupling theory. TFT will also be extended to the shear deformation process. The theory will be compared with the experimental observation of the bond-orientational anisotropy (BOA). It will be applied to elucidate the formation of the slip band. Further efforts to calculate the atomic level stresses from first principles to develop a quantum-mechanical basis for this theory.

Neutron and x-ray scattering study of heavily deformed BMG will be continued. We will carry out the study of local atomic dynamics in the liquid, using inelastic neutron scattering and the method of dynamic PDF. We will study of the origins of brittleness in bulk metallic glasses by investigating strain localization resulting from strain softening as well as the reverse process of strain hardening upon annealing. Plastic deformation of BMGs proceeds by the propagation of localized shear bands. In spite of extensive studies of the mechanical behavior of BMGs, the dynamic processes occurring during shear band deformation remain unclear. In this study, shear band initiation and propagation will be carefully monitored using a well-tuned testing machine equipped with a fast data collection system. This study is expected to contribute to a fundamental understanding of the deformation and fracture behavior of BMGs. It is known that the mechanical and physical properties of bulk metallic glasses can be substantially improved by precipitation of nano-sized crystalline particles in the glass matrix. Based on phase relationships and thermodynamics and kinetics, we intend to develop criteria and strategies to attain nanocrystalline composites by direct casting and subsequent heat treatments.

#### **Publications (2005-07)**

#### *Refereed Journal Publications:*

1. T. Egami, S. J. Poon, Z. Zhang and V. Keppens, "Glass Transition in Metallic Glasses: A Microscopic Model of Topological Fluctuations in the Bonding Network," *Phys. Rev. B*, **76**, 024203-1-6 (2007).
2. W. Dmowski and T. Egami, "Observation of Structural Anisotropy in Metallic Glasses Induced by Mechanical Deformation," *J. Mater. Res.* **22**, 412-418 (2007).
3. M. B. Tang, H. Y. Bai, W.H. Wang, D. Bogdanov, K. Winzer, K. Samwer and T. Egami, "Heavy-Fermion Behavior in Cerium Based Metallic Glasses," *Phys. Rev. B*, **75**, 172201-1-4 (2007).
4. D. B. Miracle, T. Egami, K. F. Kelton and K. M. Flores, "Structural Aspects of Metallic Glasses," *Mat. Res. Bull.*, **32**, 629- 634 (2007).
5. T. Egami, "Icosahedral Order in Liquids," *J. Non-Cryst. Sol.* **353**, 3666-3670 (2007).
6. J. R. Morris, U. Dahlborg and M. Calvo-Dahlborg, "Recent developments and outstanding challenges in theory and modeling of liquid metals," *J. Non-cryst. Sol.* **353**, 3444-3453 (2007).
7. J. R. Morris, M. I. Mendeleev and D. J. Srolovitz, "A comparison of crystal-melt interfacial free energies using different Al potentials," *J. Non-cryst. Sol.* **353**, 3565-3569 (2007).
8. Z. Zhang, V. Keppens and T. Egami, "A Simple Model to Predict the Temperature Dependence of Elastic Moduli of Bulk Metallic Glasses", *J. Appl. Phys.*, **102**, 123508 (2007).
9. X. H. Du, J. C. Huang, C. T. Liu, and Z. P. Lu, "New criterion of glass forming ability for bulk metallic glasses," *J. Appl. Phys.* **101**, 086108-1-3 (2007).
10. T. Egami, V. Levashov, R. Aga and J. R. Morris, "Atomic Dynamics in Metallic Liquids and Glasses," *Mater. Trans. JIM*, **48**, 1729-1733 (2007).
11. J. R. Morris, F. Jiang, P. Liaw, "A simple model for examining composition effects in eutectic nucleation," *Mater. Trans. JIM*, **48**, 1675-1679 (2007).
12. J. S. C. Jang, C. C. Tseng, L. J. Chang, C. F. Chang, W. J. Lee, J. C. Huang, and C. T. Liu, "Glass forming ability and thermal properties of the Mg-based amorphous alloys with dual rare earth elements addition," *Mater. Trans. JIM*, **48**, 1684-1688 (2007).
13. Z. P. Lu and C. T. Liu, "A Scheme to Design Multi-Component Bulk Metallic Glasses in Ideal Glass-Forming Liquids", *Mater. Trans, JIM*, **48**, 2476-2482 (2007).
14. Y. Liu, H. Bei, C. T. Liu, and E. P. George, "Cooling-Rate Induced Softening in a Zr<sub>50</sub>Cu<sub>50</sub> Bulk Metallic Glass," *Appl. Phys. Lett.* **90**, 071909-1-4 (2007).
15. Y. Liu, C. T. Liu, E. P. George, and X. Z. Wang, "The Soret Effect in Bulk Metallic Glasses," *Intermetallics* **15**, 557-563 (2007).
16. M. L. Morrison, R. A. Buchanan, P. K. Liaw, B. A. Green, G. Y. Wang, C. T. Liu and J. A. Horton, "Four-Point-Bending-Fatigue Behavior of the Zr-based Vitreloy 105 Bulk Metallic Glass," *Mater. Sci. Eng. A* **467**, 190-197 (2007).
17. M. L. Morrison, R. A. Buchanan, P. K. Liaw, B. A. Green, G. Y. Wang, C. T. Liu and J. A. Horton, "Corrosion-Fatigue Studies of the Zr-based Vitreloy 105 Bulk Metallic Glass," *Mater. Sci. Eng. A* **467**, 198-206 (2007).
18. W. Dmowski, C. Fan, M. L. Morrison, P. K. Liaw, and T. Egami, "Observation of Structural Changes after Thermal Treatment of Bilk Metallic Glasses," *Mater. Sci. Eng. A*, **471**, 125-129 (2007).
19. G. Y. Wang, P. K. Liaw, Y. Yokoyama, W. H. Peter, B. Yang, M. Freels, R. A. Bucanan, C. T. Liu, C. R. Brooks, "Influence of air and vacuum environment on fatigue behavior of Zr-based bulk metallic glasses", *J. Alloy and Compounds* **434-435**, 68-70, (2007).
20. G. Y. Wang, P. K. Liaw, Y. Yokoyama, A. Peker, W. H. Peter, B. Yang, M. Freels, Z. Y. Zhang, V. Keppens, R. Hermann, R. A. Bucanan, C. T. Liu, and C. R. Brook, "Studying fatigue behavior and Poisson's ratio of bulk-metallic glasses", *Intermetallics* **15**, 663-667, (2007)
21. T. H. Hung, Y. C. Chang, Y. N. Wang, C. W. Tang, J. N. Kuo, H. M. Chen, Y. L. Tsai, J. C. Huang, J. S. C. Jang, and C. T. Liu, "Development of Mg based amorphous alloys with higher amounts of rare earth elements", *Mater. Trans, JIM* **48**, 1621-25, (2007)
22. Y. P. Deng, Y. F. Guan, J. D. Fowlkes, S. Q. Wen, F. X. Liu, G. M. Pharr, P. K. Liaw, and P. D. Rock, "A combinatorial thin film sputtering approach for synthesizing and characterizing ternary ZrCuAl metallic glasses", *Intermetallics* **15**, 1208-1216, (2007)
23. M. I. Mendeleev, J. Schmalian, C. Z. Wang, J. R. Morris and K. M. Ho, "Interface mobility and the liquid-glass transition in a one-component system described by an EAM potential," *Phys. Rev. B* **74**, 104206-1-14 (2006).
24. Cang Fan, P. K. Liaw, T.W. Wilson, H. Choo, Y. F. Gao, and C, T. Liu, "Pair distribution function study and mechanical behavior of as-cast and structurally relaxed Zr-based bulk metallic glasses," *Appl. Phys. Lett.* **89**, 231920-1-3 (2006).
25. M. K. Miller, C. T. Liu, J. A. Wright, W. Tang and K. Hildal, "APT characterization of some iron-based bulk

- metallic gasses”, *J. Intermetallics* 14, 1019-1027, 2006
26. T. Egami, “Formation and Deformation of Metallic Glasses: Atomistic Theory,” *J. Intermetallics*, **14**, 882 (2006).
  27. V. Kireev, Y. Liu, Y. Braiman, B. Radhakrishnan, C. H. Hsueh, and P. F. Becher, “Thin-Film Adhesion Measurement Using Laser-Generated High-Power Surface Acoustic Waves,” *Appl. Phys. Lett.* **88**, 191911 (2006).
  28. S. Jeon, T. Thundat, and Y. Braiman, “Effect of Normal Vibration on Friction in the Atomic Force Microscopy Experiment,” *Appl. Phys. Lett.* **88**, 214102 (2006).
  29. R. S. Aga, J. R. Morris, J. J. Hoyt, and M. I. Mendeleev, , “A quantitative parameter-free prediction of simulated crystal nucleation time,” *Phys. Rev. Lett.* **96**, 245701 (2006).
  30. H. Bei, S. Xie, and E. P. George, “Softening Caused by Profuse Shear Banding in a Bulk Metallic Glass,” *Phys. Rev. Lett.* **96**, 105503 (2006).
  31. Q. J. Chen, H. B. Fan, J. Shen, J. F. Sun and Z. P. Lu, “Critical cooling rate and thermal stability of a Fe-Co-Zr-Y-Cr-Mo-B amorphous alloy”, *J. Alloy Comp.* **407**, 125 (2006).
  32. C. Fan, H. Li, L. J. Kecskes, K. Tao, H. Choo, P. K. Liaw, and C. T. Liu, “Mechanical Behavior of Bulk Amorphous Alloys Reinforced by Ductile Particles in Cryogenic Temperature”, *Phys. Rev. Lett.* **96**, 145506 (2006).
  33. C. Fan, P. K. Liaw, T. W. Wilson, W. Dmowski, Th. Proffen, H. Choo, and C.T. Liu, “A Structural Model of Bulk Amorphous Alloys”, *Appl. Phys. Lett.* **89**, 111905 (2006).
  34. C. Fan, P. K. Liaw, V. Haas, J.J. Wall, H. Choo, A. Inoue, and C. T. Liu, "Structures and Mechanical Behaviors of Zr<sub>55</sub>Cu<sub>35</sub>Al<sub>10</sub> Bulk Amorphous Alloys at Ambient and Cryogenic Temperatures" *Phys. Rev. B* **74**, 014205 (2006).
  35. Y. Liu, C. T. Liu, E. P. George, and X. Z. Wang, “Thermal diffusion and compositional inhomogeneity in cast Zr<sub>50</sub>Cu<sub>50</sub> bulk metallic glass,” *App. Phys. Lett.* **89**, 051919 (2006).
  36. Z. P. Lu, J. Shen, D. W. Xing, J. F. Sun, and C. T. Liu, “Binary eutectic clusters and glass formation in ideal glass-formation liquids”, *App. Phy. Lett.* **89**, 071910 (2006).
  37. G. Y. Sun, G. Chen, C. T. Liu, and G. L. Chen, “Innovative processing and property improvement of metallic glass based composites“, *Script Mater.* **55**, 375-378 (2006).
  38. J.J. Wall, C. Fan, P. K. Liaw, C.T. Liu and H. Choo, “A Combined Drop / Suction Casting Machine for the Manufacture of Bulk-Metallic Glass Materials”, *Review of Scientific Instruments*, **77**, Art. No. 033902 (2006).
  39. L. Xia, S. S. Fang, Q. Wang, Y. D. Dong, and C. T. Liu, “Thermodynamic modeling of glass formation in metallic glasses,” *App. Phys. Lett.* **88**, 171905 (2006).
  40. M. Xu, Y. Y. Ye, J. R. Morris, D. Sordelet, and M. J. Kramer, “Influence of Pd on formation of amorphous and quasicrystal phases in rapidly quenched Zr<sub>2</sub>Cu<sub>(1-x)</sub>Pd<sub>x</sub>,” *Phil. Mag.* **86**, 389 (2006).
  41. B. Yang, C. T. Liu, and T. G. Nieh, “Unified equation for the strength of bulk metallic glasses,” *App. Phys. Lett.* **88**, 221911 (2006).
  42. B. Yang, C. T. Liu, T. G. Nieh, M. L. Morrison, P. K. Liaw, R. A. Buchanan, “Localized heating and fracture criterion for bulk metallic glasses,” *J. Mater. Res.* **21** (4), 915-922 (2006).

#### Refereed Conference Proceedings

43. G. L. Chen, C. T. Liu, G. Chen, K. Lu, B. Huang, and S. L. Sass, Editors, *Advanced Intermetallic Alloys and Bulk Metallic Glasses*, Proceedings of the 6<sup>th</sup> International Workshop of Advanced Intermetallic and Metallic Materials, Special Issue of *Intermetallics*, Elsevier Ltd, 2007.
44. R. S. Aga, J. R. Morris, V. Levashov and T. Egami, “Local Structural Fluctuations in a Supercooled Liquid,” *Mater. Sci. Eng. A, Bulk Metallic Glasses*, edited by P. K. Liaw and R.A. Buchannan (TMS Society, Warrendale, Pennsylvania, 2006), p. 59-64.
45. M. L. Morrison, W. Dmowski, T. W. Wilson, P. K. Liaw, C. T. Liu, J. W. Richardson, E. R. Maxey, R. A. Buchanan, C. Fan, H. Choo, T. Egami, and W. D. Porter, “Pair Distribution Function Analyses of Structural Relaxation in a Zr-Based Bulk Metallic Glass,” *MRS Symp. Proc.*, **Vol. 840**, Q1.5.1 (2005).

#### Books and Book Chapters

46. T. Egami, “Atomistic Theory of Metallic Liquids and Glasses,“ in *Bulk Metallic Glasses*, ed. M. Miller and P. Liaw (Springer-Verlag, Berlin, 2007), p. 27-55.
47. R. Aga and J. R. Morris, “Modeling of Metallic Glasses,” in *Bulk Metallic Glasses*, ed. M. K. Miller and P. K. Liaw (Springer-Verlag, Berlin, 2007) p. 57-85.
48. Z. P. Liu, Y. Liu, and C. T. Liu, “Evaluation of Glass-forming ability,” in *Bulk Metallic Glasses*, ed. M. K. Miller and P. K. Liaw (Springer-Verlag, Berlin, 2007) p. 87-115.

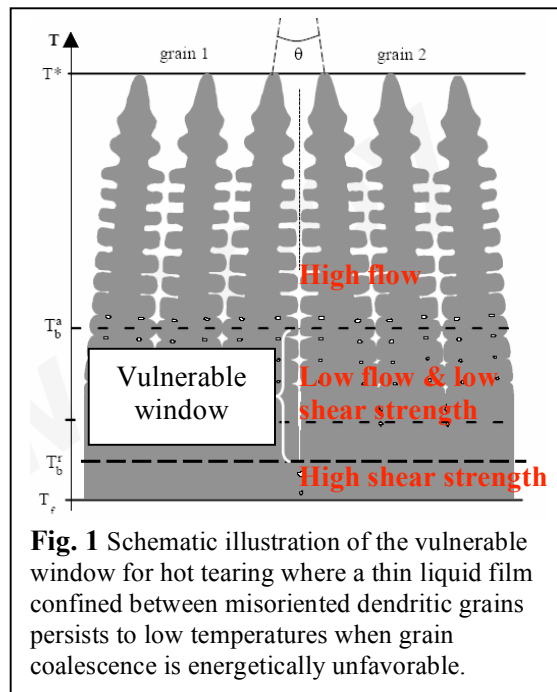
# Bridging Atomistic and Continuum Scales in Phase-Field Modeling of Solid-Liquid Interface Dynamics and Coalescence

Alain Karma

Department of Physics and Center for Interdisciplinary Research on Complex Systems,  
Northeastern University, 360 Huntington Avenue, Boston, Massachusetts 02115  
Tel/Fax: (617) 373 2929 / 2943  
Email: [a.karma@neu.edu](mailto:a.karma@neu.edu)

## Program Scope

This project seeks to understand at a fundamental level the physics governing the breakdown of crystal cohesion mediated by thin liquid films confined at grain boundaries in stressed polycrystalline materials. It focuses on the development of quantitative multi-order-parameter phase-field models and phase-field-crystal models to simulate the dynamics and coalescence of crystal melt interfaces in elemental materials and binary alloys at the long time scales and relatively low stress levels characteristic of common materials processing and aging conditions. A main goal is to combine atomistic and continuum scale methods to model these processes quantitatively building on recent progress to model anisotropic properties of isolated crystal-melt interfaces and dendritic solidification [3-5]. These studies are geared to understand thematically linked material failure processes relevant to the processing and lifetime of materials for diverse DOE-related applications ranging from energy generation to stockpile stewardship, including hot tearing, liquation cracking, and liquid metal embrittlement. These processes involve the persistence or penetration of thin liquid layers at grain boundaries under applied stress.



Hot tearing is characterized by the formation of stress-induced crack-like openings that prevent crystal cohesion at the late stage of alloy solidification. Hot cracks originate deep in the “mushy zone”, which is the mixed solid/liquid region that extends behind the tips of growing dendrites, as illustrated in Fig. 1. Thin liquid films can persist deep in this zone confined between misoriented dendritic grains when the grain boundary energy exceeds twice the crystal-melt interfacial energy, thereby rendering grain coalescence energetically unfavorable. The region of the mushy zone where these thin films are present has a low transverse shear strength and low fluid flow, which makes this region “vulnerable” to hot tearing. In particular, dendrites can be pulled apart if the flow rate cannot accommodate the large strain rates produced by thermal contraction and/or

external deformation. This phenomenon has been of long standing practical interest for the aerospace and automotive industries because solidified products, such as components of turbine blades, need to be scrapped when cracks are too large to be repaired by welding. Understanding the complex and multiscale interfacial processes that promote the formation of hot cracks and related solidification defects is crucially important for industry both to cut down processing costs improve materials safety.

Liquid metal embrittlement (LME), in turn, is a phenomenon whereby a liquid metal in contact with another, higher-melting-point polycrystalline metal, rapidly penetrates from the surface along grain boundaries. This phenomenon is known to be greatly accelerated by the application of tensile stress, resulting in the rapid propagation of intergranular cracks in normally ductile materials. While this embrittlement phenomenon has been observed in many systems, the nature of the interplay between transport, surface/grain boundary wetting, segregation and the applied stress, leading to liquid metal penetration remains incompletely understood. This topic has received increased interest recently in the context of research programs on hybrid reactors in which liquid lead acts as a cooling fluid. Understanding how penetration depends on boundary type could provide a basis to prevent failure by grain boundary engineering of these materials.

### Recent progress

Our recent studies have focused on obtaining a fundamental quantitative understanding of the interaction between two misoriented crystal grains in close contact. The range  $\delta$  of this interaction is generally set by the nanometer scale width of the crystal melt interface. For many metallic systems that have low entropy of melting, this width is especially large since crystal density waves decay slowly into the liquid phase as illustrated in the comparison of MD and phase-field-crystal simulation for Fe in Fig. 2. The interaction between crystal grains can be characterized by computing the excess free-energy  $G(h)$  (per unit area) defined as the difference between the total free-energy of the bicrystal system that includes a thin liquid layer of thickness  $h$  sandwiched between two grains, and the total free-energy of a single crystal occupying the same volume at the same temperature. This excess is the sum

$$G(h) = -L \frac{\Delta T}{T_M} h + \gamma(h)$$

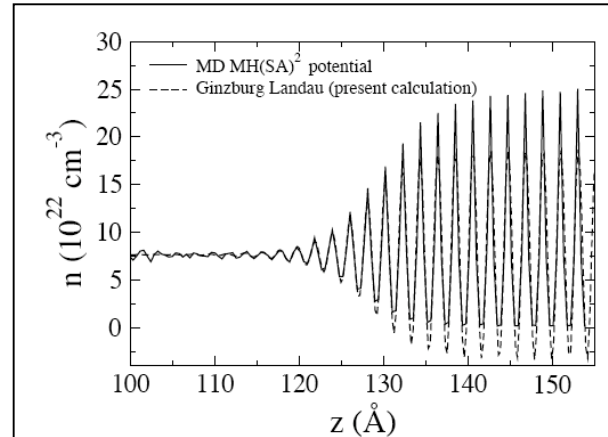


**Fig. 2** Comparison of x-y averaged density wave profile in the direction ( $z$ ) normal to the crystal melt interface of bcc Fe at the melting point computed with atomistic MD simulations (solid black line) using the MH(SA)<sup>2</sup> EAM interatomic potentials and phase-field-crystal simulations [1] (dashed line). Both predictions agree with Ginzburg-Landau theory where the order parameters are the amplitude of density waves corresponding to the principal reciprocal lattice vectors [5].

of a bulk excess free-energy proportional to  $h$ , corresponding to the first term on the right-hand-side of Eq. (1), where  $L$  is the latent heat of melting and  $\Delta T = T - T_M$ , and an interfacial excess free-energy  $\gamma(h)$ . The latter must approach  $2\gamma_{sl}$  when the crystal-melt interfaces are well separated ( $h \gg \delta$ ), where  $\gamma_{sl}$  is the excess free-energy of an isolated crystal-melt interface, and must equal the grain boundary energy,  $\gamma_{gb}$ , when the liquid layer thickness vanishes ( $h = 0$ ). The *contact potential*  $V(h) \equiv \gamma(h) - 2\gamma_{sl}$  is a fundamentally important quantity for understanding interface coalescence since its derivative governs the strength and the sign of the thermodynamic driving force that produces a net attraction or repulsion between the crystal-melt interfaces depending on whether  $-dV(h)/dh$  is negative or positive, respectively. We have used the phase-field crystal approach to calculate the contact potential in a bicrystal geometry and to study its dependence on misorientation for a symmetric tilt boundary. The order parameter in this approach is the material density with a free-energy functional that describes the fluctuations of an inhomogeneous liquid as in classical density functional theory. This functional uses simplified forms for the liquid structure factor and the variation of the liquid free-energy with density that reduce the number of reciprocal lattice vectors needed to resolve the crystal density field in each grain, thereby making computations in large system sizes accessible. Our recent studies [1] show that this approach reproduces well the properties of isolated solid-liquid interfaces as shown in Fig. 2. In addition, it is ideally suited to investigate the role of crystal structure and misorientation in grain coalescence since it provides a natural description of the overlap of crystal density waves from the two grains in the thin liquid layer sandwiched between them, as illustrated by the simulation results shown in Fig. 3. Our analysis of the phase-field crystal simulations reveals that the contact potential is always repulsive above some critical misorientation ( $\theta > \theta_c$ ), with  $-dV(h)/dh > 0$  for all  $h$ , and well-fitted in this regime by the simple exponential form  $V(h) \approx (\gamma_{gb} - 2\gamma_{sl})\exp(-h/\delta)$  that has been used previously in continuum theories of grain boundary premelting. In contrast, this exponential form does not describe well the contact potential for  $\theta < \theta_c$ . In this regime,

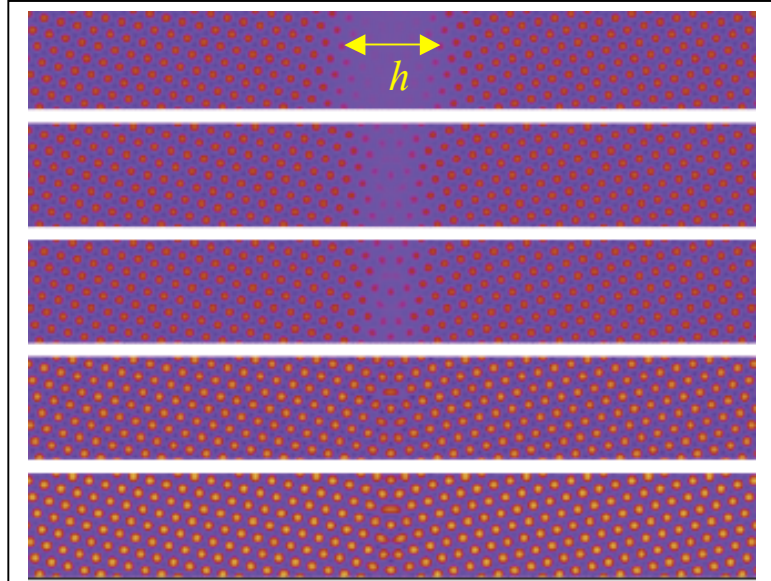


**Fig. 3** Premelting transition of a symmetric tilt boundary for hexagonal crystal symmetry in two dimensions studied by phase-field crystal simulations for a misorientation where grain coalescence is energetically unfavorable. Equilibrated crystal density fields with maxima (red peaks) corresponding to atomic positions show a sharp increase in liquid layer thickness  $h$  approaching the melting point.

the contact potential is always repulsive above some critical misorientation ( $\theta > \theta_c$ ), with  $-dV(h)/dh > 0$  for all  $h$ , and well-fitted in this regime by the simple exponential form  $V(h) \approx (\gamma_{gb} - 2\gamma_{sl})\exp(-h/\delta)$  that has been used previously in continuum theories of grain boundary premelting. In contrast, this exponential form does not describe well the contact potential for  $\theta < \theta_c$ . In this regime,

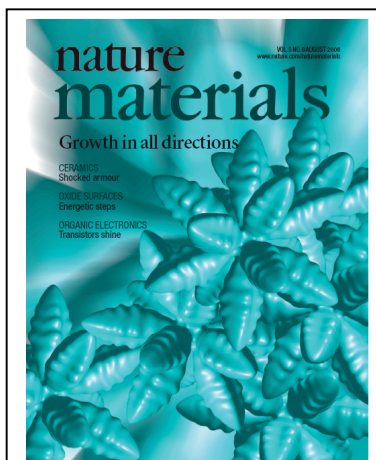
$V(h)$  shows a cross-over from attractive behavior at large  $h$  to repulsive behavior at small  $h$  with a minimum at some intermediate value of  $h \sim \delta$  that depends on misorientation. The results also show that the excess interfacial energy  $\gamma(h)$  is well described by a Read-Shockley law for small  $\theta$  with a nearly constant dislocation core radius if one incorporates the temperature dependence of the elastic constants (shear modulus and Poisson's ratio), which accounts for most of the temperature variation of  $\gamma(h)$  below the melting point in the phase-field crystal model.

## Future Plan

We plan next to extend the phase-field crystal simulations to three dimensions to carry out a more extensive study of grain coalescence for bcc ordering. Both tilt and twist boundaries will be explored in order to understand how the cross-over between the repulsive and attractive regimes is controlled by the complex interplay of crystal structure and tilt or twist angle. Quantitative comparisons with MD simulations will be carried out for parameters of Fe used in our recent studies of isolated solid-liquid interfaces. These studies will then be extended to study the role of applied stress, and subsequently to binary alloys in two and three dimensions. In parallel, we plan to develop multi-order parameter phase-field models capable to reproduce the contact potential predicted by MD and/or phase-field crystal simulations. These models will set the stage for large scale simulation studies of liquid film penetration in liquation cracking and LME.

## References to DOE sponsored publications (2005-2007)

- [1] "Phase-field crystal modeling of equilibrium bcc-liquid interfaces", K.-A. Wu and A. Karma, *Phys. Rev. B* **76**, 184107 (2007).
- [2] "Interface Mobility from Interface Random Walk", Z. T. Trautt, M. Upmanyu, and A. Karma, *Science* **314**, 632-635 (2006).
- [3] "Orientation Selection in Dendritic Evolution", T. Haxhimali, A. Karma, F. Gonzales, and M. Rappaz, *Nature Materials* **5**, 660-664 (2006).
- [4] "Crystal-melt Interfacial Free Energies in hcp Metals: A Molecular Dynamics Study of Mg", D. Y. Sun, M. I. Mendeleev, C. A. Becker, K. Kudin, T. Haxhimali, M. Asta, J. J. Hoyt, A. Karma, and D. J. Srolovitz, *Phys. Rev. B* **73**, 024116 (2006).
- [5] "Ginzburg-Landau Theory of Crystalline Anisotropy for bcc-Liquid Interfaces", K.-A. Wu, A. Karma, J. J. Hoyt, and M. Asta, *Phys. Rev. E* **73**, 094101 (2006).
- [6] "Spheroidal Particle Stability in Semi-Solid Processing", R. A. Martinez, A. Karma, and M. C. Flemings, *Metall. Mater. Trans.* **37A**, 2807-2815 (2006).
- [7] "Low Temperature Dynamics of Kinks on Ising Interfaces", A. Karma and A. E. Lobkovsky, *Phys. Rev. E* **71**, 036114 (2005).
- [8] "Crack Path Prediction in Anisotropic Brittle Materials", V. Hakim and A. Karma, *Phys. Rev. Lett.* **95**, 235501 (2005).



Nature Materials August 2006 cover "Orientation Selection in Dendritic Evolution" T. Haxhimali, A. Karma, F. Gonzales, and M. Rappaz, *Nature Materials* **5**, 660-664.

## Phase Field Approach for Strain-induced Magnetolectric Effect in Multiferroic Composites

Y.Ni <sup>a</sup>, A. G. Khachaturyan <sup>a,1</sup>

<sup>a</sup> Department of Materials Science and Engineering, Rutgers University, 607 Taylor  
Road, Piscataway, NJ 08854, USA

### **Abstract**

We have developed the Phase Field theory of the strain-mediated magnetolectric coupling in piezoelectric-piezomagnetic composites with arbitrary spatial arrangement of particles of constituent phases. The piezoelectric-piezomagnetic coupling constants are presented as a functional of a phase field that is a shape function describing an arbitrary spatial arrangement of the phases. The free energy of such composites includes the electrostatic, elastic and magnetostatic energies and is also formulated as a functional of an arbitrary microstructure. This development is a theoretical framework allowing us to address two problems, they are: (i) the finding of the two-phase architecture of a composite and the combination of intrinsic properties of the constituent phases that would optimize the ME coupling, and (ii) the realistic 3D prototyping of the evolution of the microstructure during the processing of a bulk and laminar composite.

A task (i) has been carried out by the optimization the ME coupling constant functional in a simulated 3-D virtual evolution of the composite architecture with a driving force that is formulated to eventually lead to a configuration with the best properties. This problem was mostly solved and the obtained results are published in

---

Project “Mesoscale Interfacial Dynamics in Magnetoelectric Nanocomposites”.

JAP. A further generalization and further development of this approach is currently under way. Simultaneously we have started to perform a task (ii) and plan to extend it to different multiferroic materials that are studied experimentally in this project. The extension of the theory and modeling of a spontaneous self-assembling of multiferroic composites will be along the following line.

So far the existing theories of multiferroic composites did not considered a direct contribution of a rearrangement of ferroelectric and ferromagnetic domains into extrinsic part of ME coupling—instead, they assumed phenomenological constitutive equations relating responses of homogenized grains to the applied fields. A straightforward consideration of the domain structure response is a challenge, which we will address. This is especially important in a light of the attempts to use the ferroelectrics near the morphotropic boundary in composites such as  $\text{PbZrO}_3\text{-PbTiO}_3$  (PZT) and  $\text{NiFe}_2\text{O}_4$  – according to recent studies of two PIs, the giant electrostriction in PZT phase is caused by the field-induced nano-domain rearrangement. The other development of the theory that is now in progress is the application of the theory and modeling for the determination of an optimal textures of multi-grain ME compact aggregates, in which all energy contributions we will be accurately take into account for the cases of arbitrary properties of the constituent phases.

Our other goal is the development of the computational models that realistically prototype the 3D evolution of multiphase system of complex configurations formed by decomposition of a solid solution into a mixture of magnetic and piezoelectric phases. In particular, we will study the mechanism of formation of the chessboard structure recently found in doped manganites whose decomposition can potentially produce a mixture of

DOE Basic Energy Sciences program

Project “Mesoscale Interfacial Dynamics in Magnetoelectric Nanocomposites”.  
the ferromagnetic and ferroelectric phases. The first results related to the mechanism of  
the chessboard structure are already obtained. Besides the multiferroic properties these  
materials could be used as a memory media with exceptional recording properties.

## Enhanced Thermoelectric Performance of Rough Silicon Nanowires

Allon I. Hochbaum<sup>1</sup>, Renkun Chen<sup>2</sup>, Arun Majumdar<sup>2,3,4,\*</sup>, Peidong Yang<sup>1,3,4,†</sup>

<sup>1</sup>*Department of Chemistry, University of California, Berkeley, CA 94720*

<sup>2</sup>*Department of Mechanical Engineering, University of California, Berkeley, CA 94720*

<sup>3</sup>*Department of Materials Science and Engineering, University of California, Berkeley, CA 94720*

<sup>4</sup>*Materials Sciences Division, Lawrence Berkeley National Laboratory, Berkeley, CA 94720*

\* [majumdar@me.berkeley.edu](mailto:majumdar@me.berkeley.edu)

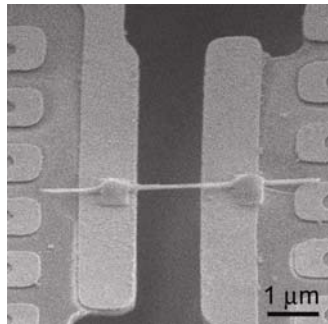
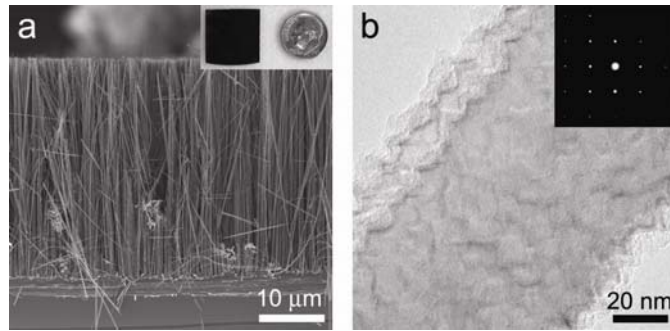
† [p\\_yang@berkeley.edu](mailto:p_yang@berkeley.edu)

Approximately 90 percent of the world's power ( $\sim 10^{13}$  Watts or 10 TW) is generated by heat engines that use fossil fuel combustion as a heat source and typically operate at 30-40 percent efficiency, such that roughly 15 TW of heat is lost to the environment. Thermoelectric modules could potentially convert part of this low-grade waste heat to electricity, which could result in significant fuel savings and reduction in carbon emissions. Their efficiency depends on the thermoelectric figure of merit ( $ZT$ ) of their material components, which is defined as  $ZT = S^2T/\rho k$  where  $S$ ,  $\rho$ ,  $k$ , and  $T$  are the Seebeck coefficient, electrical resistivity, thermal conductivity and absolute temperature, respectively. Over the past five decades it has been challenging to increase  $ZT > 1$ , since the parameters of  $ZT$  are generally interdependent<sup>1</sup>. While nanostructured thermoelectric materials have achieved  $ZT > 1$  (Refs. 2-4), the materials (Bi, Te, Pb, Sb, and Ag) and processes used are not easy to scale. Here we report the wafer-scale electrochemical synthesis of large-area arrays of rough Si nanowires that are 20-300 nm in diameter. These nanowires have  $S$  and  $\rho$  that are the same as in bulk doped Si, but those with diameters  $\sim 50$  nm exhibit 100-fold reduction in  $k$ , which yields a large  $ZT = 0.6$  at room temperature. For such nanowires, the lattice contribution to  $k$  approaches the amorphous limit for Si, which cannot be explained by current theories. Although bulk Si is a poor thermoelectric material, by greatly reducing  $k$  without significantly affecting  $S$  and  $\rho$ , Si nanowire arrays show promise as high-performance, scalable thermoelectric materials.

The most widely used commercial thermoelectric material is bulk  $\text{Bi}_2\text{Te}_3$  and its alloys with Sb, Se, etc, which have  $ZT \sim 1$ . While it is difficult to scale bulk  $\text{Bi}_2\text{Te}_3$  to large-scale energy conversion, fabricating synthetic nanostructures for this purpose is even more difficult and expensive. Si, on the other hand, is the most abundant and widely used semiconductor with a large industrial infrastructure for low-cost and high-yield processing. Bulk Si, however, has a high  $k$  ( $\sim 150 \text{ W} \cdot \text{m}^{-1} \cdot \text{K}^{-1}$  at room temperature<sup>5</sup>), making  $ZT \sim 0.01$  at 300 K (Ref. 6). The spectral distribution of phonons contributing to the  $k$  of Si at room temperature is quite broad. Because the rate of phonon-phonon Umklapp scattering scales as  $\omega^2$ , where  $\omega$  is the phonon frequency, low frequency (or long-wavelength) acoustic phonons have long mean free paths and contribute significantly to  $k$  at high temperatures<sup>7-10</sup>. Thus, by rational incorporation of phonon-scattering elements at several length scales, the  $k$  of Si is expected to decrease dramatically. Indeed, we have shown that by using roughened nanowires, one can reduce the thermal conductivity to  $\sim 1.6 \text{ W} \cdot \text{m}^{-1} \cdot \text{K}^{-1}$ , with the phonon contribution close to the amorphous limit, without significantly modifying the power factor,  $S^2/\rho$ , such that

$ZT \sim 1$  at room temperature<sup>11</sup>. Further reduction of nanowire diameter is likely to increase  $ZT > 1$ , offering the possibility of high-performance, low-cost and scalable Si-based thermoelectric devices.

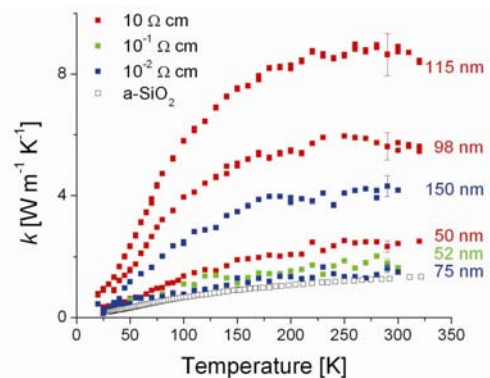
Wafer-scale arrays of Si nanowires were synthesized by an aqueous electroless etching (EE) method<sup>12</sup>. The technique is based on the galvanic displacement of Si by  $\text{Ag}^+ \rightarrow \text{Ag}^0$  reduction on the wafer surface. The reaction proceeds in an aqueous solution of  $\text{AgNO}_3$  and HF. Nanowires synthesized by this approach were vertically aligned (above, **a**), single crystalline (above, **b** inset) and consistent across large areas up to the wafer-scale (above, **a** inset). In contrast to the smooth surface of typical vapour-liquid-solid (VLS) grown, gold catalyzed Si nanowires<sup>13,14</sup>, those of the EE Si nanowires are much rougher (above, **b**). The mean roughness height of these nanowires varied wire to wire, but was typically 1 to 5 nm with a roughness period on the order of several nanometers. This roughness may be attributed to randomness of the lateral oxidation and etching in the corrosive aqueous solution. Similar results were obtained for electroless etching of both n- and p-type wafers with resistivities varying from 10 to  $10^{-2} \Omega\cdot\text{cm}$  ( $\sim 10^{14}$  to  $10^{18} \text{ cm}^{-3}$  dopant concentrations). Since thermoelectric modules consist of complementary p- and n-type materials wired in series, the generality and scalability of this synthesis indicate it is a promising method for fabrication of Si-based devices.



The thermal conductivity of these hierarchically structured Si nanowires was characterized using devices consisting of resistive coils supported on parallel, suspended  $\text{SiN}_x$  membranes<sup>13,15</sup> (left). This construction allows us to probe thermal transport in individual nanowires. The membranes are thermally connected through a bridging nanowire, with negligible leakage from heat transfer by means other than conduction through the wire. To anchor the nanowire to the membranes and reduce thermal contact resistance, a Pt-C composite was deposited on both ends.

It has been shown that the  $k$  of VLS Si nanowires is strongly diameter dependent<sup>13</sup>, which is attributed to boundary scattering of phonons. We found that EE Si nanowires exhibit a diameter dependence of  $k$  similar to that of VLS-grown wires, but the magnitude of  $k$  is five- to eight-fold lower. Since the peak  $ZT$  of semiconductor materials is predicted to occur at high dopant concentrations<sup>16</sup>, low resistivity nanowires were synthesized by post-growth gas-phase B doping of the nanowire arrays etched from  $10^{-1} \Omega\cdot\text{cm}$  wafers. The graph to the right shows the  $k$  of small diameter nanowires etched from 10,  $10^{-1}$ , and  $10^{-2} \Omega\cdot\text{cm}$  wafers.

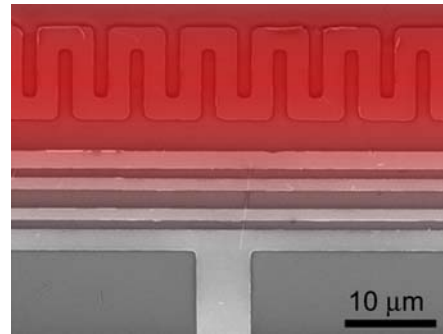
In the case of the 52 nm nanowire,  $k$  is reduced to  $1.6 \text{ W}\cdot\text{m}^{-1}\cdot\text{K}^{-1}$  at room temperature.



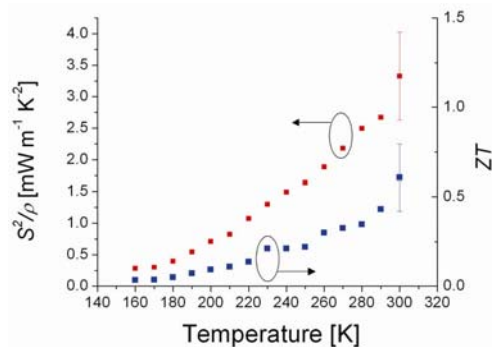
For comparison, the temperature dependent  $k$  of amorphous bulk  $\text{SiO}_2$ <sup>17</sup> is also plotted in the above graph. As can be seen from the plot,  $k$  of these single-crystalline EE Si nanowires is comparable to that of insulating glass. Indeed,  $k$  of the 52 nm nanowire approaches the minimum  $k$  predicted and measured for Si,  $\sim 1 \text{ W}\cdot\text{m}^{-1}\cdot\text{K}^{-1}$  (Ref. 18). The lattice contribution to  $k$  ( $k_l$ ) can be calculated by subtracting the electronic contribution ( $k_e$ ) as determined by the Wiedemann-Franz law<sup>19</sup>.  $k_e \approx 0.4 \text{ W}\cdot\text{m}^{-1}\cdot\text{K}^{-1}$  for these nanowires, meaning  $k_l$  ( $k_l = k - k_e$ ) is  $1.2 \text{ W}\cdot\text{m}^{-1}\cdot\text{K}^{-1}$ , remarkably close to the minimum.

To the best of our knowledge, there is currently no theory that can explain why a single-crystalline Si nanowire that is  $\sim 50 \text{ nm}$  in diameter should behave like a phonon glass. Based on the difference between VLS and EE nanowires, we suspect that surface roughness plays an important role in screening a broad spectrum of phonons, fundamentally altering phonon transmission through these confined structures. The exact mechanism, however, remains unknown.

To calculate the nanowire  $ZT$ ,  $\rho$  and  $S$  measurements were carried out on individual highly-doped nanowires. Nanowires were measured in a horizontal geometry on substrates with a micro-fabricated heating element to produce a temperature gradient, and 2- and 4-point probe electrodes to measure the Seebeck voltage and  $I$ - $V$  characteristics (at right, with false color to indicate heat gradient).



$\rho$  and  $S$  of a 48 nm nanowire were used for the  $ZT$  calculation since the diameter is close to that of the 52 nm wire for which  $k$  has been measured.  $S^2/\rho$  and  $ZT$  are plotted below as a function of temperature. The nanowire  $ZT$  is highest near room temperature at 0.6 and increasing. As compared to optimally-doped bulk Si ( $\sim 1 \times 10^{19} \text{ cm}^{-3}$ ), the  $ZT$  of the EE nanowire is nearly two orders of magnitude greater throughout the temperature range measured<sup>6</sup>. The large increase in  $ZT$  occurs because  $k$  decreases significantly, whereas  $S^2/\rho$  degrades only slightly compared to bulk. The hierarchical structuring of the EE Si nanowires allows selective scattering of phonons by dopants, nanoscale surface roughness, and dimensional confinement, while leaving electronic transport largely unaffected.



In conclusion, we have shown that it is possible to achieve  $ZT = 0.6$  at room temperature in rough Si nanowires of  $\sim 50 \text{ nm}$  diameter that were processed by a wafer scale manufacturing technique. Furthermore, by achieving broadband impedance of phonon transport, we have demonstrated that the EE Si nanowire system is capable of approaching the limits of minimum lattice thermal conductivity in Si.

This  $ZT$  enhancement can be attributed to efficient scattering throughout the phonon spectrum by the introduction of nanostructures at different length scales (diameter, roughness, and point defects). The significant reduction in thermal conductivity observed in this study may be a result of changes in the fundamental physics of heat transport in these quasi-one dimensional materials. Future experiments will focus on quantifying the effects of surface roughness and optimizing the nanowire dopant concentration. In addition, rough and thin nanowires will be thermally characterized to investigate the lower limits of thermal

conduction in such structures. P-N thermoelectric modules with the performance reported here, and manufactured from such a ubiquitous material as Si, may find wide-ranging applications in waste heat salvaging, power generation, and solid-state refrigeration. Moreover, the phonon scattering techniques developed in this study could significantly augment  $ZT$  even further in other materials to produce highly efficient solid-state thermoelectric devices.

## References

1. Majumdar, A., *Science* **303**, 777-778 (2004).
2. Hsu, K. F. *et al.*, *Science* **303**, 818-821 (2004).
3. Harman, T. C. *et al.*, *Science* **297**, 2229-2232 (2002).
4. Venkatasubramanian, R. *et al.*, *Nature* **413**, 597-602 (2001).
5. Touloukian, Y. S. *et al.*, *Thermal Conductivity: Metallic Elements and Alloys, Thermophysical Properties of Matter*, v. **1**, IFI/Plenum, New York, 339 (1970).
6. Weber, L. & Gmelin, E., *Appl. Phys. A* **53**, 136-140 (1991).
7. Nolas, G. S., Sharp, J. & Goldsmid, H. J., *Thermoelectrics: Basic Principles and New Materials Development*, Springer-Verlag, Berlin, 2001.
8. Asheghi, M. *et al.*, *Appl. Phys. Lett.* **71**, 1798-1800 (1997).
9. Asheghi, M. *et al.*, *J. Heat Transf.* **120**, 30-36 (1998).
10. Ju, Y. S. & Goodson, K. E., *Appl. Phys. Lett.* **74**, 3005-3007 (1999).
11. Hochbaum, A.I. *et al.*, *Nature* **451**, 163-167 (2008).
12. Peng, K. Q. *et al.*, *Adv. Mater.* **14**, 1164-1167 (2002).
13. Li, D. *et al.*, *Appl. Phys. Lett.* **83**, 2934-2936 (2003).
14. Hochbaum, A.I. *et al.*, *Nano Lett.* **5**, 457-460 (2005).
15. Shi, L. *et al.*, *J. Heat Transf.* **125**, 881-888 (2003).
16. Rowe, D. M. ed. *CRC Handbook of Thermoelectrics*, CRC Press, Boca Raton, ch. 5 (1995).
17. Data points used from <http://users.mrl.uiuc.edu/cahill/tcdata/tcdata.html>, agrees with measurement in Cahill, D. G. & Pohl, R. O. Thermal conductivity of amorphous solids above the plateau. *Phys. Rev. B* **35**, 4067-4073 (1987).
18. Cahill, D. G., Watson, S. K. & Pohl, R. O., *Phys. Rev. B* **46**, 6131-6140 (1992).
19. Ashcroft, N. W. & Mermin, N. D. *Solid State Physics*, Saunders College Publishing, Fort Worth, ch. 1, 2, 13 (1976).

**Electric Field Effects in Liquid Crystals with Dielectric Dispersion**  
**DE-FG02-06ER46331**

PI: Dr. Oleg D. Lavrentovich (odl@lci.kent.edu)  
Co-PI: Dr. Sergij V. Shiyanovskii (svshiyan@lci.kent.edu)  
Chemical Physics Interdisciplinary Program  
Liquid Crystal Institute  
Kent State University,  
Kent, OH 44242-0001

**Program scope**

Liquid crystals (LCs) are anisotropic fluid dielectrics. When an external field is applied, the LC director, depicting average orientation of LC molecules, reorients and thus causes optical effects that are at the heart of modern display technologies. In the physics of LCs, dielectric response is described as instantaneous: It is assumed that the electric displacement at the moment of time  $t$  is determined solely by the electric field at the very same moment  $t$ . The approach is certainly valid when the LC experiences no dielectric relaxation and the tensor of dielectric permittivity is frequency-independent. In reality, however, LCs are dielectrically dispersive. The characteristic relaxation time might vary in a broad range from millisecond to nanosecond, depending on the material. When the characteristic time with which the electric field varies becomes shorter or comparable to the characteristic time of dielectric relaxation, the classic theory is not applicable and should be replaced by an approach in which the dielectric torque depends not only on the current value of the field but also on its past values. The corresponding theories exist for isotropic fluids and solid crystals; in both cases, the dielectric properties of medium do not change with time. In LCs, the situation is more complex as the electric field causes director reorientation which in turn changes the dielectric coupling between the field and the medium. Thus the electric displacement should be a function of not only the past and present electric field, but also of the present and past director orientations.

The goal of this project is to develop physical understanding of the time-dependent dielectric response of NLCs. The research focuses on theoretical modeling and experimental testing of dielectric phenomena in the nematic LCs that occur at the time scale comparable to the time of dielectric relaxation.

Initially [1], we focused on the so-called dual-frequency nematic (DFN) materials. The dielectric anisotropy of DFN changes its sign at a certain frequency which allows one to produce the opposite signs of the “instantaneous” and “memory” contributions to the reorienting torque. In other words, the DFNs allowed us to clearly separate the predictions of the classic “instantaneous” model and the new theory that accounts for the dielectric dispersion effect and to confirm the theory experimentally.

**Recent progress**

To characterize the dielectric response of a LC with dielectric relaxation carefully, one needs to know how the temperature of the LC changes when the cell is driven by an electric field. This is why we started with the studies of how the dielectric relaxation influences of dielectric heating effects that are especially pronounced when the frequency of the applied voltage is close to the dielectric relaxation frequency [2]. We proposed a general model [2] to quantitatively describe the temperature increase of a liquid crystal as the function of the material properties of the LC (such as frequency dependence of imaginary part of the dielectric permittivity), thermal properties of the

bounding plates and the surrounding medium, as well as frequency and amplitude of the applied electric field. We verified the model experimentally, by using a thermocouple inserted directly into the nematic bulk [2].

In LCs, the dielectric heating effect is anisotropic, i.e., the temperature raise depends on the state of director orientation. We used this feature to demonstrate a thermodielectric bistability caused by the anisotropic nature of dielectric heating and director reorientation in an electric field. The bistability is a result of the positive feedback loop: director reorientation  $\rightarrow$  anisotropic dielectric heating  $\rightarrow$  dielectric anisotropy  $\rightarrow$  director reorientation. We demonstrate both experimentally and theoretically that the two states with different temperature and director orientation, namely, a cold planar state and a hot homeotropic state coexist in a liquid crystal cell for a certain frequency and amplitude range of the applied voltage [3].

We also demonstrated yet another fascinating effect of the electric field on liquid crystals, associated with the mass flow of the nematic fluid caused by the director reorientation in the applied field. This so-called “backflow” effect can be visualized when the LC is doped with micron-size colloidal inclusions. Liquid crystal molecules, reoriented by the field, set the colloidal particles into motion by pushing them into two opposite directions perpendicular to the applied field. The direction of motion is determined by the polarity of director distortions around the inclusion. The phenomenon opens the door for the study of far-from-equilibrium phenomena such as two-lane traffic, driven diffusion, etc. [4]

Most recently, we extended our studies of director reorientation by dielectric torque to the general case of dielectrically anisotropic nematic LCs, in which the dielectric anisotropy might be either positive or negative and in which the both parallel and perpendicular dielectric components might experience multiple relaxation processes at various frequencies [5]. We theoretically derived the reorienting dielectric torque acting on the director, taking into account the entire frequency spectrum of the dielectric tensor, thus generalizing the original theory, reviewed in Ref. [1], limited by the single relaxation approach. The model predicts the “dielectric memory effect” (DME), i.e., dependence of the dielectric torque on both the “present” and “past” values of the electric field and the director.

The new model allowed us to describe experimentally observed director reorientation in the case when the rise time of the applied voltage is smaller than the dielectric relaxation time.

In the typical materials such as pentylcyanobiphenyl (5CB), in which the dielectric anisotropy is positive at low frequencies, the DME slows down director reorientation in a sharply rising electric field, as the sharp front is perceived as a high-frequency excitation for which the dielectric anisotropy is small or even of a negative sign. As a result, the director reorients perpendicular to the field at the beginning of the applied voltage pulse and only

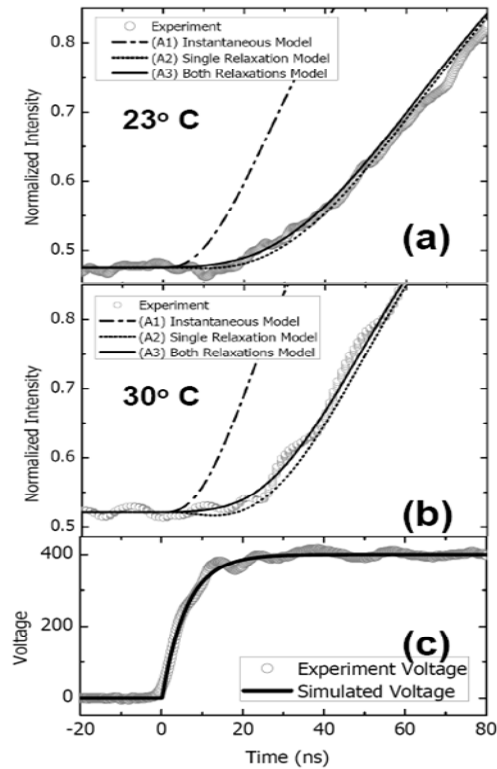


Figure 1. In a dielectrically positive liquid crystal, the DME causes a time delay before the desired director reorientation.

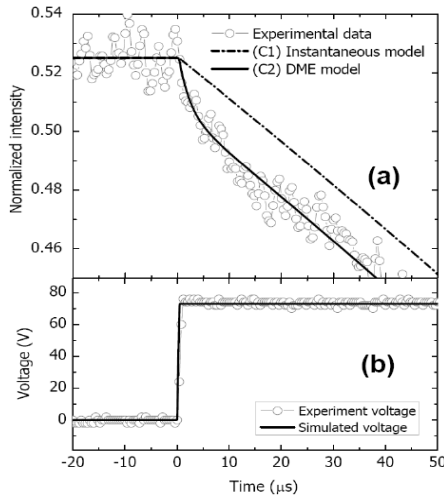


Figure 2. In a dielectrically negative liquid crystal, the DME can speed up the director reorientation.

the polarity of the electric field, which drags the reorientation of the director at the same time. The most suitable experimental situation to observe the effect is during the switching-off of the cell. When the applied voltage is switched off, the director reorients to its original state driven by surface anchoring at the bounding plates and by elastic distortions stored when the field was applied. The resulting director reorientation is just a “passive” and relatively slow effect. However, if the electric polarization does not disappear instantaneously after the field is switched off (because of the finite time of dielectric relaxation), then one can apply a very short electric pulse, with the duration of the order of the characteristic time of dielectric relaxation and accelerate the director reorientation. Figure 3 illustrates such an accelerated response.

To further verify the existence of a linear coupling between the applied electric field and the residual electric polarization in the LC, we performed a similar set of experiments on a LC that shows no dielectric relaxation in the frequency range of interest. As expected, there is no residual polarization of the sample and there is no effect of the polarity of an additional

after some time, of the order of dielectric relaxation time, starts to reorient parallel to the field, i.e., in the desired direction., Fig.1.

In the materials with negative dielectric anisotropies, the DME speeds up the response of the LCs as shown in Fig. 2. The reason is that the sharply increasing voltage pulse is perceived by the LC as a high-frequency excitation for which the absolute value of dielectric anisotropy is larger than at the low frequencies.

Our most recent result is the discovery of a dielectric torque which depends on the polarity of the electric field. The origin of this torque is the existence of a “memory” polarization as a result of the DME; unlike the director of LCs, this memory polarization can be reoriented by changing the

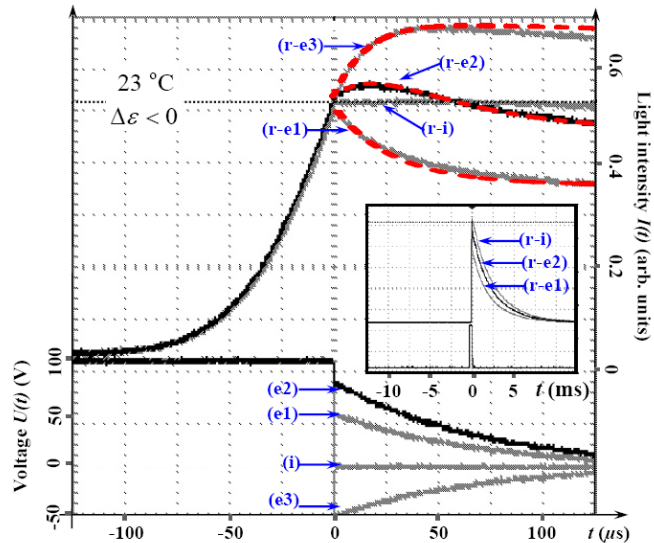


Figure 3. Electrically accelerated turn-off speed of a liquid crystal device. The conventional driving scheme is to quickly turn off the field, pulse (i), and the corresponding response is the upper “r-i” curve, which almost stay unchanged in this microsecond time range. If we use an optimized pulse (e1), the turn-off speed is noticeably faster, the upper r-e1 curve. We further check the model by using non-optimum pulses (e2, e3), and the corresponding turn-off speeds are all slower than the one under the optimized pulse.

pulse on the behavior of the cell, Fig.4.

The observation of linear dielectric effect in the nematic LCs is of importance to both the science and the industry. The existence of polarity dependent dielectric torque significantly contributes to understanding the fundamental physics of the liquid crystals, with this polar torque it opens a potential gate for more exciting research; as for the industry, the previous passive turn-off process, which solely relies on the elastic torque and surface anchoring, can now be actively controlled by an additional “turn-off” field, which enables one to reduce the turn-off time for all electrically driven liquid crystal devices, for example, the liquid crystal display may no longer suffers the motion blurs due to the long response time. We submitted our results to Physical Review Letters for publication [6].

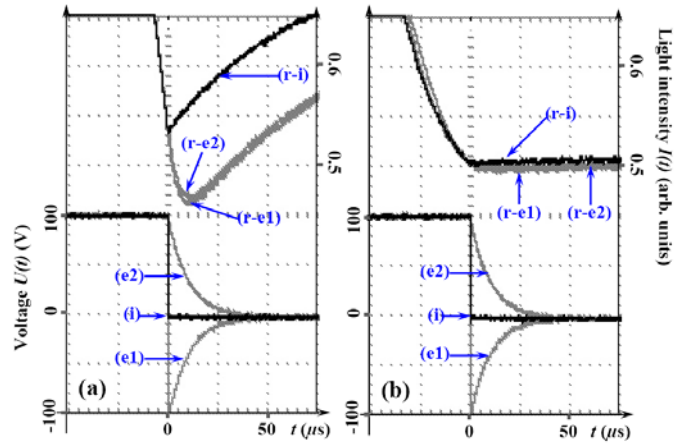


Figure 4. No observations of the electrically acceleration of the turn-off speed in a liquid crystal without dielectric relaxation.

Planned activities for the next year: To study the dynamics of the electrically induced isotropic-nematic phase transition by taking account the finite time of relaxation of permanent polarization, which is assumed to be an instantaneous process in the classic theory. We plan to develop a new model to describe the dynamics of the phase transition and to verify it experimentally.

List of publications:

1. Y. Yin, S.V. Shiyankovskii, and O. D. Lavrentovich, Fast switching of nematic liquid crystals by an electric field: Effects of dielectric relaxation on the director and thermal dynamics, Chapter 10 in: *Thermotropic Liquid Crystals*, Ed. By A. Ramamoorthy, Springer, Dordrecht, The Netherlands, ISBN 978-1-4020-5327-6, pp. 277-295 (2007).
2. Y. Yin, S.V. Shiyankovskii, O.D. Lavrentovich, Electric Heating Effects in nematic liquid crystals, *Journal of Applied Physics* **100**, 024906 (2006).
3. Ye Yin, S.V. Shiyankovskii, and O.D. Lavrentovich, Thermodielectric bistability in dual frequency nematic liquid crystal, *Phys. Rev. Lett.* **98**, 097801 (2007).
4. O.P. Pishnyak, S. Tang, J.R. Kelly, S.V. Shiyankovskii, O.D. Lavrentovich, Levitation, Lift and bidirectional motion of colloidal particles in an electrically-driven nematic liquid crystal, *Phys. Rev. Lett.* **99**, 127802 (2007).
5. Mingxia Gu, Ye Yin, S.V. Shiyankovskii, and O.D. Lavrentovich, Effects of dielectric relaxation on the director dynamics of uniaxial nematic liquid crystals, *Phys. Rev. E.* **76**, 061702 (2007).
6. M. Gu, S. V. Shiyankovskii, and O. D. Lavrentovich, Polarity dependent dielectric torque in dispersive nematic liquid crystals, *Phys. Rev. Lett.*, Submitted (2007)

## **Amorphous Structures and Polymorphs of Metallic Glasses**

**E. Ma**

**Department of Materials Science and Engineering, Johns Hopkins University,  
Baltimore, MD 21218**

**ema@jhu.edu**

### **Program Scope**

The metals and alloys we are familiar with are all crystalline and well understood. In contrast, their recently emerged amorphous counterparts, i.e., “bulk metallic glasses” (BMGs), pose new and major challenges to the materials science community [1]. Here even the basic issues, such as why they are such easy glass formers, how atoms pack inside, and how plastic deformation initiates in the absence of well-defined dislocations, have not been resolved.

This project is a continuation of our previous investigation of amorphous structure and poly(a)morphism. This is a key and fundamental scientific issue, because the macroscopic properties are all controlled by the mysterious internal atomic arrangements and their transformations. It is also a difficult problem to solve, hampering our understanding of the amorphous state of metals and the ways they behave. During the past several years, we have made significant progress in unraveling the atomic packing structures of binary metallic glasses. The short-to-medium range order involving the solute-centered quasi-equivalent clusters, and their systematic dependence on alloys for a range of atomic size ratios and chemical make-ups, have been specified [2]. We have also successfully identified a polyamorphic transition in a Ce-based metallic glass [3]. This project will take advantage of the experience we have accumulated, especially in terms of a two-pronged experimental/computational approach employing synchrotron (in situ) experiments and ab-initio/molecular-dynamics calculations.

More specifically, this project is designed to achieve the following goals. 1) We will be reaching a comprehensive understanding of the whole spectrum of the amorphous structures in metallic glasses. In particular, we are expanding our work to the newly developed multi-component BMGs, to extract packing principles and develop new structural concepts. 2) We are applying the structural knowledge gained to improve our understanding of the important properties of BMGs. First, we will clarify the structural origin of the high glass forming ability of these easy glass formers. Second, we will establish the structural basis of the various property relations observed for BMGs. Third, a correct structural description will also allow us to uncover the structural entities involved in, and the evolution of the short-to-medium range order associated with, the initiation of plastic flow during deformation, such as the formation of (cooperative) shear-transformation zones throughout the BMG sample [4] under applied stresses. 3) This research will deepen our understanding of “polyamorphism”, a new class of polymorphic transitions in amorphous matters. Emphasis will be placed on understanding the electron structure origins of the polyamorphs, and on polyamorphism in the liquid state.

This study will broaden our horizon and perspectives on the states of matter, and should significantly impact the existing theories on the atomic structure, stability and forming ability, plastic deformation, and structural evolution of amorphous metals. Our work will also help establish new, technologically useful BMGs with unusual thermodynamic, functional and rheological properties.

## Recent Progress

Recently we have made considerable progress in understanding how atoms pack in MGs, using synchrotron X-ray experiments and computer simulations. This work was published in *Nature* as a regular article [2] and made the DoE weekly news on 4/17/2006.

We constructed the three-dimensional atomic structure using reverse Monte Carlo simulations based on X-ray and EXAFS data. Independently, we carried out *ab initio* molecular dynamics modeling, without experimental input. Validations of these atomic configurations were performed by comparing the density, XANES, and partial RDFs derived from our configurations, with those determined in lab experiments. As an example, Fig. 1 demonstrates the good agreement achieved between the calculated partial RDFs of our models and those obtained before using neutron isotope experiments.

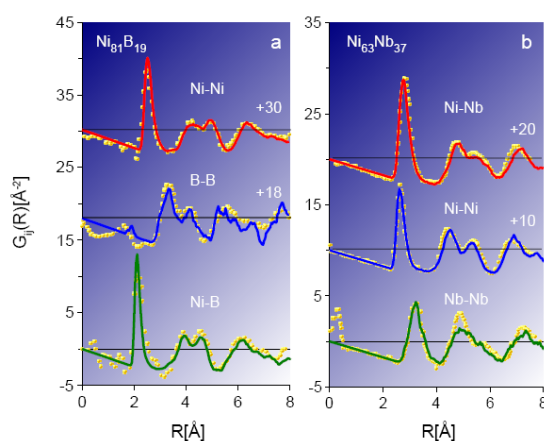


Fig. 1 Partial RDFs of our model amorphous configurations compared with experimental data for MGs.

Using the atomic coordinates, we performed structural analysis employing the Voronoi tessellation method and the common neighbor analysis (in comparison with bond orientation parameter analysis). Structural building principles have been extracted after analyzing a range of systems. We proposed the concept of “solute-centered quasi-equivalent clusters” (QECs). Their formation is a consequence of the preferred “solute avoidance” to increase the number of bonds between unlike atoms to reduce energy (there is a large negative heat of mixing in the easy glass forming systems). This avoidance is seen in the B-B correlation in Fig. 1. Fig. 2 shows examples of QECs, connected through face-sharing, edge-sharing, and vertex-sharing schemes. The intra-cluster topological short-range order (SRO) favors efficient packing, its specific type depending on the atomic size ratio ( $r^*$ ), as shown in Fig. 3.

In addition to the SRO dependence on chemistry and  $r^*$ , we also described MRO -the next level of structural organization, based on efficient dense packing of QECs, in favor of icosahedral-like ordering.

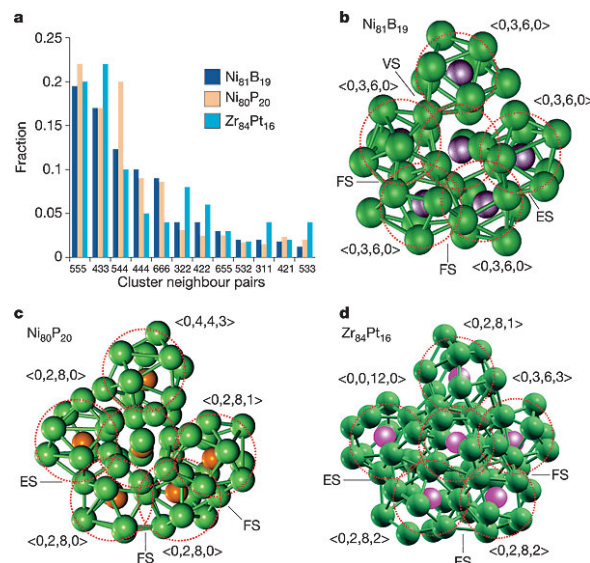


Fig. 2 Atomic packing and quasi-equivalent clusters in MGs, see [2] for details.

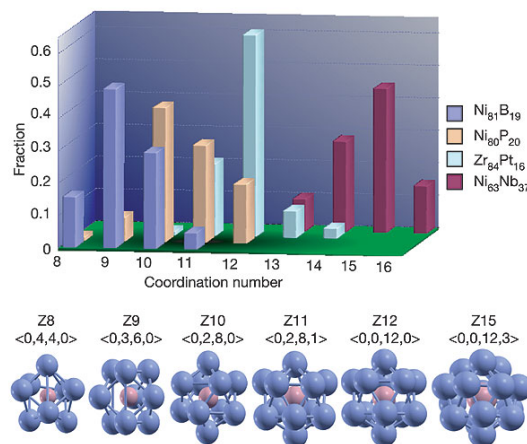


Fig. 3 Coordination number distribution depends on systems (the atomic size ratio).

In parallel studies, we observed interesting amorphous polymorphs in a MG, which is normally believed to be unlikely since MGs are already too spatially compact to transform to a higher-density phase. The results have been published in *Nature Materials* 6 (2007) 192-197 [3]. Here we only briefly summarize the main finding. We studied a melt-spun  $Ce_{56}Al_{44}$  glass because crystalline Ce is known to exhibit multiple polymorphic transitions under 1 GPa pressure with large density changes. When plotting specific volume versus pressure ( $P$ ) one observes a fast decrease of volume (corresponding to density increase, as well as to the shift of XRD peak to higher  $Q$ ) with increasing  $P$ , unusually fast when the  $P$ - $V$  equation of state is compared with the prediction given by *ab initio* simulation of the glass, when Ce is in

its “trivalent” paramagnetic state where the  $f$ -electrons are localized. At elevated  $P$  the volume in fact coincides with that expected for the same glass when all the Ce  $f$ -electrons are delocalized (the “tetravalent” state). An obvious change in slope (compressibility) is observed. Upon decompression, the volume follows nicely the prediction for the high-density phase, suggesting that the  $f$ -electrons remained delocalized, till about  $<3$  GPa where an abrupt return to the low-density phase occurred. To make sure that the data are reproducible and sufficient data points are collected to substantiate the conclusions, four different samples were studied in four separate runs at different times at the Advanced Photon Source. As shown in Fig. 4 below, for all the four data sets, the decompression data points below 13.5 GPa did not re-trace the compression ones, unlike for the BMGs studied before under pressure, where this “elastic” density increase always exactly reverses itself when the pressure is released. We therefore believe that these *in situ* synchrotron XRD experiments under pressure have captured a polyamorphic transition of the glass, much like those observed before for non-metallic glasses, from a low-density state into a high-density state, with a large density disparity (11% at  $P=15$  GPa, and 16% at  $P=0$ ) and governed by two different equations of state.

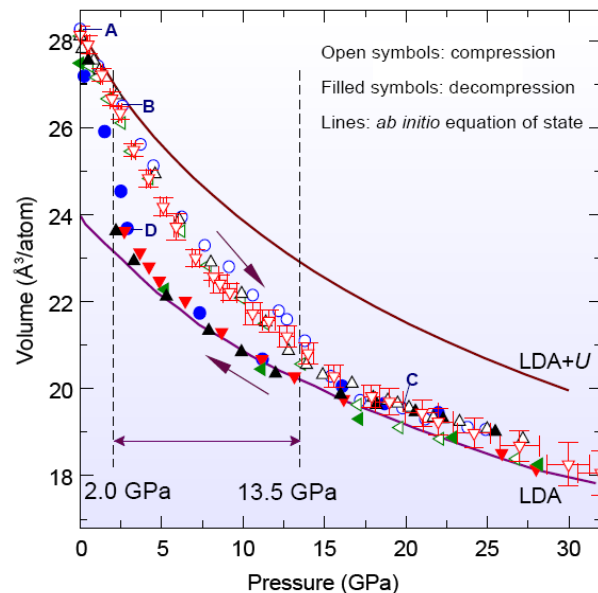


Fig. 4 Specific volume of  $Ce_{55}Al_{45}$  MG as a function of pressure. Note the abrupt transition back to the original density during decompression.

## References

- [1] A.L. Greer and E. Ma, *Bulk Metallic Glasses: at the Cutting Edge of Metals Research*, MRS Bulletin 32 (2007) 611-615.
- [2] H.W. Sheng, W.K. Luo, F.M. Alamgir, J. Bai and E. Ma, *Atomic Packing and Short-to-Medium-Range Order in Metallic Glasses*, Nature 439 (2006) 419-425.
- [3] H.W. Sheng, H.Z. Liu, Y.Q. Cheng, J. Wen, P.L. Lee, W.K. Luo, S.D. Shastri and E. Ma, *Polyamorphism in a Metallic Glass*, Nature Materials, 6 (2007) 192-197.
- [4] H. Guo, P.F. Yan, Y.B. Wang, J. Tan, Z.F. Zhang, M.L. Sui and E. Ma, *Tensile Ductility and Necking of Metallic Glass*, Nature Materials 6 (2007) 735-739.

**Title:** Mesoscale Interfacial Dynamics in Magnetoelectric Nanocomposites

**Principal Investigator:** Shashank Priya (Collaboration with Dwight Viehland, and Armen Khachaturyan)

**Mailing Address:** 304A Holden Hall, mc 0237, Virginia Tech, Blacksburg, VA 24061.

**Email:** [spriya@vt.edu](mailto:spriya@vt.edu)

**Program Scope:** Dielectric polarization of a material under the magnetic field or an induced magnetization under the electric field requires the simultaneous presence of long-range ordering of magnetic moments and electric dipoles. Single phase materials suffer from the drawback that the magnetoelectric (ME) effect is considerably weak even at low temperatures, limiting their applicability in practical devices. Better alternatives are ME composites that have large magnitudes of the ME voltage coefficient. The composites exploit the product property of the materials. Magnetoelectric particulate composites consisting of piezoelectric and magnetostrictive materials with different connectivity schemes including “3-0” and “2-0”, and laminate bulk composite with “2-2” connectivity have been investigated. However, the understanding of the physical interaction occurring at the mesoscale interfaces between the magneto-elastic stresses and elasto-electric fields has not been achieved. The lack of this understanding has limited the ability to achieve the theoretical response of the material by coordinating the local electro-magnetic couplings, via coherent elastic interactions between phases. Comprehensive understanding of such interactions would enable the development of magnetoelectric materials exhibiting giant responses at small dimensions. The specific objectives of this program are as following (i) investigation of the local magnetoelectric coefficient using magnetic force microscopy and piezo force microscopy; (ii) determine microstructure of the interfaces between magnetic and piezoelectric phases, using electron microscopies; (iii) find the correlation between local and bulk magnetoelectric responses, the interfacial microstructure for fine scale composites of various phase connectivities, and (iv) develop a 3D Phase Field model of spontaneously self-organizing nano-scale microstructures.

### Recent progress:

We initiated the program with studies on eutectic composition in the  $(1-x)\text{BTO} - x\text{CFO}$  system. The composites were synthesized near the eutectic composition for  $x = 0.30$  and  $0.35$  and a cofired bilayer composite for  $x = 0.335$  was also studied to understand how these differ in their contribution towards the ME response as shown below in Fig. 1.

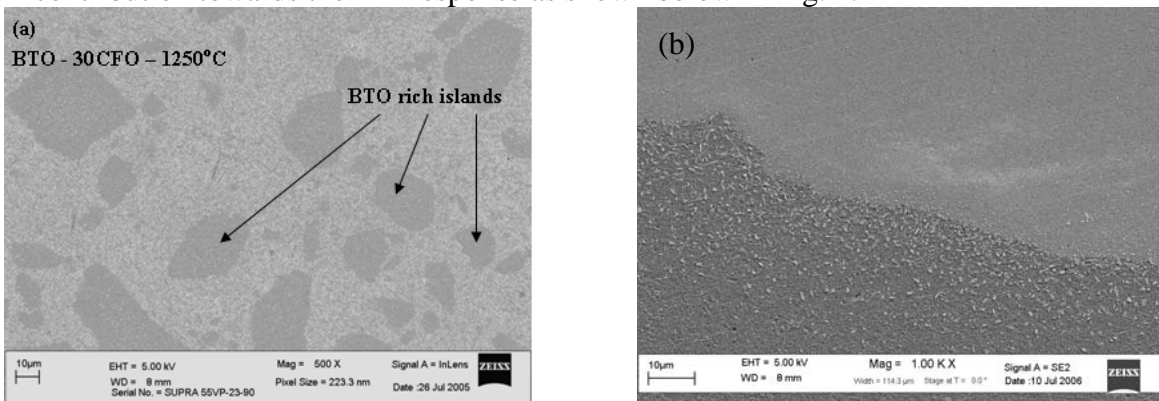


**Figure 1:** Microstructures of the synthesized BTO-CFO composites (a) eutectic decomposition, and (b) bilayer composite.

Magnified ( $10^5\times$ ) images of the microstructure taken from (a) a BTO-rich island, and (b) the CFO-rich matrix, showed that the grain sizes of both regions are quite small: the average grain size in the BTO-rich islands was  $\sim 150\text{nm}$  and that of the CFO-rich matrix region was  $\sim 215\text{nm}$ . X-ray mapping about the interfacial region revealed that the distribution of Co and Fe was more concentrated in the matrix. Standard-less quantitative analysis determined the concentrations of Co and Fe to be (i) 10at% and 7at% respectively, in the BTO-rich regions; and (ii) 18% and 35% respectively, in the matrix. Figure 2 shows the region of interest for our study. The TEM analysis of the BTO – CFO composites is in progress.

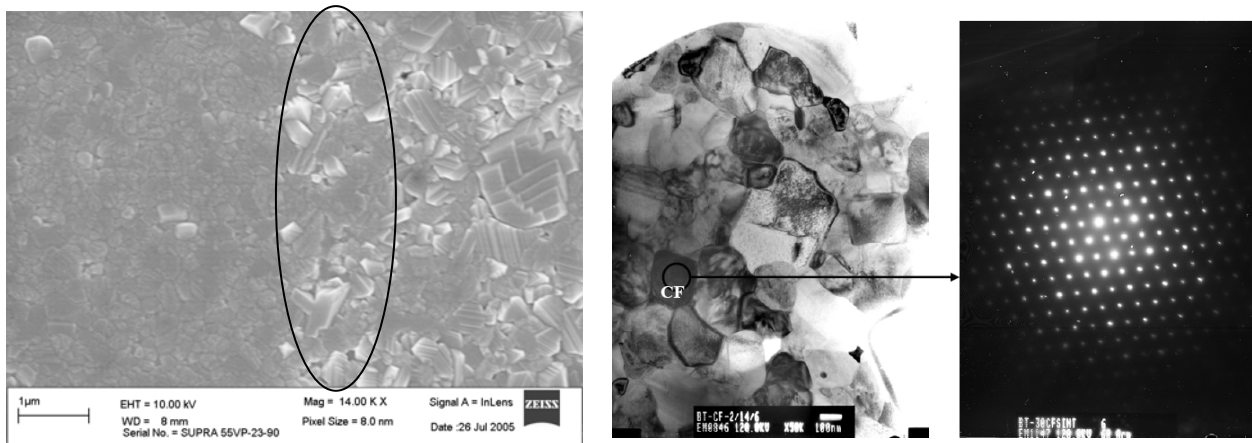


**Figure 2:** Interface structure in the BTO – CFO near eutectic composition.

However, the interesting results were: (i) bilayers exhibited significantly higher magnitude of the ME coefficients as compared to the particulates even though a high degree of coherency was observed at the interfaces, and (ii) composites exhibited higher magnitude of ME coefficient on annealing and aging. We are further investigating these observations.

Figure 3(a) shows a bright-field TEM image of as-sintered  $(1-x)\text{Pb}(\text{Zr}_{0.52}\text{Ti}_{0.48})\text{O}_3 - x\text{NiFe}_{1.9}\text{Mn}_{0.1}\text{O}_4$  (PZT-NFM) ceramic composites sample presenting a typical microstructure. This image consists of facet phases/particles (bright contrast) embedded in the matrix. The former ones (facet phases) correspond to the NFM phase, while the latter one (matrix) corresponds to the PZT phase, as identified by the EDS and SAED patterns. The NFM particles vary from 300 nm to 1500 nm. Figs. 3(c) and (d) are SAED patterns obtained from the PZT matrix, which can be identified as the [101] and [001] zone axes of the tetragonal PZT structure, respectively. The lattice parameter of this PZT structure in the sintered sample can be determined be  $a_{\text{PZT}}^{\text{s}}=3.87\text{\AA}$  and  $c_{\text{PZT}}^{\text{s}}=4.07\text{\AA}$ , with  $c/a=1.052$ . Figs. 1(e) and (f) are SAED patterns taken from NFM phase in Fig. 1(a) which can be identified as the [211] and [110] zone axes of the pseudo-cubic structure of NFM, respectively. This pseudo-cubic structure has a lattice parameter of  $a_{\text{NFM}}=8.42\text{\AA}$ , as measured from the electron diffraction pattern. Fig. 3(b) shows a bright field TEM image of the sample annealed  $800^\circ\text{C}$  for 10hrs. Fig. 3(b) shows different microstructural characteristics from those shown in Fig. 3 (a). The density of the NFM particles in this annealed sample is much less than that in the sintered sample. In addition, the NFM particles in the annealed sample have a typical size of 500 nm, much smaller than that in the sintered sample. The PZT phase in the annealed sample has a tetragonal structure with a lattice constant of  $a_{\text{PZT}}^{\text{a}}=4.07\text{\AA}$  and  $c_{\text{PZT}}^{\text{a}}=4.09\text{\AA}$ , with  $c/a=1.005$ . The samples treated by annealing at  $800^\circ\text{C}$  for 10hrs, followed by quenching in air and subsequent aging at  $300^\circ\text{C}$  shows similar microstructure to the annealed sample shown in Fig. 3(b), but the density of the NFM phase was further reduced.

Another noticeable feature observed was that in sintered sample due to the presence of large amount of defects, the grain boundaries are diffused. During annealing as the structure finds more time to reduce the defects from its structure, sharp grain boundaries were observed. The above results demonstrate that the post-sinter thermal treatments at 800°C for 10 hrs results in the reduction of the NFM phase by diffusing into the PZT structure. Meanwhile, PZT phase transfer from the tetragonal structure to a pseudo cubic structure with a larger lattice constant.

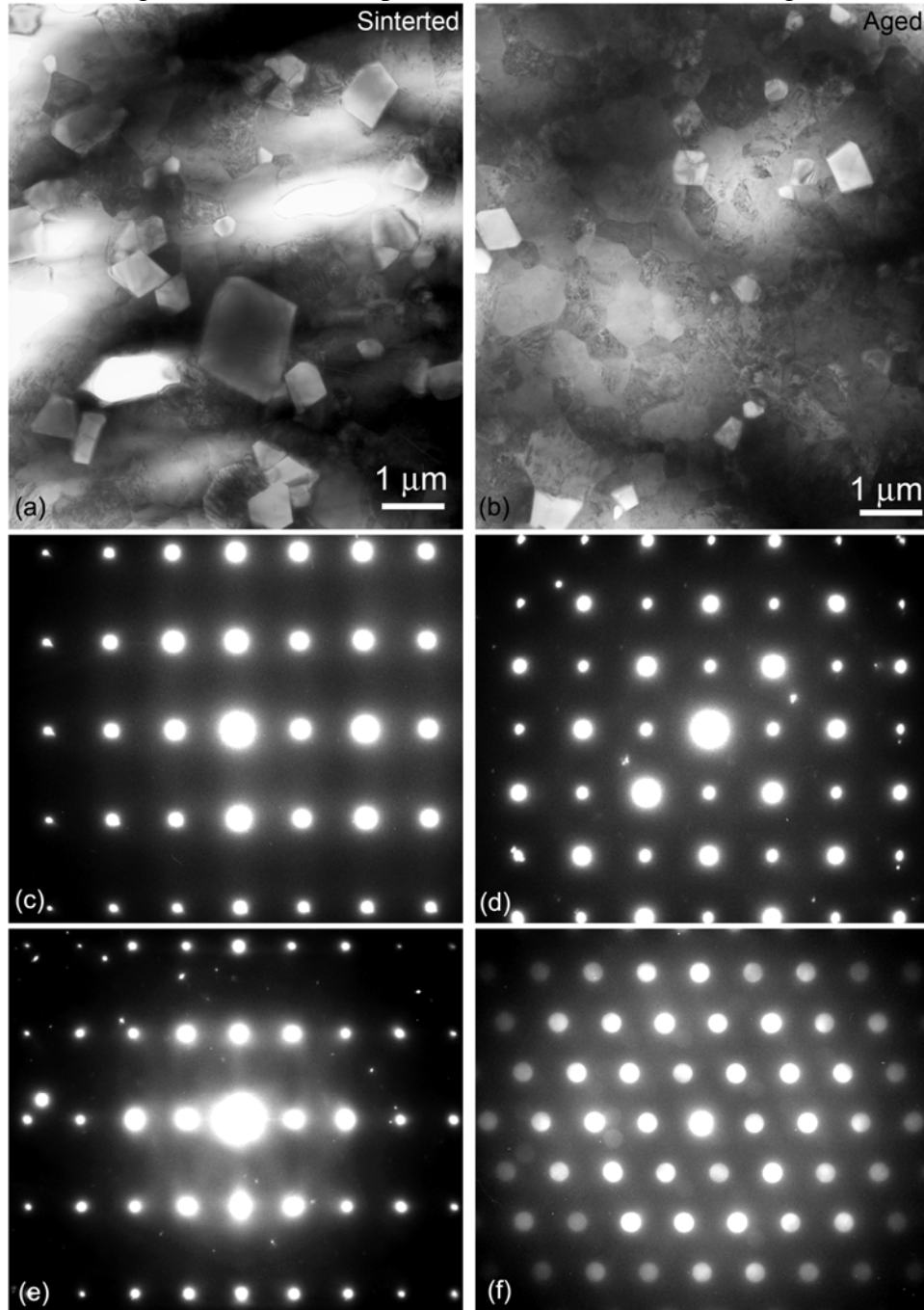


**Figure 3:** Bright field TEM images PZT – 5 NFM composites after (a) sintering, and (b) annealing. Selected area electron diffraction (SAED) pattern of PZT phase after sintering for (c) [101], (d) [001] zone axis and NFM phase after sintering (e) [211], (f) [110] zone axis.

This study is now in progress and we are planning to extend the HRTEM studies to layered composites and thin films (synthesized by our team member Dwight Viehland).

This presentation will present the progress made in first year of this program.

**Future Plans:** We are synthesizing the self-assembled and layered structures using the eutectic decomposition, co-firing, and thin film deposition. These samples are being studied using TEM, MFM and PFM, and diffraction. The results are being provided to the other team members for theoretical modeling and simulations.

**References:**

1. R. Islam, J. Jiang, F. Bai, D. Viehland, and S. Priya, “Correlation between structural deformation and magnetoelectric response in  $(1-x) \text{Pb}(\text{Zr}_{0.52}\text{Ti}_{0.48})\text{O}_3 - x \text{NiFe}_{1.9}\text{Mn}_{0.1}\text{O}_4$  particulate composites”, *Appl. Phys. Lett.* 91, 162905 (2007).
2. R. A. Islam and S. Priya, “Magnetoelectric properties of the lead-free cofired  $\text{BaTiO}_3$ – $(\text{Ni}_{0.8}\text{Zn}_{0.2})\text{Fe}_2\text{O}_4$  bilayer composite”, *Appl. Phys. Lett.* **89**, 152911 (2006).
3. S. Priya, R. Islam, S. Dong, and D. Viehland, “Advancement in the studies on magnetoelectric composites”, *J. Electrceram.* 19, 147 – 164 (2007).

## Complex amorphous transition-metal dielectrics

R. Bruce van Dover

Department of Materials Science and Engineering  
Cornell University, Ithaca, NY 14853

[vandover@cornell.edu](mailto:vandover@cornell.edu)

### Program Scope

Complex amorphous dielectrics represent a largely unexplored and incompletely understood class of materials—a class with tremendous potential advantages in electrical properties (such as charge storage or energy storage) over elemental oxides such as  $\alpha$ - $\text{SiO}_2$ . The structural degrees of freedom available in a nominally amorphous oxide or oxynitride with multiple species of metal cations offer the opportunity of identifying unpredictable *emergent behavior* such as a radically enhanced dielectric constant or breakdown field. New materials could revolutionize fields ranging from power-conditioning systems to integrated circuit technology.

Complexity has yielded valuable emergent properties in other electronic materials: we note the particularly dramatic cases of high-permittivity crystalline oxides, such as  $\text{CaCu}_3\text{Ti}_4\text{O}_{12}$ , and the cuprate superconductors, among which the four-cation compound  $\text{HgBa}_2\text{Ca}_2\text{Cu}_3\text{O}_{8+\delta}$  holds the record-high transition temperature. Indeed, it was recognized early in the investigation of the cuprates that the maximum transition temperature increased systematically as the number of unique atomic positions in the compound increased. We can expect analogous advantages in multicomponent amorphous oxides. And, unlike crystalline thin films, these materials can be deposited at low temperature which gives them a critical advantage in process simplicity for technological applications.

Complex amorphous metal-cation dielectrics have been largely overlooked in the past. Multication network glasses (e.g., silica-based glasses) have been extensively researched, as have simple single-metal-cation amorphous dielectrics such as  $\alpha$ - $\text{Ta}_2\text{O}_5$ . At present there isn't even a rough landscape of possibilities for multicomponent metal-cation systems, let alone a detailed scientific understanding of structure/property relations in this class of complex materials. This project is dramatically extending the breadth of our knowledge of the behaviors and trends in this class of materials and the depth of our understanding of their structure/property relations. Our strategy is to establish a general understanding of the relation between the properties of multicomponent amorphous oxides and their crystalline counterparts by systematic study of closely-related systems. Synthesis of multicomponent amorphous oxides is

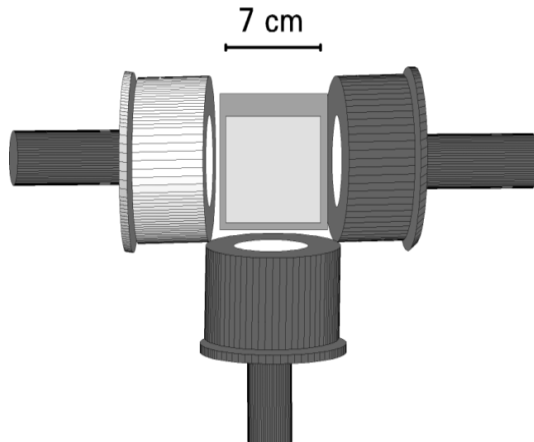


**Figure 1.** Schematic representation of sputter-gun layout. The three guns are positioned in a vacuum chamber and independently energized.

accomplished using 90° off-axis reactive cosputtering in an oxygen-containing atmosphere, illustrated in Figure 1.[1] This technique is particularly well suited to forming amorphous materials since the cations are intimately mixed as deposited and do not require high-temperature processing to ensure homogeneity.

### Current progress

An important issue is the robustness of the information we collect using composition-spread films: to what degree are the properties sensitive to subtle details of the synthesis? We have investigated this using a model system, a-Ta<sub>2</sub>O<sub>5</sub>, that has been extensively studied in the context of capacitors for dynamic random access memories. Conventional on-axis sputter deposition of this material provides a high level of ion bombardment of the growing film due to reflected neutral Ar atoms as well as negatively-charged O ions, resulting in

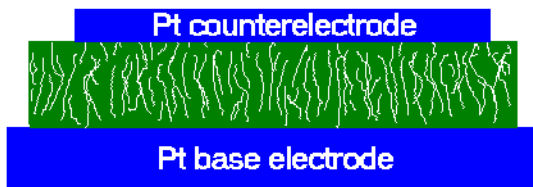


Figure 2. Schematic illustration of the fibrous structure that obtains for off-axis sputter deposition when no rf bias is applied to the substrate.

dense compressively-stressed films. We find that the low ion bombardment associated with 90° off-axis sputtering leads to formation of fibrous voids in the films, (Figure 2) and have shown that conducting channels associated with these voids produce a Maxwell-Wagner behavior and anomalous inferior dielectric properties.[2] Figure 3 illustrates this behavior, suggesting that a single relaxation time is associated with the phenomenon. We have

observed this behavior in a variety of films, including otherwise well-behaved dielectrics such as SiO<sub>2</sub> and Al<sub>2</sub>O<sub>3</sub>—clearly this microstructure should be avoided if the intrinsic properties of the dielectric are to be evaluated. We note that this film nanostructure could be useful where highly dissipative behavior is required, or where multiscale void structures are desired, as in electrodes for chemical reactions (sensors, batteries, etc.).

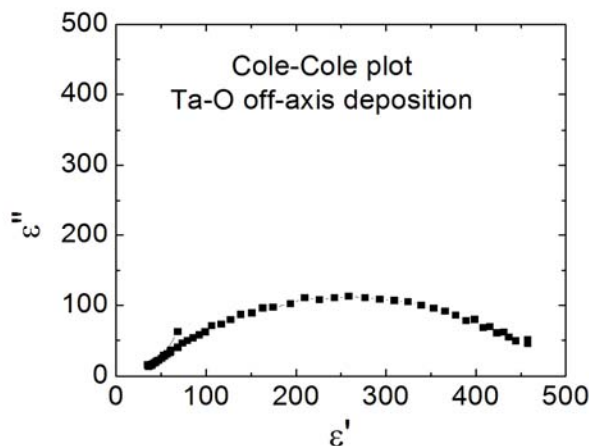
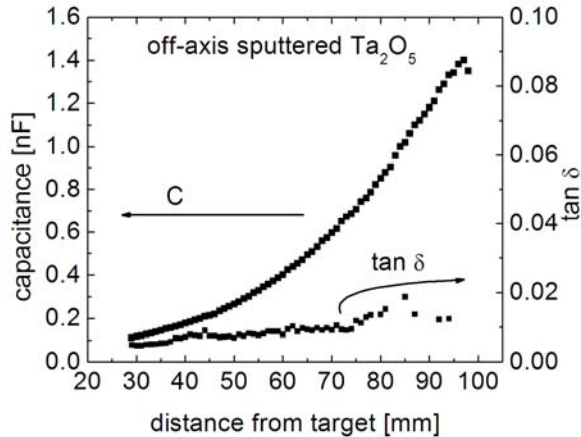


Figure 3. Cole-Cole plot for a capacitor formed with a TaO film comprising fibrous voids. The frequency range was 100 Hz – 1 MHz. The offset semicircle indicates that there is a single well-defined relaxation time (RC time constant).

We have further determined that it is possible to eliminate the low-density nanostructure in off-axis films by applying a controlled rf bias (~10 W) to the substrate during growth, thereby recovering excellent dielectric properties. This is illustrated in Figure 4, where the capacitance and dissipation factor ( $\tan \delta$ ) of 200  $\mu\text{m}$ -diameter capacitors is plotted as a function of the distance the film is from the target of the sputter gun. Note that the capacitance increases monotonically because the deposition rate, and therefore the thickness of the film, decreases with distance from the target. The dissipation factor is seen to increase gradually but even far from the target  $\tan \delta$  is quite small and the



**Figure 4. Capacitance and dissipation factor for capacitors deposited by 90° off-axis sputtering with *rf bias* applied to the substrate. The capacitance increases with distance from the target because the film is thinner. The increase in dissipation factor is small.**

these systems have been suggested for use as gate oxides in future low-power, high-performance integrated circuits based on Ge MOSFETs.[3] Figure 5 shows the variation in dielectric constant as a function of composition for a Ta-Ge-O composition spread. The cation composition range is roughly 15 at. % Ge to 60 at.% Ge across the sample, although the exact compositions have not been confirmed. The change in slope of the dielectric constant at the position  $x=40$  mm suggests either an electronic or structural transition. A similar trend in Zr-Si-O was definitively interpreted as due to a change in average atomic volume (density) associated with nanocrystallization. We speculate that the same structural effect is in play in Ta-Ge-O; that study is underway. The robustness of the films against crystallization when subject to thermal processing (e.g., during dopant activation anneals)

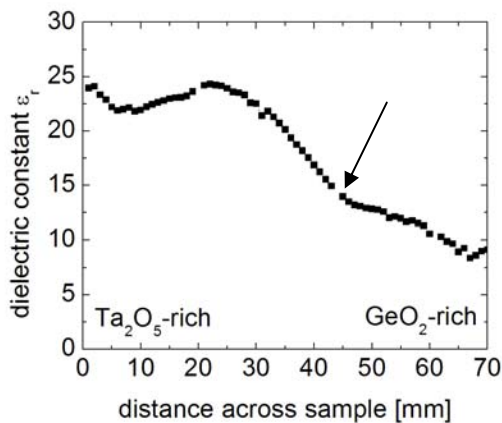


**Figure 5. Dielectric constant as a function of composition for a Ta-Ge-O composition spread. As Ta-O is added to Ge-O, the dielectric constant is seen to increase abruptly at the position ~40 mm (arrow).**

capacitance corresponds to the expected value for the dielectric constant ( $\epsilon_r=23$ ), indicating that the films do not contain fibrous voids.

This structure/property relation is also relevant to conventional on-axis sputtering where the degree of bombardment depends strongly on the location of the film with respect to the central axis. That can be an important effect but it is only poorly appreciated in the thin-film community.

We have now used the composition-spread technique to investigate novel chemical systems. For example, we are studying systems of the form  $M_1$ -Ge-O, where  $M_1$  represents a early transition metal element or main-group element such as Al or Sn. Amorphous materials in

militates for a high Ge-O content when used as a gate oxide. At the same time to avoid the environmental sensitivity of  $\text{GeO}_2$  (e.g.,  $\text{GeO}_2$  is water soluble), a high level of Ta-O is desirable. Preliminary data indicate that addition of a *third* component (i.e., Ta-Hf-Ge-O) can increase the crystallization temperature of the system even for low Ge-O content. These studies illustrate the power and versatility of our codeposited composition-spread technique.

## Challenges

Synthesis of amorphous oxides is fairly straightforward using the techniques we have developed and validated. In the future we plan to assemble a substrate fixture that

will allow ternary codeposition at up to 700 °C along with rf bias. This will enable us to study the transition from amorphous to crystalline growth, and compare this to the effect of high-temperature annealing after the deposition is completed.

Electrical measurements, such as those presented in this abstract, are also fairly straightforward, and are capable of revealing subtle behavior especially when combined with optical characterization. Future plans include characterizing the dielectric constant as a function of temperature. Variations below room temperature are likely to be associated with electronic transitions. Little is known about the prospects for electronic transitions in amorphous dielectrics—presumably many effects seen in crystalline oxides, such as charge ordering, (e.g. the Verwey transition in crystalline  $\text{Fe}_3\text{O}_4$ ) will be suppressed due to disorder. But other possibilities are viable, as seen in the case of electron-glass behavior in  $\text{Ta}_2\text{O}_5$  [4].

A greater challenge is that of obtaining detailed and useful information regarding the local structure of the amorphous films. Many techniques are useful for detailed study of individual compositions, but we are also attempting to develop a measurement that can be applied to composition spreads. For example, we have used EXAFS to obtain information about the atom-atom distances and therefore structure in dielectric films. This technique demands fairly long data acquisition times even at a synchrotron beamline, since the films have limited thickness. It requires modeling and fitting in order to develop an interpretation of the data, so it is not a robust indicator of structure. For these reasons, EXAFS is well suited to detailed studies of a particular composition, but is not an appropriate technique for broad studies of composition/structure relations. STEM, EELS, and XPS have similar issues and are not suited to broad studies as a function of composition. We are currently working to add FTIR and microRaman studies to our armamentarium, expecting that the characteristic vibrational spectra will provide robust information about bonding. Here the challenge will be to isolate the spectral features that yield important clues about the behavior of the materials. We are also looking to collaborate with computational experts who can illuminate the structural and electronic data.

We believe that the future is bright for these studies, which will dramatically extend the breadth of our knowledge of the behaviors and trends as well as the depth of our understanding of the structure/property relations in complex amorphous dielectrics.

## References

- [1] R. B. van Dover and L. F. Schneemeyer, "The Codeposited Composition Spread Approach to High-Throughput Discovery/Exploration of Inorganic Materials," *Macromolecular Rapid Communications*, vol. 25, pp. 150-157, 2004.
- [2] S. C. Barron, R. B. v. Dover, L. F. Schneemeyer, and D. Werder, "Nanostructured Thin Film Oxide by Oblique Reactive RF Sputtering," presented at MRS Fall Meeting, Boston, MA, 2007.
- [3] Y. Kamata, "High-k/Ge MOSFETs for future nanoelectronics," *Materials Today*, vol. 11, pp. 30-38, 2008.
- [4] R. M. Fleming, C. M. Varma, D. V. Lang, C. D. W. Jones, M. L. Steigerwald, and G. R. Kowach, "Coulomb glass origin of defect-induced dielectric loss in thin-film oxides," *Applied Physics Letters*, vol. 78, pp. 4016-18, 2001.

# Magnetoelectric epitaxial thin layer two phase composites

Dwight Viehland and Jiefang Li  
Virginia Tech

Dielectric polarization of a material under magnetic field, or an induced magnetization under electric field, requires the simultaneous presence of long-range ordered magnetic moments and electric dipoles. Single phase materials suffer from the drawback that their magnetoelectric (ME) effects are weak even at low temperatures, limiting their applicability in practical devices. Better alternatives are ME composites, which have been shown to have large ME voltage coefficients. Of particular interests are self-assembling two-phase nanocomposites, which have previously revealed  $\text{CoFe}_2\text{O}_4$  (CFO) nano-rods embedded in a  $\text{BaTiO}_3$  (BTO) matrix.

In this talk, we will show how epitaxial constraint can be used to design two phase morphologies in CFO- $\text{BiFeO}_3$  (or CFO-BFO) epitaxial films, and how the phase stability and properties of the two individual phases can be altered by said constraint. We have engineered various nano-structures ranging from nano-rods to nano-belts, as shown in Figure 1, by (i) orientation of substrate; (ii) epitaxial strain; and (iii) diffusion. Investigations of the mechanism of nano-structure formation over a range of temperatures revealed that (i) the first step is to grow perovskite on  $\text{SrTiO}_3$ ; (ii) the second step is nucleation of the spinel; and (iii) the third step is nano-structure evolution/growth by easy diffusion along the [110]. Our primary goal is to determine the fundamental relationship between interphase interfaces of different crystallographic symmetries and product tensor properties, such as the ME coupling of epitaxial thin layer composites: our approach to these goals are conceptually illustrated in Figure 2.

We are working with Shashank Priya (Virginia Tech) on electron microscopy and property evaluations of our films, and with Armen Khachaturyan (Rutgers University) on thermodynamic analysis of epitaxial engineering of our multiferroic layers.

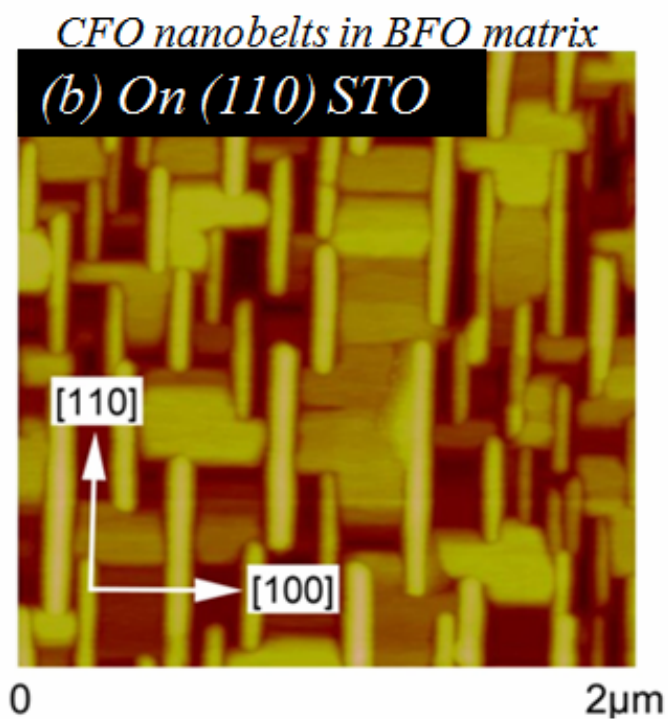
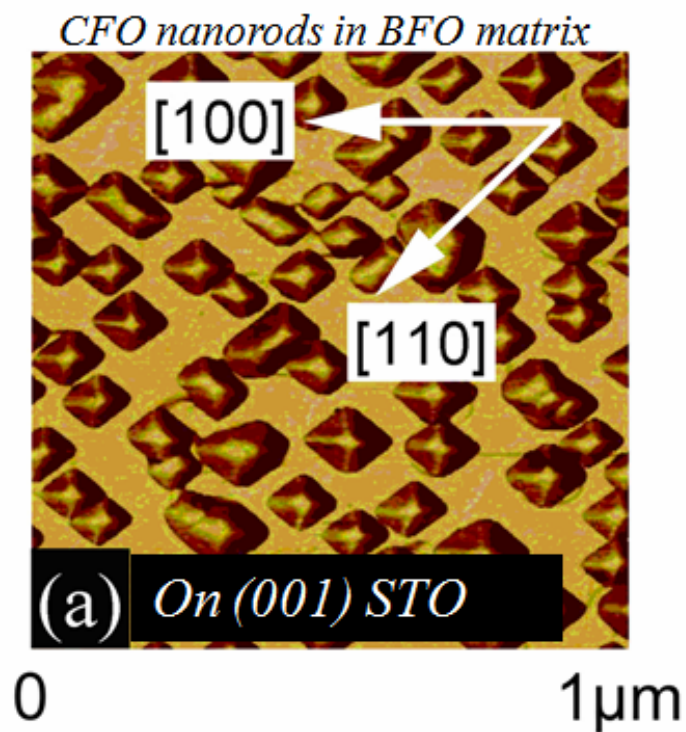
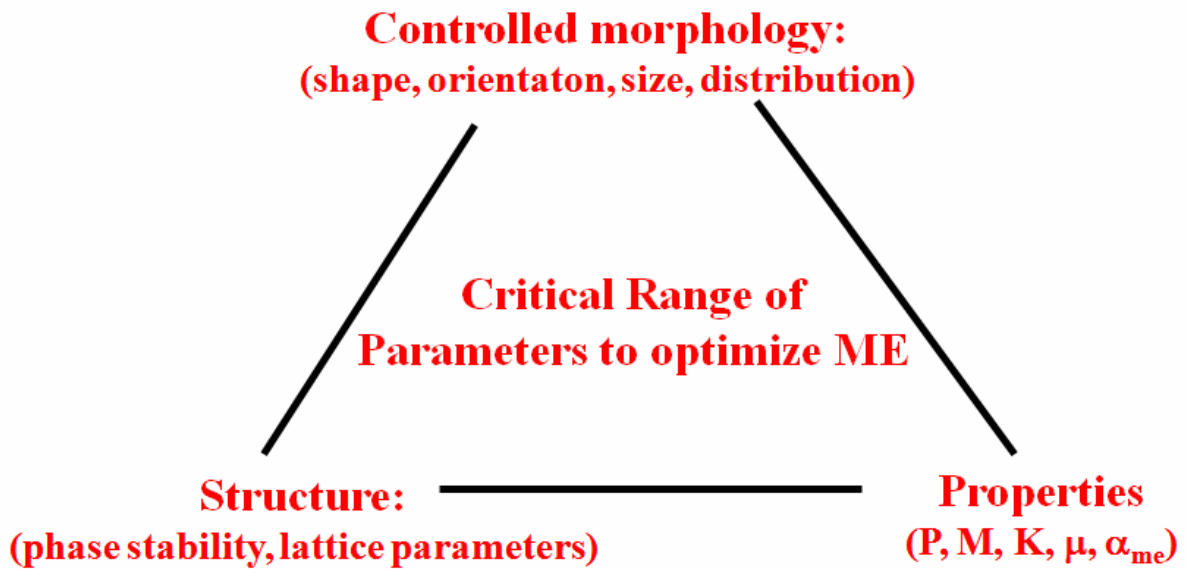


Figure 1. Atomic force image of our  $\text{CoFe}_2\text{O}_4\text{-BiFeO}_3$  nanostructures grown on (a) (001)  $\text{SrTiO}_3$  substrates, illustrating CFO nanorods in a BFO matrix; and (b) (110)  $\text{SrTiO}_3$  substrates, illustrating CFO nanobelts in a BFO matrix.



## *Engineered multi-functional nano-structures*

Figure 2. Conceptual illustration of the approach to our program goal(s).

**Project Title: Suspensions of Monodisperse Nanoparticles as Model Systems for Probing Heat Transfer Mechanisms in Nanofluids**

**PIs: Professor Bao Yang**  
Center for Environmental Energy Engineering (CEEE)  
Department of Mechanical Engineering  
University of Maryland, College Park, MD 20742  
Tel: (301) 405-6007, Fax: (301) 314-9477  
E-mail: baoyang@umd.edu

**Professor Michael R. Zachariah**  
Department of Mechanical Engineering and Department of Chemistry  
Center for NanoEnergetics Research (CNER)  
UMCP/NIST Co-Laboratory for NanoParticle Based Manufacturing and Metrology  
University of Maryland and National Institute of Standards and Technology  
Tel: (301) 405-4311, Fax: (301) 314-9477  
E-mail: mrz@umd.edu

**Program Scope:**

This proposal aims to systematically and comprehensively investigate various fundamental, but less-studied factors—Brownian motion and relaxation time of nanoparticles, fractal aggregates, and interfacial layer structure—that potentially affect thermal transport in nanofluids and nanoemulsion fluids. The program is designed to generate archival experimental data to advance fundamental understanding of transport phenomena in micro/nano systems.

**Recent Progress:**

In this report for the period *August 15, 2007 – February 20, 2008*, we present our progress on *three topics* that are currently under investigation under this DOE/BES program:

**1. ES-DMA for Characterization of Colloidal Aggregates**

During the first six-month of this program, we developed a novel method to determine the aggregation kinetics of colloidal nanoparticles by a gas phase analysis. Nanofluids can be monitored by sampling the colloidal solution via electrospray (ES), transforming a nanoparticle dispersion to a nanoparticle aerosol, followed by differential ion-mobility analysis (DMA) to determine the mobility distribution, and thus the aggregate distribution. By sampling at various times we determine the aggregation rate from which the parameters that control aggregation may be elucidated. *In contrast to other techniques, such as microscopy and static and dynamic light scattering (LS), ES-DMA can rapidly and quantitatively identify the concentration of each aggregation state (i.e. individual particles, dimers, trimers and tetramers, etc.). Moreover, ES-DMA is most effective for nano-sized particles (diameter < 100 nm), which pose a significant challenge to other methods.*

### 1.1 Theory of Aggregation Kinetics of Colloidal Nanoparticles

The model of Brownian aggregation considers three influences on the particles. The first is Brownian motion. The second influence is the van der Waals force represented by the Hamaker constant,  $A_{eff}$ . The third and final influence, the electrostatic force, depends on the surface potential,  $\psi_s$ , modulated by the ionic strength of the solution.

**Figure 1** presents  $\Phi/k_bT$  versus the separation distance,  $h$ , between two spherical Au nanoparticles for the reaction-limited (curve 1), intermediate (curve 2), and diffusion-limited (curve 3) regimes, respectively. Irreversible aggregation occurs as two particles approach each other and fall into the primary minimum near  $h = 0$ . In the reaction-limited regime, the sum of energies possesses both a maxima,  $\Phi_{max}/k_bT$  near  $r = 2a + \lambda_D$ , and a secondary minima,  $\Phi_{sec}/k_bT$  at relatively large particle separation,  $h=r_{sec}$ . The knowledge about the reaction-limited and diffusion-limited regimes is critical not only for control of the aggregate kinetics, but also for minimization of thermal interfacial resistance between nanoparticles, e.g., a liquid layer of  $h=r_{sec}$  thickness would seriously resist heat transfer between two adjacent nanoparticles.

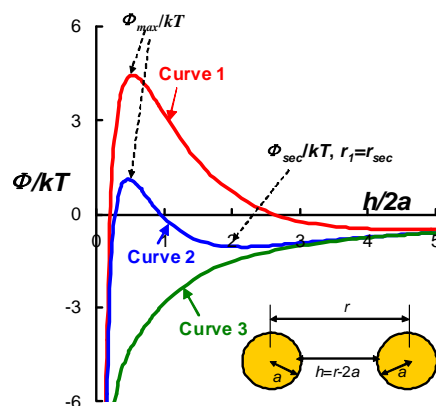


**Figure 1.** Interaction potential for two spherical colloidal nanoparticles. Curve 1: reaction-limited regime; Curve 2: intermediate regime; Curve 3: diffusion-limited regime.

### 1.2 Effect of Ionic Strength on Aggregation Kinetics

**Figure 2** presents ion-mobility spectra of Au nanofluids at various concentrations of ammonium acetate,  $C$ . Each spectrum presents up to five distinctive peaks representing clusters containing one to five individual Au particles, which we term monomer, dimer, trimer, etc. The ion-mobility of the monomer peak ( $n=1$ ) results in a diameter of 11.6 nm consistent with the original colloidal sample encrusted with salts. Further assignment of the dimer peak to 14.8 nm, the trimer peak to 17.4 nm, and the tetramer peak to 19.4 nm was confirmed by specifically depositing particles corresponding to each peak exiting the DMA on a TEM grid inside an electrostatic deposition chamber. TEM then confirms the identity (i.e the peak labeled as tetramer does contain four particles).

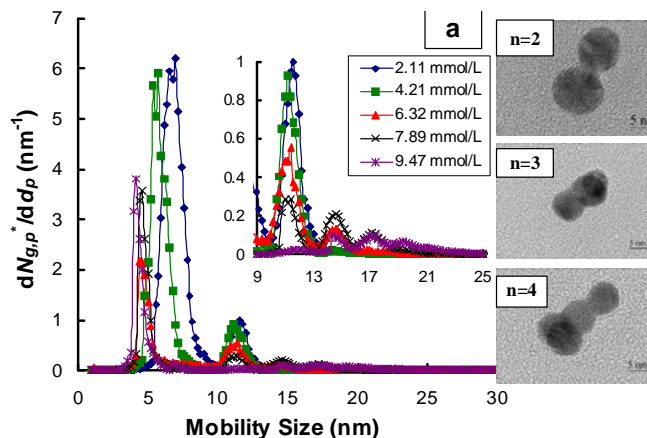


**Figure 2.** Ion-mobility spectrum of colloidal Au ammonium acetate solution at different ionic strength conditions.

## 2. Development of Self-Assembled Nanoemulsion Fluids

The strategy of adding solid particles to improve thermal conductivity of fluids has been pursued since Maxwell's theoretical work was first published more than 100 years ago. *Recently, we proposed a radically new design for heat transfer fluids that completely eliminates solid particles, and instead, uses liquid nanostructures assembled from surfactant molecules.* Initial experiments were done with a thermal fluid used in electronic cooling, termed FC-72, which is one of a line of Fluorinert™ Electronic Liquids developed by 3M Inc.. **Figure 3** shows a water nanodroplet—a reverse micelle swollen with water—in the FC-72. The water nanodroplets are stabilized by the surfactant molecules that have hydrophilic heads (grey) facing inward and hydrophobic tails facing outward into the nonpolar solvent. Dispersions of such thermal-conductive, liquid nanostructures in another immiscible, heat transfer fluids are termed “nanoemulsion fluids.”

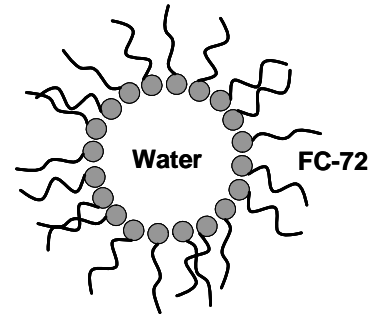


**Figure 3.** Schematic diagram of a water nanodroplet dispersed in 3M's FC-72 thermal fluid. A micelle of amphiphiles surrounds the droplet.

The preliminary results on nanoemulsion fluids are very promising. Thermal conductivity increase relative to pure FC-72 is plotted in **Fig. 4(a)** as a function of water loading. The enhancement in conductivity and viscosity of the fluids is found to be nonlinear with water loading, indicating an important role of the hydrodynamic interaction of nanodroplets. *The presence of 12 vol % of water raised the thermal conductivity by 52% compared to that of pure FC-72. Moreover, a very remarkable increase, about 126%, in effective heat capacity occurs in the fluids due to melting-freezing transition of water nanodroplets,* which is clearly evident in the results obtained by a Differential Scanning Calorimeter (DSC) (see **Fig. 4(b)**).

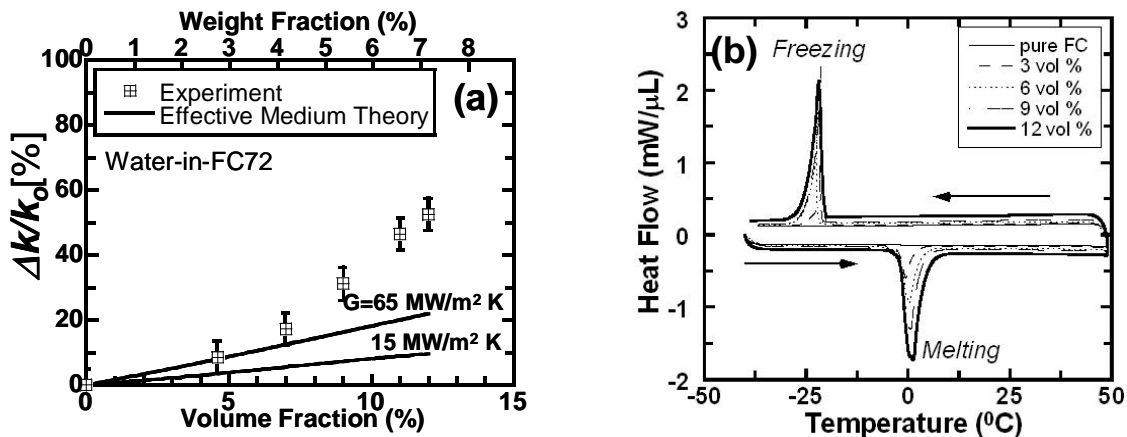


**Figure 4.** (a) Effective thermal conductivity of the water in FC-72 nanoemulsion as a function of water nanodroplet concentration. (b) Cyclic DSC heating and cooling curves for the nanoemulsion fluids. In (b), the peak at about -20  $^{\circ}\text{C}$  is the freezing peak for the water nanodroplets in these fluids.

### 3. Effects of Fractal Aggregates on Thermal Conductivity of Nanofluids

We have experimentally demonstrated the influence of fractal aggregates on thermal conductivity in nanofluids. Aqueous suspensions of monodisperse silica nanoparticles ( $d=25\pm 4\text{nm}$ ) are used as model systems, where silica nanoparticles remain as individual particles at  $\text{pH}=10.4$  due to the formation of the electrical double layer. The interaction forces between silica nanoparticles can be varied by changing the fluid  $\text{pH}$ , resulting in a very different fractal dimension of aggregates. For example, through adjustment of the fluid  $\text{pH}$  from 10.4 to 8.0, the well-dispersed nanofluids appear to be a jelly-like material where a porous network of interconnected nanoparticles spans the volume of a liquid medium.

It is experimentally evident that the thermal conductivity in the well-dispersed nanofluids ( $\text{pH}=10.4$ ) is enhanced by 10.2%, which can be well explained by the mean-field Maxwell theory. These data are in agreement with the recent reports by the MIT (Dr. Yip) and UIUC (Dr. Cahill) groups. Remarkably, we found that the conductivity enhancement increases from 10.2% to 16.3% when the  $\text{pH}$  is tuned from 10.4 to 9.22; in short, a 60% rise in thermal conductivity enhancement is possible by controlling the fractal aggregates. The ES-DMS based determination of aggregate fractal structure is underway. Fractal aggregate manipulation shows promise in raising thermal conductivity enhancement beyond the Maxwell limit.

#### Technical Plans for 2008:

- Study further how to control the aggregation kinetics in suspensions of nanoparticles
- Explore effects of fractal aggregates on thermal properties
  - Effects of the reaction-limited and diffusion limited regimes
  - Effects of the fractal dimension and size of aggregates
- Detect interfacial structure of nanoparticles
- Investigate thermal transport in nanoemulsion fluids, especially the hysteresis between the freezing and melting temperatures of the dispersed nanostructures

#### Publication:

1. Z. H. Han and B. Yang, "Thermophysical Characteristics of Water-in-FC72 Nanoemulsion Fluids," *Applied Physics Letters* **92**, 013118, 2008.
2. D-H. Tsai, R. A. Zangmeister, L. F. Pease III, M. J. Tarlov, and M. R. Zachariah, "Gas-Phase Ion-Mobility Characterization of SAM Functionalized Au Nanoparticles," *Langmuir*, accepted, 2008.
3. D-H. Tsai, L. F. Pease III, R. A. Zangmeister, M. J. Tarlov, and M. R. Zachariah, "Flocculation Kinetics of Colloidal Nanoparticles Measured by Gas-Phase Differential Mobility Analysis," *Langmuir*, submitted, 2008.

**Session VII: Photovoltaics / Photon Related**

## Overview of the Helios Solar Energy Research Center

Paul Alivisatos

Lawrence Berkeley National Laboratory

Berkeley, California, 94720

The Helios Solar Energy Research Center (SERC) is a recently-formed interdisciplinary project involving 28 senior researchers and associated graduate students and postdoctoral fellows from Lawrence Berkeley National Laboratory and UC Berkeley. Other partners are associated with Cal Tech, MIT, Arizona State University, and UC San Diego. This talk will describe the project and provide a view of research results obtained since the formation of the program.

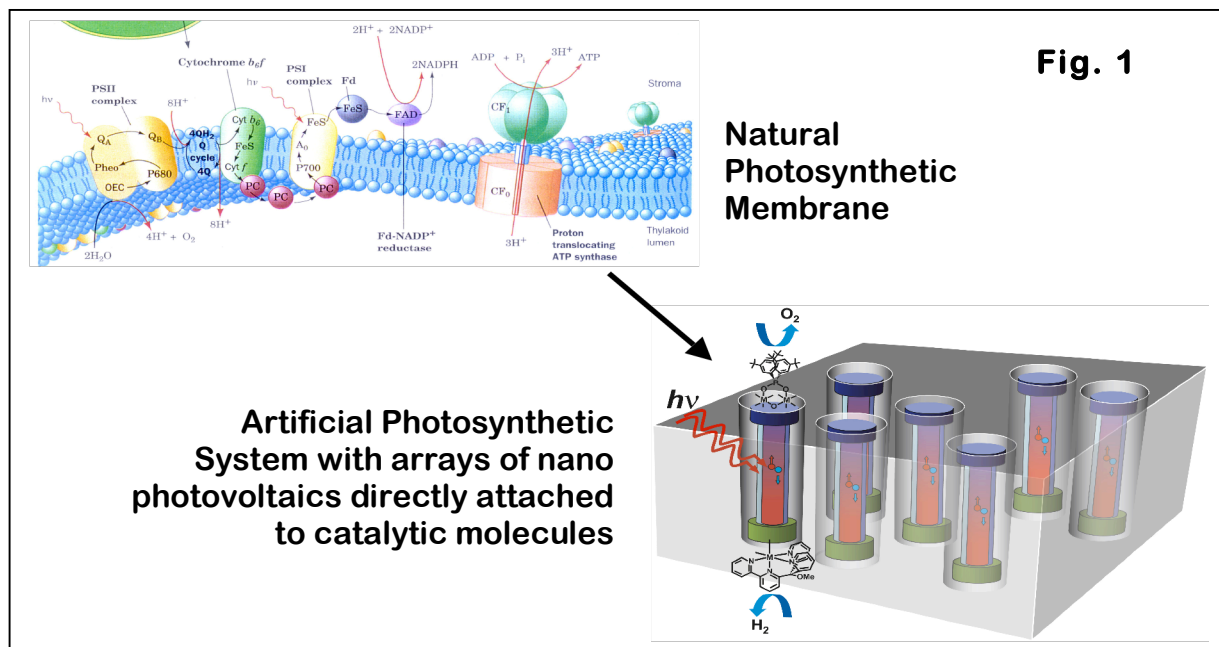
The focus of the project is the production of solar fuels, to be differentiated from biofuels. These fuels are comprised of carbon, hydrogen, and oxygen obtained from ambient carbon dioxide and water in the atmosphere and processed on a single nano-structured platform to form the fuel molecules. This pathway does not require arable land or involve crops.

Specifically, the SERC goal is to demonstrate a solar fuel generator with 1% power efficiency from photon to fuel, using abundant materials and scalable manufacturing processes, and yielding a chemically pure fuel with energy density specifications at least matching those of methanol. This is a goal we feel we can accomplish, with an adequate level of funding, within ten years.

### Artificial Photosynthetic Devices

We are planning to construct a complex membrane-like platform that will house nano-collectors and catalytic centers to split water and carbon dioxide and reform them. In this sense, the platform is much like the photosynthetic processes in leaves, and for this reason we term it an artificial photosynthetic device.

One realization of this artificial photosynthetic device is shown along with a natural PS system in Fig. 1.



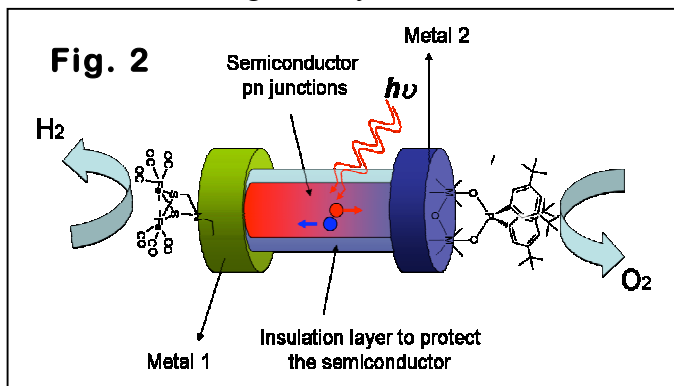
The project naturally divides into three thrusts: One is on individual components that collect light, separate charge, and catalyze reactions. A second thrust is to develop the membrane and integrate the components. Finally, there are cross-cutting theory groups to model components and processes individually, and also to model the total system. We believe that instrumentation will play a critical roll in accomplishing the SERC goal, and we have a cross-cutting instrumentation group to pool expertise to develop new instrumentation. Researchers share postdocs, and can work on more than one subproject if they feel they can contribute.

### Components

One important area of component research is the development of nanophotovoltaics, which are specially designed to provide charge to catalytic molecules. One subproject team is working to combine efficient photovoltaic charge generation in semiconductors with the corrosion resistance and catalytic activity of oxides. Another subproject team is investigating nanodot, nanorod systems to optimize charge production. A third is studying single-molecule organic photovoltaics. Recent results in these areas will be presented. In addition to nanoPV's, SERC contains a large catalysis effort, which will be discussed. There is also a project to develop light-protection mechanisms for the organic components of the integrated systems.

### Integrated Systems

Within the Integrated Systems subtask there are two efforts. One works on developing



inorganic photosynthetic units in which catalysts are joined to inorganic assemblies. Pictured in Fig. 2 is an example of this integration, actually an element in the unit shown in Fig. 1. The other effort focuses on the synthesis of artificial membranes, including polymer and inorganic assemblies.

### Theory

We believe that theoretical and computational efforts will accelerate the progress of this SERC, and seven of our colleagues are theorists. They focus on areas of chemical dynamics, reaction path techniques, self-assembly, *ab initio* electronic structure theory in liquids, and solid-state electronic structure theory. They will all contribute to individual subprojects and to the development Helios Simulator, which is an integrated multi-physics, multiscale model that will be used to determine the optimal operating parameters of the components.

## Plasmonic Photovoltaics

Harry A. Atwater

Thomas J. Watson Laboratories of Applied Physics

California Institute of Technology

MS 128-95

Pasadena, CA 91125

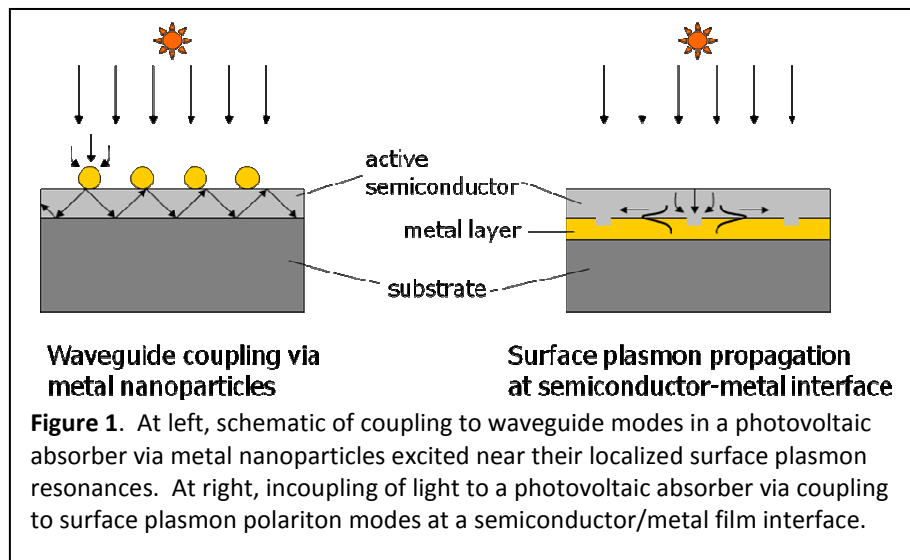
[haa@caltech.edu](mailto:haa@caltech.edu)

### Program Scope

To date, little systematic thought has been given to the question of how plasmon excitation and light localization might be exploited to advantage in photovoltaics. This proposed effort aims to change that. Using insights derived from the rapidly developing plasmonics field, we seek to dramatically modify the light absorption and carrier collection characteristics of photovoltaic materials and devices. In particular, the ability of plasmonic structures to localize light at subwavelength dimensions is synergistic with use of ultrathin quantum dot and quantum well photovoltaic absorber materials.

Conventionally, photovoltaic absorbers must be optically ‘thick’ to enable nearly complete light absorption and photocarrier current collection. They are usually semiconductors whose thickness is typically several times the optical absorption length. For silicon, this thickness is greater than 100 microns, and it is several microns for direct bandgap compound semiconductors, and high efficiency cells must have minority carrier diffusion lengths several times the material thickness. Thus solar cell design and material synthesis considerations are strongly dictated by this simple optical thickness requirement.

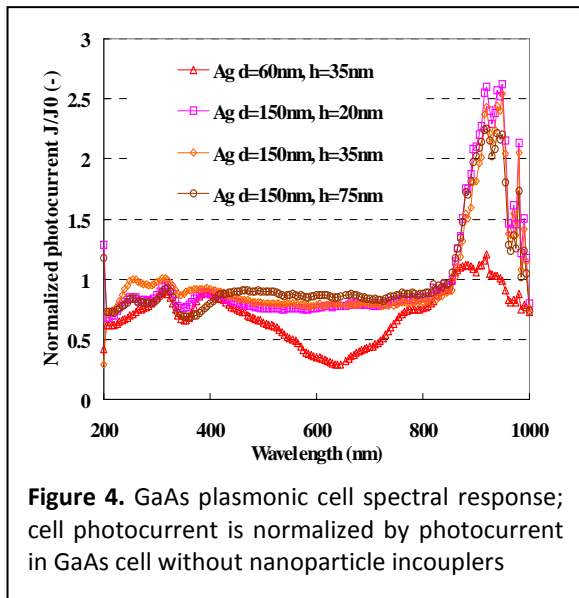
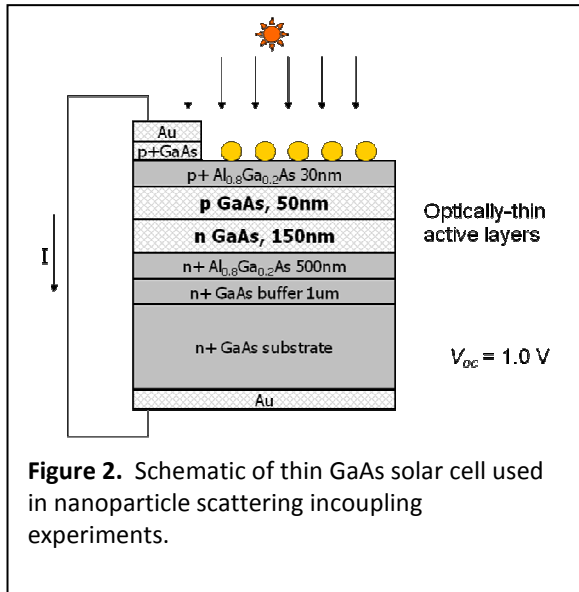
Dramatically reducing the absorber layer thickness could significantly expand the range and quality of absorber materials that are suitable for photovoltaic devices by, e.g., enabling efficient photocarrier collection across short distances in low dimensional structures such as



quantum dots or quantum wells, and also in polycrystalline thin semiconductor films with very low minority carrier diffusion lengths.

The consequences of plasmonic structure design for photovoltaics are potentially complex and far-reaching, but we choose to focus this proposed effort on modifying optical absorption in photovoltaic materials. Specifically, we will investigate two phenomena related to modifying light absorption in photovoltaic structures:

1. Ultrathin Planar Surface Plasmon Polariton Photovoltaic Absorbers

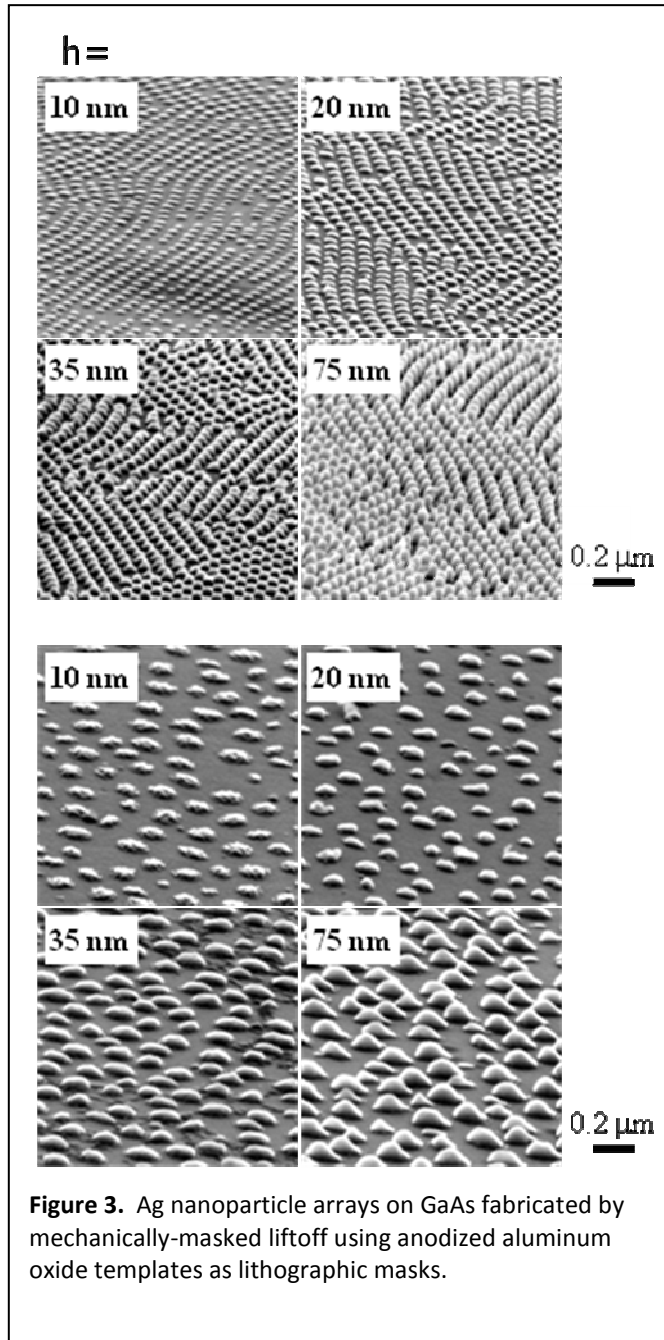


## 2. Spectral Tuning of Enhanced Absorption and Emission in Coupled Quantum Dot/Metal Nanoparticle Absorbers

Our approach combines experiments, theory, and simulation, utilizing both ‘top-down’ and ‘bottom-up’ nanofabrication, analytic theory and full-field electromagnetic simulation. We are developing prototypical solar cell structures that illustrate potential planar surface plasmon polariton absorbers and coupled quantum dot/metal nanoparticle absorbers.

### Recent Progress

We have used thin GaAs single junction solar cells as laboratory for investigation of the modification of photocurrent that results from light incoupling via nanoparticle arrays. Figures 2-4 illustrate the cell schematic, Ag nanoparticle arrays and normalized cell photocurrents



respectively. The results indicate a marked enhancement in collected photocurrent near the GaAs absorption edge at 880 nm, and a decreased photocurrent at blue wavelengths due to absorption near the metal nanoparticle localized surface plasmon resonance, particularly for the smallest particles. A simple Lambertian scattering model for the metal nanoparticle array accounts for the principal features seen experimentally in the normalized photocurrent measurements.

## Engineering Optical Conductivity in Short Period Oxide Superlattices

Xiaofang Zhai<sup>1,2</sup>, C. Mohapatra<sup>1,2</sup>, A. Shah<sup>2,3</sup>, A. Bhattacharya<sup>4</sup>, J. G. Wen<sup>2</sup>, J. M. Zuo<sup>2,3</sup>, J. N. Eckstein<sup>1,2\*</sup> (Photocatalytic Materials) eckstein@uiuc.edu

<sup>1</sup> Physics Department, and <sup>2</sup> The Frederick Seitz Materials Research Laboratory, University of Illinois at Urbana-Champaign;

<sup>3</sup> Materials Science and Engineering Department, University of Illinois at Urbana-Champaign;

<sup>4</sup> Materials Science Division, Argonne National Laboratory

Novel properties that do not exist in the bulk phases have been engineered to occur at oxide interfaces, such as ferromagnetism<sup>1</sup> and large carrier densities found at the interfaces of band insulators<sup>1-5</sup>. Oxides also have interesting optical properties, including photocatalytic activity. Artificial materials in which the electronic structure and optical absorption is controlled by layering architecture may provide a way to tailor the absorption and electron dynamics for improved performance. To study what is possible, we have fabricated digital superlattices consisting of super cells of N layers of LaMnO<sub>3</sub> and N layers of SrTiO<sub>3</sub>, N=1, 2, 3, 8, and measured their complex optical conductivity to probe the way in which the electronic structure of the superlattice depends on N. We have observed a simultaneous blue shift of the lower energy Jahn-Teller(J-T)/Mott gap absorption spectra and a corresponding red shift of the higher energy charge transferring band gap absorption spectra, becoming stronger as N decreases from 8 to 1. We have also observed a new transition peak originating from states that arise at the interfaces. This method of inventing new electronic structure appears promising for engineering new optical materials.

At the interface in a digital superlattice, the polarization symmetry is broken and the charge distribution is reconstructed<sup>5,6,7</sup>. As a result the reconstructed density of states (DoS)<sup>8-12</sup> at the interface introduces qualitatively different properties that do not exist in either of the constituent bulk phases. Many experiments have focused on the resulting DC properties, but there hasn't been exploration, as far as we know, of the optical properties of complex oxide digital superlattices. In this paper, we study how the optical band structure is controlled by interfaces by changing the period N of the interfaces in a series of digital superlattices of NLaMnO<sub>3</sub>/NSrTiO<sub>3</sub>.

SrTiO<sub>3</sub> and LaMnO<sub>3</sub> both have ABO<sub>3</sub> perovskite structure with B site in an octahedral center surrounded by oxygen, as shown in figure 1a. SrTiO<sub>3</sub> is a “charge transfer” insulator in which the valence band mainly made of oxygen states is full, while the conduction band which is mainly derived from the titanium 3d orbitals is empty<sup>13</sup>. The valence band in LaMnO<sub>3</sub> is made of higher energy 3d electrons on Mn<sup>3+</sup> sites and lower energy 2p electrons on O<sup>2-</sup> sites. Four Mn 3d electrons reside on 3 t<sub>2g</sub> orbitals and 1 e<sub>g</sub> orbital with the same spin direction because of crystal field splitting and Hund's Rule respectively. Below 700C, in single crystal LaMnO<sub>3</sub> Jahn-Teller distortion<sup>14-15</sup> lifts the degeneracy between e<sub>g</sub><sup>1</sup> (|3z<sup>2</sup>-r<sup>2</sup>>) and e<sub>g</sub><sup>2</sup> (|x<sup>2</sup>-y<sup>2</sup>>) states and forms a gap between them. On-site Coulomb repulsion also splits the filled e<sub>g</sub><sup>1</sup> band and empty e<sub>g</sub><sup>2</sup> band and causes Mott-Hubbard insulating behavior<sup>16-17</sup>. It is not clear to us which effect is more prominent in LaMnO<sub>3</sub><sup>18-20</sup>. The schematic DoS of SrTiO<sub>3</sub><sup>13</sup> and LaMnO<sub>3</sub><sup>18</sup> based on band theory are drawn in figure 1b with oxygen bands of two materials aligned.

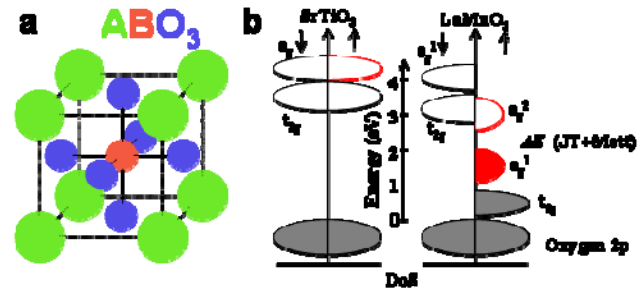


**Figure 1** The lattice structure and band structure of SrTiO<sub>3</sub> and LaMnO<sub>3</sub>. (a) The lattice structure of perovskite oxide-ABO<sub>3</sub>. A is the alkaline atom in orange color and B is the transition metal atom in green color. (b) Schematic band structure of SrTiO<sub>3</sub> and LaMnO<sub>3</sub>. The energy scale is based on band theory calculations<sup>11,16</sup>. The oxygen bands of both are aligned.

To study the electronic structure and the possible reconstruction we employed spectroscopic ellipsometry and measured the optical conductivities ( $\sigma$ ). The  $\sigma$  of  $\text{LaMnO}_3$  was scaled to half of it for better comparison with the superlattices. Figure 2a shows the effective gap energy between  $e_g^1$  and  $e_g^2$  (J-T/Mott) continuously shifted to higher energy as  $N$  decreases, from 1.6eV to 1.8eV. Simultaneously, the absorption edge of the charge-transfer gap, between Oxygen 2p states and Mn/Ti 3d states, is shifted to lower energy by about the same amount. The most provocative observation is a new absorption peak appearing at a constant energy of 2.3eV in the superlattices. The peak height of this transition linearly increases with density ( $1/N$ ), shown in figure 2b.

The  $\text{NSrTiO}_3/\text{NLaMnO}_3$  superlattices and pure  $\text{LaMnO}_3$  sample were grown on  $\text{SrTiO}_3$  substrates using ozone assisted atomic layer by layer MBE. In order to grow samples in the layer by layer way, Rutherford backscattering (RBS) was used to calibrate flux of each evaporation source to an absolute accuracy of within 1%. In-situ RHEED oscillations confirmed the layer by layer growth. The growth temperature and ozone pressure were chosen to be  $700^\circ\text{C}$  and  $2 \times 10^{-6}$  Torr in order to optimize the film growth. The superlattices and the  $\text{LaMnO}_3$  sample were all approximately 50 nm thick. DC conductivities of the superlattices and  $\text{LaMnO}_3$  sample all follow the Arrhenius law,  $1/\sigma = 1/\sigma_0 \exp(-E_g/2KT)$ , as shown in Figure 3b. The  $E_g$  values for  $\text{LaMnO}_3$ ,  $2 \times 2$  and  $1 \times 1$  superlattices are 304meV, 314meV and 330meV. The increase of the DC gap energy is consistent with an increase of the optical gap between  $e_g^1$  and  $e_g^2$ . Further more, the absence of variable range hopping indicates the samples are relatively free of disorder.

Scanning transmission electron microscopy (STEM) shows a distinct layer by layer morphology of a  $N=2$  superlattice sample in Figure 3a. It is an image taken from of a very thin sample along (1 0 0) direction on a JEOL JEM 2200FS TEM with an aberration correcting probe. The intensity of scattering is proportional to the atomic number  $Z$  of the scattering center ion. The brightest spots are from La atoms. The second brightest spots are from Sr atoms. The dimmer spots are from Ti and Mn atoms. The layer by layer distinction is kept throughout the whole sample.

The simultaneous blue shift of the J-T/Mott gap ( $e_g^1 \rightarrow e_g^2$ ) and red shift of the charge-transferring gap as  $N$  decreases can be explained by Mn and Ti 3d band hybridization at the interface, where the lower energy Mn 3d states and higher energy Ti 3d states interfere in the out-of-plane direction. The hybridization results is the lower-energy band shifting up and higher-energy band shifting down in energy. Both  $e_g^1$  and  $e_g^2$  bands of Mn shift up in energy but  $e_g^2$  shift up more since Mn  $e_g^2$  band is closer to Ti 3d band in energy. Therefore the gap between  $e_g^1$  and  $e_g^2$  increases as  $N$  decreases. The CT transition edge shifts to lower energy as the superlattice period decreases, because it is mainly composed of Oxygen

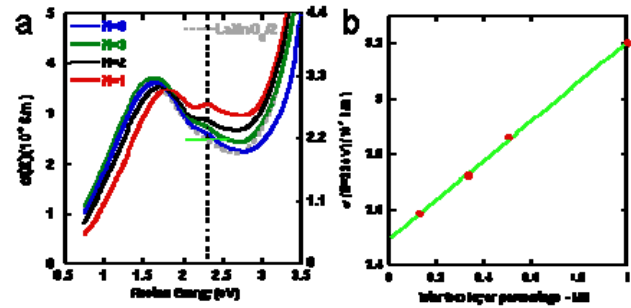


**Figure 2 Optical conductivities measured at room temperature.** (a) The optical conductivity of  $\text{NSrTiO}_3/\text{NLaMnO}_3$  superlattices plotted toward the left axis, half of the optical conductivity of a  $\text{LaMnO}_3$  thin film is plotted toward the right axis. A dashed line is drawn at 2.3eV. The green color short line is drawn at  $2.5 \times 10^4$  S/m. (b) The heights of the new transition peaks at 2.3eV of  $N=1, 2, 3, 8$  superlattices. A linear fitting (green color) extends to  $2.5 \times 10^4$  S/m at interface frequency of 0.

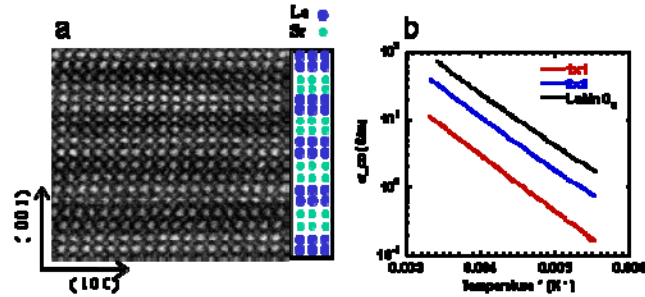


**Figure 3 STEM image and DC conductivity.** (a) STEM image of a  $2 \times 2$  superlattice sample taken along (1 0 0) direction on a JEOL JEM 2200FS TEM with a probe forming aberration corrector. (b) DC conductivity of the  $\text{LaMnO}_3$  thin film,  $2 \times 2$  superlattice and  $1 \times 1$  superlattice measured by van der Pauw method<sup>24</sup>.

2p to Ti 3d transition. This explanation is based on the assumption that Oxygen 2p states are aligned at the same energy level in LaMnO<sub>3</sub> and SrTiO<sub>3</sub>.

The linear dependence of the new peak's intensity at 2.3eV upon the interface layer density in figure 2b demonstrates this peak originates from reconstructed interface states. Furthermore, the observation in figure 2a that the peak remains at a constant energy indicates these states are localized. The sum-rule of the optical conductivity states

$$\int \sigma(\omega)d\omega = \frac{\pi e^2 N_{\text{eff}}}{2m},$$

where  $\omega$  is the frequency of the electromagnetic excitation.  $m$  is the free electron mass.  $N_{\text{eff}}$  is the number of electrons per unit volume. In order to calculate the interface electron density, we convert  $N_{\text{eff}}$  to be  $\zeta/(Na)$ .  $\zeta$  is the electron sheet density at one interface,  $N$  is the superlattice period,  $a$  is the out-of-plane lattice constant which is about 3.9Å. We make the approximation that the new absorption peak has a Gaussian distribution, then  $\int \sigma(\omega)d\omega = \sqrt{\pi}\sigma_0\Delta\omega$ , where  $\sigma_0$  is the peak intensity and  $\Delta\omega$  represents the width of the peak. The sum rule is then converted to:

$$\sigma_0 = \frac{\pi e^2 \zeta}{(\sqrt{\pi}\Delta\omega)2ma} \cdot \frac{1}{N}$$

In figure 2b  $\sigma_0$  of the 2.3eV peak is fitted as:  $\sigma_0 = (7085 \cdot \frac{1}{N} + 2.5e4)(\text{S/m})$ . Therefore  $\frac{\pi e^2 \zeta}{(\sqrt{\pi}\Delta\omega)2ma}$  is equal to 7085 S/m.  $\zeta$  is calculated to be  $1.43 \cdot 10^{12}$  #/cm<sup>2</sup> at room temperature. In semiconductor superlattices the alternating barrier and well structure give rises to so called 'mini-bands' and the band energy is dependent on the superlattice structure. In our observation the new transition peak energy doesn't depend on  $N$  and is not from 'mini-band'.

To conclude, we made digital superlattices of NSrTiO<sub>3</sub>/NLaMnO<sub>3</sub>,  $N=1, 2, 3, 8$ , and observed not only systematic blending of the density of states from the two constituent materials dependent on  $N$  but also new reconstructed interface states.

#### References:

1. A. Brinkman, H. Hilgenkamp, et al. *Nature Materials* **6**, 493-496 (2007).
2. A. Ohtomo, H. Y. Hwang, *Nature* **427**, 423-426 (2004).
3. M. Huijben, et al. *Nature Materials* **5**, 556-560 (2006).
4. J. Mannhart, et al. *Science* **317**, 1196-1199 (2007).
5. J. N. Eckstein, *Nature Materials* **6**, 473-474 (2007).
6. S. Okamoto, A.J. Millis, *Phys. Rev. B* **70**, 241104(R) (2004).
7. R. Pentcheva, W. Pickett, *Phys. Rev. Lett.* **99**, 016802 (2007).
8. A. Ohtomo, D. A. Muller, J. L. Grazul, H. Y. Hwang, *Nature* **419**, 378-380 (2002).
9. S. Smadici, P. Abbamonte, et al. *Phys. Rev. L* **99**, 196404 (2007).
10. E. Dagotto, *Rev. of Mod. Phys.* **66**, 763 (1994).
11. Y. Tokura, *Rev. of Mod. Phys.* **70**, 1039 (1998).
12. E. Dagotto, et al. *Science* **309**, 257-262 (2005).
13. L. F. Mattheiss, *Phys. Rev. B* **6**, 4718 (1972).
14. N.H. Andersen, et al. *J. of Solid States Chem.* **119**, 191-196 (1995).
15. J. Rodriguez-Carvajal, et al. *Phys. Rev. B* **57**, R3189 (1998).
16. J. Zaanen, G. Sawatzky, J. Allen, *Phys. Rev. L* **55**, 418 (1985).
17. A. Fujimori, et al. *Phys. Rev. B* **46**, 3771 (1992).
18. S. Satpathy, Z. Popovic, F. Vukajlovic, *Phys. Rev. L* **76**, 960 (1996).
19. K. H. Ahn, A. J. Millis, *Phys. Rev. B* **61**, 13545 (2000).
20. A. E. Bocquet, A. Fujimori, et al. *Phys. Rev. B* **46**, 3771 (1992)

## Program Title: Investigation of Metallic Photonic Crystals for the Modification of Thermal Emission

Dr. Shawn-Yu Lin, Rensselaer Polytechnic Institute,  
The Institute Future-Chips Constellation and Physics Department  
110 8<sup>th</sup> Street, Troy, NY 12180, USA, [sylin@rpi.edu](mailto:sylin@rpi.edu), 518/ 276-2978

In this research program, we have successfully realized 3D metallic photonic crystals for thermal emission in the infrared and visible wavelengths. We have also carried out basic material studies to allow for a successful conformal coating of high temperature metals (Pd and Ir) onto a complex 3D structure. Finally, we have grown the darkest manmade material ever for perfect solar absorption at all wavelengths-of-interest and for all angles-of-incidence.

We have implemented several methods to realize 3D metallic photonic crystal that includes both the top-down and bottom-up approaches. For the top-down method, we utilize RPI's state-of-the-art silicon micro-fabrication cleanroom for a large scale sample fabrication. We have successfully made an eight-inch 3D Cu photonic crystal, which is the largest infrared 3D photonic crystal ever been produced. We have also been successful in making 3D visible photonic crystal with a minimum feature size of 100-nano-meter.

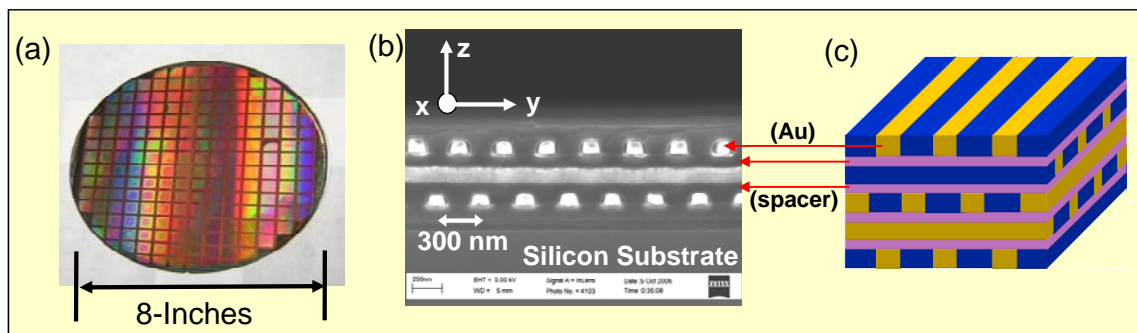


Figure 1 (a) An eight-inch diameter, large scale 3D Cu photonic crystal structure fabricated at RPI's microfabrication cleanroom; (b) A SEM image of a fabricated four layer 3D Au photonic crystal, having a minimum feature size of 100 nanometer; (c) A schematic of the layer-by-layer photonic crystal, consisting of Au nano-rods (yellow), spacer (pink) and spin-on-glass (blue)

For the bottom-up approach, we explore a new material growth method which is totally different from the traditional ones, that is, either the fabrication or self-assembly methods. Our new method is based on glancing-angle-deposition that produces a sequence of slanted rods, the spiral photonic crystal. This is an attractive way to make large scale, spatially coherent 3D structure with both low cost and high processing speed.

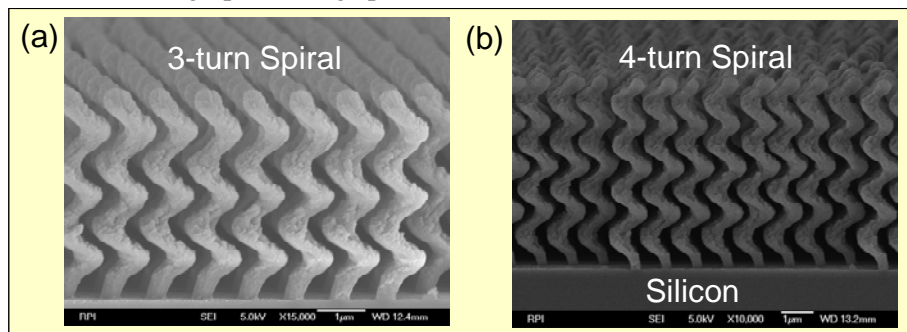


Figure 2 (a), (b) A side view image of a completed 3D spiral photonic crystal structure with 3 and 4 unit cells, respectively.

We have also investigated versatile methods for metallic material coating at the nanometer scale. The methods we have been working on include chemical vapor deposition (CVD), atomic layer deposition (ALD), electroless deposition (ELD), or a combination of these techniques. So far, we have been successful in ALD deposition of thin layer (10nm-50nm) of Pd and Ir materials.

Finally, we study a vertically-aligned carbon nanotube array as a perfect absorbing material. This material serves as an important foundation for solar utilization, as it can maximize the energy transfer from sun ray into a thermal radiator such as our metallic photonic crystal. Due to the low density array and the surface randomness of our material, we have achieved a total reflectance of 0.045% and a corresponding absorptance of 99.955% (a new world record) in the visible wavelengths. We believe these combined research efforts will enable a much improved selective thermal emission and efficiency of thermophotovoltaic energy conversion.

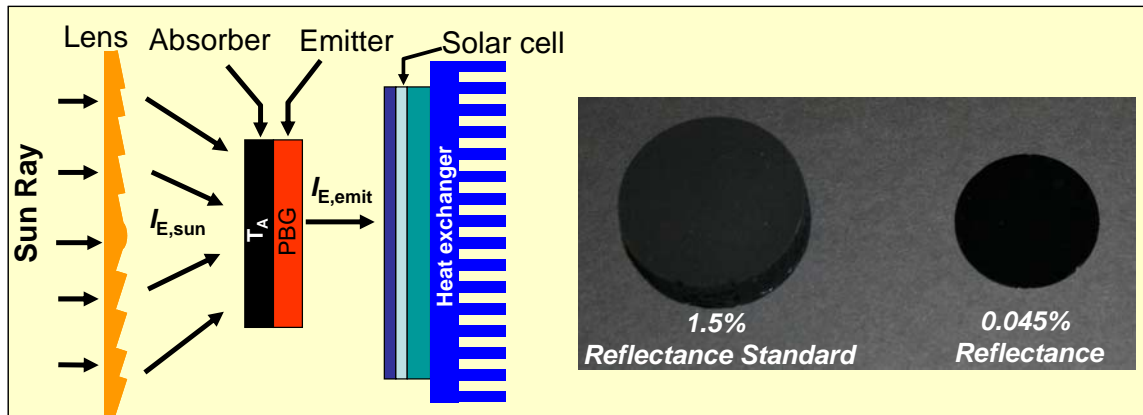


Figure 3 (Left) A schematic diagram of a system capable of achieving high efficiency (50%) solar-to-electricity conversion. The system consists of a lens for solar concentration, an all-angle, all-wavelength perfect dark absorber, a selective thermal radiator and a photovoltaic cell; (Right) A photo of a NIST certified 1.5% reflectance standard and our newly discovered nanotube array sample, having a 0.045% total reflectance. This is the darkest manmade material and has been granted a new Guinness world record in 2008.

## **Nanophosphors: Fundamental Science of Insulators in the Nanoscale Regime**

Ross E. Muenchausen  
Materials Science & Technology Division  
Los Alamos National Laboratory  
MS E-546  
Los Alamos, NM 87545  
rossm@lanl.gov

### **Program Scope:**

This research program on nanophosphors - nanostructured inorganic insulating luminescent materials - started in April 2005. While an intense investigative effort on the optical properties of nanostructured semiconductors has been carried out for more than a decade, luminescence phenomena in nanophosphors remained largely unexplored until recently. Many unique effects have been observed in nanophosphors, among them size-dependent luminescence emission, red-shifted emission and excitation bands, fluorescence lifetime dependence on the embedding medium, quenching curves shifted to higher concentrations, and larger Stokes shift. Of particular interest are nanophosphors doped or containing rare-earth (RE) ions. RE ions are particularly effective as luminescent centers and are commonly utilized to produce high quantum efficiency bulk phosphors; accordingly, these are the nanophosphors of choice for our current research. These considerations lead to the logical scientific question: How does reduced dimensionality affect the physical and chemical behavior of nanophosphors ?

In order to answer this fundamental question, nanophosphor synthesis by solution combustion and precipitation methods with high production output together with detailed structural characterization are combined with a suite of luminescence techniques, including photo- and radioluminescence, optically and thermally stimulated luminescence, and fluorescence lifetime measurements. Electron paramagnetic resonance is employed to provide additional chemical information, particularly on the local site symmetry of the luminescent center. Additionally, theoretical modeling of the temperature and dopant concentration dependence of the lifetime in nanophosphors provides fundamental insights into energy transfer and radiative processes that span timescales from nanoseconds to seconds. Of particular importance is the effect of the crystalline electric field (CEF) surrounding the luminescent center to the luminescence characteristics. This topic is presented in more detail in the next session.

### **Recent Progress:**

The structural and luminescent properties of 5at.% Eu-doped  $Gd_2O_3$  nanocrystals were investigated. The material was synthesized by the solution combustion technique and characterized by x-ray diffraction (XRD), transmission electron microscopy, and photoluminescence measurements. The as-prepared material presents predominant base-centered monoclinic structure with average crystallite size of 35 nm. Isothermal annealing at 1000 °C for up to 152 hrs. induced gradual structural transition toward the

body-centered cubic structure. Debye-Scherrer analysis of XRD results showed that annealing did not induce grain growth of monoclinic nanocrystals, while cubic nanocrystals reached 47 nm after annealing for 152 hrs. More importantly, changes in crystal size within the ~30-40 nm range are not expected to alter the optical properties of these materials (quantum confinement effects) due to the highly localized character of the 4*f*-4*f* electronic transitions in Eu<sup>3+</sup> ions. On the other hand, in RE-doped phosphors, the electronic properties of the dopants generate optical activity in the material. The RE ions are affected by the local host characteristics, including crystalline structure, local symmetry, degree of structural disorder, and defects, through the effective local CEF. In the particular case of Eu-doped Gd<sub>2</sub>O<sub>3</sub>, the forbidden 4*f* transitions become allowed by the Stark effect due to coupling of the Eu<sup>3+</sup> energy levels with the CEF of the host. Consequently, these optical transitions are very sensitive to the local symmetry and structural environment, and the observed gradual change in line emission intensity was correlated to the progressive structural transformation from monoclinic to cubic structure (Fig.1). This is further demonstrated in Fig. 2 where the 621/609 PL lines intensity ratio is linearly correlated with the (111) monoclinic/(222) cubic XRD intensity ratio. The inversion of the predominant photoluminescence emission line from 621.4 to 609.5 nm was observed and related to changes in the CEF resultant to phase transformation from cubic to monoclinic. The localized nature of the electronic distribution of the rare earth ions precludes the observation of size effects in nanocrystals tens of nanometers in size; conversely they are excellent probes of changes in the local crystal field symmetry.

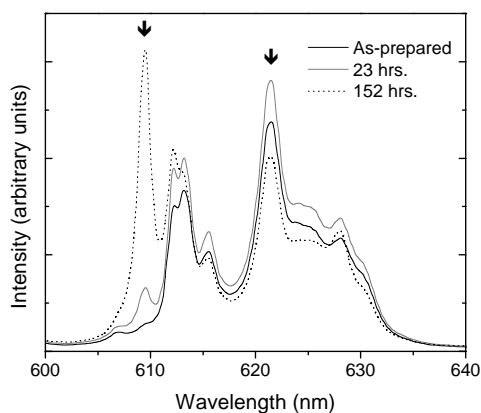


Fig. 1 - Selected high resolution PL spectra of the <sup>5</sup>D<sub>0</sub>→<sup>7</sup>F<sub>2</sub> transition from Gd<sub>2</sub>O<sub>3</sub>:Eu annealed at different times and excited at 277 nm.

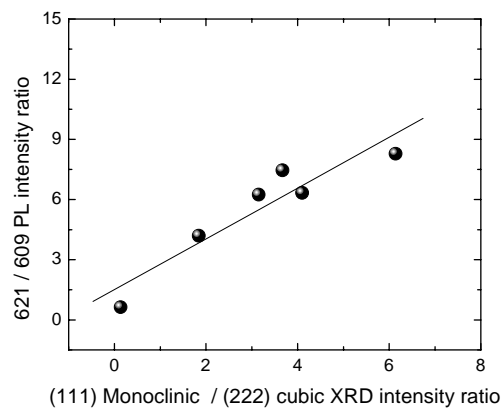


Fig. 2 - Correlation between the 621/609 PL lines intensity ratio with the XRD (111) monoclinic/(222) cubic intensity ratio.

### Future Plans:

Nanophosphors extend the materials realm for quantum confinement investigation and have already exhibited new behavior. These materials are commonly composed or doped with RE ions, whose optical transitions are of the type 4*f* → 5*d* or 4*f* → 4*f*. Thereby, they serve as a probe of reduced dimensional behavior because *f* electrons are highly localized to dimensions much smaller than the nanoscale host. Ground state *f* electrons also experience spin-orbit coupling of the electron with the magnetic field due to relative orbital motion of the nucleus and electron, whereas excited state *d* electrons

are subjected to crystal field splitting dependent on local crystalline symmetry. These two experimentally measurable effects provide additional insight into the role of reduced dimensionality on the optical properties of nanophosphors. Careful measurements of the variation in these parameters as one moves from macroscopic to nanoscale dimensions will provide fundamental information on the underlying mechanisms associated with reduced dimensionality. By exploiting conventional and photochemical-assisted solution precipitation reactions, a variety of oxide and halide nanophosphors can also be made to extend our capabilities to systematically vary materials properties.

We propose an original approach to answer the fundamental question presented in the Program Scope by using a core-shell nanoparticles-by-design approach. Core-shell nanoparticles are essentially nanoparticles with the deliberate growth of an encapsulating shell material. Our proposed Research Program comprises synthesis and characterization of oxide and halide core-shell nanophosphor structures, composition and functional properties measurements integrated with theoretical modeling of the energy transfer between luminescent sites and traps. Our capability to thoroughly address each and all of these elements makes us uniquely qualified to perform the proposed research. The potential impact of the proposed research will clarify the effects of reduced dimensionality on the optical properties on insulators, which ultimately will shape the strategies for exploiting these materials for technological advantage. Our proposed new research extends the use of core-shell nanostructures in three distinct thrusts: 1) as a means of developing a new class of nanoceramics made from non-cubic nanophosphors, 2) as a means of isolating and controlling nanophosphor surfaces, and 3) as a platform for studying and manipulating energy transfer between RE ions in nanophosphors. This proposed work strongly supports DOE's Office of Science focus on nanoscience discovery, development of fundamental scientific understanding, and conversion of this knowledge into useful technological solutions that benefit the nation.

#### **References (appeared/accepted within 2005-2007)**

##### *Science and application of nanophosphors*

R.E. Muenchausen, E.A. McKigney, L.G. Jacobsohn, M.W. Blair, B.L. Bennett and D.W. Cooke

Accepted for publication in IEEE Transactions in Nuclear Science (2007)

##### *EPR and luminescence of $F^{+}$ centers in bulk and nanophosphor oxyorthosilicates*

D.W. Cooke, M.W. Blair, J.F. Smith, B.L. Bennett, L.G. Jacobsohn, E.A. McKigney and R.E Muenchausen

Accepted for publication in IEEE Transactions in Nuclear Science (2007)

##### *Synthesis and structural transformation of luminescent nanostructured $Gd_2O_3:Eu$ produced by solution combustion synthesis*

R.E. Muenchausen, B.L. Bennett, L.G. Jacobsohn, S.C. Sitarz, J.F. Smith and D.W. Cooke

Accepted for publication (MRS Fall Meeting Proceedings - November 2007)

##### *Structure and luminescence of Ce-doped $Lu_2SiO_5$ nanophosphor*

L.G. Jacobsohn, B.L. Bennett, R.E. Muenchausen, S.C. Sitarz, J.F. Smith and D.W. Cooke

Accepted for publication (MRS Fall Meeting Proceedings - November 2007)

*Luminescent properties of nanophosphors*

L.G. Jacobsohn, B.L. Bennett, R.E. Muenchausen, J.F. Smith, and D.W. Cooke  
Radiation Measurements **42**, 675-678 (2007)

*Composite scintillators for radiation detection and nuclear spectroscopy*

E.A. McKingney, R.E. Del Sesto, L.G. Jacobsohn, P.A. Santi, R.E. Muenchausen, K.C. Ott, T.M. McCleskey, B.L. Bennett, J.F. Smith and D.W. Cooke  
Nuclear Instruments and Methods in Physics Research A **579**, 15-18 (2007)

*Effects of Tb doping on the photoluminescence of Y<sub>2</sub>O<sub>3</sub>:Tb nanophosphors*

R.E. Muenchausen, L.G. Jacobsohn, B.L. Bennett, E. A. McKigney, J.F. Smith, J.A. Valdez, and D.W. Cooke  
Journal of Luminescence **126**, 838-842 (2007)

*The central role of oxygen on H<sup>+</sup> irradiated Lu<sub>2</sub>SiO<sub>5</sub> luminescence*

L.G. Jacobsohn, B.L. Bennett, J.-K. Lee, R.E. Muenchausen, J.F. Smith, B.P. Uberuaga and D.W. Cooke  
Journal of Luminescence **124**, 173-177 (2007)

*Effects of ion beam irradiation on self-trapped defects in single-crystal Lu<sub>2</sub>SiO<sub>5</sub>*

L.G. Jacobsohn, J.-K. Lee, B.L. Bennett, R.E. Muenchausen, M. Nastasi and D.W. Cooke  
Journal of Luminescence **124**, 5-9 (2007)

*LaF<sub>3</sub>:Ce nanocomposite scintillator for gamma-ray detection*

E. A. McKigney, R.E. Muenchausen, D. W. Cooke, R. E. Del Sesto, R. D. Gilbertson, M. K. Bacrania, B. L. Bennett, L. G. Jacobsohn, T. M. McClesky, K. C. Ott, S.C. Sitarz, J. F. Smith, and S. Stange  
Hard X-Ray and Gamma-Ray Detector Physics IX, Proceedings of SPIE vol. **6706**, 67061A1-11 (2007)

*A novel method for extracting oscillator strength of rare-earth ion optical transitions in nanostructured dielectric materials*

R.E. Muenchausen, L.G. Jacobsohn, B.L. Bennett, E.A. McKigney, J.F. Smith, and D.W. Cooke  
Solid State Communications **139**, 497-500 (2006)

*Luminescent properties and reduced dimensional behavior of hydrothermally prepared Y<sub>2</sub>SiO<sub>5</sub>:Ce nanophosphors*

D.W. Cooke, J.-K. Lee, B. L. Bennett, J. R. Groves, L. G. Jacobsohn, E. A. McKigney, R. E. Muenchausen, M. Nastasi, K.E. Sickafus, M. Tang, J. A. Valdez, J.-Y. Kim and K.S. Hong  
Applied Physics Letters **88**, 103108- 1 to 3 (2006)

*Optical and structural characterization of nanostructured Y<sub>2</sub>O<sub>3</sub>:Tb*

L.G. Jacobsohn, B.L. Bennett, R.E. Muenchausen, J.F. Smith, and D.W. Cooke  
Nanophotonic Materials III, Proceedings of SPIE vol. **6321**, 63210J-1 to 9 (2006)

*Structure and optical properties of Lu<sub>2</sub>SiO<sub>5</sub>:Ce phosphor thin films*

J.-K. Lee, R.E. Muenchausen, J.-S. Lee, Q.X. Jia, M. Nastasi, J.A. Valdez, B.L. Bennett, and D.W. Cooke  
Applied Physics Letters **89**, 101905 (2006)

# Designing Nanoparticle/Nanowire Composites and “Nanotree” Arrays as Electrodes for Efficient Dye-Sensitized Solar Cells

PI: Yiyi Wu

Address: 100 W 18<sup>th</sup> Avenue, The Ohio State University, Columbus, OH 43210

e-mail: wu@chemistry.ohio-state.edu

## 1: Program Scope

The objective of this program is to design and synthesize novel porous photoelectrode structures and materials for efficient dye-sensitized solar cells (DSSCs). *The idea is to create nanostructures with both high surface area and long electron diffusion length by employing nanoparticle/nanowire (NP/NW) composites and “nanotree” arrays.* In NP/NW composites, the agglomerated nanoparticles (NPs) provide high surface area for the tethering of dye sensitizers, while the single-crystalline nanowires (NWs) provide pathways for fast electron transport. NWs can also act as light scattering centers to enhance the optical density of the electrode, and improve the mechanic strength of the film. The composite materials can, therefore, provide great flexibility in tuning the electronic, optical and mechanical properties, and thus enhance the efficiencies of DSSCs. Similarly, arrays of “nanotrees” with densely branched architecture can also provide the high surface area and efficient transport of charge carriers.

In addition, *we will also carry out a systematic investigation of multi-cation oxides for the DSSC application.* In comparison with simple binary oxides such as TiO<sub>2</sub>, SnO<sub>2</sub> and ZnO, multi-cation oxides can be prepared with tailored electric, optical, chemical and physical properties. Therefore, a full exploration of the multi-cation oxides could discover new promising phases for DSSC application.

The overall plan for carrying out this program includes (1) synthesizing single-crystalline NPs, NWs and Nanotrees. The materials that we are interested in include both binary oxide materials such as anatase TiO<sub>2</sub>, ZnO, SnO<sub>2</sub>, WO<sub>3</sub>, and also multi-cation oxide materials such as ZnSnO<sub>3</sub>, Zn<sub>2</sub>SnO<sub>4</sub> and Cd<sub>2</sub>SnO<sub>4</sub>; (2) Measuring the performance of DSSCs based on nanocrystalline multi-cation oxides; (3) Integrating NPs and NWs into composites. The NWs can be randomly oriented, or in the form of vertical NW arrays; (4) Investigating electron transport and recombination in the complex architectures probed by both time-domain and frequency-domain techniques; (5) Evaluating the energy conversion efficiency of solar cells based on the proposed complex architectures.

The proposed research program will bring progress in designing and fabricating new structures and materials at the nanoscale for energy-related application and establish an understanding of the electron transport process in the complex nanoscale architectures.

## 2: Recent Progress

### Developing complex oxides as anode materials.

In previous research reports, the anode materials have mostly been limited to simple binary oxides such as TiO<sub>2</sub>, ZnO and SnO<sub>2</sub>. The application of complex oxides in DSSC has been rarely explored. Considering the availability of a wide range of complex oxides and their tunable properties, it is interesting to investigate their applications in DSSC. Potentially, new materials with better performance than anatase TiO<sub>2</sub> could be found. The first ternary oxide that we have investigated is Zn<sub>2</sub>SnO<sub>4</sub>, considering ZnO and SnO<sub>2</sub> have both been used as anode materials. Zn<sub>2</sub>SnO<sub>4</sub> is a transparent conducting oxide material with high electron mobility and a band gap of 3.6 eV. We synthesized Zn<sub>2</sub>SnO<sub>4</sub> NPs with size in the range of 10-60 nm by a hydrothermal method. Using *cis*-bis(isothiocyanato)bis(2,2'-

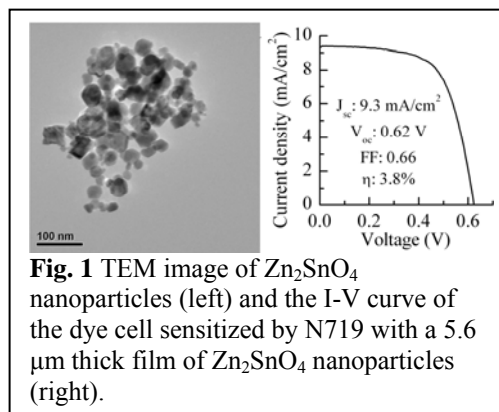


**Fig. 1** TEM image of Zn<sub>2</sub>SnO<sub>4</sub> nanoparticles (left) and the I-V curve of the dye cell sensitized by N719 with a 5.6 μm thick film of Zn<sub>2</sub>SnO<sub>4</sub> nanoparticles (right).

bipyridyl-4,4'-dicarboxylato)-ruthenium(II) bis-tetrabutylammonium (also referred to as N719) as the

Oxide	Band gap (eV)	$J_{sc}$ (mA/cm <sup>2</sup> )	$V_{oc}$ (V)	Fill factor	Efficiency (%)
Zn <sub>2</sub> SnO <sub>4</sub>	3.6	9.3	0.62	0.66	3.8
ZnGa <sub>2</sub> O <sub>4</sub>	4.0	0.030	0.26	0.55	0.0042
ZnAl <sub>2</sub> O <sub>4</sub>	3.8	0.0050	0.28	0.53	0.00074
ZnWO <sub>4</sub>	3.75	0.038	0.28	0.30	0.0033
ZnTiO <sub>3</sub>	-	0.080	0.43	0.38	0.012
ZnNb <sub>2</sub> O <sub>6</sub>	-	0.023	0.21	0.28	0.0014
MgSnO <sub>3</sub>	-	0.46	0.58	0.44	0.12
CaSnO <sub>3</sub>	4.4	0.040	0.30	0.30	0.0033
SrSnO <sub>3</sub>	4.1	0.42	0.48	0.45	0.091
BaSnO <sub>3</sub>	3.1	0.060	0.32	0.27	0.0052
TiNb <sub>2</sub> O <sub>7</sub>	3.0	2.2	0.46	0.58	0.60

**Table 1.** Summary of the performance of DSSCs based on ternary oxides sensitized by N-719 dye.

sensitizer, we have measured the performance of Zn<sub>2</sub>SnO<sub>4</sub> DSSCs with various Zn<sub>2</sub>SnO<sub>4</sub> film thicknesses and compared the results with TiO<sub>2</sub>-based DSSCs using P25 nanoparticles. When the film thickness is less than ~6 μm, the Zn<sub>2</sub>SnO<sub>4</sub> DSSCs show higher short-circuit current and efficiency than P25 DSSCs. Moreover, in comparison with ZnO as its simple component oxide, Zn<sub>2</sub>SnO<sub>4</sub> electrode is stable against acidic dye solution. Inspired by the promising performance of Zn<sub>2</sub>SnO<sub>4</sub> electrode, we have then synthesized a series of other ternary oxides. As summarized in table 1, DSSCs based on these ternary oxides sensitized by N-719 dye show low efficiencies. The possible reason could come from the

undesirable energy alignment between the conduction band of the complex oxides and the LUMO of the N-719 dye. In order to confirm and overcome this problem, we need to measure the band structure of the complex oxides as described below, and then select sensitizers with matched energy alignment to ensure the spontaneous downhill electron transfer from the sensitizers to the oxide support.

**Measuring band structure of complex oxides.** Our goal is the complete characterization of the energy levels of our semiconductors: to determine the relative dispositions of the conduction band (CB), valence band (VB) and Fermi levels ( $E_F$ ). For a DSSC, the maximum open circuit voltage ( $V_{oc}$ ) is the difference between the quasi Fermi level of the anode and the potential of the redox mediator. For a TiO<sub>2</sub>-DSSC with I<sup>-</sup>/I<sub>3</sub><sup>-</sup> couple, the  $E_{oc}$  maximum is ~0.8 V; currently, reported values are > 0.7 V, which is approaching the limit of the material. Our goal is to develop new complex oxides to increase the maximum  $V_{oc}$  and cell efficiency. Thus, we have synthesized the oxides in Table 1, and we are currently working on the band structure measurements.

We follow the usual practice to take as a first approximation that the flat band potential value ( $E_{fb}$ ) gives the position of the conduction band edge for an n-type semiconductor like TiO<sub>2</sub>. The commonly used method for measuring  $E_{fb}$  is the Mott-Schotky equation. However, the use of the Mott-Schotky equation to NP films is somewhat controversial. Our preliminary results show that its application to TiO<sub>2</sub> NPs and ZnO NWs is complicated due to the presence of additional states such as surface states and defects. Another method is to use photoelectrochemistry, in which the onset of the photocurrent is used to measure  $E_{fb}$ . In Fig. 2 we have used TiO<sub>2</sub> as a model material and determined  $E_{fb} = -0.347$  V vs Ag/AgCl (-0.150 V vs NHE), which is consistent with previous reports. We are working in reproducing  $E_{fb}$  measurements as a function of pH, and studying the dependence of  $E_{fb}$  with different solvents (e.g., acetonitrile) and electrolytes, since this is relevant to DSSC performance. We will then apply the method to the ternary

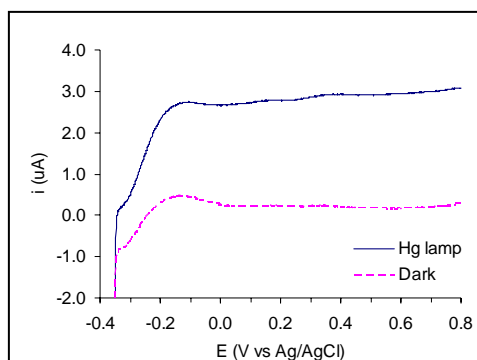


**Fig. 2.** Photoelectrochemistry experiment of TiO<sub>2</sub> NPs film in 1 M KCl, 1 M AcO<sup>-</sup> at pH 4.8 in dark and under Hg lamp illumination.

oxides that we have developed. Finally, the use of photocurrent and electrochemical impedance to measure and characterize surface and intragap states is also being pursued.

Assembling NP/NW composite architectures. DSSCs have been fabricated based on composites of anatase TiO<sub>2</sub> NPs and single-crystalline anatase TiO<sub>2</sub> NWs. NP/NW composites can possess the advantages of both building blocks, i.e. the high surface area of NP agglomerates and the rapid electron transport rate and the light scattering effect of single-crystalline nanowires. An enhancement of power efficiency from 6.7 % for pure nanoparticle cells to 8.6% for the composite cell with 20 wt% nanowires has been achieved under 1 Sun AM1.5 illumination. These results show that employing NP/NW composites represents a promising approach for further improving the efficiencies of sensitized solar cells. We have also synthesized ZnO NW arrays and then used electrophoretic deposition to infiltrate the NW arrays with TiO<sub>2</sub> NPs (Fig. 3). In this configuration, every NW is directly attached to the substrate, providing a more effective pathway for the transport of electrons than random agglomerated NWs. We are in the process of optimizing the electrophoretic deposition and testing the dye cell performance.

Developing NW-based flexible dye cells. We have found that a 20 μm thick film of TiO<sub>2</sub> NWs on FTO glass detaches when heated at 120 °C and then quickly immersed in EtOH at room temperature. The film remains complete and can be further manipulated without destroying it. The film can thus be transferred to a plastic support after it has been heat treated on glass which should improve the efficiency of flexible solar cells. This can be extended to NWs films covered with TiO<sub>2</sub> nanoparticles. This complex nanostructure can be detached and transferred to a different substrate as shown in Fig. 4. We are currently working on achieving connection to a new support for solar cell fabrication.

Optimizing Pt NP counter electrode. In the classical Grätzel cell, the counter electrode is made of Pt NPs at a loading of 5 μg/cm<sup>2</sup> on FTO-covered glass. The use of Pt is necessary as it is, to the best of our knowledge, the best catalyst for the I<sup>3</sup>/I<sup>-</sup> reduction that takes place in the cathode of the cell. This electrode is made by a “platinization” procedure by dropping H<sub>2</sub>PtCl<sub>6</sub> solution in alcohol onto FTO glass followed by annealing at 385 °C. This procedure has little control over the dispersion and size of the Pt NPs. An example of such an electrode is given in Fig. 5A. Due to the cost of Pt, it is of interest to further reduce the Pt loading that can provide the 20 mA/cm<sup>2</sup> of short circuit current density that state-of-the-art DSSCs have achieved. Our approach includes the use of mesoporous TiO<sub>2</sub> as a support for Pt NPs to achieve control of NP size and the dispersion of Pt on the surface. An example of such a support is given in Fig 5B. By varying the composition of the mesoporous TiO<sub>2</sub> precursor solutions we can achieve different mesopore sizes and shapes, and use this to control the size, dispersion, and electrocatalytic activity of the Pt

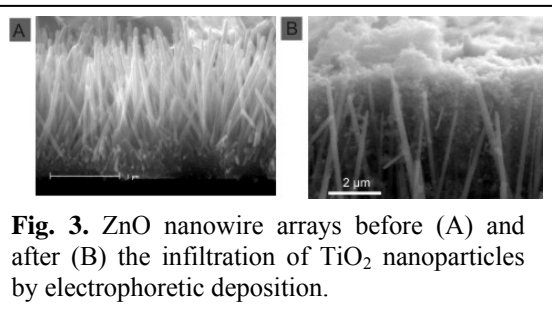


**Fig. 3.** ZnO nanowire arrays before (A) and after (B) the infiltration of TiO<sub>2</sub> nanoparticles by electrophoretic deposition.

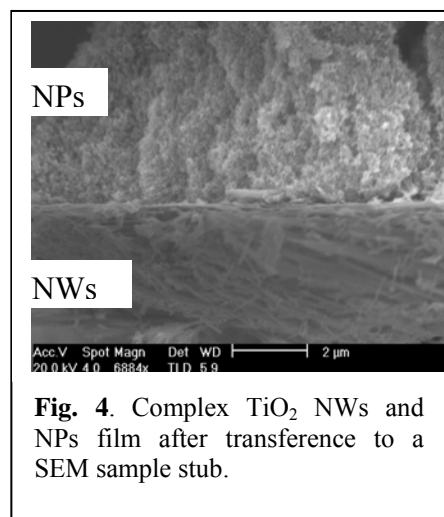


**Fig. 4.** Complex TiO<sub>2</sub> NWs and NPs film after transference to a SEM sample stub.

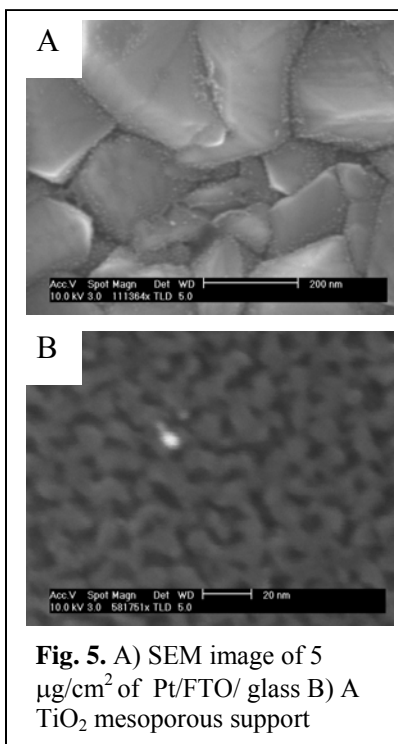


**Fig. 5.** A) SEM image of 5 μg/cm<sup>2</sup> of Pt/FTO/ glass B) A TiO<sub>2</sub> mesoporous support

NPs.

### 3: Future Plans

Measuring band structure of new anode materials. We will determine the band structure of the ternary oxides that we have synthesized (table 1) using techniques such as optical electrochemistry, photoelectron spectroscopy and diffusive reflectance measurement. The knowledge of the conduction band position will help us select sensitizers with matched energy alignment. A focus is to develop cells with increased open circuit voltage using anode materials with more negative conduction band edge than TiO<sub>2</sub>. We will also try to establish collaboration with an organic chemistry group for the synthesis of dye molecules.

Synthesizing p-type oxide nanoparticles. The goal is to investigate new p-type wide bandgap semiconductors for solid-state dye cells and p-type dye cells. Solid-state dye cells use solid hole conductor instead of the liquid electrolyte solution in order to avoid the liquid leakage issue. Recently, CuBO<sub>2</sub> has been shown to have high hole mobility ( $\sim 100 \text{ cm}^2 \text{ V}^{-1} \text{ s}^{-1}$ ), which is significantly higher than other known p-type oxides such as NiO and CuAlO<sub>2</sub>. Therefore, we will develop synthetic method to synthesize CuBO<sub>2</sub> nanoparticles, so that they can effectively penetrate into the sensitized porous anode film. We will also explore suitable dyes or quantum dots as cathode sensitizers to build p-type dye cells, which can be further assembled with normal n-type dye cells into tandem cells.

Optimizing NP/NW composite architectures. We will optimize the electrophoretic deposition method that drive charged ZnO or TiO<sub>2</sub> NPs into NW arrays. We will also pattern the growth of NW arrays in order to control the average spacing between adjacent NWs in the NW arrays. There should be a tradeoff for NW density: too high NW density reduces the open space available for NP infiltration, and thus the specific surface area, while too low NW density reduces electron collection efficiency. In addition, we will also deposit Cu<sub>2</sub>O NPs and CuBO<sub>2</sub> NPs into ZnO NW arrays to form hetero-junction solar cell and oxide solid-state dye cell, respectively.

Investigating charge transport and recombination mechanisms and surface passivation. The goal of this part is to develop fundamental understanding of the charge transport and recombination mechanism. We will measure the charge carrier lifetime and diffusivity in the new electrode materials and architectures in order to establish an understanding of the relationship between the morphology and the charge transport property of the photoelectrode. An intrinsic feature of the dye cell is the presence of extensive and diverse interfaces. The surface states play a critical role in controlling the charge transport and the operation of the solar cell. The complete energetics of the material, including that of surface and other intra-band gap states will be conducted with electrochemistry experiments. The recombination traps will be studied in novel materials and in new architectures of materials in the nanometer scale. The electrochemical behavior of the materials and their ability to mediate electrochemical reactions in the dark and under illumination will be correlated with different treatments. Changes after surface passivation and acid or base etching will confirm the presence of surface states. Deviations from the linear Mott-Schotky plots, attributed to surface states, will be further characterized as a function of frequency and potential to determine the densities of states. Finally, these findings will be compared with photo-luminescence and photo-spectroscopy data to construct the complete energy diagram of the materials.

**Program Title: Theory on Defects and Doping Bottlenecks in Semiconductors, Wide-gap Materials, and their Nanostructures**

Principal Investigator: Shengbai Zhang

Mailing Address: Department of Physics, Applied Physics, and Astronomy, Rensselaer Polytechnic Institute, 110 Eighth Street, Troy, New York 12180

Email: [zhangs9@rpi.edu](mailto:zhangs9@rpi.edu)

Program Scope: To understand doping limits in semiconductors, wide-gap materials, and their nanostructures, to propose ways to overcome these limits, and to advance the general defect, impurity, and surface physics in semiconductors. These developments are essential to the design of new-functionality in devices such as ultra high-efficiency solar cells, blue and UV LEDs, lasers, detectors, and in other solid-state photo conversion devices, with intended impacts on revolutionary energy applications, nanotechnology, and next-generation integrated circuits.

Recent Progresses: (1) Our first-principles calculation unveiled a photo-induced bistability in boron doped silicon [5], which has the undesirable effect of limiting p-type active layer Si solar cell performance. In solar-grade silicon, there commonly exist oxygen impurities which form complexes with boron under solar irradiation. Once formed, the complexes facilitate undesirable dissipation of solar energy through thermal relaxations. Our findings explain a number of experiments. (2) Nitrogen clustering has been attributed to a number of undesirable effects in dilute III-V nitride alloys ( $x \sim 1\%$ ) to hinder their use for high efficiency solar cells. What is puzzling, however, is that the clustering is an endothermic process. Recently, we showed [7] that in the presence of hydrogen, which is often the case during growth, not only the formation of the N-H complexes but also that of hydrogenated multi-N clusters is energetically favored. A post growth dehydrogenation may thus lead to the observed metastable N clusters. (3) Typically isovalent impurity has negligible interaction with charged defects. However, in highly ionic semiconductors such as ZnO, this is no longer true. In a recent yet-to-be-published work, we showed that due to the large interaction, unintentional calcium impurities can cause a reversal of the preferred proton ( $H^+$ ) sites. The large spatially undulated electric field of ionic crystal is the cause. Our results appear to resolve the longstanding experimental puzzle concerning where hydrogen resides in ZnO. (4) In collaboration with an experimental group, we applied our defect-complex doping theory to phosphorus doped zinc oxide. P-type ZnO has been obtained, which is stable over a period greater than 16 months without any apparent degradation [2]. TEM studies, however, reveal massive extended defects, which could be the reason why such p-type ZnO does not show electroluminescence. (5) In collaboration with another experimental group, we studied [8] the origin of unintentional n-type impurities in ZnO. It was found that intrinsic double donor zinc interstitials bind strongly with nitrogen acceptors to form donor complexes. This could facilitate the formation of (Zn interstitial-N) complexes during post-growth cooling. The calculated results are in good agreement with experiments. (6) Semiconductor nanostructures are full of faceted surfaces. The rule of thumb to determine the structures of the surfaces is the electron counting model. Recently, we successfully extended the model to more practical surfaces such as metal-impurity covered semiconductor surfaces [6] and to  $sp^2$  and  $sp^3$  mixed structures of carbon (such as surface steps, nano diamond and porous graphite) [1]. (7)  $TiO_2$  nanoparticles have attracted much attention for their use in dye-sensitized solar cells and for their exceptional oxidation potential in bio applications. The understanding of photo oxidation on  $TiO_2$  surface is, however, at best fragmented.

In a recent study [4], we developed a theory to unify the understanding of photooxidation from hole-scavenging, deprotonation, to self assembly of glucose covered TiO<sub>2</sub> nanorods. The results explain a number of experiments.

Future Plans: After more than eight years into the program, although we have made significant progress in *every* year, it becomes more and more clear to us that we should take the program to the next level of excellence not only to maintain its vitality but also to further broaden its impacts to real materials research. For this reason, we will steer our future research plans into two broad research areas that are currently very much “forbidden” zones to first-principles calculations: (1) kinetic doping limit theory and (2) accurate determination of defect levels beyond the density functional theory (DFT).

(1) *Kinetic doping limit theory.* With today’s growth techniques, few systems of current interest are truly under thermal equilibrium to which and only to which the current defect theory applies. This includes the doping of diamond, zinc oxide, and even gallium nitride in some cases and the growth of the entire class of nanostructures, their doping, and defect properties. The reason that such materials can exist and their electronic properties can be improved is because diffusion of the defects and impurities are rare events and will not happen significantly over the lifetime of a device. Thus, understanding atomic diffusion is the key to the development of next-generation electronic materials. In the past, we have been the advocate for such a viewpoint and have done a series of work trying to demonstrate the point with some success. However, we are yet to develop a systematic kinetic doping limit theory because it requires the knowledge of the complex energy surface, in particular, atomic diffusion pathways and barriers. Using the current DFT codes, one often needs to guess the pathways before calculating the barriers. Alternatively, one can apply molecular dynamics (MD) to determine the diffusion pathways. Here, the difficulty lies in the un-physically short simulation time— picoseconds in *ab initio* methods and nanoseconds in classical model potential methods. Over several picoseconds, most of the rare events may not even happen, rendering the MD simulation useless.

We are in the process of developing a new multi-scale method to accelerate defect dynamics, which we term stochastically accelerated MD. The point is that for rare events, one should not go through every individual steps of atomic vibration in order to accurately predict statistical trajectory of the diffusion. Thus, we employ statistical means to advance the clock without having to alter the real physical process. In a model potential study of hydrogen diffusion in silicon, we have obtained a very impressive acceleration factor  $> 10^3$ . Yet, we are confident that another three orders of magnitude increase is feasible. Such acceleration factors should be sufficient to cover most of the rare events in statistically meaningful way. Moving forward, we will further develop the method such that it can be incorporated into first-principles calculations. Among the first systems to apply our new approach, we will consider zinc oxide again to see which impurities or impurity complexes are stable enough to yield p-type conductivity. If not, what might be the likely cause for the conversion from p-type to n-type over a relatively short time period? We will consider silicon and binary semiconductor quantum dots such as those of GaAs or ZnSe to determine dopant outdiffusion, segregation, and thereby statistically most meaningful distributions of the impurities and defects. Because we are dealing with kinetic processes, indiffusion during the growth and out diffusion after growth can be drastically different. Therefore, we also need to explore dopant incorporation processes in order to determine what are the most effectively ways to incorporate them into the host.

(2) *Accurate determination of defect levels.* For a longtime, first-principles defect calculations suffer from the too small band gaps due to the use of the local density approximation (LDA). In the case of silicon, the calculated band gap (0.6 eV) is only half of that of experimental value (1.2 eV). In the case of oxides, the errors can even be larger. For example, the calculated band gap for zinc oxide (0.9 eV) is more than 73% smaller than the experimental value (3.4 eV). In the past, people have used a scissors operator to artificially open up the band gap while maintaining the LDA defect level positions fixed with respect to the top of valence band. Such a practice may be reasonable for shallow acceptor states as they are mainly valence band derived states. For deep levels (which are of particular importance) and for donor states derived mainly from the conduction band, however, the errors could be severe. For example, LDA gives the oxygen vacancy donor level 0.1 eV about the LDA conduction band minimum (CBM). In the scissors operator approach, however, the level sinks 2.4 eV below the CBM.

To break the impasse, we plan to carry out GW quasiparticle calculations. While quasiparticle calculations for Si and GaAs have been done 20 years ago, however, only recently it is possible to calculate the quasiparticle band gap of ZnO with adequate treatment of Zn *d* states which were too shallow in previous GW calculations. The resulting band gap is in good agreement with experiment. We have teamed up with the group of original development to recalculate the defect levels in semiconductors including ZnO. The unique computing facilities at Rensselaer Polytechnic Institute Computational Center for Nanotechnology Innovations (CCNI), IBM BlueGene with 32,000 CPUs, enable us to do this in a timely fashion. Not only we will calculate the one-particle energy levels, but we will also develop a method to integrate the GW quasiparticle results with those of DFT to quantitatively include the charge and lattice relaxation effects. If successful, this could represent a big leap in defect physics.

References to publications of DOE sponsored research (2005-2007):

1. H. X. Yang, L. F. Xu, Z. Fang, C. Z. Gu, and S. B. Zhang, "Bond Counting Rule for Carbon and Its Application to the Roughness of Diamond (001)", *Phys. Rev. Lett.* **100**, 026101 (2008).
2. A. Allenic, W. Guo, Y. B. Chen, M. B. Katz, G. Y. Zhao, Y. Che, Z. D. Hu and B. Liu, S. B. Zhang, X. Q. Pan, "Amphoteric phosphorus doping for stable p-type ZnO", *Advanced Materials* **19**, 3333 (2007).
3. X. Ma, P. Jiang, Y. Qi, J. Jia, Y. Yang, W. Duan, W.-X. Li, X. Bao, S. B. Zhang, Q.-K. Xue, "Experimental observation of quantum oscillation of surface chemical reactivities", *PNAS* **104**, 9204-9208 (2007).
4. M.-H. Du, J. Feng, S. B. Zhang, "Photo-Oxidation of polyhydroxyl molecules on TiO<sub>2</sub> surfaces: From hole scavenging to light-Induced self-assembly of TiO<sub>2</sub>-cyclodextrin wires", *Phys. Rev. Lett.* **98**, 066102 (2007).
5. M.-H. Du, H. M. Branz, R. S. Crandall, S. B. Zhang, "Bistability-mediated carrier recombination at light-induced boron-oxygen complexes in silicon", *Phys. Rev. Lett.* **97**, 256602 (2006).
6. L. Zhang, E. G. Wang, Q. K. Xue, S. B. Zhang, and Z. Zhang, "Generalized electron counting in determination of metal-induced reconstruction of compound semiconductor surfaces", *Phys. Rev. Lett.* **97**, 126103 (2006).
7. M.-H. Du, S. Limpijumnong, and S. B. Zhang, "Hydrogen-mediated nitrogen clustering in dilute III-V nitrides", *Phys. Rev. Lett.* **97**, 075503 (2006).
8. D. C. Look, G. C. Farlow, P. Reunchan, S. Limpijumnong, S. B. Zhang, and K. Nordlund, "Evidence for native-defect donors in n-type ZnO", *Phys. Rev. Lett.* **95**, 225502(2005).
9. Y.-H. Kim, S. B. Zhang, Yang Yu, L. F. Xu, and C. Z. Gu, "Dihydrogen bonding, p-type conductivity, and the true origin of workfunction change on hydrogenated diamond (001) surfaces", *Phys. Rev. B* **74**, 075329 (2006).

10. W. E. McMahon, I. G. Batyrev, T. Hannappel, J. M. Olson, and S. B. Zhang, "5-7-5 line defects on As/Si(100): A general stress-relief mechanism for V/IV surfaces", *Phys. Rev. B* **74**, 033304 (2006).
11. S. Na-Phattalung, M. F. Smith, K. Kim, M. H. Du, S. H. Wei, S. B. Zhang, S. Limpijumnong, "First-principles study of native defects in anatase TiO<sub>2</sub>", *Phys. Rev. B* **73**, 125205 (2006).
12. M.-H. Du and S. B. Zhang, "DX centers in GaAs and GaSb", *Phys. Rev. B* **72**, 075210 (2005).
13. M.-H. Du, S. Limpijumnong, and S. B. Zhang, "Hydrogen pairs and local vibrational modes in H-irradiated GaAs:N", *Phys. Rev. B* **72**, 073202 (2005).
14. L. Zhang, S. B. Zhang, Q.-K. Xue, J.-F. Jia, and E. G. Wang, "Electronic structure of identical metal cluster arrays on Si(111) - 7 x 7 surfaces", *Phys. Rev. B* **72**, 033315 (2005).
15. Y. Jiang, Y.-H. Kim, S. B. Zhang, P. Ebert, S. Yang, Z. Tang, K. Wu, and E. G. Wang, "Growing extremely thin bulklike metal film on a semiconductor surface: Monolayer Al(111) on Si(111)", *Appl. Phys. Lett.* **91**, 181902 (2007).
16. Y. Qi, X. Ma, P. Jiang, S. Ji, Y. Fu, J.-F. Jia, Q.-K. Xue, and S. B. Zhang, "Atomic-layer-resolved local work functions of Pb thin films and their dependence on quantum well states", *Appl. Phys. Lett.* **90**, 013109 (2007).
17. S. Limpijumnong, M. F. Smith, and S. B. Zhang, "Characterization of As-doped, p-type ZnO by x-ray absorption near-edge structure spectroscopy: Theory", *Appl. Phys. Lett.* **89**, 222113 (2006).
18. J. G. Lu, Z. Z. Ye, G. D. Yuan, Y. J. Zeng, F. Zhuge, L. P. Zhu, B. H. Zhao, and S. B. Zhang, "Electrical characterization of ZnO-based homojunctions", *Appl. Phys. Lett.* **89**, 053501 (2006).
19. Y. J. Zeng, Z. Z. Ye, W. Z. Xu, J. G. Lu, H. P. He, L. P. Zhu, B. H. Zhao, C. Che, and S. B. Zhang, "p-type behavior in nominally undoped ZnO thin films by oxygen plasma growth", *Appl. Phys. Lett.* **88**, 262103 (2006).
20. W. Z. Xu, Z. Z. Ye, Y. J. Zeng, L. P. Zhu, B. H. Zhao, L. Jiang, J. G. Lu, H. P. He, and S. B. Zhang, "ZnO light-emitting diode grown by plasma-assisted metal organic chemical vapor deposition", *Appl. Phys. Lett.* **88**, 173506 (2006).
21. M.-H. Du and S. B. Zhang, "Topological defects and the Staebler-Wronski effect in hydrogenated amorphous silicon", *Appl. Phys. Lett.* **87**, 191903 (2005).
22. F. Zhuge F, L. P. Zhu, Z. Z. Ye, D. W. Ma, J. G. Lu, J. Y. Huang, F. Z. Wang, Z. G. Ji, and S. B. Zhang, "ZnO p-n homojunctions and ohmic contacts to Al-N-co-doped p-type ZnO", *Appl. Phys. Lett.* **87**, 092103 (2005).
23. G. D. Yuan, Z. Z. Ye, L. P. Zhu, Q. Qian, B. H. Zhao, R. X. Fan, C. L. Perkins, and S. B. Zhang, "Control of conduction type in Al- and N- co-doped ZnO thin films", *Appl. Phys. Lett.* **86**, 202106 (2005).
24. T. J. Coutts, X. Li, T. M. Barnes, B. M. Keyes, C. L. Perkins, S. E. Asher, S. B. Zhang, S.-H. Wei, and S. Limpijumnong, "Synthesis and characterization of nitrogen-doped ZnO films grown by MOCVD", Chapter 3 in *Zinc Oxide Bulk, Thin Films and Nanostructures*, C. Jagadish and S. J. Pearton, eds. (Elsevier, Amsterdam, 2006), pp. 43-84.
25. X. N. Li, S. E. Asher, S. Limpijumnong, S. B. Zhang, S.-H. Wei, T. M. Barnes, T. J. Coutts, R. Noufi, "Unintentional doping and compensation effects of carbon in metal-organic chemical-vapor deposition fabricated ZnO thin films", *J. Vac. Sci. Technol A* **24**, 1213 (2006).
26. X. Li, S. Asher, S. Limpijumnong, B. Keyes, C. L. Perkins, H. Moutinho, J. Luther, S. B. Zhang, S.-H. Wei, and T. J. Coutts, "Impurity effect in ZnO and nitrogen doped ZnO thin films fabricated by MOCVD", *J. Crystal Growth* **287**, 94 (2006).

## **Author Index**

## Author Index

Ager, III, J. W. ....	44, 48	Fong, D. D. ....	89
Ali, N. ....	203	Frechet, J.M.J. ....	2
Alivisatos, P. ....	249	Frey, N. ....	182
Allcock, H. R. ....	125	Friesen, C. ....	146
Anderson, R. ....	175	Fuoss, P. H. ....	89
Angst, M. ....	182	Gass, J. ....	182
Antropov, V. ....	190	George, E. ....	211
Armstrong, A. M. ....	33	Goldman, A. I. ....	167
Atwater, H. A. ....	251	Gschneider, K. A. ....	167
Barnett, S. A. ....	129	Gungor, M. R. ....	105
Benesi, A. J. ....	125	Haller, E. E. ....	44, 48
Bergman, L. ....	72	Han, J. ....	76
Berseth, P. ....	163	Harmon, B. N. ....	167
Bhattacharya, A. ..	254, 89	Harris, V. ....	182
Bowman, R. C. ....	133	Hochbaum, A. I. ....	1, 222
Brédas, J-L. ....	52	Horn, K. ....	80
Bridges, F. ....	37	Houston, J. E. ....	93
Bustamante, C. ....	2	Hwang, S.-J. ....	133
Carter, S. ....	37	Jena, P. ....	150, 155
Ceder, G. ....	41, 137	Kahn, A. ....	52
Chen, G. ....	207	Karma, A. ....	215
Chen, R. ....	1, 122	Kellogg, G. L. ....	97
Chinnasamy, C. N. ....	182	Kerr, L. L. ....	56
Chrzan, D. C. ....	44, 48	Khachaturyan, A. G. ....	219, 234
Chumbley, L. S. .	155, 167	Kim, C. ....	133
Cohen, M. L. ....	2	Koleske, D. D. ....	60
Conradi, M. S. ....	138	Kotula, P. G. ....	121
Coutts, T. J. ....	56	Krishnan, K. M. ....	171
Crawford, M. H. ....	60	Lauhon, L. J. ....	10
Crommie, M. F. ....	2	Lavrentovich, O. D. ....	226
Cronin, S. ....	6, 20	Lee, D. ....	125
De Jonghe, L. C. ....	142	Lee, S. R. ....	60
Dubón, O. D. ....	48	Li, J. ....	242
Duggal, A. ....	52	Li, Q. ....	64
Eastman, J. A. ....	89	Li, X. ....	56
Eckstein, J. N. ....	254	Liliental-Weber, Z. ....	48
Egami, T. ....	211	Lin, S-Y. ....	257
Ellis, D. ....	129	Lin, V.S.-Y. ....	155
Fang, Z. ....	56	Liu, F. ....	101
Feibelman, P. J. ....	121	Lograsso, T. A. ....	167
Fleming, R. M. ....	33	Look, D. C. ....	56
Follstaedt, D. M. ....	60	Louie, S. G. ....	2

Ma, E. ....	230	Sommer, A. ....	56
Macdonald, D. D. ....	125	Srikanth, H. ....	182
Majumdar, A. ....	1, 222	Stadler, S. ....	203
Malliaras, G. ....	52	Stephenson, G. B. ....	89
Mandrus, D. ....	182	Stowe, A. ....	163
Marks, L. D. ....	129	Suzuki, Y. ....	186
Maroudas, D. ....	105	Tan, X. ....	190
Martin, J. E. ....	175	Thaler, G. ....	60
Mascarenhas, A. ....	68	Trauner, D. ....	2
Mason, T. O. ....	129	Tsui, F. ....	194
McCallum, R. W. ....	190	Tyson, T. A. ....	198
McCluskey, M. D. ....	72	Van Dover, R. B. ....	238
McMahon, W. E. ....	68	Vasiljevic, N. ....	121
McQueeney, R. J. ....	167	Venturini, G. ....	175
Miller, G. J. ....	167	Viehland, D. ....	234, 242
Mishin, Y. ....	109	Virkar, A. V. ....	159
Missert, N. A. ....	60, 121	Voorhees, P. W. ....	129
Mohapatra, C. ....	254	Walukiewicz, W. ....	48
Moodenbaugh, A. ....	64	Wei, S.-H. ....	8
Morris, J. R. ....	211	Wen, J. G. ....	254
Muenchausen, R. E. ..	259	Wright, A. F. ....	33
Myers, S. M. ....	33	Wu, Y. ....	263
Ni, Y. ....	219	Xi, X. ....	27
Nurmikko, A. V. ....	76	Yang, B. ....	245
Ohta, T. ....	80	Yang, P. ....	1, 31, 222
Pecharsky, V. K. ....	155, 167	Yang, Z-L. ....	24
Petford-Long, A.K. ....	113	Yap, Y. K. ....	84
Phan, M. H. ....	182	Yu, K. M. ....	48
Poeppelmeir, K. ....	129	Zachariah, M. R. ....	245
Priya, S. ....	234	Zapol, P. ....	89
Pruski, M. ....	155	Zavadil, K. R. ....	121
Qiang, Y. ....	72	Zettl, A. ....	2
Read, D. ....	175	Zhai, X. ....	254
Reimer, J. A. ....	142	Zhang, J. Z. ....	37
Ren, Z. ....	14	Zhang, S. ....	267
Ross, P. N. ....	142	Zidan, R. ....	163
Rotenberg, E. ....	80	Zuo, J. M, ....	254
Sales, B. ....	182		
Schmid, A. K. ....	80		
Seyller, T. ....	80		
Shah, A. ....	254		
Shi, J. ....	179		
Shi, L. ....	20		
Shiyanovskii, S. V. ....	226		
Si, W. ....	64		
Smith, D. L. ....	117		

## **Participant List**

## Participant List

First Name	Last Name	Organization	Phone	Email
Joel	Ager	Lawrence Berkeley National Lab	510-486-6715	<a href="mailto:jwager@lbl.gov">jwager@lbl.gov</a>
Paul	Alivisatos	Lawrence Berkeley National Lab	510-486-4999	<a href="mailto:apalivisatos@lbl.gov">apalivisatos@lbl.gov</a>
Harry	Allcock	The Pennsylvania State University	814-865-3527	<a href="mailto:hra@chem.psu.edu">hra@chem.psu.edu</a>
Andrew	Armstrong	Sandia National Laboratories	505-284-7757	<a href="mailto:aarmstr@sandia.gov">aarmstr@sandia.gov</a>
Christie	Ashton	Basic Energy Sciences	301-903-0511	<a href="mailto:christie.ashton@science.doe.gov">christie.ashton@science.doe.gov</a>
Harry	Atwater, Jr.	CalTech	626-395-2197	<a href="mailto:haa@daedalus.caltech.edu">haa@daedalus.caltech.edu</a>
Scott	Barnett	Northwestern University	847-491-2447	<a href="mailto:s-barnett@northwestern.edu">s-barnett@northwestern.edu</a>
Scott	Barnett	Northwestern University	847-491-2447	<a href="mailto:s-barnett@northwestern.edu">s-barnett@northwestern.edu</a>
Leah	Bergman	University of Idaho	208-8857317	<a href="mailto:Lbergman@uidaho.edu">Lbergman@uidaho.edu</a>
Robert	Bowman	Jet Propulsion Laboratory/Caltech	818-354-7941	<a href="mailto:robert.c.bowman-jr@jpl.nasa.gov">robert.c.bowman-jr@jpl.nasa.gov</a>
Robert	Bowman	Jet Propulsion Laboratory/Caltech	818-354-7941	<a href="mailto:robert.c.bowman-jr@jpl.nasa.gov">robert.c.bowman-jr@jpl.nasa.gov</a>
Frank	Bridges	University of California, Santa Cruz	831-459-2893	<a href="mailto:bridges@physics.ucsc.edu">bridges@physics.ucsc.edu</a>
Gerbrand	Ceder	Massachusetts Inst of Technology	617-253-1581	<a href="mailto:gceder@mit.edu">gceder@mit.edu</a>
Gang	Chen	Massachusetts Inst of Technology	617-253-0006	<a href="mailto:gchne2@mit.edu">gchne2@mit.edu</a>
Renkun	Chen	University of California, Berkeley	510-643-6512	<a href="mailto:rkchen@me.berkeley.edu">rkchen@me.berkeley.edu</a>
Renkun	Chen	University of California, Berkeley	510-643-6512	<a href="mailto:rkchen@me.berkeley.edu">rkchen@me.berkeley.edu</a>
Daryl	Chrzan	University of California, Berkeley/LBL	510-643-1624	<a href="mailto:dcchrzan@berkeley.edu">dcchrzan@berkeley.edu</a>
Mark	Conradi	Washington University	314-935-6292	<a href="mailto:msc@wuphys.wustl.edu">msc@wuphys.wustl.edu</a>
Michael	Crommie	Lawrence Berkeley National Lab	510-642-9392	<a href="mailto:crommie@berkeley.edu">crommie@berkeley.edu</a>
Stephen	Cronin	University of Southern California	213-740-8787	<a href="mailto:scronin@usc.edu">scronin@usc.edu</a>
Lutgard	De Jonghe	University of California, Berkeley/ Lawrence Berkeley National Lab	510-486-6138	<a href="mailto:dejonghe@lbl.gov">dejonghe@lbl.gov</a>
Lutgard	De Jonghe	Lawrence Berkeley National Lab/ University of California, Berkeley	510-486-6138	<a href="mailto:dejonghe@lbl.gov">dejonghe@lbl.gov</a>

Mildred	Dresselhaus	Massachusetts Inst of Technology	617-253-6864	millie@mgm.MIT.edu
Jeffrey	Eastman	Argonne National Laboratory	630-252-5141	jeastman@anl.gov
James	Eckstein	Universtiy of Illinois	217-244-7709	eckstein@uiuc.edu
Takeshi	Egami	Oak Ridge National Laboratory/ University of Tennessee	865-974-7204	egami@utk.edu
Cody	Friesen	Arizona State University	480-965-3954	Cody.Friesen@asu.edu
Bonnie	Gersten	DOE-BES-DMSE	301-903-0002	Bonnie.Gersten@science.doe.gov
Karl	Gschneider, Jr.	Iowa State University	515-294-7931	cagey@ameslab.gov
Carlos	Gutierrez	Sandia National Laboratories	505-284-2971	cgutie@sandia.gov
Eugene	Haller	University of California, Berkeley/ Lawrence Berkeley National Lab	510-486 5294	eehaller@lbl.gov
Allon	Hochbaum	University of California, Berkeley	510-642-2867	hochbaum@berkeley.edu
Jack E.	Houston	Sandia National Laboratories	505-844-8939	jehouston@sandia.gov
Luiz	Jacobsohn	Los Alamos National Laboratory	505-667-8011	lgjacob@lanl.gov
Purusottam	Jena	Virginia Commonwealth University	804-828-8991	pjena@vcu.edu
Antoine	Kahn	Princeton University	609-258-4642	kahn@princeton.edu
Alain	Karma	Northeastern University	617-373-2929	a.karma@neu.edu
Alain	Karma	Northeastern University	617-373-2929	a.karma@neu.edu
Gary	Kellogg	Sandia National Laboratories	505-844-2079	gkkello@sandia.gov
Lei	Kerr	Miami University	513-529-0768	kerrll@muohio.edu
Armen	Khachaturyan	Rutgers University	732-445-4711	khach@jove.rutgers.edu
Refik	Kortan	Office of Basic Energy Sciences	301-903-3308	refik.kortan@science.doe.gov
Kannan	Krishnan	University of Washington	206-543-2814	kannanmk@u.washington.edu
Lincoln	Lauhon	Northwestern University	847-491-2232	lauhon@northwestern.edu
Oleg	Lavrentovich	Liquid Crystal Institute	330-672-4844	odl@lci.kent.edu
Stephen	Lee	Sandia National Laboratories	505-844-7307	srlee@sandia.gov

Qiang	Li	Brookhaven National Laboratory	631-344-4490	qiangli@bnl.gov
Qiang	Li	Brookhaven National Laboratory	631-344-7090	lperagine@bnl.gov
Shawn	Lin	Rensselaer Polytechnic Institute	518-276-2978	sylin@rpi.edu
Feng	Liu	University of Utah	801-587-7719	fliu@eng.utah.edu
Evan	Ma	Johns Hopkins University	410-516-8601	ema@jhu.edu
DiMassachusetts	Maroudas	University of Mass, Amherst	413-545-3617	maroudas@ecs.umass.edu
James	Martin	Sandia National Labs	505-844-9125	jmartin@sandia.gov
Angelo	Mascarenhas	NREL	303-384-6608	angelo_mascarenhas@nrel.gov
Angelo	Mascarenhas	NREL	303-384-6608	angelo_mascarenhas@nrel.gov
Matthew	McCluskey	Washington State University	509-335-5356	mattmcc@wsu.edu
Yuri	Mishin	George Mason University	703-993-3984	ymishin@gmu.edu
Nathan	Moore	Sandia National Laboratories	505-844-0278	nwmoore@sandia.gov
Ross	Muenchausen	Los Alamos National Laboratory	505-667-0391	rossm@lanl.gov
Arto	Nurmikko	Brown University	401-863-2869	Arto_Nurmikko@brown.edu
Taisuke	Ohta	Sandia National Laboratories	505-284-3167	tohta@sandia.gov
Vitalij	Pecharsky	Ames Lab, Iowa State University	515-294-8220	vitkp@ameslab.gov
Amanda	Petford-Long	Argonne National Laboratory	630-252-5480	petford.long@anl.gov
Kenneth	Poeppelmeier	Northwestern University	847-491-3505	krp@northwestern.edu
Shashank	Priya	Virginia Tech	540-231-0745	spriya@vt.edu
Zhifeng	Ren	Boston College	617-552-3575	renzh@bc.edu
Jing	Shi	UC-Riverside	951-827-1059	jing.shi@ucr.edu
Li	Shi	University of Texas at Austin	512-471-3109	lishi@mail.utexas.edu
Jerry	Simmons	Sandia National Laboratories	505-844-8402	jsimmon@sandia.gov
Darryl	Smith	LANL	505 667 2056	<a href="mailto:dsmith@lanl.gov">dsmith@lanl.gov</a>

Hariharan	Srikanth	University of South Florida	813-974-2467	sharihar@cas.usf.edu
Shane	Stadler	Southern Illinois University	618-453-5110	sstadler@physics.siu.edu
Yuri	Suzuki	Lawrence Berkeley National Lab/ University of California, Berkeley	510-643-0087	ysuzuki@berkeley.edu
Xiaoli	Tan	Iowa State University	515-294-3355	xtan@iastate.edu
Frank	Tsui	University of North Carolina	919-962-0305	ftsui@physics.unc.edu
Trevor	Tyson	New Jersey Institute of Technology	973-642-4681	tyson@adm.njit.edu
R. Bruce	van Dover	Cornell University	607-255-3228	vandover@cornell.edu
Yana	Vaynzof	Princeton University	609-258-2056	yvaynzof@princeton.edu
Dwight	Viehland	Virginia Tech	540-231-2276	viehland@mse.vt.edu
Anil	Virkar	University of Utah	801-581-5396	anil.virkar@m.cc.utah.edu
David	Waldeck	University of Pittsburgh	412-624-8430	dave@pitt.edu
Wladyslaw	Walukiewicz	Lawrence Berkeley National Lab	510-486-5329	W_Walukiewicz@lbl.gov
Zhong Lin (Z.L.)	Wang	Georgia Institute of Technology	404-894-8008	zlwang@gatech.edu
Lane	Wilson	DOE/BES	301-903-5877	lane.wilson@science.doe.gov
Yiyi	Wu	Ohio State University	614-247-7810	wu@chemistry.ohio-state.edu
Xiaoxing	Xi	Penn State University	814-863-5350	xxx4@psu.edu
Bao	Yang	University of Maryland	301-405-6007	baoyang@umd.edu
Peidong	Yang	Lawrence Berkeley National Lab	510-643-1545	p_yang@berkeley.edu
Yoke Khin	Yap	Michigan Technological University	906-487-2900	ykyap@mtu.edu
Michael	Zachariah	University of Maryland and NIST	301-405-4311	mrz@umd.edu
Kevin	Zavadil	Sandia National Laboratories	505-845-8442	krzavad@sandia.gov
Shengbai	Zhang	Rensselaer Polytechnic Institute	518-276-6127	zhangs9@rpi.edu
Jane	Zhu	DOE-BES	301-903-3811	jane.zhu@science.doe.gov
Ragaiy	Zidan	Savannah River National Laboratory	803-646-8876	ragaiy.zidan@srl.doe.gov